CONTENTS

BULLETIN OF THE
MINERAL RESEARCH AND EXPLORATION

CONTENTS

Bulletin of the Mineral Research and Exploration

http://bulletin.mta.gov.tr

Syn-sedimentary tectonic markings in the Oligocene Datça-Kale-Acı Göl basin, Western Anatolia

Gülşen ELMAS[a*] , Gürol SEYİTOĞLU[a] , Nizamettin KAZANCI[a]   and Veysel IŞIK[a]

[a]Ankara University, Department of Geological Engineering, Tectonic Research Group, Gölbaşı, Ankara, Turkey.

Research Article

ABSTRACT

In southwest Turkey, the Oligocene sedimentary sequence is located on the Datça-Kale-Acı Göl basin between the Menderes Massif and Lycian nappes. To understand the nature of this basin is important for tectonic models that explain the exhumation of the Menderes massif. In the northeast extension of this basin, the sedimentary sequence is interpreted as alluvial fan, fan-delta, beach, marine input, inner shelf carbonates and offshore deposits. The Oligocene Datça-Kale main breakaway fault bounding the south eastern margin of the basin is represented by İnceler and Acı Göl faults in the study area. The wedge geometry of the sequence thickening towards the İnceler normal fault is an evidence of syn-tectonic deposition. The northwest margin of the basin is controlled by two en-echelon faults. The sedimentary sequence has a wedge geometry thickening towards the normal fault and at the same time its upper layers overlap the fault. As a result, the northeast extension of the Datça-Kale-Acı Göl Oligocene basin is an elongated fjord like depositional area containing the shallow marine environments controlled by normal faults located in its southeast and northwest margins. It was demonstrated that the southeast basin margin limited by the Datça- Kale main breakaway fault performed dominant tectonic control. The similar kinematic indicators that is used for the model explaining the exhumation of the Menderes massif by the upward bending of Datça-Kale main breakaway fault are also observed in the northwest of the basin as top to the north-northeast.

1. Introduction

The Datça-Kale-Acı Göl Oligocene basin is located between the Menderes massif and the Lycian nappes in southwestern Anatolia and has a northeast-southwest extension (Figure 1). The outcrops of Oligocene basin units in the region can be traced from the Gökova Gulf to Kale and from the northeast of Denizli to Dinar area, and have been studied in the literature giving different basin names (eg. Lycian molasse basin, Kale basin, Kale-Tavas basin, Çardak-Tokça basin, Çardak-Dazkırı basin, Denizli basin) (Figure 1). It was interpreted that Datça-Kale-Acı Göl basin was developed on the hanging wall block of the

Datça-Kale main breakaway fault, which is associated with the exhumation as an asymmetric core complex of the Menderes massif (Seyitoğlu et al., 2004).

The outcrops belonging to Oligocene sedimentary units were mapped in the north of the Gökova Bay (Gürer and Yılmaz, 2002). The Datça fault located in the south of the bay in the submarine seismic reflection studies carried out in the Gulf of Gökova, is seen in listric normal fault geometry dipping northward (Kurt et al., 1999). The seismic reflection sections obtained along the hanging wall block of the fault and perpendicular to the Datça fault reveal the presence of a sedimentary sequence which is 2500 m thick and
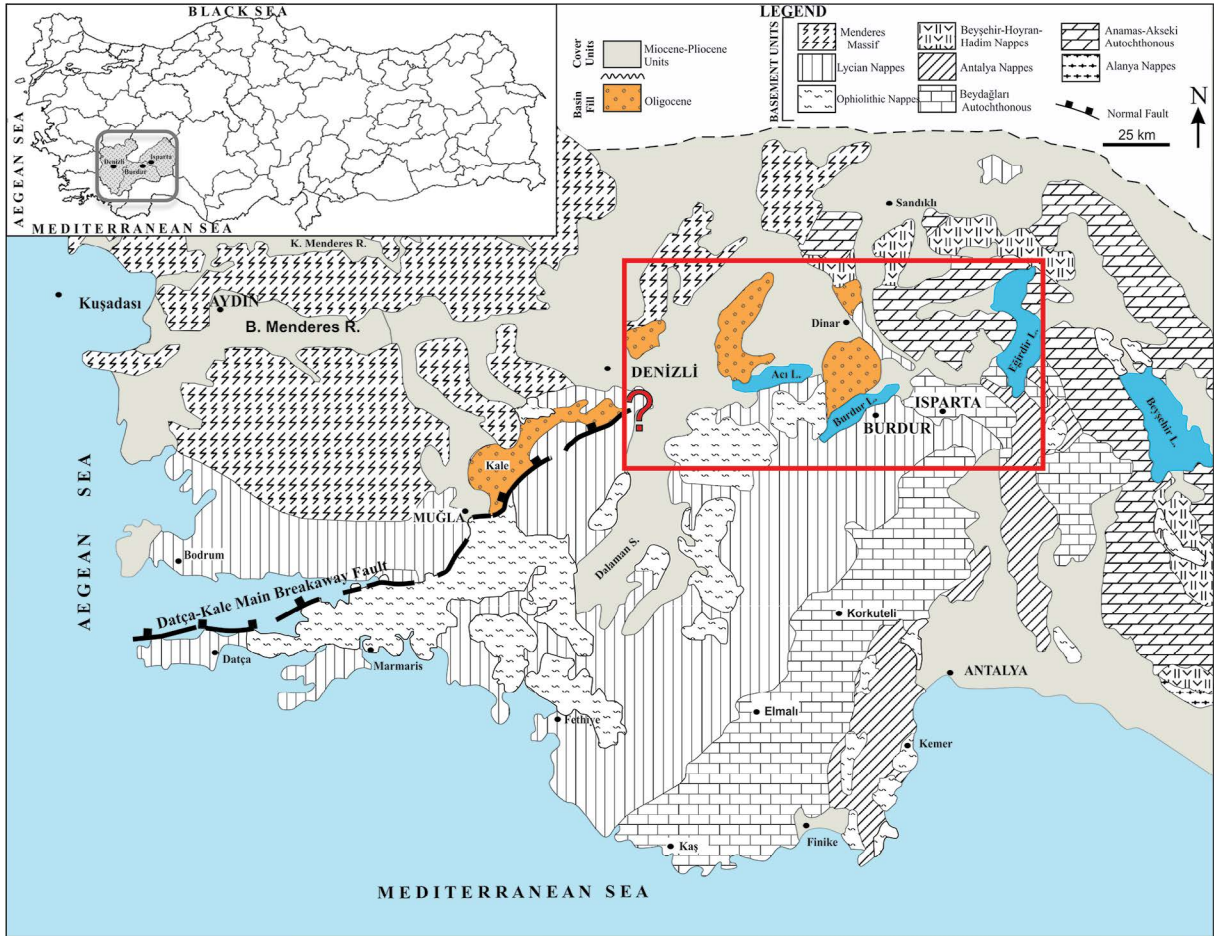
Figure 1- Study area in the northeast of Datça-Kale-Acı Göl basin in southwestern Anatolia (Datça-Kale main breakaway fault from Seyitoğlu et al. (2004), regional geology from Konak, 2002; Turhan, 2002; Konak and Şenel, 2002; Şenel, 2002).

thickens towards the fault with a wedge geometry (Kurt et al., 1999, see line 11). The sediment thickness and its geometry show that basin units here were deposited as syn-sedimentary in the control of the Datça fault and it was interpreted that this deposition occurred in the Oligocene period (Seyitoğlu et al., 2004). The data related to continuation of faulting observed in the submarine in the Gökova Bay and associated formations on land in the east were shown by the geophysical data by Çağlar and Duvarcı (2001).

The Kale section of the northeastern most of the Datça-Kale-Acı Göl basin was studied by Hakyemez (1989) and Yılmaz et al. (2000). Yılmaz et al. (2000) and Gürer and Yılmaz (2002) stated that the Kale-Tavas basin was developed under the control of northeast - southwest trending normal faults dipping northwest. They interpreted this basin as a "piggy-back" basin which developed on the Lycian nappes

and also suggested that it had been developed under tectonic regime representing a contraction in north-south directions in general.

The Oligocene successions in Denizli and Çardak-Dazkırı basins in the northeast together with Kale-Tavas basins were investigated by Sözbilir (2005). Suggesting that these basins were formed by the southward detachment of the Lycian nappes over the Menderes massive under the extensional tectonic regime, it was stated that folds observed in basin fills were related with the rootless movement of the Lycian nappes towards the south. Although not explicitly stated in the text, it is understood that Sözbilir (2005) agrees with the "Lycian detachment fault" associated with the first exhumation of Menderes massif in the symmetrical core complex model of Ring et al. (2003). Sözbilir (2005) in his study explained the reported observation of the basement rocks thrusting on the

Oligocene sequence in two separate places (Tokça and Kuzunkaya locations) with the renewing movements of the Lycian nappes and indicated the presence of extensional basins in the Menderes massif at the same time. Although the relationship between the basement rocks and the Oligocene sedimentary sequence around Tokça was mapped as a steep angle normal fault (Göktaş et al., 1989), Akkiraz et al. (2010) presenting detailed maps showing that this relationship is a thrust and indicate that this sedimentary sequence is Rupelian-Early Chattian (Oligocene) in age.

In previous studies, it is observed that the Datça-Kale-Acı Göl basin was divided into sub-basins and different stratigraphies were proposed. The studies supplying age data for sedimentary successions rely on the facts of palynology (Akgün and Sözbilir, 2001; Akkiraz and Akgün, 2005) nannoplankton, foraminifera, mollusk (İslamoğlu et al., 2006; Gedik, 2008; İslamoğlu, 2008), palynology and benthic foraminifera (Akkiraz, 2008; Akkiraz et al., 2010, 2011).

Göktaş et al. (1989), revealing the stratigraphy of the Çardak-Tokça basin, reported that they were formed by deltaic shallow marine sediments where terrigenous inputs in places are available. Hakyemez (1989) indicates that the Karadere formation, which developed as the lowermost alluvial fan in the Kale basin, is conformably overlain by the coal-bearing Mortuma formation developed in lagoon environment consisting of braided and meandering stream deposits. He stated that these deposits are then unconformably overlain by the lower Miocene Yenidere formation.

Toker (2008) studied the Oligocene sequence in the Çardak-Dazkırı basin from bottom to top as Armutalanı, Çardak, Hayrettin, Tokça formations. Armutalan and Çardak formations were considered as the alluvial fan deposits (Toker and Yağmurlu, 2010).

Karadenizli et al. (2009, 2017) presents the generalized stratigraphy for Oligocene Datça-Kale-Acı Göl basin by the distinction of Mortuma, Çardak and Hayrettin formations. The Üçtepe reef member was also included in the Hayrettin formation. In facies analysis of the formations, the alluvial fan and fluvial, fan delta, sandy beach, shallow sea clastics, inner shelf carbonates and offshore deposits were determined (Figure 2).
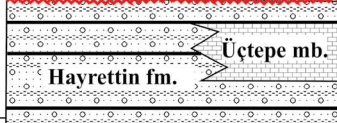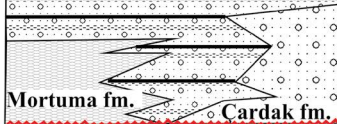
Figure 2- Generalized stratigraphical section of the Datça-Kale-Acı Göl basin [from Karadenizli et al. (2009)].

In this article, tectono-sedimentary development of the NE section of Datça-Kale-Acı Göl basin, where its basin-margin relationships were relatively less studied, will be explained by using the field observations carried out at key locations (Figure 3). Unlike previous studies, the margins, size and geometry of the basin will also be emphasized because the Oligocene period of time has a critical importance in the geology of Turkey.

2. Field Observations on the Southeast Margin of the Datça-Kale-Acı Göl Basin

2.1. Southwest of Çardak: İnceler-Söğütköy area (Figures 3 and 4a)

Datça-Kale main breakaway fault, turns into north-northeast direction and starts to be clearly observed in the western İnceler-Söğütköy area (Figures 1 and 3) after limiting the Kale-Tavas basin from the south (Yılmaz et al., 2000; Gürer and Yılmaz, 2002). The northwest dipping İnceler normal fault form the contact between the basement units consisting of the Lycian nappes and the Eocene sedimentary units

3
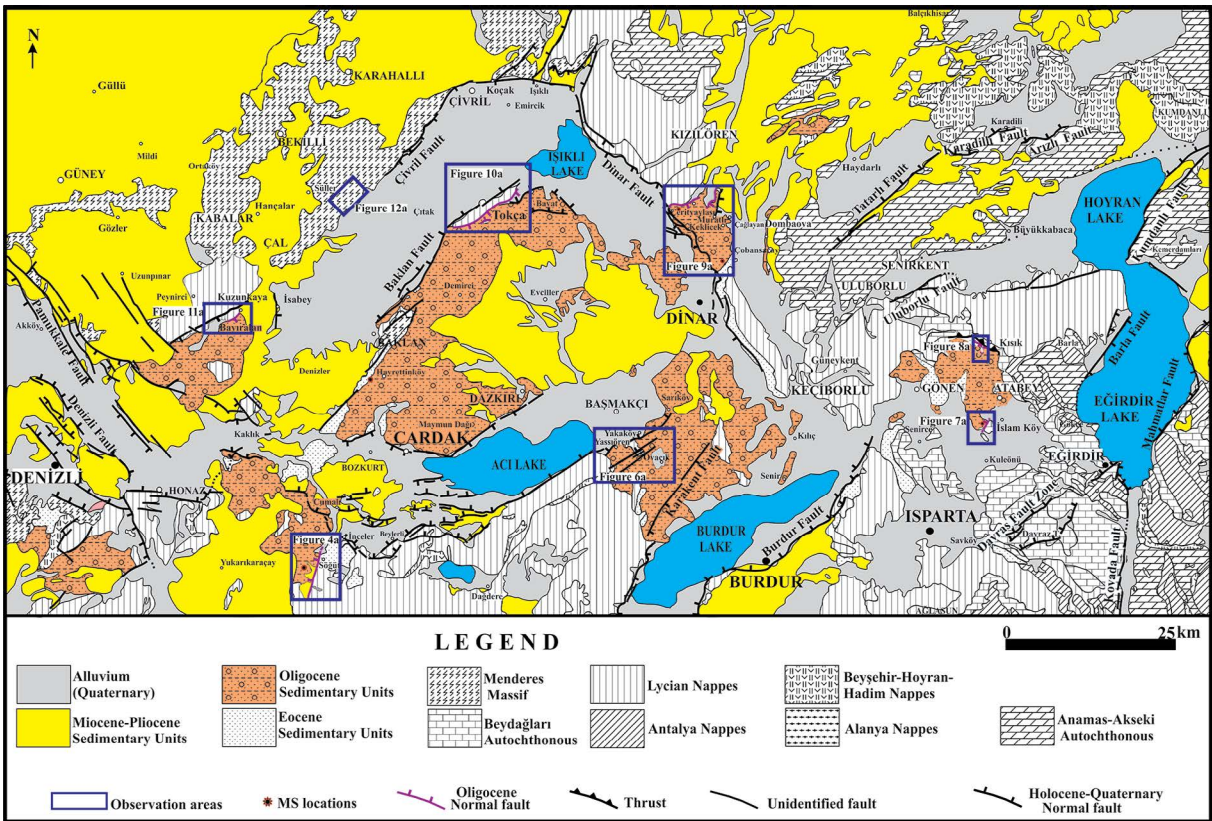
Figure 3- The simplified geological map of the northeastern part of the Datça-Kale-Acı Göl basin and the location of the detailed observation areas. See figure 1 for location. (from Konak, 2002; Turhan, 2002; Konak, and Şenel, 2002; Şenel 2002; Emre et al., 2013).

and the Oligocene-Neogene sequence (Figure 4a). While the lower levels of the sequence belonging to the Çardak formation, dominantly consisting of Oligocene coarse conglomerate and sandstone alternation, have high to medium dipping values (55-37º), it becomes low dipping (10º) as the dip value decreases transitionally towards upper layers (Figure 4b). The succession is disconformably covered by a probable Neogene sequence formed by red mudstones, armored mud-balls, limestone with plant parts and loose conglomerate. It is possible to see the Oligocene succession dominantly composed of conglomerates in the wedge geometry thickening towards the İnceler fault in deeply incised valley slopes (Figure 5a, b). This situation clearly shows that the İnceler fault was developed as a growth fault in the Oligocene and controls the deposition of the Oligocene sedimentary sequence. The İnceler fault should have continued its activity during and after the Neogene period.

The data, which is the first field observation and reveal the relationship between the tectonism and sedimentation in the Oligocene along the breakaway

fault, similar to this observation is also observed in the submarine seismic reflection sections in the Gulf of Gökova (Kurt et al., 1999; Seyitoğlu et al., 2004; Seyitoğlu and Işık, 2015).

2.2. East and Southeast of Başmakçı: Yassıören-Atabey Area (Figure 3 and 6a)

In the south of Başmakçı, the footwall block of the active Acı Göl normal fault consists of the Lycian nappes, while the hanging wall block consists of the Quaternary deposits and the recent deposits of Acı Göl, which cover a large area in the region (Figure 3). The indirect data showing that the Acı Göl normal fault, working as active fault today, acts as a part of Datça-Kale main breakaway fault during the Oligocene period are given below.

The Maymun Dağ fault, located in the northwest of the Acı Göl, is the antithetic fault of the Acı Göl fault. In the footwall of Maymundağ fault, the apparent thickness of the Oligocene succession, which has low dipping angle, is at least 789 m and can be measured
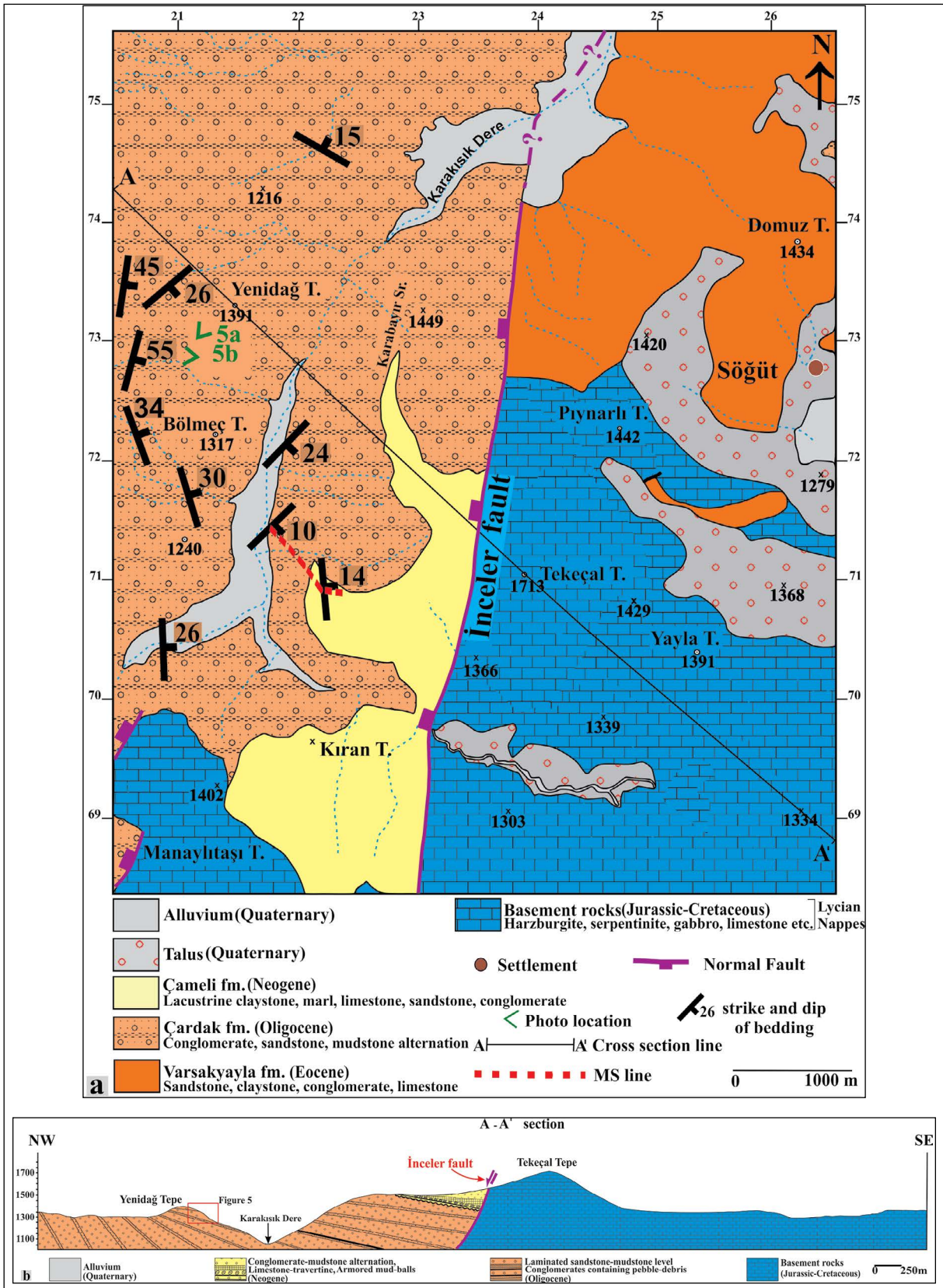
Figure 4- a) Geological map of İnceler-Söğütköy (from Şenel, 2010). See figure 3 for location and see figures 4b and 5a for photo location, b) Geological cross section showing the relationship between the İnceler fault and the basement rock and the Oligocene-Neogene units (red rectangle shows the location of the photograph in figure 5a).
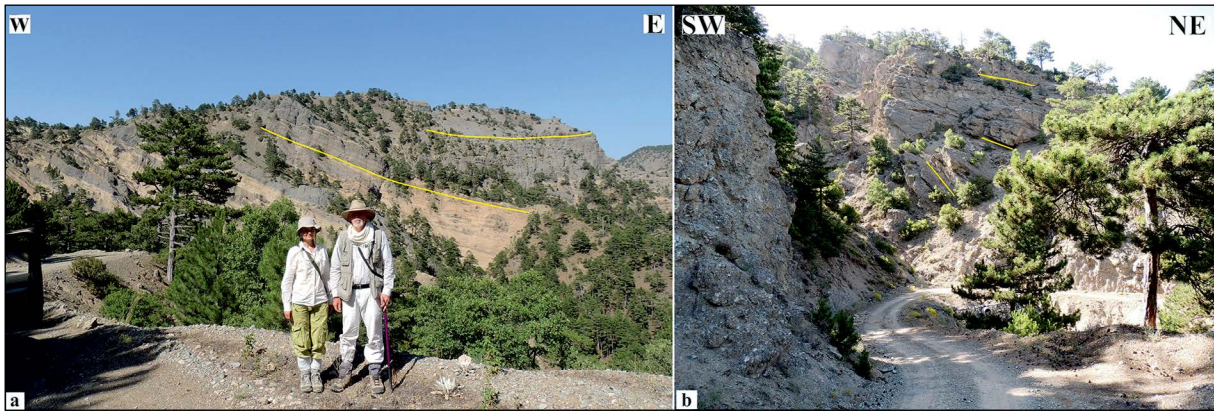
Figure 5- a) The thickening wedge geometry of the Oligocene succession in İnceler-Söğütköy area, towards the İnceler fault outside the photo frame, b) Close-up view of the wedge geometry. Yellow lines indicate bedding planes.
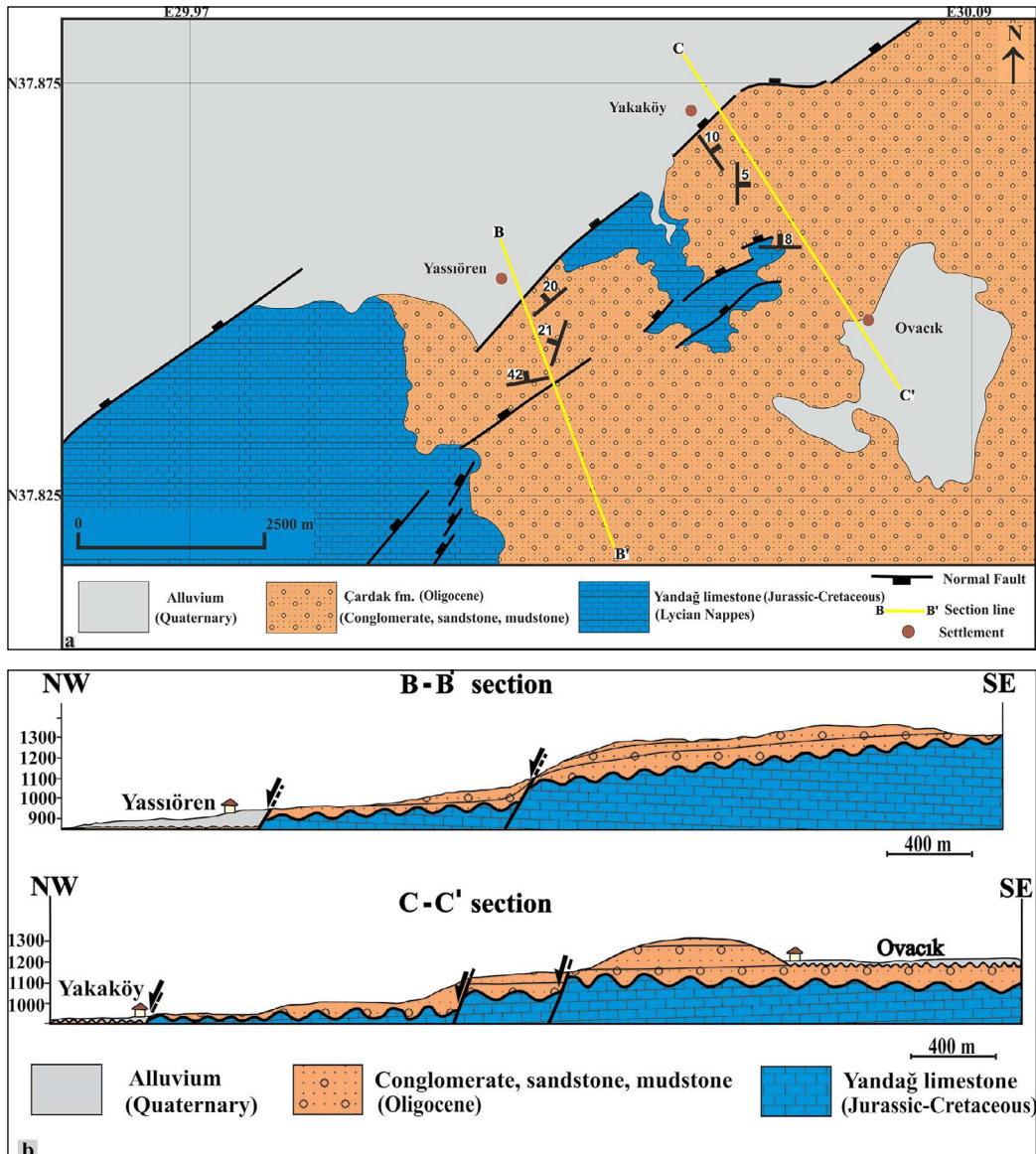
Figure 6- a) Geological map of Yassıören, see figure 3 for location, b) Geological cross sections of Yassıören and Yakaköy (See figure 6 for location).

between the summit of the Maymun Dağ and the Acı Göl level. It is concluded that there should be an Oligocene succession as much as observed on the Maymun Dağ below the Quaternary plain in the Acı Göl and its close vicinity. Accordingly, it can be suggested that the Acı Göl fault behaved as a segment of the Datça-Kale main breakaway fault in the Oligocene and controlled the deposition of the Oligocene successsion by benefiting from the thickness difference of the Oligocene succession at the footwall and hanging wall blocks of this fault. This recommendation is supported by field observations in the vicinity of Yassıören Village (Figures 3 and 6). The segments of the Acı Göl fault separates the rocks of the Lycian nappes and the unconformably overlying Oligocene clastic sequence from the Acı Göl Quaternary sequence (Figures 6a, 6b). The observation of Oligocene succession both at the footwall and hanging wall blocks of this active fault and that the Oligocene succession observed at the footwall block is thinner (250-500) than the succession observed at the Maymun Dağ (798 m) shows that the Oligocene succession at the footwall block of the Acı Göl fault is the overlapping/overlying section on the uplifting block of the normal fault (Acı Göl Oligocene segment) limiting the basin in the Oligocene period (Figure 6a, 6b). It is observed that the succession overlying the Acı Göl Oligocene segment of Datça-Kale main breakaway fault extends to Atabey, north of Isparta (Figure 3).

The bottom of the Oligocene succession (Akkiraz et al., 2011), which generally consists of conglomerates at the Kırkdağ Tepe area (Figure 7) in the south-southwest of Atabey, is observed in the hanging wall of a northeast-southwest trending normal fault dipping northwest (Figure 7a, 7b, 7c). The relationship of the upper levels of this sequence with the pre-Oligocene basement is observed in the north of Atabey (Figure 8a, 8b). The basement rocks composed of recrystallized limestones in this area thrust over Eocene sandstone-mudstone alternation (Figure 8c). The east-west trending south dipping normal fault developed immediately in front of the thrust limit the Oligocene conglomeratic succession that overlies folded Eocene units with an angular unconformity. In the hanging wall of this fault, another normal fault is overlapped by the Oligocene sediments (Figure 8a, 8b, 8c, 8d, 8e). This feature is a sign of a syn-tectonic sedimentation in the Oligocene.

The main breakaway fault, which limits the Datça-Kale-Acı Göl basin from the southeast, cannot be clearly traced towards the northeast due to the younger northwest-southeast extending Dinar fault. The Oligocene succession located at the footwall block of the Dinar fault unconformably overlies the horst in the north of Senirkent as a relatively thin sequence. As this situation resembles the situation at the footwall block of the Acı Göl fault it is possible that the main breakaway fault is located around Tatarlı in further northwest, and even if it extends further northeast under the Quaternary deposits, it will have to be cut in the northeast by the northwest-southeast trending Afyon-Akşehir graben (Figure 3).

3. Field Observations on the Northwestern Margin of Datça- Kale-Acı Göl Basin

3.1. Cerityaylası Area (Figures 3 and 9)

The succession of the Oligocene Çardak formation on the footwall block of the Dinar normal fault, which also produced the Dinar earthquake on the 1st of October in 1995, overlies the Eocene sediments to the west of Çobansaray with an angular unconformity (Figure 3). As heading towards further northwest, it was observed that this succession was limited by northeast-southwest trending southeast dipping enechelon Cerityaylası and Muratlı normal faults (Figure 9a, 9b). The dip of the Oligocene succession decreases in up section and overlies the Muratlı fault (Figure 9e). This shows that the deposition of Oligocene succession is controlled by the Cerityayla and Muratlı faults (Figure 9b, 9c).

3.2. Tokça Area (Figures 3 and 10)

There are different opinions about the characteristic of the tectonic contact forming the northwestern boundary of the Datça-Kale-Acı Göl Oligocene basin between the Triassic - Cretaceous recrystallized limestones and the Oligocene sedimentary sequence in the footwall block of the Baklan graben, which is confined by the Baklan fault (Figure 3) around Tokça. This contact was mapped as thrust by Sözbilir (2005) and Akkiraz et al. (2010) and the sedimentary sequence at the footwall block was found to be of Rupelian-Early Chattian (Oligocene) age. On the other hand, the same contact was mapped as the steep angle normal fault by Göktaş et al. (1989). According
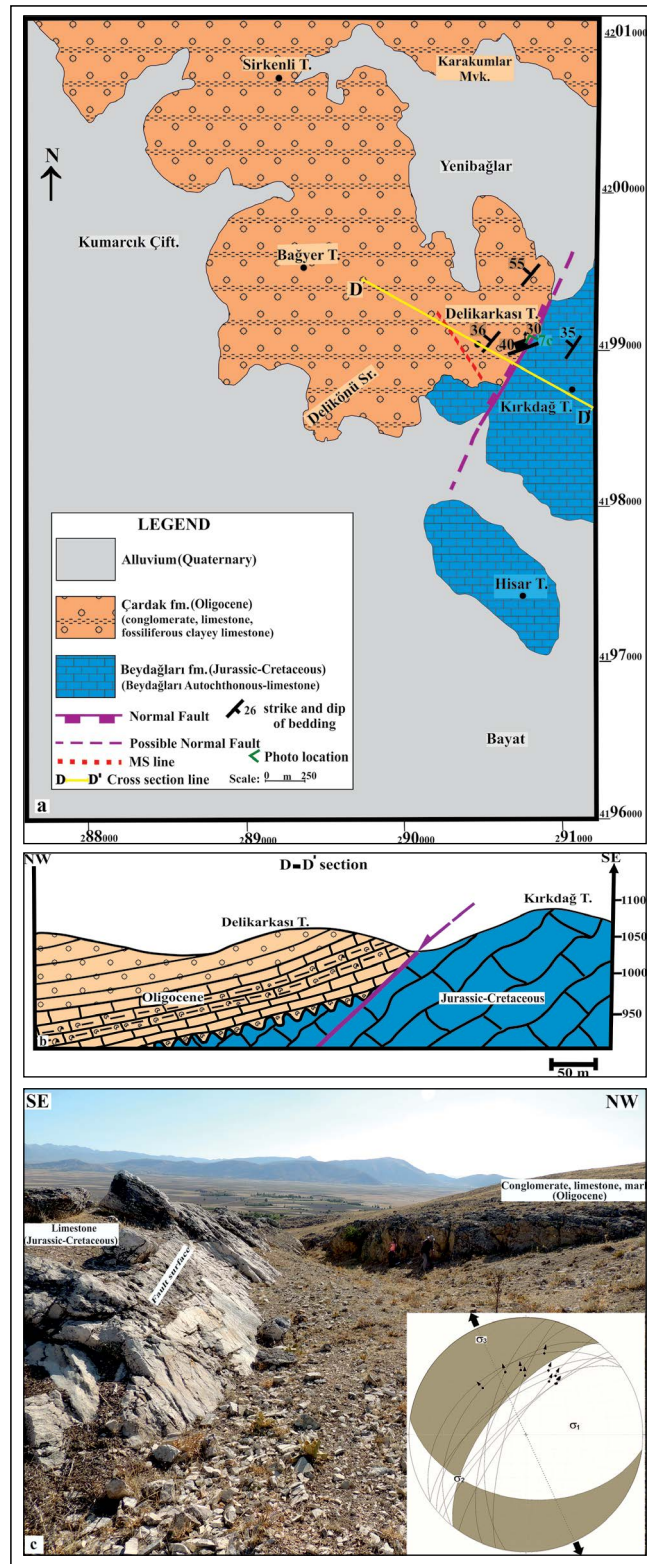
Figure 7- a) Geological map of Atabey-Kırkdağ. (from Şenel, 2010). See figure 3 for location, b) Geological cross-section of the Kırkdağ Tepe area. See figure 7a for location, c) The field view of the normal fault between Jurassic-Cretaceous units and Oligocene Çardak formation and the fault plane solution indicating the normal fault based on measurements taken from the fault plane (looking from NNE).

Figure 8- a) Geological map of the north of Atabey, see figure 3 for location, b) Geological cross section, the north of Atabey, c) Thrust between Jurassic-Cretaceous Recrystallized limestone and Eocene sandstones, looking west (Thrust plane is measured as E-W 40N), d) Normal fault contact between the Eocene sandstones and the conglomerates of the Oligocene Çardak formation, e) Normal fault overlapped by the conglomerates of the Oligocene Çardak formation.

Figure 9- a) Geological map showing the Cerityaylası-Muratlı faults, see figure 3 for the location, b) Geological cross section of Cerityaylası, c) the view of Cerityaylası fault on the field, d) The wedge geometry thickening towards the Muratlı fault in the Oligocene Çardak formation, e) the overlapping of the Muratlı normal fault by the Çardak formation.
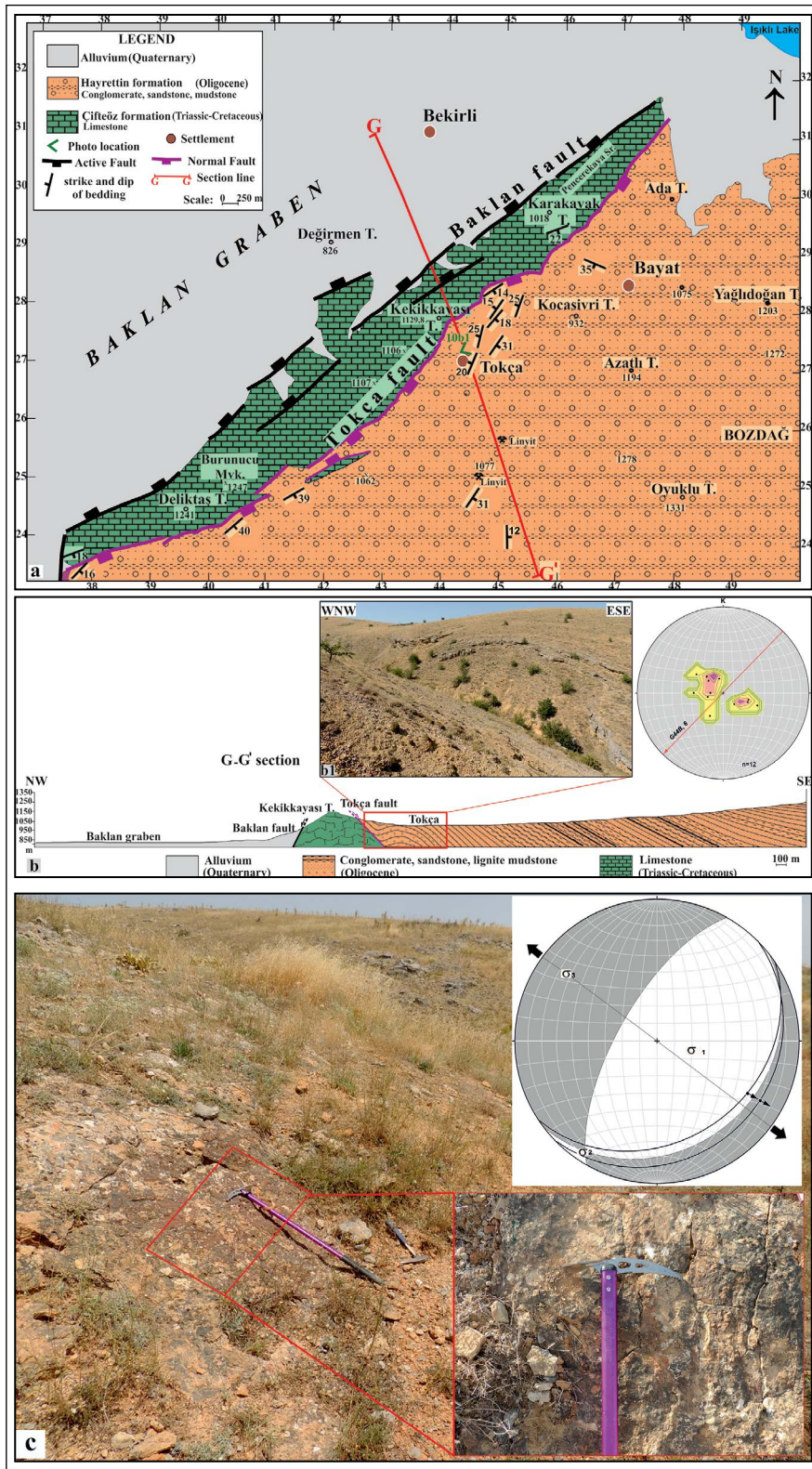
Figure 10- a) Geological map of Tokça, for the location see figure 3, b) the geological cross section and the structural data belonging to fold axes developed parallel to the fault between the Oligocene Hayrettin formation and Triassic-Cretaceous Çifteöz formation, the average trend of fold axes: N44E, plunge: 6°, c) The oxidized fault plane on limestones and the solution of the fault plane indicating normal fault (the fault plane: N56E, 31SE, and slip striations: N63W, 26SE).

to our field observations, the tectonic contact between the Triassic-Cretaceous recrystallized limestone and the Oligocene sedimentary units is a northeast-southwest trending normal fault dipping southeast. Tokça fault can be followed along 13 km and consists of 4 segments (Figure 10a, 10b). There are traces of hydrothermal activity in breccias in the fault zone. It has been possible to measure the fault plane and slip striations at one location in the fault zone. It is very clear that the dip direction of the Tokça fault surface and the movement on it indicate a normal fault character (Figure 10c). The Oligocene sedimentary units in the Tokça normal fault contact are composed of carbonate cemented, sub-rounded, grain supported, coarse pebbly conglomerates and show open folds. The fact that the fold axes are parallel to the Tokça normal fault (Figure 10b) also indicates that these folds are related to normal faulting. As moving away from Tokça normal fault towards southeast, the Oligocene sedimentary sequence is found to be uniformly dipping to the southeast (Figure 10b).

3.3. Kuzunkaya Area (Figures 3 and 11)

It was reported that the ophiolitic basement had thrusted over the Oligocene sedimentary units at Kuzunkaya, the north of Bayıralan in the west of İsabey (see Sözbilir, 2005, figure 15). However, the field observations carried out in the region indicate that the boundary between the ophiolitic basement and the Oligocene sedimentary units is an east northeast-west southwest trending normal fault dipping steeply southeast. (Figures 3, 11a, b, c). The drag fold syncline in the hanging wall block of the fault was used to determine the direction of movement (Figures 11b, c).

Generally the field observations on the northwest side of the Datça-Kale-Acı Göl basin indicate that the margin of the basin is limited to an antithetic normal fault system of Datça-Kale main breakaway fault. Cerityaylası and Muratlı faults served as growth faults (Figure 9d).

4. **Microtectonic Findings within the Northwest Extension of the Datça-Kale Main Breakaway Fault**

The lithology of the metamorphic rocks in study areas is marble, calc-schist and calc-silicate schist. Our mesoscopic and microscopic studies in these rocks reveal that the rocks were affected by the mylonitization with varying grades. Carbonate minerals (calcite) constitute the common mineral composition of these rocks. Phyllosilicate minerals (biotite, chlorite, muscovite, sericite), quartz, feldspar and amphibole accompany rock composition in different proportions. Epidote and opaque mineral are also found as an accessory mineral in the rock.

The primary foliation of the rock protolith is defined by the elongation of the phyllosilicate minerals. These foliation planes are largely overprinted and cut and/or deflected by mylonitic foliation. Mylonitic foliation is characterized by recrystallized calcite minerals aligned in foliation surfaces. Also the recrystallized phyllosillicate minerals accompany the formation of mylonitic foliation which showing folding in geometries. Stretched mineral clusters along the mylonitic foliation represent the mylonitic lineation. The isolated mineral groups with extensional geometry on mylonitic foliation planes represent the mylonitic lineation.

The mylonitization in rocks is depend on the primary composition and textural properties of the rock. The mylonitic rocks which are wholly or mainly of carbonate composition contain the recrystallized calcite minerals. Some of the mylonitic rocks are formed by fine and medium grained recrystallized calcites. In some of the mylonitic rocks, these fine and medium grained recrystallized calcites and very fine-grained recrystallized calcites occur as matrix material which surround large calcites known as porphyroclast. These rocks also include intensively altered amphibole porphyroclasts, some opaque minerals and altered coarse phyllosilicate porphyroclasts. Development of fractures particularly in calcite porphyroclasts and the presence of recrystallized calcite and quartz grains in opening areas suggest that the deformation of these minerals occurred during extensional regime.

Undulatory extinction and twinning development is remarkable in calcite porphyroclasts, which indicates that the temperature is between 200 and 300 °C during deformation. The quartz grains, in some thin sections also display partly recrystallization and typically undulatory extinction. These properties of minerals suggest that the temperature is at 250°C or above during the deformation. When we consider the regional geothermal gradient as 30°C/km, it is possible to say that the deformed minerals in the mylonitic rocks may be deformed at depths of 6-10 km.
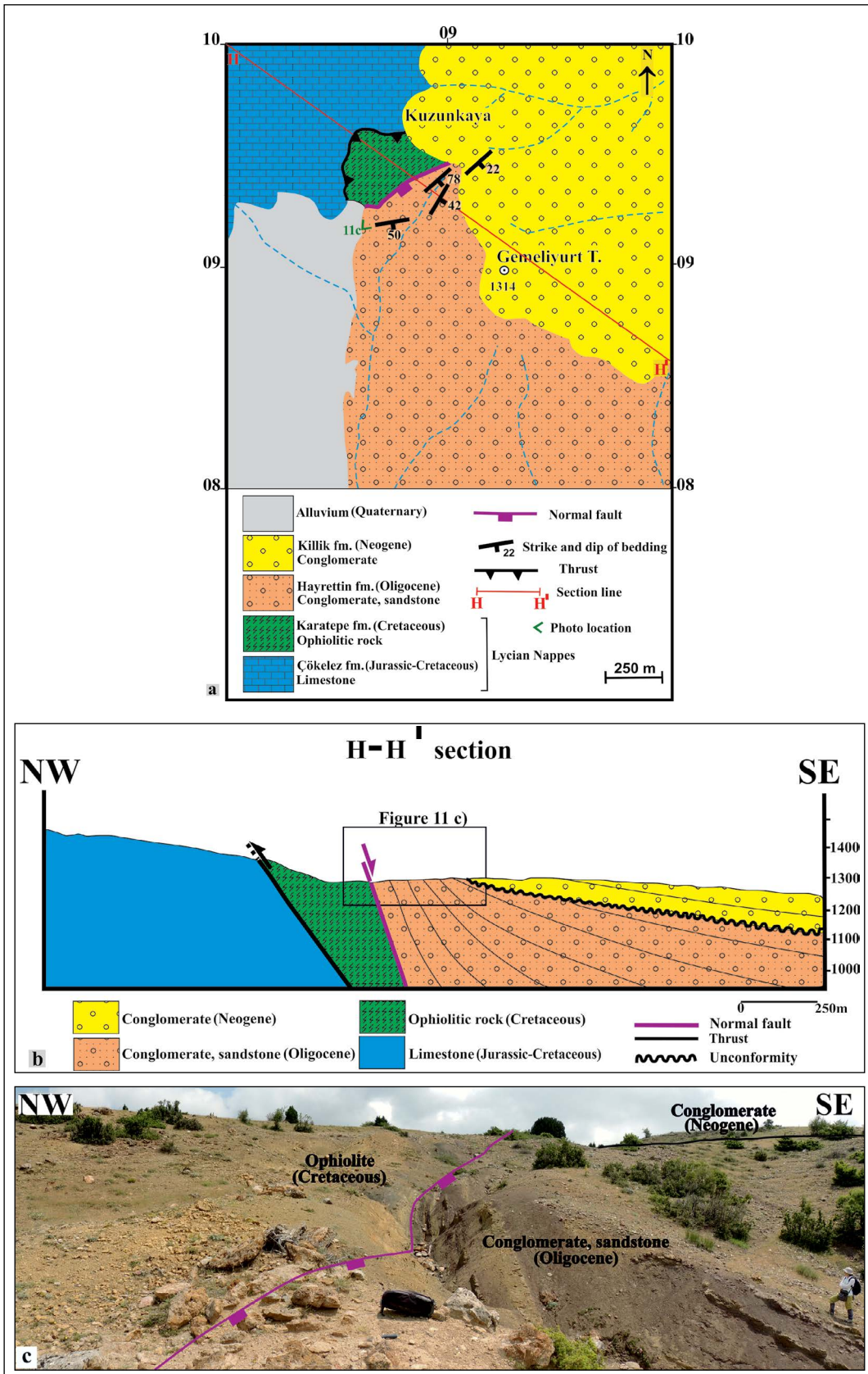
Figure 11- a) Geological map of the vicinity of Kuzunkaya, see figure 3 for location, b) the geological cross section of the Kuzunkaya. (The reverse fault relationship from Konak et al., 1986, the black rectangle is the photo location in figure 11c), c) Photo showing the normal fault boundary between the Oligocene Hayrettin formation and the ophiolitic basement (Karakaya formation) (see figure 11b for location).

The thin sections with parallel to the stretching (mylonitic) lineation include some data on the kinematics of ductile deformation in the rock. The S-C structure and the asymmetric porphyroclast formations are dominant kinematic indicators in the study area (Figure 12a, b). It is also seen typical oblique foliation. Kinematic indicators suggest that mylonitization has top-to-the-N-NE sense of shearing. In other words, during the development of the ductile shear zone, the lithologies above the zone might be moved toward the North. At the same time, the kinematic indicators designate that ductile deformation in the region is related to simple shear. All these findings are consistent with the well known kinematic indicators and sense of shearing in the regional extensional regime obtained from the Menderes core complex (Işık et al., 2001, 2003, 2004; Işık, 2004).

5. Tectono-Sedimentary Evolution of the Northeastern Datça-Kale-Acı Göl Oligocene Basin

For the northeastern part of the Datça-Kale-Acı Göl basin, the Cerityayla, Çobansaray, Hayrettin, Söğütköy and Atabey measured stratigraphic sections were prepared (Figures 3, 13a, b). The relative location of these measured stratigraphic sections in the basin and the location evaluation related to the area where microtectonic observations are made is presented in figure 14.

It is possible to mention about three separate Oligocene successions of the northeastern part of the Datça-Kale-Acı Göl basin. The first of these is the İnceler-Söğütköy sequence to the south of the Acı Göl, where thick coarse clastics are present. This sequence, which is observed as two separate outcrops and highly probable that they are the continuation of each other, is composed of normal graded beddings with a thickness of 15 - 50 cm mainly dominated by coarse sand-medium pebbles.

Two most striking features of the succession are the minority of silt-clay size grains and the decreasing of the primary bedding dip from bottom to top. Clay leaching is a good reagent for high energy aqueous environments. The decrease of the layer dipping can be data for rapid accumulation and active tectonism during deposition. In the upper continuation of this outcrop, the sedimentary structure and textural characteristics observed in the beach sediments (the abundance of well-rounded but weakly spherical platy, long axis orientation in grains, and unavailability of clay and silt grains) were seen. Taken together, it is understood that this coarse grained sequence was deposited as a coarse-grained delta and/or fan delta in a shallow marine environment.

The coal bearing Oligocene successions in the vicinity of Maymun Dağ and Tokça have thinner grain size. The characteristics of sequence observed as fine grained conglomerate-sandstone in the vicinity of Maymun Dağ is that it has impoverished by clay, which is well washed. This situation is an expression of relatively high energy and indicates that the sediments were accumulated in a shallow sea or coastal environment. The coal bearing sequence
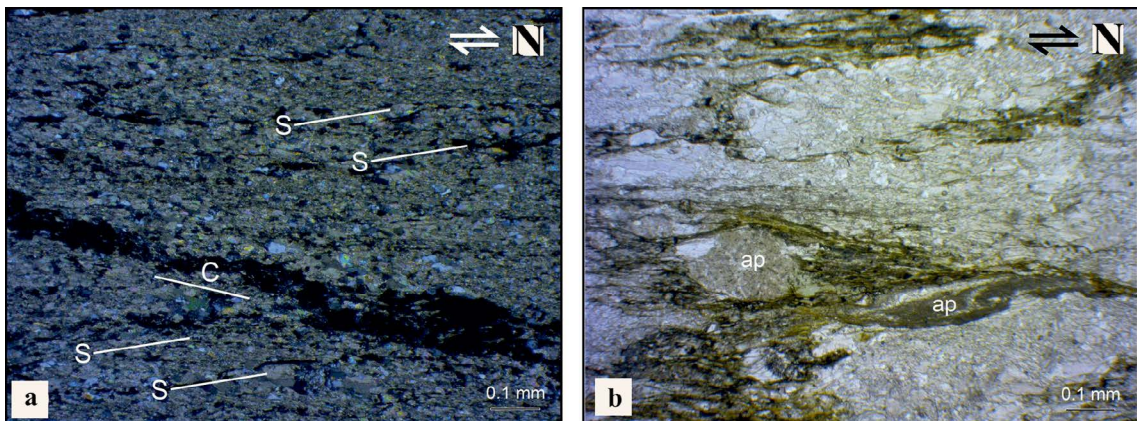
Figure 12- Microscopic view of some microstructures commonly observed in metamorphics forming the basement rocks in the study area, see figure 3 for location. The kinematic indicators in the oriented sample show that the movement in the regional deformation is upper-north, a) S-C structure. (Cross nicol), b) Asymmetric porphyroclast (single nikol). ap: asymmetric porphyroclast; N: North.
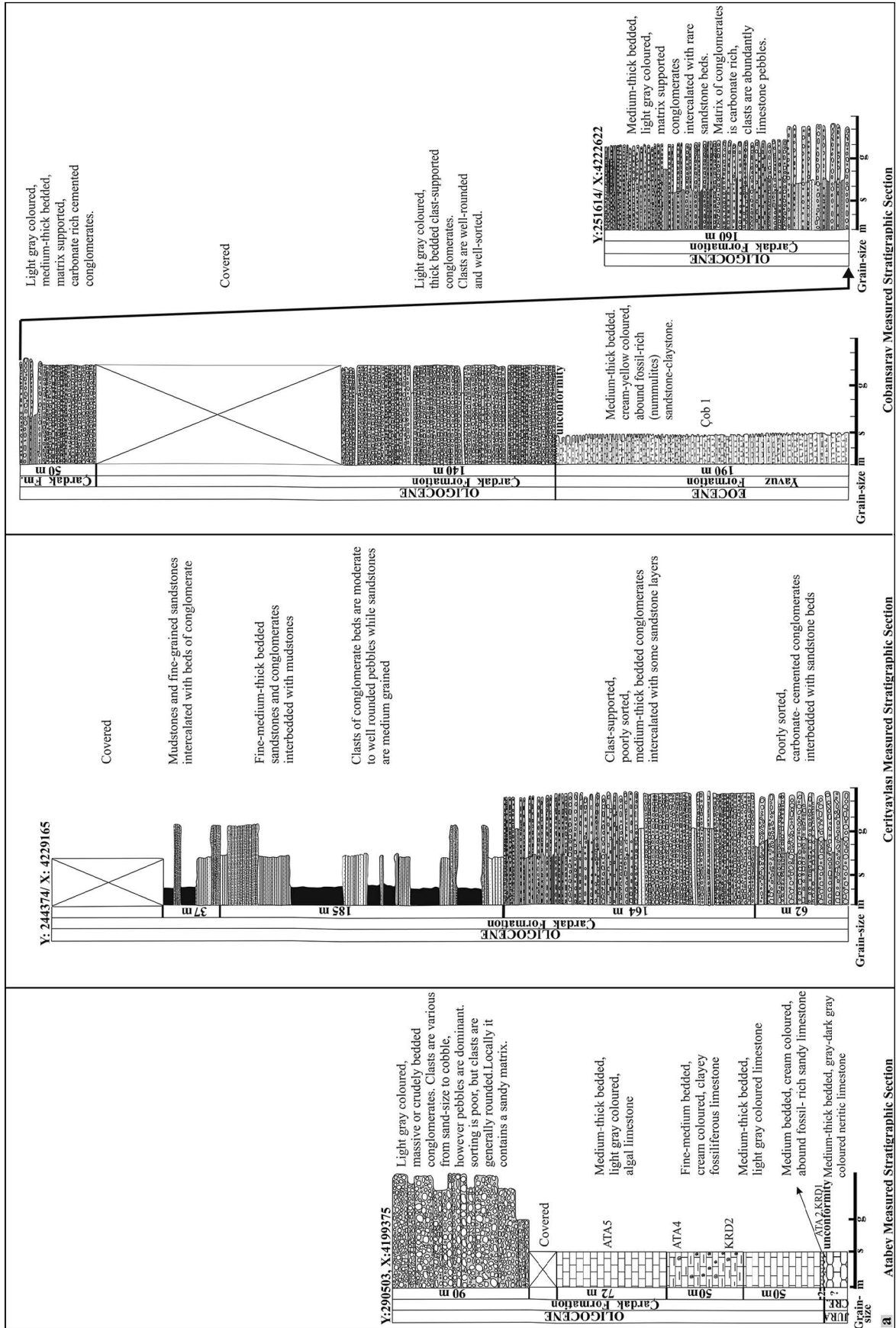
Figure 13- a) The measured stratigraphic sections taken from the NE section of the Datça-Kale-Acı Göl basin. See figure 3 for location.

Figure 13- continue, b) The measured stratigraphic sections taken from the NE section of the Datça-Kale-Acı Göl basin. See Figure 3 for location.
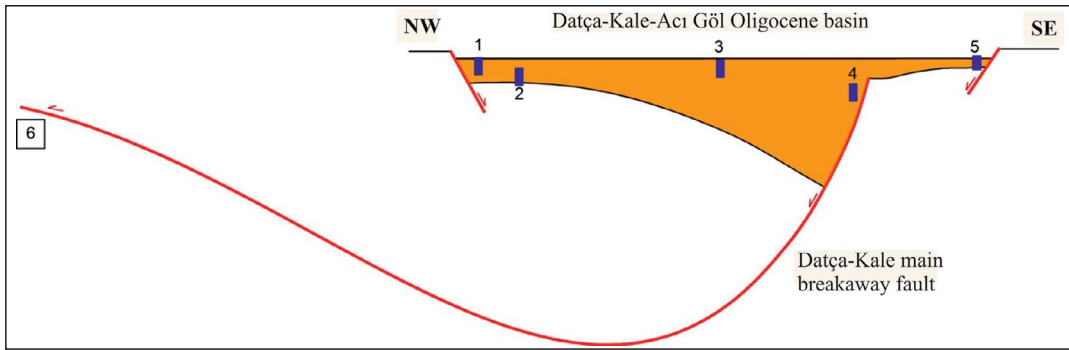
Figure 14- Representative cross-section showing the relative positions of measured stratigraphic sections in the northeastern part of the Datça-Kale-Acı Göl basin. 1-Cerityaylası, 2- Çobansaray, 3-Hayrettin, 4- Söğütköy, 5-Atabey measured stratigraphic sections, 6-Location of microtectonic observations in the vicinity of Süller in the lower plate of Datça-Kale Main breakaway fault.

around Tokça is different from the previous ones with marl - claystone - siltstone lithology. Lamination and soft sedimentary deformation structures are evident. It is composed of clay dominated sediments. It is low in energy and probably indicate marine-marsh environments. It is possible to interpret the coals as paralic environment products.

In the horst of the Dinar graben, Oligocene units in the vicinity of the Cerityaylası show similarities with the Söğütköy sequence in terms of grain size. These units to be in red color in places are secondary and it is not a depositional characteristics. In addition to this, the clay grains were washed less. It is possible to interpret them as alluvial fan - fan delta sediments.

In general, these deposits represent shallow marine coastal environments. It would be appropriate to talk about a tectonically controlled deposition. The excess thickness in narrow range is an indication of tectonism.

Considering all field observations and measured stratigraphical sections, it is clear that there is an effective tectonic control on the SW margin of the Oligocene Datça-Kale-Acı Göl basin. This situation was achieved by the İnceler and Acı Göl faults which are the continuation of Datça-Kale main breakaway fault in NE. Cerityayla and Tokça faults, which are developed as antithetic to these normal faults, are lower profile structures that limit the basin from NE (Figure 15).
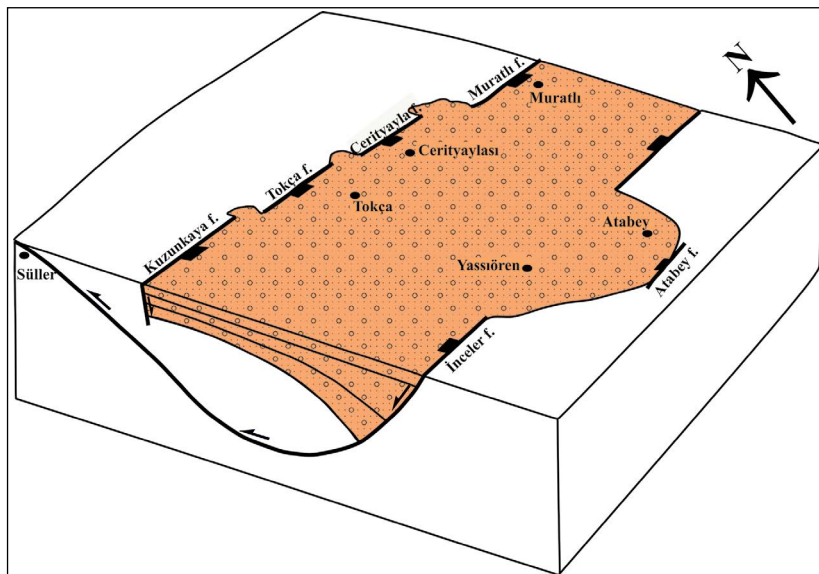
Figure 15- Schematic block diagram showing the status of the northeastern part of the Datça-Kale-Acı Göl basin in the Oligocene.

6. Discussion and Results

Considering the covered and eroded outcrops in addition to their areal distribution, the Oligocene Datça-Kale-Acı Göl basin is interpreted to be a marine deposition area with a geometry of 50-75 km wide, about 300 km long. Special depositional systems provided by the geometry of narrow and long sedimentary areas are in concern. The modern examples of these are fjords and there is observed sediment only on basin axes as basin margins are in the form of slope (Hansen et al., 2007). However, Miocene Köprü and Manavgat basins can be given as examples for the old basins (Çiner et al., 2008). While the sedimentary centers of these are relatively long, the basin margins accumulate more and various sediments (Kostaschuk and McCann, 1983; Hansen, 2004). The additional feature of Datça-Kale-Acı Göl Oligocene basin is that the two sides of the basin are faulted but the activity of the fault on one side is dominant and accumulates more sediment due to tectonism. In summary, the presence of different successions in different localities is the usual result of the basin geometry and forms a good example for old fjord type basins.

The field observations carried out in northeast of the Oligocene Datça-Kale-Acı Göl basin show that the Datça-Kale main breakaway fault, which limits the basin from the southwest, is represented by İnceler and Acı Göl faults. The Oligocene sequence showing the wedge geometry in the hanging wall block of the İnceler fault reveals that this fault developed as syn-sedimentary. The fact that the Oligocene succession on the footwall block of the Acı Göl fault is very thin in comparison with the succession observed on the Maymun Dağ led to the evaluation that the Oligocene deposits in this section were formed by overlying the basin-margin faults. The relationships of the Oligocene deposits of Cerityaylası and Muratlı faults, which are located in the northwest margin of the basin as an antithetic of the Oligocene Datça-Kale main breakaway fault, show that they are syn-sedimentary faults (Figure 9d). It was determined that Tokça fault was not a thrust fault as claimed in previous studies but it had a normal fault character and represented the northwestern edge of Datça-Kale-Acı Göl basin together with Cerityaylası and Muratlı faults. The Menderes massif was exhumed with the bending of Datça-Kale main breakaway fault and it was revealed that up to the north-northeast movement took place also in the vicinity of the Süller by means of microtectonic studies performed on the lower plate.

References

Akgün, F., Sözbilir, H. 2001. A palynostratigraphic approach to the SW Anatolian molasse basin: Kale-Tavas molasse and Denizli molasse. Geodynamica Acta 14, 71-93.

Akkiraz, M.S. 2008. Palynological investigations and foraminifer contents of the Eocene– Miocene deposits in the Çardak–Tokça, Burdur and İncesu Areas, Western Anatolia. PhD Thesis, Dokuz Eylül Üniversitesi, 484p. İzmir.

Akkiraz, M.S., Akgün, F. 2005. Palynology and age of the Early Oligocene units in Çardak–Tokça Basin, Southwest Anatolia: Paleoecological implications. Geobios 38, 283-299.

Akkiraz, M. S., Akgün F., Örçen, S. 2010. Çivril doğusunda (Denizli) yüzlek veren Rupeliyen–erken Şattiyen (Oligosen) yaşlı Tokça formasyonunun Paleoekolojisi: Sayısal iklimsel karşılaştırmalar. Türkiye Jeoloji Bülteni 53(1), 63-95.

Akkiraz, M.S., Akgün, F., Örçen, S. 2011. Stratigraphy and palaeoenvironment of the Lower-middle Oligocene units in the northern part of the Western Taurides (İncesu area, Isparta, Turkey). Journal of Asian Earth Sciences 40, 452–474.

Çağlar, I., Duvarcı, E. 2001. Geoelectric structure of inland area of the Gökova rift, southwest Anatolia and its tectonic implications. J. Geodynamics 31, 33–48.

Çiner, A., Karabıyıkoğlu, M., Monod, O., Deynoux, M, Tuzcu, S. 2008. Late Cenozoic Sedimentary Evolution of the Antalya Basin, Southern Turkey. Turkish Journal of Earth Sciences 17, 1–41.

Emre, Ö., Duman, T.Y., Özalp, S., Elmacı, H., Olgun, Ş., Şaroğlu, F. 2013. Açıklamalı Türkiye Diri Fay Haritası, Ölçek 1:1.250.000. Maden Tetkik ve Arama Genel Müdürlüğü Özel Yayın Serisi 30, Ankara.

Gedik, F. 2008. Foraminiferal description and biostratigraphy of the Oligocene shallow marine sediments in Denizli region, SW Turkey. Revue de Paleobiologie, Geneve 27, 25-41.

Göktaş, F., Çakmakoğlu, A., Tan, E., Sütçü, Y.F., Sarıkaya, H. 1989. Çivril-Çardak arasının Jeolojisi: Maden Tetkik ve Arama Genel Müdürlüğü Rapor No: 8701, 109s. Ankara (unpublished).

Gürer, F., Yılmaz, Y. 2002. Geology of the Ören and surrounding areas, SW Anatolia. Turkish Journal of Earth Sciences 11, 1-13.

Hakyemez, Y. 1989. Kale-Kurbalık (GB. Denizli) bölgesindeki Senozoyik yaşlı çökel kayaların jeolojisi ve stratigrafisi. Maden Tektik ve Arama Dergisi 109, 9-21.

Hansen, L. 2004. Deltaic Infill of a Deglaciated Arctic Fjord, East Greenland: Sedimentary Facies and Sequence Stratigraphy. Journal of Sedimentary Research 74, 422-437.

Hansen, L., Eilertsen, R.S., Solberg, I. L., Sveian, H., Rokoengen, K. 2007. Facies characteristics, morphology and depositional models of clay-slide deposits in terraced fjord valleys, Norway. Sedimentary Geology 202, 710-729.

Işık, V. 2004. Micro-tectonic features of Simav shear zone, northern Menderes massif, western Turkey. Geological Bulletin of Turkey 47 (2), 49-91.

Işık, V., Çemen, I., Tekeli, O., Seyitoğlu, G. 2001. Ductile-brittle transition in Salihli granitoid below the Karadut detachment surface, Menderes massif, Western Turkey. 24 - 28 September 2001. 4th Int. Turkish Geology Sym., Çukurova University, Adana, Turkey, 213 p.

Işık, V., Seyitoğlu, G., Çemen, I. 2003. Ductile-brittle transition along the Alasehir shear zone and its structural relationship with the Simav detachment, Menderes massif, western Turkey. Tectonophysics 374, 1-18.

Işık, V., Tekeli, O., Seyitoğlu, G. 2004. The $^{40}Ar/^{39}Ar$ age of extensional ductile deformation and granitoid intrusions in the northern Menderes core complex: Implications for the initiation of extensional tectonics in western Turkey. Journal of Asian Earth Science 23 (4), 555-566.

İslamoğlu, Y. 2008. Molluscan biostratigraphy and paleoenvironmental reconstruction of Oligocene deposits in the Denizli and Kale-Tavas subbasins (SW Turkey). Geodiversitas 30 (2), 261-285.

İslamoğlu, Y., Gedik, F., Aydın, A., Atay, G., Hakyemez, A., Babayiğit, S. 2006. Denizli Bölgesi'ndeki (GB Türkiye) Oligosen Yaşlı Lagüner ve Denizel Çökellerin Mollusk, Foraminifera, Nannoplankton, Mercan ve Ostrakoda Biyostratigrafisi. 20-24 Mart 2006. 59. Türkiye Jeoloji Kurultayı. Bildiri Özleri Kitabı 245-249. Ankara.

Karadenizli, L., Saraç, G., Şen, Ş., Seyitoğlu, G., Gedik, F., Kangal, Ö., Kayakıran, İ., Kazancı, N., Gül, A., Erten, H. 2009. Batı ve Orta Anadolu Oligosen Paleocoğrafyası. Maden Tetkik ve Arama Genel Müdürlüğü Rapor No: 11225. 271s. Ankara (unpublished).

Karadenizli, L., Saraç, G., Şen, Ş. 2017. DAKAC (Datça-Kale-Acıgöl) Havzasının Oligosen Paleocoğrafyası ve Tektonik Önemi. 10-14 Nisan 2017. 70. Türkiye Jeoloji Kurultayı. Bildiri Özleri Kitabı 696-697. Ankara.

Kostaschuk, R. A., McCann, S. B. 1983. Observations on delta-forming processes in a fjord- head delta, British Columbia, Canada. Sedimentary Geology 36, 269-288.

Konak, N. 2002. Türkiye Jeoloji Haritası. 1:500.000 ölçekli İzmir paftası, No 7. Maden Tetkik ve Arama Genel Müdürlüğü, Ankara.

Konak, N., Şenel, M. 2002. Türkiye Jeoloji Haritası. 1:500.000 ölçekli Denizli paftası, No 13. Maden Tetkik ve Arama Genel Müdürlüğü, Ankara.

Konak, N., Akdeniz, N., Çakır, M.H. 1986. Çal - Çivril - Karahallı dolayının jeolojisi, Maden Tetkik ve Arama Genel Müdürlüğü Raporu No: 8945.Ek:1, 133p. (unpublished).

Kurt, H., Demirbaş, E., Kuşçu, I. 1999. Investigation of submarine active tectonism in the Gulf of Gökova, southwest Anatolia-southeast Aegean sea, by multi-channel seismic reflection data. Tectonophysics 305, 477-496.

Ring, U., Johnson, C., Hetzel, R., Gessner, K. 2003. Tectonic denudation of a Late Cretaceous-Tertiary collisional belt: Regionally symmetric cooling patterns and their relation to extentional faults in Anatolide belt of western Turkey: Geological Magazine, 140(4), 21-441.

Seyitoğlu, G., Işık, V. 2015. Late Cenozoic extensional tectonics in western Anatolia: Exhumation of the Menderes core complex and formation of related basins [Batı Anadolu'da Geç Senozoyik Genişleme tektoniği: Menderes çekirdek kompleksinin yüzeylemesi ve ilişkili havza oluşumu]. Bulletin of the Mineral Research and Exploration 151, 49-109.

Seyitoğlu, G., Işık, V., Çemen, İ. 2004. Complete Tertiary exhumation history of the Menderes massif, western Turkey: an alternative working hypothesis. Terra Nova 16, 358-364.

Sözbilir, H. 2005. Oligo-Miocene extension in the Lycian orogen: evidence from the Lycian molasse basin, SW Turkey, Geodinamica Acta 18, 255-282.

Şenel, M. 2002. Türkiye Jeoloji Haritası. 1:500.000 ölçekli Konya paftası, No 14. Maden Tetkik ve Arama Genel Müdürlüğü, Ankara.

Şenel, M. 2010. Türkiye Jeoloji Haritası. 1:100.000 ölçekli Denizli M23 paftası, No 16. Maden Tetkik ve Arama Genel Müdürlüğü, Ankara.

Şenel, M. 2010. Türkiye Jeoloji Haritası. 1:100.000 ölçekli Isparta M25 paftası, No 14. Maden Tetkik ve Arama Genel Müdürlüğü, Ankara.

Turhan, N. 2002. Türkiye Jeoloji Haritası. 1:500.000 ölçekli Ankara paftası, No 8. Maden Tetkik ve Arama Genel Müdürlüğü, Ankara.

Toker, E. 2008. Acıgöl- Çardak (Denizli) grabeninin kuzeyindeki Tersiyer çökellerinin tektono-sedimanter gelişiminin incelenmesi. Doktora Tezi, Süleyman Demirel Üniversitesi, Fen Bilimleri Enstitüsü, Jeoloji Mühendisliği Anabilim Dalı, 264 s. Isparta.

Toker, E., Yağmurlu, F. 2010. Oligocene alluvial sedimentation in the northern of Acıgöl basin, SW Turkey: facies analysis and palaeogeographical evolution. 18-22 October 2010. 7th International Symposium on Eastern Mediterranean Geology. 67. Adana.

Yılmaz, Y., Genç, Ş.C., Gürer, F., Bozcu, M., Yılmaz, K., Karacık, Z., Altunkaynak, Ş., Elmas, A. 2000. When Did The Western Anatolian Grabens Begin to Develop? Tectonics and Magmatism in Turkey and Their Surrounding Area. Geological Society in London 173, 353-384.

Bulletin of the Mineral Research and Exploration

Sedimentological properties and depositional environments of the Holocene sequence in Yenikapı, İstanbul

Meltem SEZERER BULUT[a*] , M. Namık YALÇIN[b]   and Oya ALGAN[c]

[a]STFA Temel Araştırma ve Sondaj AŞ, Istanbul, Turkey.
[b]İstanbul University, Department of Geological Engineering, Istanbul, Turkey.
[c]İstanbul University, Institute of Marine Sciences and Management, Istanbul, Turkey.

Research Article

ABSTRACT

During the salvage excavations in the area of the former Theodosian harbor in Yenikapı-İstanbul several ship wrecks from the Byzantine period, archaeological objects from different periods and a Holocene aged sedimentary sequence have been uncovered. In this study the lithological, lithostratigraphical and facies properties of the Holocene sequence are investigated in detail and its depositional environment is determined. For this purpose along four profiles (S1, S2, S3, S4) 14 different sections of a total thickness of 17.75 m are studied and 100 samples are collected. The grain size distribution and mineralogical composition of the samples are defined by sieve and sedigraph analysis and by XRD method, respectively. Results of these analyses and facies characteristics of this poorly known Holocene sequence are used for the definition of the depositional environment. Accordingly, the marine sediments are deposited in a near-shore environment, with a natural embayment or estuary transgressively. Terrigenous and anthropogenic material carried by the Lycos River, at the mouth of this natural embayment, resulted in first a regression and then a high-energy fluvial system in the study area.

1. Introduction

In the excavations carried out under the management of the Istanbul Archaeological Museum in Yenikapı (Figure 1) for the Marmaray Project, which connects both sides of the Bosphorus with the rail-tube, 36 shipwrecks belonging to the Byzantine Theodosian Harbor and various remains were found (Kızıltan, 2007; 2010; 2014; Asal, 2010; Çelik, 2007; Kocabaş, 2015; Pulak et al., 2015). In addition to numerous wrecks and various archaeological findings, a Quaternary sedimentary sequence, which was encountered in some of the drillings for engineering geology in Istanbul and its vicinity were also uncovered. In the excavation site, there are also Paleozoic and Cenozoic units together with the Quaternary sequence. Here, the sequence from bottom to top consists of the Trakya formation (Paleozoic), Miocene deposits, marsh clay (Holocene), marine deposits (Holocene), fluvial deposits of the Bayrampaşa (Lycos) River (Holocene), agricultural soil and artificial filling deposits.

The lithological, stratigraphic and geo-archaeological features of these units have been investigated by various researchers (Algan, et al., 2007; 2009; 2010; 2011; 2014; Perinçek, 2010a; 2010b; Yalçın et al., 2015, 2019). The sequence uncovered in the ancient Thedosian Harbor excavation contains important evidences of the Holocene sedimentary environments and their changes. However, the studies on the analysis of sedimentological conditions and depositional environment of the Holocene units were limited in number and scope.
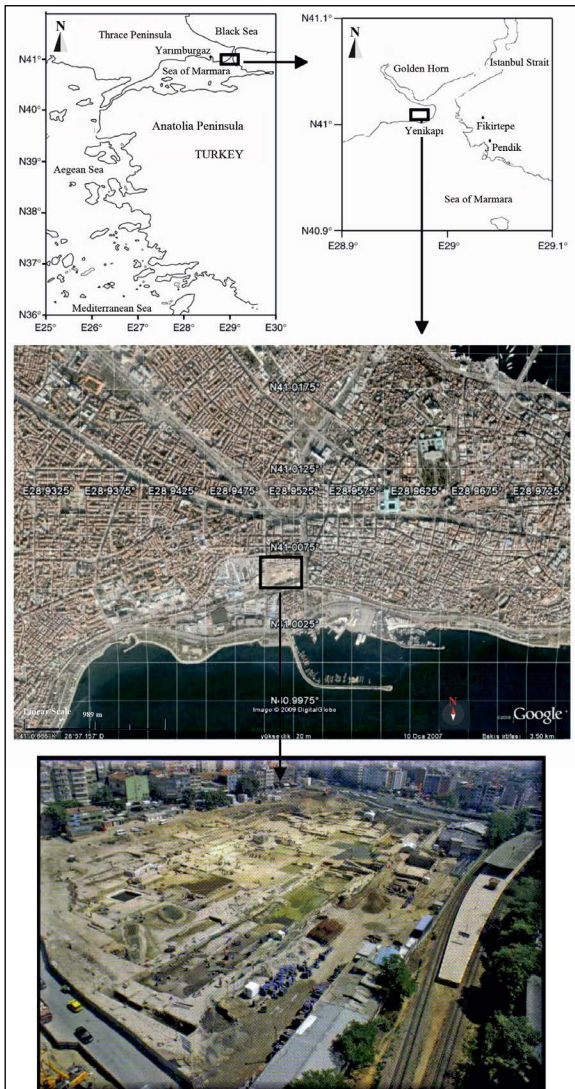
Figure 1- Location map of the study area.

In this study, it is aimed to investigate Holocene marine and fluvial deposits uncovered during the archaeological excavations in detail, to reveal their sedimentological properties and to determine depositional environments.

2. Material and Methods

In order to determine geological, stratigraphic and sedimentological features of the Holocene succession, a total of 17.75 m in 4 profiles (S1, S2, S3, S4) were measured in the excavation site, and 100 samples were collected for different analyzes along the sections. The location of profiles in which the section measurements are made and the samples collected are shown in figure 2.

In order to determine the grain size distribution of samples, the sieve analysis for the grain size between (-8) and (4) ɸ and Micromeritics Sedigraph analysis for the grain sizes between (4) - (10) ɸ were performed. For this purpose, the coarse fraction (-8 to 4 ɸ) was divided into different sizes by the sieve analysis, then their percentage amounts were estimated by weighing them. Fine grain size (4 to 10 ɸ) group was analyzed on the Micrometritics Sedigraph device and the grain size distribution was obtained. As a result of these two analyses, the grain size distribution in the range of 256-0.001 mm was determined.

In order to determine mineralogical composition of the rocks, representative samples of each unit were milled and analyzed by X-ray diffractometer (XRD) Philips PW-1430 in the Mineralogy and Petrography Laboratory of the Geological Engineering Department of Istanbul University. In this device, the Cu Kα radiation was performed using Ni filter, 36 kV voltage, 20 mA current, $2\Theta = 1°/d$ goniometer speed and at certain C.P.S. sensitivities. For each sample, the measurement was made between 2Θ values in 5-65 ranges.

The results of XRD analyses can be evaluated in two ways as qualitative and semi-quantitative. The quantitative/semi-quantitative method is not very reliable as different crystal systems have different diffraction properties. In addition, the errors due to overlapping of instrumental conditions and some pixels are also effective in the evaluation (Hooton and Giorgetta, 1977). Therefore, it is tried to eliminate these errors with various factor calculations (Hooton and Giorgetta, 1977). In this study, though it is not very detailed, an assessment was made in order to make an approach to the mineralogical composition of the samples without making a factor estimation according to the abundance of samples. In this evaluation, the peak intensities of all minerals in the sample were determined based on peak heights obtained as a result of XRD analysis. Then, using the direct proportions between the peak heights of the minerals in each sample, the mineral percentages from the highest to lowest peaks were determined. Thus, a ranking was made according to the abundance of minerals in the composition of each sample.

3. General Geology

The rock assemblages outcropping in Yenikapı, located on the southern margin of the Historic Peninsula
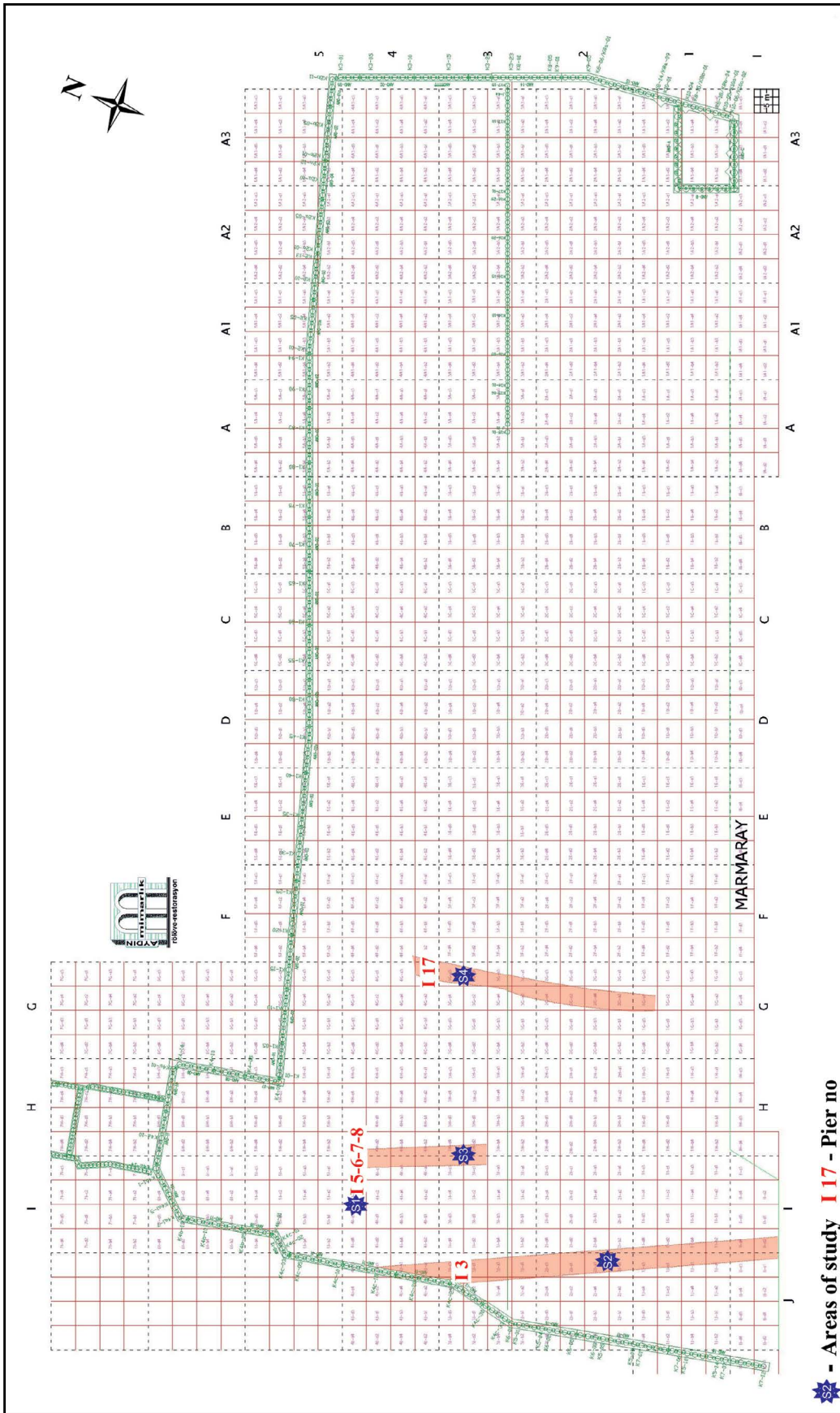
Figure 2- The locations of the piers (I3, I5-6-7-8, I17) studied in the excavation area and the sections examined in these areas (S1, S2, S3, S4) (used under the permission of the Directorate of Archaeological Museums).

in Istanbul, are composed of Paleozoic and Cenozoic units (Figure 3). The Paleozoic Trakya formation is represented by sandstone, siltstone, claystone alternation and forms the basement in the study area. After a long gap, the Çukurçeşme, Güngören and Bakırköy formations were distinguished (Gedik and Aksay, 2002) in Miocene deposits unconformably overlying the basement. The Çukurçeşme formation is composed of greenish gray, silty sandy clays consisting of yellow to beige sand and clayey sand bands. The Güngören formation is composed of greenish gray, clay laminated in places and contains sandy silty levels. These two formations are overlain by the Bakırköy formation which is composed of Mactra limestones with clay interlayers. The Belgrad formation, which is composed of red to brown and yellow pebbles and sands, and the Kuşdili formation consisting of blackish gray pebble, sand, clay and muds overlie the older units with an angular unconformity. At the top, the fluvial deposits and artificial fillings are confined to stream or river valleys exist.

Paleozoic and Cenozoic rock units are only partly represented in the study area and its vicinity. Therefore, only the units in Yenikapı and its vicinity were introduced in this study. The unit called as the basement rock in the Yenikapı excavation site is the Early Carboniferous Trakya formation forming the uppermost part of the Istanbul Paleozoic sequence. Although this unit did not naturally outcrop in the study area, it was encountered during excavations. The Trakya formation is generally composed of grayish, lead-green and brown greywacke and shales and is thin-medium-thick bedded. The lower boundary of the unit was not encountered in shallow drillings excavated for foundation and engineering geology purposes. There is an unconformable relationship with the overlying Güngören formation.

Among Miocene units, the unit outcropping in the Yenikapı excavation site is the Late Miocene Güngören formation. The unit has also large exposures in the study area. The Güngören formation consists of light green and yellowish green claystone, siltstone,
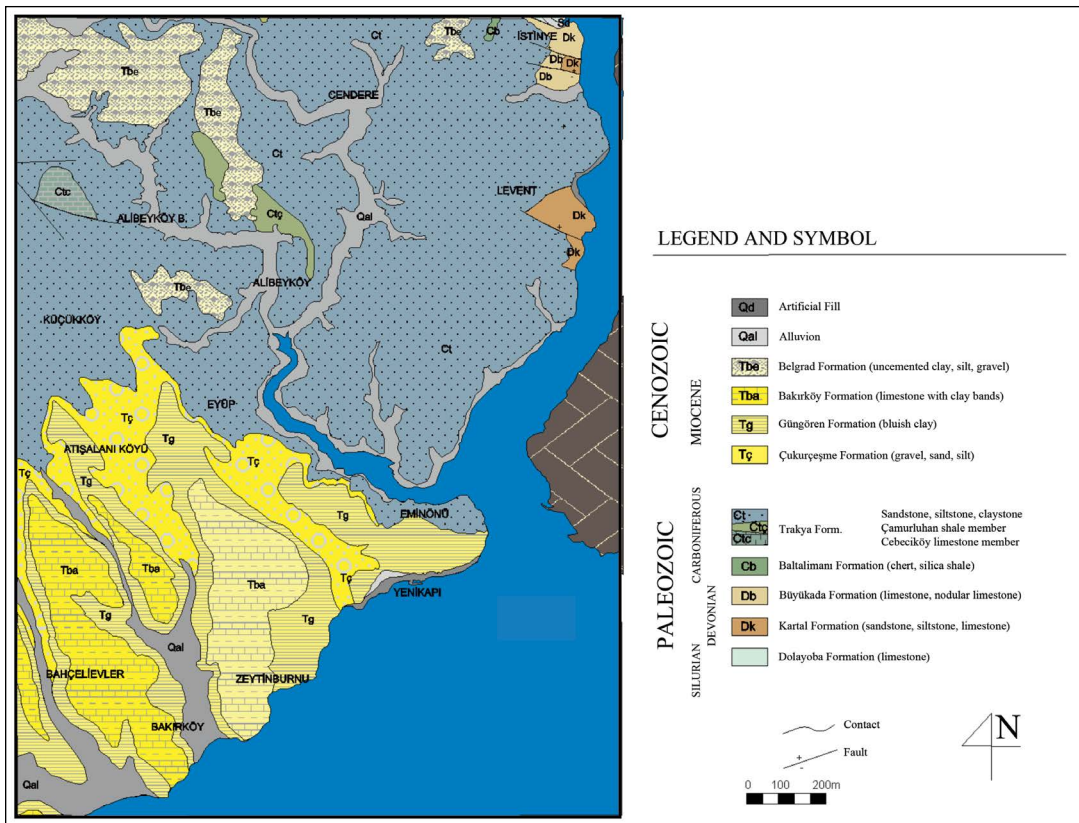
Figure 3- General geology map of the Yenikapı area and its vicinity (Sayar, 1977; Gedik and Aksay, 2002; Gedik et al., 2005; Algan et al., 2011) (The geology map for the Anatolian side was not shown, instead this region was shown with ▨ symbol).

sandstone and limestone layers. There are also observed plant stems, leaf traces, silt and sand lenses in clays. In the study area, the upper and lower contacts of the Güngören formation are unconformable. The unit is overlain by the Holocene marine unit (Kuşdili formation) and/or dark colored clay unit.

The clay unit consisting of dark gray, black and rarely brown homogeneous fine clastic sediments overlying the Güngören formation is observed in a limited area in the study area. The black clay unit has a maximum thickness of up to 9 m in the area and thins out towards the edges. The dominant lithology of the unit is clay, and lamination or layering was not distinctively encountered. In the uppermost part of the unit at the contact with the marine unit, sand fillings in cracks are observed as a result of activities of marine organisms living on the sea floor and/or due to the drying. In the lower parts of the sequence, sandy levels and sand mats are observed developed as local and small-scale channel fills (Yalçın et al., 2015).

The Holocene sedimentary sequence overlying the Miocene Güngören formation and the black clay in occasions can be divided into two units as marine and fluvial. The Holocene marine unit begins with gray, white coarse gravels, and continues with light yellow to beige sand with shells and sand, sandy silty clayey sand and consist of occasionally scattered fragments of amphora, ceramic, bone, glass and coins belonging to 5th-7th centuries (Kızıltan, 2010; 2014; Algan et al., 2011). The overlying unit is a typical fluvial deposit composed of badly to medium rounded cobbles, pebbles and coarse sands. Several ceramic pieces and anthropogenic materials belonging to 8th-11th centuries were found in it (Kızıltan, 2010; 2014; Algan et al., 2011). The artificial infill located on top of the succession contains the fillings of the Byzantine and Ottoman Periods, the agriculture soil, and the residues of concrete-rubble in the near term (20th century) (Figure 4).

4. Holocene Sedimentary Sequence and its Properties

Holocene sedimentary deposits will be studied under titles of lithostratigraphy, lithological features, mineralogical composition, grain size distribution, fossil content and sedimentary structures. The sequence begins with different sizes of gravels and passes in upward direction to yellow to beige, fine grained sand and fluvial coarse sand and pebble at
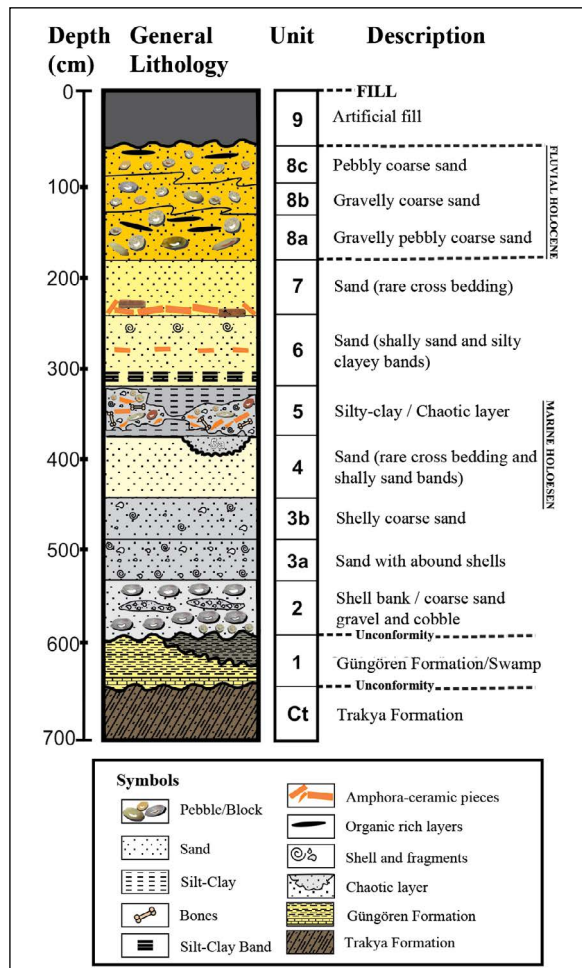
Figure 4- Generalized stratigraphical section of the Yenikapı sedimentary sequence.

the top. The Holocene sedimentary sequence was investigated separating them into 7 sub units from bottom to top as a result of detailed studies (Units 2-8).

4.1. Lithostratigraphy

The stratigraphy and lithological features of the Holocene sequence are presented below from old to young. The bottom of the sequence consists of the Miocene Güngören formation and Holocene marshy clay called the Unit 1 (Figure 4).

Unit 2 (bottom clastics) begins to deposit with light yellow to beige, coarse sand and/or blocks-coarse cobbles-pebbles and consists of medium to coarse grained sand, sand lenses with many shells and shell fragments that have no lateral continuity and coarse pebbles and blocks forming a second level (Figure 5). Angular, flat, large pebbles and blocks consisting
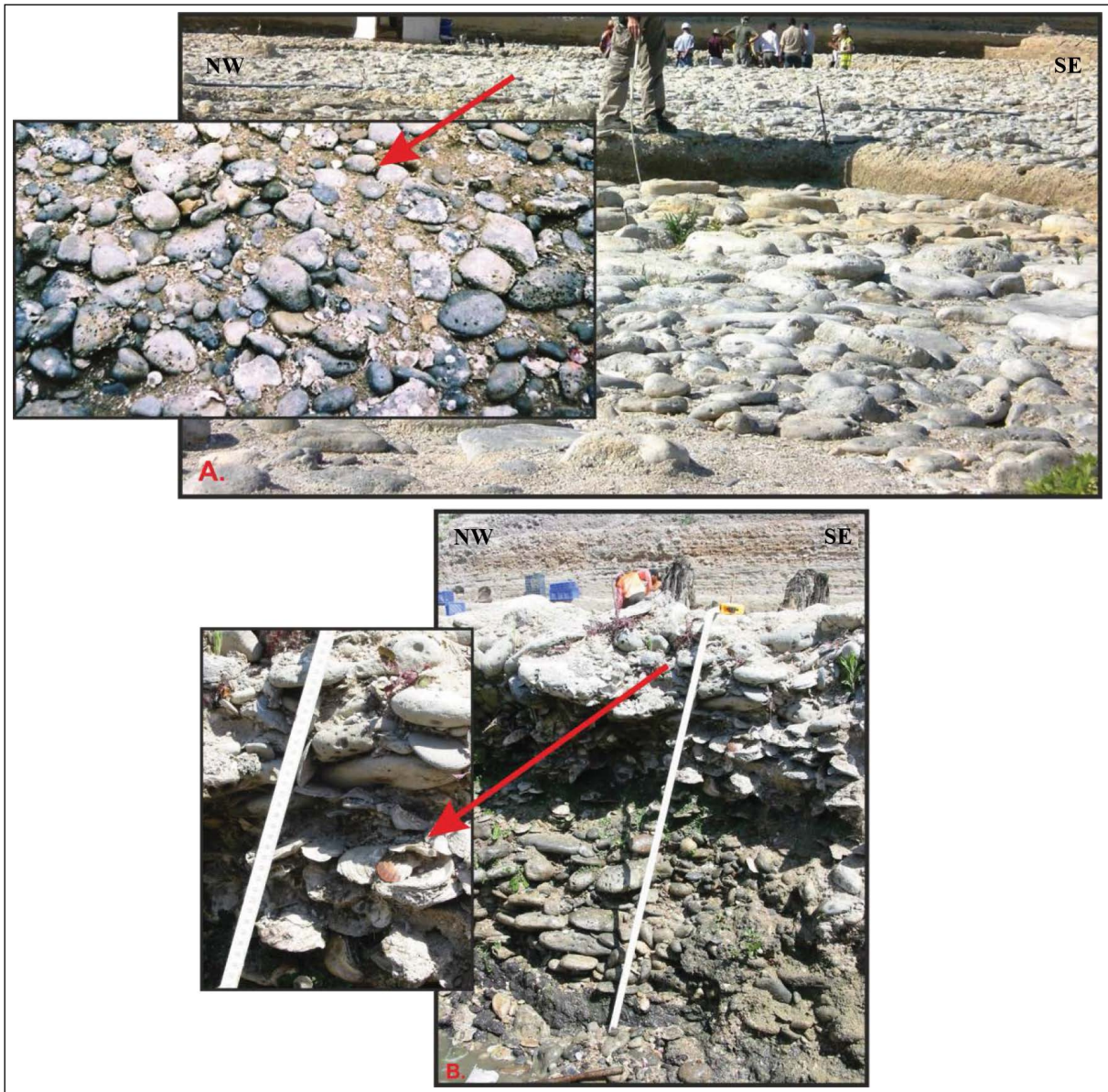
Figure 5- Flat block and coarse pebbles (A) observed in two levels, and rounded pebbles with coarse shells presenting imbricated structures (B) in Unit 2.

of bioperforation holes appear at the bottom of Unit 2. The presence of bioperforation holes of a marine benthic fauna on these blocks and pebbles, arranged in two levels, indicates that they have remained in the marine environment for a long time. These pebbles are derived from the Paleozoic-Cenozoic rocks in Istanbul (Algan et al., 2010). Yalçın et al. (2015) stated that the functional purposes of these very large and angular blocks could be recognized despite the sea and/or wave effect, that they could have been carried by human hands and used in the Neolithic period buildings. In addition, there are smaller (nearly 10 cm), rounded basal pebbles, which could present

imbricated structures and were transported by the sea transgressing landward due to the rising sea level on the black clay here (Yalçın et al., 2015). The unit overlies both the Miocene Güngören formation and the black clay in the study area. The total thickness of this coarse pebble and blocks, the sand in between and the lenticular sand layer that have not any lateral continuity is about 25-50 cm. The pebble ratio decreases to the south towards the sea and the first level pebble and sand layer intertongue with each other and the second level smaller pebbles directly overlie the basement.

Unit 3 (sands with shells); begins with 30-70 cm thick coarse sand (3a) with many shells and shell fragments then grades into coarse sand unit (3b) of which its sand amount reaches nearly 30-60 cm and consist of disseminated shells. In studied profiles (S1-S2-S3-S4) oxidized layers as thin bands were observed on the upper section of the unit 3 (Figure 6). These levels, which are especially oxidized in profiles S3 and S4, are very prominent. This is due to paint of sands of the unit 3 at the bottom as a result of the oxidation of materials such as amphora etc. in unit 4 located on top of the Unit 3.

Unit 4 (Sandy level) is a light yellow, coarse sandy unit and contains locally silty, clayey layers, small scale cross beddings and occasionally clay-mud pellets. Particularly, at the lower parts of the unit there are abundant shell lenses, few amphora pieces, bone and rotten wood fragments and rare pebbles (Figures 6 and 7). Although the thickness of Unit 4 shows variations laterally in short distances within the study area, it generally varies between 50-100 cm.

Unit 5 (Chaotic level) is composed of silty-clayey sands with an erosional bottom and a chaotic association of a complex depositional process. Unit 5 is formed by chaotic levels in S1, S2 and S4 profiles, however this level is observed within a fine grained matrix in the S3 profile. This chaotic unit contains plenty of amphorae-ceramic pieces, animal bones, coins, broken or fully preserved glassware, marble pebble and blocks. These ceramics and amphorae belong to the 5th and 7th centuries (Algan et al., 2011). The thickness of Unit 5 generally varies in 20-50 cm's in the studied S 2-3-4 profiles, whereas the thickness of the S1 profile (north of the S2-3-4 profiles) does not exceed 20 cm (Figure 7).

This unit, which is formed by a complex depositional process is a tsunami deposit of the earthquake in 557 AD according to Perinçek (2010*a*) and Bony et al. (2011). Algan et al. (2011), though not ignoring the possibility of flood or tsunami, stated that this material was subsided as a result of daily activities within the Byzantine Theodosian harbor. Yalçın, et al. (2015) indicated that there was needed more data to understand the depositional mechanism, and it was unlikely that there would be a usual port fill when the unit's characteristics and chaotic structure had been considered. They also suggested that a flood that would drag all sorts of materials into the sea would create a
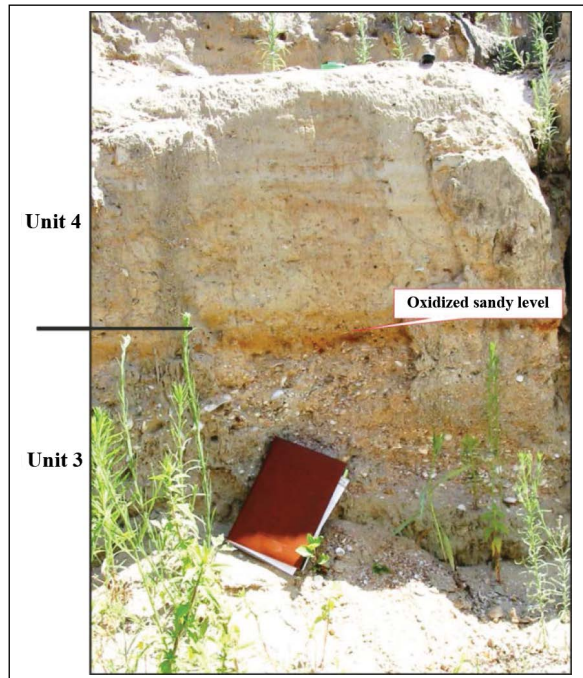
Figure 6- View of Units 3 and 4 in the field.

Figure 7- View of the level containing chaotic-anthropogenic additives in Unit 5 in S1 profile located in the northern part of the study area.

similar set of sediments. Göktürk et al. (2011) showed that rainfall was effective in the mentioned period. Pearson et al. (2012) and Kuniholm et al. (2014; 2015) stated in the light of dendrochronological data that chaotic unit was younger than 557 earthquake which was thought to cause tsunami. It is concluded that there is a need for new data to clarify the process leading to the deposition of Unit 5.

Unit 6 (silt and clay interlayered sands with shells) consists of light yellow to beige, fine grained sands. There are lenticular layers composed of shells and silty-clayey bands in places (Figure 8). The transition between the Units 5 and 6 is gradational. Because the

Unit 6 has been removed earlier than this study during the archeological investigations carried out in the study area in S2 and S4 profiles, it was observed only in S1 and S3 profiles. The thickness of the unit in the study area reaches up to 100 cm.

Unit 7 (sparsely cross-layered sands) begins with amphorae-ceramic fragments, pebble and blocks at the bottom and passes into homogeneous light yellow, medium to fine grained sands with similar characteristics to the Unit 6 in the upper parts (Figure 8). In sandy layers of the Unit 7, the cross stratifications and silty-clayey bands can be seen as well . The amphorae and ceramics at the bottom of this unit belong to the 10th and 11th centuries (Algan et al., 2007). According to Perinçek (2008), the shores of Istanbul were subjected to the influence of two big storms in the 10th and 11th centuries, and these pottery levels were formed as a result of storm waves. The unit was observed only in S1 and S3 profiles due to the previous archaeological excavations and has a thickness of 40-70 cm.

Unit 8 (coarse clastics), named as the fluvial Holocene, conformably and gradually overlies the sequence representing the Holocene marine units ranging from Unit 2 to Unit 7 (Figure 4). The fluvial Holocene unit is generally represented by yellow to brown, coarse grained deposits of natural clastic and anthropogenic material transported by the Lycos River. The Unit 8 is divided into three sub units as; 8a, 8b, 8c (Figure 9). Unit 8a is composed of coarse grained sand with well to medium rounded coarse pebbles that does and/or does not offer gradation based on the location. The overlying Unit 8b consists of well-rounded pebbles and granules at a certain level

Figure 9- The view of lithological properties of three sub Units (8a, 8b, 8c) of the Unit 8 in S1 profile.

Figure 8- The views of Unit 6 and its silty layers, and the bottom layers of Unit7.

and well sorted sands better than the Unit 8a. At the topmost level 8c the grain size increases. The unit is represented by well-poorly rounded pebbly coarse sands. Unit 8 is usually red, black and beige in color. It also includes fine, well-rounded ceramics, pottery, bones and shells, and thin levels rich in black organic matter. The unit is then overlain by an artificial fill (Unit 9, soil cover). The average thickness of the fluvial unit in the study area is 1 m. It was determined that the thickness increases towards the west of the study area.

4.2. Lithological Properties

The results of sieve analyses of the samples collected from the studied S1, S2, S3 and S4 profiles were used in order to redefine the lithological definitions based on macro observations given above as numerical data. In this context, the results of sieve analysis of the samples collected from each unit were evaluated with the help of Folk and Ward (1957) diagrams. In these ternary diagrams, gravel (G) -sand (S) - mud (M) percentages are used to determine coarse grain content and the sand (S) - silt (Z) - clay (C) percentages are considered for fine grained content. Figures 10a and 10b illustrate the ternary diagrams for each profile and lithologies of the units.
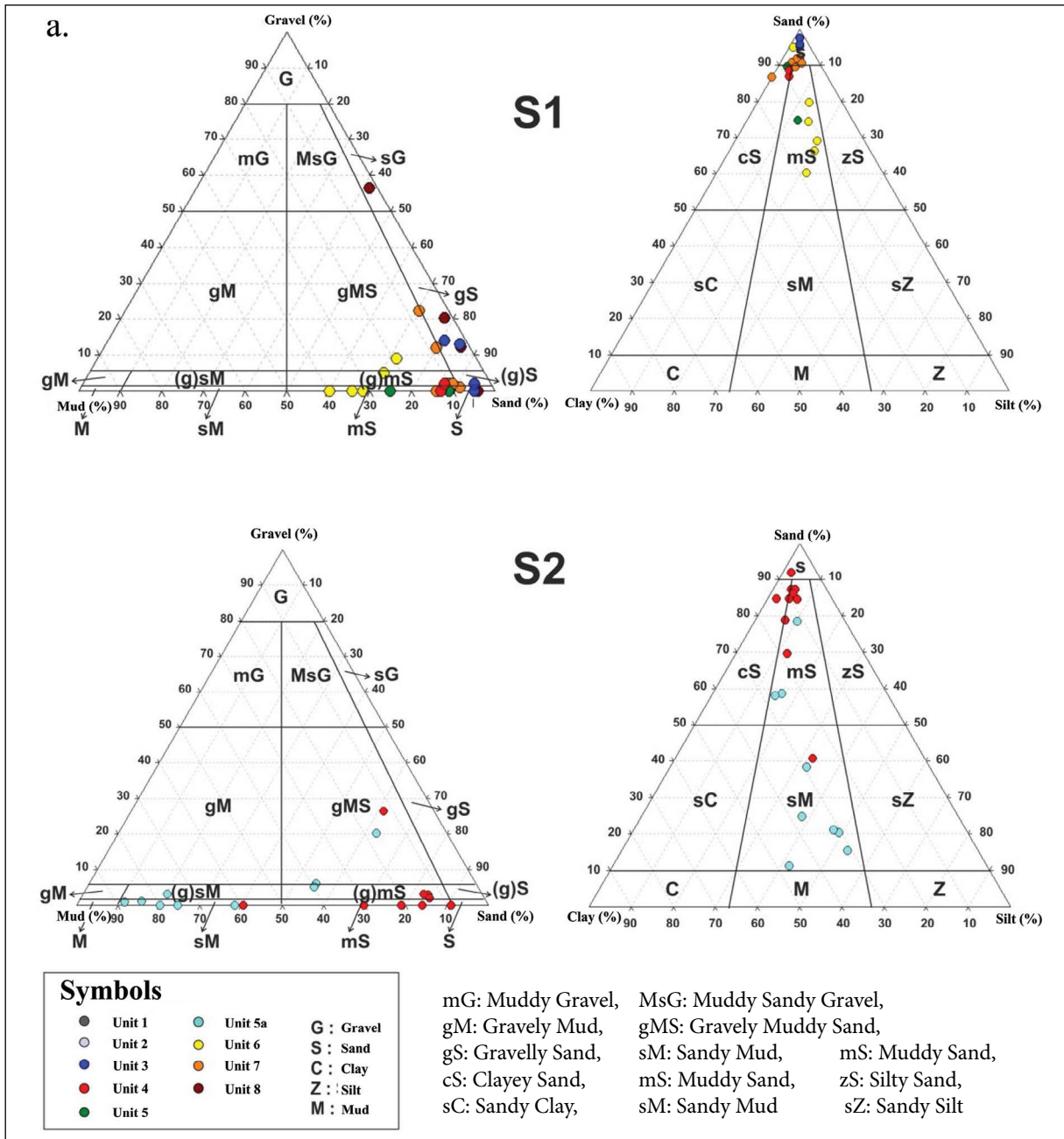
Figure 10- a) Descriptions of marine and fluvial Holocene sediments for each unit in S1 and S2 profiles in ternary diagrams of Folk and Ward (1957).

According to figures 10a and 10b, the Unit 2 is represented by blocks and coarse pebbles due to the grain size greater than 8mm. The dominant lithology in Unit 3 is pebbly sand and sand. Depending on the decrease in the grain size starting from Unit 4, the lithologies such as sand, clayey-silty sand, silty-clayey sand, sandy-silty clay and sandy mud come to the fore in later units. The marine phase ends with the dominant lithology of sand, clayey sand of Unit 7. Starting with the pebbly sand, the grain size,

which first thins out then becomes thick towards the end, indicates that the deposition, which began with shallow and high energy environment then turned into a lower energy environment and then again became a high energy environment. In the continuation of this process, the dominant lithologies defined as the fluvial Holocene in Unit 8 indicate that the energy of the environment further increased and the deposition period was completed.
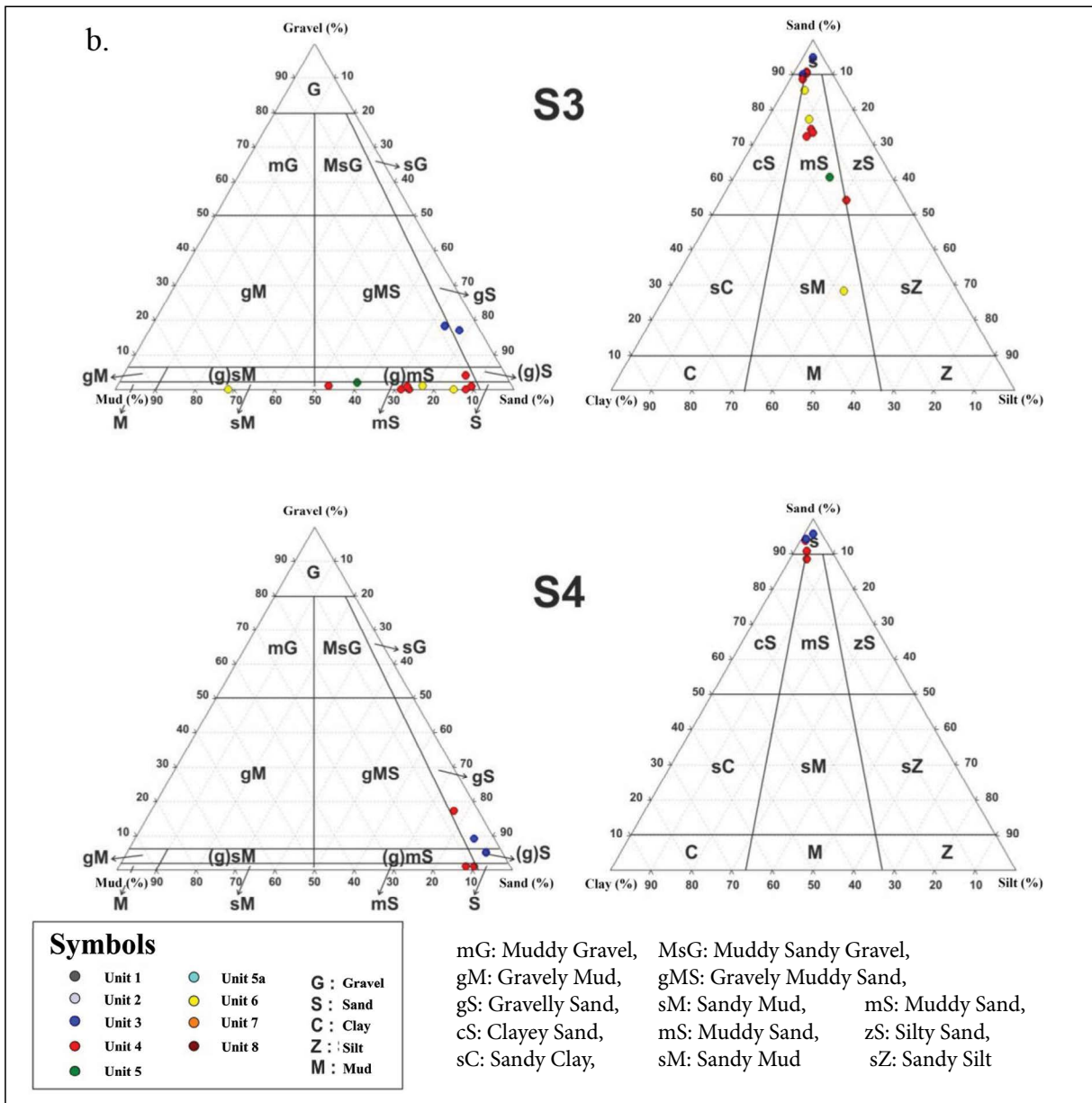
Figure 10- b- Descriptions of marine and fluvial Holocene sediments for each unit in S3 and S4 profiles in ternary diagrams of Folk and Ward (1957).

4.3. Grain Size Distribution

In order to evaluate the energy level in a depositional environment and interpret the mechanisms effective in deposition, the grain size distribution of the units is utilized (Spencer, 1963; Blott and Pye, 2001). In this study, the grain size analysis was performed for representatively selected 62 samples from 100 specimens collected from the Holocene units. The samples were collected along the profiles S1, S2, S3 and S4 to represent differentiated units. The grain size distributions determined according to the results of the sieve and sedigraph analysis will be presented by means of histogram and total cumulative grain size curves on the basis of units. Although such diagrams were prepared for all of the 62 samples, only one or two representative diagrams for each unit will be mentioned.

Since the Unit 2 at the bottom of Holocene sequence is composed of block and coarse pebbles, this unit was not evaluated in terms of grain size characteristics.

Unit 3 was evaluated using 8 samples collected from S1-S3-S4 profiles. The grain size distribution in these 8 samples does not differ significantly and the fine grained sand (φ=3) with a share of approximately 45% constitutes the dominant grain size. In the light of histograms, it was found that the samples of Unit 3 exhibited a unimodal distribution (Figure 11). This shows that there is a single mechanism controlling the grain size in the depositional environment. In this context, it should be noted that the material in the neck
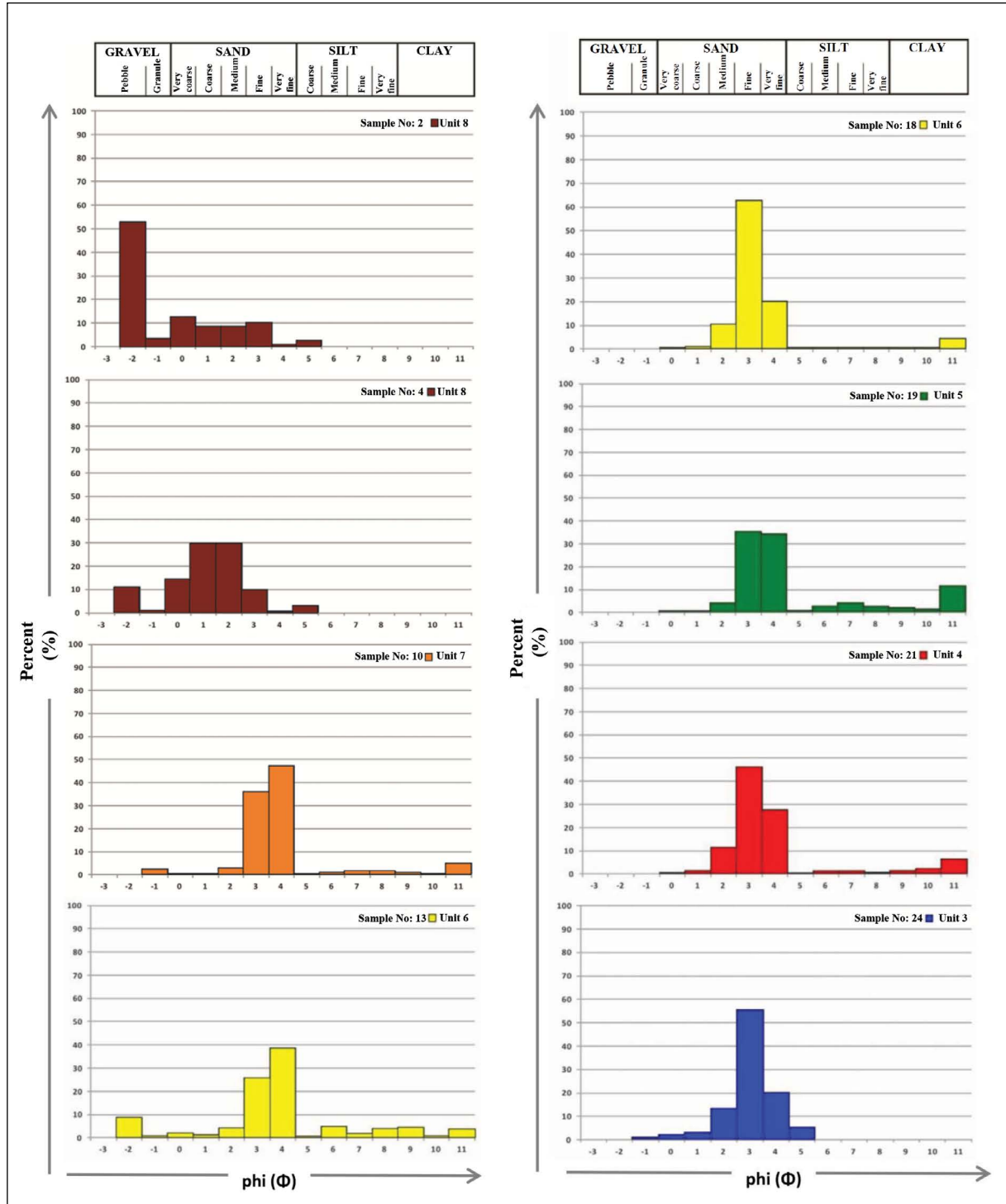
Figure 11- Grain size distributions of the samples selected to represent different units.

of fine grained pebble-granule (<φ = -1) with less than 10% in profiles represents shells and shell fragments in the unit.

The analysis of grain size distribution of the Unit 4 was performed for 22 samples collected from S1, S2, S3 and S4 profiles. As a result, the dominant grain size of Unit 4 was determined as fine to very fine grained sand (φ=3, φ= 4) with a share of approximately 50% to 40% (Figure 11).

Unit 4 contains about 10% of clay and lesser amounts of silt grain size fractions in places, reflecting the silt and clay bands in the unit. For this reason, a bimodal distribution can be recognized in histograms, though not very clear and this can be interpreted as an indication that material has come from two different sources. Especially the increasing pebble ratio (5-10%) in the samples taken from the lower levels of the Unit 4 in S2, S3 and S4 profiles belong to the level containing pebble, marble piece and shell fragments at a level at the bottom of Unit 4. It should be noted that this level is the result of anthropogenic activities at the harbor and therefore does not reflect a change in the energy level of the environment.

Unit 5, which contains the chaotic community in a matrix of silty-clayey sand, was investigated in the study area with three samples collected from S1 and S3 profiles. These samples were collected from the matrix of Unit 5. The histograms showing the particle size distribution showed that the matrix of Unit 5 displayed a bimodal distribution. Approximately 45% of the dominant grain size is fine to very fine sand (φ= 3, φ= 4) and approximately 10% of silt-clay size material is seen as well (Figure 11). Thus, it was understood that the matrix of Unit 5 was composed of clayey-silty fine grained sand. However, it has not been possible to make an assessment on the formation mechanism of the chaotic community characterizing the Unit 5.

Unit 6 was evaluated using 9 samples collected from S1 and S3 profiles. In figure 11, two samples taken from different sections of Unit 6 show that the dominant grain size is fine to very fine grained sand (φ= 3, φ= 4). However, all the other grain size fractions are also represented even they are at very low percentages (Figure 11). This distribution indicates that different elements have started to be effective in the depositional environment.

The histograms of Unit 7 generated by using 6 samples from S1 profile exhibit a unimodal distribution (Figure 11). The mod value of this distribution consists of fine to very fine sand size material with percentage of 30-55%. In some examples, the fine grained pebble material reaching up to 20% represents a level in which the amphora, coin, glass fragments and animal bones are present within the unit and do not show a rising energy level in the environment.

The grain size distribution of Unit 8 evaluated by means of 4 samples from S1 profile begins with well sorted fine grained sand at 80% and extends badly sorted, coarse to medium grained sand and pebble size material in the upper layers (Figure 11). This distribution indicates that there have been a high energy environment.

The grain size distribution of units was evaluated also by forming the cumulative grain size curves along with histograms (Figure 12). The cumulative curves show that Unit 3 is medium grained sand, Unit 4 is fine grained sand, Unit 5 (matrix) and Unit 6 are fine to very fine grained sand, silt and clay, Unit 7 is fine grained sand and Unit 8 is coarse grained sand-pebble and created different clusters from each other. In this sense, the cumulative grain size curves correspond to the histogram results as expected.

The grain size distribution data were statistically evaluated in the next step. These statistical parameters help to determine the depositional environment (Blott and Pye, 2001). The average grain size (median) (value that divides the curve into two equal areas), sorting (whether the distribution curve is spread or narrow), skewness (which direction the curve is tilted, + or - skewness) and curtosity (whether the curve is (+) lepto or (-) platy) values for the samples collected from S1-S2-S3-S4 profiles were determined. The change in depth for the samples belonging to S1 profile in which all the units are represented is given in figure 13. Unit 3, which is medium to badly sorted, (-) skewed, lepto and platycurtic, coarse to medium grained sand, at the bottom of S1 profile underlies the Unit 4, which is badly sorted, symmetrical to (+) skewed, leptokurtic fine grained sand. Unit 5 is very badly sorted, (+) skewed, leptokurtic, coarse grained silt-clay. This is followed by Unit 6 which is very badly sorted, (+) skewed, leptocurtic very fine sand. On top of that, the Unit 7, which is badly-very badly sorted, (+) - (-) skewed, leptocurtic fine grained sand
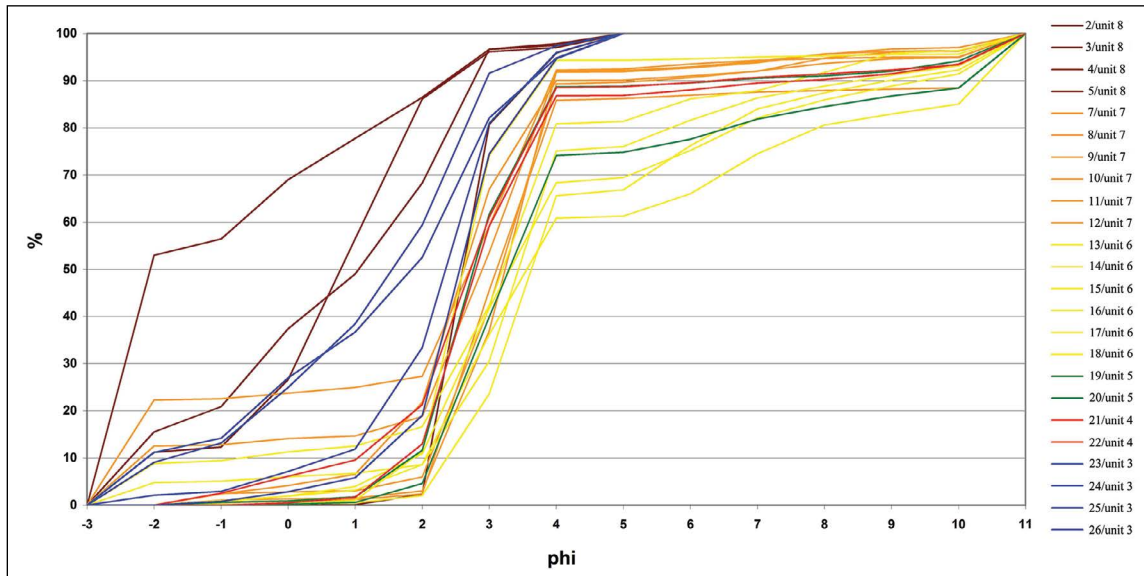
Figure 12- The grain size distribution of the units along the S1 profile by means of cumulative grain size curves.

is observed. Unit 8 at the top of this sequence is poorly sorted, (+) - (-) skewed, lepto and platycurtic pebble-granule.

When the statistical parameters of the average grain size for all profiles are evaluated together, it is noticed that all the units are generally badly to medium sorted, and that the dominant type of sediment, generally represented by sand is also accompanied by

the coarse and/or clay-silt size material. The Units 8, 7 and 6 have all types of skewness values, however the Units 5 and 4 have only (+)/very (+) skewness. The Unit 3 is separated from the other units only with (-) skewness values. It is observed that a more complicated sedimentation mechanism develops after Unit 3, which has (-) skewness, and the (+) skewness occurs in Units 4 and 5 (Figure 13). This situation has
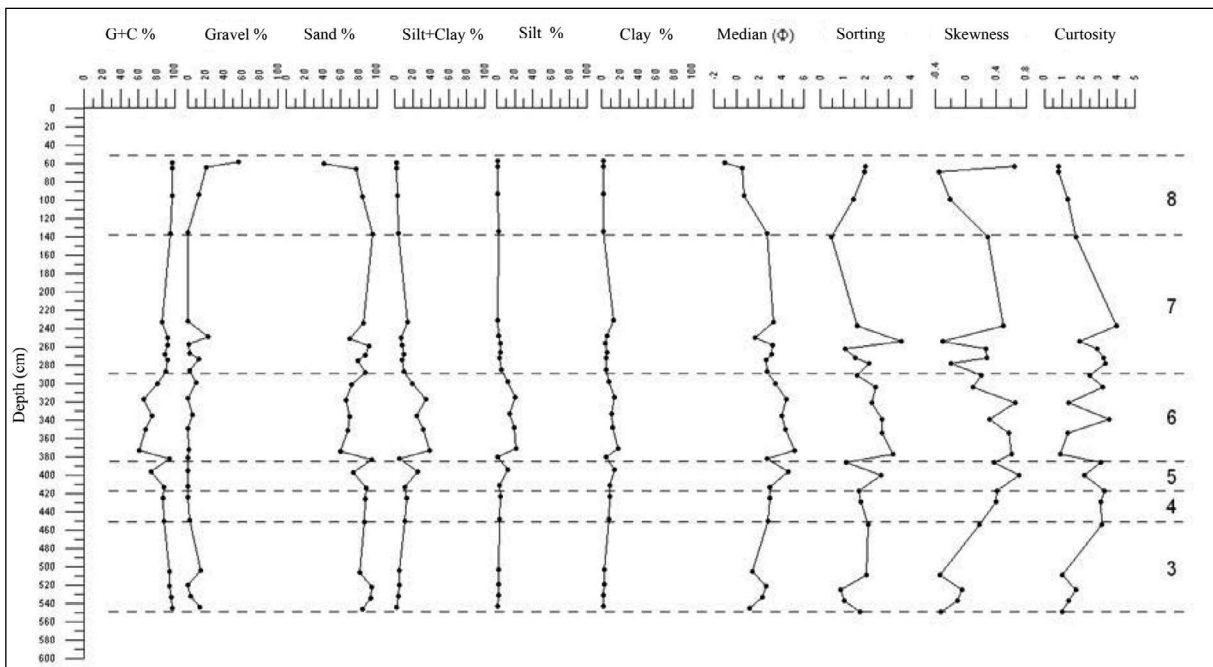
Figure 13- The change of grain size and statistical parameters of samples collected from S1 section based on units and depth.

continued during the deposition of the upper parts of the sequence.

As a result, it can be said that the sand, which shows unimodal distribution, was generally deposited in the marine Holocene sequence in Yenikapı. From time to time the energy level of the environment decreased and thin silt and clay bands were formed in the succession. In addition, a complex deposition also occurred as well due to the harbor activities and tsunami/flood events in the marine Holocene sequence in Yenikapı. It is concluded that Unit 8, which was located in the upper part of the sequence, was formed by the deposition of the material transported by the Lycos stream in a high-energy fluvial environment.

4.4. Fossil Content

In this study, the fossil assemblage in the sequence was not studied in detail and the fossil content of the Yenikapı sedimentary sequence was compiled from Algan et al. (2011), Bony et al. (2011), Meriç et al. (2009) and Perinçek et al. (2007). The Yenikapı sedimentary sequence generally consists of foraminifera, ostracod, pelecypod and gastropod shells.

Among benthic foraminifers; *Ammonia* sp., *Elphidum* sp. and *Quinqueloculina* sp. are dominant and *Adelosina carinata striata, Cycloforina contorta, Massilina secans, Miliolinella subrotunda, Pseudotriloculina* spp., *Rosalina* spp., *Porosononion subgranosum* and *Haynesina depressula* are encountered in few amounts. The foraminifer assemblage has poor genus diversity and a low population, and the dominant genera are *Ammonia sp.*, then *Elphidium sp.* Although the diversity starts to increase starting from Unit 7, the total benthic foraminifer amount reaches the maximum in Unit 5.

The ostracod fauna with general features consist of marine (*Aurila convexa, Paracytheridea depressa, Urocythereis oblonga, Pontocythere elongate, Semicytherura inverse, Semicytherura sulcata, Callistocythere intricatoides, Carinocythereis carinata, Hiltermannicythere turbida, Pseudocytherura calcarata, Loxoconcha elliptica, L. rhomboidea, L. stellifera, Xestoleberis comunis, X. dispar, Henryhowella asperrima, Leptocythere* sp.), oligohaline (*Candona neglecta, Heterocypris salina,*

Euxinocythere sp., *Ilyocypris gibba*) and eurihalina (*Cyprideis torosa*) species. The most spread of them are *Aurila* sp., *Semicytherura* sp., *Urocythereis* sp., *Callistocythere* sp., *Pseudocytherura* sp. and *Pontocythere* sp. which prefers sandy floors. The genera diversity and population are high in Units 5, 4 and 3, and reaches the maximum in Unit 6. The diversity and population decrease over these values. At the topmost Unit 8, a couple of marine species and genera such as; *Candona* sp., *Heterocypris* sp. and *Ilyocypri*s sp. indicating the fresh water input are observed (Algan et al. , 2011).

Benthic foraminifer assemblage shows that there is a transition from marine to fluvial environment from bottom to top. Species such as; *Ammonia* and *Elphidium* can adopt itself to salinity conditions in a large interval ranging from hyposaline to hypersaline and they are largely observed in inner shelf, lagoon and tidal flats (Murray, 1973). *Massilina, Quinqueloculina, Miliolinella* and *Rosalina* prefers salinity conditions less than 32‰ (Murray, 1973). *Elphidium, Ammonia* and *Quinqueloculina*, which are seen in Units 3 and 4 below the succession, are dominant and the assemblage that possess rich species diversity characterizes shallow marine environment. *A. para*sovica and *A. tepida* are known as eurihaline species and can tolerate low salinities (1-26%) (Yanko, 1990). The fossil assemblage that has low population and species diversity of which these species are dominant are located at the top part of the succession (Units 8 and 7) and reflect the decreasing salinity conditions. The ostracod fauna shows that marine forms are dominant in the lower parts of the succession. However, the oligohaline species become dominant towards the upper layers and support a change from marine to fluvial conditions (Algan et al., 2011).

4.5. Sedimentary Structures

The sand lenses with abundant shells and shell fragments, which have no lateral continuity are the first conspicuous sedimentary structure in Unit 2 forming the bottom of the marine Holocene unit. In addition, there are rounded pebbles with diameters of nearly 5-10 cm that present imbricated structures in the lowermost parts of the unit. These levels represent basal conglomerates of the transgressing sea. The typical sedimentary structure identified in Unit 3 is the

lenticular shell aggregations, which do not have lateral continuity, and represent the sedimentation in a shore (beach) environment. In the upper parts of Unit 4, the silt-clay bands are noticed. Besides, the mud pellets were determined (Figure 14) and these pellets were possibly associated with bioturbation. The chaotic level within Unit 5, which is erosional at the bottom, offers extremely complex structure. For this reason, as mentioned earlier, it has been thought that this structure had occurred as a result of a very high energy, sudden and effective event. Unit 6 as well, includes silt-clay bands with occasionally disseminated or arranged shells like Unit 4. Within Unit 7, where marine sand is dominant, the micro-scale cross-bedding associated with decayed and charred plant material and macro-scale, cross-bedded sand levels were observed. In addition, there are sedimentary structures called the "seismite" in lower parts of the unit 7. The seismites are structures formed as a result of the segregation of water from unconsolidated sediments and deterioration of stratification as a result of earthquakes (Figure 15).
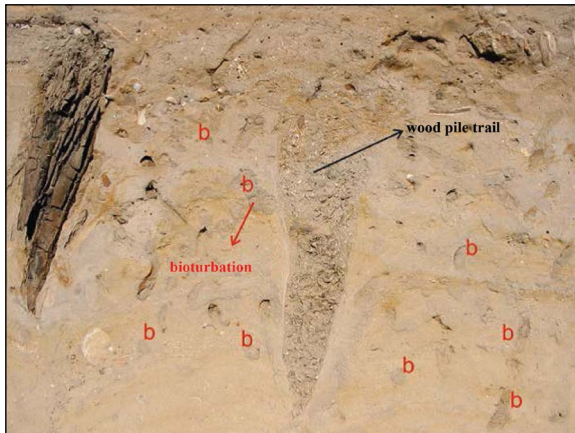
Figure 14- Mud pellets resulting from the bioturbation in Unit 4 (b).

Figure 15- Seismite structure seen in Unit 7 (Algan et al., 2009)

The most striking sediment structure in Unit 8 is the channel structures in different sizes which are typical indicators for a fluvial environment. Since the majority of channel fillings consist of anthropogenic material transported by the Lycos River, these structures were clearly visible in the exposed sections (Figure 16).

Figure 16- Channel filled with organic rich material in Unit 8.

4.6. Mineralogical Composition

The mineralogical composition of the representative samples selected from Bakırköy, Çukurçeşme and Trakya formations, which form the basis of this sequence with the Holocene succession in the Yenikapı excavation area, and have outcrops in the immediate vicinity were determined and a correlation was made between the Holocene sequence and the source area.

The XRD analyzes showed that quartz, calcite, albite and aragonite minerals were most commonly found in the composition of all samples taken from the Holocene sequence. The amount of quartz (SiO_2) and calcite ($CaCO_3$) in the samples ranges from 10% to 90%, while the amount of albite ($NaAlSi_3O_8$) and aragonite ($CaCO_3$) reaches a maximum of 30%. In three representative samples selected from Bakırköy, Çukurçeşme and Trakya formations mainly the calcite, quartz and albite minerals were detected. In the light of these findings, it was concluded that the grains of Holocene sequence originated mainly from the Trakya formation and from Miocene units. The source of aragonite mineral should be the shells which are abundant in Holocene units. In addition, the hematite (Fe_2O_3), dolomite ($CaMg(CO_3)_2$), rutile (TiO_2), pyrite (FeS_2) and orthoclase ($KAlSi_3O_8$) minerals in nearly 10% were determined in Yenikapı samples.

It was possible to conclude that the mineralogical composition of the Holocene units may vary depending on the activities of the harbor and the city as well as the natural resource area. While there is orthoclase mineral in Units 3 and 4, it was not found in the upper part of the sequence (Figure 17). This situation shows that the participation of the orthoclase mineral into the environment discontinued after the construction of the port. When it is considered that the harbor is protected with one or two breakwaters, it can be said that the orthoclase was transported to the environment by sea and its source is the Pliocene-Pleistocene units at the
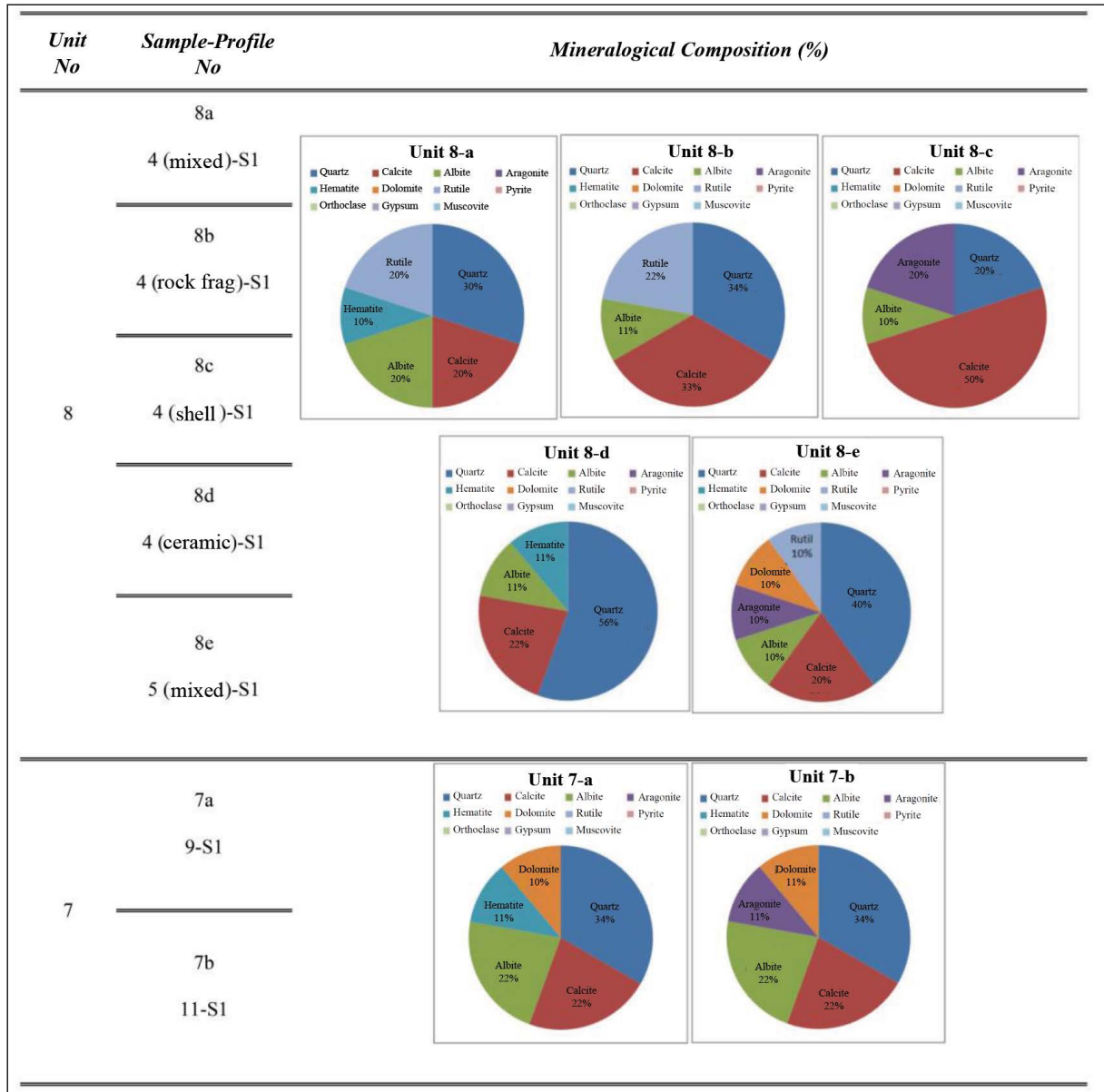
Figure 17- The mineralogical composition of the samples collected from the Holocene sequence and from Bakırköy, Çukurçeşme and Trakya formations, which have outcrops in the vicinity of Yenikapı.

base of the Sea of Marmara. The dolomite, hematite and pyrite minerals occurring in Units 6, 7 and 8 are very likely to originate from harbor and urban activities (Figure 17) because these minerals are not present in units (units 2-4) where there was no harbor or city and/or when they were very small. The reveal of these minerals as well are among the first indicators

that the material transported by the Lycos stream began to fill the harbor gradually. The rutile should be derived from two sources, both natural (Trakya formation) and anthropogenic because of its presence in Unit 4. The increase in the amount of rutile in young units supports this (Figure 17).

Figure 17- Continue.

Unit No	Sample-Profile No	Mineralogical Composition (%)
4	4a 22-S1 4b 75-S2 4c 53-S2 4d 86-S3 4e 77-S4 4f 80-S4	
3	3a 23-S1 3b 24-S1 3c 26-S1 3d 81-S4 3e 83-S4	
Bakırköy, Trakya and Çukurçeşme Formations		
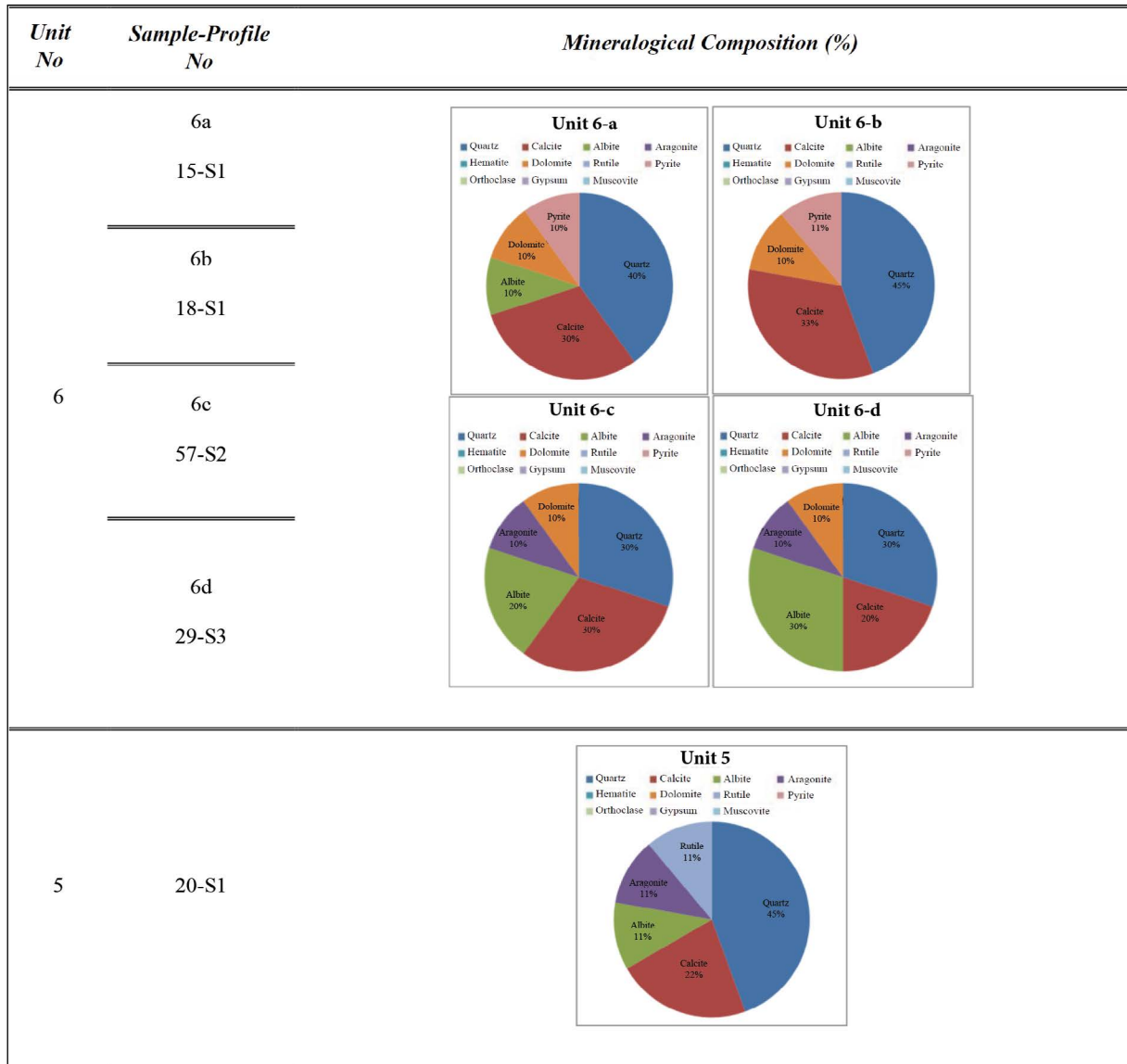
Figure 17- Continue.

5. Discussion

The depositional environment of the Holocene sequence in Yenikapı, İstanbul were defined by means of properties such as; stratigraphy, lithology, grain size, fossil content, sedimentary structures and mineralogical compositions of this sequence defined above.

The Holocene sequence overlying the Miocene Güngören formation and the Early-Middle Holocene marsh clay was deposited in two different environments as marine (from Unit 2 to Unit 7) and fluvial (Unit 8). All the signs indicate that this differentiation is doubtless. However, it should be noted that there is not any gap between these two environments. The deposition began as marine then turned into a fluvial by gradual shoaling and completed its deposition. Hence, it can be said that the Yenikapı Holocene sequence was deposited in an environment shaped as a result of first the sea level rise then by the seaward regression of the shore due to the material transported and deposited by the river. The pebbles, which present rounded, imbricated structures consisting of the large marine pelecypod shells occasionally observed at the bottom of Unit 2, represent the beginning of transgression. This transgression should have developed due to the global sea level rise which began at the end of the last glacial age. The sea level in the last glacial age, which was 120 m (Lambeck et al., 2004) lower than today, caused the Sea of Marmara and Black Sea to turn into a lake (Çağatay et al., 2000). The sill, which is at -65 m in the entrance of the Çanakkale (Dardanelles) Strait, was exceeded nearly 12000 years ago. So, the Marmara Lake then turned into a sea and the sea level began to rise (Çağatay et al., 2000, 2003, 2009). The rising sea then began to pervade the shores of the ancient Marmara Lake. The period when the rising sea reached the study area in Yenikapı was determined as 6650-7080 cal years from the shells at the bottom of Unit 2 by Algan et al. (2011) using the ^{14}C method. The age determinations carried out on shells, which are preserved in nests carved on coarse blocks again gave the age of 7330-6980 years by using the ^{14}C method (Perinçek, 2010b). In the light of these data, it was understood that the sea began to invade Yenikapı approximately 7000 years ago. The age determined for the uppermost part of the clay unit observed in the area is about 7400 cal years (Yalçın, et al., 2015). Considering that some of the top sections

of the clay unit may have been eroded, it can be said that there is a few hundred years of gap between the marine deposits and marsh clays. The rising sea level must have invaded the valley of the Lycos River and flooded its mouth and turned the valley into a wide estuary or embayment. The aggregation of lenticular shells and shell fragments at the bottom of Unit 2 indicate a depositional environment very close to the shoreline in a shallow marine environment. The ^{14}C ages taken from the sections in slightly upper parts of Unit 2 are clustered 3000 years ago than today (Algan et al., 2009; 2011). This situation shows the fact that the sea level, which is commonly observed in submerging coastal regions, rises and pushes the river load backward for a certain time by flooding the river mouths and the deposition rate becomes extremely low (Nichols, 1999; Coe and Church, 2003) have also been experienced in Yenikapı. For this reason, it can be said that during the following 4000 years, the working area has remained as a coastal environment where almost no deposit was recovered. Starting from 3000 years ago, since the material influx into the environment has reached the normal levels, the shell bearing sands belonging to the Unit 3 has started to be deposited in a foreshore-near shore environment in the embayment entrance. Although these conditions have continued to be effective during the deposition of the sands of the Unit 4, the transformation of this embayment into a harbor protected by breakwater towards the last stages of the unit caused the environmental conditions to change. The clay and silt bands observed in the uppermost part of the Unit 4 are the preliminary signs of a protected harbor environment (Marriner and Morhange, 2006; 2007; Marriner et al., 2008; 2010). The absence of orthoclase mineral in the deposited sequence after Unit 4 is another indication of the fact that the connection of the environment with the offshore is greatly cut off. The similar environmental conditions have continued in the period when the Unit 5 was deposited. The chaotic community observed in this unit represented by very fine sand, silt and clay size material does not reflect the essential properties of the sedimentation environment as it represents a short-term and high-energy process such as the flood or tsunami. Sand again began to deposit in this protected harbor environment with Unit 6. This situation, which seems contradictory at the first glance, can be evaluated as a meaningful process considering the existence of the Lycos River flowing into the embayment. The fact

that the well sorted, fine grained sand is relatively the dominant grain size indicates that the energy of the environment increased and the detrital source started to be more effective. Considering that the harbor is intensely being used, it was understood that the source was mainly the Lycos River which caused the propagation of delta towards the sea. In addition to both proximity and natural processes, the increase in the material transported by the stream due to anthropogenic processes is the cause of the change in the depositional regime. Another source of the sand is the sand transported to the harbor with huge waves exceeding the breakwater of an extraordinary storm (Pulak et al., 2015), which has been identified as the cause of the sinking of several wrecks in Units 6 and 7. These waves and sand caused both the sinking of ships and allowed them to be protected by rapidly covering the wrecks (Perinçek, 2010*a, b*; Algan, 2009; 2011; Kocabaş, 2010; Kocabaş, 2015; Pulak, et al., 2015). Another indication of the fact that the delta of the Lycos River filling the embayment became very close to the section near to the sea of the harbor is the large-scale cross-stratification due to the currents observed in the upper parts of the Unit 7. The approaching delta has reached the study area shortly after. The fluvial sequence of Unit 8, which overlies the Unit 7, was deposited as a product of typical fluvial-delta environment. Thus, the sedimentation, which began in a clastic foreshore environment, has evolved into a near shore environment where the very high sedimentation occurs as a result of the rising sea level flooding this coastal environment containing the large cove/estuary. After the construction of a harbor protected by a breakwater in the study area, a protective harbor environment emerged and the units with relatively much smaller grain sizes were deposited. Due to the fluvial activity that began to fill the cove, the sand began to be deposited again in the harbor and then the depositional period was completed with fluvio-deltaic sediments.

6. Results

According to sedimentological properties seven units were distinguished in the Holocene sediments in the Yenikapı district. The sequence begins with pebbles in varying sizes at the bottom then passes into yellow to beige, fine grained sand in the upward and again to coarse grained sand and pebble at the top.

In order to determine the depositional environment and environmental changes of this sequence, the grain size distribution, lithologies, fossil content, sedimentary structures and mineralogical compositions of differentiated units were investigated. The sieve analysis and grain size distribution determined by the sedigraph revealed that the Units of 3 and 4 were formed by medium-fine-very fine grained sands, the Units of 5, 6 and 7 consisted of silt and clay in addition to sand, and the Unit 8 was composed of pebble and coarse to medium grained sands at the bottom.

The pebble, coarse shells and lenticular shell aggregations presenting the clast imbrication at the bottom, the traces of bioturbation, the cross stratification and the seismites in the sandy unit in intermediate sections and the channel structures and fills in the upper sections of the Holocene sequence were observed.

In previous studies, generally the foraminifers, ostracod, pelecypod and gastropod fossils were detected in the Holocene sequence in Yenikapı. These fossils are mostly presented by benthic genera and species indicating the shallow marine and transition zones. The typical marine forms in the lower section of the sequence turn into brackish water forms towards the upper sections.

It was determined that the minerals in non-natural environment in a Holocene sequence had come out due to antropogenic activities within younger units. It was seen that the variations were controlled by the antropogenic activities in Byzantine city in addition to Paleozoic and Tertiary units in the source area.

The deposition of Holocene sequence in Yenikapı-Istanbul began in a clastic foreshore environment, but the rising sea level submerged this shore consisting of large embayment/estuary and changed it into a near shore environment where the sedimentation had become very slow. At the beginning of the 5th century, the clay-silt containing units were deposited in this sheltered environment after the installation of a harbor protected by the breakwater. The sand began to be deposited again in the harbor due to the Lycos River which began to fill the embayment and due to the increasing anthropogenic activities. As a result, the shoreline began to regress towards the sea, and a fluvio-deltaic environment developed after the river plain had reached the study area.

Acknowledgements

References

Algan, O., Yalçın, M.N., Yılmaz, Y., Perinçek, D., Özdoğan, M., Yılmaz, İ., Meriç, E., Sarı, E., Kırcı-Elmas, E., Ongan, D., Bulkan-Yeşiladalı, Ö. Günhan, D., Özbal, H. 2007. The geoarchaeological significance of the ancient port Theodosius at Yenikapı: Late-Holocene environmental changes and the cultural history of Istanbul over the last ten thousand years. In: Kızıltan, Z. (Ed.), Istanbul: 8000 years brought to daylight; Marmaray, Metro, Sultanahmet excavations, pp.242-245. Vehbi Koç Foundation, ISBN 978-975-6959-39-8.

Algan, O., Yalçın, M.N., Özdoğan, M., Yılmaz, İ., Sarı, E., Kırcı-Elmas, E., Ongan, D., Bulkan-Yeşiladalı, Ö., Yılmaz, Y., Karamut, İ. 2009. A short note on the geo-archaeological significance of the ancient Theodosius Harbor (İstanbul-Turkey). Quaternary Research, 72, pp.457–461.

Algan, O., Yalçın, M.N., Yılmaz, İ., Kırcı-Elmas, E., Sarı, E., Ongan, D., Bulkan-Yeşiladalı, Ö., Perinçek, D., Özdoğan, M., Yılmaz, Y., Karamut, İ. 2010. Geoarchaeology of the Theodosian Harbor at Yenikapı. In: Kocabaş, U. (Ed), Proceedings of the 1st Symposium on Marmaray-Metro Salvage Excavations, 5th– 6th May 2008, Istanbul, pp.175–181, Directorate of Istanbul Archaeological Museums, ISBN 978-605-60853-6-9.

Algan, O., Yalçın, M.N., Özdoğan, M., Yılmaz, Y., Sarı, E., Kırcı-Elmas, E., Yılmaz, İ., Bulkan, Ö., Ongan, D., Gazioğlu, C., Nazik, A., Polat, M.İ., Meriç, E. 2011. Holocene coastal change in the ancient harbor of Yenikapı–İstanbul and its impact on cultural history. Quaternary Research, 76, pp.30-45.

Algan, O., Yalçın, M.N., Özdoğan, M. 2014. Yenikapı Kazıları Jeoarkeoloji Çalışmaları-Son Buzul Döneminden Günümüze Çevre Koşullarındaki Değişimler ve Kültür Tarihine Yansımaları. Ş. Baltaş, Ş. Altun (Eds.), Hayalden Gerçeğe Bir İstanbul Öyküsü-Marmaray, pp.130-139. ISBN 978-605-64547-1-4.

Asal, R. 2010. Theodosian harbor and sea trade in Byzantine Istanbul. In: Kocabaş, U. (Ed) Proceedings of the 1st Symposium on Marmaray-Metro Salvage Excavations, 5th– 6th May 2008, Istanbul, pp.153-160, Directorate of Istanbul Archaeological Museums, ISBN 978-605-60853-6-9.

Blott, S.J. Pye, K. 2001. GRADISTAT: a grain size distribution and statistics package for the analysis of unconsolidated sediments. Earth Surface Processes and Landforms, 26, pp.1237-1248.

Bony, G., Marriner, N., Morhange, C., Kaniewski, D., Perinçek, D. 2011. A high-energy deposit in the Byzantine harbour of Yenikapı. Quaternary International, 266, pp.117-130, doi: 10.1016/j.quaint.2011.03.031.

Coe, A.L., Church, K.D. 2003. Sequence stratigraphy and sea-level change (part 2). In: Coe, A.L. (Ed.), The Sedimentary Record of Sea-Level Change. Cambridge University Press, The Open University, pp.57–98.

Çağatay, M.N., Görür, N., Algan, O., Eastoe, C., Tchapalyga, A., Ongan, D., Kuhn, T., Kuşcu, İ. 2000. Last glacial–Holocene palaeoceanography of the Sea of Marmara: timing of the last connections with the Mediterranean and the Black Sea. Marine Geology, 167, pp.191–206.

Çağatay, M.N., Görür, N., Polonia, A., Demirbağ, E., Sakınç, M., Cormier, M.-H., Capotondi, L., McHugh, C., Emre, Ö., Eriş, K. 2003. Sea level changes and depositional environments in the İzmit Gulf, eastern Marmara Sea, during the late

glacial–Holocene period. Marine Geology 202, pp.159–173.

Çağatay, M.N., Eriş, K., Ryan, W.B.F., Sancar, Ü., Polonia, A., Akçer, S., Biltekin, D., Gasperini, L., Görür, N., Lericolais, G., Bard, E. 2009. Late Pleistocene-Holocene Evolution of the Northern Shelf of the Sea of Marmara. Marine Geology, 265, pp.87-100.

Çelik, G.B. 2007. Daily Life in Yenikapı. In: Kızıltan, Z. (Ed.), Istanbul: 8000 years brought to daylight; Marmaray, Metro, Sultanahmet excavations, pp.216-229. Vehbi Koç Foundation, ISBN 978-975-6959-39-8.

Folk, R. L., Ward, W. C. 1957. Brazos River Bar: a Study of Significance of Grain Size Parameters. Journal of Sedimentary Petrology 27, pp.3-26.

Gedik, İ., Aksay, A. 2002. 1:100 000 Ölçekli Türkiye Jeoloji Haritaları Adapazarı-G25 Paftası: Pafta No.32, Maden Tetkik Arama Enstitüsü Yayını, Ankara.

Gedik, İ., Pehlivan, Ş., Timur, E., Duru, M. 2005. 1:50 000 Ölçekli Türkiye Jeoloji Haritaları, No.12, İstanbul F23d Paftası, Maden Tetkik Arama Enstitüsü Yayını, Ankara.

Göktürk, O., Fleitmann, D., Badertscher, S., Cheng, H., Edwards, R., Leuenberger, M., Fankhauser, A., Tüysüz, O., Kramers, J. 2011. Climate on The Southern Black Sea Coast During The Holocene, Implications from The Sofular Cave Record. Quaternary Science Reviews, pp.1-13.

Hooton, D.H., Giorgetta, N.E. 1977. Quantitative X-Ray Diffraction Analysis by a Direct Calculation Method. X-Ray Spectrum. V.6, pp.2-5.

Kızıltan, Z. 2007. Marmaray Project and the 8000 Years of Istanbul "brought to daylight". In: Kızıltan, Z. (Ed.), Istanbul: 8000 years brought to daylight; Marmaray, Metro, Sultanahmet excavations, pp.18-27. Vehbi Koç Foundation, ISBN 978-975-6959-39-8.

Kızıltan, Z. 2010. Excavations at Yenikapı, Sirkeci and Üsküdar within Marmaray and Metro Project. . In Kocabaş,U (Ed.), Proceedings of the 1st Symposium on Marmaray-Metro Salvage Excavations, 5th– 6th May 2008, İstanbul, pp.1-17, Directorate of Istanbul Archaeological Museums, ISBN 978-605-60853-6-9.

Kızıltan, Z. 2014. Marmaray-Metro Projesi Kurtarma Kazıları: Yenikapı-Sirkeci ve Üsküdar İstasyonları Arkeoloji Çalışmaları ve İstanbul'un 8 Bin Yılı. In Ş. Baltaş, Ş. Altun (Eds.), Hayalden Gerçeğe Bir İstanbul Öyküsü-Marmaray, ISBN 978-605-64547-1-4, pp.54-76.

Kocabaş, U. 2010. Istanbul University Yenikapı shipwrecks project: ships. In Kocabaş,U (Ed.), Proceedings of the 1st Symposium on Marmaray-Metro Salvage 27 Excavations, 5th-6th May 2008, İstanbul, pp.23-35, Directorate of Istanbul Archaeological Museums, ISBN 978-605-60853-6-9.

Kocabaş, U. 2015. The Yenikapı Byzantine-Era Shipwrecks, Istanbul, Turkey: a preliminary report and inventory of the 27 wrecks studied by Istanbul University. The Int. J. of Nautical Archaeology, 44, 1, p.p5-38. doi: 10.1111/1095-9270.12084.

Kuniholm, P.I., Pearson, C.L., Wazny, T.J. 2014. Yenikapı ve diğer Marmaray Proje Alanlarında Dendrokronoloji Araştırmaları. Ş. Baltaş, Ş. Altun (Eds.), Hayalden Gerçeğe Bir İstanbul Öyküsü-Marmaray, pp.154-159. ISBN 978-605-64547-1-4.

Kuniholm, P.I., Pearson, C.L., Wazny, T.J., Griggs, C.B. 2015. Of Harbors and Trees: The Marmaray Contribution to a 2367-Year Oak-Tree-Ring Chronology from 97 Sites for the Aegean, East Mediterranean, and Black Seas . Ancient Near Eastern Studies, Supplement Series V. 47, pp.47-90, ISBN: 978-90-429-3062-9.

Lambeck, K., Antonioli, F., Purcell, A., Silenzi, S. 2004. Sea-Level Change Along The Italian Coast for The Past 10.000 yr. Quaternary Science Reviews 23, pp.1567-1598.

Marriner, N., Morhange, C. 2006. The 'Ancient Harbor Parasequence': anthropogenic forcing of the stratigraphic highstand record. Sedimentary Geology 186, pp.13–17.

Marriner, N., Morhange, C. 2007. Geoscience of ancient Mediterranean harbors. Earth-Science Reviews 80, pp.137–194.

Marriner, N., Morhange, C., Carayon, N. 2008. Ancient Tyre and its harbors: 5000 years of human–environment interactions. Journal of Archaeological Science 35, pp.1281–1310.

Marriner, N., Morhange, C., Goiran, J.P. 2010. Coastal and ancient harbor geoarchaeology. Geology Today 26 (1), pp.21–27.

Meriç, E., Perinçek, D., Avşar, N., Nazik, A., Yücesoy-Eryılmaz, F., Barut, İ., F., Dinçer, F. 2009. Yenikapı Eski Kıyılarında 5-12. Yüzyıllar Arasındaki Çevre Kirliliğinin Bentik Foraminiferlerle Belirlenmesi. Türkiye Petrol Jeologları Derneği Bülteni 21, Sayı 1, No.1, pp.1-22.

Murray, J. W. 1973. Distribution and Ecology of Living Benthic Foraminiferids, Crane Russak and Co, 247p., New York.

Nichols, G. 1999. Sedimentology and Stratigraphy. Blackwell Science Ltd, 355p.

Pearson, C., L., Griggs, C., B., Kunıholm, P.I., Brewer, P., W., Wazny, T., Canady, L. 2012. Dendroarchaeology of the Mid-First Millennium AD in Constantinople. Journal of Archaeological Science, 39, pp.3402-3414.

Perinçek, D. 2008. Yenikapı Antik Liman Kazılarıda Jeoarkeloji Çalışmaları ve Doğal Afetlerin Jeolojik Kesitteki İzleri. 1. Ulusal Doğal Afetler ve Yerbilimleri Sempozyumu Bildiriler Kitabı, pp.31-49, Sakarya.

Perinçek, D. 2010a. Geoarchaeology of the excavation site for the last 8000 years and traces of natural catastrophes in the geological profile. In: Kocabaş, U. (Ed.), Proceedings of the 1st Symposium on Marmaray-Metro Salvage Excavations, 5th–6th May 2008, Istanbul, pp.191–219, Directorate of Istanbul Archaeological Museums, ISBN 978-605-60853-6-9.

Perinçek, D. 2010b. The geoarcheology of the Yenikapı excavation site in the last 8000 years and geological traces of natural disasters (Istanbul - Turkey). Bull.Min.Res.Exp., 141, pp.69-92.

Perinçek, D., Meriç, E., Pulak, C., Körpe, R., Yalçıner, A.C., Gökçay, M., Avşar, N., Nazik, A., Kozanlı, C., Kapan-Yeşilyurt, S., Gökgöz, Z. 2007. Yenikapı Antik Liman Kazılarında Jeoarkeoloji Çalışmaları ve Yeni Bulgular. Türkiye Jeoloji Kurultayı, 60, pp.16–22. April 2007, Ankara.

Pulak, C., Ingram, R., Jones, M., Matthews, S. 2015. Eight Byzantine Shipwrecks from the Theodosian Harbour Excavations at Yenikapı in Istanbul, Turkey: an introduction. Int. J. of Nautical Archaeology, 44, 1, pp.39–73. doi: 10.1111/1095-9270.12083.

Sayar, C. 1977. İstanbul Yeni İskan Yöreleri Geoteknik ve Sismik Etüdü. Boğaziçi Üniversitesi, Deprem Mühendisliği Araştırma Enstitüsü Raporu, Cilt 1., 119p.

Spencer, D.W. 1963. The interpretation of grain size distribution curves of clastic sediments. Journal of Sedimentary Petrology, 33, 1, pp.180-190.

Yanko, V.V. 1990. Stratigraphy and paleogeography of marine Pleistocene and Holocene deposits of the Northern seas of the USSR, Memorie della Societa Geologica Italiana 44:167-187.

Yalçın, M., N., Sezerer, M., Pearson, C., L., Algan, O., Kuniholm, P. 2013. Establishment of a High-Resolution Stratigraphy with the Help of Dendrochronology: An Example From The Marine Holocene Sequence in The Ancient Thedosian Harbor (Istanbul, Turkey), Geological Society of America Abstracts With Programs, Vol.45, No.7 (Abstract).

Yalçın, M.N., Bulkan, Ö., Algan, O., Konak, A. 2015. A Holocene aged swamp area in Yenikapı-Istanbul and it's relation with the neighboring Neolithic settlement. Ancient Near Eastern Studies, Supplement Series V. 47, pp.31-46, ISBN: 978-90-429-3062-9.

Yalçın, M.N., Sezerer Bulut, M., Pearson, C., Kuniholm, P., Algan, O., Wazny, T. 2019. Establishing a high-resolution stratigraphy in the Holocene marine sequence of the ancient Theodosian harbor of Istanbul with the help of dendrochronology, Geoarchaeology, 34:360–374.

Bulletin of the Mineral Research and Exploration

Paleoenvironmental features and ostracod investigation of Paleogene-Neogene sequences in Babaeski-Lüleburgaz- Muratlı-Çorlu region (Southeastern Thrace, Turkey)

Ümit ŞAFAK[a*]

[a]Çukurova University, Faculty of Engineering and Architecture, Department of Geology Engineering, Adana.

Research Article

ABSTRACT

Aim of the study is to evaluate the Paleogene-Neogene sequences of Babaeski- Lüleburgaz-Muratlı-Çorlu (Southeastern Thrace, Turkey) region using the micropaleontological analysis on two borehole samples collected by Mineral Research and Exploration (MTA), measured sections and point samples taken from the neighborhood of Silivri, Türkmenli-Çorlu, Babaeski-Lüleburgaz, Edirne –Babaeski regions and Tekirdağ-Hayrabolu road. There the lignite sandstone, siltstone (Early Oligocene aged Danişmen Formation) and silts (Late Miocene-Pliocene aged Ergene Formation) with well-preserved ostracod fauna obtained from the the upper levels of the sequence along with some micro-Mollusca at some levels. The study results showed that lacustrine and lagoonal ostracods including marine species were generally found in the claystone, siltstone and marl of the lower and upper levels of lignite cuts in borehole. The ostracod assemblages identified in the study were compared with other ostracod studies in the Thrace Basin and other parts of Turkey as well as in the Oligocene in Paris, the Akiten Basin, Belgium. In the Early Oligocene sediments, the presence of the Tethys effect was observed in the investigated area. In addition, the ostracod species defined in the Late Miocene-Pliocene are compared with other ostracod studies carried out in the Thrace Basin and other parts of Turkey as well as in the Western and Eastern Carpathians, Caspian Basin and Baltic Sea. According to obtained fauna, the Paratethys effect was determined more than in Tethys in Late Miocene-Pliocene in the studied region.

1. Introduction

In the southeast of Thrace Basin, this research, which is mainly used from Tertiary (Paleogene-Neogene) stratigraphy, ostracod assemblage is as follows; the study was conducted in the neighborhood of Çorlu-Muratlı-Lüleburgaz-Babaeski region in southeastern Thrace (Figure 1). The aim of this study is to identify the micropaleontological features and an environmental condition of the Paleogene-Neogene rocks of the Çorlu-Muratlı-Lüleburgaz-Babaeski-Malkara and Silivri regions. For this purpose, a detailed micropaleontological study was

accomplished in the regions above. During this study, twenty three of the ostracod samples were taken from the Danişmen Formation and five of them were taken from the Ergene Formation. In this study, species found in the Oligocene include ostracods *Neocyprideis apostolescui*, *N. williamsoniana*, *Cladarocythere apostolescui*, *Cytheromorpha zinndorfi*, *Hemicyprideis elongata*, *H. helvetica*, *H. montosa*, *Cytheridea crassa*, *C. pernota*, *Sphenocytheridea gracilis*, *Serrocytheridea eberti*, *Krithe angusta*, *Cushmanidea scrobiculata*, *Loxoconcha* sp.1, *Loxocorniculum decorata*, *Hirschmannia* sp., *Candona* (*Lineocypris*) sp., *Candona* (*Pseudocandona*) sp., *Candona*

Figure 1- Location of measured sections from study area (Google earth, 2018).

(*Pseudocandona*) *fertilis, Ilyocypris cranmorensis, I. boehli, Virgatocypris tenuistriata, Novocypris striata, Verticypris jacksoni, Cypridopsis soyeri* and *Eucypris pechelbronnensis*; gastropods; and micro-pelecypods (*Valvata, Viviparus* and *Avimactra*). In addition, *Eucypris dulcifons, Heterocypris salina, Ilyocypris bradyi,* and *Candona* (*Caspiocypris*) *alta*, they were identified in between Late Miocene–Pliocene.

2. Material and Methods

During the study, measured sections, spot samples and washed cutting samples of the two boreholes completed by the Mineral Research and Exploration General Directorate were taken from the most important unit of the area, the Danişmen Formation and the unconformably overlying Ergene Formation. A total of 22 ostracod genera and 28 ostracod species were identified in the sections, spot samples and drilling samples from 153 washed samples.

The study was conducted on measured sections in Bıyıkali, Beşer Tuğla, Silivri Sahil, Malkara-Tekirdağ and Silivri-Değirmenköy regions selected from 1:25000-scale E19c4, F17b2, F17b4, F18c3, F18c4, F19c4, F20d3, F20d4, G17b1, G18a1, and G18b1 map areas; 2 borehole samples and spot samples

from outcrops at different localities (Figure1). During all the sampling, particular attention was given to layers with fossils and lithology types. The washing method was used for a total of 153 samples taken from the measured sections, spot samples and drilling samples for that reason. Samples were disaggregated in the laboratory in order to obtain loose Ostracoda specimens. Hard samples and samples with medium hardness samples were split into 150 g. batches and wrapped with thick paper for being crushed by using a rock hammer. Crushed samples were then placed into 1 L glass beakers and treated with hot water and 15% diluted hydrogen peroxide (H_2O_2) for at least 24 hours. Disaggregated residues were later washed over a mesh of 0.60,0.120, and 0.230 mm sieves, and placed in sample bags upon oven drying. Following the separation of microfossils from grains, Ostracoda were placed on slides for identification of genera and species. Identified Ostracoda genera and species were counted in order to determine their lateral and vertical distribution and abundance**.** Finally, the Ostracoda genera and species contents of each sample were determined (Morkhoven, 1963; Witt, 2003, 2011; Freels, 1980; Esteoulle-Choux et al., 1986; Rückert-Ülkümen et al., 2009; Meisch, 2000) and Hartmann and Puri (1974) systematic has been used.

Plate 1, 2, 3 and 4 were prepared from the selected (Scanning Electron Microscope) SEM images of different Ostracoda genera, species and Mollusca genera.

The paleogeographical environment datas of this study were determined by using the statistical results which identified ostracoda genera and species evaluated in order to determine their lateral and vertical distribution and abundance. The frequency table of ostracode species modified from Sissingh (1972) and correlative interpretation of these data as well as the salinity criteria of Remane, 1958; Morkhoven, 1963; Freels 1980; Athersuch et al., 1989; Witt, 2011; Rückert-Ülkümen et al., 2009. In particular, mollusc genera compatible with lacustrine conditions were described based on the studies of Taner, 1980; Bremer, 1978; Sayar, 1991; Wenz, 1922.

3. Geological Setting

The Thrace Basin is surrounded by the Istranca Massif in the north, the Rhodope massif in the west, and the Menderes Massif in the south (Figure 1). The Istranca massif is composed of gneisses and metamorphosed Paleozoic and Mesozoic sedimentary rocks on the greenschist facies that overlies it (Üşümezsoy, 1982; Taner and Çağatay, 1983). The sedimentary rocks that form the basement of the massif are affected by the Upper Cretaceous granodiorite rocks and are covered by an Upper Cretaceous volcano-sedimentary unit (Perinçek et al., 2015).

The basement in the study area and surroundings (Çorlu-Babaeski-Lüleburgaz-Silivri) is made up of the Istranca metagranite (Figure 2). It is overlain unconformably by cover sediments of the Paleogene (MTA Stratigraphy Committee Lithostratigraphy Unit Series, 2006; Siyako, 2006b; Siyako and Huvaz, 2007; Şafak and Güldürek, 2016a,b).

Miocene and later units cover the Eocene-Oligocene sequence in the Central and Northern Thrace. Öztunalı and Üşümezsoy (1979) reported that Taner and Çağatay, 1983 had studied granitic rocks in the southern slope of the Istranca Massif. Miocene and later units in Central and Northern Thrace cover the Eocene-Oligocene sequence. Siyako (2006b) suggested that the lithostratigraphic roof of the Thrace Basin can be established using the data obtained from

southern Thrace, Gökçeada, Bozcaada and Gallipoli Peninsula and the seismic sections and exploration wells in North Thrace. A clear description has yet to be given for the Eocene-Oligocene deposits belonging to the outcrops of the Thrace Basin in the Armutlu Peninsula (Akartuna, 1968), between Mudanya and Trilye in the Biga Peninsula (Siyako et al., 1989) in the south of the Marmara Sea, which shows the southern border of the Thrace Basin.

The basin sedimentation probably started as a transgressive sequence during the Early Eocene (Saner, 1985; Turgut and et al., 1983; Doust and Arıkan, 1974; Keskin, 1974). A metamorphic complex presents the foundation of the basin. The Strandja Mountains are 9,000 meters in thickness, starting from the southern skirts and extending to cover almost all of the Thrace (Figure 1) (Perinçek et al., 2011; Siyako, 2006a,b; Siyako, 2005; Görür and Okay, 1996; Turgut and Eseller, 2000; Turgut et al., 1991; Kopp et al., 1969; Perinçek, 1987).

The Paleogene-Neogene units of Thrace are generally composed of clastic rocks but also contain carbonates in the shelf areas and on the ridge and peaks in the middle of the basin. These units were deposited in basins in seven separate time periods, with significant phases of uplift and erosion (Perinçek et al., 2015). The sedimentation in the central part of the basin is partly continuous and in some parts, discontinuities and erosion phases can be observed. The basin floods very quickly and is filled up as it sinks. Turgut et al. (1983) and Keskin (1974) reported that Eocene transgression reached maximum levels in the Early Oligocene as carbonates were deposited at the northern shelf and at the Kuleli - Babaeski elevation, while the deep parts of the basin were filled with turbidity currents in the Middle Eocene - Early Oligocene. Turgut et al. (1983) observed that the Thrace Basin was influenced by delta system formed by a great river, with submarine fans having been formed accordingly.

Keskin (1974), Ediger (1982, 1988), Turgut et al. (1983) and Saner (1985) reported that the regression period of the Eocene transgression occurred in between Middle Oligocene-Lower Miocene stage interval. The terrestrial palynofacies of the Late Miocene-Early Pliocene of the Ergene and Kırcasalih formations were reported by Ediger (1982) to have been deposited after a sedimentation in the Middle Miocene. It has also

Figure columns (left to right): UPPER SYSTEM | SYSTEM | SERIES | STAGE | GROUP | FORMATION | MEMBER | LITOLOGY | (lithology labels) | Ostracoda species

CENOZOIC

System	Series	Stage	Group	Formation	Member	Lithology
NEOGENE	Quaternary (Holocene)				Kırcasalih	alluvium / conglomerate clay
	Quaternary (Pleistocene)					basalt
	Late Miocene-Pliocene	Tortonian-Messinian		ERGENE	Karatepe bazaltı	
					Sinanlı	lacustrine limestone
				Çelebi		clayey limestone / sandstone
				Çantaköy		siltstone / tuff
PALEOGENE	OLIGOCENE	Rupelian-Stampian	Yeni muhacir	Danişmen	Armutburnu	lignite
					Pınarhisar	lignite / clayey limestone / sandstone / marl
					Taşlı sekban	marl
				Mezardere	Osmancık	siltstone
					Teslimköy	sandstone / marl
	EOCENE	Lutetian-Priabonian		Osmancık		sandstone
				Ceylan	Soğucak / Koyunbaba	reefal limestone

Left vertical labels: Paleo-Meso.

Ostracoda species:

Eucypris dulficons Diebel ve Pietrzeniuk
Ilyocypris bradyi (Norman)
Candona (Caspiocypris) alta (Zalanyi)
Candona (Caspiolla) sp.
Cladarocythere apostolescui (Margerie)
Neocyprideis williamsoniana (Bosquet)
Neocyprideis apostolescui (Margerie)
Hemicyprideis montosa (Jones and Sherborn)
Hemicyprideis elongata (Keen)
Hemicyprideis helvetica (Lienenklaus)
Candona (Pseudocandona) fertilis (Lienenklaus)
Candona (Pseudocandona) sp.
Candona (Lineocypris) sp.
Candona sp.
Cytheridea pernota (Margerie)
Cytheridea crassa Terquem
Serrocytheridea eberti (Lienenklaus)
Cytheromorpha zinndorfi (Lienenklaus)
Cytheridea pernota Oertli and Keij
Cytheromorpha sp.
Cushmanidea cf. *scrobiculata* Lienenklaus
Loxocorniculum decorata Lienenklaus
Cytheropteron sp.
Ilyocypris boehli Triebel
Ilyocypris cranmorensis Keen
Hirchmannia sp.
Loxoconcha sp.1 Sönmez-Gökçen
Sphenocytheridea gracilis Keij
Cypria sp.
Heterocypris salina (Bradyi)
Krithe angusta Brady ve Norman
Eucypris pechelbronnensis Stchepinsky
Novocypris striata Guernet
Cypridopsis soyeri (Margerie)
Cypridopsis modesta Sönmez-Gökçen
Virgatocypris tenuistriata (Dollfus)
Verticypris jacksoni Keen

Candona (Pseudo candona) fertilis

Loxoconcha sp.
Candona (Pseudo candona) fertilis

Figure 2- Generalized measured section of the study area.

been observed that the Late Miocene, Early Pliocene - Pleistocene units, which developed after subduction in the Middle Miocene, are a sedimentary products that followed the subduction phase, with a less obvious discrepancy being observed between Late Miocene and Pliocene (Perinçek et al., 2015).

The basin is an area where intensive geological investigations have been carried out on account of the lignite it contains. Some of the major studies that have been conducted on this issue in the Thrace Basin include those by Lebküchner (1974), Perinçek et al. (2011), Sütçü et al. (2009), Rückert-Ülkümen

et al. (2009), Şengüler et al. (2000), İslamoğlu et al. (2008), Kara et al. (1996), Şengüler et al. (2003), Şengüler (2008, 2013), Atalay (2002), Perinçek et al. (2015) and Şafak and Güldürek (2016*a,b*), together with the study of a regional geology team, determined the fossil coverage and age of the lignite sandstone formation unit. Furthermore, Kara (1996) reported the general geology of the province and the important coal lands in the Thrace Basin, while Şengüler et al. (2000) conducted a study on the coal deposits and the samples taken from coal mined in Keşan, Malkara and Uzunköprü.

In a separate study by Şengüler (2008), an investigation of the Thrace Basin coals was carried out, and in addition to providing a description of their characteristics, it was determined that coals of the Thrace Basin had been deposited in the delta marshes of the lacustrine environments of the coals. While the rate of the collapse of the product is high, there is excessive sediment thickness, making the correlation of the coal veins difficult. Another study conducted by Şengüler (2013) showed that the environmental conditions of the river were optimal during the settlement of the Danişmen Formation and therefore prevented lignite sedimentation.

4. Paleostratigraphical Results

4.1. Stratigraphy

Units exposed in the study area from base to top are Danişmen Formation, Çantaköy Formation, Ergene Formation, Kırcasalih Formation and alluvium.

The Danişmen Formation is widely exposed in the study area and it is the top unit of the regressive delta system that begins with the Mezardere Formation. The formation consists of Taşlısekban, Pınarhisar and Armutburnu members. The Çantaköy Formation overlies the Danişmen Formation unconformably and it is expressed by siltstone and tuffs.

In this study, the average thickness of the units was measured as 200 m.

In this study the Danişmen Formation contains ostracod species such as *Cytheromorpha zinndorfi* (Lienenklaus) from family Cytheridea; *Cladarocythere apostolescui* (Margerie) from family Limnocytheridae; *N. williamsoniana* (Bosquet),

Neocyprideis apostolescui (Keij), *Hemicyprideis helvetica* (Lienenklaus), *H. elongata* Keen, *H. montosa* (Jones & Sherborn), *Cytheridea crassa* Ducasse, *C. pernota* Oertli & Keij, *Sphenocytheridea gracilis* Keij and *Serrocytheridea eberti* (Lienenklaus) from family Cytherideidae; *Cushmanidea scrobiculata,* (Lienenklaus) from family Cuchmanideidae; *Krithe angusta* Deltel from family Krithidae; *Loxocorniculum decorata*, *Hirschmannia* sp., and *Loxoconcha* sp.1 Sönmez-Gökçen from family Loxoconchidae; *Candona (Lineocypris)* sp., *Candona (Pseudocandona)* sp., and *Candona (Pseudocandona) fertilis* Triebel from family Candonidae; *Novocypris striata Ilyocypris cranmorensis* Keen, and *I.boehli* Triebel from family Ilyocyprididae; *Verticypris jacksoni* Keen, *Virgatocypris tenuistriata* (Dollfus), and *Eucypris pechelbronnensis* Stchepinsky from family Cyprididae; and *Cypridopsis soyeri* (Margerie) from family Cypridopsidae. In addition, there are pelecypod and gastropod genera such as *Avimactra, Viviparus,* and *Valvata* of Oligocene age (Figure 2).

The Ergene Formation is widespread in the study areas, and it also has cross-layered conglomerate, sandstone containing abundant plant material, mudstone, and claystone. The formation is composed of Çelebi and Sinanlı members and is overlied by Karatepe volcanics.The thickness is approximately 50 m as obtained in this study.

The samples from the Ergene Formation contain ostracod assemblages dominated by *Candona (Caspiocypris) alta* Zalanyi from family Candonidae, *Ilyocypris bradyi* Sars from family Ilyocyprididae, *Eucypris dulcifons* Diebel & Pietrzenuik, and *Heterocypris salina* (Brady) from family Cyprididae. These ostracod species indicate Late Miocene–Pliocene age. Kırcasalih Formation contains conglomerate, clay and overlies the Ergene Formation uncomformably.

4.1.1. Measured Stratigraphic Sections, Boreholes And Their Ostracod Contents

Bıyıkali measured section (Tekirdağ-Hayrabolu way): Scale layouts used were taken from the 1:25000 map area F18-c4, beginning with coordinates X_1: 533558.16 E, Y_1: 4541547.36, N Z_1: 226 m and finishing with coordinates X_2: 533561.93 E, Y_2: 4540723.42 N, Z_2: 255 m. From the 35 m thick measured section ten samples were taken for washing. The section consists

of yellowish siltstone, sandstone, and claystone. In the section of the Danişmen Formation, following ostracod species *Cytheromorpha zinndorfi* (samples 1, 7, 10); *Neocyprideis apostolescui* (sample 5); *Hemicyprideis montosa* (samples 2, 6, 7); *Cytheridea pernota* (samples 1, 6 ,10); and *Serrocytheridea eberti* (samples 6,7) were identified. In accordance with the identified ostracod fauna, age is determined as Rupelian/Stampian (Figure 3).

Beşer Tuğla measured section: Scale layouts used were taken from the 1:25000 map area G18b1, beginning with coordinates X1:526628.13 E, Y1: 4533404 N, Z_1: 216 m and finishing with coordinates X2:526490.57 N, Y2: 4535116.81 N, Z_2: 115 m. Five washed samples were taken from the measured section, which is 22 m thick. The well-known Mezardere (No.1) clay is at the base of the section and shows concretion and lamination features. There are siltstone beds containing sandstone interbeds in this unit. The succession continues upward with sandstone.

The section is represented by *Loxoconha* sp. and *Candona (Pseudocandona)* sp. (rare) in sample 1; *Cladarocythere apostolescui* and *Neocyprideis williamsoniana* (rare), *Cytheridea pernota* and *Candona (Pseudocandona)* sp. (common), and *Hemicyprideis montosa* and *Ilyocypris boehli* (very common) in sample 2; *Cytheridea pernota* (very rare) in sample 3; and *Loxoconcha* sp.1 Sönmez-Gökçen (common) in sample 4 (Figure 4).

Silivri coast measured section: Scale layouts used were taken from the 1:25000 map area F20-d3, beginning with coordinates X1:604945.43 E, Y_1: 4547371.95 N, Z_1: 97 m and finishing with coordinates X_2: 604128.86 E, Y_2: 4547360.30 N, Z_2: 122 m. Three samples were taken from the 28 m thick measured section. The section is dominated by yellowish, leaf-tracked, lignite-veined sandstone. Sample 2 taken from the lignite sandstone contains *Cladarocythere apostolescui* (common), *Hemicyprideis montosa* (frequent), *Eucypris pechelbronnensis, H. elongata, Candona (Pseudocandona)* sp., *Candona (Pseudocandona) fertilis* Triebel (rare). *Hemicyprideis montosa* (very rare) is both observed in the samples 2, 3 are observed in the study area (Figure 5).

Malkara-Tekirdağ measured section (Malkara Surface Mining): Scale layouts used were taken from the

1:25000 map area G17-b1, beginning with coordinates X_1:458312.02 E, Y_1: 4534233.48 N, Z_1: 134 m and finishing with X_2: 488382.20 E, Y_2. 4534264.20 N, Z_2: 115 m. Eight washed samples were taken from the 70 m thick measured section. The section was measured from beginning to top.

Sample 1, taken from the carbonate, includes abundant silicified wood fossils and contains very rare *Cytheridea pernota, Hemicyprideis montosa, H. elongata,* and rare *Cushmanidea scrobiculata.* Claystone with the sample number 2 contains, contains rare *Cytheromorpha zinndorfi* and very rare *Cushmanidea scrobiculata* and *Krithe angusta.* Sample 3, which was taken from caesious siltstone, contains rare *Cytheridea pernota.* Sample 4, from the claystone, includes very common *Hemicyprideis montosa* and very rare *Hemicyprideis elongata.* Sample 5 contains very rare *Sphenocytheridea gracilis* and rare *Krithe angusta.* Samples 6, 7, and 8, were taken from the bottom of the section, contain rare to common *Cytheromorpha zinndorfi,* very rare to common *Serrocytheridea eberti,* rare to common *Cytheridea pernota,* common *Haplocytheridea helvetica,* very common *Hemicyprideis montosa,* very rare to common *Hemicyprideis elongate* (Figure 6).

Silivri-Değirmenköy measured section (western part of Silivri region): Scale layouts used were taken from the 1:25000 map area F20-d4, beginning with coordinates X_1:584992.95 E, Y_1: 4552551.85 N, Z_1: 157 m and finishing with coordinates X_2: 584952.24 E, Y_2: 4552613.53 N, Z_2: 210 m. Nine washed samples were taken from the measured section, which is 75 m thick. The section contains light-colored siltstone, tuffaceous siltstone, and sandstone. The fauna is composed of frequent to common *Cytheromorpha zinndorfi* in samples 2, 3, 5 and 7; common *Cytheromorpha* sp. in sample 6; frequent *Cytheridea pernota* in samples 4 and 7; very common *Hemicyprideis montosa* in samples 2, 3, 4, 5 and 7; common *Cushmanidea scrobiculata* in samples 2 and 5; common *Loxocorniculum decorata* and *Cytheropteron* sp. in samples 2 and 3; rare *Candona (Caspiocypris) alta, Candona (Caspiolla)* sp., and *Heterocypris salina* in sample 9 from the Ergene Formation (Figure 7).

TB-57 (Hacısungur) drilling log: This drilling was carried out at coordinates X: 4538398, Y: 501100 and
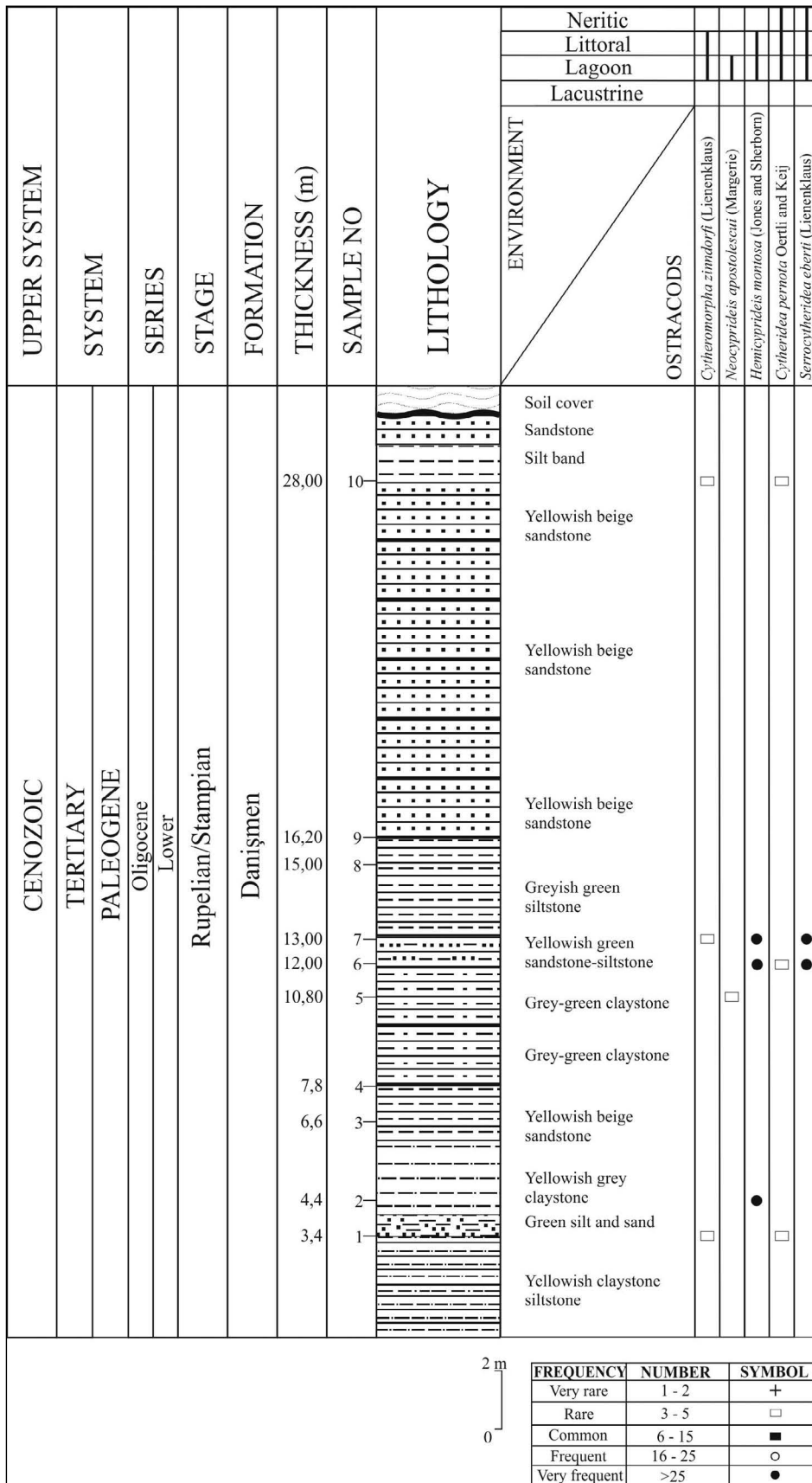
Figure 3- The distribution of ostracod species in Bıyıkali measured section.
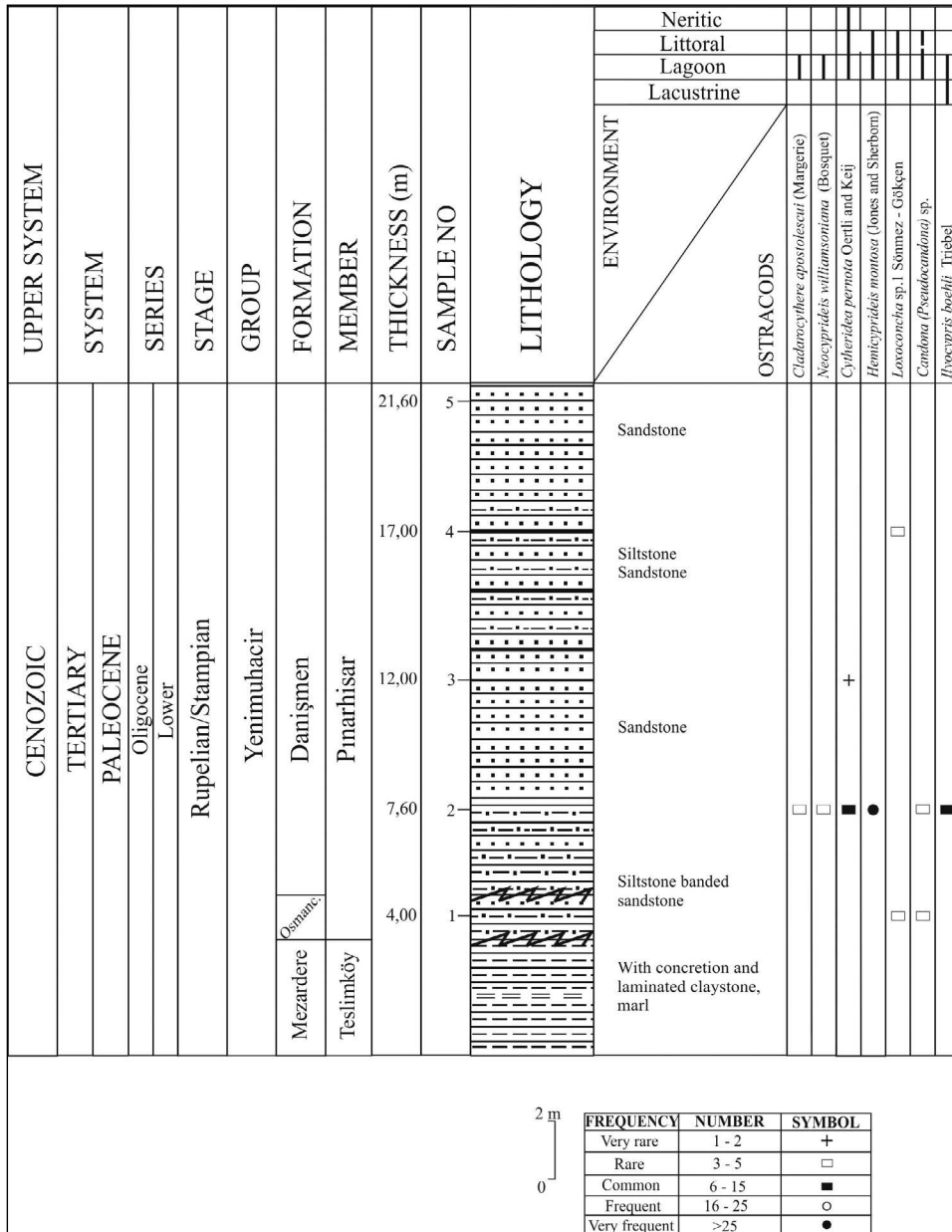
Figure 4- The distribution of ostracod species in Beşer Tuğla measured section.

Z: 134 m of 1:25000 map area G18-a1. Drilling depth is 557 m, and 90 wash samples were taken from the drilling log. The borehole penetrated the Danişmen and Ergene formations. The Danişmen Formation and its Pınarhisar Member were drilled from the depth 557 m. to 11.50m.

Only 11.50 m of the Ergene Formation and Çelebi Member were cut in borehole.

Ostracod species and genera obtained from the Danişmen Formation include *Neocyprideis*

apostolescui, *Neocyprideis williamsoniana*, *Hemicyprideis helvetica*, *Hemicyprideis montosa*, *Cytheromorpha zinndorfi***,** *Loxocorniculum decorata***,** *Hirchmannia* sp., *Candona (Lineocypris)* sp., *Candona (Pseudocandona)* sp*., Candona (Pseudocandona) fertilis*, *Verticypris jacksoni*, *Ilyocypris cranmorensis*, *Ilyocypris boehli*, *Virgatocypris tenuistriata*, *Cypridopsis soyeri*, and *Eucypris pechelbronnensis* (Figure 8).

TD- 58 drilling log: This borehole was located at coordinates X: 4538750, Y: 502300, and Z: 142 m
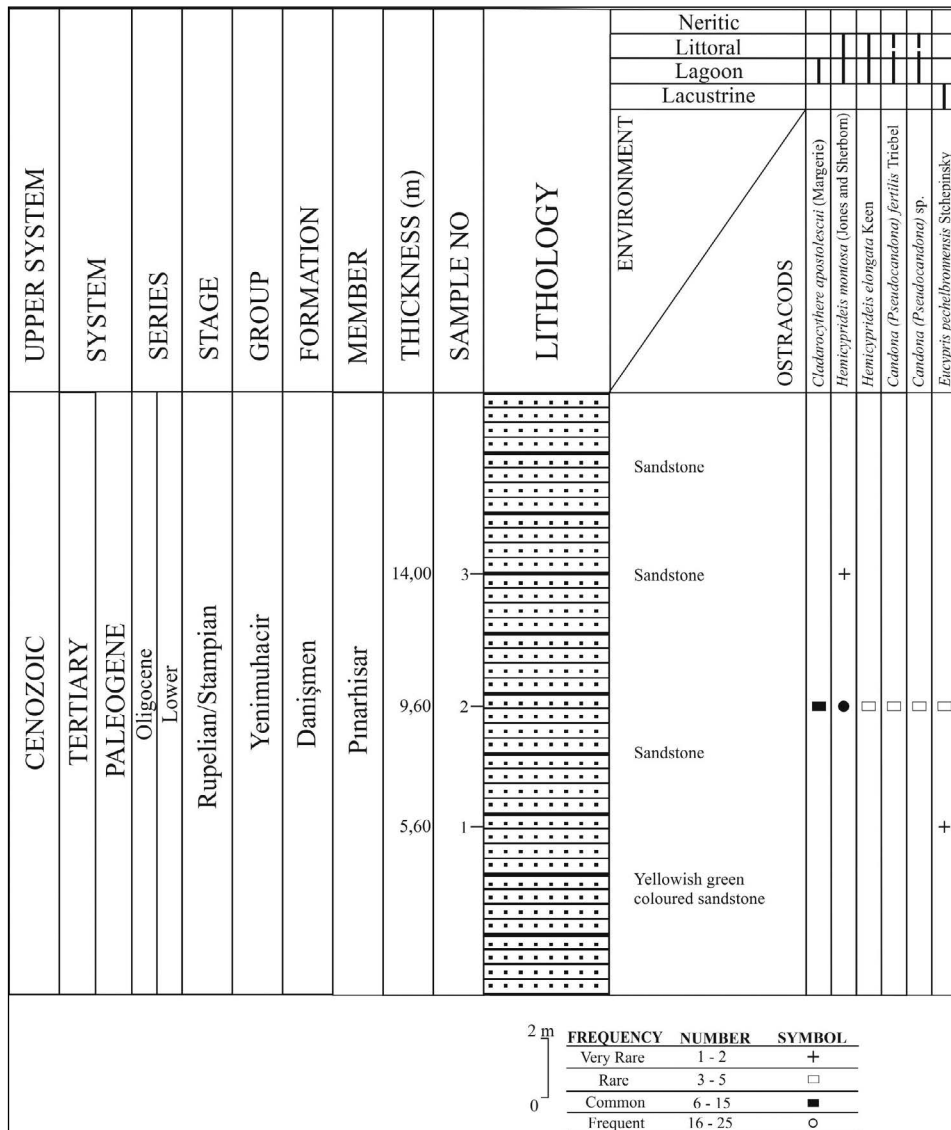
Figure 5- The distribution of ostracod species in Silivri measured section.

of 1:25000 map area G18-a1. Drilling depth was 47 m, and 16 wash samples were taken. In this borehole, the Ergene and Danişmen formations were cut. The upper 24.40 m penetrated the Ergene Formation, with Danişmen Formation from 24.40–46.30 m.

Ostracod genera and species found in this drilled section in the Ergene Formation were *Eucypris dulcifons*, *Ilyocypris bradyi*, and *Heterocypris salina*. Ostracod genera and species in the Danişmen Formation were *Cladarocythere apostolescui*, *Hemicyprideis montosa*, *Cytheridea pernota*, *Neocyprideis* a*postolescui*, *Serrocytheridea eberti*, *Candona (Pseudocandona)* sp., *Candona (Pseudocandona)*

fertilis, *Ilyocypris boehli*, and *Cypria* sp (Figure 9).

Lithological descriptions and fossil contents of spot samples: Two spot samples were taken from the clay unit along the Lüleburgaz–Babaeski road at map area F18-a₁ with coordinates X: 4586180, Y: 508038 and X: 4586074, Y: 516298. They contain *Candona (Caspiocypris) alta* and *Heterocypris salina* (Ergene Formation).

One spot sample was taken from the claystone unit along the Babaeski–Edirne road at F18-a₁ with coordinates X: 4593295, Y: 497759, Z: 101 m. It also contains *Candona (Caspiocypris) alta* and *Heterocypris salina* (Ergene Formation).

Stratigraphic column — Malkara-Tekirdağ measured section

UPPER SYSTEM	SYSTEM	SERIES	STAGE	GROUP	FORMATION	MEMBER
CENOZOIC	TERTIARY	PALEOGENE (Oligocene, Lower)	Rupelian/Stampian	Yenimuhacir	Danişmen	Pınarhisar

Environment classes: Bathyal, Neritic, Littoral, Lagoon, Lacustrine

Ostracod species distribution:

Thickness (m)	Sample No	Lithology	Cytheromorpha zinndorfi (Lienenklaus)	Servocytheridea eberti (Lienenklaus)	Sphenocytheridea gracilis Keij	Cytheridea pernota Oertli and Keij	Haplocytheridea helvetica (Lienenklaus)	Hemicyprideis montosa (Jones and Sherborn)	Hemicyprideis elongata (Keen)	Cushmanidea scrobiculata Lienenklaus	Krithe angusta Brady and Norman
		Alluvium									
12,50	1	Carbonated claystone				+		+	+	□	
20,00	2	Claystone	□							+	+
30,00	3	Greyish green siltstone					□				
36,00	4	Yellowish beige coloured claystone						●	□		
40,00	5				+						□
		Fossiliferous greyish green siltstone									
60,00	6					+	□	●	+		□
67,50	7	Siltstone	□			○		●	○	+	+
75,00	8		■	○	○	○		■	●	○	■

FREQUENCY	NUMBER	SYMBOL
Very rare	1 - 2	+
Rare	3 - 5	□
Common	6 - 15	■
Frequent	16 - 25	○
Very frequent	>25	●

5 m / 0

Figure 6- The distribution of ostracod species in Malkara-Tekirdağ measured section.

Two spot samples were taken from the claystone and clay-silt unit along the Babaeski–Edirne road at F17-b$_2$ with coordinates X: 4590755, Y: 502277, Z: 79 m. They contain *Eucypris dulcifons* and *Ilyocypris bradyi* (Ergene Formation).

Three spot samples were taken from the claystone unit along the Babaeski–Lüleburgaz road at F18-a$_2$ with coordinates X: 4585760, Y: 519085, Z: 77 m. The *Cyprideis* sp., *Candona* (*Caspiocypris*) *alta*, and *Cypridopsis* sp. were observed in the samples (from the Ergene Formation).

One spot sample was taken from the sandstone-siltstone unit along the Tekirdağ–Hayrabolu road at F18-c$_3$ with coordinates X: 4540670, Y: 539937, Z: 200 m. The sample contains *Hemicyprideis montosa*, *Cytheridea pernota*, and *Cypria* sp. (from the Danişmen Formation).

Figure 7- The distribution of ostracod species in Silivri-Değirmenköy measured section.

One spot sample was taken at Türkmenli Village, F18-c$_4$ with coordinates X: 4543542, Y: 570530, Z: 125 m. It contains *Hemicyprideis montosa* and *Candona (Pseudocandona) fertilis* (from the Danişmen Formation).

One spot sample was taken from the sandy pebble unit at Çiftlikköy at F20-d$_4$ with coordinates X: 4553023, Y: 589258, Z: 228 m. It contains *Heterocypris* sp. (from the Ergene Formation).

One spot sample was taken from the sandstone at İbribey, G18-a$_2$ with coordinates X: 4534500, y: 510640, Z: 206 m. It was barren.

Two spot samples were collected from conchoidal hard siltstone and claystone from the Barbaros-Nayip area at G18-b$_2$ with coordinates X1: 4525479, Y1: 534791/X2: 4525235, Y2: 534327 *Cladarocythere apostolescui* and *Cytheromorpha* sp. (from the Danişmen Formation) (Figure 10).
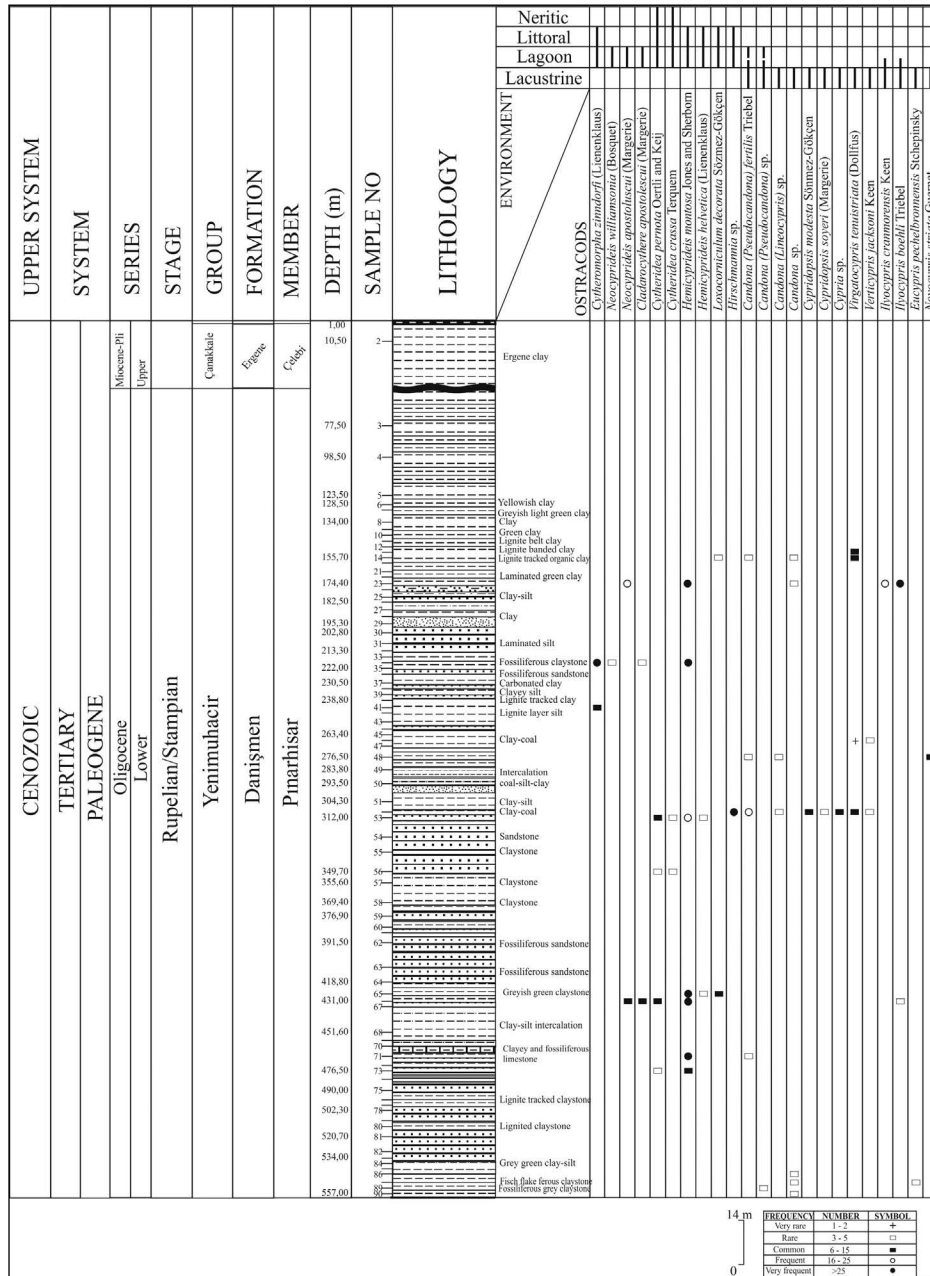
Figure 8-The distribution of ostracod species in Hacısungur (TB-57) drilling log.

5. Chronostratigraphical and Paleogeographical Distributions of Ostracoda

The ranges of the fossils observed in this study are as follows (Table 1): *Cytheromorpha zinndorfi* in Germany at the Rupelian–Aquitanian (Lienenklaus, 1905; Keij 1957); in Belgium at the Eocene (Keij, 1957); in France and Turkey at the Early Oligocene (Sönmez-Gökçen, 1973; Apostolescu, 1964; Gökçen, 1975; Estéoule et al., 1986; Şafak, 1997; Şafak and Güldürek, 2016a; Şafak,

2008; Şafak, 2016; Şafak, 2010a; Şafak et al., 2015; and Şafak and Güldürek, 2016b; and in Switzerland at the Oligocene (Oertli, 1956).

Neocyprideis apostolescui in England, France, and Turkey at the Middle Eocene (Şafak, 1990; Şafak, 2008; Şafak, 2010b; Şafak and Güldürek, 2016a,b; Şafak et al., 2015; Oertli, 1985; Haskins, 1969; Nazik, 1993; Şafak, 2010a; Şafak, 2016).

UPPER SYSTEM | SYSTEM | SERIES | STAGE | GROUP | FORMATION | MEMBER | DEPTH (m) | SAMPLE NO | LITHOLOGY | ENVIRONMENT | OSTRACODS

Environment categories: Neritic, Littoral, Lagoon, Lacustrine

Ostracod species:
- Cladarocythere apostolescui (Margerie)
- Neocyprideis apostolescui (Margerie)
- Hemicyprideis montosa (Jones and Sherborn)
- Cytheridea pernota Oertli and Keij
- Sermocytheridea eberti (Lienenklaus)
- Candona (Pseudocandona) fertilis Triebel
- Candona (Pseudocandona) sp.
- Ilyocypris boehli Triebel
- Cypria sp.
- Eucypris dulcifons Diebel and Pietrzeniuk
- Ilyocypris bradyi (Norman)
- Heterocypris salina (Brady)

CENOZOIC — TERTIARY

NEOGENE: Pliocene (Lower); Miocene, Upper, Tortonian/Messinian; Ergene Group; Çelebi Member — Claystone

PALEOGENE: Oligocene, Lower, Rupelian/Stampian, Yenimuhacir, Danişmen, Pınarhisar

Depth (m) / Sample No / Lithology:
- 0,5 / 1 / Claystone
- 6,0 / 2 / Claystone
- 3 / Claystone
- 16,00 / 4
- 18,00 / 5
- 20,00 / 6 / Claystone
- 22,60 / 7
- 24,40 / 8
- 27,00 / 9 / Greenish siltstone / Clay
- 29,00 / 10 / Greyish green claystone
- 31,20 / 11 / Clay
- 33,80 / 12 / Clay
- 36,00 / 13 / Clay
- 38,00 / 14 / Clay-silt
- 40,00 / 15
- 42,00 / 16 / Clay-silt
- Clay-silt

2,5 t

Figure 9- The distribution of ostracod species in TD-58 drilling log.

Neocyprideis williamsoniana in England and France at the Early Oligocene (Keen, 1972; Haskins, 1969; Oertli, 1985; Şafak, 1993; Şafak, 2008; Şafak, 2010a; Şafak, 2010b; Şafak et al., 2015; Şafak and Güldürek, 2016a,b; Şafak, 2016).

Cladarocythere apostolescui in England and Turkey at the Early Oligocene (Keen, 1972; Şafak and Güldürek, 2016a; Şafak et al., 2015; Şafak and Güldürek, 2016b; Şafak, 2016).

Cytheridea pernota in Romania, Hungary, France, England and Turkey at the Late Eocene–Early Oligocene (Jiricek, 1983; Monostori, 1983; Oertli, 1985; Keen, 1972; Şafak, 2010a; Şafak, 2008; Şafak et al., 2015; Şafak and Güldürek, 2016a,b; Şafak, 2016).
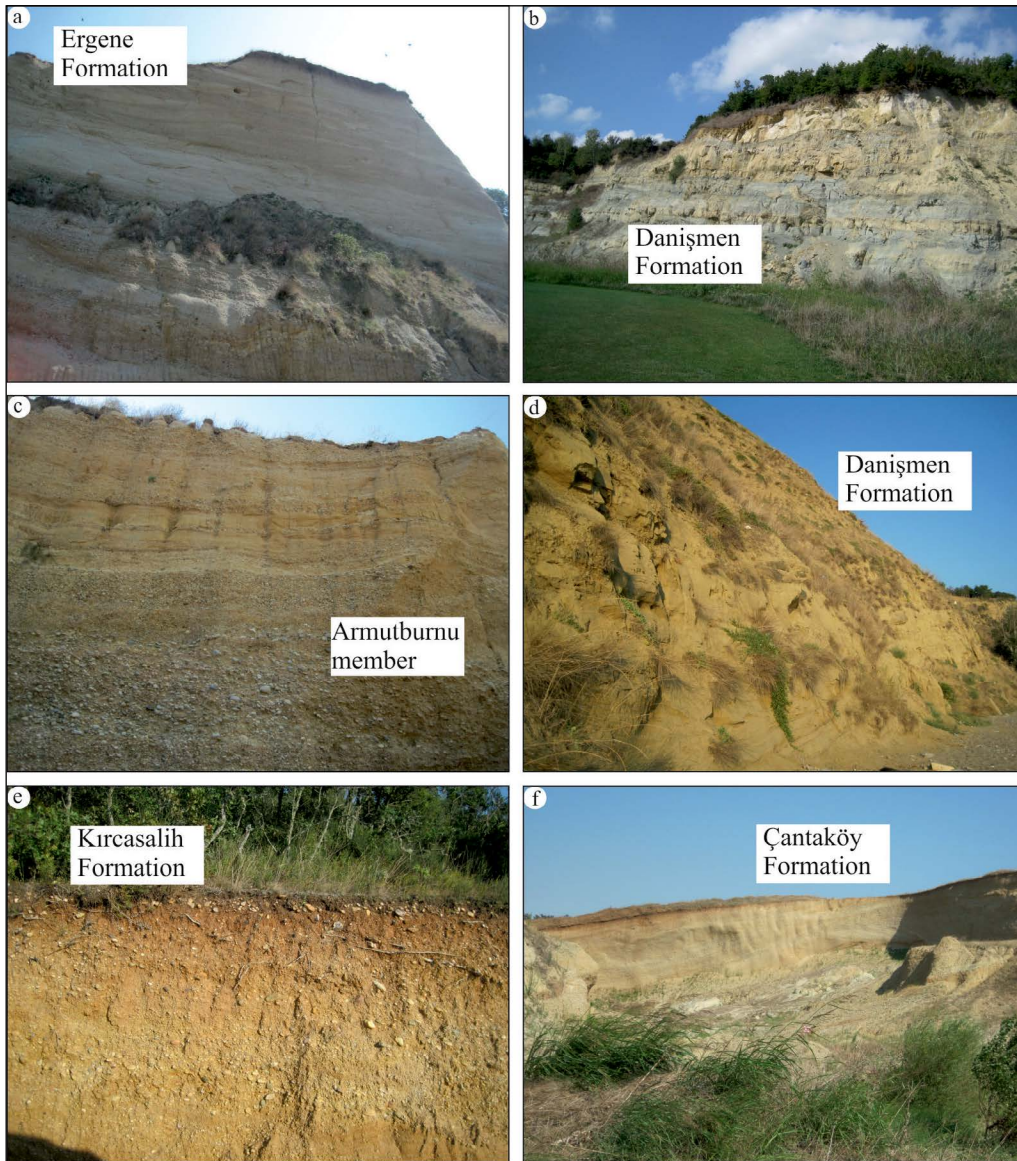
Figure 10- Outcrops of the studied formation.a. Çiftlikköy, Ergene; b. Bıyıkali village, Danişmen; c. Barbaros-Nayip area, Armutburnu-Danişmen; d. Silivri coast, Danişmen; e: Çorlu-Türkmenli village, Kırcasalih; f: Silivri-Değirmenköy-Çantaköy village, Çantaköy.

Cytheridea crassa in Turkey/Malatya at the Middle Eocene (Şafak, 1990) and in France/Aquitaine Basin at the Eocene (Oertli, 1985).

Serrocytheridea eberti in Germany at the late Oligocene (Colin and Carbonnel, 1992), at the Rupelian (Lienenklaus, 1894; Uffenorde and Radtke, 2008); in the Paris Basin at the Stampian (Oertli, 1985); and in France at the Aquitanian (Colin and Carbonnel, 1992); in Switzerland at the Rupelian-Chattian (Oertli, 1956); in Turkey/Thrace at the Sannoisian, at the Oligocene (Sönmez-Gökçen, 1973; Witt, 2011)

Sphenocytheridea gracilis in the Paris Basin at the Lutetian (Keij, 1957, Oertli, 1985)

Haplocytheridea helvetica in Switzerland at the Rupelian–Chattian (Oertli, 1956); in Germany at the Chattian (Goerlich, 1953); in western Europe at the Oligocene (Oertli and Key, 1955); in Belgium at the Tongrian–Rupelian (Keij, 1957); in Holland at the Tongrian (Keij, 1957); in China/Tarim Basin at the Late Eocene (Bosboom et al., 2011); in Turkey/Thrace at the Sannoisian (Sönmez-Gökçen, 1973);

Table 1- The correlation of ostracod species span in Eocene-Oligocene-Pliocene sediments in Turkey with other European basins.

OSTRACOD SPECIES	EOCENE			OLIGOCENE		MIOCENE			PL.	QUA.
	LOWER	MIDDLE	UPPER	LOWER	UPPER	LOWER	MIDDLE	UPPER		
Cytheromorpha zinndorfi (Lienenklaus)			€€€	+++ *** ### $$$	$$$					
Neocyprideis apostolescui (Margerie)		ééé *** ###								
Neocyprideis williamsoniana (Bosquet)				ééé ***						
Cladarocythere apostolescui (Bosquet)			ééé ###	ééé ###						
Cytheridea pernota Oertli and Keij			ééé *** <<< >>> ###	ééé *** <<< >>> ###						
Cytheridea crassa Terquem	***	*** ###	***							
Serrocytheridea eberti (Lienenklaus)				+++ $$$ ###	+++ $$$ ###					
Sphenocytheridea gracilis Keij		***								
Haplocytheridea helvetica (Lienenklaus)			^^^	OOO €€€ !!! $$$ ###	+++ OOO $$$ ###					
Hemicyprideis montosa (Jones and Sherborn)				ééé *** ###						
Hemicyprideis elongata (Keen)				ééé *** ###						
Hemicyprideis helvetica (Lienenklaus)				ééé *** ###	### >>>					
Loxocorniculum decorata Sönmez-Gökçen				###						
Ilyocypris boehli Triebel				ééé ###	###					
Ilyocypris bradyi (Norman)						QQQ ??? AAA JJJ	QQQ ??? AAA JJJ	QQQ ??? AAA JJJ ###	###	###
Ilyocypris cranmorensis Keen				ééé						
Novocypris striata Guernet	***	***	***	###	###					

Germany	+++	Lienenklaus, 1896, 1905; Goerlich, 1953; Keij, 1957; Carbonel ve Ritzkovski, 1969
France	***	Apostolescu, 1964; Estéoulle et al., 1986
Belgium	€€€	Keij, 1957
England	ééé	Haskins, 1969; Keen, 1972
Sweden	$$$	Oertli, 1956; Carbonel, Weidmann ve Berger, 1985
Turkey	###	Sönmez-Gökçen, 1973; Gökçen, 1975; Şafak, 1990, 1997, 2003, 2008, 2010, 2010 a,b, 2013; Şafak et al., 1999, 2005, 2013; Şafak ve Güldürek, 2014; Nazik, 1993; Tanar ve Gökçen, 1990; Ünlügenç ve diğ., 1991; Witt, 2003, 2011; Freels, 1980; Şafak ve diğ., 1992, 1999, 2015; Nazik et al., 1992, 1999, 2008; Avşar ve diğ., 2006; Matzke-Karasz&Witt, 2005
Hungary	<<<	Monostori, 1983
Romania	>>>	Jiricek, 1983; Vasiliev et al., 2005
Europe	OOO	Triebel, 1963; Oertli et al., 1955)
Netherlands	!!!	Keij, 1957
China	^^^	Bosbom et al., 2011, Xiangzhong et al., 2010; Mischke et al., 2003
Serbia	===	Krstic, 1972
Slovakiaa	&&&	Pipik, 2001
Baltic Sea	\\\	Meisch, 2000; Annette and Strahl, 2011
Kaspik Basin	///	Zalanyi, 1929
Urals	DDD	Danukalova et al., 2007
Africa	QQQ	
Asia	???	
USA	AAA	
Middle East	JJJ	

Hemicyprideis montosa and *H. elongata* in France, England, and Turkey at the Early Oligocene (Oertli, 1985; Keen, 1972; Şafak et al., 2005; Şafak, 1993; Şafak, 2010*a*; Şafak, 2008; Şafak, 2010*b*; Şafak et al., 2015; Şafak and Güldürek, 2016*a,b*; Şafak, 2016);

H. helvetica in Paris and England at the Early Oligocene (Oertli, 1985; Keen, 1972); in Romania at the Late Oligocene (Jiricek, 1983); and in Turkey (in the Mut Basin, Karsanti Basin, Tekirdag, Denizli and Thrace) at the Oligocene (Tanar and Gökçen, 1990; Şafak et al., 2005; Şafak, 1993; Şafak, 2008; Şafak, 2010*a*; Şafak and Güldürek, 2016*a,b*; Şafak, 2016);

Loxocorniculum decorata in Turkey/Thrace SE at the Sannoisian (Sönmez-Gökçen, 1973; Şafak, 2016; Şafak et al., 2015)

Candona (Pseudocandona) fertilis in Germany at the Early and Late Oligocene (Carbonnel and Ritzkovski, 1969); in Switzerland and France at the Late Oligocene (Carbonnel and Ritzkovski, 1969); in Europe at the Oligocene (Triebel, 1963); and in Turkey (Karsantı Basin, İstanbul, Thrace Basin) at the Early-Late Oligocene (Şafak, 1997; Şafak et al., 2015; Şafak and Güldürek, 2016*a,b*; Şafak, 2016; Şafak, 2010*a*; Ünlügenç et al., 1991)

Cypridopsis modesta in Turkey/Thrace SE at the Sannoisian (Sönmez-Gökçen, 1973).

Virgatocypris tenuistriata in France/Paris Basin at the Late Eocene (Oertli, 1985); in England at the Sannoisian (Keen, 1972); and in Turkey at the Rupelian/Stampian (Şafak et al., 2015; Şafak, 2016).

Verticypris jacksoni and *Ilyocypris cranmorensis* in Turkey (İstanbul and Thrace Basin) at the Rupelian/Stampian (Şafak, 2016; Şafak et al., 2015); in England at the Sannoisian (Oertli, 1985)

Cypridopsis soyeri in Turkey (NW Thrace Basin and İstanbul) at the Oligocene (Şafak et al., 2015; Şafak and Güldürek, 2016*a*; Şafak, 2016); in England at the Sannoisian (Keen, 1972);

Ilyocypris boehli in Turkey (Thrace Basin, İstanbul, Mut Basin, Karsantı Basin) at the Early and Late Oligocene (Sönmez-Gökçen, 1973; Şafak et al., 2015; Şafak and Güldürek, 2016*a;* Şafak, 2016; Tanar and Gökçen, 1990; Şafak et al., 2005; Şafak, 1993; Ünlügenç et al., 1991); in England at the Early Oligocene (Keen, 1972)

Eucypris pechelbronnensis in Turkey (Thrace Basin and İstanbul) at the Rupelian/Stampian (Şafak et al., 2015; Şafak, 2016); England and France at the Sannoisian (Stchepinsky, 1960; Keen, 1972)

Novocypris striata in the Aquitaine Basin at the Eocene; in the Paris Basin at the Stampian–Early Eocene (Oertli, 1985); and in Turkey/Thrace NW and İstanbul at the Oligocene (Şafak et al., 2015; Şafak and Güldürek, 2016*a,b*; Şafak, 2016).

Eucypris dulcifons in NW China Recent and in China at the Pleistocene (Li et al., 2010) in the Baltic Sea at the Pleistocene–Holocene (Kossler and Strahl, 2011); in NW China at Recent (Mischke et al., 2003); in the South of the Ural Mountains at the Late–Middle Pleistocene (Danukalova et al., 2007); in Turkey (İstanbul, Kayseri) at the Late Miocene, Tortonian, and Pliocene (Şafak, 1997; Şafak et al., 1999*a,b*; Nazik et al., 1992) and in Akyatan Lagoon the Recent (Nazik et al., 1999).

Heterocypris salina in the North and Baltic Seas at the Late Miocene–Recent (Meisch, 2000); in Serbia at the Middle Miocene (Krstic, 1972); in Slovakia at the Late Miocene (Pipik, 2001); in W Anatolia at the Late Miocene–Pliocene (Witt, 2003); in SW Anatolia at the Late Miocene (Freels, 1980); in NW Anatolia at the Pannonian–Pleistocene (Matzke-Karasz and Witt, 2005); in Turkey/Malatya at the Upper Miocene (Nazik et al., 2008); in the Bakırköy Basin at the Tortonian (Şafak, 1997); in W Istanbul at the Pliocene (Şafak et al., 1999*a*), (Şafak et al., 1999*b*); and in Denizli at the Late Miocene (Şafak, 2010*a*); in Thrace at the Late Miocene –Pliocene (Şafak and Güldürek, 2016*b*).

Ilyocypris bradyi in Middle East, South America, Middle Asia, North Africa, and Europe at the Miocene–Recent (Meisch, 2000); in Turkey (İstanbul, Kayseri, Thrace Basin) at the Pliocene (Şafak et al., 1999*a,b*); in the Bakırköy Basin at the Tortonian (Şafak, 1997); in Kayseri at the Pliocene (Şafak et al., 1992; Nazik et al., 1992); in the west of Istanbul at the Pliocene (Şafak et al., 1999*a,b*) and in Yumurtalık Bay the Recent (Şafak, 2003); in Thrace at the Late Miocene –Pliocene (Şafak and Güldürek, 2016*b*).

Candona (Caspiocypris) alta in the Caspian Basin at the Late Miocene (Zalanyi, 1929); in the south of the Carpathian Mountains at the Miocene–Pliocene (Vasiliev et al., 2005); in Romania at the Sarmatian (Hanganu, 1974); in Turkey (Sivas and

Şebinkarahisar) at the Upper Miocene (Freel, 1980); in Sarız and Tufanbeyli at the Pliocene (Şafak et al., 1992; Nazik et al., 1992); in Hınıs/Erzurum at the Pliocene–Early Pleistocene (Şafak, 2013).

It was stated by Islamoğlu et al. (2008) that Paratethys sea, a branch of the Tethys, dominated Thrace during Eocene epoch in the form shallow marine carbonate platforms, and the three-stage isolation process started later during Oligocene Epoch. Some ostracods, such as *Neocyprideis apostolescui*, *Cytheridea crassa*, *C. pernota*, *Haplocytheridea helvetica*, were the samples observed within the Tethys ocean in different parts of the UK and Turkey. Ostracod fauna, which were also described in this study, were found in the shallow marine carbonate platforms during Middle and Late Eocene (Lutetian-Priabonian) and considered remarkable to investigate Eocene-Oligocene transition. It is stated that during the early Rupelian period Thrace Region still contained the seas of Western Tethys, then the isolation from Tethys began and finally the eastern Paratetis endemic fauna and the third stage developed in the form of an increasing continent. The ostracods species, namely *Cytheromorpha zinndorfi*, *Cladarocythere apostolescui*, *Serrocytheridea eberti*, *Hemicypreidis montosa*, *H. helvetica*, *Candona (Pseudocandona) fertilis*, *Ilyocypris boehli*, are the samples observed in the UK, Switzerland, Romania, Hungary and Turkey to showing the characteristics of the Tethys- Paratethys. These species are the examples defined in this study in the Eastern Paratethys section, where the isolation of the early Oligocene (Rupelian) was stated to initiate.

The Late Oligocene period is explained to be observed in the formation of pure freshwater marshes and coastal marshes by the stream. The ostracod species of *Haplocytheridea helvetica*, *Hemicyprideis helvetica*, *Candona (Pseudocandona) fertilis*, *Ilyocypris boehli*, which show Paratethys properties, are observed in Hungary, Caspian basin and in various parts of Turkey. These species are the examples identified in the Late Oligocene by the authors, indicating the formation of fresh water marshes and the coastal marshes by the stream. It is stated that a sedimentary basin system originating from the changing tectonic regimes extended from the Western Mediterranean coasts, which lied in front of the Alps, to the areas including the Carpathians, and from there to the Caucasus, Caspian Sea and the Pontides in the East. These sedimentary strata are told

to be firstly called as Paratethys by Laskarev (1924) (Kovac et al., 2017). It is stated that the Paratethys emerged in the early Oligocene and associated with the complete isolation of internal-continental Seas (Kovac et al., 2017), and low-organic carbon deposits were mentioned for the north of Central Paratethys.

In Neogene, the connection between the Mediterranean and the individual basins was very unstable, and the partial or total isolation of these basins must have led to the emergence of endemic fauna in each watershed system, and that the division of these internal seas were in three regions: Western (Alpine), Central (Carpathian, Balkan) and Eastern (Crimean-Caucasian) Paratethys. During the Late Miocene, the Central Paratethys sedimentary environment gradually changed into bitter and fresh water due to the isolation of Lake Pannon (Kovac et al., 2017). The area was filled with a large amount of deltaic sediment from the edges of the basin, thus the deep water lake environment gradually turned into shallow water (Kovac et al., 2017). At the end of this period, in the Mediterranean, the impact of Messinian salinity crisis and sea level on the Mediterranean was tectonically effective in the closed lake system, and alluvial plains began to develop (Kovac et al., 2017). Ostracod species such as *Ilyocypris bradyi*, *Heterocypris salina*, *Candona (Caspiocypris) alta* are the examples observed in Tethys-Paratethys during the studies carried out in the different parts of England and Turkey. These species are also described in this study as indicators of the development water fauna, which were transformed into shallow water due to the unstable and Pannonian insulations.

6. Lithostratigraphy and Paleoenvironmental Interpretation

The General Directorate of Mineral Research and Exploration Stratigraphy Committee published a book in 2006 entitled Thrace Lithostratigraphy Units within Lithostratigraphy Units Series-2.

Tertiary units in this basin were studied in detail by Kasar et al. (1983), Siyako (2002), Türkecan and Yurtsever (2002) and Siyako (2006b). The results of these studies show that the age of the Danişmen Formation is Middle Eocene–Lower Miocene (Yenimuhacir Group) and the age of the Ergene Formation (Çanakkale Group) is Late Miocene–

Pliocene. This study examined the Danişmen and Ergene formations (Figure 2).

The Danişmen Formation forms top unit in the Yenimuhacir Group (Siyako, 2002, 2006b). The Yenimuhacir Group was firstly named as a formation (Esso Standard, 1960; Holmes, 1961), then redefined by Ünal (1967) and Kasar et al. (1983) as a group.

The Yenimuhacir Group consists of the Mezardere, Osmancık, and Danişmen formations. The Mezardere Formation is composed of shale and marl facies of the delta front, and the Ceylan-Keşan formations underlie the Istranca metagranite. The Osmancık Formation lies above and is gradational with the underlying Yenimuhacir Group; it was first identified by Ünal (1967). The formation contains interbedded tuffs and sandstones. Teslimköy member is formed by sandstone and marl. The Osmancık Formation, observed from the north of Keşan to Tekirdağ, was aged as Late Eocene–Early Oligocene by Sümengen et al. (1987), Alişan and Gerhard (1987), and Batı et al. (1993, 2002). The Osmancık Formation was described by Ünal (1967) and Holmes (1961) as the Osmancık Sandstone, which lies above the Mezardere Formation, transitional with the Danişmen Formation. The Osmancık Formation was deposited as a progressive delta front facies, which has been aged as Oligocene by Akyol and Akgün (1995), Batı et al. (1993, 2002), Gerhard and Alişan (1987, 1985).

The Danişmen Formation was defined by Boer (1954) and decribed by Beer and Right (1960) and used as a formation by Kasar et al. (1983) and Ünal (1967). It is transitional and lies above the Osmancık Formation and is covered by younger units (Atalay, 2002; Siyako, 2006b).

The formation consists of claystone, sandstone, lignite, and marl beds of Early Eocene age (Kemper, 1961; Ozansoy, 1962; Lebküchner, 1974; Saraç,1987; Şafak, 2008, Şafak and Güldürek, 2016a); Middle Oligocene (Umut et al., 1983, Sümengen et al., 1987); Late Oligocene by (Kasar and Eren, 1986; Batı et al., 2002); and Late Oligocene–Early Miocene (Alişan, 1985; Gerhard and Alişan, 1987; Batı et al., 1993; Şenol 1980; Bear and Wright 1960; Şafak, 2008) determining the thickness of the unit reach up to 200-250-670-150 m.

The Ergene Formation was defined by Boer (1954). Sediments of this formation is transitional with the overlying Çantaköy Formation and is unconformable with the older underlying units (Siyako, 2006b). The unit was described as the Ergene Group by Ünal, 1967; Turgut et al., 1983; Kasar et al., 1983; Şentürk et al., 1988b; Şentürk et al., 1988a; Sümengen et al., 1987 and as the Velimeşe Formation by Umut et al. (1983).

Among the ostracod genera, the genus Cushmanidea represents epineritic; Cytheridea represents lagoonal-epineritic; such as Krithe represents the infraneritic-bathyal range while others represent different ranges; Hirschmannia, Hemicyprideis, Loxoconcha, and Cytheromorpha represent lagoonal-littoral; Neocyprideis and Cladarocythere represent lagoonal; Ilyocypris lacustrine-lagoonal; Virgatocypris, Candona (Lineocypris), Heterocypris, Cypridopsis, Eucypris, Novocypris, Candona (Pseudocandona), and Verticypris represent lacustrine. Furthermore, three genera (Valvata, Viviparus, and Avimactra) that belong to the gastropod and pelecypod classes represent lagoonal and lacustrine environments, respectively.

Ambient conditions required for the distribution of ostracods found in the measured sections of the study area are as follows:

In the Bıyıkali section, the ostracod taxa represent the following environments Hemicyprideis represents lagoonal-littoral, Neocyprideis represents lagoonal, and Cytheridea represents lagoonal-epineritic. The section indicates lagoonal environment.

In the Beşer Tuğla section, the genera of ostracods represent the following environments: and Ilyocypris and Candona (Pseudocandona) represent lacustrine, Neocyprideis and Cladarocythere represent lagoonal, Loxoconcha and Hemicyprideis represent lagoonal-littoral, and Cytheridea represents lagoonal-epineritic. The section indicates lagoon environment.

In the Silivri section, identified ostracods represent the following environments: Eucypris represents lacustrine, Candona (Pseudocandona) represents lacustrine-lagoonal, Cladarocythere represents lagoonal, and Hemicyprideis represents lagoonal-littoral. This section indicates deposition dominated by freshwater up to lagoonal conditions.

The ostracods of the Malkara-Tekirdağ section represent the following environments: Cytheromorpha, Cytheridea, and Hemicyprideis represent lagoonal-littoral; Sphenocytheridea, Serrocytheridea, and Cytheridea represent lagoonal-neritic; Cushmanidea represents neritic; and Krithe represents neritic-

bathyal. This section reflects the conditions of a shallow marine environment generally.

In the Silivri-Değirmenköy section, the ostracod taxa represent the following environments: *Candona* (*Caspiocypris*), *Candona* (*Caspiolla*), and *Heterocypris* represent lacustrine; *Cytheromorpha*, *Hemicyprideis*, and *Loxocorniculum* represent lagoonal-littoral; *Cytheridea* represents lagoonal-neritic; *Cushmanidea* represents neritic; and *Cytheropteron* represents neritic-bathyal. The transition from lagoonal condition to marine environment was observed in this section.

In the TB-57 drilling log, the ostracods represent the following environments: *Candona* (*Lineocypris*), *Cypridopsis, Eucypris, Verticypris Candona, Cypria, Novocypris* and *Virgatocypris* represent lacustrine; *Neocyprideis* and *Cladarocythere* represent lagoonal; *Cytheromorpha, Hemicyprideis, Loxocorniculum,* and *Hirschmannia* represent lagoonal-littoral; and *Cytheridea* represents lagoonal-neritic. The sequence developed under closed-basin brackish water conditions, which are indicative of a rare shallow marine environment.

In the TB-58 borehole, the ostracod genera represent the following environments:

Cypria, Eucypris, and *Heterocypris* represent lacustrine; *Candona* (*Pseudocandona*)*, Ilyocypris* represent lacustrine-lagoonal; *Cladarocythere, Neocyprideis* represent lagoonal; *Hemicyprideis* represents lagoonal-littoral; and *Cytheridea* and *Serrocytheridea* represent lagoonal-neritic. The sequence indicates a shallow marine condition and together with lake to lagoon conditions.

7. Discussion

The Istranca massif and the massif of the Tertiary Thrace basins, which constitute the southern slope of the deposition (Okay and Yurtsever, 2006) are composed of two main units in the north-east of the Black Sea. The Istranca massif is represented by gneiss and metamorphosed Paleozoic and Mesozoic sedimentary rocks that overlie the greenschist facies (Taner and Çağatay, 1983; Üşümezsoy, 1982). Starting from the southern Istranca Mountains, Tertiary deposits reach 9000 meters of thickness, covering all of Trakya and outcropping (Şengüler et al., 2000; 2003; Turgut et al., 1983; 1991; Kopp et al., 1969). Paleocene-Early Eocene sediments in the region have been observed in

a very narrow area of Southwestern Thrace, but they were incompatible with the Middle Eocene limestones. The Middle Eocene-Early Miocene sediments were part of the Koyunbaba and Soğucak formations that had developed transgressively. The Ceylan Formation precipitated in places where the basin deepened, while the delta system that developed later is included in the Yenimuhacir Group and consists of Mezardere, Osmancık and Danişmen Formations from top to bottom. The Çantaköy Formation is another unit that had been deposited within this age range. Miocene units have been studied as part of the Çanakkale and Çekmece groups and the Ergene Formation. The uppermost Miocene-Pliocene is represented by the Kırcasalih Formation, which spreads widely throughout Northern Thrace (Siyako, 2006*b*).

Siyako (2006*b*) reported that Paleocene-Pleistocene sediments in the Thrace Basin had separated from each other by angular unconformities, and that Paleocene-Lower Eocene sediments were present in a very narrow area in southwest Thrace and the Gelibolu Peninsula.

Additionally, Siyako (2006*a,b*) stated that this stack was covered unconformably by the Middle Eocene limestone.

Various units in the basin that had collapsed in the early-Middle Eocene period in terrestrial and marine environments have been observed to be vertically and laterally transitional to each other (Siyako, 2006*a*, Siyako, 2005).

In the Late Eocene, the Keşan Formation and the Ceylan Formation corresponding to the upper levels of this unit were deposited, and thereafter, the sediment referred to the Yenimuhacir Group started to deposit – with lithological differences observed between them in a shallow environment during the latter part of the Late Eocene-early Oligocene period (Kopp et al., 1969, Kasar et al., 1983; Atalık, 1992; Sümengen and Terlemez, 1991; Siyako, 2006*b*, 2005).

The Mezardere, Osmancık and Danişmen formations were deposited in this shallow system up to the Early Miocene (Siyako, 2005; Ünal, 1967; Kasar et al., 1983). Siyako (2006*b*) stated that at the end of this phase, the region became completely filled and ascended to land, with the sedimentation of young Miocene-Pliocene units beginning as a result of erosion.

Volcanic outcrops observed by Siyako (2006*b*) in the Hisarlıdağ Formation in Southwestern Thrace deposited in the Early-Middle Miocene and also outcrops observed in Çanakkale and Çekmece groups and the Ergene Formation deposited in the Upper Miocene; outcrops observed in Karatepe Basalt deposited in the Miocene; and outcrops observed in the Kırcasalih Formation, with wide expanses in Northern Thrace, deposited in the Pliocene. The Marmara Formation formed by the marine terraces defined around the Marmara Sea deposited in the Pleistocene.

Studies by Maravelis et al. (2007) and Maravelis and Zelilidis (2012) on the paleoclimatology and paleoecology of the Eocene / Oligocene border in the Thrace Basin and Northeastern Aegean Sea, showed that the Eocene sediments orginated in deeper marine conditions than the Oligocene sediments.

Siyako and Huvaz (2007) performed a study on the Eocene stratigraphy and evolution of the Thrace Basin, while İslamoğlu et al. (2008) studied the storage environment in the Oligocene sediments in the Thrace Basin, from Tethys up to the Eastern Paratethys, researching their paleoclimatology and palaeogeography.

Rückert-Ülkümen et al. (2009) described the palaeobiogeographical properties of the Eastern Paratethys in the Ergene Basin (NW Turkey) and reported on the Neogene biostratigraphy of the Ergene Basin (Eastern Paratethys) coastal zone.

Witt (2011) presented systematics of ostracod faunas of marine Oligocene and terrestrial Miocene formations in the study of the Thrace-Pınarhisar sediments.

It was revealed that an ostracod community, which was explored by Şafak and Güldürek (2016*a*), and significant consolidation in Oligocene compared to the previously identified Eocene in the west of Thrace, as determined by Maravelis et al. (2007) and Maravelis and Zelilidis (2012), could be observed in the south-eastern part of the area.

Akgün et al. (2013) studied the vegetation structure and composition during the Oligocene period in the south and west of the Thrace Basin, and the Basin's climate characteristics as well. The first palynomorph and mollusc assemblages were identified during the Rupelian and Chattian. The annual average temperature of palynomorphs was investigated to explain the transition during the Rupelian and Chattian, which revealed climatic cooling, vegetation and pollen changes of the pollen assemblages in coastal deposits.

Demirtaş et al. (2015) studied the late Oligocene palynomorphs from the Middle Miocene coals of the Gelibolu Peninsula. Samples were taken from coal zones in two different regions; coal petrography was used to examine the storage conditions of the two coal zones along with their organic petrography, compositions, maceral ratios and palynological characteristics. The maceral compositions of the Oligocene coals were similar to those of the Miocene; the two different communities were distinguished by the percentages of palynomorphs. The first assemblage was found in the late Oligocene sediments, and the second one was found in the sediments of the Middle Miocene period**.**

In this study, a micropaleontological evaluation of the Paleogene-Neogene sediments of Babaeski-Muratlı-Çorlu-Lüleburgaz (Southeastern Thrace) region was carried out.

This study was carried out on drilled sections taken from Silivri, Türkmenli-Çorlu, Babaeski- Lüleburgaz, Edirne –Babaeski, Tekirdağ-Hayrabolu road, and two drilling washing samples, prepared by MTA, of which the drilling procedure was carried out with point samples. In addition to well-preserved ostracod fauna, obtained from greenish, yellowish claystone, , leafy, lignite sandstone, yellowish beige colored sandstone, organic colored clay, and silt (Early Oligocene Danişmen Formation), and the clays (Late Miocene-Pliocene Ergene Formation), all of which are widely found in the area, micro-molluscs were also observed in some levels. The clay lithology of the Yenimuhacir Group under the Danişmen Formation and lenticular sandstone of the Teslimköy Member feature siltstone intercalated sandstone (Osmancık Formation) above it. In the study area, the Danişmen Formation of the Taşlısekban and Armutburnu Member were very small, while the Pinarhisar Member was fossilized and thicker.

The ostracod community within the Danişmen Formation and its members, and their location in the stack, which was indicated to belong to the Rupelian / Stampian, Late Oligocene (Chattian) according to Şafak and Güldürek, 2016*a,b*, were not included in this study.

The stack is unconformably overlain by the Ergene Formation. The unit in the area of investigation, particularly the top layer of the stack, is well-known, and in addition to well-preserved ostracod fauna, micro-mollusks were found in some levels.

It was observed that the Çelebi Formation of the study was fossilized, and Sinanlı Member and Karatepe Basalt were found to have very little thickness. With this study, it was found that the Ergene Formation was Late Miocene-Pliocene. The Kırcasalih Formation that developed over this unit was Pleistocene. The Danişmen Formation was determined to have collapsed in Early Oligocene, while the Miocene fauna mentioned in the literature was not found.

The Ergene Basin in Neogene described by Rückert-Ülkümen et al. (2009) did not have a *Congeria ornithopsis* location that was similar to that of the basins in Bulgaria, North Yugoslavia and Vienna, and the examined Ergene site contained clayey levels as well as scarce fossiliferous levels in both measured sections according to drilling data.

The ostracod species identified in the study were compared with other ostracods in the Thrace Basin and other parts of Turkey, as well as with other ostracods in the Oligocene in Europe, Northwest and Paris-Aquitain Basin, Belgium, England, Romania and Switzerland. Based on this fauna, the Early Oligocene region was shown to have been influenced by the Tethys effect.

The ostracod species identified in the study area in the Late Miocene-Pliocene were compared against other ostracod studies in the Thrace Basin and other parts of Turkey, as well as in the Baltic Sea, Caspian Basin, Romania and Carpathians. According to these fauna assemblages, the Paratethys effect was determined to be much more higher than the effect of Tethys in the Late Miocene-Pliocene period.

8. Conclusions

A micropaleontological analysis of the Tertiary sediments from the Çorlu-Muratlı-Lüleburgaz-Babaeski region (Southeast Thrace) was completed in this study. The dominant conditions of depositional environment were identified.

Yellow-green claystone, yellow-beige sandstone, leaf-imprinted lignite bearing sandstone, organic colored clay, silt, and clay of the Danişmen and Ergene formations are widespread throughout the area, constituting the upper layers of the sediments. They provided well-preserved ostracod fauna, with micro-molluscs observed in some layers. According to the microfauna content of all samples, the age of the sedimentation was identified as the early Oligocene-Pliocene.

Species of Oligocene age include ostracods *Cytheromorpha zinndorfi*, *Cladarocythere apostolescui*, *Neocyprideis apostolescui*, *N. williamsoniana*, *Hemicyprideis montosa*, *H. elongata, H. helvetica*, *Serrocytheridea eberti*, *Sphenocytheridea gracilis*, *Cytheridea pernota*, *C. crassa*, *Cushmanidea scrobiculata*, *Krithe angusta*, *Loxocorniculum decorata*, *Hirschmannia* sp., *Loxoconcha* sp.1, *Candona* (*Pseudocandona*) *fertilis, Candona* (*Pseudocandona*) sp., *Candona* (*Lineocypris*) sp., *Ilyocypris boehli, I. cranmorensis*, *Novocypris striata*, *Eucypris pechelbronnensis, Virgatocypris tenuistriata*, *Verticypris jacksoni* and *Cypridopsis soyeri*; micro-pelecypods and gastropods such as *Avimactra*, *Viviparus*, and *Valvata*. Meanwhile, ostracods *Candona* (*Caspiocypris*) *alta*, *I. bradyi*, *E. dulcifons*, and *H. salina* were identified to be from the Late Miocene–Pliocene. Among the ostracod genera, the genus *Krithe* represents the infraneritic-bathyal range, whereas others represent different ranges, specifically: *Cushmanidea* epineritic*; Cytheridea* lagoonal-epineritic; *Cytheromorpha, Hemicyprideis, Hirschmannia, and Loxoconcha* lagoonal-littoral*; Cladarocythere* and *Neocyprideis* lagoonal*; Ilyocypris* lacustrine-lagoonal; and *Novocypris*, *Eucypri*s, *Virgatocypris*, *Verticypris*, *Heterocypris*, *Candona (Pseudocandona)*, *Candona* (*Lineocypris*), and *Cypridopsis* lacustrine. In addition, three genera (*Avimactra, Viviparus,* and *Valvata*) of pelecypods and gastropods represent lagoonal and lacustrine environments, respectively.

The faunal study showed that the measured sections used in the study and the marl, siltstone, and claystone in the upper and lower layers of lignite intersected by the boreholes containing lagoonal and lake ostracods generally.

This study showed a similar age–environment relationship when compared with other studies conducted in the Thrace Basin, northwestern Europe, the Paris/Aquitaine Basins, Belgium, England, Romania, and Sweden.

References

Akartuna, M. 1968. Armutlu yarımadasının jeolojisi. İstanbul Üniversitesi Fen Fakültesi Monografileri 20, 105 s.

Akgün, F., Akkiraz, M. S., Üçbaş, S. D., Bozcu, M., Sevinç Kapan-Yeşilyurt, S., Bozcu, A. 2013. Oligocene vegetation and climate characteristics in north-west Turkey: data from the south-western part of the Thrace. Turkish Journal of Earth Sciences 22, 277-303.

Akyol, E., Akgün, F. 1995. Trakya karasal Tersiyeri'nde yaş tayinleri. Trakya Havzası Jeolojisi Sempozyumu Bildiriler Kitabı, 28-29.

Alişan, C. 1985. Trakya ''I'' Bölgesi'nde Umurca-1, Kaynarca-1, Delen-1 kuyularında kesilen formasyonların palinostratigrafisi ve çökelme ortamlarının değerlendirilmesi. TPAO Araştırma Grubu Arşivi, Rapor no 386, 60s. Ankara (unpublished).

Alişan, C., Gerhard, J.E. 1987. Kuzey Trakya Havzası'nda açılan üç kuyunun palinostratigrafisi ve kaynak kaya özellikleri. Türkiye 7. Petrol Kongresi Bildiriler Kitabı, 461-474.

Apostolescu, V. 1964. Répartition stratigraphique générale des ostracodes du Paléogene des Bassins de Paris et Bruxelles, Collogue Paléogene. Mémoires. B.R.G.M., no. 28.

Atalay, Z. 2002. Trakya bölgesindeki linyit formasyonların (Danışmen ve Ağaçlı Formasyonları) stratigrafisi fasiyes ve çökelme ortamı özellikleri. Cumhuriyet Üniversitesi Mühendislik Fakültesi Dergisi Seri-A Yerbilimleri C. 19, S. 1, 61-80.

Atalık, E. 1992. Depositional systems of the Osmancık formation in the Thrace Basin. Doktora Tezi, Orta Doğu Teknik Üniversitesi, 343 s. (unpublished).

Athersuch, J., Horne, D.J., Whittaker, J.E. 1989. Marine and Brackish Ostracods. Synopses of the British Fauna (N.S.), 43.

Batı, Z., Alişan, C., Ediger, V. Ş., Teymur, S., Akça, N., Sancay, H., Ertuğ, K., Kirici, S., Erenler, M., Aköz, Ö. 2002. Kuzey Trakya havzasının Palinomorf, Foraminifer ve Nannoplankton Biyostratigrafisi. Türkiye Stratigrafi Komitesi Çalıştayı (Trakya Bölgesi'nin Litostratigrafi Adlamaları) Özleri, s. 14.

Batı, Z., Erk, S., Akça, N. 1993. Trakya Havzası Tersiyer birimlerinin palinomorf, foraminifer ve nannoplankton biyostratigrafisi. TPAO Araştırma Grubu Arşivi, Rapor no 1947, 92s. Ankara (unpublished).

Bear, H., Wright J.A. 1960. Stratigraphy of the Ganosdağ, Korudağ and Keşan Hills District. (Thrace), TPAO Arşiv no 736, (unpublished).

Boer, N.P. de 1954. Report on geological reconnaissance in Turkish Thrace. G.A. Report no Ç 25373, Petrol Dairesi, The Hague.

Bosboom, E.R., Dupont-Nivet, G., J.P. Houben, A., Brinkhuis, H., Villa, G., Mandic, O., Stoica, M., Jan Zachariasse, W., Guo, Z., Li, C., Krijgsman, W. 2011. Late Eocene sea retreat from the Tarim Basin (est China) and concomitant Asian paleoenvironmental change, Palaeogeography, Palaeoclimatology, Palaeoecology 299, 385-398.

Bremer, H. 1978. Paleontoloji. Ege Üniversitesi Fen Fakültesi Kitapları Serisi, No 46.

Carbonnel, G., Ritzkovski, S. 1969. Ostrokodes Lacustres de l'Oligocene (Melanienton) de la Hesse (Allemagne). Arch.Sc. 22:1, 55-82.

Carbonnel, G., Weidmann, M., Berger, J.P. 1985. Les Ostrakodes lacustres et saumatres de la molasse de suisse occidentale. Revue de Paleobiologie 4:2, 215-251.

Colin, J.P., Carbonnel, P. 1992. Inventaire des ostracodes fossiles de la Réserve Naturelle Géologique de saucats-La Brède. Bulletin de la Société linnéenne de Bordeaux 20, 1, 3-35.

Danukalova, G. A., Yakovlev, A. G., Morozova, E. M., Alimbekova, L. I. 2007. Biostratigraphy of the Late Middle Pleistocene (Middle Neopleistocene) of the Southern Urals region. Quaternary International 160, 17–29.

Demirtaş, F., Bozcu, M., Koşun, E., Akkiraz, M. S. 2015. Petrography and palynology of Late Oligocene and Middle Miocene coals in the Gelibolu Peninsula, NW Turkey. Turkish Journal of Earth Sciences 24, 383–397.

Doust, H., Arıkan, Y. 1974. The geology of the Thrace Basin. Türkiye İkinci Petrol Kongresi Tebliğleri Kitabı, 119-136.

Ediger, V. Ş. 1982. Kuleli Babaeski sırtının (KB Trakya) Paleo-ortamsal incelemesi ve Kuzey Trakya havzasının hidrokarbon potansiyelinin değerlendirilmesinde yeni yaklaşım: Türkiye Petrolleri Anonim Ortaklığı Rapor No: 1995, 194 s., Ankara (unpublished).

Ediger, V. Ş. 1988. Biga Yarımadası'ndaki kömürlü birimlerden alınan örneklerin palinolojik analizi. TPAO Araştırma Merkezi Grubu Rapor No: 809, Ankara (unpublished).

Esso Standard, 1960. 1 sayılı Marmara petrol bölgesi AR/EST/105, 106, 108 ve 109 hak sıra numaralı sahalara ait terk raporu. TPAO Arama Grubu Arşivi rapor no: 1031, Ankara (unpublished).

Estéoule-Choux, J., Margerel, J-P., Guernet, C. et Rıvoalland, H. 1986. Données sur le bassin stampien de Quessos (massif armoricein), Etude sédimentologique et micropaléontologique du gisement du moulin de Boguet. Revue de Micropaléontologie, V. 28, N. 4, 243-254.

Freels, D. 1980. Limnische Osrakoden aus jungtertiar und Quartarder Turkey. Geologische Jahrbuch, Reihe B, Heft 39, 172 p.

Gerhard, J.E., Alişan, C. 1987. Palynostratigraphy, Paleoecology, and visual organic geochemistry Turgutbey-2, Değirmencik-3 and Pancarköy-1, Thrace Basin, Turkey. TPAO Araştırma Merkezi Grubu Arşivi rapor no 983, 33s. Ankara (unpublished).

Goerlich, F. 1953. Ostrakoden der Cytherideinae aus dem Tertiären Molasse Bayerns, Senckenbergiana, Bd. 34, no. 1/3.

Gökçen, N. 1975. Pınarhisar Formasyonu'nun yaşı ve ortam şartlarında görülen yanal değişmeler (Kuzey, Kuzeydoğu Trakya). Cumhuriyetin 50. Yılı Yerbilimleri Tebliğleri, 128-142.

Görür, N., Okay, A.I. 1996. Fore-arc origin of the Thrace basin, northwest Turkey. Geologische Rundschau 85, 662-668.

Hanganu, E. 1974. Observations sur l'ostracofaune pontienne de la région entre la vallée du Danube et la vallée du Motru. Revista Espanola Micropaleontologia 6, 3, 335-345, 3 Taf., Madrid.

Haskins, C.W. 1969. Tertiary Ostracoda from the Isle of Wight and Barton, Hampshire, England. Revue de Micropaléontologie, Part IV, N. 3, Paris.

Holmes, A.W. 1961. A stratigraphic review of Thrace. TPAO Arama Grubu Arşivi rapor no. 368, Ankara (unpublished).

İslamoğlu, Y., Harzhauser, M., Gross, M., Jimenez-Moreno, G., Coric, S., Kroh, A., Rögl, F., Van M., J. 2008. From Tethys to Eastern Paratethys: Oligocene depositional environments, paleoecology and paleobiogeography of the Thrace Basin (NW Turkey). Int J Earth Sci (Geol Rundsch), DOI 10.1007/s00531-008-0378-0.

Jiricek, R. 1983. Redefinition of the Oligocene and Neogene Ostracod Zonation of the Paratethys. Knihovnicka Zemniho plynu a nafyt (Nr.4) pp. 195-236/6, Hodonin.

Kara, H., Tuncalı, E., Narin, R., Gürsoy, B., Dümenci, S. 1996. Trakya Tersiyer kömür havzası raporu. Maden Tetkik ve Arama Genel Müdürlüğü Rapor No: 9974, Ankara (unpublished).

Kasar, S., Eren, A. 1986. Kırklareli-Saray-Kıyıköy bölgesinin jeolojisi, TPAO Arama Grubu Arşivi rapor no: 2208, 45s., Ankara (unpublished).

Kasar, S.,Bürkan, K., Siyako, M., Demir, O. 1983. Tekirdağ-Şarköy-Keşan-Enez bölgesinin jeolojisi ve hidrokarbon olanakları. TPAO Arama Grubu Arşiv no:1771, Ankara (unpublished).

Keen, M.C. 1972. The Sannoisian and some other Upper Palaeogene Ostracoda from North-west Europe. Palaeontology, V. 15, Part 2, London.

Keij, A. 1957. Eocene and Oligocene Ostracoda of Belgium. Institut Royale Science Naturelles Belgique, Brussels, Mémoires No. 136:1-210.

Kemper, E. 1961. The Kırklareli Limestone (Upper Eocene) of the northern basin rim. G. Deilman Bergbau GMBH jeolojik raporu, T37.

Keskin, C. 1974. Kuzey Trakya Havzası'nın Stratigrafisi. Türkiye İkinci Petrol Kongresi Tebliğleri Kitabı, 137-163.

Kopp, K.O., Pavoni, N., Schindler, C. 1969. Geologie Thrakiens IV: Das Ergene-Becken. Beih zum Geol. Jahrb., Heft 76, 136 p., Hannover.

Kossler, A., Strahl J. 2011. The Late Weichselian to Holocene succession of the Niedersee (Rügen, Baltic Sea) – new results based on multi-proxy studies. E&Gquaternary Science Journal ,Volume 60, Number 4, 434–454.

Kováč, M., Hudáčková, N., Halásová, E., Kováčová, M., Holcová, K., Oszczypko-Clowes, M., Báldi, K., Less, G., Nagymarosy, A., Ruman, A., Klučiar, T, Jamrich, M. 2017. The Central Paratethys palaeoceanography: a water circulation model based on microfossil proxies, climate, and changes of depositional environment. Acta Geologica Slovaca, 9(2), 75–114.

Krstic, N. 1972. Neue Ostracoden aus der Obermiozän von Donja mutnica (Paracin, Serbien). Bulletin Scientifique A17, 153-155.

Laskarev, V. 1924. Sur les équivalens du sarmatiien supérieur en Serbie. In: Vuj vić P. (Ed.): Receuil de traveaux offert à M.Jovan Cvijic par ses amis et collaborateurs. Drzhavna Shtamparija, Belgrade, 73—85.

Lebküchner, R.F. 1974. Orta Trakya Oligoseninin jeolojisi Hakkında. Maden Tetkik ve Arama Genel Müdürlüğü Rapor No. 2983, Ankara (unpublished).

Li, X., Liu, W., Zhang, L., Sun, Z. 2010. Distribution of Recent ostracod species in the Lake Qinghai area in orthwestern China and its ecological significance. Ecological Indicators 10, 880-890.

Lienenklaus, E. 1894. Monographie der Ostrakoden des Nordwestdeutschen Tertiaers. Zeitschrift der Deutschen Geologischen Gesellschaft 46.

Lienenklaus, E. 1905. Die Ostrakoden des Mainzer Tertiärbeckens. Abhandlungen der Senckenbergischen Naturforschenden Gesellschaft, 1-67.

Maden Tetkik ve Arama Genel Müdürlüğü Trakya bölgesi Litostratigrafi Birimleri, Stratigrafi Komitesi, Litostratigrafi Birimleri Serisi-2, 2006.

Maravelis, A., Zelilidis, A. 2012. Discussion: Unravelling provenance from Eocene–Oligocene sandstones of the Thrace Basin, North-east Greece" by Caracciolo et al. (2011). Sedimentology 58, 1988–2011.

Maravelis, A., Konstantopoulos, P., Pantopoulos, G., Zelilidis, A. 2007. North aegean sedimantary basin evolution during the Late Eocene to Early Oligocene based on sedimentological studies on Lemnos Island (NE Greece). Geologica Carpathica 58, 455-464.

Matzke-Karasz, R., Witt, W. 2005. Ostracods of the Paratethyan Neogene Kılıç and Yalakdere Formations near Yalova (İzmit Province, Turkey). Zitteliana, A45, 115-133, 2 figs, 3pls, 1 tab, München.

Meisch, C. 2000. Freshwater Ostracoda of Western and Central Europe, Süsswasserfauna von Mitteleuropa 8/3. Akademischer Verlag, Heidelberg.

Mischke, S., Herzschuh, U., Kürschner, H., Fuchs, D., Chen, F.H., Meng, F., Sun, Z.C. 2003. Sub-Recent Ostracoda from Qilian Mountains (NW China) and their ecological significance. Limnologica 33, 280–292.

Monostori, M. 1983. Ostracodes of Eocene/Oligocene Boundary profiles in Hungary. Annales Universities Scientiarum Budapestinensisde roland, Eötvös Nominatae Sectio Geologica tomus XXV.

Morkhoven, F.P.C.M. 1963. Post-Palaeozoic Ostracoda. V.II, 478 p., Newyork.

Nazik, A. 1993. Darende Havzası Tersiyer İstifinin Mikropaleontolojik (Ostrakod ve Foraminifer) İncelenmesi. TJK Bülteni, Cilt 36, Sayı 1, Ankara.

Nazik, A., Şafak, Ü., Şenol, M. 1992. Micropaleontological Investigation (Ostracoda) of the Pliocene sequence of the Tufanbeyli (Adana) Area. Yerbilimleri, 1992 1st International Symposium on Eastern Mediterranean Geology, proceedings and abstracts, 281-304, Adana.

Nazik, A., Evans, G., Gürbüz, K. 1999. Sedimentology and palaeontology with special reference to the ostracoda fauna of Akyatan Lagoon (Adana-SE Turkey). Geosound 35, 127-147.

Nazik, A., Türkmen, İ., Koç, C., Aksoy, E., Avşar, N., Yayık, H. 2008. Fresh and Brackish Water Ostracods of Upper Miocene Deposits, Arguvan/Malatya (Eastern Anatolia). Turkish Journal of Earth Sciences, Vol. 17, pp. 481-495.

Oertli, H.J. 1956. Ostrakoden aus der oligozänen und miozänen Molasse der Schweiz. Abhandlungen der Schweizerischen paläontologischen Gesellschaft 74: 1-119, Basel.

Oertli, H.J. 1985. Atlas des Ostracodes de France. Bull. centres rech. explor.-prod. Elf-Aquitaine, Mem. 9. Pau 1985. Mémoires Elf-Aquitaine 9, 17-311, Paléogéne.

Oertli, H.J. Key, A.J. 1955. Drei neue Ostrakoden-Arten aus dem Oligozän Westeuropas. Bulletin der Schweizerische Vereinigung von Petroleum-Geologen und –Ingenieuren 22(62): 19-28.

Okay, A., İ., Yurtsever, A. 2006. Istranca Masifinin Metamorfik Kaya Birimleri ile Metamorfizma Sonrası Kretase Kaya Birimleri. Stratigrafi Komitesi Litostratigrafi Birimleri Serisi-2, Trakya Bölgesi Litostratigrafi Birimleri. Maden Tetkik ve Arama Genel Müdürlüğü Yayınları, 1-41.

Ozansoy, F. 1962. Doğu Trakya Alt Oligosen Antrakoterienleri, Maden Tetkik Arama Enstitüsü Dergisi 58, 85-96, Ankara.

Öztunalı, Ö., Üşümezsoy, Ş. 1979. Istranca Masifi'nin "Çekirdek" kayaçları ve petrojenetik evrimleri, Türkiye Jeoloji Kurumu-İstanbul Üniversitesi Yerbilimleri Fakültesi, Altınlı Sempozyumu, 37-44.

Perinçek, D. 1987. Trakya Havzası Renç Fay Zonunun Sismik Özellikleri. Türkiye 7. Petrol Kongresi Bildirileri, 11-20.

Perinçek, D., Ataş, N., Karatut, Ş., Erensoy, E. 2015. Geological factors controlling potential of lignite beds within the danişmen formation in the Trace basin. Bulletin of the Mineral Research and Exploration 150, 77-108.

Perinçek, D., Ataş, N., Erensoy, E., Karatut, Ş. Kösebalaban, A., Ergüder İ., Ünal., Y. 2011. Trakya Havzası'nın linyit potansiyeli ve bunu kontrol eden jeolojik faktörler. 64. Türkiye Jeoloji Kurultayı Bildiri Özetleri, 93-94.

Pipik, R. 2001. Les ostracodes d'un lac ancien et ses paléobiotopes au-Mioène supérieur: Le Bassin de Turiec (Slovaquie). Thèse Université Claude Bernard Lyon, 337.

Remane, A. 1958. Die Biologie des Brackwassers. In: THIENEMANN, A: Die Binenge wasser, Einzeldarstellungen aus der Limnologie und ihren Nachbagebieten, 22: 1-348.

Rückert-Ülkümen, N., Özkar-Öngen, İ., Çevik-Öner, B. 2009. Doğu Paratetis'in Ergene Havzası'ndaki paleobiyocoğrafik özellikleri. İstanbul Yerbilimleri Dergisi C. 22, s.2, 119-140.

Saner, S. 1985. Saros Körfezi dolayının çökelme istifleri ve tektonik yerleşimi, Kuzeydoğu Ege Denizi, Türkiye. Türkiye Jeoloji Kurumu Bülteni 28, 1-10.

Saraç, G. 1987. Kuzey Trakya bölgesinde Edirne-Kırklareli-Saray-Çorlu-Uzunköprü-Dereikebir yörelerinin memeli paleofaunası. Ankara Üniversitesi Fen Bilimleri enstitüsü Jeoloji Müh. Anabilim Dalı Yüksek Lisans Tezi, Ankara (unpublished).

Sayar, C. 1991. Paleontoloji Omurgasız Fosiller. İstanbul Teknik Üniversitesi Kütüphanesi Sayı: 1435, İstanbul.

Siyako, M. 2002. Trakya ve yakın çevresinin Tersiyer litostratigrafisi, Türkiye Stratigrafi Komitesi Çalıştayı, Trakya Bölgesi'nin Litostratigrafi Adlamaları, Özler, Maden Tetkik ve Arama Genel Müdürlüğü, Ankara, s. 4.

Siyako, M. 2005. Trakya ve yakın çevresinin Tersiyer stratigrafisi. TPAO Arama Grubu Rapor No: 4608, 104 s. Ankara (unpublished).

Siyako, M. 2006a. Trakya Havzası'nın linyitli kumtaşları. Maden Tetkik Arama Dergisi 132, 63-73.

Siyako, M. 2006b. Trakya Bölgesi Litostratigrafi Birimleri (Tersiyer Bölümü). Stratigrafi Komitesi, Litostratigrafi Birimleri Serisi-2. Maden Tetkik ve Arama Genel Müdürlüğü yayını. 70 s.

Siyako, M., Huvaz, O. 2007. Eocene stratigraphic evolution of the Thrace basin, Turkey, Sedimentary Geology, 198, 75-91.

Siyako, M., Bürkan, K.A., Okay, A.İ. 1989. Biga ve Gelibolu Yarımadaları'nın Tersiyer Jeolojisi ve Hidrokarbon olanakları. TPJD Bülteni, c:1/3, s: 183-199.

Sönmez-Gökçen, N. 1973. Etude paléontologique (ostracodes) et stratigraphique de niveaux du Paléogéne du Sud-Est de la Thrace, Maden Tetkik ve Arama Genel Müdürlüğü Yayınlarından, No.147, Ankara.

Stchepinsky, A. 1960. Etude des Ostracodes du Sannoisien d'Alsace. Bulletin Service. Carte geologique Alsace Lorraine, 16, 3, 151-174, 1 pl.

Sümengen, M., Terlemez, İ. 1991. Güneybatı Trakya Yöresi Eosen Çökellerinin stratigrafisi. Maden Tetkik Arama Dergisi 113, 17-30, Ankara.

Sümengen, M., Terlemez I., Şentürk, K., Karaköse, C. 1987. Gelibolu Yarımadası ve Güneybatı Trakya Tersiyer Havzası'nın Stratigrafisi, Sedimantolojisi ve Tektoniği, Maden Tetkik ve Arama Genel Müdürlüğü Rapor No: 8128 (unpublished).

Sütçü, E., Paker, S., Nurlu, Y., Kumtepe, P., Cengiz, T. 2009. Tekirdağ-Malkara havzasında CBS yöntemleriyle potansiyel kömür sahalarının belirlenmesine yönelik iki değişkenli istatistiksel yaklaşım. TMMOB Coğrafi Bilgi Sistemleri Kongresi, İzmir, 8 s.

Şafak, Ü. 1990. Malatya Kuzeybatısının (Medik-Ebreme yöresi) Üst Lütesiyen Ostrakod Faunası. Ç.Ü. Müh-Mim. Fak. Dergisi, Cilt 5, Sayı 1, 135-149, Adana.

Şafak, Ü. 1993. Karsantı yöresinde (KKD Adana) yüzeyleyen Tersiyer istifinin Ostrakod dağılımı ve ortamsal özellikleri. Türkiye Jeoloji Bülteni, c.36 s. 1.

Şafak, Ü. 1997. Bakırköy Havzası (İstanbul) Tersiyer Çökellerinin Ostrakod Faunası. Yerbilimleri 30, 255-285.

Şafak, Ü. 2003. Yumurtalık Koyu (Adana) Ostrakod Topluluğu. Maden Tetkik Arama Dergisi 126, 1-10, Ankara.

Şafak, Ü. 2008. Malkara (Tekirdağ) yöresi Erken/Alt Oligosen çökellerinin ostrakod faunası ve ortamsal özellikleri. Ç.Ü. Yerbilimleri Dergisi 52, s 263-282, Adana.

Şafak, Ü. 2010a. Güney-Buldan-Babadağ-Yenicekent-Kale (Denizli, GB Anadolu) Çevresi Tersiyer Çökellerinin Ostrakod Topluluğu ve Ortamsal Özellikleri. KSÜ Mühendislik Bilimleri Dergisi 13 (2), 44-62.

Şafak, Ü. 2010b. Pınarhisar-Vize/Kırklareli (KB Anadolu) Yöresi Oligosen Yaşlı Linyitli Çökellerin Ostrakod Faunası ve Ortamsal Özellikleri. TPJD Bülteni, Cilt:22, Sayı:2, s. 11-29, Ankara.

Şafak, Ü. 2013. Hınıs (Erzurum, Doğu Anadolu) yöresindeki volkano-sedimanter Yolüstü Formasyonu ostrakod faunası ve ortamsal özellikleri. Maden Tetkik Arama Dergisi 146, 55-81, Ankara.

Şafak, Ü. 2016. Yedikule-İstanbul Bölgesi Tersiyer (Miyosen-Pliyosen) Çökellerinin Ostrakod Faunası ve Ortamsal Özellikleri. Maden Tetkik ve Arama Genel Müdürlüğü Dergisi 152, 39-63, Ankara.

Şafak, Ü., Güldürek, M. 2016a. The Ostracoda assemblage of the Eocene-Oligocene transition in northwestern Thrace: Kırklareli-Edirne area (northwestern Turkey). Journal of African Earth Sciences 117, 62-85.

Şafak, Ü., Güldürek, M. 2016b. Edirne- (Trakya) Bölgesi Paleojen-Neojen Çökellerinin (Edirne-Keşan, Uzunköprü, Meriç, Süloğlu sondajları) mikropaleontolojik incelenmesi. Ç.Ü.Müh. Mim. Fak Dergisi, Cilt 31 (1), Sayı 2, 17-33, Adana.

Şafak, Ü., Avşar, N., Meriç, E. 1999a. Ostracoda and benthic foraminifera of tertiary sequence of western part of İstanbul. Yerbilimleri Dergisi, 4 th European Ostracodologists Meeting No:35, p. 173-201, Adana.

Şafak, Ü., Avşar, N., Meriç, E. 1999b. Batı Bakırköy (İstanbul) Tersiyer Çökellerinin ostrakod ve foraminifer topluluğu. Maden Tetkik Arama Dergisi No. 121, s. 17-33, Ankara.

Şafak, Ü., Nazik, A., Şenol, M. 1992. Kayseri Güneydoğusu (Sarız) Pliyosen Ostrakod ve Gastropod Faunası. Ç. Ü. Müh. Mim. Fak. Dergisi, Cilt 7, Sayı 1, s. 171-195, Adana.

Şafak, Ü., Kelling, G., Gökçen, N.S., Gürbüz, K. 2005. The mid-Cenozoic succession and evolution of the Mut basin, southern Turkey, and its regional significance. Sedimantary Geology 173, 121-150.

Şafak, Ü., Özsarı, F., Yıldız, C.E. 2015. Tekirdağ yöresi Oligosen çökellerinin (Hacısungurlu Sondajı) ostrakod faunası ve ortamsal özellikleri. 68th Türkiye Jeoloji Kurultayı Bildiri Özleri Kitabı, 552-553, Ankara.

Şengüler, İ. 2008. Trakya Havzası Kömür Aramaları Projesi Raporu (2005-2006-2007 Yılı Sondajları). Maden Tetkik ve Arama Genel Müdürlüğü Rapor No: 11069, Ankara (unpublished).

Şengüler, İ. 2013. Ergene (Trakya) Havzası'nın jeolojisi ve kömür potansiyeli. Maden Tetkik ve Arama Doğal Kaynaklar ve Ekonomi Bülteni 16, 109-114.

Şengüler, İ., Toprak, S., Kara, H., Öner, A., Tuncalı, E., Kır, N. 2000. Güney Trakya Bölgesindeki Kömürlerin Petrografik İncelemesi ve Ortamsal Yorumu. Türkiye 12. Kömür Kongresi Bildiriler Kitabı, 173-180, Karadeniz Ereğlisi, Zonguldak.

Şengüler, İ., Akman, Ü., Taka, M., Dümenci, S., Kalkan, İ., Kır, N., Sulu, K. 2003. Güney Marmara Neojen Havzalarının Kömür Potansiyeli. 56. Türkiye Jeoloji Kurultayı Bildiri Özleri Kitabı, 212-213, Ankara.

Şenol, M. 1980. Keşan (Edirne) ve Marmara Ereğlisi (Tekirdağ) Yörelerinde Oligosen Yaşlı Birimlerin Çökel Ortamları ve Linyit Oluşumları. TJK Bülteni 23, 133-140, Ankara.

Şentürk, K., Sümengen, M., Terlemez, İ., Karaköse, C. 1998a. Çanakkale-D3 paftası, 1: 100000 ölçekli açınsama nitelikli Türkiye jeoloji haritaları. 63. Maden Tetkik ve Arama Müdürlüğü, Ankara.

Şentürk, K., Sümengen, M., Terlemez, İ., ve Karaköse, C. 1998b. Çanakkale-D3 paftası, 1: 100000 ölçekli açınsama nitelikli Türkiye jeoloji haritaları. 64. Maden Tetkik ve Arama Müdürlüğü, Ankara.

Tanar, Ü., Gökçen, N. 1990. Mut-Ermenek Tersiyer İstifinin Stratigrafisi ve Mikropaleontolojisi. Maden Tetkik Arama Enstitüsü Dergisi 110, 175-181, Ankara.

Taner, F., Çağatay, A. 1983. Istranca masifindeki maden yataklarının jeolojisi ve minerolojisi. Türkiye Jeoloji Kurumu Bülteni 26, 31-40, Ankara.

Taner, G. 1980. Das Neogen der Umgebung Yalova. Communications de la Faculté des Sciences de l'Université d'Ankara, Série C1, Géologie, Tome 23, Ankara.

Triebel, E. 1963. Ostrakoden aus dem Sannois und Jungeren Schichten des Mainzer Beckens: 1. Cypritidae. Senckenbergiana, Bd. 44, Frankfurt.

Turgut, S., Eseller, G. 2000. Sequence stratigraphy, tectonics and depositional history in Eastern Thrace Basin, NW Turkey. Marine and Petroleum Geology 17, 61-100.

Turgut, S., Siyako, M., Dilki, A. 1983. Trakya havzasının jeolojisi ve hidrokarbon olanakları. Türkiye Jeoloji Kongresi Bülteni 4, 35-46.

Turgut, S.,Türkaslan, M., Perinçek, D. 1991. Evolution of the Thrace sedimentary basin and its hydrocarbon prospectivity. In: Spencer AM (ed) Generation, accumulation, and production of Europes hydrocarbons. Special Publication of European Association of Petroleum Geoscientists 1, 415-437.

Türkecan, A., Yurtsever, A. 2002. İstanbul paftası, 1: 500000 ölçekli Türkiye Jeoloji Haritası Serisi. Maden Tetkik Arama Genel Müdürlüğü, Ankara.

Uffenorde, H., Radtke, G. 2008. On noding in Serrocytheridea and Hemicyprideis (Cytherideinae) from the Early Oligocene (Mainz Basin, Germany). Senckenbergiana lethaea 88, 77–92.

Umut, M., Kurt, Z., İmik, M., Özcan, I., Sarıkaya, H., Saraç, G. 1983. Tekirdağ, Silivri (İstanbul), Pınarhisar alanının jeolojisi. Maden Tetkik ve Arama Genel Müdürlüğü Derleme Rapor no: 7349, Ankara (unpublished).

Ünal, O.T. 1967. Trakya jeolojisi ve petrol imkanları. TPAO Arama Grubu Arşivi, rapor no 391, 80 s., Ankara (unpublished).

Ünlügenç, U.C., Demirkol, C., Şafak, Ü. 1991. Adana Baseni K-KD'nda yer alan Karsantı Baseni Çökellerinin Stratigrafik-Sedimantolojik Nitelikleri. A. Suat Erk Jeoloji Simpozyumu (2-5 Eylül 1991), Bildirileri, 1993, 215-227, Ankara.

Üşümezsoy, Ş. 1982. Igneous and metamorphic geology and mineralization of Istranca region (Geotectonic setting and mineralization of the Istranca masif). İstanbul University Earth Sciences Review, v.3, no. 1-2, 227-294.

Vasiliev, J., Krigsman, W., Stoica, M., Langereis, Cor, G. 2005. Mio-Pliocene magnetostratigraphy in the southern Carpathian foredeep and Mediterranean-Paratethys correlations. Terra Nova 17, 376-384.

Wenz, W. 1922. Zur Nomenklatür tertiärer Land und Süsswassergastropoden. Senkenbergiana, Bd. IV, Heft 5, 2, 75-86, Frankfurt.

Witt, W. 2003. Freshwater ostracods from Neogene deposits of Develiköy (Manisa, Turkey). Zitteliana A43, 93-108.

Witt, W. 2011. Mixed ostracod faunas, co-occurrence of marine Oligocene and non-marine Miocene taxa at Pınarhisar, Thrace, Turkey. Zitteliana A51, 237-254.

Zalanyi, B. 1929. Morpho-systematische Studien über fosil: Muschelkrebse. Geological of Hungary Services Paleontology 5:1-153.

PLATES

PLATE - I

1-3. *Cytheromorpha zinndorfi* (Lienenklaus)

    1. Carapace, left side view, Hacısungurlu Borehole, 34th sample

    2. Carapace, left side view, Malkara-Tekirdağ Measured Section, 8th sample

    3. Carapace, right side view, Bıyıkali Measured Section, 7th sample

4. *Cytheromorpha* sp.

    4. Carapace, right side view, Silivri-Değirmenköy Measured Section, 6th sample

5. *Cladarocythere apostolescui* (Margerie)

    5. Left valve, side view, Hacısungurlu Borehole, 34th sample

6. *Neocyprideis apostolescui* (Keij)

    6. Left valve, outside view, Hacısungurlu Borehole, 23rd sample

7. *Neocyprideis williamsoniana* (Bosquet)

    7. Left valve, outside view, Hacısungurlu Borehole, 66th sample

8-9. *Cytheridea pernota* (Oertli and Keij)

    8. Right valve, outside view, Hacısungurlu Borehole, 53rd sample

    9. Left valve, outside view, Hacısungurlu Borehole, 53rd sample
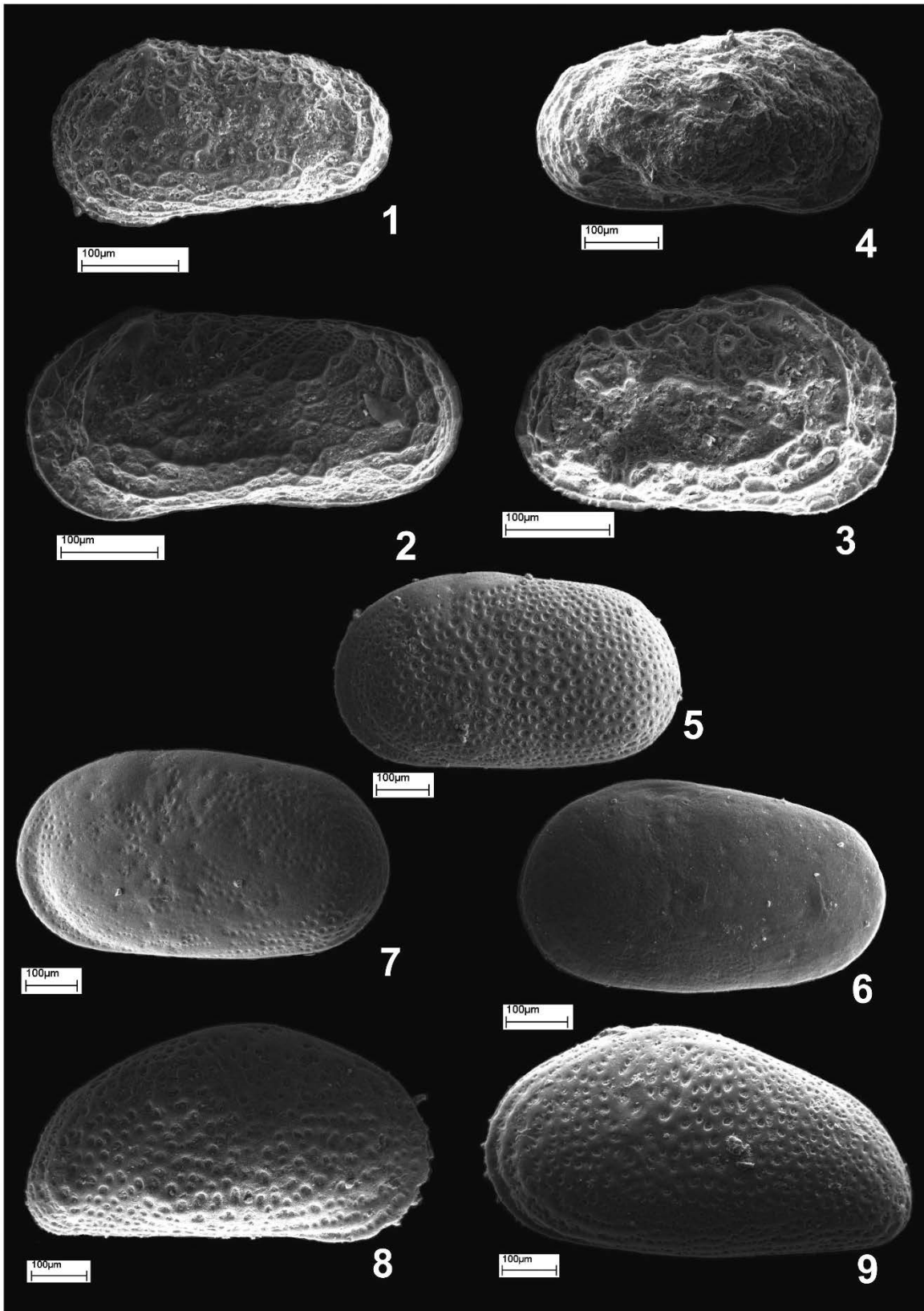
PLATE - 2

1. *Cytheridea crassa* Terquem

    1. Carapace, right side view, Hacısungurlu Borehole, 56th sample

2-4. *Hemicyprideis montosa* (Jones and Sherborn)

    2. Left valve, outside view, Hacısungurlu Borehole, 65th sample

    3. Right valve, outside view, Silivri Measured Section, 2nd sample

    4. Carapace, left side view, Hacısungurlu Borehole, 53rd sample

5. *Hemicyprideis elongata* Keen

    5. Carapace, right side view, Silivri Measured Section, 2nd sample

6-8. *Serrocytheridea eberti* (Lienenklaus)

    6. Carapace, left side view, Malkara-Tekirdağ Measured Section, 8th sample

    7. Carapace, right side view, TD-58 Borehole, 9th sample

    8. Carapace, left side view, Malkara-Tekirdağ Measured Section, 6th sample
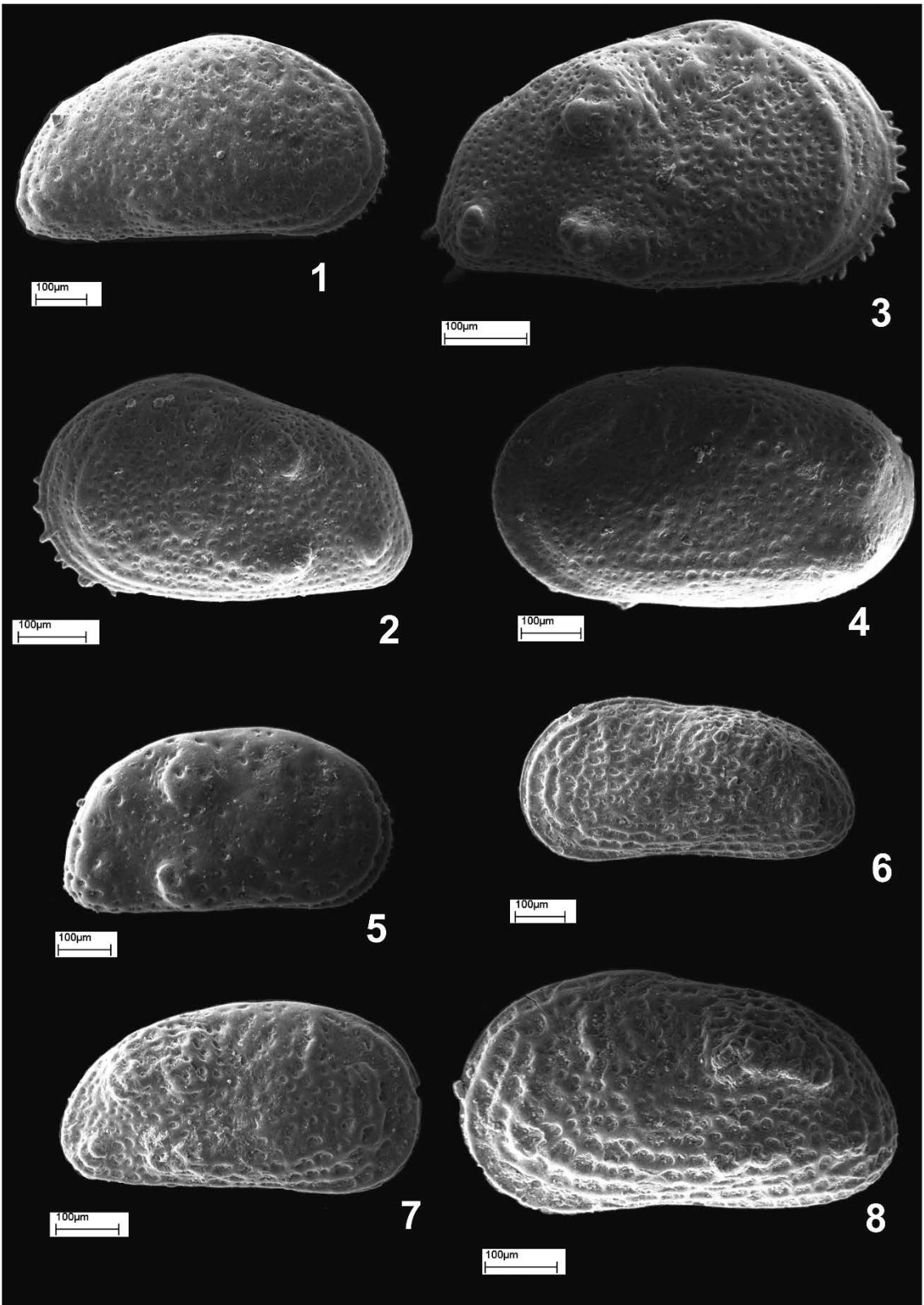
PLATE - 3

1-2. *Krithe angusta* Brady and Norman

  1. Carapace, right side view, Malkara-Tekirdağ Measured Section, 6th sample

  2. Carapace, left side view, Malkara-Tekirdağ Measured Section, 6th sample

3. *Candona (Pseudocandona) fertilis* Triebel

  3. Left valve, outside view, Hacısungurlu Borehole, 52nd sample

4. *Candona (Lineocypris)* sp.

  4. Left valve, outside view, Hacısungurlu Borehole, 48th sample

5. *Virgatocypris tenuistriata* (Dollfus)

  5. Carapace, left side view, Hacısungurlu Borehole, 14th sample

6. *Ilyocypris boehli* Triebel

  6. Right valve, outside view, Hacısungurlu Borehole, 66th sample

7. *Candona (Caspiocypris) alta* (Zalanyi)

  7. Left valve, outside view, Silivri-Değirmenköy Measured Section, 9th sample

8. *Heterocypris salina* (Brady)

  8. Left valve, outside view, Babaeski-Edirne Road, 1st point sample
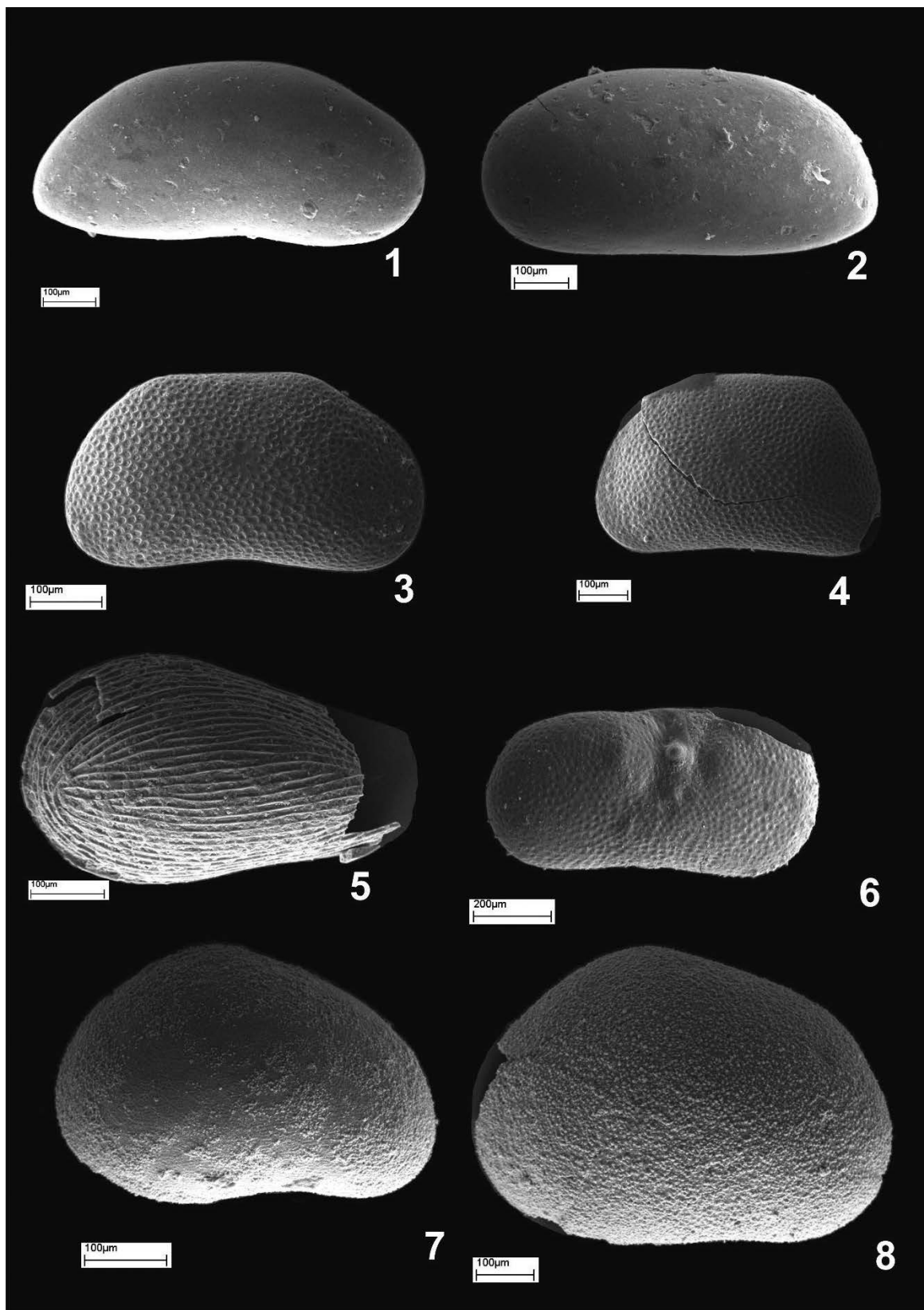
PLATE - 4

1. *Eucypris dulcifons* Diebel and Pietrzenuik

    1. Carapace, left side view, TD-58 Borehole, 2nd sample

2. *Candona (Caspiolla)* sp.

    2. Left valve, outside view, Silivri-Değirmenköy Measured Section, 9th sample

3. *Gyraulus* sp.

    3. Carapace, dorsal view, Hacısungurlu Borehole, 89th sample

4. *Potamides* sp.

    4. Carapace, side view, Hacısungurlu Borehole, 56th sample

5. *Viviparus* sp.

    5. Carapace, oral view, Hacısungurlu Borehole, 56th sample

6. *Avimactra* sp.

    6. Valve, outside view, Hacısungurlu Borehole, 87th sample

7. *Modiolus* sp.

    7. Valve, outside view, Hacısungurlu Borehole, 87th sample

Bulletin of the Mineral Research and Exploration

http://bulletin.mta.gov.tr
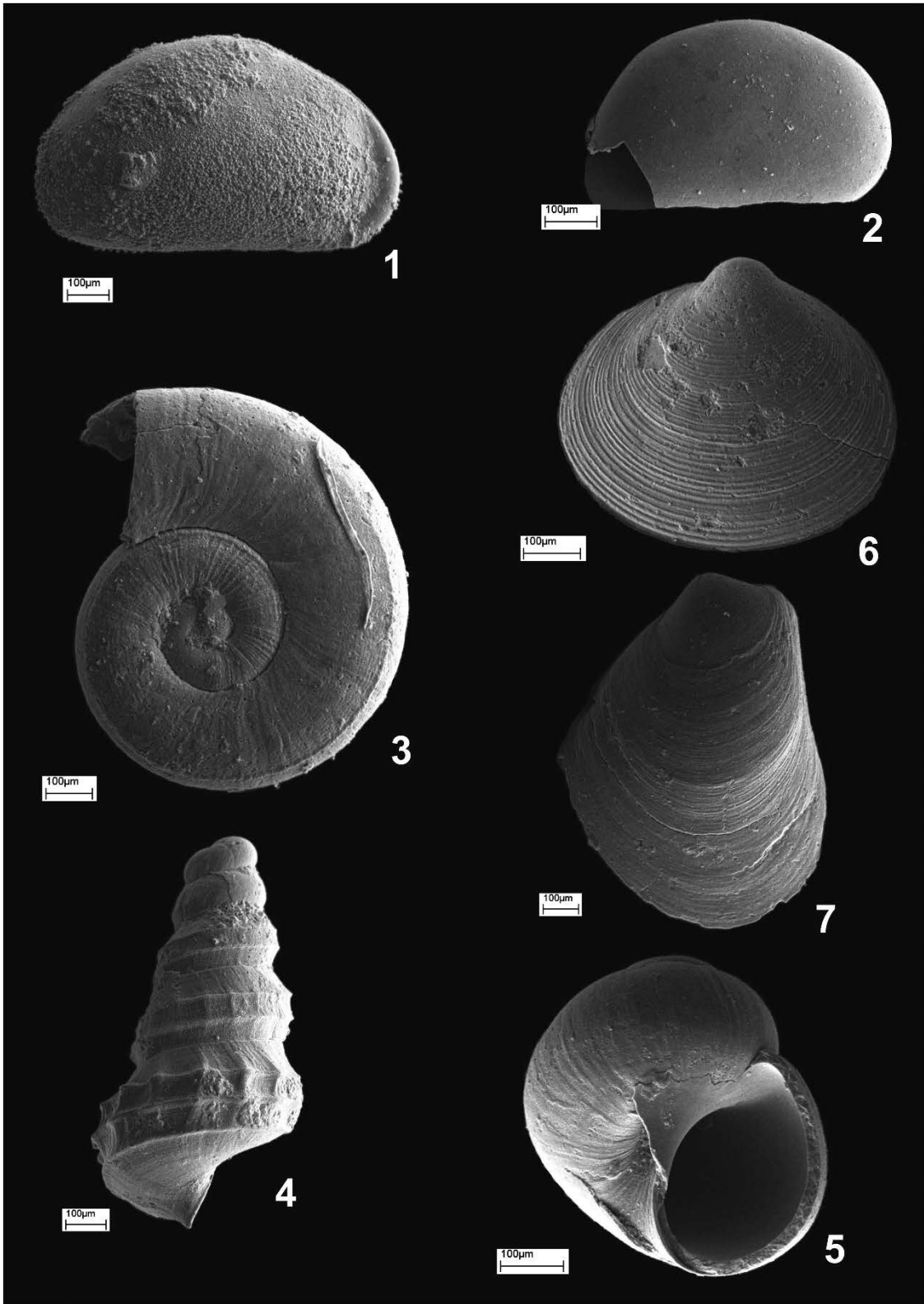
Petrological and geochemical features of Biga Peninsula granitoids, NW Anatolia, Turkey

Ümit AYDIN[a] , Pınar ŞEN[*a] , Öner ÖZMEN[a]   and Erdal ŞEN[b]

[a]*General Directorate of Mineral Research and Exploration, Mineral Research and Exploration Department, 06800, Ankara, Turkey.*
[b]*Hacettepe University, Faculty of Engineering, Geological Enginerirng Department, 06532, Ankara, Turkey.*

Research Article

ABSTRACT

In Northwest Anatolia, widespread magmatism developed due to collision between Anatolide-Tauride platform and Sakarya continent during Late Cretaceous-Early Tertiary period. The granitoids in Biga Peninsula are products of post-collisional magmatism following the convergence of the northern branch of Neotethyan Ocean and developed in two different stages as Eocene and Oligo-Miocene. Eocene Karabiga, Güreci, Kuşçayır and Dikmen granitoids are granite and diorite-granodiorite; Oligo-Miocene Sarıoluk, Yenice, Kestanbol, Eybek, Evciler, Çamyayla and Alanköy granitoids are diorite, granodiorite, monzonite and Q-monzonite in composition. Metaluminous and peraluminous granitoids have similar geochemical variations and exhibit post-collisional geochemical signatures. Trace element patterns are almost similar to those observed in upper crust and GLOSS (Global Subducting Sediment) patterns with depletion in high field strength (HFS) elements (Nb, Ta, Ti, Zr, Hf). But, Oligo-Miocene Sarıoluk, Yenice-Çakıroba, Kestanbol, Evciler, Çamyayla, Alanköy and Eocene Karabiga, Güreci and Kuşçayır granitoids have higher Th and U contents relative to upper crust and GLOSS. Dikmen, Yenice-Hamdibey, Yenice-Eskiyayla and Eybek granitoids have lower Th content. Geochemical variations indicate that partial melting and fractional crystallisation-crustal contamination processes are effective in their genesis and evolution. Trace element ratios also indicate subduction signatures in their genesis and Rb/Ba, Rb/Sr ratios suggest mantle melting rather than crustal melting. Accordingly, post-collisional Biga Peninsula granitoids were derived from a previously metasomatised lithospheric mantle source, which was enriched during northward subduction and closure of the northern branch of Neo-Tethys Ocean beneath the Sakarya continent, since variations in Rb, Cs, Th, La and Sm reveal that lithospheric mantle was mesomatised by both aqueous fluids and sediment melts.

1. Introduction

The closure of the Neo-Tethys ocean at the end of the Late Cretaceous and the following continental collision played an important role in the tectonic evolution of Anatolia. As a result of the subduction of the northern branch of the Neo-Tethys beneath the Sakarya continent to the north, continent-continent collision occurred between the Anatolide-Tauride platform and the Sakarya continent. This collision occurring along the northern section of Anatolia is represented by the İzmir-Ankara-Erzincan suture zone (IAESZ) and this suture zone separates the Sakarya zone from the Anatolide-Tauride platform (Okay and Tüysüz, 1999; Şengör and Yılmaz, 1981). The continent-continent collision is thought to have occurred before the Middle Eocene (Genç and Altunkaynak, 2007; Altunkaynak et al., 2012*a*) in the Palaeocene-Early Eocene period (Okay et al., 2001; Okay, 2008). Latest Early Eocene is accepted as the time of post-collisional extensional tectonics (Yılmaz et al., 1995; Genç and Yılmaz, 1997;

Karacık et al., 2008). After this collision, widespread magmatic activity occurred in northwest Anatolia (Yılmaz, 1989; 1990; Güleç, 1991; Harris et al., 1994; Seyitoğlu and Scott, 1996; Altunkaynak et al., 2012*a, b*). After collision, the first products of magmatism comprised Middle Eocene-aged granitic plutons and intermediate-composition calcalkaline volcanic rocks (Harris et al., 1994; Delaloye and Bingöl, 2000; Altunkaynak and Dilek, 2006; Okay and Satır, 2006; Altunkaynak, 2007; Altunkaynak and Genç, 2008; Yılmaz Şahin et al., 2010; Altunkaynak et al., 2012*b*; Altunkaynak and Dilek, 2013; Ersoy and Palmer, 2013; Gülmez et al., 2013; Aysal, 2015; Ersoy vd., 2017*a, b*). It is known that the Late Oligocene-Early Miocene period magmatism produced granitic plutons and coeval volcanic rocks commonly observed in NW Turkey (Genç, 1998; Aldanmaz et al., 2000; Karacık et al., 2008; Hasözbek et al., 2010*a, b*; Yılmaz Şahin et al., 2010; Altunkaynak et al., 2012*a*; Erkül and Erkül, 2012; Aldanmaz et al., 2015; Aysal, 2015). Upper Miocene-Pliocene magmatism generally has alkaline basaltic composition (Yılmaz et al., 2001; Aldanmaz et al., 2015; Kürkcüoğlu et al., 2008).

There are two different opinions about the origin and tectonic setting of magmatism in northwest Turkey. According to the first of these, Middle Miocene magmatic rocks formed in a magmatic arc environment (Peccerillo and Taylor, 1976; Yılmaz et al., 1981; Ercan et al., 1995; Köprübaşı et al., 2000; Okay and Satır, 2006; Ustaömer et al., 2009). The second view is that these are post-collisional magmatism products and formed due to lithospheric delamination or slab break-off mechanisms (Aldanmaz et al., 2000; Köprübaşı and Aldanmaz, 2004; Dilek, 2006; Altunkaynak, 2007; Keskin et al., 2008; Kürkcüoğlu et al., 2008; Dilek and Altunkaynak, 2009; Gülmez et al., 2013). In recent years, the second view has gained more acceptance.

As the Biga Peninsula is a region where subduction, continent-continent collision and post-collisional processes may be observed, it forms a good area to research geochemical dynamics of magmatism and to reveal the effects of these processes on the genesis and the evolution of the magmatism. This study assessed the mineralogical-petrographical and geochemical features of granitic plutons located in the Biga Peninsula with the aim of determining magma source based on major oxides, trace elements and rare earth elements to explain the source properties and magmatic evolution.

2. Regional Geology

The Late Cretaceous-Early Eocene period was a tectonically active period and Tethyan evolution was effective in Western Anatolia with ophiolite emplacement, high pressure/low temperature metamorphism, subduction, arc magmatism and continent-continent collision processes occurring (Okay et al., 2001). As a result, northwest Turkey is located in an important orogenic belt where different tectonic assemblages and belts can be observed together (Şengör and Yılmaz, 1981; Okay, 1989; Okay et al., 1996; Okay and Tüysüz, 1999; Okay et al., 2001). These tectonic assemblages are separated from each other by sutures represented by ophiolites, metamorphic rocks and accretionary complexes (Okay et al., 2001). The Biga Peninsula comprises two different tectonic assemblages separated from each other by the Intra-Pontide Suture Zone in the northwest; these assemblages are the Rhodope-Istranca massif to the north and the Sakarya assemblage to the south (Figure 1a). The Sakarya assemblage is bounded by the Intra-Pontide suture zone to the north and the İzmir-Ankara-Erzincan suture zone to the south (Figure 1a). The basement of the assemblage is Palaeozoic-aged metamorphic and plutonic rocks (Okay et al., 1996; Delaloye and Bingöl, 2000; Okay et al., 2006; Topuz et al., 2007; Okay, 2008) and the Permo-Triassic-aged (subduction/addition complex) accretionary complex known as the Karakaya complex which underwent severe deformation and partial metamorphism (Okay et al., 1996; Okay and Göncüoğlu, 2004; Okay et al., 2006; Okay, 2008). The complex basement is unconformably overlain by Lower-Middle Jurassic continental-shallow marine clastic sedimentary rocks (Altıner et al., 1991; Okay, 2008) and Middle-Upper Jurassic platform-type neritic limestones, Lower Cretaceous limestones and Upper Cretaceous-Palaeocene volcanic and sedimentary rocks (Akyüz and Okay, 1996; Okay et al., 1996; Okay and Tüysüz, 1999; Okay, 2008).

The Biga Peninsula has complicated geology comprising variable metamorphic, magmatic and sedimentary rocks with ages from the Palaeozoic to the Cenozoic. Since the main subject of this study comprises the mineralogical-petrographical and geochemical features of Eocene and Oligo-Miocene-aged granitoids in the Biga Peninsula, the geology of the region has been simplified (Figure 1). Rocks outcropping in the Biga Peninsula may be divided in

two as pre-Tertiary basement rocks and Tertiary rocks (Duru et al., 2012). In the study area, pre-Tertiary basement rocks outcrop within NE-SW striking tectonic zones (Duru et al., 2012). These zones are the Çetmi melange, Ezine zone and Sakarya Zone from west to east (Figure 1b).

The Sakarya Zone forming the basement in the study area comprises the underlying Kazdağ metamorphics and tectonically associated Kalabak

Group and Karakaya complex. All these units are unconformably overlain by Jurassic-Cretaceous-aged neritic carbonates (Figure 1b). Ezine Zone which is outcropped in the NW of the peninsula, is represented by the Karadağ Group, Çamlıca metamorphics and the Denizgören ophiolite overlying these units with a tectonic contact. The Ezine and Sakarya zones are overlain by the Upper Cretaceous-aged Çetmi Melange (Duru et al., 2012) (Figure 1b).
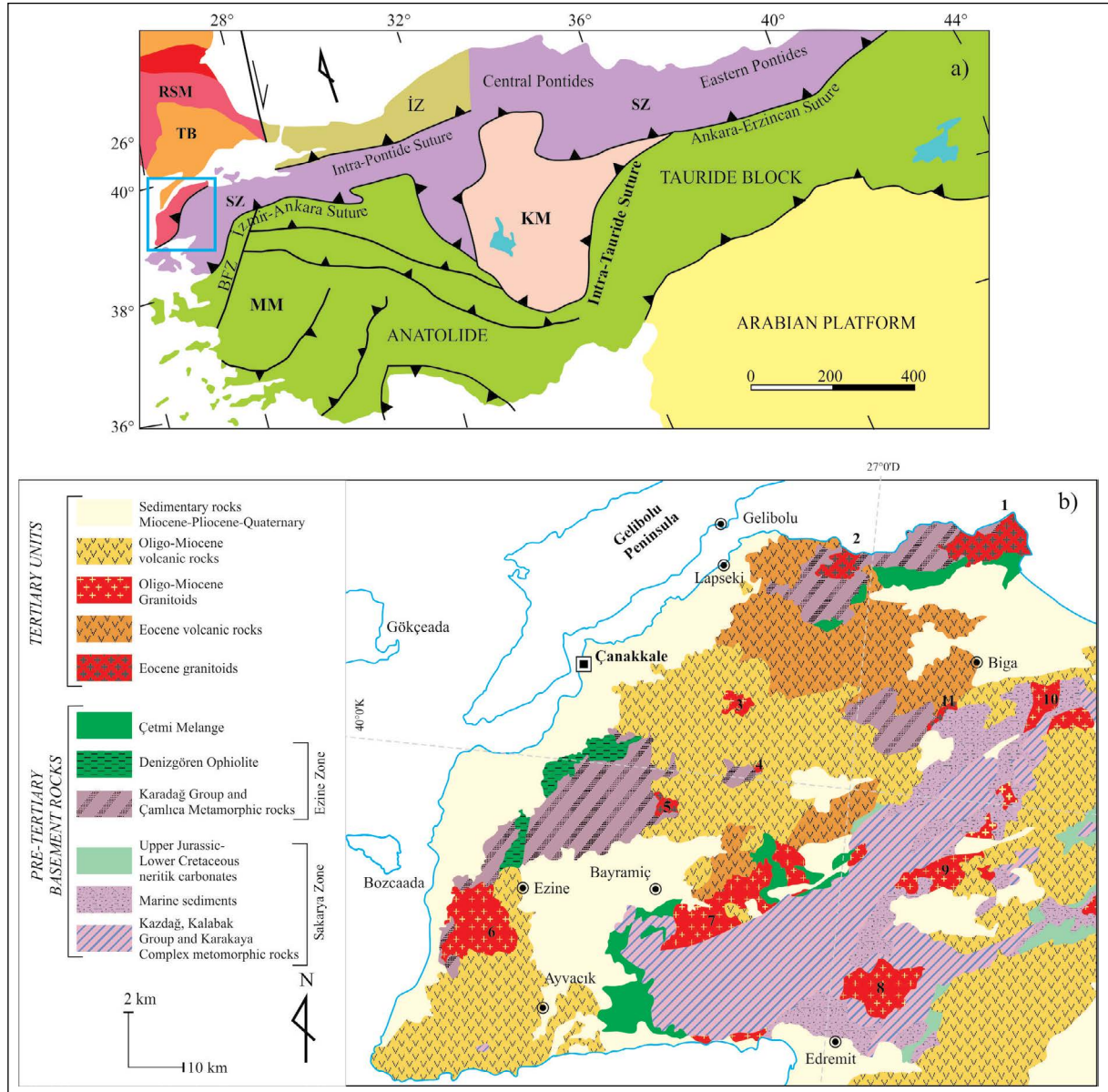
Figure 1- a) Tectonics of Turkey (Okay and Tüysüz, 1999). RSM: Rhodope-Strandja Massif; TB: Thace basin; İZ: İstanbul Zone; SZ: Sakarya Zone; MM: Menderes Massif; KM: Kırşehir Massif; BFZ: Bornova Flysch Zone. b) Generalised geological map of Biga Peninsula (Konak et al., 2016; Duru et al., 2012; Ersoy et al., 2017a, b). 1: Karabiga pluton; 2: Güreci pluton; 3: Çamyayla pluton; 4: Alanköy pluton; 5: Kuşçayır pluton; 6: Kestanbol pluton; 7: Evciler pluton; 8: Eybek pluton; 9: Yenice pluton; 10: Sarıoluk pluton; 11: Dikmen pluton.

Above these pre-Tertiary basement rocks in the study region, magmatic and sedimentary rocks occurred during the Eocene-Quaternary time interval were emplaced (Duru et al., 2012; Ilgar et al., 2012). In the Biga Peninsula, Tertiary plutonic and volcanic rock units are widespread throughout the region. The Tertiary period begins with Eocene granitoids and andesitic-dacitic calcalkaline volcanic rocks and continues in the Upper Miocene with alkaline character basaltic volcanic rocks (Yılmaz, 1990).

Magmatism developing as a result of collision between the Sakarya continent and Anatolide-Tauride platform in the Late Cretaceous-Early Tertiary period produced its first products in the Middle Eocene and continued until the end of the Miocene (Yılmaz, 1997; Karacık and Yılmaz, 1998; Genç and Altunkaynak, 2007; Yılmaz Şahin et al., 2010). The granitoids forming the subject of the study and outcropping over large areas were emplaced in the region in the Eocene and Oligocene-Miocene time interval. The age of the granitoid rocks in the Biga Peninsula becomes younger from Middle Eocene in the north to Oligo-Miocene in the south. This study focuses on the mineralogical, petrographical and geochemical features of the Eocene granitoid rocks of the Karabiga and Güreci granitoids outcropping east of Lapseki and around Karabiga in the north of the Biga Peninsula, Kuşçayır granitoid to the north of Bayramiç, Dikmen granitoids to the south of Biga and the Oligo-Miocene Eybek, Evciler, Kestanbol, Çamyayla, Alanköy, Sarıoluk and Yenice granitoids generally outcropping in the south of the peninsula.

Karabiga granitoid is located north of Karabiga, covering nearly 75 km² area and generally has granitic composition. There are many dikes (pegmatite and aplite dikes) extending in different directions within the pluton. Aplite dikes are elongated mainly N-S direction, with a thickness up to 1.5 m. Pegmatite dikes are generally extending in N60-80°W direction. The basement rocks in the area of the Karabiga granitoid comprises lithologic units such as mica schist, amphibolite schist and gneiss belonging to Permo-Triassic-aged Çamlıca metamorphic rocks. The Upper Cretaceous Çetmi ophiolite tectonically overlies this unit (Duru et al., 2012) and the Karabiga granitoid has been emplaced by cutting both these units.

Güreci granitoid outcropping over 22 km² area around the Çavuşköy and Güreci were first called the Şevketiye granitoid by Delaloye and Bingöl (2000). They are petrographically classified as granodiorite, monzonite and quartz diorite. The Güreci granitoid has experienced intense alteration, fresh outcrops are found only in some stream beds. There are dioritic mafic enclaves hosted within the rock.

Kuşçayır granitoid is mostly represented by dark colored diorite, diorite-porhyry and light colored granodiorite type rocks and it is white, gray and yellowish in color due to weathering. Contact metamorphic zone representing the hornblende hornfels and albite-epidote hornfels facies is developed along the contact with host rock. Plutonic rocks, cutting quartzite and mica-schist, are overlain by volcanic rocks at the ENE of Kuşçayır village.

Dikmen granitoid with a NE-SW trending in the east of Dikmen fault has coarse grained crystals and is greyish white in color. They are usually cut by quartz veins/veinlets which have up to 50 cm. thickness and aplites. The number of quartz veins/veinlets increase from north to south.

Sarıoluk granitoid is located west of Gönen County between Balıkesir and Çanakkale provinces. The unit is brownish-greenish colour, highly weathered, with abundant biotite flakes, metagranite with clear foliation and gneissic granite appearance and petrographically granodiorite composition. Pegmatite veins containing abundant quartz and alkali feldspar are observed cutting the base of the unit in the study area. The unit has tectonic contacts with all surrounding units.

Yenice granitoids, which are usually light colored, are mostly represented by monzonitic and granodioritic rocks, and generally extending in NE-SW direction in the vicinity of Yenice, Hamdibey, Eskiyayla and Çakıroba. Contact metamorphism developed at the contact of plutons. They are abundantly cracked and articulated, and often cut by aplite dykes.

Kestanbol granitoid is grey-brown in colour, with occasional K-feldspar of 4-5 cm cut by lamprophyre in the study area that typically outcrops around Kestanbol and Koçali village. The Kestanbol granitoid is lithologically homogeneous comprising quartz monzonite, monzonite, monzonite porphyry and granite rock types. Aplite, lamprophyre and mafic dikes were emplaced into the fracture planes in the Kestanbol granitoid. The pluton was emplaced within metamorphic basement rocks and there is a

contact metamorphic zone and skarn mineralization at the contact with basement rocks. There are many lamprophyre dikes within the pluton.

Eybek granitoid is a pluton represented by granite, Q-monzonite and granodiorite rocks with N-S, NW and NE trending veins in the east section. Some sections of the pluton are weathered and rounded forms with 30-50 cm diameter are observed due to weathering. Additionally, mafic enclaves are enclosed.

Evciler granitoid is an elliptical body covering nearly 180 km^2 area with WSW-ENE trending. Topography in the area of outcrops is smooth. It was emplaced into the basement rocks and lower volcanic units. An albite-epidote-hornfels facies zone reaching up to 200 m width developed on the contact with Kazdağ metamorphic rocks. Mafic enclaves of various size are observed.

Çamyayla granitoid outcrops around Çan and is coeval with the adjacent Dededağ volcanic assemblage. Products developing during this process are defined by both cross-cutting and overlapping associations. A contact metamorphic zone with actinolite hornfels and quartz-alkali feldspar hornfels facies developed around the pluton.

Alanköy granitoid represented by granodioritic rocks has well developed skarn zones and Q-stockworks as well.

3. Petrographic Features of Biga Peninsula Granitoids

The granitoids in the study area are mostly classified as granite and granodiorite (Appendix 1). In addition, the Güreci, Kestanbol, Kuşçayır, Alanköy and Çamyayla granitoids are called as monzonite, Q-monzonite, Q-monzodiorite and Q-diorite rock types. The granitoids in the region occur as widespread plutonic bodies, and aplite and porphyry dikes having mineralogical composition similar to granitoids occurred as planar intrusions are observed as well. The majority of this type of dikes are observed in the Karabiga, Kestanbol and the Çamyayla granitoids. Almost all samples have holocrystalline texture. Most of the samples having moderate-large grain size exhibit granular texture, whereas dikes have fine-moderate grain size and porphyric texture. The main mineral phases are quartz, plagioclase, orthoclase,

hornblende and biotite, with relatively lesser amounts of microcline and clinopyroxene minerals (Figure 2). Titanite, apatite and opaque minerals are common accessory minerals. Secondary chlorite, sericite, calcite and clay minerals are observed in almost all rocks due to alteration.

Quartz is generally anhedral and crystallised as space-fillings between other minerals. Typically it has undulatory extinction. It is subhedral in Karabiga aplitic rocks and significant reduction is observed in grain size.

Plagioclase is the main component of the granitoids. Many plagioclase minerals have polysynthetic twinning in addition to zoned texture. Generally, there is little or partial sericitisation. Especially in the Evciler granitoids, common myrmekitic texture is observed along grain boundaries. In the Yenice-Eskiyayla granitoids, sieve texture is observed due to excessive alteration. The alteration effect is very limited in the Sarıoluk granitoids.

Alkali feldspar is mainly observed as orthoclase minerals. Microcline is only observed in the Yenice-Eskiyayla granitoids. In all samples, orthoclase generally found as large crystals, has experienced alteration, and more argillized or sericitized than plagioclase minerals. Due to large grain size, they have poikilitic texture enclosing quartz and hornblende minerals especially in the Güreci, Eybek, Kestanbol and Evciler granitoids. In the Karabiga, Yenice-Eskiyayla, Çamyayla, Alanköy and Sarıoluk granitoids, perthitic texture, graphic texture and rare granophyric texture developed.

Hornblende is generally found as long prismatic crystals. They are less common in the Karabiga and Kestanbol granitoids than in other regions. Some of the hornblendes in the Evciler, Yenice-Çakıroba and Sarıoluk granitoids formed from the edges and the cleavages of the pyroxene. As the transformation of pyroxene to amphibole is not complete, pyroxene residues remain. This situation may be explained by rapid volatile loss from granitic magmas (Poutiainena and Scherbakovab, 1998). In some samples, and especially in the Dikmen and Yenice-Hamdibey region, poikilitic texture containing plagioclase minerals has developed. Exsolution of opaque from the cleavage is noteworthy in Eybek and Kuşçayır granitoids. Hornblende in the Çamyayla, Alanköy
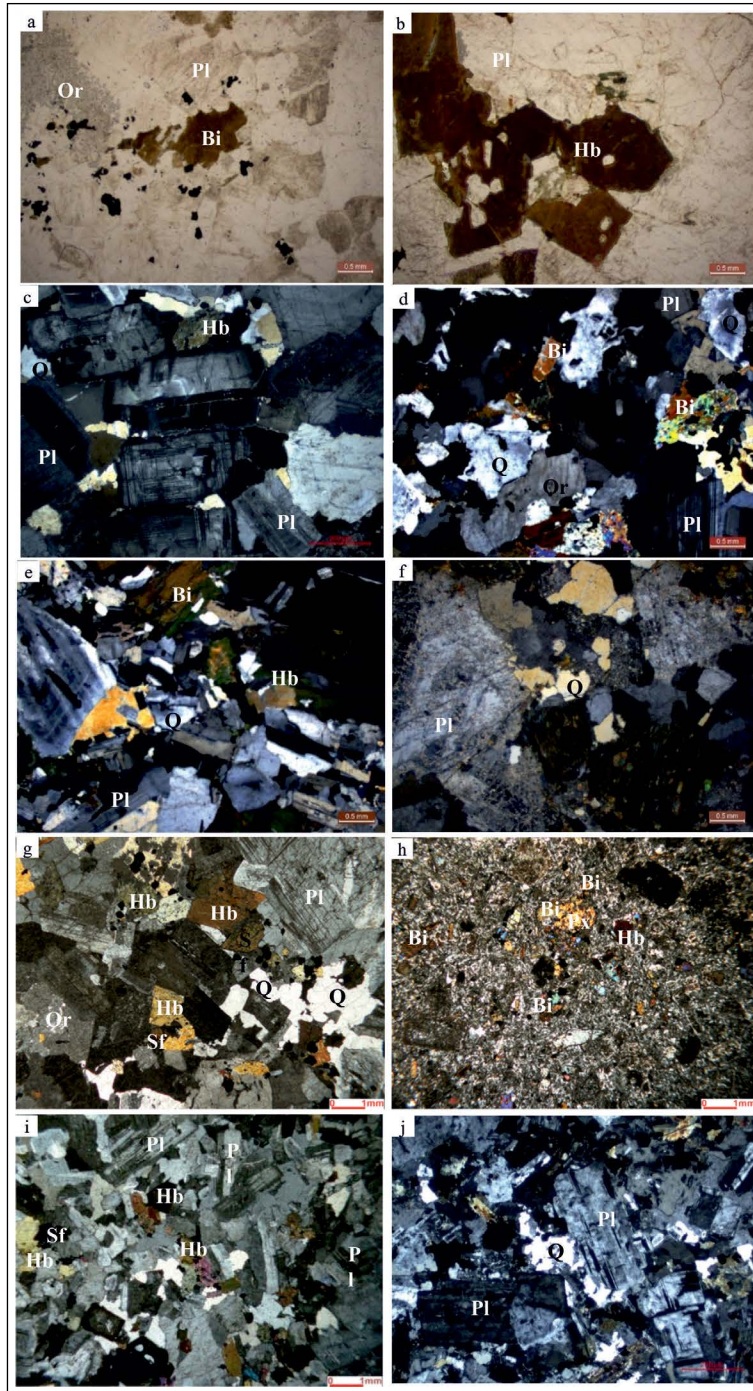
Figure 2- Microphotographs from Biga Peninsula granitoids; a) Granite with a granular texture from Karabiga (plane polarised x 2.5); b) Granite with a granular texture from Güreci granitoid (plane polarised x 2.5); c) Granodiorite with a granular texture from Dikmen granitoid (cross polarised x 2.5); d) Granodiorite sample from Sarıoluk (cross polarised x 2.5); e) Granodiorite from Evciler granitoid (cross polarised x 2.5); f) Q-diyorit sample from Alanköy granitoid (cross polarised x 2.5); g) Q-monzonite sample from Kestanbol granitoid (cross polarised x 2.5); h) Porphyric lamprophyr sample from Kestanbol granitoid (cross polarised x 2.5); i) Monzonite with a holocrystalline granular texture from Kestanbol granitoid (cross polarised x 2.5); j) Q-monzodiorite with a holocrystalline porphyric texture from Kuşçayırı granitoid (cross polarised x 2.5). Bi: biotite; Hb: hornblende; Or: orthoclase; Pl: plagioclase; Px: pyroxene; Q: Quartz; Sf: sphene (titanite).

and Sarıoluk granitoids have been carbonatised and in some parts they are altered to chlorite.

Clinopyroxene minerals have not remained stable, and largely transformed to hornblende minerals. In some samples (Sarıoluk granitoid), though they retain their original crystal form, they are generally observed as residues in the hornblende minerals.

Biotite is found less than hornblende but is the dominant dark-coloured mineral in the Karabiga granitoid, especially, and in dikes in other regions. Generally, they have been chloritised by alteration in the Yenice-Çakıroba, Hamdibey and Evciler granitoids.

Titanite is euhedral crystals in nearly all rocks. Apatite which is rarely observed in the samples, is found as needle-like and prismatic crystals, and it mainly occur as inclusions.

4. Analytical Techniques

Major oxides, trace and rare earth element analyses were performed in General Directorate of Mineral Research and Exploration (MTA), Mineral Analysis and Technology Department. Major oxide analyses were performed by using a Thermo ARL XRF device with 3 g samples mixed with cellulose binder (0.9 g), pressed into pellet form at 40 kN pressure.

Trace and rare earth element analyses were performed by Plasma Quant MS Elite Analytic Jena ICP-MS device. Samples of 0.25 g were dissolved in HCl, HNO_3, $HClO_4$ and HF acids and the dissolved sample was completed to 50 ml for analysis. JG 1a Certified Reference Material was used for quality control of the analysis. The values measured during analysis of certified standard reference material are given in table 1.

5. Geochemical Features of Biga Peninsula Granitoids

The major oxide, trace and rare earth element analysis for granitoids in the Biga Peninsula are given in Table 1. To classify the rocks, the major oxides were normalised to 100% on an anhydrous basis and plotted on a total alkali (Na_2O+K_2O %) - SiO_2% diagram (Figure 3). According to Middlemost (1994)'s volcanic rock classification diagram, Eocene Karabiga, Güreci, Kuşçayır and Dikmen granitoids in Biga Peninsula

are granite, diorite and granodiorite in composition, respectively and Oligo-Miocene granitoids are diorite, granodiorite, monzonite and Q-monzonite in composition. They all exhibit subalkaline major-oxide character (Figure 3). Subalkaline rocks exhibit calcalkaline signature according to the AFM diagram with calcalkaline-tholeiitic dividing line (Irvine and Baragar, 1971) (Figure 3).

Variation diagrams for major oxides and some selected trace elements against SiO_2 (Harker diagrams) are shown in figure 4. Increasing SiO_2 is correlated with (i) decreasing Fe_2O_3, MgO, CaO, Al_2O_3, Sr and Nb and (ii) increasing K_2O and Rb. These observed variations in Fe_2O_3, MgO, CaO, Al_2O_3, Sr, and the relative increase in K_2O and Rb with increasing SiO_2 may indicate fractional crystallisation processes. Na_2O exhibits a relatively horizontal trend with increasing SiO_2. This situation may be due to weathering. It can be concluded that fractional crystallisation processes played a role in the evolution of Biga granitoids.

In the plot of Shand (1943)'s A/NK – A/CNK diagram (Figure 5a), Karabiga samples are generally metaluminous, samples from other granitoids are metaluminous to peraluminous. Most of the samples clearly plot in the I-type granite field. On the ASI-Fe_{tot} diagram of Norman et al. (1992), the majority of samples also represent I-type granite features (Figure 5b). As a result, the Biga Peninsula granitoids exhibit both metaluminous and peraluminous composition. They have MgO/MnO and MgO/Fe_2O_{3t} ratios generally varying from 3 to 27 and 0.20 to 0.52, respectively and Na_2O/CaO ($\leq$4.86) and A/NK (>1.2) values, reflecting the characteristics of continental arc granites (Maniar and Piccoli, 1989).

Primitive mantle (Sun and McDonough, 1989) normalised trace element distribution diagrams of Biga Peninsula granitoids are shown in figure 6. As can be seen on the diagrams, the common features to all the granitoids in the Biga Peninsula are the depletion in Nb, Ta, Zr and Ti elements and the enrichment in Pb and U elements. These observed variations are common geochemical features of arc magmatism and also may form as a result of contamination by continental crust during the upwelling of mantle-derived magmas. Accordingly, negative anomalies in Nb, Ta and Ti and positive anomalies in Pb and U are the most typical features of crustal contamination and/or sediment contribution to mantle-derived

Table 1- Major-oxide (wt.%), trace and rare earth elements (ppm) analysis of Biga Peninsula granitoids (wt. %: weight %; LOI: Loss on ignition)

Sample No	KARABİGA GT						GÜRECİ GT							
	ASM-K11	ASM-K12	ASM-K13	ASM-K14	ASM-K15	ASM-K16	ASM-K01	ASM-K02	ASM-K03	ASM-K04	ASM-K05	ASM-K06	ASM-K07	ASM-K08
SiO_2 (wt.%)	76.1	73.9	73.9	74	72.5	75.4	65.1	64.6	66.1	67.2	62.8	54.2	60.2	59
TiO_2	0.1	0.2	0.2	0.2	0.2	0.1	0.5	0.5	0.5	0.4	0.5	0.5	0.6	0.7
Al_2O_3	13.2	14	13.7	14	15.1	13.6	16.4	16.3	16.2	16.2	16.8	20	17.4	18.3
CaO	0.4	1.6	1.7	1.5	2.1	2.4	4.8	2.2	4.4	3.8	5.9	7.6	5.9	7.7
Fe_2O_3t	1	1.5	1.5	1.5	1.5	0.9	4.6	5.3	4.2	3.5	5.1	8	5.9	4.6
Na_2O	3.1	3.4	3.2	3.4	3.8	3.3	3.2	3.2	3.3	3.2	2.9	4.9	3	3.9
K_2O	5.2	4	4.9	4.4	3.7	3.2	2.6	3.6	2.8	3.2	2.8	1	2.9	1.8
MgO	0.1	0.3	0.3	0.3	0.3	0.3	1.6	1.8	1.5	1.1	1.9	2.3	2.2	2.4
MnO		0.1					0.1	0.2	0.1	0.1	0.1	0.1	0.1	0.1
P_2O_5		0.1	0.1	0.1	0.1	0.1	0.2	0.2	0.2	0.1	0.2	0.3	0.3	0.3
LOI	0.45	0.45	0.35	0.35	0.5	0.35	0.7	1.9	0.6	0.8	0.7	0.8	1.1	1
Total	99.65	99.55	99.85	99.75	99.8	99.65	99.8	99.8	99.9	99.6	99.7	99.7	99.6	99.8
A/CNK	1.15	1.09	1.00	1.07	1.07	1.02	0.97	1.24	0.98	1.03	0.91	0.87	0.92	0.82
A/NK	1.23	1.41	1.29	1.35	1.47	1.53	2.03	1.78	1.91	1.85	2.15	2.19	2.15	2.19
Sc (ppm)	13	14	2	2	2	2	14	13	10	9	12	27	4	12
V	31	21	25	24	26	19	101	112	105	93	132	218	151	166
Cr	163	211	124	220	195	190	155	141	184	173	148	40	93	68
Rb	211	146	166	144	125	75	76	112	94	98	78	34	96	67
Sr	48	116	96	93	136	228	249	229	284	273	351	579	515	544
Y	17	18	12	10	14	13	23	20	16	15	15	97	7	15
Zr	45	24	21	32	17	11	13	12	11	10	14	11	10	13
Nb	17	14	12	14	11	11	10	11	11	11	8	23	8	9
Cs	4	4	5	4	5	1	2	2	3	4	3	2	3	3
Ba	73	330	218	229	248	679	483	748	624	772	733	104	753	254
La	33	31	28	30	29	33	36	27	32	22	23	30	10	22
Ce	61	58	49	47	52	56	66	52	56	44	43	72	21	43
Pr	6	6	4	4	5	5	6	5	5	4	4	8	2	4
Nd	22	22	14	14	14	15	20	17	16	16	15	38	7	15
Sm	4	4	2	2	2	3	4	3	3	3	3	12	1	3
Eu	1.06	1.22	0.25	0.47	0.54	0.47	1.01	0.92	0.8	0.91	0.87	2.27	0.44	0.82
Gd	3.2	3.6	2.2	2.2	2.3	2.4	3	2.7	2.4	2.3	2.4	9.6	1.1	2.3
Tb	0.54	0.56	0.34	0.31	0.35	0.35	0.57	0.52	0.43	0.41	0.45	2.39	0.2	0.42
Dy	3.1	3.1	2	1.7	2.2	2	3.5	3.2	2.5	2.5	2.6	15.9	1.2	2.5
Ho	0.58	0.59	0.4	0.34	0.42	0.4	0.68	0.62	0.49	0.46	0.51	3.07	0.22	0.49
Er	1.96	2	1.55	1.23	1.58	1.45	2.33	2.11	1.67	1.55	1.68	10.34	0.75	1.63
Tm	0.2	0.2	0.2	0.2	0.2	0.2	0.3	0.3	0.2	0.2	0.2	1.4	0.1	0.2
Yb	1.7	1.7	1.9	1.3	1.8	1.6	2.1	1.9	1.5	1.4	1.5	9.2	0.7	1.5
Lu	0.26	0.25	0.31	0.2	0.29	0.25	0.32	0.3	0.23	0.22	0.24	1.3	0.1	0.22
Hf	3.2	1.6	1.3	1.8	1.0	0.8	1.3	1.2	1.1	0.9	1.4	1.7	1.0	1.3
Ta	1.9	1.3	1.2	1.1	1.0	0.6	0.8	0.8	0.7	0.8	0.7	1.8	0.5	0.6
Pb	37	776	25	24	20	22	17	252	20	18	16	13	16	14
Th	77	61	132	76	96	97	95	72	73	74	63	92	37	64
U	18	18	18	19	18	18	21	18	16	17	17	22	9	17

Table 1- (Continued)

Sample No	KUŞÇAYIR GT							DİKMEN GT			SARIOLUK GT			
	ASM-K09	ASM-K10	ASM-K48	ASM-K49	ASM-K50	ASM-K51	ASM-K52	ASM-K56	ASM-K57	ASM-K58	ASM-K25	ASM-K26	ASM-K27	ASM-K28
SiO_2 (wt.%)	60.8	61.6	61.4	61.2	61.2	61.7	56.7	66.2	65.6	64.5	64	64	64	66.2
TiO_2	0.5	0.6	0.5	0.6	0.5	0.6	0.7	0.3	0.3	0.4	0.6	0.5	0.6	0.5
Al_2O_3	17.4	17.2	17	17.3	17.3	16.8	17.6	17.6	18.2	18.7	16.4	16.3	16.2	15.8
CaO	5.7	6	6	5.7	6.3	5.9	6.8	4.5	4.9	4.5	4.4	4.3	4.5	3.8
Fe_2O_3t	5.6	5.5	5.2	5.5	5.3	5.5	7	2.8	2.6	2.7	4.3	4.4	4.4	3.8
Na_2O	3.1	3.1	3.1	3	3.2	3.1	2.9	4.5	4.9	4.6	3.5	3.5	3.4	3.3
K_2O	2.8	2.8	2.9	2.7	2.6	2.8	2	1.8	1.3	1.5	3.9	3.8	3.8	3.9
MgO	2.1	2	2.1	2.2	2.1	2.1	3	1.2	1.1	1.4	1.7	1.7	1.8	1.5
MnO	0.1	0.1	0.1	0.2	0.1	0.1	0.2	0.1	0.1	0.1	0.1	0.1	0.1	0.1
P_2O_5	0.3	0.2	0.2	0.3	0.3	0.3	0.3	0.2	0.1	0.2	0.3	0.3	0.3	0.2
LOI	1.15	0.65	1.15	1.2	0.8	0.95	2.55	0.6	0.6	1.15	0.45	0.65	0.55	0.55
Total	99.55	99.75	99.65	99.9	99.7	99.85	99.75	99.8	99.7	99.75	99.65	99.55	99.65	99.65
A/CNK	0.94	0.90	0.89	0.95	0.88	0.89	0.91	1.00	0.99	1.08	0.91	0.92	0.90	0.95
A/NK	2.14	2.11	2.06	2.20	2.14	2.06	2.54	1.88	1.92	2.03	1.64	1.65	1.67	1.64
Sc (ppm)	15	18	12	10	14	19	23	7	6	8	2	2	10	9
V	151	141	147	149	140	4	4	3	3	4	120	117	122	108
Cr	97	117	87	92	80	21	8	35	25	35	119	127	131	163
Rb	94	88	98	44	54	116	61	63	36	62	161	146	160	157
Sr	489	517	528	514	541	951	974	841	728	988	572	543	584	511
Y	16	21	16	12	25	22	20	15	9	12	11	9	13	13
Zr	9	11	13	18	12	23	100	4	4	5	5	6	7	6
Nb	8	8	10	10	9	11	50	2	2	2	17	15	16	14
Cs	3	4	4	2	3	3	2	9.5	1	1	10	8	8	8
Ba	594	711	681	707	751	844	642	481	352	462	1155	1112	1235	1138
La	30	32	32	38	37	38	27	24	21	15	27	27	26	21
Ce	58	62	67	73	76	68	51	44	37	28	47	45	47	41
Pr	5	6	7	7	8	7	6	5	4	3	4	4	4	4
Nd	21	24	28	26	33	29	25	19	14	13	14	13	17	15
Sm	4	5	5	4	6	5.5	5	3.3	2.4	2.6	2	2	3	3
Eu	1.16	1.37	1.62	1.35	1.52	1.6	1.5	1	0.8	1	0.43	0.55	1.03	0.88
Gd	3.1	3.8	5.9	5.2	7.4	5.1	4.8	3.5	2.6	2.6	2.4	2.4	3.2	2.8
Tb	0.51	0.67	0.67	0.55	0.94	0.8	0.7	0.5	0.3	0.4	0.33	0.3	0.44	0.42
Dy	2.8	3.9	3.1	2.5	4.8	4.2	3.8	2.7	1.8	2.2	1.9	1.6	2.4	2.4
Ho	0.53	0.73	0.57	0.45	0.92	0.7	0.6	0.4	0.3	0.4	0.35	0.31	0.47	0.46
Er	1.75	2.42	2.11	1.67	3.34	2.2	2.1	1.5	1	1.3	1.32	1.16	1.66	1.62
Tm	0.2	0.3	0.3	0.2	0.4	0.4	0.3	0.2	0.2	0.2	0.2	0.2	0.2	0.2
Yb	1.5	2	1.9	1.5	2.9	2.5	2.2	1.6	1	1.3	1.5	1.3	1.5	1.5
Lu	0.21	0.29	0.26	0.21	0.39	0.4	0.4	0.3	0.2	0.3	0.23	0.19	0.22	0.22
Hf	1.1	1.2	1.0	1.4	1.0	1.6	2.8	0.4	0.3	0.4	0.5	0.7	0.9	0.7
Ta	0.6	0.6	0.5	0.5	0.5	1	0.6	0.7	0.4	0.6	1.2	1.0	1.0	1.0
Pb	18	20	73	36	18	43	29	12	10	9	89	41	43	67
Th	63	55	96	107	92	0.9	0.6	0.3	0.2	0.2	86	77	70	73
U	17	18	26	22	24	4.8	3.1	1.1	0.7	1	19	20	21	20

Table 1- (Continued)

Sample No			YENİCE GT										
			Çakıroba	Çakıroba	Çakıroba	Hamdibey	Hamdibey	Hamdibey	Hamdibey	Hamdibey	Eskiyayla	Eskiyayla	Eskiyayla
	ASM-K29	ASM-K30	ASM-K31	ASM-K32	ASM-K33	ASM-K59	ASM-K60	ASM-K61	ASM-K62	ASM-K63	ASM-K53	ASM-K54	ASM-K55
SiO$_2$ (wt.%)	63.9	63.1	63.7	61.2	63	63.1	64.5	63.1	62.3	62.2	69.7	67.8	65.3
TiO$_2$	0.6	0.6	0.6	0.6	0.6	0.6	0.5	0.7	0.6	0.7	0.3	0.3	0.4
Al$_2$O$_3$	15.9	16	16.2	16	16.3	16	15.9	15.5	16.1	16.1	15.7	15.8	15.9
CaO	4.8	5	4.5	4.9	5.1	4.7	4.3	5	5.1	5.2	1.3	2.8	4.5
Fe$_2$O$_3$t	4.3	4.5	4.7	4.6	4.9	4.8	4.5	5	5.2	5.2	2.8	3.3	3.7
Na$_2$O	3.1	3.2	3.2	3.2	3.3	3.4	3.2	2.8	3.2	3.3	4.3	3.9	3.7
K$_2$O	4.2	4.1	3.8	3.9	3.5	3.7	4	4.5	3.8	3.6	3.2	3	2.3
MgO	1.9	2	2	2.2	2	2	1.8	2.1	2.1	2.2	0.8	1.3	1.5
MnO	0.1	0.1	0.1	0.1	0.1	0.1	0.1	0.1	0.1	0.1	0.1	0.1	0.1
P$_2$O$_5$	0.3	0.3	0.3	0.3	0.3	0.3	0.3	0.3	0.3	0.3	0.1	0.1	0.2
LOI	0.6	0.7	0.6	2.7	0.65	0.95	0.5	0.45	0.8	0.75	1.35	1.4	2.05
Total	99.7	99.6	99.7	99.7	99.75	99.65	99.6	99.55	99.6	99.65	99.65	99.8	99.65
A/CNK	0.86	0.85	0.92	0.87	0.88	0.88	0.91	0.83	0.86	0.86	1.22	1.07	0.95
A/NK	1.65	1.65	1.73	1.68	1.77	1.67	1.66	1.63	1.71	1.72	1.49	1.63	1.85
Sc (ppm)	17	14	12	13	13	16	12	13	17	17	5	8	7
V	114	114	122	117	125	4	4	4	5	4	3	3	3
Cr	54	60	132	128	117	26	26	13	28	23	32	27	26
Rb	156	151	151	162	130	188	164	166	189	165	97	101	53
Sr	587	579	546	506	564	1184	806	800	1150	1048	439	686	653
Y	32	22	23	23	22	24	21	26	24	28	11	23	18
Zr	7	7	7	5	7	12	10	10	12	11	7	10	7
Nb	18	16	15	15	14	6	5	5	6	6	4	5	3
Cs	10	8	8	12	6	5	5	7	7	8	2	1	1
Ba	1239	1197	1030	1107	1201	1591	1014	888	1432	1261	773	1141	948
La	54	88	42	40	39	67	44	51	66	65	40	38	31
Ce	117	163	86	80	80	123	92	93	121	126	70	64	55
Pr	12	17	9	8	8	13	11	11	13	14	7	7	6
Nd	45	66	34	31	32	52	42	44	53	57	26	27	23
Sm	8	11	6	6	6	8.7	7.2	8.1	9.2	10	4.2	4.7	4.1
Eu	1.99	2.46	1.45	1.37	1.33	2.3	1.6	1.7	2.3	2.3	1.1	1.4	1.3
Gd	8.3	10.9	6.3	6	6.1	8.8	7.3	7.9	9.3	10	3.9	4.7	4.2
Tb	1.12	1.17	0.83	0.78	0.82	1	0.9	1	1.1	1.2	0.5	0.7	0.6
Dy	5.9	4.8	4.4	4.1	4.2	4.9	4.2	5.3	5.2	5.9	2.2	3.9	3.2
Ho	1.09	0.79	0.81	0.78	0.81	0.8	0.7	0.8	0.8	0.9	0.3	0.7	0.5
Er	3.86	2.77	2.85	2.74	2.82	2.6	2.3	2.9	2.8	3.2	1.3	2.4	1.9
Tm	0.5	0.3	0.4	0.3	0.3	0.4	0.3	0.4	0.4	0.5	0.2	0.4	0.3
Yb	3.4	2	2.5	2.4	2.4	2.6	2.3	2.9	2.7	3.1	1.3	2.6	2
Lu	0.48	0.27	0.35	0.34	0.34	0.5	0.5	0.5	0.5	0.6	0.3	0.5	0.4
Hf	0.8	0.7	1.0	0.5	0.9	0.9	0.8	0.8	0.9	1	0.5	0.7	0.5
Ta	1.5	0.9	1.0	1.1	0.9	1.6	1.4	1.7	1.5	2.1	0.7	0.8	0.6
Pb	47	42	33	30	32	35	27	44	47	42	18	21	18
Th	110	182	97	92	89	2.3	2.1	2.3	2.3	2.6	1.1	1.1	0.8
U	23	33	22	21	21	11	12.6	12.4	14.9	18.9	4.4	4.8	4

Table 1- (Continued)

Sample No	KESTANBOL GT					EYBEK GT						EVCİLER GT		
	ASM-K41	ASM-K42	ASM-K43	ASM-K44	ASM-K45	ASM-K64	ASM-K65	ASM-K66	ASM-K67	ASM-K69	ASM-K70	ASM-K34	ASM-K35	ASM-K36
SiO_2 (wt.%)	63.1	62.1	64.3	64.2	63.7	57.1	63.9	63.5	62.3	63.1	60.9	60.3	63.8	60.9
TiO_2	0.5	0.5	0.5	0.5	0.5	0.8	0.7	0.6	0.6	0.6	0.7	0.6	0.5	0.5
Al_2O_3	16.8	16.7	16.3	16.2	16.4	17.5	15.6	15.8	16.4	16.4	16.9	17.6	16.2	16.6
CaO	4.2	4.3	4	4	4.1	5.9	4.6	4.4	5	4.8	5.5	6	5	5.7
Fe_2O_3t	4.6	4.3	3.8	4	4	7.2	4.6	5	5.3	4.9	5.5	5.9	4.6	5.6
Na_2O	3.7	3.6	3.8	3.6	3.6	3.6	3	3.2	3.2	3.3	3.4	3.5	3.4	3.3
K_2O	4	4.7	4.5	4.5	4.4	2.8	4.2	3.8	3.6	3.5	3.4	3	3.1	2.9
MgO	1.7	2	1.5	1.6	1.7	2.7	2	2.2	2.1	2	2.4	1.9	1.7	2.5
MnO	0.1	0.1	0.1	0.1	0.1	0.1	0.1	0.1	0.1	0.1	0.1	0.1	0.1	0.1
P_2O_5	0.2	0.5	0.4	0.4	0.4	0.3	0.3	0.3	0.3	0.3	0.3	0.3	0.2	0.3
LOI	0.7	0.85	0.35	0.55	0.6	1.55	0.7	0.75	0.7	0.65	0.55	0.5	1.25	1.15
Total	99.6	99.65	99.55	99.65	99.5	99.55	99.7	99.65	99.6	99.65	99.65	99.7	99.85	99.55
A/CNK	0.93	0.89	0.88	0.90	0.90	0.89	0.87	0.91	0.90	0.91	0.88	0.88	0.90	0.88
A/NK	1.61	1.52	1.46	1.50	1.53	1.95	1.64	1.68	1.79	1.78	1.82	1.95	1.81	1.94
Sc (ppm)	12	15	14	12	16	17	14	14	16	13	20	13	11	11
V	140	138	118	124	125	4	4	4	4	4	5	145	129	137
Cr	81	127	106	107	127	10	15	21	25	21	24	105	157	136
Rb	151	213	205	186	193	136	163	166	164	141	164	107	112	87
Sr	393	819	793	770	788	1261	930	864	1039	899	1412	511	428	620
Y	18	21	23	21	14	19	42	25	24	20	26	26	20	20
Zr	22	14	10	10	12	25	13	10	11	10	13	7	6	6
Nb	13	18	18	16	15	12	6	5	6	5	7	12	11	9
Cs	7	7	8	4	4	9	4	5	5	5	4	6	3	3
Ba	844	1373	1116	1309	1301	618	1477	1079	1358	1068	1846	751	834	1145
La	46	52	31	29	22	37	66	56	63	50	65	54	59	53
Ce	92	102	65	60	45	71	151	109	118	93	123	106	109	98
Pr	10	10	7	6	5	8	19	12	13	11	14	11	10	10
Nd	36	40	30	25	21	34	78	49	53	43	58	40	38	36
Sm	6	7	6	5	4	6.3	14.4	8.6	9.1	7.8	10.4	7	6	6
Eu	1.62	1.92	1.48	1.35	1.45	1.7	2.6	1.9	2.2	1.9	2.9	1.81	1.61	1.52
Gd	6.8	7.9	5.7	5.3	4.4	6.5	14.5	9	9.1	8.2	10.8	7.9	6.3	6.3
Tb	0.81	0.94	0.84	0.72	0.56	0.8	1.8	1.1	1.1	0.9	1.3	1	0.78	0.78
Dy	3.8	4.4	4.6	4	2.7	4.3	9.1	5.2	5.2	4.5	6	5.1	3.8	3.8
Ho	0.69	0.78	0.85	0.77	0.51	0.7	1.4	0.8	0.8	0.7	0.9	0.98	0.69	0.71
Er	2.43	2.82	2.94	2.74	1.8	2.3	4.9	2.8	2.8	2.5	3.1	3.44	2.51	2.46
Tm	0.3	0.3	0.4	0.4	0.2	0.3	0.7	0.4	0.4	0.4	0.4	0.4	0.3	0.3
Yb	2	2.4	2.7	2.5	1.6	2.2	4.7	2.7	2.7	2.3	2.9	3	2.2	2.1
Lu	0.28	0.33	0.38	0.37	0.22	0.4	0.9	0.6	0.5	0.4	0.5	0.44	0.32	0.3
Hf	1.3	1.8	1.4	1.3	1.7	1.3	1.1	1	0.9	0.8	1	0.8	0.8	0.6
Ta	0.8	1.1	1.2	1.0	1.0	0.9	4.4	2.4	1.6	1.6	1.6	0.7	0.8	0.3
Pb	45	66	80	55	50	20	42	32	33	34	41	22	24	19
Th	134	109	78	78	76	0.8	3.1	2.5	2.3	2.1	1.7	138	147	133
U	31	26	24	25	23	12.2	27.3	20.4	14.9	14.3	11.1	31	28	27

Table 1- (Continued)

Sample No	ÇAMYAYLA GT									ALANKÖY GT			JG-1a (CRM Standard)
	ASM-K37	ASM-K38	ASM-K39	ASM-K40	ASM-K20	ASM-K21	ASM-K22	ASM-K23	ASM-K24	ASM-K17	ASM-K18	ASM-K19	
SiO_2 (wt.%)	75.2	73.8	64.6	64.8	63.4	62.1	64.5	63.8	63.8	65.7	66.3	65.2	
TiO_2	0.1	0.1	0.4	0.4	0.5	0.6	0.5	0.5	0.5	0.4	0.4	0.5	
Al_2O_3	14	14.4	15.9	16.1	16.9	16.3	17	17	17	16	16.3	16.5	
CaO	0.7	1.1	4.7	4.2	4	4.4	3.5	4.1	4	3.9	3.1	4.1	
Fe_2O_3t	0.8	1.2	4.3	3.9	4	4.3	3.8	4	4.2	3.9	3.8	4	
Na_2O	3.4	3.1	3.2	3.2	3.4	3.5	3.5	3.4	3.3	2.8	3.2	2.6	
K_2O	5	5.3	3.6	3.6	4	5	4.2	3.9	4.1	3.7	3.5	3.6	
MgO	0.2	0.3	1.8	1.7	1.8	2	1.5	1.7	1.6	1.6	1.4	1.6	
MnO			0.1	0.1	0.1	0.1	0.1	0.1	0.1	0.1	0.1	0.1	
P_2O_5			0.3	0.3	0.2	0.5	0.2	0.2	0.2	0.2	0.2	0.2	
LOI	0.3	0.35	0.75	1.6	1.45	0.7	0.95	0.8	0.9	1.4	1.4	1.35	
Total	99.7	99.65	99.65	99.9	99.75	99.5	99.75	99.5	99.7	99.7	99.7	99.75	
A/CNK	1.14	1.12	0.90	0.96	0.98	0.85	1.02	0.98	0.99	1.02	1.11	1.05	
A/NK	1.27	1.33	1.73	1.76	1.70	1.46	1.65	1.73	1.72	1.86	1.80	2.02	
Sc (ppm)	10	11	13	13	11	2	2	10	1	2	3	13	7
V	33	23	124	118	92	132	105	123	119	103	98	128	
Cr	204	162	158	236	66	144	75	80	92	145	145	92	
Rb	167	162	128	139	95	237	132	138	132	115	116	135	125
Sr	133	240	573	518	307	873	361	370	347	398	339	448	98
Y	18	19	21	20	15	9	11	19	9	11	10	23	35
Zr	13	11	5	5	10	10	21	9	10	15	12	12	92
Nb	8	8	10	9	11	21	14	14	14	11	9	12	
Cs	2	3	3	6	4	10	5	6	3	2	4	6	2
Ba	555	1030	1243	1030	725	1517	945	786	761	860	730	829	399
La	54	47	46	50	32	37	22	29	17	31	41	38	20.5
Ce	101	92	92	103	56	58	38	59	30	52	67	77	42
Pr	10	9	10	10	5	5	3	6	3	5	5	7	4.5
Nd	35	35	38	39	18	15	11	22	9	15	17	27	20
Sm	6	6	7	7	3	2	2	4	2	2	2	5	4
Eu	1.55	1.53	1.78	1.61	1.02	0.74	0.44	1.14	0.36	0.61	0.83	1.37	0.7
Gd	6.3	6.5	7.6	7.4	2.9	2.4	2	3.8	1.7	2.4	2.7	4.5	3.8
Tb	0.75	0.79	0.89	0.88	0.46	0.28	0.29	0.59	0.23	0.33	0.32	0.72	0.7
Dy	3.6	3.8	4.2	4.1	2.6	1.4	1.7	3.4	1.4	1.8	1.7	4.1	4
Ho	0.65	0.68	0.76	0.74	0.5	0.28	0.34	0.64	0.27	0.34	0.32	0.8	0.8
Er	2.29	2.39	2.68	2.65	1.75	1.03	1.26	2.26	1.04	1.29	1.19	2.81	2
Tm	0.3	0.3	0.3	0.3	0.2	0.1	0.2	0.3	0.2	0.2	0.2	0.4	0.3
Yb	2	2.1	2.2	2.3	1.6	1	1.5	2.1	1.2	1.4	1.1	2.5	3.5
Lu	0.29	0.29	0.31	0.31	0.24	0.15	0.23	0.31	0.19	0.2	0.17	0.37	0.4
Hf	0.7	0.6	0.6	0.6	0.8	0.9	1.3	0.7	0.7	1.3	1.1	1.1	2.9
Ta	0.7	0.6	0.7	0.7	0.7	1.3	0.9	0.9	0.8	0.9	0.6	0.8	2.5
Pb	23	23	28	20	18	89	41	32	19	84	17	66	
Th	150	114	124	168	80	61	76	79	66	85	66	94	15
U	28	25	26	32	20	15	17	21	17	20	16	22	4.1
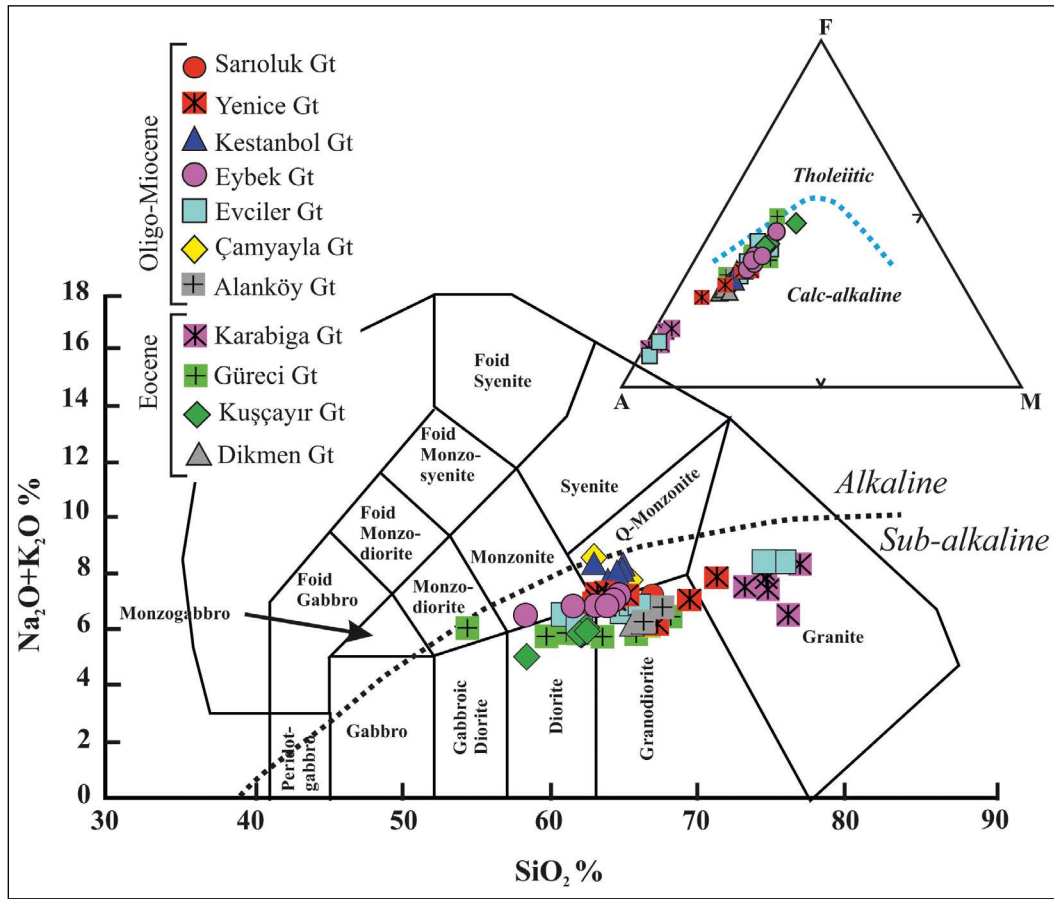
Figure 3- Total alkali-SiO$_2$ classification diagram for the Biga Peninsula granitoids (Middlemost, 1994). Insert figure is the AFM ternary diagram of Irvine and Baragar (1971); (A: Na$_2$O+K$_2$O, F: Fe$_2$O$_3$t, M: MgO)
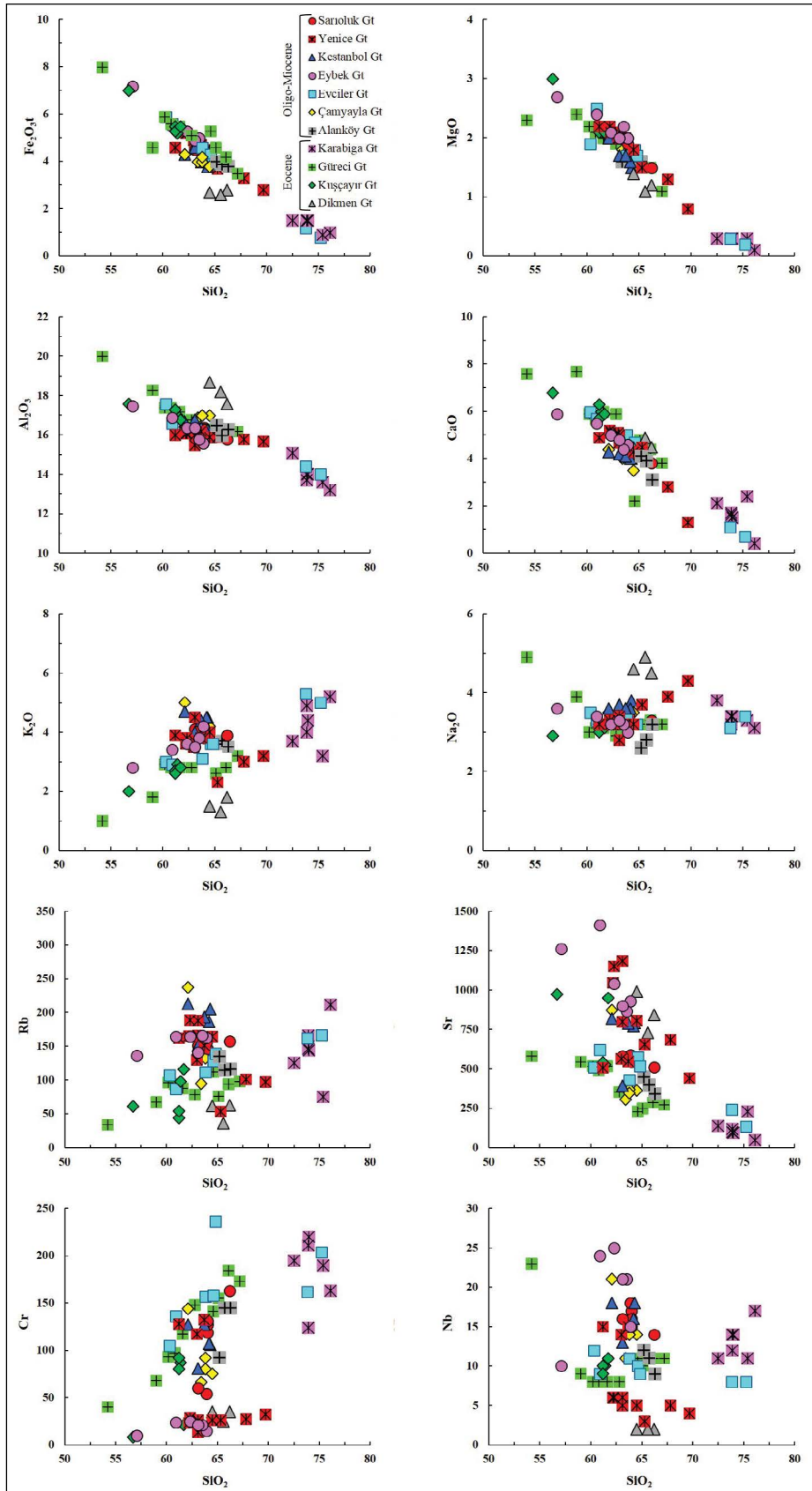
Figure 4- SiO$_2$ variation diagrams for the selected major-oxides and trace elements of the Biga Peninsula granitoids.
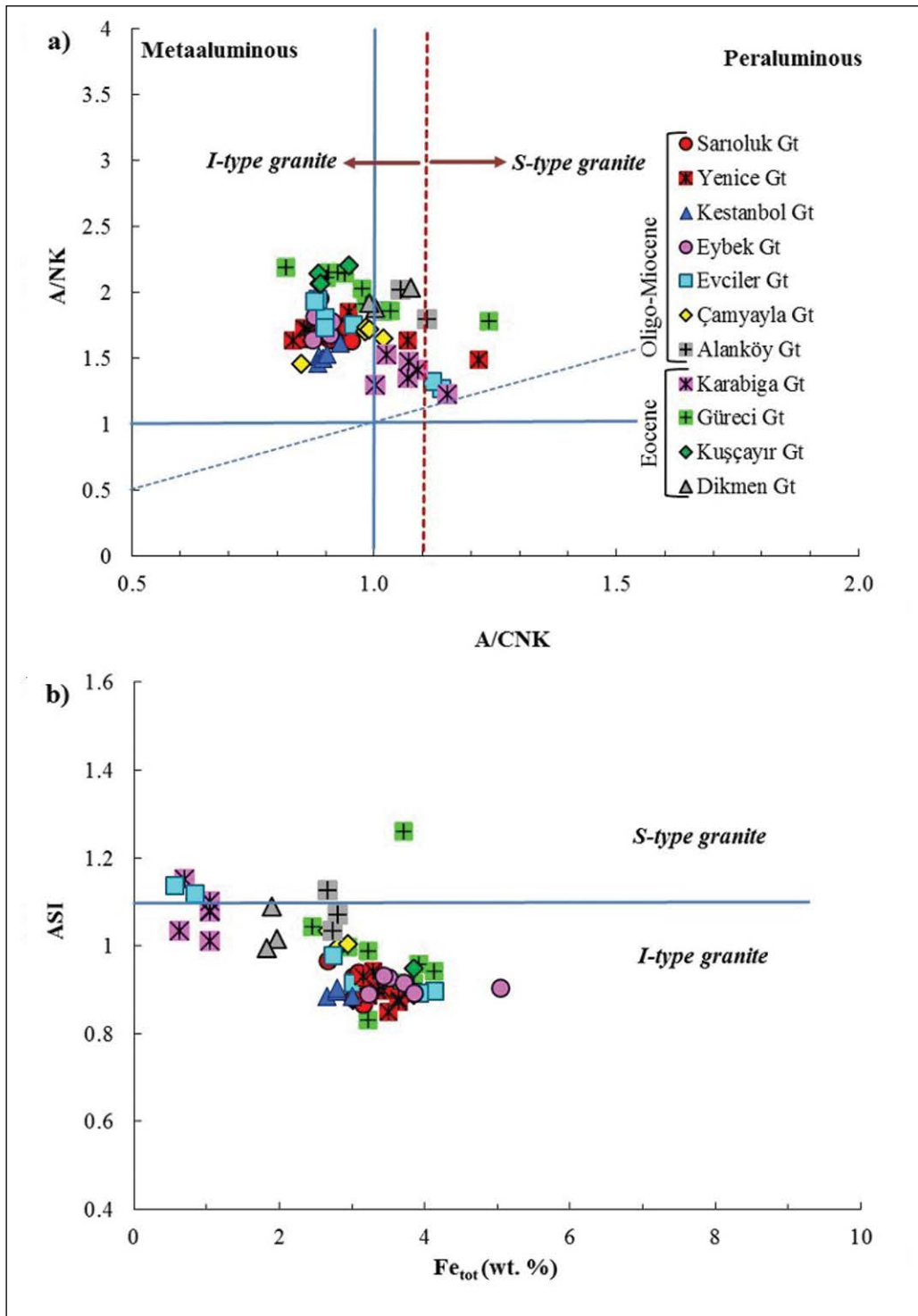
Figure 5- a) A/NK (molar) – A/CNK (molar) diagram (Shand, 1943); b) ASI (molar) – Fe_tot diagram (Norman et al., 1992) of the Biga Peninsula granitoids.
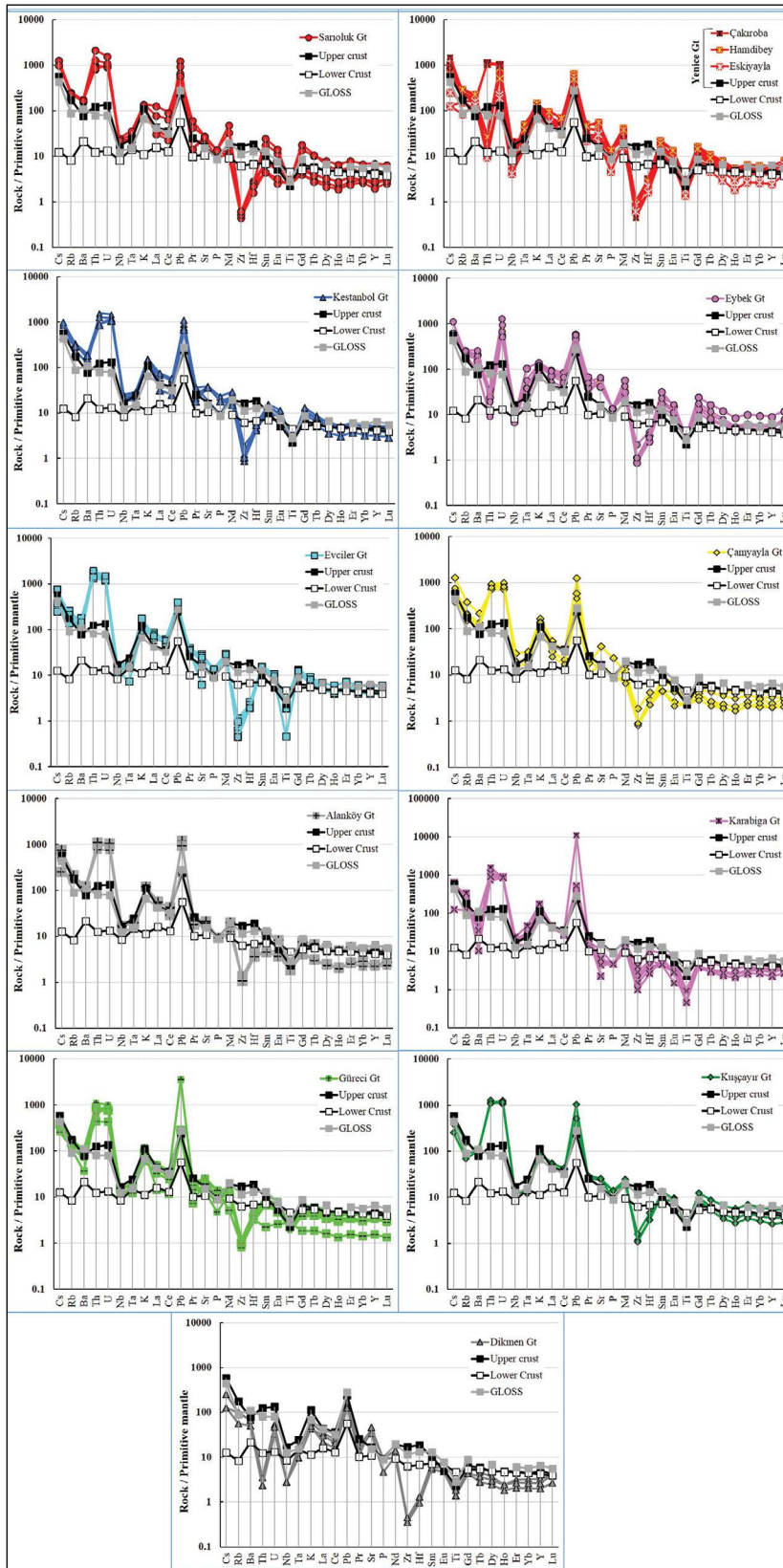
Figure 6- Primitive mantle normalised (Sun and McDonough, 1989) trace element patterns of Biga Peninsula granitoids. Upper crust, lower crust and GLOSS (*Global Subducting Sediment)* data are from Taylor and McLennan (1995), McLennan (2001) and Plank and Langmuir (1998).

material (Gill, 1981; Thompson et al., 1983; Fitton et al., 1988). In addition to above variations, while the Eocene Karabiga and Güreci granitoids have significant Th anomalies, Dikmen granitoids represent negative Th anomalies. Oligo-Miocene Sarıoluk, Yenice-Çakıroba, Kestanbol, Evciler, Çamyayla and Alanköy granitoids are characterised by significant Th positive anomalies, whereas Oligo-Miocene Yenice-Hamdibey, Yenice-Eskiyayla and Eybek granitoids are depleted in Th. Accordingly, the positive Th and U anomalies together with negative Nb, Ta and Ti anomalies may indicate the role of crustal/sediment contributions in the evolution of granitoids.

Figure 7 displays the chondrite-normalised (McDonough and Sun, 1995) rare earth element (REE) distribution diagrams of the selected samples from the Biga Peninsula granitoids. The great majority of the samples are enriched in light rare earth elements (LREE) relative to heavy rare earth elements (HREE) and they have $(La/Yb)_N$ ratios varying from 8 to 29. But, the low $[(La/Yb)_N = 2.17]$ ratio of a sample (ASM-K06) from Güreci granitoid can reflect the unfractionated nature of the sample. Most of the samples do not have significant negative Eu anomaly, but Karabiga and Sarıoluk granitoids have slight negative Eu anomaly, possibly indicating the fractionation of plagioclase (Figure 7).

6. Discussion

6.1. Identification of Magmatic Processes: Fractional Crystallization, Partial Melting and Crustal Contamination

Major oxide, trace element variation diagrams, trace and REE distribution patterns indicate that the Biga Peninsula granitoids were affected by fractional crystallisation processes during the evolution of the magmatism. But, the majority of samples had no clear negative Eu and Sr anomalies, indicating that plagioclase fractionation was not significant in the evolution of the Biga granitoids. As a result, in order to determine the effects of fractional crystallisation, the Rb-Sr and K/Rb-SiO_2 diagrams (Figure 8) is used, since Rb/Sr ratio is a good marker for fractional crystallisation and high Rb/Sr ratio indicates advanced degrees of fractionation (Imeokparia, 1981; Blevin, 2003). Most of the samples have Rb/Sr ratios varying from 0.1 to 1.0, whereas the Rb/Sr ratios in Karabiga
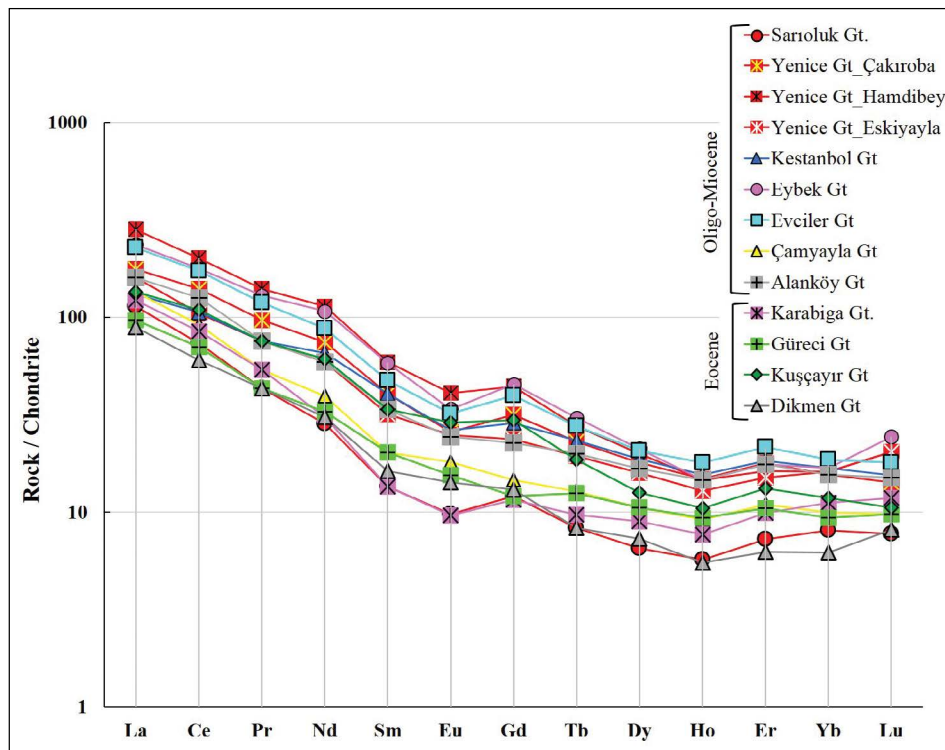
Figure 7- Chondrite normalised (McDonough and Sun, 1995) rare earth element patterns of the Biga Peninsula granitoids.
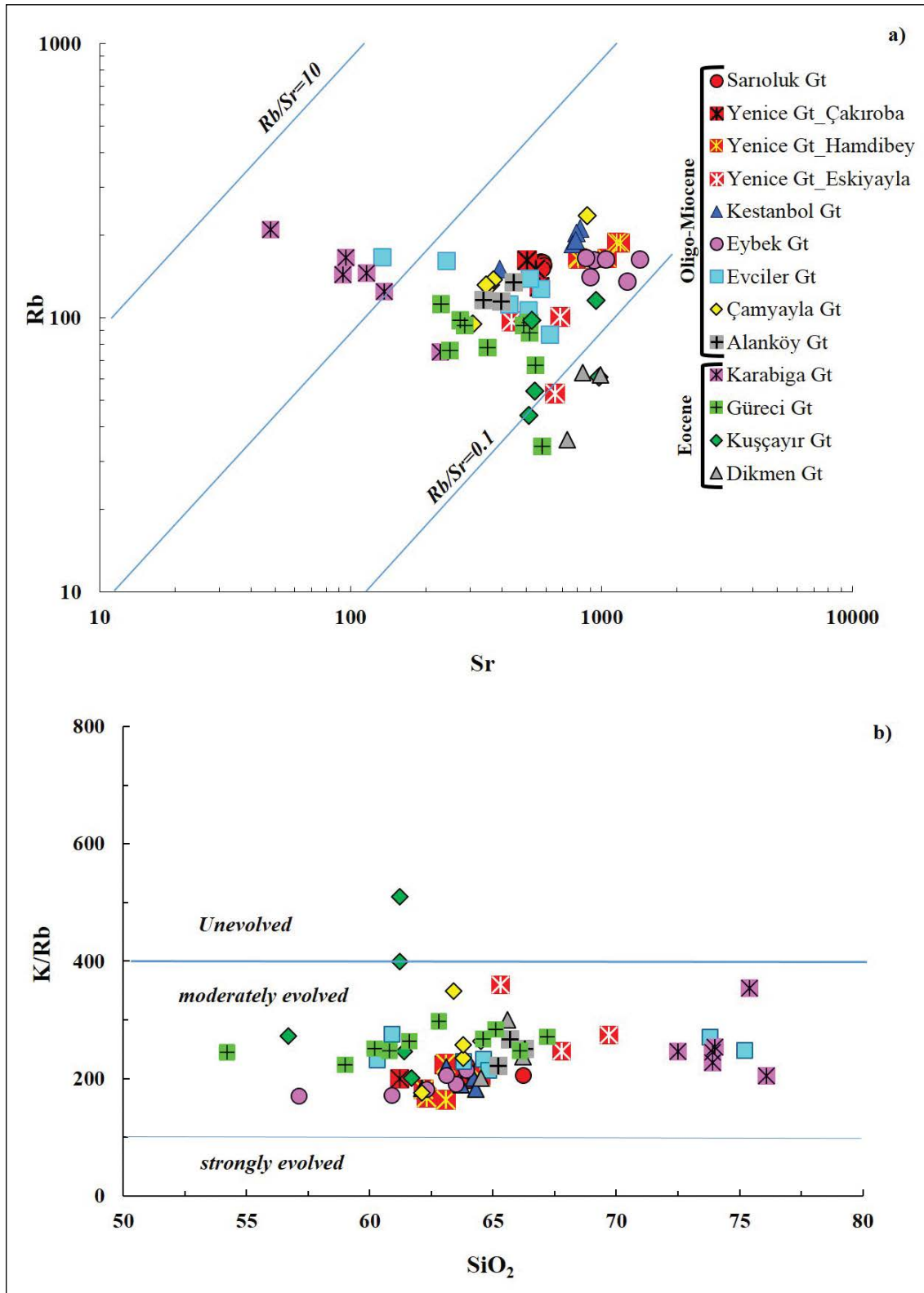
Figure 8- a) Rb-Sr and, b) K/Rb-SiO$_2$ diagrams (Blevin, 2003) for the Biga Peninsula granitoids.

and Dikmen samples range between 0.33-4.40 and 0.05-0.07, respectively (Figure 8a). Accordingly, while there is relatively strong fractionation for the Karabiga granitoids, the effects of this process are mildly in the Dikmen granitoids. Similarly, the K/Rb-SiO$_2$ diagram (Figure 8b) is one of the important indicators used to determine the degree of fractionation in granitic melts as low K/Rb and increasing SiO$_2$ content indicates strong fractionation (Blevin, 2003; Rossi et al., 2011). As seen on the figure 8b, the Biga Peninsula granitoids show moderate levels of fractionation.

The Rb-Ba-Sr triangular diagram adapted from El Bouseily and El Sokkary (1975) (Figure 9) (Karapetian et al., 2001; Xiang et al., 2017) is used to assess the magmatic differentiation process and tectonic setting features in the evolution of granitoids. The majority of samples display quartz diorite and granodiorite composition and are plotted in the I-type granite field, but the Karabiga granitoids fall in the area between S- and I-type granites and show strong

fractionation (Figure 9). Samples having I-type granite characteristics show moderate level of fractionation. It can be concluded that the effects of the fractional crystallisation process were at moderate levels during the evolution of Biga Peninsula granitoids.Moreover, in order to asses the partial melting processes in the genesis of magmatism, the La – La/Yb diagram of Thirlwall (1994) is utilised (Figure 10). While horizontal trends give fractional crystallisation, the increasing La/Yb with increasing La indicates the partial melting processes. We conclude that partial melting is also thought to play a significant role.

Figure 8, 9 and 10 reveal the effects of fractional crystallisation and partial melting processes in the evolution and genesis of the magmatism. Besides, Ce/Pb – Pb and Rb/Ba – Rb/Sr diagrams were used to determine the effects of crustal contamination on magmatism (Figure 11). Low Ce/Pb ratio is one of the most characteristic features of crustal contribution and/or sediment contribution to mantle material because
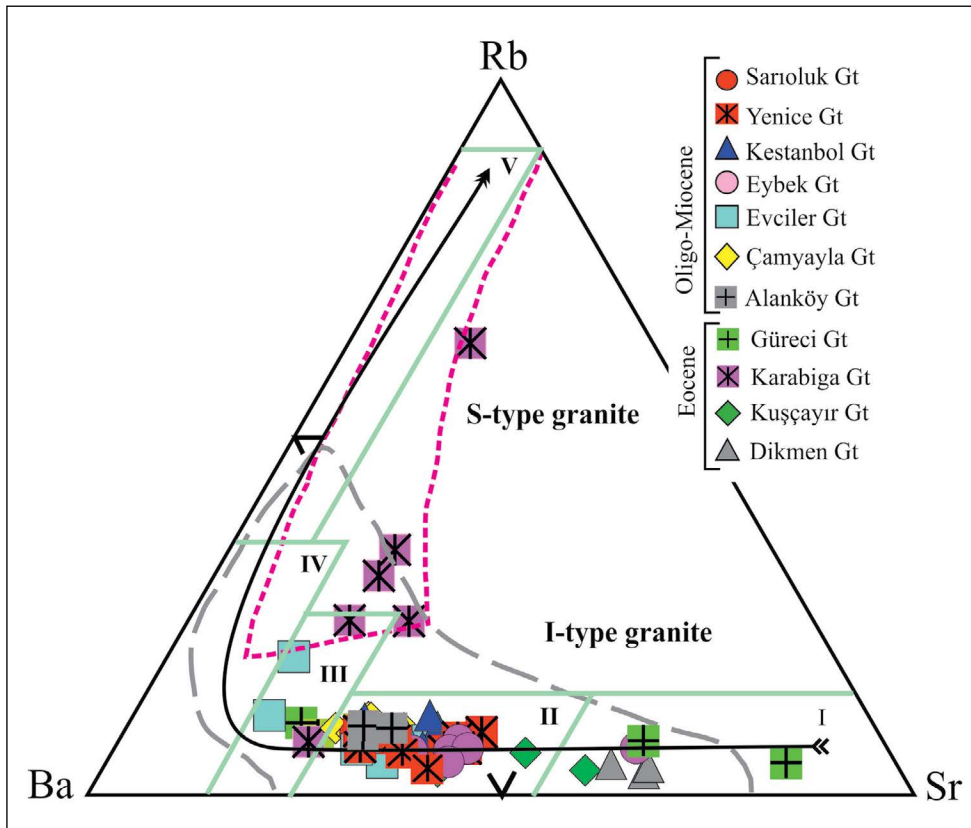
Figure 9- Rb-Ba-Sr ternary discrimination diagram of the Biga Peninsula granitoids (adapted from El Bouseily and El Sokkary, 1975; Karapetian et al., 2001 and Xiang et al., 2017). Roman numerals from I to V indicate poorly evolved granite to strongly evolved granite. I: Diorite; II. Granodiorite-Quartz-diorite; III. Anomalous granite; IV. Normal granite; V: strongly evolved granite.
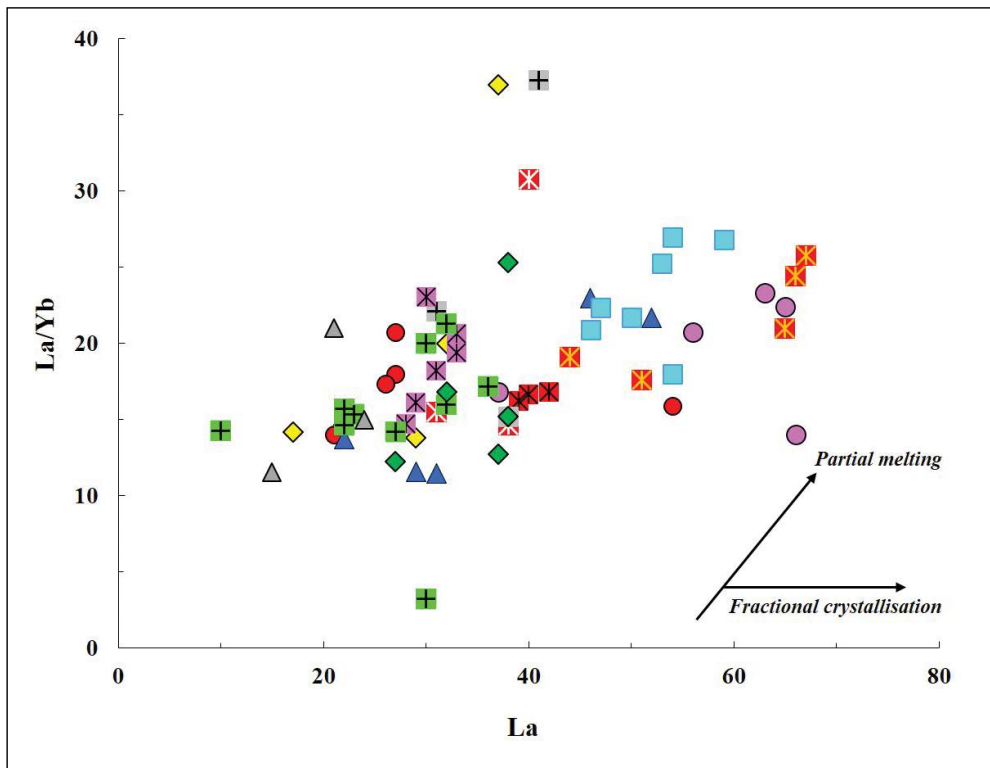
Figure 10- La – La/Yb diagram (Thirwall, 1994) of Biga Peninsula granitoids. Symbols as in figure 9.

the Pb content of crustal material is clearly higher compared to the mantle (Taylor and McLennan, 1985; Hofmann et al., 1986). Hofmann et al. (1986) showed that ocean island basalt (OIB) and mid-ocean ridge basalt (MORB) have high and relatively constant Ce/Pb ratios (~ 25), while the upper crust (UC) has lower Ce/Pb ratio (~3.2) (Taylor and Mc Lennan, 1985). In order to determine the role of crustal contamination in the evolution of Biga Peninsula granitoids, binary mixing modelling of Langmuir et al. (1978) was applied. In the mixing model, OIB&MORB and UC were used as end-members and two component binary mixing diagram between Pb and Ce/Pb were created. Biga Peninsula granitoids are plotted on the mixing curve between OIB&MORB and UC and shifted towards the UC end-member on the curve (Figure 11a).

Biga Peninsula granitoids show trace element distribution patterns similar to that of upper crust (Taylor and McLennan, 1985; McLennan, 2001) and GLOSS (Plank and Langmuir, 1998). But, there are some significant differences in detail. Sarıoluk, Yenice-Çakıroba, Kestanbol, Evciler, Çamyayla, Alanköy, Karabiga, Güreci and Kuşçayır granitoids are enriched in Th, whereas Yenice-Hamdibey,

Yenice-Eskiyayla, Eybek and Dikmen granitoids are depleted in Th. Accordingly, high Th and Pb concentrations do not appear to be explained solely by crustal contamination processes. As a result, Rb/Ba – Rb/Sr diagrams has been used to distinguish the mantle-derived melts from crustal derived melts (Li et al., 2015; Chen et al., 2017) (Figure 11b). The diagram includes Sylvester (1998)'s basalt and pelite-derived melt curves. Most of the studied samples are plotted in the clay-poor source field but Karabiga samples are shifted towards the pelite-derived melt composition and clay rich source. According to this diagram (Figure 11b), derivation from crustal melting does not seem plausible explanation for the genesis of Biga Peninsula granitoids. Furthermore, although the crustal contribution may have played a role in the evolution of magmatism (Figure 11a), the negative anomalies in Nb, Ta and Ti and positive anomalies in Th and U, GLOSS-like trace element distributions and Rb/Ba-Rb/Sr variations essentially reflect the source characteristics rather than crustal contamination processes (Figure 11b).

Consequently, the observed geochemical variations – such as depletion in Nb, Ta, Ti, enrichment in Th,
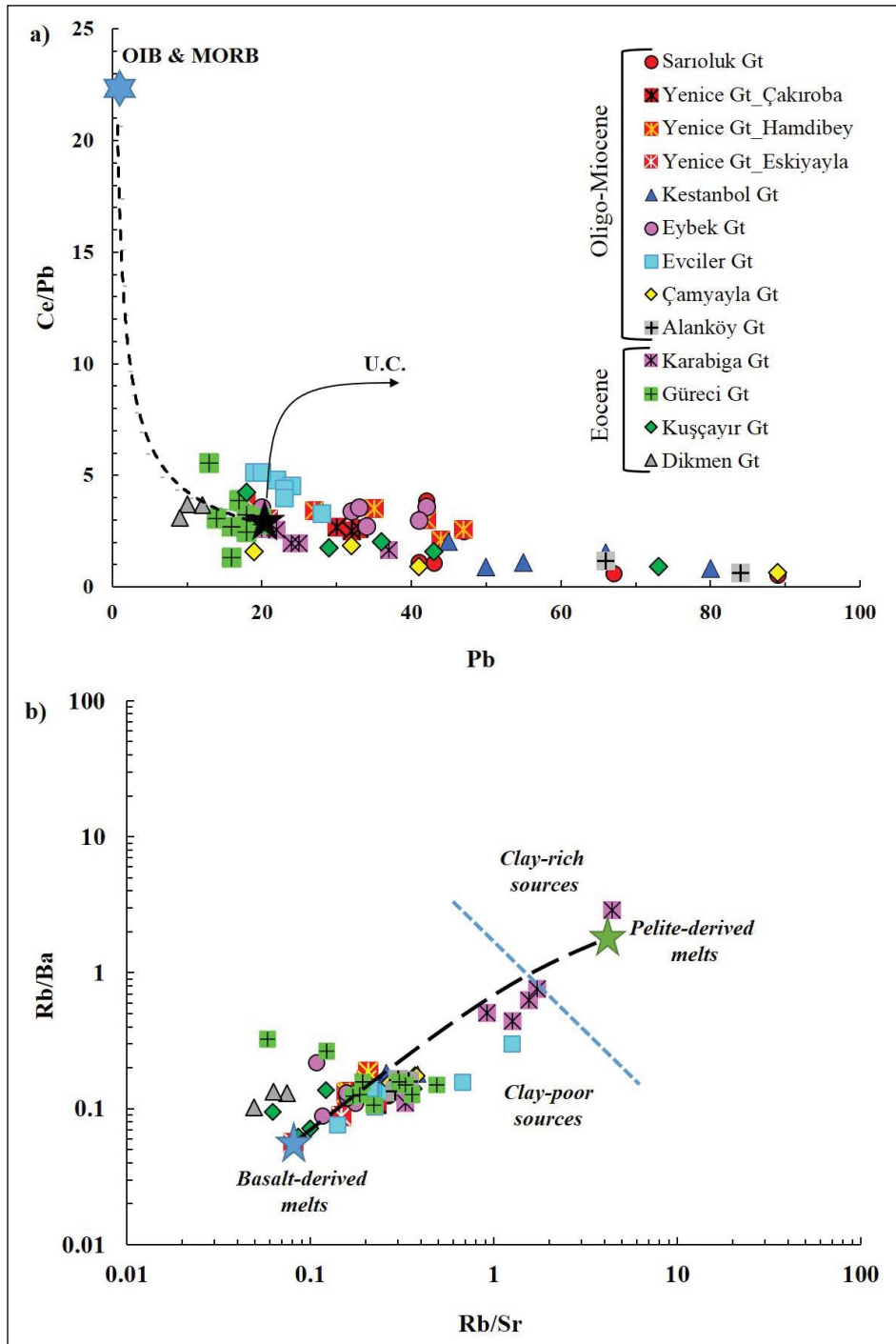
Figure 11- Biga Peninsula granitoids a) Ce/Pb – Pb binary mixing diagram. Binary mixing curve between OIB and MORB [average values of Normand and Garcia (1999)] and upper crust (UC) (Taylor and McLennan, 1985) is calculated from Langmuir et al. (1978); b) Rb/Ba – Rb/Sr diagram. Basalt- and pelite-derived melt curve from Sylvester (1998).

U and Pb and UC and GLOSS-like trace element distributions – are unlikely to be explained solely by crustal contamination. Because, magmas derived from mantle-source metasomatised by subduction components may retain these types of geochemical features. As a result, the source characteristics of the magmas generating the Biga Peninsula granitoids are assessed in the following section.

6.2. Tectonic Setting and Source Characteristics

In order to determine the tectonic setting of the Biga Peninsula granitoids, the tectonic discrimination diagram for granitic rocks of Pearce et al. (1984) is used (Figure 12). According to this diagram, samples are generally plotted in the volcanic arc granite (VAG) field. However, the tectonic setting of rocks falling at the intersection of within plate granites (WPG), arc granites (VAG) and syn-collisional granites (syn-COLG) is still controversial and this intersecting field is accepted as the post-collisional granite (post-COLG) field (Pearce, 1996). Accordingly, the Biga Peninsula granitoids can be clearly classified as post-collisional granites (Figure 12).

Nb/La – Ba/Rb and Ce/Pb – Ce diagrams have been used to reveal the role of subduction components on the samples exhibiting geochemical features similar to post-collisional granites (Figure 13). Low Nb/La and Ce/Pb ratios indicate subduction components. As can be clearly seen on the figures, the Biga Peninsula granitoids are plotted within the field represented by global subducted sediment (*GLOSS*). According to these diagrams, the variatons in Nb/La, Ba/Rb and Ce/Pb can be attributed to subduction zone process and

interpreted as that the post-collisional granitoids in the study area were derived from mantle source carrying subduction zone components.

In order to determine the process responsible for Th enrichment and the subduction components in Biga Peninsula granitoids, the element associations indicating different geochemical behaviour in aqeous fluid and sediment melt phases have been utilised. Ratios of slab-derived fluid/melt mobile elements (e.g. Th, Ba, Rb, Cs and La) to slab-derived fluid immobile element (e.g. Sm) are good markers for following the subduction zone components, since Ba, Rb and Cs elements mobilise with the aqueous fluid phases (McCulloch and Gamble, 1991; Ribiero et al., 2013), whereas Th and La are solely mobilise with sediment melting (Johnson and Plank, 1999; Ribeiro et al., 2013). Thus, Th/La and La/Sm are used by many researchers to determine the involvement of subducting sediment and sediment melts in subduction zones (Plank, 2005; Tommasini et al., 2011; Labanieh et al., 2012; Chen et al., 2017) and involvement of slab sediment into the overlying mantle wedge assigns the La/Sm ratios of the source (Labanieh et al., 2012). According to these criterion, La/Sm ratios (4.6-20.5) of almost
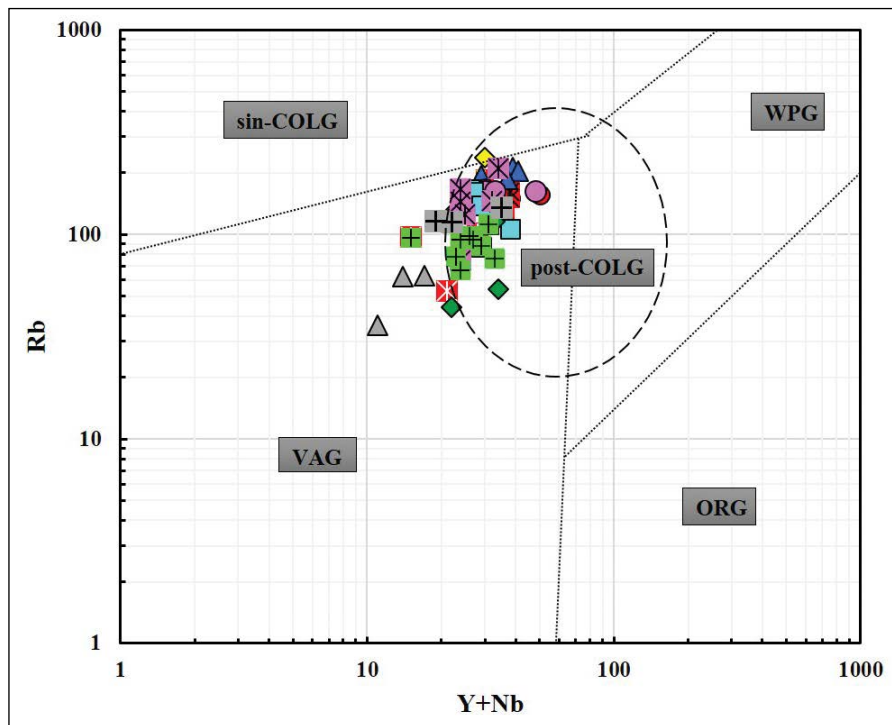
Figure 12- Rb- Y+Nb tectonic discrimination diagram of Biga Peninsula granitoids (Pearce et al., 1984; Pearce, 1996). VAG: Volcanic arc granites; syn-COLG: syn-collisional granites; WPG: within-plate granites; post-COLG: post-collisional granites. Symbols as in figure 11.
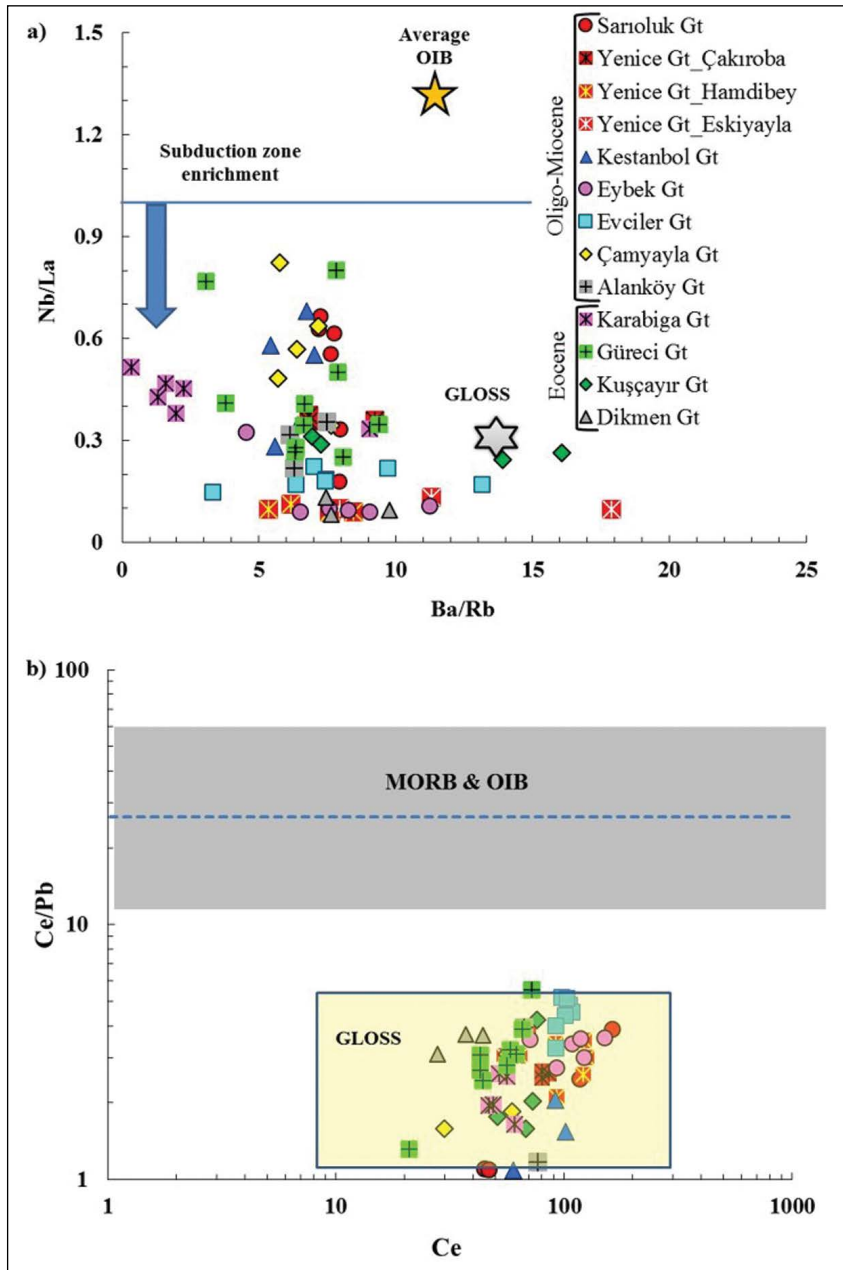
Figure 13- a) Nb/La-Ba/Rb (Wang et al., 2004) diagram of the studied samples. GLOSS (*Global Subducting Sediment*) values are from Plank and Langmuir (1998) and average OIB (Ocean island basalts) values are from Sun and McDonough (1989); b) Ce/Pb – Ce diagram of the studied samples. GLOSS field from Su et al. (2017) and references therein.

all samples and Th/La ratios (1.6-4.7) of Sarıoluk, Yenice-Çakıroba, Kestanbol, Evciler, Çamyayla, Alanköy, Karabiga, Güreci and Kuşçayır granitoids are sufficiently high to imply sediment involvement. But, La/Sm ratio also increase as a result of some processes such as weathering, fractional crystallisation and partial melting (Labanieh et al., 2012). As a result, to eliminate factors such as weathering and fractional

crystallisation causing high La/Sm ratios in Biga Peninsula granitoids, the La/Sm – loss on ignition (LOI) and La/Sm - SiO$_2$ diagrams have been utilised (Figure 14). As the LOI values are directly related to degree of weathering, it increases with increasing weathering. Thus, LOI is a good marker to distinguish weathered sample from fresh sample (Chauvel et al., 2005). Labanieh et al. (2012) also demonstrate that
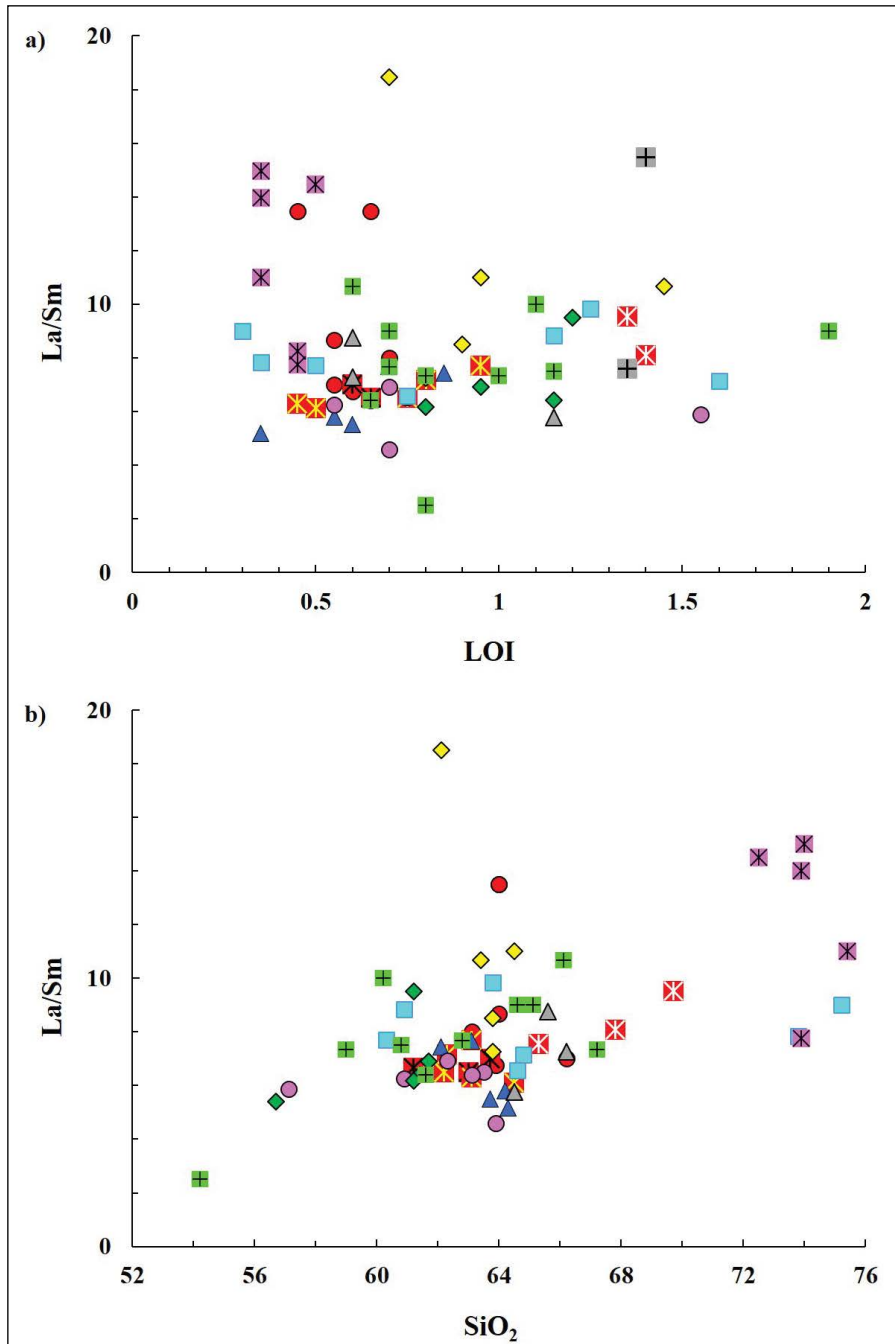
Figure 14- a) La/Sm – Loss on Ignition (LOI) and, b) La/Sm – SiO₂ diagrams of Biga Peninsula granitoids. Symbol as in figure 13.

La/Sm values increase with increasing weathering. As can be clearly seen on the figure 14a, there is no clear correlation between La/Sm and LOI. The lack of correlation between LOI and La/Sm indicates that weathering do not play a significant role on the ratio of La/Sm. In the plot of La/Sm versus SiO_2 (Figure 14b), there is a mild positive correlation with increasing SiO_2, but it does not adequate to explain the high La/

Sm ratios in the samples. Consequently, the high La/Sm ratios (5-20) in Biga Peninsula granitoids can be attributed to sediment contribution (Labanieh et al., 2012).

Similarly, the Rb/Th, Cs/Th – La/Sm diagrams (Figure 15) are used to discriminate aqeous fluids from the sediment-derived melts in the samples (Ribeiro et
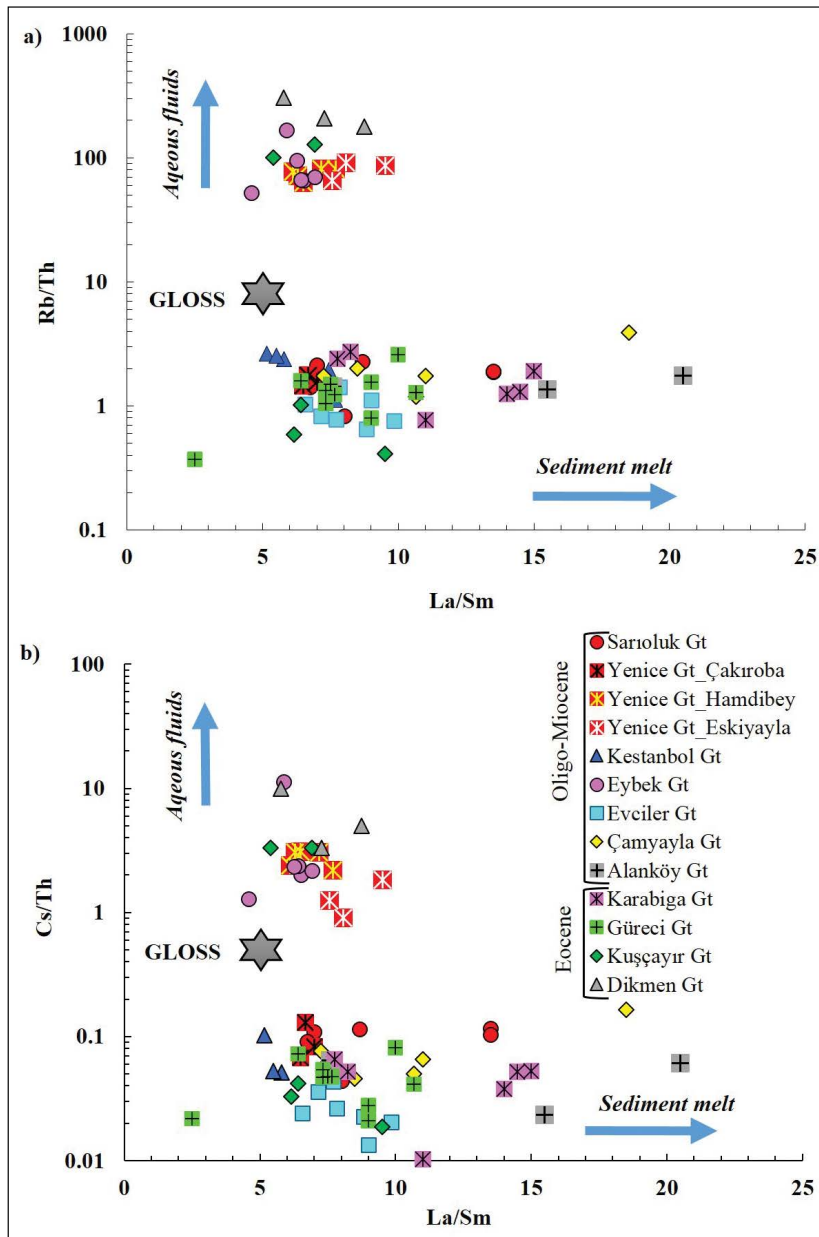
Figure 15- a) Rb/Th – La/Sm; b) Cs/Th – La/Sm diagrams (Ribeiro et al., 2013) of Biga Peninsula granitoids. GLOSS values from Plank and Langmuir (1998).

al., 2013). It can be interpreted that aqueous fluids were effective in the genesis of the Yenice-Hamdibey, Yenice-Eskiyayla, Eybek and Dikmen granitoids since they are characterised by low Th contents, whereas sediment melting appear to be the dominant process in the genesis of Th-enriched samples (Figure 15a, b).

6.3. Assesment of Ore-Formation Potential

Undoubtedly, granitic rocks and/or granitoids are very important in terms of ore potential. Many mineral

deposits of economic significance are associated with granitic rocks, and the most important of these are copper (Cu)-molybdenum (Mo), Cu-Au, tin (S)-tungsten (W)-uranium (U) and rare metals (Ta-Cs-Li-Nb-Be-Sn-Mo-W) deposits. The Biga Peninsula, located in the Tethyan metallogenic belt containing the world's important ore deposits, is the most important metallogenic region in Turkey (Yiğit, 2012) As a result, to determine the mineralisation potential of Biga Peninsula granitoids, which have post-collisional features and exhibit both metaluminous

and peraluminous composition, and were derived from lithospheric mantle metasomatised by aqeous fluids and sediment melts, Ballouard et al.(2016)'s Nb/Th – Zr/Hf diagram has been used. Ballouard et al. (2016) suggested that peraluminous granites with low Nb/Ta ratios had experienced fluid interactions leading to enrichment in strongly incompatible elements such as Cs, Sn, F, Li, Rb and W and the Nb/Ta ratio may be used to distinguish barren granites from ore-bearing granites. They also demonstrated that low Nb/Ta content (<5) indicates concomitant effect of fractional crystallisation and magmatic-hydrothermal alteration, and F-rich acidic reduced fluids of magmatic origin are responsible for these types of processes. It is apparent on the Nb/Ta – Zr/Hf diagram (Figure 16), Yenice-Hamdibey and Eskiyayla, Eybek and Dikmen granitoids have low Nb/Ta and Zr/Hf contents and are shifted towards the rare metals related granites field. This case indicates that fluids of magmatic origin have played significant role in Dikmen, Eybek, Yenice-Hamdibey and Yenice-Eskiyayla granitoids and reflects the concomitant effect of fractional crystallisation along with magmatic-hydrothermal

alteration. This is also supported by the observed variations in Rb/Th – La/Sm and Cs/Th – La/Sm diagrams (Figure 15) that aqeous fluids have played a significant role in the genesis of Yenice-Hamdibey and Yenice-Eskiyayla, Eybek and Dikmen granitoids.

7. Conclusions

Following the collision of the Sakarya continent with the Anatolide-Tauride platform in the Late Cretaceous-Early Tertiary, widespread magmatic activity developed in northwest Anatolia. Plutons in the Biga Peninsula are products of this magmatism and were emplaced in the time interval from the Eocene and Oligo-Miocene. The Biga Peninsula granitoids are products of a post-collisional environment, generating due to partial melting of a lithospheric mantle source metasomatised by aqueous fluids and sediment-melts released during the previous subduction. In addition, trace element distributions and trace element ratio diagrams demonstrate that crustal contamination and fractional crystallisation processes have also mildly effects in the evolution of the granitoids.
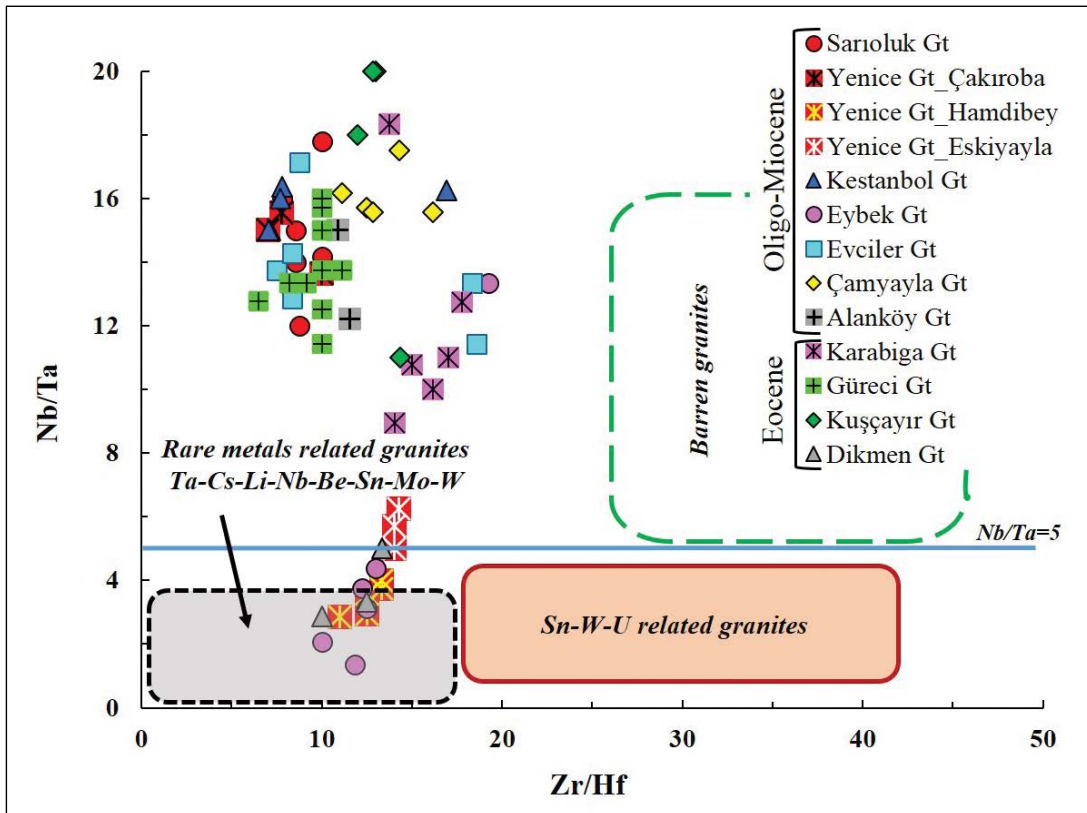
Figure 16- Nb/Ta-Zr/Hf diagram of diagram of Biga Peninsula granitoids (Ballouard et al., 2016).

Acknowledgements

References

Akyüz, H.S., Okay, A.İ. 1996. A section across a Tethyan Suture in Northwestern Turkey. International Geology Review 38, 405-418.

Aldanmaz, E., Pearce, J. A., Thirlwall, M.F., Mitchell, J. G. 2000. Petrogenetic evolution of late Cenozoic, post-collision volcanism in western Anatolia, Turkey. Journal of Volcanology and Geothermal Research, 102, 67– 95.

Aldanmaz, E., Pickard, M., Meisel, T., Altunkaynak, Ş., Sayıt, K., Şen, P., Hanan, B.B., Furman, T. 2015. Source components and magmatic processes in the genesis of Miocene to Quaternary lavas in western Turkey: constraints from HSE distribution and Hf–Pb–Os isotopes. Contribution to Mienarlogy and Petrology 170(2), 1-20.

Altıner, D., Koçyiğit, A., Farinacci, A., Nicosia, U., Conti, M.A. 1991. Jurassic– Lower Cretaceous stratigraphy and paleogeographic evolution of the southern part of northwestern Anatolia: Geologica Romana 28, 13–80.

Altunkaynak, Ş. 2007. Collision-driven slab breakoff magmatism in Northwestern Anatolia, Turkey. Journal of Geology 115, 63–82.

Altunkaynak, Ş., Dilek, Y. 2006. Timing and nature of postcollisional volcanism in western Anatolia and geodynamic implications. In: Dilek, Y., Pavlides, S. (Eds.), Post collisional tectonics and magmatism in the Mediterranean region and Asia: Geological Society of America Special Paper 409, 321–351.

Altunkaynak, Ş., Genç, Ş.C. 2008. Petrogenesis and time-progressive evolution of the Cenozoic continental volcanism in the Biga Peninsula, NW Anatolia (Turkey). Lithos 102, 316-340.

Altunkaynak, Ş., Dilek, Y. 2013. Eocene mafic volcanism in northern Anatolia: its causes and mantle sources in the absence of active subduction. International Geology Review 55 (13), 1641-1659.

Altunkaynak, Ş., Dilek, Y., Genç, Ş.C., Sunal, G., Gertisser, R., Furnes, H., Foland, K. A., Yang, J. 2012a. Spatial, temporal and geochemical evolution of Oligo-Miocene granitoid magmatism in western Anatolia, Turkey. Gondwana Research 21, 961-986.

Altunkaynak, Ş., Sunal, G., Aldanmaz, E., Genç, Ş.C., Dilek, Y., Furnes, H., Foland, K. A., Yang, J., Yıldız, M. 2012b. Eocene Granitic Magmatism in NW Anatolia (Turkey) revisited: New implications from comparative zircon SHRIMP U–Pb and 40Ar-39Ar geochronology and isotope geochemistry on magma genesis and emplacement. Lithos 155, 289-309.

Aysal, N. 2015. Mineral chemistry, crystallization conditions and geodynamic implications of the Oligo–Miocene granitoids in the Biga Peninsula, Northwest Turkey. Journal of Asian Earth Science 105, 68-84.

Ballouard, C., Pojol, M., Boulvais, P., Branquet, Y., Tartese, R., Vigneresse, J-L. 2016. Nb-Ta fractionation in peraluminous granites: A marker of the magmatic-hydrothermal transition. Geology 44(3), 231-234.

Blevin, P. 2003. Metallogeny of granitic rocks, The Ishihara Symposium, Granites and Associated Metallogenesis 14, 5-80.

Chauvel, C., Dia, A. N., Bulurde, M., Chabaux, F., Durand, S., Ildefonse, P., Gerard, M., Deruelle, B., Ngounouno, I. 2005. Do decades of tropical rainfall affect the chemical compositions of basaltic lava flows in Mount Cameroon? Journal of Volcanology and Geothermal Research 141, 195-223.

Chen, B., Long, X., Wilde S.A., Yuan, C., Wang, Q., Xia, X., Zang, Z. 2017. Delamination of lithospheric mantle evidenced by Cenozoic potassic rocks in Yunnan, SW China: A contribution to uplift of the Eastern Tibetan Plateau. Lithos 284-285, 709-729.

Delaloye, M., Bingöl, E. 2000. Granitoids from western and northwestern Anatolia: geochemistry and modeling of geodynamic evolution. International Geology Review 42, 241– 268.

Dilek, Y. 2006. Collision tectonics of the Mediterranean region: causes and consequences. Geological Society of America, Special Paper 409, 1-13.

Dilek, Y., Altunkaynak, Ş. 2009. Geochemical and temporal evolution of Cenozoic magmatism in western

Turkey: mantle response to collision, slab break-off, and lithospheric tearing in an orogenic belt. Geological Society, London, Special Publications 311, 213-233.

Duru, M., Pehlivan, Ş., Okay, A.İ., Şentürk, Y., Kar, H. 2012. Biga Yarımadası'nın Tersiyer öncesi jeolojisi. Biga Yarımadası'nın Genel ve Ekonomik Jeolojisi MTA Özel Yayın Serisi-28, 7-77.

El Bouseily, A.M., El Sokkary, A.A. 1975. The relation between Rb, Ba and Sr in granitic rocks. Chemical Geology 16, 207-219.

Ercan, T., Satır, M., Steinitz, G., Dora, A., Sarıfakıoğlu, E., Adis, C., Walter, H.J., Yıldırım, T. 1995. Biga Yarımadası ile Gökçeada, Bozcaada ve Tavşan adalarındaki KB Anadolu Tersiyer volkanizmasının özellikleri. Bulletin of Mineral Research and Exploration 117, 55-87.

Erkül, S.T., Erkül, F. 2012. Magma interaction processes in syn-extensional granitoids: the Tertiary Menderes Metamorphic core complex, western Anatolia, Turkey. Lithos 142-143, 16-33.

Ersoy, E.Y., Palmer, M.R. 2013. Eocene–Quaternary magmatic activity in the Aegean: implications for mantle metasomatism and magma genesis in an evolving orogeny. Lithos 180-181, 5–24.

Ersoy, E.Y., Palmer, M.R., Can Genç, Ş., Prevelic D., Akal, C., Uysal, İ., 2017a. Chemo-probe into the mantle origin of the NW Anatolia Eocene to Miocene volcanic rocks: Implications for the role of, crustal accretion, subduction, slab roll-back and slab break-off processes in genesis of post-collisional magmatism. Lithos 288-289, 55-71.

Ersoy, E.Y., Akal, C., Can Genç, Ş., Candan, O., Palmer, M.R., Prelevic, D., Uysal, İ., Mertz-Kraus, R., 2017b. U-Pb zircon geochronology of the Paleogene-Neogene volcanism in the NW Anatolia: Its implications for the late Mesozoic-Cenozoic geodynamic evolution of the Aegean. Tectonophysics 717, 284-301.

Fitton, J. G., James, D., Kempton, P.D., Ormerod, D.S. Leeman, W.P. 1988. The role of lithospheric mantle in the generation of late Cenozoic basic magmas in the Western United States. Journal of Petrology Special Lithosphere Issue 331-349.

Genç, Ş. C. 1998. Evolution of the Bayramiç magmatic complex. Journal of Volcanology and Geothermal Research, 85 (1- 4), 233-249.

Genç, Ş. C., Yılmaz, Y. 1997. An example of Post-collisional Magmatism in Northwestern Anatolia: the Kızderbent Volcanics (Armutlu peninsula, Turkey). Turkish Journal of Earth Science 6, 33-42.

Genç, Ş. C., Altunkaynak, Ş. 2007. Eybek graniti (Biga yarımadası, KB Anadolu) üzerine: Yeni jeokimya verileri ışığında yeni bir değerlendirme. Yerbilimleri 28 (2), 75-98.

Gill, J.B. 1981. Orogenic andesites and Plate tectonics. Springer - Verlag, New York.

Güleç, N. 1991. Crust-mantle interaction in western Turkey: implications from Sr and Nd isotope geochemistry of Tertiary and Quaternary volcanics. Geological Magazine 123, 417-435.

Gülmez, F., Genç, Ş.C., Keskin, M., Tüysüz, O. 2013. A post-collision slab-breakoff model for the orgin of the Middle Eocene magmatic rocks of the Armutlu-Almacık belt, NW Turkey and its regional implications. Geological Society, London, Special Publications 372, 107-139.

Harris, N.B.W., Kelley, S., Okay, A.İ. 1994. Post-collsion magmatism and tectonics in northwest Anatolia. Contributions to Mineralogy and Petrology 117, 241-252.

Hasözbek, A., Satır, M., Erdoğan, B., Akay, E., Siebel, W. 2010a. Early Miocene granite formation by detachment tectonics or not? A case study from the northern Menderes Massif (Western Turkey). Journal of Geodynamics 50, 67–80.

Hasözbek, A., Satır, M., Erdoğan, B., Akay, E., Siebel, W. 2010b. Early Miocene postcollisional magmatism in NW Turkey: geochemical and geochronological constraints. International Geology Review 53, 1098–1119.

Hofmann, A.W., Jochum, K.P., Seufer, M., White W.M. 1986. Nb and Pb in oceanic basalts: new constraints on mantle evolution. Earth and Planetary Science Letters 79, 33-45.

Ilgar, A., Sezen Demirci, E., Demirci, Ö. 2012. Biga Yarımadası Tersiyer istifinin stratigrafisi ve sedimantolojisi. Biga Yarımadası'nın Genel ve Ekonomik Jeolojisi Maden Tetkik ve Arama Genel Müdürlüğü Özel Yayın Serisi-28, 75-120.

Imeokparia, E.G. 1981. Ba/Rb and Rb/Sr ratios as indicators of magmatic fractionation, postmagmatic alteration and mineralization-Afu Younger Geranite Complex, Northern Nigeria. Geochemical Journal 15, 209-219.

Irvine, T. N., Baragar, W. R. A. 1971. A guide to the chemical classification of the common volcanic rocks. Canadian Journal of Earth Science 8, 523-548.

Johnson, M.C., Plank, T., 1999. Dehydration and melting experiments constrain the fate of subducted sediments. Chemical Geology 130, 289-299.

Karacık, Z., Yılmaz, Y. 1998. Geology of the ignimbrites and the associated volcano–plutonic complex of the Ezine area, northwestern Anatolia. Journal of Volcanology and Geothermal Research 85(1), 251-264.

Karacık, Z. Yılmaz, Y., Pearce, J., Ece, Ö.I. 2008. Petrochemistry of the South Marmara granitoids, northwest Anatolia, Turkey. International Journal of Earth Science 97, 1181-1200.

Karapetian, S.G., Jrbashian, R.T., Mnatsakanian A.K. 2001. Late collision rhyolitic volcanism in the north-eastern part of Armenian Highland: Journal of Volcanology and Geothermal Research 112, 189-220.

Keskin, M., Genç, Ş.C., Tüysüz, O. 2008. Petrology and geochemistry of post-collisional Middle Eocene volcanic units in North-Central Turkey: Evidence for magma generation by slab breakoff following the closure of the Northern Neotethys Ocean. Lithos 104, 267-305.

Konak, N., Alan, İ., Bakırhan, B., Bedi, Y., Dönmez, M., Pehlivan, Ş., Sevin, M., Türkecan, A., Yusufoğlu, H. 2016. 1/1.000.000 Ölçekli Türkiye Jeoloji Haritası. Maden Tetkik ve Arama Genel Müdürlüğü Yayını, Ankara-Türkiye.

Köprübaşı, N., Aldanmaz, E. 2004. Geochemical constraints on the petrogenesis of Cenozoic I-type granitoids in Northwest Anatolia, Turkey: evidence for magma generation by lithospheric delamination in a post-collisional setting. International Geology Review 46, 705–729.

Köprübaşı, N., Şen, C., Köprübaşı, N. 2000. Geochemistry of Fıstıklı (Armutlu–Yalova) granitoid. Bulletin of Earth Sciences Application and Research Centre of Hacettepe University, 22, 33–42.

Kürkcüoğlu, B., Furman, T., Hannan, B. 2008. Geochemistry of post-collisional mafic lavas from the North Anatolian Fault zone, Northwestern Turkey. Lithos 101, 416-434.

Labanieh, S., Chauvel, C., Germa, A., Q., X. 2012. Martinique: a clear case for sediment melting and slab dehydration as a function of distance to the trench. Journal of Petrology 53 (12), 2411-2464.

Langmuir, C.H., Vocke, R.D., Hanson, G.N., Hart, S.R. 1978. A general mixing equation with applications to İcelandic basalts. Earth and Planetary Science Letters 37, 380-392.

Li, D., He, D., Fan, C. 2015. Geochronology and Sr-Nd-Hf isotopic composition of the granites, enclaves, and mafic dykes in the Karamaya area, NW China: Insights into late Carboniferous crustal growth of West Junggar. Geoscience Frontiers 6 (2), 153-173.

Maniar, P. D., Piccoli, P.M. 1989. Tectonic discrimination of granitoids. Geological Society of America Bulletin 101, 635–643.

McDonough, W.F., Sun, S.S. 1995. The composition of the Earth. Chemical Geology 120, 223-253.

McCulloch, M.T., Gamble, J.A. 1991. Geochemical and geodynamical constraints on subduction zone magmatism. Earth and Planetary Science Letter 102, 358-374.

McLennan, S.M. 2001. Relationship between the trace element composition of sedimenatry rocks and upper continental crust. Geochemistry Geophysics Geosystems 2, article no. 2000GC000109.

Middlemost, E. A. K. 1994. Naming materials in magma/ igneous rock system. Earth-Science Reviews 37, 215-224.

Normand, M.D., Garcia, M.O. 1999. Primitive magmas and source characteristivs of the hawaiian plume: petrology and geochemistry of shield picrites. Earth and Planetary Science Letters 168, 27-44.

Normand, M. D., Leeman, W. P., Mertzman, S. A. 1992, Granites and rhyolites from the northwestern USA: Temporal variation in magmatic processes and relations To tectonic setting: Transactions of the Royal Society of Edinburgh, Earth Science 83, 71–81.

Okay, A.İ. 1989. Tectonic units and sutures in the pontides, Northern Turkey. In: Sengör AMC (ed) Tectonic evolution of the Tethyan region, Kluwer academic publishers, pp 109-116.

Okay, A.İ. 2008. Geology of Turkey: A synopsis, Anschitt 21, 19-42.

Okay, A.İ., Tüysüz, O. 1999. Tethyan sutures of northern Turkey. In: Durand, B., Jolivet, L., Horvath, F., Seranne, M. (Eds.), The Mediterranean Basin: Tertiary Extansion within the Alpine Orogen, 156. Geological Society, Special Publications, London, pp. 75– 515.

Okay A.İ., Göncüoğlu, M.C. 2004. Karakaya Complex: A review of data and concepts. *Turkish Journal of Earth Sciences* 13: 77-95.

Okay, A.İ., Satır, M. 2006. Geochronology of Eocene plutonism and metamorphism in northest Turkey: evidence for a possible magmatic arc. Geodinamica Acta 19, 251– 266.

Okay, A.İ., Satır, M., Maluski, H., Siyako, M., Monie, P., Metzger, R., Akyüz, S. 1996. Palaeo- and Neo-Tethyan events in northwest Turkey. *In* Yin E & Harrison M (eds) Tectonics of Asia, Cambridge University Press, 420-441.

Okay, A.İ., Tansel, İ., Tüysüz, O. 2001. Obduction, subduction and collsion as reflected in the Upper Cretaceous-Lower Eocene sedimentary record of western Turkey. Geological Magazine 138(2), 117-142.

Okay, A.İ., Satır, M., Siebel, W. 2006. Pre-Alpide Palaezoic and Mesozoic orogenic events in the Eastern Mediterranean region. In: Gee, D.G. & Stephenson, R.A. (eds), European Lithosphere Dynamics. Geological Society, London, Memoirs 32, 389-405.

Pearce, J.A. 1996. Sources and settings of granitic rocks. Episodes 19 (4), 120-125.

Pearce, J.A., Harris, N.B.W., Tindle, A.G. 1984. Trace element discrimination diagrams for the tectonic interpretation of granitic rocks. Journal of Petrolology 25, 956-983.

Peccerillo, A., Taylor, S.R. 1976. Geochemistry of Eocene calcalkaline volcanic rocks from the Kastamonu area, northern Turkey. Contributions to Mineralogy and Petrology 58, 63–81.

Plank, T. 2005. Constraints from thorıum/lanthanum on sediment recycling at subduction zones and the evolution of the continents. Journal of Petrology 46 (5), 921-944.

Plank, T., Langmuir, C.H. 1998. The chemical composition of subducting sediment and its consequences for the crust and mantle. Chemical Geology 145, 325-394.

Poutiainen, M., Scherbakov, T.F. 1998. Fuid and melt inclusion evidence fort he origin of idiomophic quartz crystals in topaz-bearing granite from the Salmi batholih, Karelia, Russia. Lithos 44, 141-151.

Ribeiro, J. Stern, R.J., Kelley, K.A., Martinez, F., Ishizuka, O., Manton, W.I., Ohara, Y. 2013. Nature and distribution of slab-derived fluids and mantle sources beneath the Southeast Mariana forearc rift. Geochemistry Geophysics Geosystems 14, 4865-4607, doi:10.1002/ggge.20244.

Rossi, J.N., Toselli, A.J., Basei, M.A., Sial, A.N., Baez, M. 2011. Geochemival indicators of metalliferpus fertility in the Carboniferous San Blas pluton, Sierra de Velasco, Argentina. In: Sial, A. N., Bettencourt, J. S., De Campos, C. P. & Ferreira, V. P. (eds), Granite-Related Ore Deposits. Geological Society, London, Special Publications 350, 175–186.

Seyitoğlu, G., Scott, B.C. 1996. The cause of N-S extensional tectonics in West Turkey. Tectonic escape vs. Back-arc spreading vs. Orogenic collapse. Journal of Geodynamics, 22, 145 - 153.

Shand, S.J. 1943. The eruptive rocks: 2nd edition, John Wiley, New York, 444 p.

Su, H-M., Jiang S-Y., Zhang, D-Y., Wu, X-K. 2017. Partial Melting of Subducted Sediments Produced Early Mesozoic Calc-alkaline Lamprophyres from Northern Guangxi Province, South China. Scientific Reports 7: 4864 (DOI:10.1038/s41598-017-05228-w).

Sun, S.S., McDonough, W.F. 1989. Chemical and isotopic systematics of oceanic basalts: implications for mantle composition and processes. In: Saunders, A.D. and Norry, M.J. (eds.), Magmatism in ocean basins. Geological Society of London Special Publication 42, 313-345.

Sylvester, P.J., 1998. Post-collisional strongly peraluminous graites. Lithos 45, 29-44.

Şengör, A.M.C., Yılmaz, Y. 1981. Tethyan evolution of Turkey: a plate tectonic approach. Tectonophysics, 75, 181-241.

Taylor S., R., Mc Lennan, S.M. 1985. The continental crust: its composition and evolution. An examination of the geochemical record preserved in sedimentary rocks. Blackwell Scientific Publications 46, pp.838.

Thompson R. N., Morrison M. A., Dickin A. P., Hendry, G. L. 1983. Continental flood basalts… Arachnids rule OK?, *in* Hawkesworth, C. J., and Norry, M. J. (eds.), Continental basalts and mantle xenoliths: Nantwich, UK, Shiva, 158–185.

Tommasini, S., Avanzinelli, R., Conticelli, S. 2011. The Th/La and Sm/La conundrum of the Tethyan realm lamproites. Earth and Planetary Science Letters 301, 469-478.

Topuz, G., Altherr, R., Schwartz, W.H., Dokuz, A., Meyer, H.-P. 2007. Variscan amphibolites-facies rocks from the Kurtoğlu metamorphic complex (Gümüşhane area, Eastern Pontides, Turkey). International Journal of Earth Science 96, 861–873.

Ustaömer, P.A., Ustaömer, T., Collins, A.S., Reischpeitsch, J. 2009. Lutetian arc-type magmatism along the southern Eurasian margin: new U–Pb LA-ICPMS and whole-rock geochemical data from Marmara Island, NW Turkey. Mineralogy and Petrology 96, 177– 196

Wang, K.-L., Chung, S.-L., O'Reilly, S. 2004. Geochemical Constraints for the Genesis of Post-collisional Magmatism and the Geodynamic Evolution of the Northern Taiwan Region. Journal of Petrology 45(5), 975-1011.

Xiang, Y-X., Yang, J-H., Chen J-Y., Zhang, Y. 2017. Petrogenesis of Lingshan highly fractionated granites in the southeast China: Implication for

Nb-Ta mineralization. Ore Geology Review 89, 495-525.

Yılmaz, Y. 1989. An approach to the origin of young volcanic rocks of western Turkey. In: Şengör AMC (eds) Tectonic evolution of the Tethyan Region. Kluwer, Dordrecht, pp. 159.

Yılmaz, Y. 1990. Comparison of the young volcanic associations of the West and the east Anatolia under the compressional regime: a review. Journal of volcanology and geothermal Research 44, 69-87.

Yılmaz, Y. 1997. Geology of western Anatolia. Active tectonics of northwestern Anatolia. The Marmara poly-project, a multidisciplinary approach by space-geodesy, geology, hydrogeology, geothermic and seismology. Vdf Hochschulverlag AG an der Zurich, pp 31–53.

Yılmaz, Y., Tüysüz, O., Gözübol, A.M., Yiğitbaş, E. 1981. Abant (Bolu)-Dokurcan (Sakarya) arasındaki Kuzey Anadolu Fay Zonunun kuzey ve güneyinde kalan tektonik birliklerin jeolojik evrimi: İst. Yerbilimleri 1, 23, 9-261.

Yılmaz, Y., Genç, Ş.C., Yiğitbaş, E., Bozcu, M. Yılmaz, K. 1995. Geological evolution of the Late Mesozoic continental margin of Northwestern Anatolia. Tectonophysics 243, 155-171.

Yılmaz, Y., Genç Ş.C., Karacık, Z., Altunkaynak, Ş. 2001. Two contrasting magmatic associations of NW Anatolia and their tectonic significance. Journal of Geodynamics 31, 243-271.

Yılmaz Şahin, S., Örgün, Y., Güngör, Y., Göker, A.F., Gültekin, A.H., Karacık, Z. 2010. Mineral and Whole-rock Geochemistry of the Kestanbol Granitoid (Ezine-Çanakkale) and its Mafic Microgranular Enclaves in Northwestern Anatolia: evidence of felsic and mafic magma interaction. Turkish Journal of Earth Science 19, 101-122.

Yiğit, Ö. 2012. A prospective sector in the Tethyan Metallogenic Belt: Geology and geochronology of mineral deposits in the Biga Peninsula, NW Turkey. Ore Geology Reviews 46, 118-148.

Appendix 1- Location and description of samples. Abbreviations: Q: Quartz; plag: plagioclase.

Sample No	Location		Sampling	Petrographical classification	Texture	Grain size	Description				
							Felsic minerals	Mafic minerals	Accessory minerals	Alteration	Others
Karabiga Gt.											
ASM-K11	40°25'10".69	27°16'4".77	Dike	Granite Aplite	Holocrystalline granular texture	fine	Q, orthoclase, plag	biotite	opaque min., zircon	low sericitization, argillisation	Some orthoclase minerals exhibit graphic texture.
ASM-K12	40°25'50".49	27°11'36".83	Stock	Granite Aplite	Holocrystalline granular texture	fine-medium	Q, orthoclase, plag	biotite	opaque min.	moderate sericitization, argillisation	
ASM-K13	40°25'47".23	27°11'13".48	Dike	Granite-porphyry	Holocyrstalline porphyric texture	medium-coarse	Phenocrysts: Q, orthoclase, plag Groundmass: Q, orthoclase, plag	biotite	opaque min.	low sericitization, argillisation	Some orthoclase minerals exhibit graphic texture.
ASM-K14	40°25'57".76	27°12'13".05									
ASM-K15	40°25'49".56	27°13'6".21									
ASM-K16	40°26'50".84	27°15'7".22									
Güreci Gt.											
ASM-K01	40°21'32".34	26°56'19".59	Stock	Granite	Holocrystalline granular texture	medium	plag, orthoclase, Q	biotite, hornblende	opaque min.	low sericitization, argillisation, chloritisation	Some orthoclase minerals exhibit poikilitic texture.
ASM-K02	40°21'18".11	26°56'38".97	Stock	Granite	Holocrystalline granular texture	medium	plag, orthoclase, Q	biotite, hornblende	sphene (titanite), opaque min.	moderate-high sericitization, argillisation, chloritisation, epidotization	Some orthoclase minerals exhibit poikilitic texture.
ASM-K03	40°21'28".95	26°56'40".19	Stock	Granite	Holocrystalline granular texture	medium	plag, orthoclase, Q	biotite, hornblende	sphene (titanite), opaque min.	low sericitization, argillisation, chloritisation	Some orthoclase minerals exhibit graphic texture.
ASM-K04	40°21'22".14	26°53'3".61									
ASM-K05	40°20'57".90	26°53'28".87									
ASM-K06	40°17'0".84	26°52'9".47	Stock	Monzonite	Holocrystalline granular texture	fine-medium	plag, orthoclase, Q	hornblende	sphene (titanit), opaque min.	moderate sericitization, argillisation	
ASM-K07	40°17'0".27	26°52'21".58	Stock	Q-diorite	Holocrystalline granular texture	medium-coarse	plag, orthoclase, Q	hornblende, biotite	sphene (titanit), opaque min.	low-moderate sericitization, argillisation, chloritisation	Some orthoclase minerals exhibit poikilitic texture. The sample has been subjected to cataclasm and recyrstallisation occurred in Q minerals
ASM-K08	40°17'2".67	26°52'25".89									
ASM-K09	40°17'4".19	26°52'20".10									
ASM-K10	40°17'14".58	26°52'23".56									
Kuşçayır Gt.											
ASM-K48	39°55'39".38	26°36'13".92	Stock	Q-monzodiorite	Holocrystalline porphyric texture	medium-coarse	Q, plag, K-feldspar	hornblende	opaque min.	low argillisation, opacification	Hornblende contains the exsolution lamellae of opaque mineral
ASM-K49	39°55'51".22	26°36'15".29	Stock								

Appendix 1- (Continue)

Sample No	Location		Sampling	Petrographical classification	Texture	Grain size	Description				
							Felsic minerals	Mafic minerals	Accessory minerals	Alteration	Others
ASM-K50	39°56'5".17	26°36'6".40	Stock	Q-monzodiorite	Holocrystalline porphyric texture	medium-coarse	Q, plag, K-feldspar	hornblende	opaque min.	low argillisation, opacification	Hornblende contains the exsolution lamellae of opaque mineral
ASM-K51	39°56'11".99	26°35'50".06	Stock								
ASM-K52	39°56'13".68	26°35'12".84									
Dikmen Gt.											
ASM-K56	40°8'58".88	27°10'36".98	Stock	Granodiorite	Holocrystalline granular texture	medium	Q, plag, orthoclase	biotite, hornblende	opaque min.	low-moderate sericitization, chloritisation	Plagioclase minerals have biotite inclusions and, fragmention occurs along grain boundary. Hornblende has poikilitic texture and some have plagioclase inclusions. Chloritisation of biotite from the cleavages is observed and some hornblende minerals were transfomed into biotite
ASM-K57	40°8'57".66	27°10'32".37									
ASM-K58	40°8'54".75	27°10'27".58									
Sarulok Gt											
ASM-K25	40°7'32".58	27°23'26".72	Stock	Granodiorite	Holocrystalline granular texture	fine-medium	Q, plag, orthoclase	biotite, pyroxene	opaque min.	low-moderate argillitisation, uralitisation	micrographic texture in some orthoclase minerals
ASM-K26	40°7'43".98	27°23'58".85									
ASM-K27	40°8'34".90	27°26'39".11	Stock	Granodiorite	Holocrystalline granular texture	fine-medium	Q, plag, orthoclase	biotite, hornblende	opaque min., sphene (titanite)	low-moderate argillitization, carbonatisation	micrographic texture in some orthoclase minerals
ASM-K28	40°8'43".66	27°27'11".58									
ASM-K29	40°8'49".31	27°28'6".56									
ASM-K30	40°8'48".91	27°28'26".63									
Yenice Gt											
ASM-K31 (Çakıroba)	39°57'13".05	27°17'36".26	Stock	Granite	Holocrystalline granular texture	medium-coarse	plag, orthoclase, Q	biotite, hornblende (pyroxene residue)	opaque min., sphene (titanite)	moderate sericitization, chloritisation	
ASM-K32	39°57'21".68	27°17'20".62									
ASM-K33	39°57'19".96	27°16'44".03									
ASM-K59	39°55'19".40	27°16'14".13									
ASM-K60 (Hamdibey)	39°53'59".90		Stock	Granodiorite	Holocrystalline granular texture	medium	Q, plag, orthoclase	biotite, hornblende	sphene (titanite), opaque min.	low-moderate sericitization, chloritisation	Hornblende with a poikilitic texture has plagioclase inclusions. Chloritisation of biotite through cleavages is observed, some hornblendes are transfromed into biotite
ASM-K61	39°51'51".19	27°12'59".33	Stock	Granodiorite	Holocrystalline granular texture	medium	Q, plag, orthoclase	biotite, hornblende	opaque min.	low argillisation	Grain size reduction due to cataclastism
ASM-K62	39°52'21".40	27°13'20".38									
ASM-K63	39°52'49".06	27°12'54".25									

Appendix 1- (Continue)

Sample No	Location		Sampling	Petrographical classification	Texture	Grain size	Description				
							Felsic minerals	Mafic minerals	Accessory minerals	Alteration	Others
Eskişehir Gt.											
ASM-K53	39°54'53".61	27°1'22".26	Stock	Granite	Holocrystalline granular texture	fine	Q, microcline, orthoclase, plag.	biotite, hornblende	opaque min.	low sericitization, carbonatisation	sieve texture in plagioclase, perthitic texture in orthoclase
ASM-K54	39°54'33".83	27°1'11".66									
ASM-K55	39°54'10".15	27°1'34".63									
Kestanbol Gt.											
ASM-K41	39°44'45".76	26°18'35".99	Stock	Q-monzonite	Holocrystalline granular texture	fine	Q, plag, K-feldspar	biotite	opaque min.		mafic minerals forms glameroporphyric texture
ASM-K42	39°43'28".16	26°17'44".59									
ASM-K43	39°42'53".64	26°17'0".97	Stock	Granite	Holocrystalline granular texture	medium-coarse	Q, plag, K-feldspar	biotite, hornblende	sphene (titanite), opaque min.		poikilitic and perthitic texture in K-feldspars
ASM-K44	39°42'38".41	26°15'55".74									
ASM-K45	39°42'54".89	26°1'56".05									
ASM-K46	39°46'24".24	26°16'3".48	Dike	Lamprophyre/ Kersantite	Porphyric texture	fine	Plag, K-feldspar	pyroxene, biotite, olivine (?)	opaque min.	low argillisation	
ASM-K47	39°46'24".24	26°16'3".48	Dike								
Eybek Gt.											
ASM-K64	39°42'39".60	27°10'18".18	Stock	Q-monzonite	Holocrystalline granular texture	fine	plag, orthoclase, Q	biotite, hornblende	sphene (titanite), opaque min., zircon	low sericitization, chloritisation, opasitleşme	Orthoclase minerals exhibit poikilitic texture, and contains plagioclase and hornblende inclusions. Hornblende contains the exsolution lamellae of opaque mineral and exhibit chloritisation and some are also transformed into biotite
ASM-K65	39°42'30".52	27°9'55".90	Stock	Granite	Holocrystalline granular texture	medium	Q, orthoclase, plag	biotite, hornblende	sphene (titanite), opaque min.	low-moderate sericitization, opasitleşme	Orthoclase minerals exhibit poikilitic texture. Hornblende contains the exsolution lamellae of opaque mineral.
ASM-K66	39°41'11".92	27°9'39".01	Stock	Granodiorite	Holocrystalline granular texture	medium	Q, plag, orthoclase	biotite	sphene (titanite), opaque min.	low argillitization	
ASM-K67	39°40'53".68	27°9'20".45									
ASM-K69	39°40'53".58	27°9'9".07									
ASM-K70	39°41'10".94	27°8'30".36									
Eviler Gt											
ASM-K34	39°46'36".54	26°41'32".06	Stock	Granodiorite	Holocrystalline granular texture	medium	Q, plag, orthoclase	biotite, hornblende	sphene (titanite), opaque min.	moderate sericitization, argillitization, chloritisation	poikilitic texture in some orthoclase minerals

Appendix 1- (Continue)

Sample No	Location		Sampling	Petrographical classification	Description						
					Texture	Grain size	Felsic minerals	Mafic minerals	Accessory minerals	Alteration	Others
ASM-K35	39°47'5".71	26°42'24".94	Stock	Granodiorite	Holocrystalline granular texture	medium-coarse	Q, K-feldspar, plag	biotite, hornblende	sphene (titanite), opaque min.	low chloritisation, sericitization	Myrmekitic texture developed between quartz and plagioclase. Chloritisation of biotite and hornblende through the cleavages is observed. Q minerals have plagioclase inclusions.
ASM-K36	39°47'41".25	26°45'41".61			Holocrystalline granular texture	medium					
ASM-K37	39°48'3".02	26°46'49".15	Stock	Granite Aplite	Holocrystalline granular texture		Q, K-feldspar, plag	rare biotite	opaque min.	low argillisation, sericitization	Perthitic and graphic texture
ASM-K38	39°48'35".70	26°47'18".57									
ASM-K39	39°48'35".70	26°47'18".57									
ASM-K40	39°50'22".06	26°54'12".47									
Çamyayla Gt											
ASM-K20	40°6'37".02	26°44'57".02									
ASM-K21	40°6'30".98	26°44'39".98	Stock	Q-monzodiorite porphyry	Holocyrstalline porphyric texture	medium-coarse	Phenocrysts: plag Groundmass: plag, orthoclase, Q	Groundmass: biotite, hornblende	opaque min.	Orta sericitization, argillisation, chloritisation	Some orthoclase minerals exhibit micrographic texture.
ASM-K22	40°6'42".23	26°44'23".59	Stock								
ASM-K23	40°7'2".05	26°44'12".24	Stock	Q-monzodiorite	Holocrystalline granular texture	fine-medium	plag, orthoclase, Q	biotite, hornblende	opaque min.	low-moderate sericitization, argillisation, chloritisation	Some orthoclase minerals exhibit micrographic texture.
ASM-K24	40°7'14".47	26°44'51".73	Stock								
Alanköy Gt											
ASM-K17	40°1'18".71	26°46'32".43	Stock	Q-diorite	Holocrystalline granular texture	medium	plag, Q, orthoclase	hornblende	sphene (titanite), opaque min.	high sericitization, argillisation, chloritisation, epidotization	
ASM-K18	40°1'12".34	26°46'41".86									
ASM-K19	40°1'18".55	26°46'31".72	Stock								

Bulletin of the Mineral Research and Exploration

http://bulletin.mta.gov.tr

The gas hydrate potential of the Eastern Mediterranean basin

Şükrü MEREY[a*]   and Sotirios Nik. LONGINOS[b]

[a]Department of Petroleum and Natural Gas, Batman University, Batman, Turkey.
[b]Department of Petroleum and Natural Gas, Middle East Technical University, Ankara, Turkey.

Research Article

ABSTRACT

Gas hydrate exploration studies have increased substantially since last decade. Gas hydrate reservoirs are commonly found in the marine environment and permafrost. Studies related to natural gas hydrates in the Mediterranean Basin are rare compared to those released on the continental margins of the United States of America, Japan, India, China and Korea. This study provides an evaluation of the gas hydrate potential of the Mediterranean Basin using available literature data such as scientific drilling data (Ocean Drilling Program Leg 160 and Leg 161), sediment data, geothermal data, geochemical data, gas seepage data, mud volcano data etc., It is shown that there is a high producible gas hydrate potential (~ 98.16 standard trillion cubic meter) in the Mediterranean Basin. The Eastern Mediterranean basins have the highest gas hydrate potential due to its high amount of source gas potential and lower geothermal gradient compared to those in the Western Mediterranean.

1. Introduction

Gas hydrate reservoirs are deemed as likely future energy source due to the fact that they can be found amply mostly in permafrost regions and sediments in the oceans, both occupying huge areas of the Earth. According to calculations for hydrate bearing sands globally, there is a great range of global gas hydrate resource between 133 standard trillion cubic meter (tcm) and 8891 tcm (Johnson, 2011). Although through the years, the estimations of gas hydrates have been reduced by the majority of the scientists from their initial findings (Milkov, 2004), it can be stated that even the most pessimistic calculations of total quantity of gas in gas hydrates are much larger than the conventional gas resources (404 tcm) and shale gas (204-456 tcm) (Chong et al., 2016). On the other hand, almost 80% of global natural gas demand is met by conventional sources, with unconventional sources increasing only in recent years. Global energy demand will be ameliorated significantly in the next decades

as earth population grows. It has been projected that the global energy consumption will rise by 56% from 524 quadrillion British Thermal Unit (BTU) in 2010 to 820 quadrillion BTU in 2040 (IEA, 2011). Due to its huge potential all over the world, gas hydrates unconventional resources are quite important.

Gas hydrates are crystalline compounds formed from water and suitably-sized gas molecules at high pressure and low temperature conditions. Depending on which gas molecules are present, hydrates form different crystal structures. Cubic structure I (sI), structure II (sII) and hexagonal structure H (sH) are three gas hydrate structures found in nature (Sloan and Koh, 2008). sI hydrate has two types of cavities: a small pentagonal dodecahedral cavity consisting of 12 pentagonal rings of water and a large tetrakaihedral cavity consisting of 12 pentagonal and two hexagonal rings of water. sII hydrate also has two cavity sizes: the pentagonal dodecahedral cavity and the larger hexakaidecahedral cavity consisting of 12 pentagonal

and four hexagonal rings of water. sH hydrate is composed of 3 small (5^{12}), 2 medium ($4^35^66^3$) and 1 large cages ($5^{12}6^8$) (Carroll, 2009). Approximately 46, 136 and 34 water (H_2O) molecules are essential for sI, sII and sH hydrates respectively. Gas hydrates formed by only one type of gas are defined as simple or pure gas hydrates. Simple hydrates of methane (CH_4), ethane (C_2H_6), carbon dioxide (CO_2), hydrogen sulfide (H_2S), and xenon (Xe) are called a sI type of gas hydrate. Moreover, propane (C_3H_8), i-butane (i-C_4H_{10}), nitrogen (N_2), and oxygen (O_2) form the sII type of gas hydrate. Different than sI and sII hydrates, for the formation of sH hydrates, a gas such as CH_4 and other large molecules that have diameters greater than those of isobutane (i-C_4H_{10}), such as isopentane (i-C_5H_{12}) are needed (Carroll, 2009). sI and sII hydrates are common all over the world, while sH hydrates are not common and they were only found in a few regions such as the Gulf of Mexico, Cascadia, and the Caspian Sea (Hester and Brewer, 2009).

Even though gas hydrate reservoirs are examined as contingent energy sources for future, until now there have been only a few short-term production tests and there is no commercial gas production. Gas hydrates are in solid form at reservoir conditions, so conventional oil and gas production techniques cannot be implemented in gas hydrate reservoirs (Chen et al., 2018). Gas hydrate reservoirs are classified in four classes. Class 1 hydrate reservoir has a stable hydrate layer and an underlying free gas zone. Class 2 hydrate reservoir has a stable hydrate layer and an underlying free water zone. Class 3 hydrate reservoir has a stable hydrate layer bounded by permeable or impermeable shale or clay zones. Class 4 hydrate reservoirs are distributed near sea floor with low hydrate saturation and they are not regarded as the productive reservoirs (Worthington, 2010; Moridis et al., 2013). Among these classes, Class 1 hydrates are considered as the most promising gas hydrate reservoirs due to their gas potential in both hydrate section and free gas section. The expected proportions of Class 1, Class 2, Class 3, and Class 4 reservoirs in nature are 14 percentages (%), 5 %, 6 % and 75 % respectively (Yang et al., 2017).

There are four gas production methods for gas hydrate reservoirs: thermal injection, depressurization, chemical injection and CH_4-CO_2 replacement. In thermal injection method, the temperature is accrued with electrical heating, hot fluids injection and microwave heating. The main drawbacks of thermal

injection method are the loss of heat in non-hydrate sections, the low injection rates and the expensive cost of thermal injection (Chong et al., 2016). In depressurization method, there is production of free water and or free gas in the pores of gas hydrate reservoirs by using pumps (i.e. electrical submersible pump), hence the reservoir pressure is diminished below hydrate equilibrium pressure and creates the gas hydrate dissociation and the release of gas and water. The drawbacks of depressurization method are sand production, geomechanical risks and slow gas production (Yin et al., 2018). In chemical injection method, chemicals such as methanol, ethylene glycol, brine etc. are used to shift the gas hydrate equilibrium curve leading to gas hydrate dissociation. However, chemical injection method is noxious in marine environments (Xu and Li, 2015). In CH_4-CO_2 method when CO_2 is injected into CH_4 gas hydrate reservoir, CH_4 molecules leave their hydrate cages and CO_2 molecules fill these void cages because of thermodynamic stability difference between CH_4 hydrate and CO_2 hydrate. The low injection rate and low replacement rate are the disadvantages for CH_4-CO_2 method (Kvamme, 2015).

The number of studies related to these gas hydrates in the Mediterranean Sea is low compared to those from the continental margins of the United States of America (USA), Japan, India, China and Korea. This study aims at evaluating the gas hydrate potential of the Mediterranean Basin (especially the Eastern Mediterranean) by using the available literature data such as drilling data, geothermal data, and geochemical data.

2. Gas Hydrate Potential of the Eastern Mediterranean Sea

Recently, there have been many conventional gas reserve discoveries in the Mediterranean Basin most of which are in the Eastern Mediterranean indicating a huge conventional gas potential (Lo, 2017). In order to propose the producible gas hydrate potential of the Eastern Mediterranean Sea, the following criteria should be satisfied:

- Source gas potential (generally biogenic CH_4)
- Migration paths (if source rock and reservoir rock are different, there should be a migration path from source rock to reservoir rock)

- Reservoir rock within gas hydrate stability zone (GHSZ)
- Porous and permeable coarse sands
- Water in porous media

It is essential to study the Eastern Mediterranean Basin literature data to conclude that whether the Eastern Mediterranean Sea has producible gas hydrate potential or not.

2.1. Source Gas Potential in the Eastern Mediterranean Sea

The source gas potential in the Mediterranean Sea was proved with recent conventional gas discoveries. For instance, in the Nile Delta of the Mediterranean Sea, there are 126 gas fields with proven reserves about 1.8 tcm. In the Levantine basin of the eastern Mediterranean, recent gas discoveries have been made. Similarly, it is known that there are potential gas reserves in the south part of Crete and Cyprus (Foscolos et al., 2011). There are widespread gas seepages across the seafloor of the eastern Mediterranean Sea. These extensive gas seepages were mostly observed in mud volcanoes. Mud volcanoes (and/or gas chimneys) are defined as the result of massive mud/fluid expulsion on the seafloor (Praeg et al., 2011). There is a link between mud volcanoes and hydrocarbon occurrences. As the number of mud volcanoes increases, the possibility of hydrocarbon existence increases as well (Kopf, 2002).

Although a few mud volcanoes were detected in the Western Mediterranean Basin, many mud volcanoes were found in the Eastern Mediterranean. According to Milkov (2005), mud volcanoes are important indicators of gas hydrate existence because they show the high source gas potential in the study area. The number of mud volcanoes in the Eastern Mediterranean Sea exceeds 200, which is one of the world's highest abundances of mud volcanoes as seen in figure 1 (Woodside et al., 1998; Kopf, 2002; Charlou et al., 2003; Camerlenghi and Pini, 2009). All of these indicate that there is no problem in the Eastern Mediterranean Sea in terms of source gas potential.

The gas released at the seafloor of the Eastern Mediterranean Basin is originated by two mechanisms: biogenic and thermogenic gas generation. In the Eastern Mediterranean Basin, part of the gas plumbing system is related to plate convergence between Africa and Eurasia (Farla, 2006). Gas hydrate dissociation may be related to this geological process. The other mechanism responsible for gas migration that is the sedimentary loading within the Nile Deep Sea fan. Huge amount of gas hydrate dissociations occurred due to the increase in the seafloor temperature of the Mediterranean Sea (Poort et al., 2005). Global warming causes gas hydrate dissociations in the different part of the world (Ruppel and Kessler, 2017). Woodside et al. (1998) proposed that most of the mud volcanoes in the Eastern Mediterranean Sea are
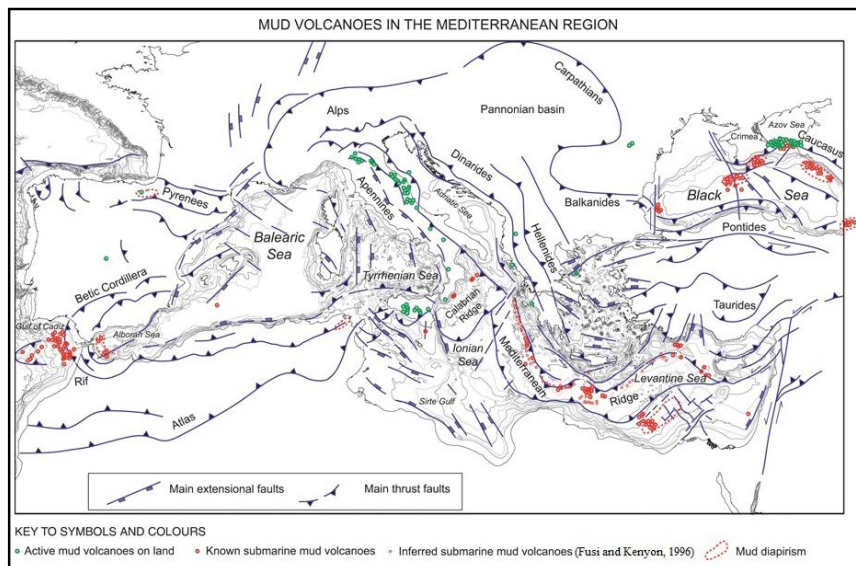
Figure 1- Distribution of mud volcanoes in the Mediterranean region (Camerlenghi and Pini, 2009).

related to tectonic forces and the rest amount is related to gas hydrate dissociation.

Table 1 lists some locations where gas seepages detected in the Eastern Mediterranean Sea (Gontharet et al., 2009; Makovsky et al., 2013; Aloisi et al., 2000; Lykousis et al., 2009; Pape et al., 2010; Werne et al., 2004). As seen in table 1, mostly CH_4 was detected in almost all gas seepages. This is an important sign of biogenic source gas (Charlou et al., 2003). However, there is also thermogenic gas potential in Amsterdam mud volcano (MV) (Anaximander Mountain in the Eastern Mediterranean Sea) in table 1 because gas is composed of 84 % CH_4, 13 % C_2H_6, and 3 % C_3H_8.

While taking gas samples in gas seepage areas in table 1, the core samples were also taken in the seafloor by using gravity corer. Figure 2-a shows the gas hydrate sample collected in Thessaloniki MV (1315 meter (m) below sea level) in the Eastern Mediterranean Sea (Lykousis et al., 2004). Similarly, the gas hydrate was collected from Amsterdam MV (2025 m below sea level) as shown in figure 2-b (Lykousis et al., 2009). Gas hydrate detected in Amsterdam MV is sII hydrate.

In some cores taken from the seafloor of the Eastern Mediterranean Sea, gas hydrate was not found but the sediments were mousy and soupy (Pape et al., 2010). While sampling core samples with the gravity corer, pressure is not preserved so gas hydrate mostly dissociates until it reaches to the sea surface. However, mousy and soupy sediments are also considered as important signs of gas hydrate existence (Merey and Sinayuc, 2016a).

Farla (2006) proposed that the amount of CH_4 stored in the Eastern Mediterranean Sea varies from 61×10^9 cubic meter (m^3) to 490×10^9 m^3. This indicates huge source gas potential in the Eastern Mediterranean Sea. It is expected that important amount of this source gas is also stored as gas hydrates inside the sediments within gas hydrate stability zone (GHSZ).

2.2. Migration Paths

Conventional petroleum systems are composed of source rock, migration paths, reservoir rock and trap rock (Hunt, 1995). For gas hydrates, source rock and reservoir may coincide. Especially, within the gas hydrate stability zone, source gas may be formed after biogenic processes, so gas migration may not be needed to feed a reservoir. With the necessary pressure and temperature condition, gas hydrates

Table 1- Some gas seepages in the Eastern Mediterranean Sea.

Location	Sea Depth, m	Gas Type	Source
Nile Delta Sea Fan	500 to 3000	Mostly CH_4	Gontharet et al., 2009
Levantine Basin	1100 to 1300	Mostly CH_4	Makovsky et al., 2013
Olimpi Area	1700 to 2000	Mostly CH_4	Aloisi et al., 2000
Thessaloniki MV	1260 to 1320	Mostly CH_4	Lykousis et al., 2009
Amsterdam MV	2025	84 % CH_4, 13 % C_2H_6, 3 % C_3H_8	Pape et al., 2010
Kazan MV	1700	CH_4	Werne et al., 2004
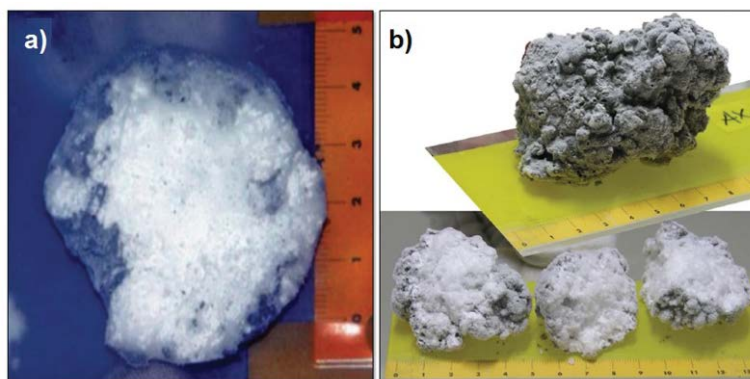
Figure 2-   a) Gas hydrate sample in Thessaloniki MV, Eastern Mediterranean (Lykousis et al., 2004) b) Gas hydrate sample in Amsterdam MV (Lykousis et al., 2009)

may form within the source rock. A cap rock is not a must for gas hydrate because gas hydrates are in solid form. However, gas seepages at the seafloor show that there are many migration systems like faults and permeability changes in the Eastern Mediterranean Basin.

2.3. Gas Hydrate Stability Zone (GHSZ)

Gas hydrate stability zone is defined as the interval where gas hydrates form and GHSZ thickness depends on sea depth, sea salinity, geothermal gradient, chemical composition of the gas and the water. Above GHSZ, gas hydrate cannot exist because there is not enough hydrostatic pressure. Below GHSZ, gas hydrate cannot exist as well because temperature raises with depth due to geothermal gradient but hydrostatic pressure is not enough to form gas hydrate (Max and Johnson, 2016).

In order to determine the thickness of GHSZ of the Mediterranean Sea, it is essential to get information about seafloor temperature, geothermal gradient, water depth (pressure), and salinity. The seafloor temperature of the Mediterranean Sea varies from 12.5 Celsius (°C) to 14 °C. The pore water salinity is approximately 3.86 weight % (Praeg et al., 2017). It is known that gas hydrates generally follow hydrostatic pressure and generally they are not over-pressurized as conventional gas reservoirs (Max and Johnson, 2016).

The type of gas hydrate affects GHSZ. sII hydrate formed from natural gas mixtures is much more stable than CH_4 (sI) hydrate (Sloan and Koh, 2008) so GHSZ of sII is thicker. Moreover, water depth is an important factor affecting the thickness of GHSZ. As sea depth increases, the thickness of GHSZ increases. Therefore, GHSZ is thinner in sea slopes. For example, Thessaloniki MV is located between 1260 m and 1320 m below sea surface and GHSZ is very thin at this MV. Figure 3 shows the Mediterranean Sea bathymetry. As seen in this figure, the Eastern Mediterranean Sea is deeper than the Western Mediterranean Sea. This also proves the higher possibility of gas hydrate existence in the Eastern Mediterranean Sea compared to the Western Mediterranean Sea.

The high average water depth in the Mediterranean Sea favors the a thicker GHSZ. However, the sea floor temperature of the Mediterranean Sea is high (~14°C) relatively to the global ocean (Küçük et al., 2016), and this reduces the thickness of GHSZ. The geothermal gradient in the Mediterranean Basin is highly variable (Merey and Longinos, 2018). In the Western Mediterranean Sea, heat flow varies from 50 to >100°C/kilometer (km). However, the Eastern Mediterranean Sea has a geothermal gradient less than 50°C/km (Eckstein, 1978; Praeg et al., 2011). The reason of very high geothermal gradients in the Western Mediterranean Sea is explained with volcanism activity
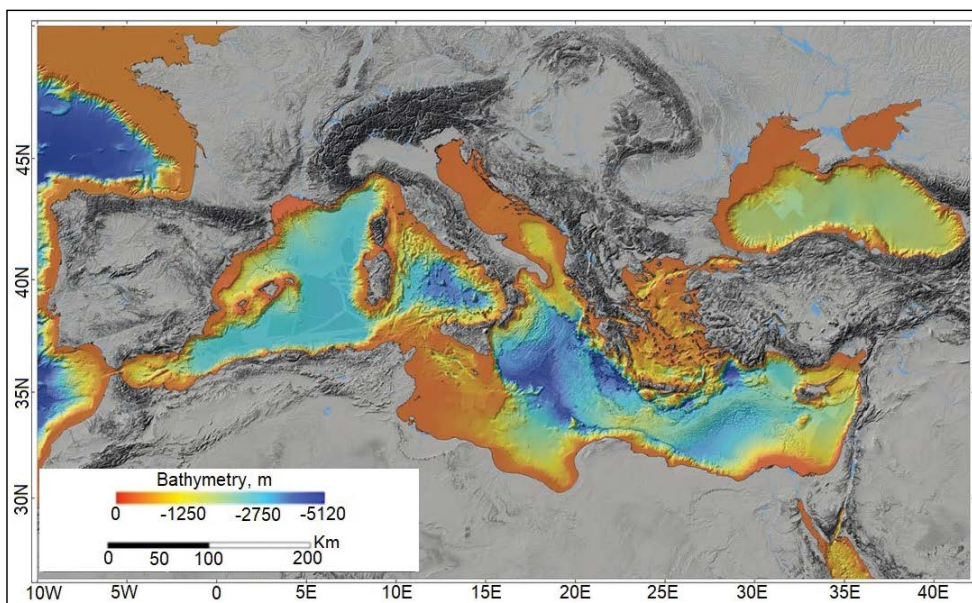
Figure 3- Mediterranean sea bathymetry (Brosolo et al., 2012).

in this area (higher upper mantle temperature below this zone) (Cermak and Rybach, 2012).

Due to its deeper water depth and lower geothermal gradient, the Eastern Mediterranean Sea has thicker GHSZ compared to the Western Mediterranean Sea. Methane gas hydrate stability curve in the conditions of the Mediterranean Sea with an average of 3.86 wt. (weight) % salinity was drawn in figure 4 by using HEP software developed by Merey and Sinayuc (2016b). For 500 m-thick methane hydrate stability zone (MHSZ), the temperature in the bottom of MHSZ was calculated as 20°C and 39°C for 12°C/km and 50°C/km geothermal gradients respectively (when seafloor temperature is 14°C and sea depth is 2000 m). For 39°C, methane hydrate equilibrium pressure should be 164.5 mega Pascal (MPa). It is not possible to obtain this pressure in gas hydrates because gas hydrates follow hydrostatic pressure gradients and they are not overpressurized as conventional gas reservoirs (Max and Johnson, 2016). In this example, the hydrostatic pressure at 500 meter below seafloor (mbsf) is 26.5 MPa, which is below 164.5 MPa. For this reason, gas hydrate stability zone in the Western Mediterranean Sea is thin as seen in figure 5. However, in the Eastern Mediterranean Sea, there are locations with 12°C/km geothermal gradient. In these conditions, at 500 mbsf (in the example above), hydrostatic pressure and methane hydrate equilibrium pressure in figure 4 are close to each other (~26.5 MPa) so it is possible to observe 500 m thick-MHSZ in the Eastern Mediterranean Sea.

Furthermore, there are many mud volcanoes and gas seepages in the Eastern Mediterranean Sea and gas hydrate samples were collected in the Eastern Mediterranean Sea (Figure 2). All of these supports the widespread existence of gas hydrates in the Eastern Mediterranean Sea. Kopf (2002), Ocakoğlu (2009) and Praeg et al. (2011) proposed this potential as well.

Table 2 lists some of GHSZ predictions in the Mediterranean Sea (Klauda and Sandler, 2003; Praeg et al., 2017; Wood and Jung, 2008; Praeg et al., 2011; Max and Johnson, 2016). Considering all of these variations over the Mediterranean Sea, Praeg et al. (2011) proposed the GHSZ thickness map of the Mediterranean Sea for methane hydrate in figure 5. As expected according to the outcomes of this study, there are huge amounts of gas seeps in figure 1 in the Eastern Mediterranean Sea. Moreover, the thickness of GHSZ in the Western Mediterranean Sea is less than 150 m. On the other hand, the thickness of GHSZ varies from 175 m to 500 m in the Eastern Mediterranean Sea. When figure 3 and figure 5 are analyzed together,

Table 2- GHSZ Predictions in the Mediterranean Sea.

Source	GHSZ, m
Klauda and Sandler, 2003	100 to 400
Praeg et al., 2007	Average 200
Wood and Jung, 2008	100 to 250
Praeg et al., 2011	200 to 500
Max and Johnson, 2016	Maximum 400
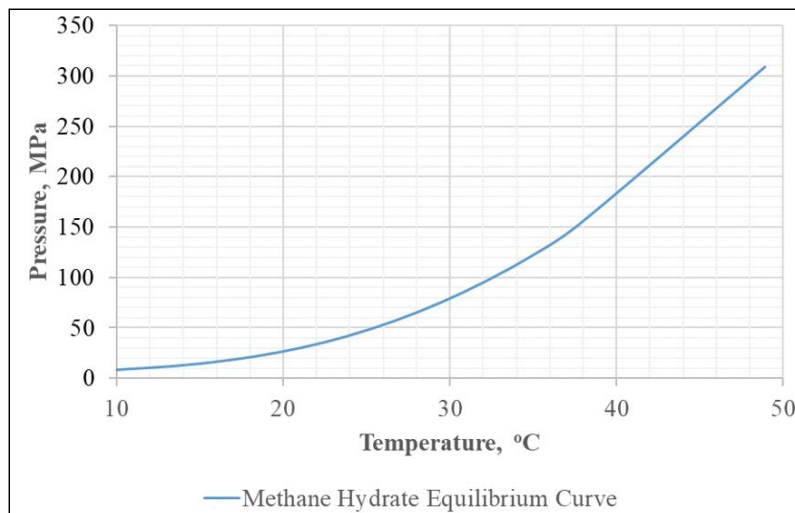
Figure 4- Methane hydrate stability curve in the conditions of the Mediterranean Sea with an average of 3.86 wt. % salinity.
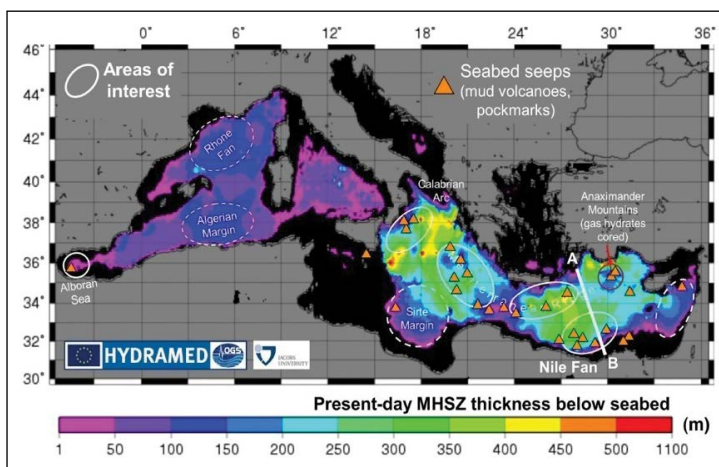
Figure 5- Methane Hydrate Stability (MHSZ) in the Mediterranean Sea; orange triangles indicating the general locations of known seabed gas seeps (Praeg et al., 2011).

it can be concluded that GHSZ strongly depends on water depth because in deeper part of the Eastern Mediterranean Sea, GHSZ is thicker. Furthermore, due to higher geothermal gradient (50-100°C/km) in the Western Mediterranean Sea, GHSZ is thin in this part of the Mediterranean Sea. To summarize, the Eastern Mediterranean Sea has thicker GHSZ and it has a good potential of gas hydrate existence.

2.4. Porous and Permeable Coarse Sands

The type of sediments where gas hydrate deposited is quite important for hydrate morphology in porous media. Generally, the permeability of clays and shales is associated to mud volcanoes. CH_4 formed in this geological environment is forced through the host formation by overpressure and hydrofracturing, forming fracture filling gas hydrates and nodular gas hydrates. These gas hydrates are common in the world but they are not considered as producible gas hydrate because the permeability, porosity and hydrate saturations in these types of gas hydrates are very low.

With current technology, gas production from gas hydrates deposited inside the porous media of coarse sands is possible in terms of feasibility. This is because permeability, porosity and gas hydrate saturations are high in coarse sands (Merey and Sinayuc, 2016a; Max and Johnson, 2016). In recent short-term gas production trials from gas hydrates in Canada, USA and Japan, gas hydrates deposited in coarse sands were chosen (Boswell et al., 2017).

According to the outcomes in this study, the Eastern Mediterranean Sea has high amount of source gas potential, migration paths, and thick GHSZ and these are significant indicators of a gas hydrate potential. However, coarse sands within GHSZ in the Eastern Mediterranean Sea should be detected for the producible gas hydrate potential. Max and Johnson (2016) proposed that the presence of coarse sands with high reservoir quality is possible in the Mediterranean Sea because of its Neogene and younger history.

Although geophysical methods are helpful for detecting coarse sands in GHSZ, the drilling data is necessary to detect these coarse sands possibly including gas hydrates. In this study, the open-source drilling and coring data of Ocean Drilling Program (ODP) Leg 160 and Leg 161 in 1995 were investigated in detail. The wells were drilled in the Eastern Mediterranean Sea during ODP Leg 160 program and the wells were drilled in the Western Mediterranean Sea during ODP Leg 161 program (ODP Leg 160, 1995; ODP Leg 161, 1995). Figure 6 shows the locations of the wells drilled during ODP Leg 160 and Leg 161 programs.

The detection of sands in the lithology of the wells drilled during ODP Leg 160 and Leg 161 are shown in table 3 (Emeis et al., 1996; Robertson, 1998a; Kopf et al., 1998; Robertson and Kopf, 1998). in the Western Mediterranean Sea, no sand section was detected during the drilling of the sediments up to 199.4 meter below seafloor (mbsf). However, this is
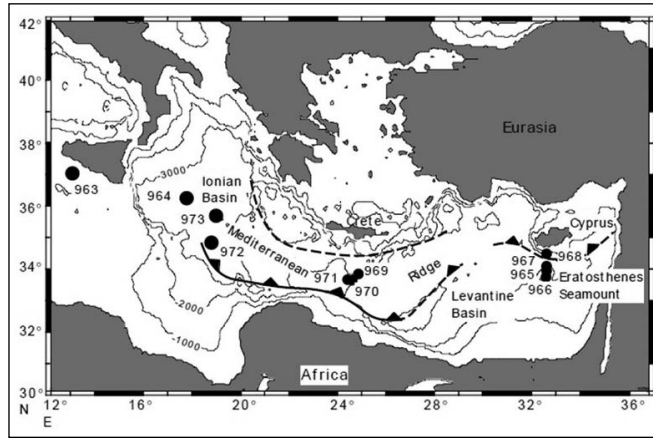
Figure 6- The drilling sites in ODP Leg 160 in the Mediterranean Sea (ODP
Leg 160, 1995; ODP Leg 161, 1995).

Table 3- Detection of sands in the lithology of the wells drilled during ODP Leg 160 and Leg 161.

Site Number	Depth, mbsf	Sand	Source
963	199.4	No detected	Emeis et al., 1996
964	112	Limited interval of foraminifer sand	Emeis et al., 1996
965	250.4	Not detected	Emeis et al., 1996
966	350	Relatively rare intervals of crudely stratified coarse carbonate sand	Robertson, 1998a
967	600.3	Not detected	Spezzaferri et al., 1998
968	301	Fine sands (up to tens of centimeters thick) (167-301 mbsf)	Robertson, 1998b
969	110	Not detected	Emeis et al., 1996
970	200	Poorly consolidated thin- to medium-bedded sands	Kopf et al., 1998
971	200	Thin layers that correspond to relatively sandy	Robertson and Kopf, 1998
972	95.4	Fine sands up to 50 cm in thickness	Robertson and Kopf, 1998
973	150	Interbeds of sands, silts, and nannofossil clays, and a single 14-m-thick interval of sand	Kopf et al., 1998

the data from only one site and the sediments are very heterogeneous. Therefore, with the increase of drilling activities around Site 963 and other sites, there is a possibility to detect coarse sand sections. In Site 964 in the Western Mediterranean Sea, limited interval (centimeter scale) of foraminifer sand was observed. In Site 965 in the Eastern Mediterranean Sea, no sand section was found. However, near Site 965, relatively rare intervals of crudely stratified coarse carbonate sands were detected in Site 966. Even though no sand section was detected in Site 967 in the South of Cyprus, fine sands (up to tens of centimeters thick between 167 and 301 mbsf) were observed in Site 968 in the South of Cyprus. Similarly, poorly consolidated thin- to medium-bedded sands were detected in Site 970

in the South of Crete but near Site 970, sand section was not discovered in Site 969. Near Site 970, thin layers that correspond to relatively sandy sediments were detected in Site 971. In Site 972, fine sands up to 50 cm in thickness were detected but the thickest sand section (14 m) in ODP Leg 160 and Leg 161 was found in Site 973.

The cores recovered from Site 970 and Site 971 were mainly "mousse-like" muddy sediments. It is hard to see gas hydrates in sediments if the core samples are taken to the surface with conventional coring techniques instead of new pressurized coring techniques. However, the appearance of the sediments after conventional coring can be a proxy for the

presence of gas hydrates. With gas hydrate dissociation after conventional coring, "soupy" and "mousse-like" sediments are seen as a proxy for the gas hydrate existence (Melgar, 2009; Merey, 2017). Soupy sediments include high amount of water, and high hydrate content might be reason of this when nodular and massive gas hydrate exists. Different from soupy sediments, mousse like sediments are considered to include disseminated gas hydrates in fine sediments (Melgar, 2009). Therefore, the appearance of core samples is one of good indicators of gas hydrates even if they are conventional core samples and these indicators are available in the Mediterranean Sea.

Figure 7 shows the sand % in Site 966, Site 967, Site 969, Site 970 and Site 971. The drilling results of ODP Leg 160 and Leg 161 indicate that there is a potential of coarse sand section within GHSZ. If these sand sections were invaded with source gas, gas hydrate deposition is highly possible inside these coarse sands. Thus, these coarse sand sections in the Mediterranean Sea should be targets for the exploration of producible gas hydrates as in Canada, USA, India, and Japan (Merey and Sinayuc, 2016a; Merey and Longinos, 2018)

2.5. Other Indicators

The existence of gas hydrates might be investigated by using different methods. One of them is geophysical method. Bottom-simulating reflections (BSR) are commonly used to detect gas hydrates in marine environment. Above the bottom of GHSZ, gas hydrate is stable but below the bottom of GHSZ, gas hydrate is not stable and gas is available as free gas in the pores of the sediments. Hence, at the bottom of GHSZ, there is a transition from solid phase and gaseous phase of methane. This creates a large acoustic impedance contrast generating a high amplitude reflector called bottom simulating reflector (Thakur and Rajput, 2011) because it mimics sea bottom. Majumdar et al. (2016) proposed that the detection of BSR increases the possibility of gas hydrate detection 2.6 times..

Even though BSRs are widely detected along the world continual margins, only one BSR has been tentatively detected so far in the Mediterranean Sea (Merey and Longinos, 2018). This BSR (Figure 8) is in the Nile Deep Sea Fan in the Eastern Mediterranean Sea (Praeg et al., 2011). The reasons of rare occurrence of BSR in the Mediterranean Sea might be due to (Miles, 1995; Merey and Longinos, 2018):
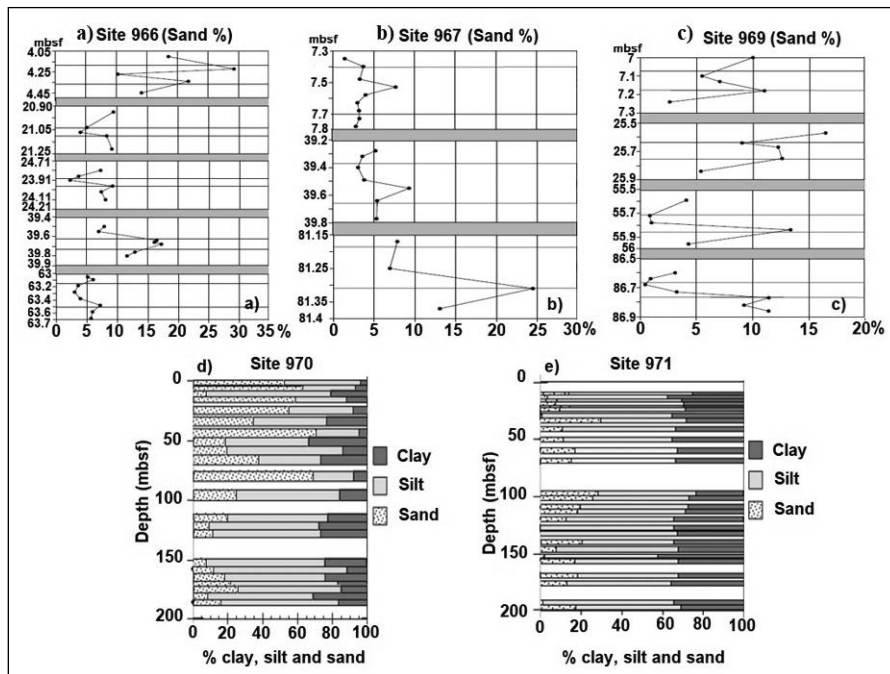
Figure 7- a) Sand % in Site 966 (Robertson, 1998a) b) Sand % in Site 967 (Spezzaferri et al., 1998) c) Sand % in Site 969 (Diester-Haass et al., 1998) d) Clay, Silt and Sand % in Site 970 (Kopf et al. 1998) e) Clay, Silt and Sand % in Site 971 (Robertson and Kopf, 1998).
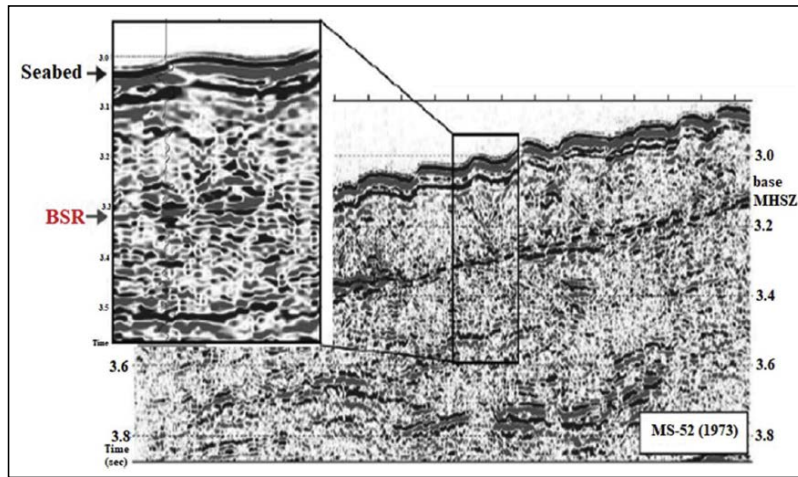
Figure 8- The BSR observed in the central Nile Delta, Eastern Mediterranean Sea (Praeg et al., 2008).

- Less Class 1 hydrate occurrence
- Less shallow geophysical studies

During the drilling of marine sediments, core samples are collected. Chlorine (Cl) content of pore water of cores might be an indicator to determine gas hydrate saturations in cores (Haese et al., 2006; Merey and Sinayuc, 2016a). During gas hydrate formation, only pure water is taken to the structure of gas hydrate and salt stays inside the rest of pore water. Although initially Cl content of pore water increases due to gas hydrate formation, it is balanced with the neighbor sediments within geological history. When gas hydrate dissociates and it releases pure water to porous media so Cl content decreases within gas hydrate zones. It is possible to calculate gas hydrate saturation in porous media by using Cl content in porous media and average Cl trend content. In Site 970, Cl content decreased near Milano MV and this is an important indicator of gas hydrate existence (Kopf et al., 1998). Furthermore, Cl content reduction in pore water was observed in Kazan MV and Amsterdam MV in Anaximander Mountain of the Eastern Mediterranean Sea. However, it was proposed that there is an another reason of Cl content reduction, which is due to clay mineral diagenesis (Haese et al., 2006).

3. Gas in-Place in the Potential Mediterranean Sea Gas Hydrates

Since the consideration of gas hydrates as energy resources, they have been many gas-in place calculations in gas hydrates in the world. Although small variations in parameters change gas-in place amount enormously, these calculations are essential to show the gas potential in the study area. It is not enough to calculate gas potential in gas hydrates deposited in all sediments because it is considered that feasible gas production is possible from gas hydrates deposited in coarse sands with current technology. For this reason, in this study, gas amount in producible gas hydrate was also calculated for the Mediterranean Sea and the Eastern Mediterranean Sea.

In order to make gas-in place calculations from the potential Mediterranean Sea gas hydrates, the following parameters were obtained from the literature for this study: Porosity, gas type, average gas hydrate saturation, seafloor temperature, geothermal gradient, sea depth, sea salinity, sediment salinity, pressure gradient, and GHSZ thickness

Equation 1 and Equation 2 are commonly used to calculate CH_4-in place in gas hydrate reservoirs (GIP) (Boswell and Collett, 2011);

$$GIP = \varphi \times h \times A \times EF \times CR \times S_h \qquad (1)$$

$$EF = \frac{MW_{CH_4}}{MW_{CH_4} + N_H MW_{H_2O}} \times \frac{V_H \rho_H}{\rho_{CH_4}} \qquad (2)$$

where;

φ: porosity, fraction

h: thickness of hydrate zone, m

A: cross-sectional area of hydrate zone, m^2

CR: cavity fill ratio of CH_4

EF: Expansion factor of CH_4 in hydrate to surface standard conditions, ratio

S_h: gas hydrate saturation, fraction

$MWCH_4$: Molecular weight of CH_4, g/mol

ρ_H: CH_4 hydrate density, kg/m³

MWH_2O: Molecular Weight of H_2O, g/mol

N_H: Hydration Number of CH_4 hydrate

ρ_{CH_4}: CH_4 gas density at standard conditions (0.717935 kg/m³ at 0°C and 1 atm)

V_H: unit hydrate volume (1 m³)

In the literature, there are two GIP calculations in the Mediterranean Sea (Klauda and Sandler, 2003; Bruneton et al., 2012). In these studies, rough estimations were made. According to Klauda and Sandler (2003), 590 tcm CH_4 is deposited inside the potential Mediterranean Sea gas hydrates. Bruneton et al. (2012) estimated producible CH_4 from CH_4 hydrates in the Mediterranean Sea as 51 tcm. Compared to these two estimations, a detailed literature review in Mediterranean Sea was made for the purpose of this study and table 4 was obtained. Table 4 includes the necessary parameters for Equation 1 and Equation 2. By using the core data and porosity log data in ODP Leg 160 and 161 (ODP Leg 160, 1995; ODP Leg 161, 1995), largest, most likely and lowest porosity values were found for the Mediterranean Sea sediments within MHSZ. As discussed earlier, the thickness of MHSZ varies depending on geothermal gradient, sea salinity and bathymetry. HEP software developed by Merey and Sinayuc (2016b) was used to estimate MHSZ at different geothermal gradient (Eckstein, 1978), sea salinity (Praeg et al., 2011) and bathymetry (Brosolo et al., 2012). Then, the range in MHSZ in the Mediterranean Sea in table 4 was obtained. CH_4 was obtained from the core samples recovered in ODP Leg

160 and Leg 161 (ODP Leg 160, 1995; ODP Leg 161, 1995). From the amount of CH_4 recovered from the cores, the range of gas hydrate saturations (S_h) in table 4 was found. For these estimations, expansion factors estimated with HEP were used.

By using the parameters in table 4, Monte Carlo simulations were made with Equation 1 and Equation 2 to calculate CH_4 stored in CH_4 hydrates deposited in all sediments of the Mediterranean Sea and the Eastern Mediterranean Sea. It is known that the surface of area of the Mediterranean Sea is 2.5 million km² and the surface area of the Eastern Mediterranean Sea is 1.65 million km² (Simav et al., 2008). The gas hydrate area of the Eastern Mediterranean Sea is shown in table 4 as well. According to the calculations in this study, it was estimated that the potential Mediterranean Sea gas hydrates deposited in all types of sediments (shales, clays, silt, sands, etc.) includes 623.466 tcm (median) (varying from 11.505 tcm to 2091.560 tcm) of CH_4 as shown in table 5. In the Eastern Mediterranean Sea, the amount of CH_4 deposited in gas hydrates deposited in all types of sediments is 552.3 tcm (median) (ranging from 9.96 tcm to 1954 tcm) as seen in table 5. Table 5 indicates the minimum GIP and maximum GIP. Huge variations are due to the variations in the parameters in table 4. With the increase of exploration and drilling studies, these variations will be decreased and much more exact GIP values will be obtained.

As discussed previously, gas hydrates deposited in coarse sands are targets for feasible gas production from gas hydrates with current technology because of coarse sands' high permeability and high porosity. ODP Leg 160 and ODP Leg 161 data is quite helpful

Table 4- Parameters used for the calculation of the amount of CH_4 in the Mediterranean Sea gas hydrates in all sediments.

	Lowest	Most Likely	Largest	Reference
Porosity, fraction	0.4	0.5	0.7	ODP Leg 160 (1995); ODP Leg 161 (1995)
Average hydrate filling, fraction	0.01	0.1	0.5	ODP Leg 160 (1995); ODP Leg 161 (1995)
MHSZ Thickness, m	100	175	500	Eckstein (1978); Praeg et al., 2011; Brosolo et al., 2012
Cavity fill ratio calculated with HEP	0.989	0.99	0.994	ODP Leg 160 (1995); ODP Leg 161 (1995)
Expansion Factor with HEP	167.549	167.697	169.206	ODP Leg 160 (1995); ODP Leg 161 (1995)
Hydrate Area, m² (Whole Mediterranean Sea)	4.817E+08	2.000E+11	2.151E+11	Bruneton et al. (2012)
Hydrate Area, m² (Eastern Mediterranean Sea)	3.315E+08	1.570E+11	1.851E+11	Bruneton et al. (2012)
Sand Fraction %	1	15	35	ODP Leg 160 (1995); ODP Leg 161 (1995)

Table 5- CH$_4$ potential of the Mediterranean Sea Hydrates.

Source	GIP in the Mediterranean Sea Hydrates, tcm in all sediments	GIP in the Mediterranean Sea Hydrates, tcm in sands	GIP in the Eastern Mediterranean Sea Hydrates, tcm in all sediments	GIP in the Eastern Mediterranean Sea Hydrates, tcm in sands
Klauda and Sandler (2003)	590	-	-	-
Bruneton et al. (2012)	-	51	-	-
This Study	623.466 (11.505-2091.560)	98.160 (1.606-458.868)	552.3 (9.96-1954)	81.2 (1.36-313.8)

to determine average sand contents. In table 4, it was shown that the sand fraction varies from 1 % to 35 % in the Mediterranean Sea. By using Equation 1, Equation 2 and sand content data in table 4, Monte Carlo simulations were run in order to calculate GIP in gas hydrate deposited in the possible sand sections of the Mediterranean Sea and the Eastern Mediterranean Sea. The amount of CH$_4$ in the Mediterranean Sea hydrates deposited in sands was found as 98.16 tcm (median) (ranging from 1.606 tcm to 458.868 tcm). This amount in the Eastern Mediterranean Sea was estimated by Monte Carlo simulation as 81.2 tcm (median) (varying from 1.36 tcm to 313.8 tcm).

According to GIP estimations in this study, it is shown that the Eastern Mediterranean Sea has a great potential of gas hydrates and producible gas hydrates. In order to evaluate this potential, further geophysical studies, drilling studies, coring studies and well logging studies are requisite.

4. Gas Production Potential from the Eastern Mediterranean Sea Hydrates

Coarse sands have good reservoir properties such as high permeability and high porosity so they are targets for gas hydrate studies in terms of energy. This is because gas hydrates are in solid phase and they decrease intrinsic permeability of the sediments. There should be a huge data (i.e. drilling data, coring data, well log data, seismic data, etc.) to decide on the optimum production method of gas production from gas hydrates (Max and Johnson, 2016; Merey, 2017). Nevertheless, it is necessary to predict possible production methods from gas hydrates in the Mediterranean Sea. According to Boswell et al. (2017), depressurization method is the most widely chosen production method. Generally, chemical injection method is not preferred in marine environment due to their harm to the environment (Xu and Li, 2015). Thermal injection is not feasible when it is applied alone but it is suggested that it might be helpful if it is applied with depressurization method together (Chong et al., 2016). In light of all of these discussions in this study about the Mediterranean Sea, depressurization method might be chosen for gas production from the possible gas hydrates in the Mediterranean Sea. When seafloor temperature is high, this means thin GHSZ. However, the sediments with higher temperature cause the higher gas production with depressurization method due to heat fluxes from the boundaries (Han et al., 2017). The seafloor temperature of the Mediterranean Sea is in the classification of high temperature-seafloor. For this reason, depressurization should be considered as one candidate production method in the Mediterranean Sea.

CH$_4$-CO$_2$ replacement method has been considered as a good alternative to depressurization method (Boswell et al., 2017). Basically, especially below 10.3^{o}C, CO$_2$ hydrate is much more stable compared to CH$_4$ hydrate so when CO$_2$ is injected to CH$_4$ hydrate, there is a replacement between CH$_4$ and CO$_2$ molecules. This method was tried in Ignik Sikumi field of Alaska in 2012 but CO$_2$/N$_2$ mixture was preferred for better replacement efficiency. After the replacement of CO$_2$/N$_2$ and CH$_4$ in CH$_4$ hydrate, new mixed hydrate of CO$_2$-N$_2$-CH$_4$ should be stable as well. Figure 9 shows the hydrate equilibrium of different mixed gas hydrates of CO$_2$-N$_2$-CH$_4$ and pressure-temperature data of the Mediterranean Sea sediments. In order to prepare Figure 9, HEP (Hydrate Equilibrium Point Prediction) software of Merey and Sinayuc (2016b) was used. Figure 9 indicates that the replacement of CO$_2$/N$_2$-CH$_4$ in CH$_4$ hydrate is not possible because the seafloor temperature (~14°C) and geothermal gradient of the Mediterranean Sea are high. Even if this replacement occurred, mixed gas hydrate cannot stay in equilibrium in the conditions of the Mediterranean Sea. In this study, it was shown that CO$_2$/N$_2$-CH$_4$ replacement method is not applicable in the Mediterranean Sea. Among four gas hydrate production methods, depressurization with/without wellbore heating is suggested for the Mediterranean Sea gas hydrates.
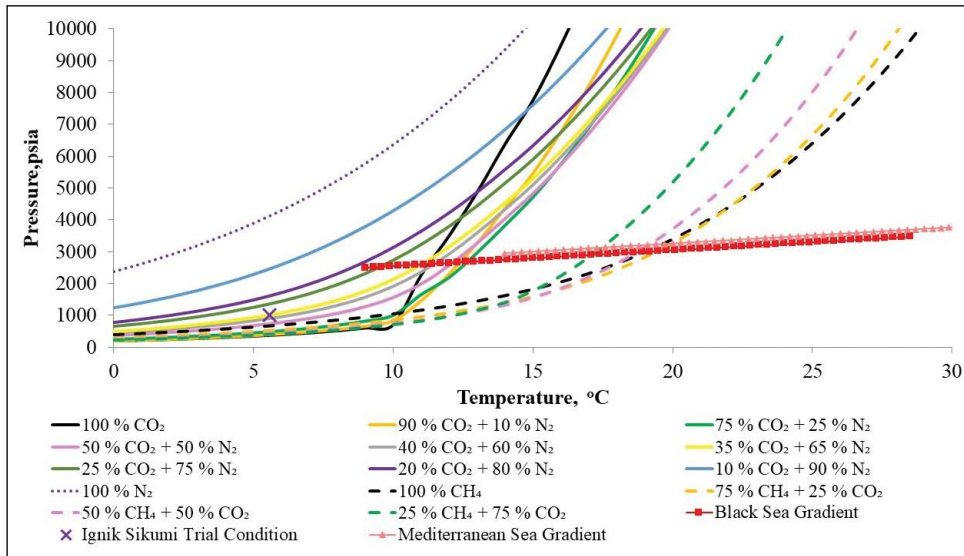
Figure 9- Hydrate equilibrium curves of CO_2, CH_4, N_2 and the pressure and temperature profile of Mediterranean Sea.

5. Conclusions

Gas hydrate reservoirs are considered as near-future energy resources. Although there are many exploration, research and development studies related to gas hydrates in the world, there are not enough studies about the Mediterranean Sea. Initially, it is important to indicate the gas hydrate potential of the Mediterranean Sea. In this study, the following concluding remarks were obtained:

- The Mediterranean Sea has all necessary conditions for the existence of gas hydrates: enough source gas, migration paths, enough thick GHSZ, and water in porous media.

- Source gas potential is higher in the Eastern Mediterranean Sea compared to the Western Mediterranean Sea because most of the gas seepages and mud volcanoes were detected in the Eastern Mediterranean Sea.

- GHSZ in the Eastern Mediterranean Sea is thicker than GHSZ in the Western Mediterranean Sea because sea depth is higher and geothermal gradient is lower in the Eastern Mediterranean Sea.

- According to the analysis of ODP Leg 160 and Leg 161 drilling data, it is concluded that the Mediterranean Sea might include coarse sand sections which might include producible gas hydrates.

- The Mediterranean Sea gas hydrates might include 623.466 tcm of CH_4 in all sediments and 98.16 tcm (median) of CH_4 in coarse sands.

- The Eastern Mediterranean Sea gas hydrates might include 552.3 tcm of CH_4 in all sediments and 81.2 tcm (median) of CH_4 in coarse sands.

- Depressurization method with/without thermal heating production method is suitable for the Mediterranean Sea gas hydrates because the seafloor temperature of the Mediterranean Sea is high and this is advantageous due to the heat transfer from the boundaries during gas production.

- CH_4-CO_2/N_2 replacement production method is not applicable in the conditions of the Mediterranean Sea because of its high seafloor temperature.

The huge gas hydrate potential of the Eastern Mediterranean Sea should be evaluated with geophysical and exploration studies. With further studies, gas hydrate prospects in the Eastern Mediterranean will be known in detail so better production strategies can be made.

References

Aloisi, G., Pierre, C, Rouchy, J.M., Foucher, J.P., Woodside, J. 2000. Methane-related authigenic carbonates of eastern Mediterranean Sea mud volcanoes and their possible relation to gas hydrate destabilisation. Earth and Planetary Science Letters 184 (2000), 321-338.

Bruneton, A., Konofagos, E., Foscolos, A.E. 2012. Cretan Gas Fields – A new perspective for Greece's hydrocarbon resources. Pytheas Market Focus. https://images.derstandard.at/2013/08/21/greece_crete.pdf. October 21, 2018.

Boswell, R., Collett, T.S. 2011. Current perspectives on gas hydrate resources. Energy & Environmental Science 4, 1206-1215.

Boswell, R., Schoderbek, D., Collett, T.S., Ohtsuki, S., White, M.D., Anderson, B.J. 2017. The Ignik Sikumi Field Experiment, Alaska North Slope: Design, Operations, and Implications for CO_2-CH_4 Exchange in Gas Hydrate Reservoirs. Energy Fuels 31 (1), 140-153.

Brosolo, L., Mascle, J., Loubrieu, B. 2012. Morpho-bathymetry of the Mediterranean Sea. Commission for The Geological Map Of The World. https://ccgm.org/en/catalogue/130-carte-morpho-bathymetrique-de-la-mediterranee-9782917310120.html. September 20, 2018.

Camerlenghi, A., Pini, G.A. 2009. Mud volcanoes, olistostromes and Argille scagliose in the Mediterranean region. Sedimentology 56, 319–365.

Carroll, J. J. 2009. Natural Gas Hydrates: A Guide for Engineers. Gulf Professional Publishing.

Cermak, V., Rybach, L. 2012. Terrestrial Heat Flow in Europe. Springer Science and Business Media, 2012.

Charlou, J.L., Donval, J.P., Zitter T., Roy, N., Jean-Baptiste, P., Foucher, J.P., Woodside, J. 2003. Evidence of methane venting and geochemistry of brines on mud volcanoes of the eastern Mediterranean Sea. Deep-Sea Research I 50 (8), 941-958.

Chen, L., Feng, Y., Kogawa, T., Okajima, J., Komiya, A. 2018. Maruyama. Construction and simulation of reservoir scale layered model for production and utilization of methane hydrate: The case of Nankai Trough Japan. Energy 143 (2018), 128-140.

Chong, Z.R., Hern, S., Yang, B., Babu, P., Linga, P., Li X. 2016. Review of natural gas hydrates as an energy resource: prospects and challenges. Applied Energy 162 (2016), 1633–1652.

Diester-Haass, L., Robert, C., Chamley, H. 1998. Paleoproductivity and Climate Variations during Sapropel Deposition in the Eastern Mediterranean Sea. Robertson, A.H.F., Emeis, K.C., Richter, C., Camerlenghi, A. (Eds.). 1998. Proceedings of the Ocean Drilling Program, Scientific Results 160.

Eckstein, Y. 1978. Review of heat flow data from the eastern mediterranean region. Pageoph 117 (150).

Emeis, K.C., Robertson, A., Richter, C., Fox, P.J., Baldauf, J.,Francis, T.J.G. 1996. Ocean Drilling Program Leg 160 Preliminary Report Mediterranean I. http://www-odp.tamu.edu/publications/prelim/160PREL.PDF/. January 26, 2018.

Farla, R. 2006. Investigation on clathrates localised in the Eastern Mediterranean mud volcanoes. http://geoverse.eu/downloads/clathrates.pdf/. April 10, 2018.

Foscolos, A., Konofagos, E., Bruneton, A. 2011. The Occurrence of Converging Plates, Mud Flow Volcanoes and Accretionary Prism Complexes in the Mediterranean Ridge. Their Relationship to Possible Hydrocarbon Accumulations Offshore Crete. A New Respective for Greece's Oil and Natural Gas Resources. http://www.rieas.gr/images/aoz2.pdf/. August 27, 2017.

Fusi, N., Kenyon, N.H. 1996. Distribution of mud diapirism and other geological structures from longrange sidescan sonar (GLORIA) data, in the Eastern Mediterranean Sea, Mar. Geol., 132, 21-38.

Gontharet, S., Stadnitskaia, A., Bouloubassi, I., Pierre, C., Damsté, J.S. 2009. Palaeo methane-seepage history traced by biomarker patterns in a carbonate crust, Nile deep-sea fan (Eastern Mediterranean Sea). Marine Geology 261 (2009), 105-113.

Haese, R.R., Hensen, C., de Lange, G.J. 2006. Pore water geochemistry of eastern Mediterranean mud volcanoes: Implications for fluid transport and fluid origin. Marine Geology 225 (2006), 191-208.

Han, D., Wang, Z., Song, Y., Zhao, J., Wang, D. 2017. Numerical analysis of depressurization production of natural gas hydrate from different lithology oceanic reservoirs with isotropic and anisotropic permeability. Journal of Natural Gas Science and Engineering 46 (2017), 575-591.

Hester, K. C., Brewer, P. G. 2009. Clathrate Hydrates in Nature. Annual Review of Marine Science 1, 303-327.

Hunt, J. M. 1995. Petroleum Geochemistry and Geology. Freeman.

International Energy Agency (IEA). 2011. World energy outlook special report: are we entering the golden age of gas? 2011, Paris.

Johnson, A.H. 2011. Global resource potential of gas hydrate- a new calculation. 7. International Conference on Gas Hydrates 17-21 July 2011, Edinburgh.

Klauda, J.B., Sandler, S.I. 2003. Predictions of gas hydrate phase equilibria and amounts in natural sediment porous media. Marine and Petroleum Geology 20 (2003), 459-470.

Kopf A. 2002. Significance of mud volcanism. Reviews of Geophysics 40 (2), 1-51.

Kopf, A., Clennell, B., Camerlenghi, A. 1998. Variations in Sediment Physical Properties and Permeability of Mud-Volcano Deposits from Napoli Dome and Adjacent Mud Volcanoes. Robertson, A.H.F., Emeis, K.C., Richter, C., Camerlenghi, A. (Eds.). 1998. 1998 Proceedings of the Ocean Drilling Program, Scientific Results, 160.

Küçük, H.M., Goldberg, D.S., Haines, S.S., Dondurur, D., Guerin, G., Çifçi, G. 2016. Acoustic Investigations of Shallow Gas and Gas Hydrates: Comparison Between the Black Sea and the Gulf of Mexico. Gordon Research Seminars - Natural Gas Hydrate Systems 28 February 28- 4 March 2016, Houston.

Kvamme, B. 2015. Feasibility of simultaneous CO_2 storage and CH_4 production from natural gas hydrate using mixtures of CO_2 and N_2. Canadian Journal of Chemistry 93 (8), 897–905.

Lykousis, V., Alexandri, S., Woodside, J., Nomikou, P., Perissoratis, C., Sakelllariou, D., de Lange, G., Dahlmann, A., Casas, D., Rousakis, G., Ballas, D., Ioakim, C. 2004. New evidence of extensive active mud volcanism in the Anaximander Mountains (Eastern Mediterranean): The "ATHINA"mud volcano. Environmental Geology 46, 1030–1037.

Lykousis, V., Alexandri, S., Woodside, J., de Lange, G., Dahlmann, A., Perissoratis, C., Heeschen, K., Ioakim, C., Sakellariou, D., Nomikou, P., Rousakis, G., Casas, D., Ballas, D., Ercilla, G. 2009. Mud volcanoes and gas hydrates in the Anaximander mountains (Eastern Mediterranean Sea). Marine and Petroleum Geology 6 (6), 854-872.

Lo, C. 2017. Timeline: game-changing gas discoveries in the eastern Mediterranean.https://www.offshore-technology.com/features/timeline-game-changing-gas-discoveries-eastern-mediterranean/. April 7, 2018.

Majumdar, U., Cook, A.E., Shedd, W., Frye, M. 2016. The connection between natural gas hydrate and bottom simulating reflectors. Geophysical Research Letters 43, 7044-7051.

Makovsky, Y., Tibor, G., Herut, B., Waldmann, N.D., Spiro, B., Antler, G., Sivan, O., Ballard, R.D., Coleman, D., Huebscher, C., Avraham, Z.B. 2013. Pervasive Seafloor Gas Flow along the Periphery of the Southeastern Mediterranean. AAPG European Regional Conference 8-10 April 2013, Barcelona.

Max, M.D., Johnson, A.H. 2016. Exploration and Production of Oceanic Natural Gas Hydrate: Critical Factors for Commercialization. Springer.

Melgar, E.P. 2009. Sedimentology and Geochemistry of Gas Hydrate-rich Sediments from the Oregon Margin (Ocean Drilling Program Leg 204). PhD Thesis, Universitat de Barcelona 253 p. Barcelona (unpublished).

Merey, S., Sinayuc, C. 2016a. Analysis of the Black Sea sediments by evaluating DSDP Leg 42B drilling data for gas hydrate potential. Marine and Petroleum Geology 78 (2016), 151-167.

Merey, S., Sinayuc, C. 2016b. New Software That Predicts Hydrate Properties and Its Use in Gas Hydrate Studies. Journal of Chemical & Engineering Data 61 (5), 1930-1951.

Merey, S. 2017. Analysis of the Black Sea Gas Hydrates. PhD Thesis, Middle East Technical University, Department of Petroleum and Natural Gas Engineering 376 p. Ankara (unpublished).

Merey, S., Longinos, S.N. 2018. Numerical simulations of gas production from Class 1 hydrate and Class 3 hydrate in the Nile Delta of the Mediterranean Sea. Journal of Natural Gas Science and Engineering 52(2018), 248-266.

Miles, P.R. 1995. Potential distribution of methane hydrate beneath the European continental margins. Geophysical Research Letters 22(23), 3179-3182.

Milkov, A.V. 2004. Global estimates of hydrate-bound gas in marine sediments: how much is really out there? Earth-Science Reviews 66 (3–4), 183-197.

Milkov, A.V. 2005. Global Distribution of Mud Volcanoes and Their Significance in Petroleum Exploration as a Source of Methane in the Atmosphere and Hydrosphere and as a Geohazard. Martinelli, G., Panahi, B. (Eds.). 2005. Mud Volcanoes, Geodynamics and Seismicity. NATO Science Series (Series IV: Earth and Environmental Series), 51. Springer.

Moridis, G.J., Collett, T.S., Boswell, R., Hancock, S., Rutqvist, J., Santamarina, C., Kneafsey, T., Reagan, M.T., Darvish, M.P., Kowalsky, M., Sloan, E.D., Coh, C. 2013. Gas Hydrates as a Potential Energy Source: State of Knowledge and Challenges. Lee, W.J. (Ed.) Advanced Biofuels

and Bioproducts. Springer Science Business Media.

Ocakoğlu, N. 2009. Gas Hydrates and Their Importance: Investigation of Gas Hydrates and Shallow Gas in Seas around Turkey. Istanbul Yerbilimleri Dergisi 22 (1), 29-47.

ODP (Ocean Drilling Program) Leg 160. 1995. Mediterranean Sea I: The Eastern Mediterranean Sites 963-973, 3 March-3 May 1995. http://www-odp.tamu.edu/publications/leg_ndx/160ndex.htm/. April 1, 2018.

ODP (Ocean Drilling Program) Leg 161. 1995. Mediterranean Sea II - The Western Mediterranean Sites 974-979. 3 May-2 July 1995 http://www-odp.tamu.edu/publications/leg_ndx/161ndex.htm/. April 1, 2018.

Pape, T., Kasten, S., Zabel, M., Bahr, A., Abegg, F., Hohnerg, H-J., Bohrmann, G. 2010. Gas hydrates in shallow deposits of the Amsterdam mud volcano, Anaximander Mountains, Northeastern Mediterranean Sea. Geo-Marine Letters 30, 187-206.

Praeg, D., Unnithan, V., Camerlenghi, A. 2007. PROJECT: HYDRAMED. Gas hydrate stability and prospectivity in the Mediterranean Sea. www.dur.ac.uk/ey.go/general_public/AAPG_Newsletter_June.pdf/. 12 February 2018.

Praeg, D., Geletti, R., Mascle, J., Unnithan, V., Harmegnies, F. 2008. Geophysical Exploration for Gas Hydrates in the Mediterranean Sea and a Bottom Simulating Reflection on the Nile Fan. GNGTS 2008 SESSIONE 3.2. pp. 467–469.

Praeg, D., Geletti, R., Wardell, N., Unnithan, V., Mascle, J., Migeon, S., Camerlenghi, A. 2011. The Mediterranean Sea: A Natural Laboratory to Study Gas Hydrate Dynamics? 7.International Conference on Gas Hydrates 17-21 July 2011, Edinburgh.

Praeg, D., Migeon, S., Mascle, J., Unnithan, V., Wardell, N., Geletti, R., Ketzer, J.M. 2017. Geophysical evidence of gas hydrates associated with widespread gas venting on the central Nile Deep-Sea Fan, offshore Egypt. 9. International Conference on Gas Hydrates, June 25-June 30, 2017, Denver.

Poort, J., Vassilev, A., Dimitrov, L. 2005. Did postglacial catastrophic flooding trigger massive changes in the Black Sea gas hydrate reservoir? Terra Nova 17(2), 135–140.

Robertson, A.H.F. 1998a. Significance of Lower Pliocene Mass-Flow Deposits for the Timing and Process of Collision of the Eratosthenes Seamount with the Cyprus Active Margin. Robertson, A.H.F., Emeis, K.C., Richter, C., Camerlenghi, A. (Eds.). 1998. 1998 Proceedings of the Ocean Drilling Program, Scientific Results, 160.

Robertson, A.H.F. 1998b. Late Miocene Paleoenvironments and Tectonic Setting of the Southern Margin of Cyprus and the Eratosthenes Seamount. Robertson, A.H.F., Emeis, K.C., Richter, C., Camerlenghi, A. (Eds.). 1998. 1998 Proceedings of the Ocean Drilling Program, Scientific Results, 160.

Robertson, AH.F., Kopf, A. 1998. Origin of Clasts and Matrix within the Milano and Napoli Mud Volcanoes, Mediterranean Ridge Accretionary Complex. Robertson, A.H.F., Emeis, K.C., Richter, C., Camerlenghi, A. (Eds.). 1998. 1998 Proceedings of the Ocean Drilling Program, Scientific Results, 160.

Ruppel, C. D., Kessler J. D. 2017. The interaction of climate change and methane hydrates, Rev. Geophys., 55, 126-168.

Simav, M., Yildiz, H., Arslan, E. 2008. Doğu Akdeniz'de Uydu Altimetre Verileri İle Deniz Seviyesi Değişimlerinin Araştırılması. Harita Dergisi 139 (1), 1-31.

Sloan, E. D., Koh, C.A. 2008. Clathrate Hydrates of Natural Gases. CRC Press.

Spezzaferri, S., Cita, M.B., McKenzie, J.A. 1998. The Miocene/Pliocene Boundary in the Eastern Mediterranean: Results from Sites 967 and 9691. Robertson, A.H.F., Emeis, K.-C., Richter, C., and Camerlenghi, A. (Eds.) 1998. 1998 Proceedings of the Ocean Drilling Program, Scientific Results 160.

Thakur, N.K., Rajput, S. 2011. Exploration of Gas Hydrates: Geophysical Techniques. Springer.

Werne, J.P., Haese, J.P., Zitter, T., Aloisi, G., Bouloubassie, I., Heijs, S., Fiala-Medioni, A., Pancost, R.D., Damsté, J.S.S., de Lange, G., Forney, L., Gottschal, J.C., Foucher, J.P., Mascle, J., Woodside, J. 2004. Life at cold seeps: a synthesis of biogeochemical and ecological data from Kazan mud volcano, eastern Mediterranean Sea. Chemical Geology 2050 (3-4), 367-390.

Worthington, P.F. 2010. Petrophysical evaluation of gas-hydrate formations. Petroleum Geoscience 16, 53-66.

Wood, W.T., Jung, W.Y. 2008. Modeling the extent of Earth's marine methane hydrate cryosphere. 6. International Conference on Gas Hydrates 6-20 July 2008, Vancouver.

Woodside, J.M., Ivanov, M.K., Limonov, A.F. 1998. Shallow gas and gas hydrates in the Anaximander Mountains region, Eastern Mediterranean Sea. Henriet, J.P., Mienert, J. (Eds). 1998. Gas Hydrates: Relevance to World Margin Stability and Climate Change. Geological Society Special Publication 137, 177–193.

Xu, C.G., Li, X. 2015. Research progress on methane production from gas hydrates. RSC Advances 5, 54672–54699.

Yang, Y., He, Y., Zheng, Q. 2017. An analysis of the key safety technologies for natural gas hydrate exploitation. Advances in Geo-Energy Research 1 (2), 100-104.

Yin, Z., Moridis, G., Chong, Z.R., Tan, K., Linga, P. 2018. Numerical Analysis of Experiments on Thermally Induced Dissociation of Methane Hydrates in Porous Media. Industrial & Engineering Chemistry Research 57 (17), 5776-5791.

Bulletin of the Mineral Research and Exploration

http://bulletin.mta.gov.tr

Rare earth elements and yttrium geochemistry of the geothermal fields in the Eastern Black Sea Region (Ordu, Rize, Artvin), NE Turkey

Esra HATİPOĞLU TEMİZEL[a*] , Fatma GÜLTEKİN[a] and Arzu FIRAT ERSOY[a]

[a]Karadeniz Techincal University, Department of the Geological Engineering, 61080 Trabzon, Turkey.

ABSTRACT

In this study, behavior and migration processes of rare earth elements (REEs) were determined in the thermal and cold waters of the geothermal fields in the Eastern Black Sea Region.The temperatures of the geothermal waters are between the range of 38 and 60 °C. The water types are $Na\text{-}Ca\text{-}SO_4$ for Sarmaşık (Ordu) field, $Na\text{-}Ca\text{-}HCO_3$ for Ikizdere (Rize) field, $Na\text{-}Ca\text{-}CO_3\text{-}SO_4$, for Ayder (Rize) field and $Na\text{-}HCO_3\text{-}Cl$ for Savsat (Artvin) field. All geothermal fields are in alkaline geothermal character (pH: 7-9.3) and have very low REE + Y concentrations, slightly significant Ce contens and significantly positive Eu anomalies (except for Ayder geothermal field). REE+Y content, fractionation and positive Eu anomalies of the investigated water are controlled by water/rock ratio, pH and minerals in the host rocks. According to the thermodynamic calculations, it was determined that the mobility of the REEs in geothermal fields were mainly controlled by Ln^{3+}, $LnOH^{2+}$, $LnCl^{2+}$, $Ln(SO_4)_2^-$, $LnSO_4^+$, $LnHCO_3^{2+}$, $Ln(CO_3)_2^-$ and $LnCO_3^+$ complexes.

1. Introduction

Rare earth elements (REE) are compatible group elements that have similar physicochemical properties with atomic numbers ranging from 57 to 71 (La-Lu). Yttrium exhibits chemical behaviors similar to REE and is used in geochemical studies. In recent studies related to the hydrothermal systems conducted by many researchers, significant information about the geochemical behaviors of waters were determined like the change in chemical composition of geothermal waters during underground circulation by examining the behavior of REE and Y (REE+Y), the sources of this composition, alteration, secondary mineral deposition conditions, condition and motion of particulate materials (Hass et al., 1995; Bau and Dulski, 1999; Embley et al., 2007; Craddock and Batch, 2010; Göb et al., 2013, Shakari, 2015; Bragin et al., 2018).

The events such as the rate of interaction between the water and host rock, the absorption processes and chemical complexation reactions in hydrothermal systems affect the distribution models of REE. As known, the equilibrium and decomposition conditions of REE bearing minerals cause the mobility and release of REE during the alteration of host rock. The solubility of REE depends on the presence of anionic ligands, which complicates and stabilizes these elements in the groundwater. Therefore, the chemical speciation calculations based on the thermodynamic principles can reveal more information about the chemical processes of REE+Y in the geothermal waters (Wood, 1990). REE+Y are used to understand the processes such as the water-rock-magmatic gas interaction, primary mineral dissolution, secondary mineral deposition (Bragin et al., 2018).

In the Eastern Black Sea Region, there are many studies on the mineralogy and petrography of the rocks in the areas where volcanic and magmatic rocks generally outcrop (Özbeşikçi et al., 1981; Gedik et al., 1992; Göksu, 1996; Temizel, 2002; Karslı et al., 2004; Arslan and Aslan, 2006; Temizel et al., 2012; Evcimen and Karslı, 2012). NE-SW trending strike-slip faults, which control the flow of hot water to the surface at the same time form the catchment routes. The General Directorate of Mineral Research and Exploration (MTA) and the other researchers have conducted many researches in their close vicinities to investigate and use these hot springs (Kartal, 1972; Büyük, 1978; Terlemez and Yılmaz, 1980; Erzenoğlu and Tangaç, 1986; Gürsel, 1991; Kara, 1997; Uzel et al., 1998; Gündüz, 1999; Fırat Ersoy, 2001; Akkuş et al., 2005). Unlike the studies carried out in the literature, the REE+Y contents and fractionation of the Sarmaşık geothermal field (SGF), Ayder geothermal field (AGF), İkizdere geothermal field (İGF) and Şavşat geothermal field (ŞGF) waters were detected in this study. In addition to these, the calculation of chemical speciation of the waters and the geochemical processes controlling the REE+Y contents in the water were also evaluated.

2. Material and Methods

The field studies were conducted between April 2016 and October 2017 as geological studies, in-situ measurement and sampling. The sampling was carried out in 20 locations as being 4 hot spring wells, 2 hot springs, 6 cold springs and 8 surface waters. During the in-situ measurements at the water sampling points, the measurements of T (temperature), EC (electrical conductivity), pH, TDS (Total Dissolved Solids) were made by YSI-556 model multi-parameter measuring instrument.

The probes used during measurements were kept by being washed with pure water before and after each measurements and were run with buffer solutions after daily calibrations before each field study. In order to determine the major anion-cation and trace element contents of the waters, the sampling was made with 500 mL polyethylene bottles.

The chemical and REE+Y analyzes of water samples were carried out in the Water Chemistry Laboratory of the Hydrogeology Engineering Department of Hacettepe University (Ankara, Turkey)

by the ion chromatography technique and Inductively Coupled Plasma – Mass Spectrometry (ICP-MS) methods, respectively. The major cations (Ca^{2+}, Mg^{2+}, Na^+ and K^+) were determined by the Cl^- and sulfate ion chromatography system. The alkalinity was however determined by the standard titration method. SiO_2 was analyzed by the spectrophotometric method. The ion balance error of the analyzes is below 5%. The rock geochemical analyzes were performed using Inductively Coupled Plasma – Mass Spectrometry (ICP-MS) in the ACME Laboratory (Canada).

The selected complexes of REE (Ln^{3+}, $LnCO^{3+}$, $Ln(CO_3)_2^-$, $LnCl^{2+}$, $LnSO_4^+$, $LnHCO_3^{2+}$, $LnOH^{2+}$, LnO^+, LnO_2^- ve LnO_2H^*; Ln represents any of the Lantanides) were calculated by using the database of the thermodynamic parameters in the Visual MINTEQ software (Gustafsson, 2012) . It was calculated by using database. The modeling process was carried out for the actual groundwater composition by using the temperature and pH values measured in water in the atmospheric pressure. The major ions, Fe, Mn, Al and REE+Y were used in the calculations. Ce and Eu anomalies ($Ce/Ce^* = Ce_{CN}/(La_{CN}*Pr_{CN})^{0.5}$) were calculated using ($Eu/Eu^* = Eu_{CN}/(Sm_{CN}*Gd_{CN})^{0.5}$) equations (CN: Chondrite normalized value (Sun and McDonough, 1989)).

3. Geological and Hydrogeological Structures

The Eastern Black Sea Region located to the east of Turkey is geologically called as the eastern Pontide tectonic unit (Ketin, 1966). The Pontides are divided into two as the Western Pontides and Eastern Pontides in the west and east of Samsun (Özsayar et al., 1981). The tectonic unit of the Eastern Pontides is divided into two zones as; the "North" and "South" with the Ardanuç-İspir-Kemaliye-Reşadiye border by Özsayar et al. (1981). While the magmatic and volcano-sedimentary rocks are dominant in the Northern Zone of the Eastern Pontide, the sedimentary rocks are dominant in the Southern Zone. SGF, İGF, AGF and ŞGFs studied within the framework of this study are located in the Northern Zone of the Eastern Pontides. The units belonging to the Paleozoic, Mesozoic and Cenozoic periods outcrop in the northern zone (Figure 1). The Paleozoic granitoids form the oldest unit in the Eastern Pontides. These units are unconformably overlain by the Jurassic volcanics and volcaniclastics. The Late Cretaceous in the region is represented mainly by the volcanic (basalt, andesite and pyroclastics)

and clastic sedimentary rocks (sandstone, siltstone and mudstone). The Late Cretaceous granitoids were emplaced by cutting these units. The age of the clastic sedimentary rocks (conglomerate, sandstone, mudstone), volcanic rocks (andesite, basalt and pyroclastics) and granitic rocks which cut them are Eocene. The Miocene units are composed of clastic sedimentary rocks interbedded with tephrite, basalt and pyroclastics. Pliocene clastic deposits consisting of conglomerate, sandstone, siltstone and marl alternation (Figure 1).

The primary porosity of the volcanic rocks, generally composed of basalts of the Late Cretaceous, is very low in SGF and its surround. The fractured structures, which they have because of tectonic activities, provide secondary porosity to the rocks and permeability in places. These non-homogeneous permeable levels throughout the units allow the surface waters to flow deeper along the faults. In the areas, where slant topography is dominant, the waters flowing to shallow depths emerge from the slopes in the form of low discharge springs. Therefore, the volcanic rocks are important in fractured grounds in terms of groundwater.

The units consisting of clastic rocks like conglomerate, sandstone and siltstone of the Jurassic age in and around İGF are permeable. The Late

Cretaceous and Eocene units, which are generally volcano-sedimentary in character, are permeable in areas where pyroclastic rocks represented by agglomerate and tuff outcrops. The permeability of rocks such as granite and granodiorite, which form the granitoid widely exposed in the study area, are very low in non-fractured and unweathered areas. However, the three directional fracture systems developed in these rocks gave the granitoid a permeable property. In addition, the bonds between the minerals have become weak and the rocks have dispersed on the surface and shallow depths in the rocks where different degrees of weathering are observed. Therefore, the granitoid is permeable in areas where it is fractured and weathered, and impermeable in unfractured and unweathered areas.

The units of Late Cretaceous basaltic and andesitic rocks have not permeability in AGF, but the pyroclastics outcropping in the form of tuffs are permeable. The well-developed fracture systems of the granitoid outcropping in a large area have provided permeability to the unit. The spring waters discharging from cracks every season prove this.

The clastic sedimentary and volcanic rocks generally crop out in ŞGF. The fact that the rocks such as; conglomerate, sandstone and siltstone of which their primary porosities are high permeable, show variation according to their degree of cementation.
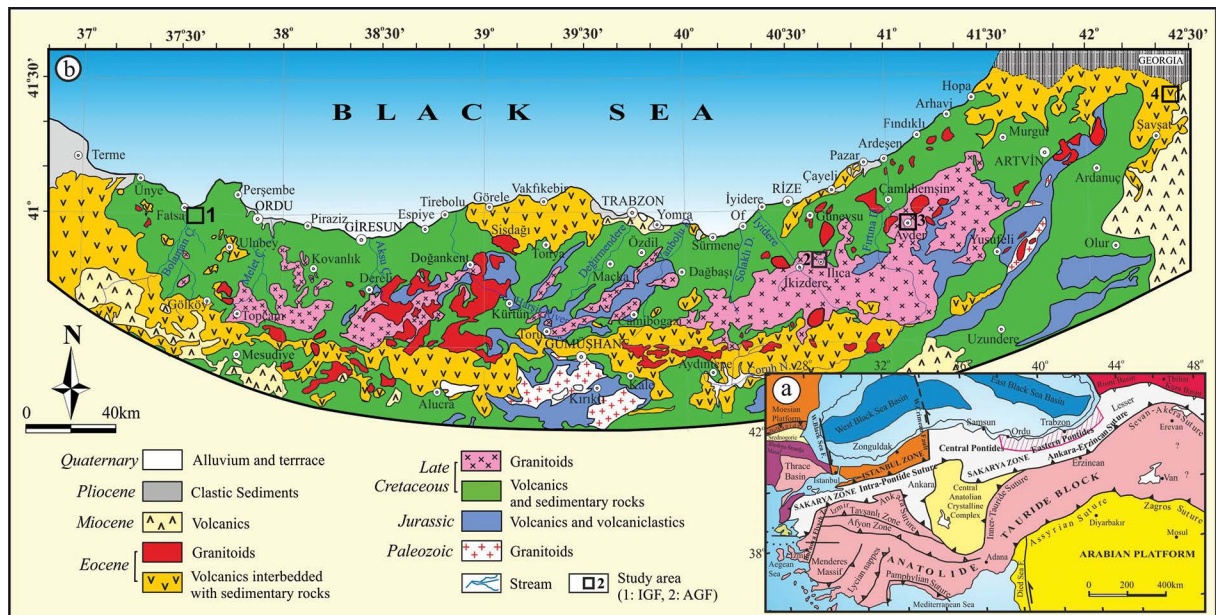
Figure 1- a) The tectonic map of Turkey (modified from Okay and Tüysüz, 1999), b) distribution of volcanic and intrusive rocks in East Pontides (modified from Güven, 1993; Arslan et al., 2013; Yücel, 2013 and Temizel et al., 2016).

The primary porosities of the volcanic rocks are low, but their improved structures and tectonic activities during cooling provided them to be in fractured. The tuffs of the Late Cretaceous units in the area are permeable, and volcanic rocks such as dacite and rhyodacite are impermeable.

4. Major Ions

In order to determine the chemical properties of the waters in the investigated areas, the samples were taken from the geothermal wells, hot and cold springs and surface waters. In SGF, the sampling and in-situ measurements were made from hot spring (SARKAP), two cold springs (SSK, QK), and the surface water draining the basin (IDD-IDB). The sampling and measurement studies in İGF were made from the geothermal well (ILKAP), one from the cold spring (ISK) and from the surface water near the geothermal drilling (IDERY-IDERA). In AGF, one sample from the geothermal well (AYKAP), two samples from hot springs (AYKÖPK, AYESH), one from cold spring (HOŞSU) and from the surface water (AYDEREY-AYDEREA) were taken and measured.

The in-situ measurement and sampling was carried out from geothermal wells (ILICAS), mineral water (CDMS), cold spring (SKSK) and from the surface water (CERDERY-CERDEA). The descriptions, coordinates and elevation values of the sample points taken are given in table 1.

The hot spring (SARKAP) in SGF has the temperature of 47°C, EC of 1935 μs/cm and pH value of 8.05 from in situ measurements. Mg ions are quite low values (Table 2) in dominant anion and cations of the Na and SO_4 ions in the hot spring. The temperatures of two different cold springs (SSK and ÇK) in this area is approximately 14°C and EC values are 174 and 337 μS/cm, respectively. Ca and HCO_3 ions are dominant in cold springs with pH values of about 7. The surface waters (IDD-IDB) in the field has a pH of about 8 and EC of 84-94 μS/cm and Ca and HCO_3 ions are dominant in these waters.

60°C temperature and 7.03 pH value were measured in the geothermal well in IGF. Dominated anions and cations in the hot spring are Na and HCO_3 ions with EC of 6633 μS/cm (Table 2). Ca and HCO_3 ions are dominant in the cold spring in IGF with a pH

Table 1- Sampling coordinates in the study area.

	Sample No	Coordinate (UTM 37 T WGS84)	Elevation (m)
Sarmaşık (Ordu) Geothermal Field	SARKAP (Hot spring)	0383154 - 4536830	102
	SSK (Cold spring)	0383064 - 4536784	101
	ÇK (Cold spring)	0375853 - 4532828	225
	IDD (Surface water)	0383619 - 4536877	100
	IDB (Surface water)	0383071 - 4536795	104
İkizdere (Rize) Geothermal Field	ILKAP (Geothermal well)	0635840 - 4515969	848
	ISK (Cold spring)	0637838 - 4516474	995
	IDERY (Surface water)	0636570 - 4516090	966
	IDERA (Surface water)	0635555 - 4516034	821
Ayder (Rize) Geothermal Field	AYKAP (Geothermal well)	0676703 - 4535711	1228
	AYKÖPK (Hot spring)	0673100 - 4541100	825
	AYESH (Hot spring)	0676356 - 4535638	1200
	HOŞSU (Cold spring)	0677192 - 4535639	1271
	AYDEREA (Surface water)	0673500 - 4539500	1050
	AYDEREY (Surface water)	0678212 - 4535863	1300
Şavşat (Artvin) Geothermal Field	ILICAS (Geothermal well)	0282740 - 4586153	1495
	CDMS (Mineral spring)	0281351 - 4573470	1145
	ŞSSK (Cold spring)	0282628 - 4588250	1550
	CERDERY (Surface water)	0282940 - 4585958	1496
	CERDERA (Surface water)	0281280 - 4586418	1490

Table 2- Physicochemical parameters of the analyzed waters.

Sample No	Temperature (°C)	pH	EC (µS/cm)	TDS mg/L	Ca mg/L	Mg mg/L	Na mg/L	K mg/L	Cl mg/L	Alkalinity (HCO$_3$+CO$_3$) mg/L	SO$_4$ mg/L	% Error
Sarmaşık Geothermal Field												
SARKAP	47	8.05	1935	1260	213.13	0.33	261.90	3.79	97.12	11.76	875.8	1.43
SSK	14.5	7.8	174	141	51.86	7.55	14.06	3.39	2.35	203.33	5.24	2.90
CK	14	7.08	337	272	112.23	7.18	15.02	3.86	5.27	370.78	8.49	1.95
IDD	15.2	8.27	94	69	25.82	4.34	6.69	0.66	2.15	101.66	3.66	0.47
IDB	15.8	7.87	84	66	23.29	3.76	5.37	0.54	1.52	89.70	3.42	0.62
İkizdere Geothermal Field												
ILKAP	60	7.03	6633	2587	331.31	79.01	965.65	140.66	464.12	2810	296.2	3.03
ISK	11.8	7.34	22	19	7.24	0.71	3.09	0.40	0.30	23.92	1.49	2.98
IDERY	9.1	6.4	17	16	6.82	0.72	1.32	0.37	0.14	23.92	2.38	2.46
IDERA	9.2	7.4	19	17	7.08	0.80	1.71	0.53	0.38	23.92	2.49	4.76
Ayder Geothermal Field												
AYKAP	55	9.15	233	97	8.74	0.06	39.93	0.73	2.69	35.3	38.1	2.97
AYKOPK	31.7	9.32	296	171	16.77	0.26	63.66	1.06	9.77	24	118	0.93
AYESH	20	8.16	33	24	8.26	1.24	12.8	0.36	1.36	30.5	12.5	4.29
HOSSU	10.8	7.56	35	31	9.25	1.73	3.83	0.89	0.48	36.6	1.51	3.91
AYDEREA	7.7	6.84	22	21	5.19	0.5	1.21	0.31	0.13	18.3	1.96	1.42
AYDEREY	10.3	7.3	19	17	7.49	1.03	2.07	0.61	0.10	0.49	1.62	3.34
Şavşat Geothermal Field												
ILICAS	39	6.9	5734	3044	288	46.35	1323	35.14	1052	2601	166	0.90
SSSK	9.2	7.59	155	144	55.75	8.07	11.46	0.08	1.25	191.37	4.79	1.81
CDMS	12	6.2	2741	2369	369.4	60.07	1003	22.28	771.89	2379	150	2.89
CERDERA	13.8	8.53	411	340	50.9	9.07	116.46	2.91	83.69	251.18	17.6	4.45
CERDERY	8.6	7.92	122	116	43.15	6.55	13.4	0.42	1.13	155.49	4.9	4.26

value of 7.34, an EC of 22 µS/cm (Table 2). Ca and HCO$_3$ ions are dominant in the surface water draining the basin with a pH value of 6.7 and EC value of 18 µS/cm.

During the in-situ measurements in AGF, where Na, CO$_3$ and SO$_4$ ions are dominant, the temperature of the geothermal well is 55°C, the pH value is 9.15 and EC value is 233 µS/cm (Table 2). Looking at two naturally hot springs discharging in this field, AYESH has a temperature of 20°C, pH value of 8.16 and EC value of 33 µS/cm. The other hot spring, AYKÖPK, has the temperature of 30°C, pH of 9.32 and EC of 266 µS/cm. In AYESH, Na and HCO$_3$ ions are dominant, whereas in AYKÖPK, Na and SO$_4$ ions are dominant (Table 2). The cold spring (HOŞSU) in the field has dominant Ca and HCO$_3$ ions with a pH value of 7.56 and an EC of 35 µS/cm. The pH of the surface water in the field is around 7, and the EC value is 19 µS/cm in upper elevations and 22 µS/cm in lower elevations and the dominant anions and cations are Ca and HCO$_3$.

The geothermal well water (ILICAS) has a temperature of 39°C, a pH value of 6.9 an EC of 5734 µS/cm in ŞGF. Na and HCO$_3$ ions are dominant in the well water. The pH of the mineral water (CDMS) is 6.2, the EC value is 2741 µS/cm and the dominant anions and cations are Na and HCO$_3$. The pH and EC values of the cold spring (ŞSSK), which is dominant in Ca and HCO$_3$ ions, are 7.59 and 155 µS/cm, respectively. The chemical properties of the river water are different from each other before (CERDERY) and after (CERDERA) the mixing of the hot spring (Table 2). CERDERY has a pH of 7.92, an EC value of 122 µS/cm with dominant anions and cations are Ca and HCO$_3$. However, CERDERA has the EC value of 411 µS/cm with dominant anions and cations of Na and HCO$_3$. The drill water flowing out has physically and chemically influenced the river water that runs nearby.

When the plots of waters in the Piper Diagram for the geothermal fields of the Eastern Black Sea Region are evaluated, the earth alkaline elements in the hot waters (Ca+Mg) in the SGF and strong acid (Cl + SO$_4$) roots are higher than alkaline elements (Na+K) and weak acid roots (CO$_3$ + HCO$_3$), respectively. However, the opposite situation is observed in cold spring and surface waters (Figure 2). In IGF, AGF and ŞGF hot
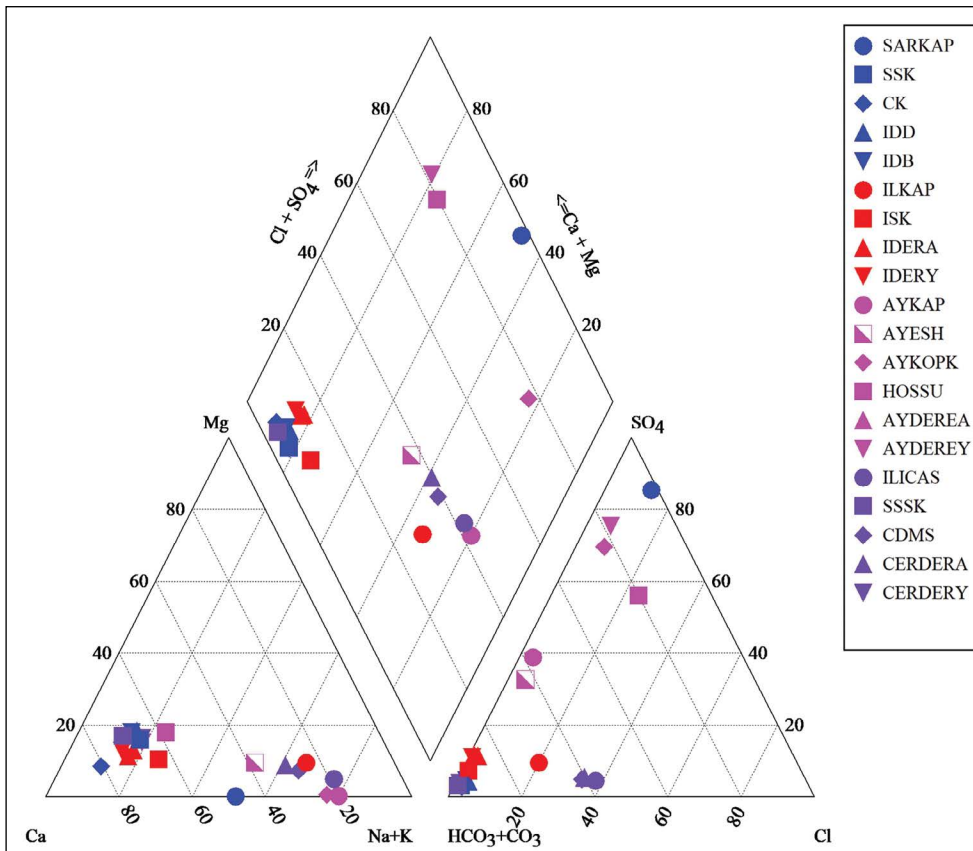

Figure 2- Piper diagrams of the investigeted water samples

springs, the alkaline elements (Na+K) and weak acid roots (CO_3+HCO_3) are more than the earth alkaline elements (Ca+Mg) and strong acid (Cl+SO_4) roots. CO_3 and SO_4 values in the Ayder hot springs with very low Cl content, are approximately the same, however; Cl and HCO_3 ions in the Şavşat hot springs with low SO_4 are in the same values. In all three areas, the earth alkaline elements (Ca + Mg) and weak acid roots (CO_3 + HCO_3) in cold springs and surface waters are more than the alkaline elements (Na + K) and strong acid (Cl + SO_4) roots respectively (Figure 2).

The saturation indices for different minerals were calculated by using thermodynamic modeling to estimate the degree of interaction of the waters in the study area with host rocks (Table 3). The primary minerals, which are determined microscopically in volcanic rocks that are exposed in geothermal fields, are silicate minerals like; plagioclase, alkaline feldspar, augite, hornblende and quartz, and the secondary minerals are; calcite, quartz and chlorite. The sedimentary rocks in the surrounding are formed by the lacustrine deposits which the limestone, sandstone, marl, cherty limestone and gypsum lenses are observed. The saturation index (SI) values belonging to the selected minerals considering these lithologies were calculated using the pH and chemical analysis results in the field utilizing the PHREEQC software included in the AquaChem 2014.1 software (Table 3).

When the SI values are examined, hot and cold waters in the studied areas are not saturated with sulphate minerals such as anhydrite and gypsum. Sarmaşık hot and cold springs show a tendency for slight oversaturation to dolomite and calcite, but unsaturated with dolomite. The surface waters are approximately in equilibrium state with calcite (Figure 3a). İkizdere geothermal well water is saturated with aragonite, calcite, barite and dolomite minerals. Cold spring and surface waters are not saturated with any of the selected minerals (Figure 3b). While the Ayder hot geothermal well water is slightly saturated with aragonite, calcite and dolomite, the cold spring and surface waters are unsaturated (Figure 3c). Şavşat geothermal water and Ciritdüzü mineral water are saturated with aragonite, calcite and dolomite, however; the surface waters are not saturated (Figure 3d). While the hot springs of İkizdere and Şavşat are saturated with K-feldspar representatively selected for silicate minerals, the Sarmaşık and Ayder hot springs are not saturated. All hot and cold springs except the Ayder hot spring are saturated with K-mica mineral. All hot and cold waters except for the hot springs of Ayder are saturated with clay minerals such as; kaolinite and illite. All warm waters except the Şavşat hot springs are saturated with talc mineral. All hot waters except the Ayder geothermal well water shows a slight tendency to oversaturation to quartz mineral, whereas the Ayder geothermal well water show a slight tendency towards sub-saturation. All hot and cold waters show a super saturation to minerals such as goethite and hematite (Table 3).

5- Rare Earth Elements (REEs) and Yttrium

Although their positions in the periodic table are close to each other, the REE+Y have different physicochemical properties and are widely used in the interpretation of geochemical processes in water-rock interaction. In addition, these elements may reflect changes in response to anthropogenic or natural anomaly effects in hydrogeological environments (Bragin et al., 2018).

REE+Y concentrations of the waters analyzed in the studied geothermal fields and their close vicinities and the exposed samples collected are shown in table 4. REE+Y distribution models normalized to chondrite (Sun and McDonough, 1989) are given in figure 4. When the figures 4b, d, f and h are examined, REE+Y patterns in the waters in all areas are almost similar to each other except for the minor differences. This situation shows that the host rocks in which the water is circulating are of similar type.

When the table 4 and figure 4 are evaluated, the ∑REE concentrations in the analyzed waters are 0.06-1.83 ppb in SGF, 0.64-2.13 ppb in IGF, 0.01-0.3 ppb in AGF, and 0.03-2.13 ppb in SGF. The highest ∑REE concentration in geothermal waters was measured in ILKAP (İkizdere) and ILICAS (Şavşat) (∑REE = 2.13 ppb) samples. The lowest REE concentrations (∑REE = 0.01-0.3 ppb) were measured in AGF waters with the highest pH value (8.60-9.86), and the lowest TDS value (52-173 mg/L).

The chondrite normalized La_{CN}/Gd_{CN} ratios are higher than 1 (except CERDERA and IDD) and Yb_{CN}/Gd_{CN} ratios (excluding ILICAS) are less than 1 in all

Table 3- Saturation index calculations for some minerals in the analyzed waters.

Minerals	Formula	Sarmaşık Geothermal Field				İkizdere Geothermal Field		
		SARKAP	SSK	CK	IDD	ILKAP	ISK	IDERY
Albite	$NaAlSi_3O_8$	-0.85	-0.98	-2.33	-1.40	0.49	-2.71	-4.40
Anhydrite	$CaSO_4$	-0.63	-3.15	-2.72	-3.52	-1.06	-4.33	-4.15
Aragonite	$CaCO_3$	0.38	0.09	-0.09	0.01	1.43	-1.36	-3.09
Barite	$BaSO_4$	1.09	-1.76	-0.56	-1.85	0.43	-1.34	-1.59
Ca-Montmorillonite	$Ca0.165Al_2,33Si_3,67O_{10}(OH)_2$	-0.75	4.33	3.58	3.41	3.40	3.54	3.79
Calcite	$CaCO_3$	0.51	0.24	0.06	0.16	1.55	-1.93	-2.93
Celestine	$SrSO_4$	-0.86	-3.53	-2.52	-3.99	-1.1	-4.9	-4.82
Dolomite	$CaMg(CO_3)_2$	-1.36	-0.15	-0.89	-0.24	2.99	-4.71	-6.73
Flourite	CaF_2	-0.13	-2.77	-2.86	-3.57	-1.22	-3.70	-5.04
Gypsum	$CaSO_4:2H_2O$	-0.54	-2.90	-2.47	-3.27	-1.08	-4.08	-3.90
Goethite	$FeOOH$	7.57	8.07	7.01	7.91	7.91	6.60	3.77
Halite	$NaCl$	-6.29	-9.01	-8.66	-9.36	-5.13	-10.51	-11.21
Illite	$K0.6Mg0.25Al_2,3Si_3,5O_{10}(OH)_2$	-0.74	3.62	2.32	2.67	3.35	1.86	1.40
K-Feldsar	$KAlSi_3O_8$	-0.61	0.88	-0.44	0.06	1.61	-1.08	-2.40
K-Mica	$KAl_3Si_3O_{10}(OH)_2$	4.55	10.02	9.13	8.65	9.67	8.49	8.94
Kaolinite	$Al_2Si_2O_5(OH)_4$	0.59	5.36	5.22	4.59	4.17	5.57	6.26
Quartz	SiO_2	0.13	0.49	0.21	0.39	0.49	0.24	-0.16
Rhodochrosite	$MnCO_3$	-1.63	-3.14	-	-	-0.06	-	-4.56
Siderite	$FeCO_3$	-6.70	-0.99	-0.34	-2.43	-0.52	-2.32	-3.16
Talc	$Mg_3Si_4O_{10}(OH)_2$	4.50	-1.38	-7.12	0.54	3.14	-8.49	-
Viterite	$BaCO_3$	-3.00	-4.01	-3.43	-3.81	-1.99	-4.60	-6.08

Table 3- (continue)

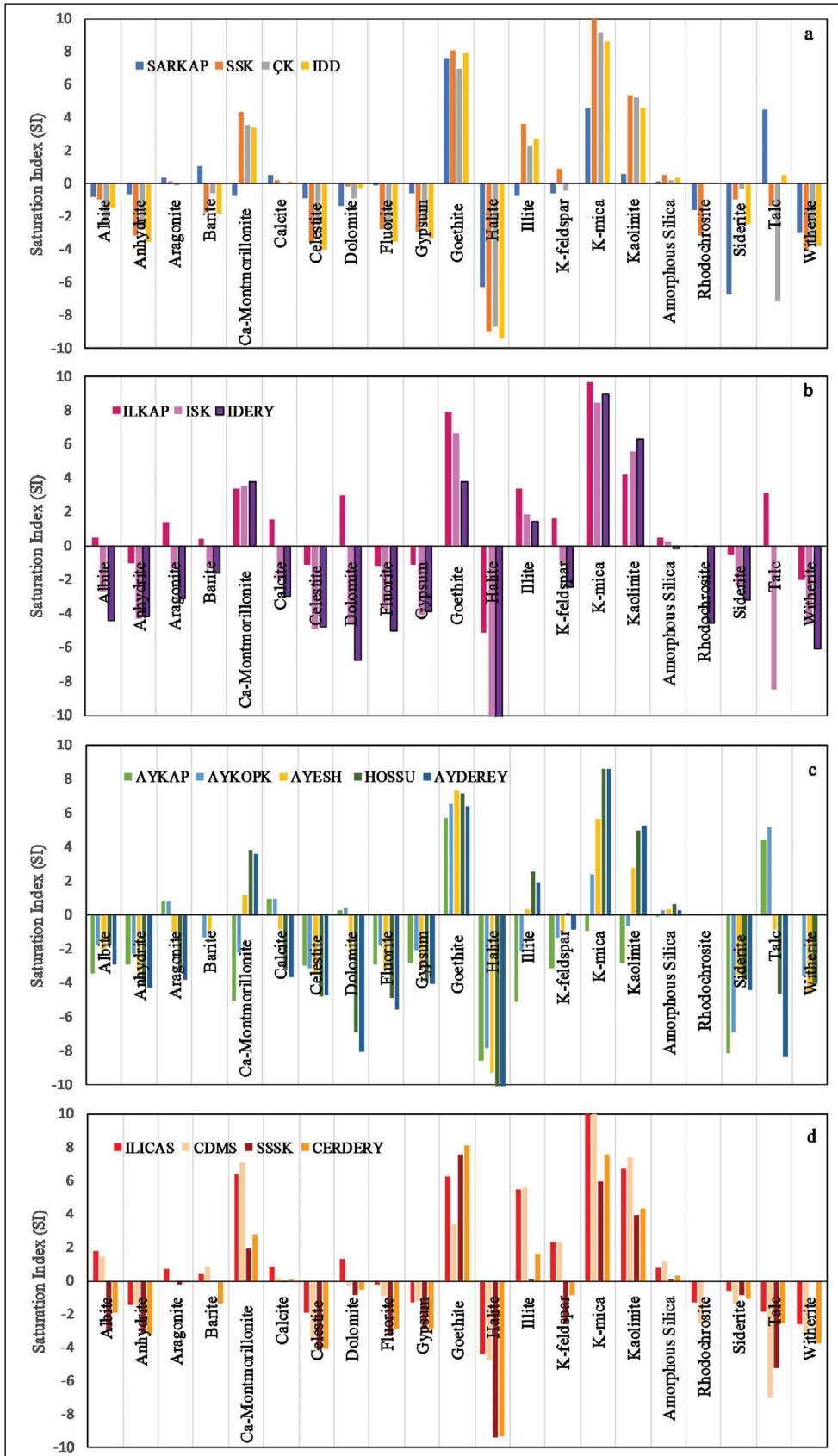| Minerals	Formula	Ayder Geothermal Field						Şavşat Geothermal Field		
		AYKAP	AYKOPK	AYESH	HOSSU	AYDEREY	ILICAS	CDMS	SSSK	CERDERY
Albite	$NaAlSi_3O_8$	-3.42	-1.79	-1.99	-1.79	-2.89	1.75	1.48	-3.01	-1.90
Anhydrite	$CaSO_4$	-2.88	-2.30	-3.39	-4.22	-4.27	-1.47	-1.47	-3.15	-3.22
Aragonite	$CaCO_3$	0.81	0.78	-1.01	-3.32	-3.82	0.69	0.00	-0.20	-0.07
Barite	$BaSO_4$	-	-1.30	-1.01	-	-	0.41	0.82	-	-1.41
Ca-Montmorillonite	$Ca0.165Al3.33Si3.67O_{10}(OH)_2$	-5.05	-2.22	1.20	3.79	3.56	6.40	7.10	1.91	2.78
Calcite	$CaCO_3$	0.94	0.92	-0.86	-3.17	-3.66	0.83	0.16	-0.04	0.09
Celestine	$SrSO_4$	-2.99	-3.16	-3.45	-4.76	-4.70	-1.94	-3.49	-4.17	-4.07
Dolomite	$CaMg(CO_3)_2$	0.28	0.45	-2.26	-6.93	-8.05	1.28	-0.32	-0.82	-0.54
Flourite	CaF_2	-2.94	-1.77	-3.24	-4.89	-5.56	-0.23	-0.94	-3.27	-2.91
Gypsum	$CaSO_4{:}2H_2O$	-2.85	-2.11	-3.16	-3.97	-4.01	-1.33	-1.21	-2.90	-2.96
Goethite	$FeOOH$	5.71	6.51	7.32	7.18	6.40	6.24	3.38	7.54	8.10
Halite	$NaCl$	-8.59	-7.79	-9.28	-10.22	-11.12	-4.40	-4.77	-9.37	-9.33
Illite	$K0.6Mg0.25Al2.3Si3.5O_{10}(OH)_2$	-5.11	-2.14	0.31	2.51	1.97	5.49	5.54	0.12	1.63
K-Feldsar	$KAlSi_3O_8$	-3.14	-1.30	-1.14	0.09	-0.89	2.31	2.33	-2.62	-0.85
K-Mica	$KAl_3Si_3O_{10}(OH)_2$	-0.93	2.36	5.66	8.58	8.60	12.28	12.20	5.95	7.54
Kaolinite	$Al_2Si_2O_5(OH)_4$	-2.80	-0.60	2.79	4.98	5.27	6.72	7.41	3.93	4.30
Quartz	SiO_2	-0.08	0.26	0.38	0.63	0.28	0.78	1.15	0.07	0.34
Rhodochrosite	$MnCO_3$	-	-	-	-	-	-1.32	-2.51	-	-
Siderite	$FeCO_3$	-8.12	-6.90	-3.54	-3.85	-4.40	-0.60	-1.37	-0.88	-1.04
Talc	$Mg_3Si_4O_{10}(OH)_2$	4.43	5.16	-0.83	-4.63	-8.33	-1.84	-7.00	-5.26	-2.55
Viterite	$BaCO_3$	-	-3.56	-4.61	-4.06	-	-2.63	-3.23	-	-3.80

Figure 3- Saturation indices of some selected minerals a) Sarmaşık geothermal field, b) İkizdere geothermal field c) Ayder geothermal field, d) Şavşat geothermal field.

Table 4- REE+Yttrium concentrations of the analyzed waters (rocks:ppm, waters:ppb, bdl: below detection limit).

		La	Ce	Pr	Nd	Sm	Eu	Gd	Tb	Dy	Y	Ho	Er	Tm	Yb	Lu
SARMAŞIK GEOTHERMAL FIELD (SGF)																
F-3	Tuffite	7.9	12.6	1.64	6.8	1.47	0.48	1.55	0.24	1.56	7.9	0.26	0.94	0.11	0.75	0.12
F-5	Sandy Lst.	4	6.1	0.8	3.2	0.59	0.14	0.64	0.09	0.54	3.9	0.13	0.36	0.06	0.36	0.05
F-8	Basaltic tuff	16	34.2	4.5	20.1	4.43	1.42	4.77	0.75	4.56	24.6	0.95	2.67	0.4	2.47	0.4
F-10	Basalt	29.6	51.3	5.26	17.5	3.21	0.57	2.86	0.47	2.83	18.7	0.61	2.07	0.33	2.24	0.39
SARKAP	Hot spring	0.129	0.486	0.058	0.773	0.054	0.224	0.02	0.007	0.015	0.17	0.007	0.018	0.002	0.017	0.023
SSK	Cold spring	bdl	bdl	0.004	0.025	0.008	0.005	0.006	0.001	0.006	0.044	0.001	0.004	0	0.003	0.001
ÇK-	Cold spring	bdl	bdl	bdl	0.016	0.023	0.044	bdl	0.001	bdl	0.085	bdl	0.002	bdl	0.002	bdl
IDD	Surface water	0.013	0.074	0.01	0.043	0.012	0.005	0.017	0.002	0.013	0.069	0.001	0.009	0.001	0.004	0.001
IDB	Surface water	0.023	0.065	0.017	0.06	0.014	0.005	0.015	0.002	0.012	0.083	0.002	0.01	0	0.008	0.001
İKİZDERE GEOTHERMAL FIELD (IGF)																
IK-1	Granite	31.6	57.2	6.06	20.6	3.6	0.75	3.66	0.58	3.74	22.2	0.77	2.36	0.38	2.57	0.4
IK-2	Granite	15.2	27.8	3.09	11.4	2.36	0.5	2.63	0.43	2.99	18.3	0.64	2.08	0.31	2.14	0.36
ILKAP	Geothermal well	0.126	0.61	0.054	0.762	0.089	0.286	0.043	0.01	0.039	0.432	0.005	0.039	0.005	0.032	0.027
ISK	Cold spring	0.155	0.273	0.046	0.17	0.039	0.017	0.039	0.004	0.027	0.183	0.003	0.022	0.003	0.018	0.003
IDERA	Surface water	0.1	0.217	0.039	0.141	0.035	0.009	0.027	0.004	0.03	0.18	0.004	0.016	0.002	0.015	0.004
IDERY	Surface water	0.083	0.316	0.033	0.113	0.023	0.01	0.019	0.004	0.022	0.157	0.003	0.014	0.002	0.012	0.004
AYDER GEOTHERMAL FIELD (AGF)																
AY-1	Granodiorite	0.9	2.6	0.52	3	1.21	0.92	1.84	0.34	2.3	12.4	0.49	1.53	0.21	1.35	0.2
AY-2	Granodiorite	30.4	45.9	4.66	15	2.18	0.6	1.62	0.22	1.31	7.1	0.25	0.74	0.11	0.8	0.13
AY-3	Basalt	17.5	36.7	4.97	21	5.04	1.44	6.16	1.1	7.17	42.5	1.62	4.99	0.74	5.1	0.81
AYKAP	Geothermal well	bdl	bdl	0.003	bdl	0.003	0.002	bdl	0	0.0035	0.004	0	0.003	0	0	0.001
AYESH	Hot spring	bdl	bdl	bdl	bdl	0.001	0.004	bdl	0	0	0.004	0	0.001	0	0	bdl
AYKOPK	Hot spring	bdl	bdl	0.002	0.011	0.002	0.002	0.002	0.001	0.009	0.01	0	0.003	0	0.0035	0
HOSSU	Cold spring	bdl	bdl	0.003	0.006	0.0015	0.001	bdl	0.0005	0.003	0.003	0	0.002	0	0	0.001
AYDEREY	Surface water	0.028	0.091	0.005	0.0116	0.004	0.0035	0.014	0.001	0.002	0.0193	bdl	0.0013	0	0.0025	0.0005
AYDEREA	Surface water	0.077	0.122	0.0115	0.0525	0.009	0.006	0.0095	0.001	0.0105	0.0535	0	0.0105	0	0.0075	0.002

Table 4- (continue)

		La	Ce	Pr	Nd	Sm	Eu	Gd	Tb	Dy	Y	Ho	Er	Tm	Yb	Lu
						ŞAVŞAT GEOTHERMAL FIELD (SGF)										
SV-1	Sandstone	5.4	11.2	1.56	7.1	2.07	0.72	2.28	0.38	2.45	13.6	0.52	1.53	0.23	1.45	0.22
SV-2	Sandstone	8.8	17.8	2.47	10.7	2.96	0.89	3.19	0.54	3.24	18.2	0.73	2.02	0.3	1.88	0.3
TD-1	Trachyandesitet	16.1	29.2	3.13	11.2	1.86	0.53	1.17	0.13	0.65	3	0.11	0.27	0.03	0.25	0.03
TD-3	Trachyandesitet	14.9	25.5	2.73	9.5	1.52	0.53	0.92	0.11	0.5	2.4	0.1	0.18	0.03	0.19	0.03
C-1	Volcanogenic sst.	4.4	9.1	1.3	6.4	1.77	0.71	2.17	0.36	2.43	12.9	0.5	1.5	0.2	1.33	0.2
C-7	Volcanogenic sst.	5.3	11.1	1.54	7.2	1.9	0.72	2.38	0.38	2.38	13.9	0.53	1.57	0.21	1.42	0.22
TRV-1	Travertine	2.5	3.5	0.53	2	0.55	0.2	0.93	0.18	1.3	13.2	0.29	0.92	0.12	0.85	0.13
ILICAS	Geothermal well	0.358	0.593	0.051	0.649	0.047	0.272	0.027	0.004	0.042	0.396	0.004	0.029	0.002	0.033	0.024
CDMS	Mineral spring	0.18	0.615	0.0575	0.8075	0.038	0.1955	0.0585	0.0075	0.043	0.301	0.002	0.0285	0.0025	0.016	0.003
ŞSSK	Cold spring	ȯla	ȯla	0.003	0.016	0.0025	0.0015	0.002	0.001	0	0.0103	0	0.002	0	0.002	0.0015
CERDERA	Surface water	0.005	0.02	0.038	0.138	0.021	0.118	0.0285	0.002	0.0225	0.124	0.005	0.0055	0.001	0.013	0.028
CERDERY	Surface water	0.068	0.27	0.02	0.039	0.013	0.005	0.014	0.002	0.013	0.12	0.002	0.008	0.001	0.006	0.004
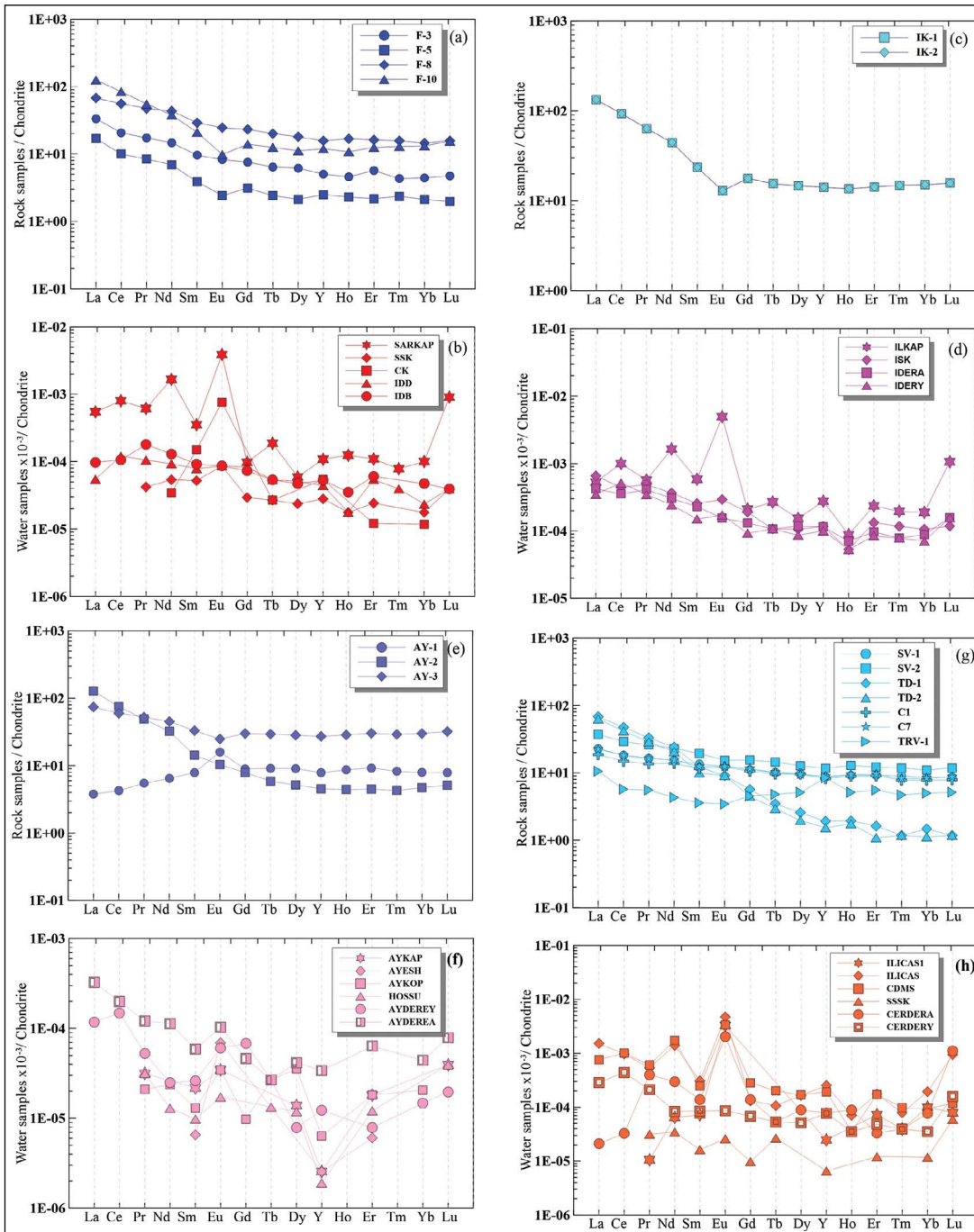
Figure 4- Distribution of Chondrite-normalized REE patterns of rocks (a, c, e and g) and waters (b, d, f and h) (Sun and McDonough, 1989) (a, b:Sarmaşık geothermal fields; c,d: İkizdere geothermal fields; e,f: Ayder geothermal fields; g,h: Şavşat geothermal fields).

waters in the study area (Sun and McDonough, 1989). These ratios show that the majority of the waters are enriched in the Light Rare Earth Elements (La-Eu, LREE) whereas they are poor in terms of the Heavy Rare Earth Elements (Gd-Lu, HREE) (Figures 4b, d, f and h). Similar to many other studies in the literature

in recent years (Gammons et al., 2005; Shakeri et al., 2015; Zhang et al., 2016; Bragin et al., 2018) the TDS amounts and ∑REE values have increased in SGF, IGF and AGF waters with increasing temperature. AGF waters, which are basic in character (pH ~9) compared to other sites, have very low TDS amounts

(~97 mg/L) despite the measured high temperature (55°C). The clay minerals, which formed as a result of the argillization of feldspars observed in granitic host rocks within the waters in this field, to absorb elements in the water have caused the decrease of TDS amount of waters and accordingly very low ∑REE concentration.

The most common feature of all the geothermal waters analyzed (except for the Ayder area) is that they have a distinct Eu anomaly. The Eu anomalies calculated in geothermal waters (Eu/Eu*) are 20.84 in SGF, 14.13 in IGF and 23.34 in ŞGF. In the case of AGF, the Eu anomaly was calculated around 3.057 only in the AYKÖPK sample. In addition, the positive Ce anomalies observed in the geothermal waters examined (Sarmaşık: 1.37, İkizdere: 1.81, Şavşat: 1.07, Ayder: not calculated) reflect the reducing conditions in the hydrothermal system. Desorption of Fe oxyhydroxides in hot waters explains high saturation values (Figure 3) and positive Ce anomalies to Fe minerals such as goethite.

The REE+Y contents of the surface water and cold springs in the study areas are changing parallel to the thermal waters in lower concentrations. The fractionation between LREE and HREE concentrations in surface waters is less than that of the geothermal waters.

REE+Y distribution models determined in host rocks in the investigated areas are shown in figures 4a, c, e and g. Tuffite, (F-3), sandy limestone (F-5), basaltic tuff and basalts (F-8, F-10) in SGF, granitic (IK-1, IK-2) and granodioritic (AY-1, AY-2) host rocks, sandstone (SV-1, SV-2), trachyandesite (TD-1, TD-3), volcanogenic sandstone (C1-C7) and travertine (TRV-1) type rocks at İkizdere and Ayder geothermal fields show negative Eu and less distinct Ce anomaly. In addition to these, while the host rocks are enriched in LREE similar to waters they are depleted in HREE.

6. Cerium and Europium Anomalies

In the absorption process Ce^{3+} is easily oxidized to Ce^{4+} in iron hydroxides (Bau and Dulski, 1999). Ce anomalies depend on pH and, are observed in alkaline waters (Moller, 2001). Since the Ce^{4+} is preferably adsorbed by Mn oxides (De Carlo et al., 1998), the low temperature surface waters generally show negative Ce anomalies compared to +3 valence REE.

Analyzes of REE+Y behaviors in studies conducted worldwide showed the presence of positive Eu anomaly in high temperature chlorine systems (T>230°C, pH<7). The REE+Y distribution models in these systems are similar, and are not affected by the host rock types. On the other hand, the hydrothermal systems with pH>7 show significant negative Eu anomaly (Klinkhammer et al., 1994). The thermodynamic calculations showed that Eu had a +2 valence in high-temperature fluids (T>300°C) and formed chloride complexes. These complexes are more stable than the complexes formed with +3 valence REE (Haas et al., 1995).

Many studies have shown that REE+Y (especially Eu) fractionation is a complex process, and the behavior of these elements is dependent on the physicochemical environmental parameters (Bragin et al., 2018). REE+Y contents and fractionation of the aquifer composition in high-temperature hydrothermal reservoirs are subject to less impact and consequently the pH and pressure cause the occurrence of complex compound formation (Hass et al., 1995). In low temperature hydrothermal areas close to the surface (T<100°C), the REE+Y contents and distributions are controlled by pH, rock composition and water/rock ratio.

All waters in the study area show a less distinct Ce anomaly (Ce / Ce * = Ce_{CN} / (La_{CN} * Pr_{CN}) 0.5) and distinctively positive Eu (Eu / Eu * = Eu_{CN} / (Sm_{CN} * Gd_{CN}) 0.5) anomaly except for AGF (Figure 4). It is considered that Eu anomaly originated from the Eu rich minerals (plagioclase ± K-feldspar) present in host rocks of geothermal fields. Ce anomalies in water and host rocks are compatible with each other.

7- Transportation Routes of the Rare Earth Elements

REE concentrations in the groundwater are mostly dependent on the solubility of minerals containing REE in the host rock and the degree of decomposition of the host rock. The duration of contact of water with the host rock, the absorption processes and chemical complexation reactions are effective in transporting REE to water. The visual MINTEQ (Gustafsson, 2012) software was used to determine REE transportation processes in the investigated areas. The thermodynamic calculations showed that Ln^{3+}, $LnOH^{2+}$, $LnCl^{+}$, $Ln(SO_4)_2^{-}$, $LnSO_4^{+}$, $LnHCO_3^{2+}$,

Ln(CO$_3$)$_2^-$ and LnCO$_3^+$ complexes were present for each type of REE. The results of the derivation model where the contribution of the major aqueous species of the total dissolved REE to the geothermal and cold springs are shown as the percentage for all studied areas is given in table 5.

Table 5- REE transportation types in hot and cold waters in the study areas (values < 0.05 %).

	SARKAP	SSK	ILKAP	ISK	AYKAP	AYESH	AYKOPK	HOŞSU	ILICAS	SSSK	CDMS
La^{3+}	8.62	90.20	38.96	95.44	0.23	68.90	0.43	93.65	44.68	93.27	76.39
LaOH^{2+}	2.16	3.39	1.36	1.27	1.84	9.56	1.38	1.98	0.40	1.54	0.03
LaCl^{2+}	0.03	0.01	0.57	-	-	-	-	-	1.28	-	1.49
La(SO$_4$)$_2^-$	15.94	-	3.82	-	-	0.09	0.05	-	0.67	-	0.33
LaSO$_4^+$	59.83	6.39	51.31	3.28	0.37	21.44	1.02	4.37	22.49	5.19	21.76
LaHCO$_3^{2+}$	0.16	-	0.53	-	0.03	-	0.02	-	5.23	-	-
La(CO$_3$)$_2^-$	0.49	-	0.01	-	61.63	-	54.37	-	0.55	-	-
LaCO$_3^+$	12.77	-	3.43	-	35.90	-	42.73	-	24.70	-	-
Ce^{3+}	7.31	86.17	35.33	93.97	0.09	59.44	0.17	91.49	34.36	91.74	76.52
CeOH^{2+}	7.92	7.79	6.54	2.85	3.41	22.13	1.81	4.32	1.15	3.27	0.07
CeCl^{2+}	0.03	0.01	0.46	-	-	-	-	-	0.99	-	1.79
Ce(SO$_4$)$_2^-$	8.07	-	2.01	-	-	0.05	0.01	-	0.32	-	0.22
CeSO$_4^+$	52.18	6.02	48.53	3.17	0.15	18.37	0.41	4.18	17.60	4.99	21.40
CeHCO$_3^{2+}$	0.13	-	0.45	-	-	-	-	-	3.75	-	-
Ce(CO$_3$)$_2^-$	1.21	-	0.03	-	67.30	-	61.67	-	1.21	-	-
CeCO$_3^+$	23.16	-	6.65	-	29.06	-	35.93	-	40.62	-	-
Pr^{3+}	6.59	85.60	34.38	93.71	0.05	58.60	0.09	91.09	28.58	91.42	76.60
PrOH^{2+}	6.97	8.41	6.00	3.12	1.74	23.25	1.01	4.74	0.96	3.61	0.08
PrCl^{2+}	0.03	0.01	0.45	-	-	-	-	-	0.82	-	1.79
Pr(SO$_4$)$_2^-$	6.14	-	1.92	-	0.08	0.03	-	-	0.20	-	0.11
PrSO$_4^+$	47.03	5.98	47.24	3.16	-	18.11	0.22	4.16	14.64	4.97	21.42
PrHCO$_3^{2+}$	0.10	-	0.38	-	-	-	-	-	2.72	-	-
Pr(CO$_3$)$_2^-$	2.27	-	0.06	-	75.16	-	69.86	-	2.11	-	-
PrCO$_3^+$	30.87	-	9.57	-	22.97	-	28.81	-	49.97	-	-
Nd^{3+}	5.92	82.38	32.24	92.31	0.04	53.15	0.08	89.03	26.64	89.77	77.42
NdOH^{2+}	7.96	11.68	6.84	4.49	1.78	29.71	1.13	6.80	1.17	5.23	0.12
Nd(SO$_4$)$_2^-$	6.91	-	1.99	-	-	0.05	-	-	0.25	-	0.21
NdSO$_4^+$	45.49	5.94	48.40	3.20	0.07	17.09	0.19	4.18	14.55	5.00	22.26
NdHCO$_3^{2+}$	0.10	-	0.38	-	-	-	-	-	2.72	-	-
Nd(CO$_3$)$_2^-$	2.51	-	0.07	-	76.71	-	71.62	-	2.42	-	-
NdCO$_3^+$	31.12	-	10.07	-	21.39	-	26.94	-	52.26	-	-
Sm^{3+}	4.75	70.12	29.48	86.15	0.02	38.05	0.04	80.19	20.23	82.51	76.85
SmOH^{2+}	10.97	24.71	9.46	10.79	1.34	49.40	1.10	15.96	1.66	12.79	0.29
Sm(SO$_4$)$_2^-$	4.44	-	1.30	-	-	0.04	-	-	0.17	4.70	0.25
SmSO$_4^+$	37.34	5.17	45.27	3.06	0.03	12.52	0.10	3.85	11.31	-	22.61
SmHCO$_3^{2+}$	0.09	-	0.40	-	-	-	-	-	2.37	-	-
Sm(CO$_3$)$_2^-$	4.62	-	0.15	-	83.27	-	79.10	-	4.20	-	-
SmCO$_3^+$	37.79	-	13.94	-	15.34	-	19.66	-	60.07	-	-
Eu^{3+}	3.95	67.46	26.96	84.80	-	34.90	0.03	78.40	17.78	81.08	75.30
EuOH^{2+}	11.77	27.55	11.56	12.19	0.74	53.55	0.96	17.84	1.83	14.29	0.33
EuCl^{2+}	0.02	0.01	0.35	-	-	-	-	-	0.51	-	1.76
Eu(SO$_4$)$_2^-$	7.80	-	2.58	-	-	0.06	-	-	0.30	-	0.46
EuSO$_4^+$	31.09	4.98	41.41	3.01	0.01	11.48	0.07	3.76	9.94	4.62	22.15
EuHCO$_3^{2+}$	0.15	-	0.92	-	-	-	-	-	3.63	-	-
Eu(CO$_3$)$_2^-$	8.42	-	0.41	-	91.46	-	83.90	-	6.64	-	-
EuCO$_3^+$	36.80	-	15.82	-	7.78	-	15.05	-	59.37	-	-
Gd^{3+}	4.82	72.28	28.62	87.64	0.02	39.02	0.04	82.41	22.18	84.58	76.51
GdOH^{2+}	15.04	22.50	14.36	9.32	2.22	48.40	1.39	13.72	2.23	10.71	0.25

Table 5- (continue)

$GdCl^{2+}$	-	-	0.20	-	-	-	-	-	0.34	-	0.96
$Gd(SO_4)_2^-$	6.17	-	1.80	-	-	0.04	-	-	0.24	-	0.29
$GdSO_4^+$	37.04	5.21	42.96	3.04	0.04	12.54	0.11	3.87	12.12	4.71	22.00
$Gd(CO_3)_2^-$	4.18	-	0.13	-	83.10	-	79.57	-	4.11	-	-
$GdCO_3^+$	32.65	-	11.52	-	14.62	-	18.89	-	56.06	-	-
$GdHCO_3^{2+}$	0.10	-	0.41	-	-	-	-	-	2.72	-	-
Tb^{3+}	4.27	63.69	27.57	82.90	0.01	30.63	0.02	75.94	19.37	79.25	77.65
$TbOH^{2+}$	19.24	31.86	19.27	14.30	1.69	59.87	1.15	20.59	2.88	16.44	0.41
$Tb(SO_4)_2^-$	4.58	-	1.50	-	-	0.03	-	-	0.18	-	0.23
$TbSO_4^+$	30.46	4.45	37.88	2.80	0.02	9.47	0.05	3.47	9.92	4.31	21.72
$TbHCO_3^{2+}$	0.11	-	0.50	-	-	-	-	-	2.99	-	-
$Tb(CO_3)_2^-$	7.38	-	0.25	-	89.06	-	86.66	-	7.16	-	-
$TbCO_3^+$	33.96	-	13.04	-	9.22	-	12.11	-	57.51	-	-
Dy^{3+}	3.69	63.71	24.60	83.30	-	29.63	0.02	76.60	16.43	80.13	79.20
$DyOH^{2+}$	22.75	32.20	26.06	14.12	1.83	61.87	1.03	20.20	3.11	15.90	0.41
$Dy(SO_4)_2^-$	2.55	-	0.98	-	-	0.01	-	-	0.09	-	0.10
$DySO_4^+$	25.30	4.09	32.91	2.58	0.01	8.49	0.04	3.20	8.00	3.97	20.29
$DyHCO_3^{2+}$	0.10	-	0.49	-	-	-	-	-	2.78	-	-
$Dy(CO_3)_2^-$	8.61	-	0.30	-	89.50	-	87.50	-	8.19	-	-
$DyCO_3^+$	37.00	-	14.65	-	8.65	-	11.41	-	61.41	-	-
Ho^{3+}	3.81	59.76	26.79	80.54	-	27.45	0.01	72.78	16.49	76.71	79.82
$HoOH^{2+}$	19.98	36.57	21.39	17.09	1.20	65.03	0.85	24.31	2.88	19.66	0.52
$Ho(SO_4)_2^-$	2.97	-	1.14	-	-	0.02	-	-	0.10	-	0.13
$HoSO_4^+$	24.92	3.67	34.22	2.38	0.01	7.51	0.03	2.91	7.66	3.63	19.53
$HoHCO_3^{2+}$	0.10	-	0.48	-	-	-	-	-	2.54	-	-
$Ho(CO_3)_2^-$	10.93	-	0.41	-	91.73	-	89.80	-	10.11	-	-
$HoCO_3^+$	37.30	-	15.58	-	7.04	-	9.30	-	60.22	-	-
Er^{3+}	3.45	56.73	26.23	78.40	-	25.47	0.01	69.98	14.66	74.18	79.68
$ErOH^{2+}$	18.25	39.79	20.22	19.29	0.91	67.54	0.70	27.23	2.66	22.31	0.60
$Er(SO_4)_2^-$	3.81	-	1.49	-	-	0.02	-	-	0.13	-	0.23
$ErSO_4^+$	22.57	3.48	33.51	2.31	-	6.97	0.02	2.79	6.81	3.51	19.50
$ErHCO_3^{2+}$	0.09	-	0.51	-	-	-	-	-	2.42	-	-
$Er(CO_3)_2^-$	13.05	-	0.52	-	92.87	-	91.05	-	11.84	-	-
$ErCO_3^+$	38.78	-	17.52	-	6.21	-	8.22	-	61.47	-	-
Tm^{+3}	2.87	50.84	22.98	74.44	-	20.93	-	65.19	12.50	70.10	78.27
$TmOH^{2+}$	22.25	46.03	27.14	23.36	0.98	73.33	0.70	32.21	3.23	26.57	0.75
$TmCl^{2+}$	-	-	0.26	-	-	-	-	-	0.31	-	1.59
$Tm(SO_4)_2^-$	2.84	-	1.10	-	-	0.02	-	-	0.11	-	0.24
$TmSO_4^+$	18.76	3.12	29.36	2.20	-	5.73	0.02	2.60	5.81	3.32	19.15
$TmHCO_3^{2+}$	0.08	-	0.48	-	-	-	-	-	2.21	-	-
$Tm(CO_3)_2^-$	15.32	-	0.65	-	93.80	-	92.35	-	14.26	-	-
$TmCO_3^+$	37.88	-	18.03	-	5.22	-	6.93	-	61.57	-	-
Yb^{3+}	2.46	40.34	22.10	65.17	-	15.50	-	54.23	10.18	59.73	79.19
$YbOH^{2+}$	22.11	57.36	27.17	33.04	0.98	80.59	0.85	43.76	3.27	37.62	1.22
$YbCl^{2+}$	-	-	0.20	-	-	-	-	-	0.20	-	1.28
$Yb(SO_4)_2^-$	3.07	-	1.33	-	-	0.02	-	-	0.11	-	0.31
$YbSO_4^+$	14.30	2.29	24.68	1.79	-	3.89	0.01	2.02	4.24	2.64	18.00
$Yb(CO_3)_2^-$	14.10	-	0.67	-	92.54	-	90.57	-	12.46	-	-
$YbCO_3^+$	43.89	-	23.39	-	6.48	-	8.56	-	67.69	-	-
$YbHCO_3^{2+}$	0.07	-	0.47	-	-	-	-	-	1.85	-	-
Lu^{3+}	2.63	41.88	23.79	66.56	-	16.39	-	55.75	10.99	61.18	80.58
$LuOH^{2+}$	21.75	55.90	26.84	31.73	0.78	79.75	0.69	42.32	3.27	36.29	1.17
$LuCl^{2+}$	-	-	0.14	-	-	-	-	-	0.14	-	0.82
$Lu(SO_4)_2^-$	2.93	-	1.21	-	-	0.02	-	-	0.11	-	0.34
$LuSO_4^+$	14.22	2.22	24.79	1.70	-	3.84	0.01	1.93	4.27	2.52	17.10
$LuHCO_3^{2+}$	0.07	-	0.46	-	-	-	-	-	1.82	-	-
$Lu(CO_3)_2^-$	17.66	-	0.84	-	94.32	-	92.80	-	15.79	-	-
$LuCO_3^+$	40.75	-	21.93	-	4.90	-	6.50	-	63.62	-	-

In SGF with a pH value of ~8 and a temperature of 47°C, the total dissolved REE in hot waters dominantly formed the sulfate complexes ($LnSO_4^+$). In general, the REE have been transported to the geothermal water with the main anion sulfate. These complexes gradually decreased from LREE (~59-31%; La-Eu) to HREE (~37-14%; Gd-Lu). In this area, it is seen that the free metal ions (Ln^{3+}) are dominant in the cold spring in this field (~90-67%; La-Eu, ~72-41%; Gd-Lu).

Similar to the SGF, the total dissolved REE dominantly formed sulfate complexes ($LnSO_4^+$) in the geothermal well water (ILKAP) which has a pH of ~7 and a temperature of 60°C. These complexes gradually decreased from LREE (~51-41%; La-Eu) to HREE (~42-24%; Gd-Lu). In this area, it is seen that free metal ions (Ln^{3+}) are dominant in cold spring (~95-84%; La-Eu, ~87-66%; Gd-Lu).

In AGF, the bicarbonate ($LnHCO_3^{2-}$) complexes formed dominant species by increasing with the increased atomic numbers of the REE in the AYKAP geothermal well water with a pH value of ~9 and temperature of 55°C (~61-91%; La-Eu, ~83-94; Gd-Lu). The free metal ions (Ln^{3+}) gradually decreased from La to Nd, and formed dominant species in AYESH geothermal spring water with a pH of ~8 and the temperature of 20°C. $LnOH^{2+}$ complexes from Sm to Lu have become dominant by increasing with the increasing atomic number. In the hot spring of AYKOPK (pH: 9.3, temperature: 31.7°C), the carbonate ($LnCO_3^+$) complexes have formed dominant species by increasing with the increasing atomic numbers of REE (~54-83%; La-Eu, ~79-92%; Gd-Lu). The concentrations of carbonate complexes of REE have also increased with high pH values in AGF. The cold spring (HOŞSU) in the field gradually decreases with increasing atom numbers (~93-78%; La-Eu, ~82-55%; Gd-Lu) and form dominant species of free metal ions (Ln^{3+}).

In the ILICAS well (pH: 6.9, temperature: 38.8°C) in ŞGF, the carbonate ($LnCO^{3+}$) complexes increased with increasing atom numbers of REE (~44-59%; La-Eu, ~56-63%; Gd-Lu) and formed dominant species. Free metal ions (Ln^{3+}) in cold springs in the field decreased with the increasing atomic numbers of the REE in the SSSK spring (pH: 7.5, temperature: 9.2°C) (~93-81%; La-Eu, ~84-61%; Gd-Lu) formed dominant complexes without changing too much

(~76%; La-Eu,: ~79%; Gd-Lu) in the CDMS spring (pH: 6.2, temperature: 12°C).

8. Results

The thermal waters located in the Eastern Black Sea Region, which are controlled by tectonic lines in magmatic (plutonic and volcanic) rocks are as follows; SGF thermal waters in Na-Ca-SO_4 type with a temperature of 47°C; İGF thermal waters in Na-Ca-HCO_3 type with a temperature of 60°C; AGF thermal waters in Na-Ca-CO_3-SO_4 type with a temperature of 55°C and ŞGF thermal waters in Na-HCO_3-Cl type with a temperature of 39°C. The ∑REE contents in these geothermal waters with pH values varying in between 7-9 are at very low (0.02-2.13 ppb) concentrations. The highest ∑REE concentration was determined in the ILKAP (İkizdere) and ILICAS (Şavşat) geothermal waters where the TDS values were also high. Low REE concentrations, typically detected in alkaline thermal waters, were observed in AGF geothermal water with a high pH (8.60-9.86). The REE contents of the cold springs are lower than the geothermal waters and vary between 0.02-0.82 ppb. In the cold water with a high ion content (TDS: 2369 mg/L) in ŞGF, the ∑REE is 2.05 ppb. The ∑REE values in surface waters vary between 0.1-0.64. This situation indicates that the total ion concentration is more effective than the temperature on ∑REE values.

The majority of waters in the studied areas showed LREE/HREE fractionation towards the LREE enrichment. Except for the Ayder area, all geothermal waters have a distinct positive Eu, less significant Ce anomaly. It is considered that the source of Eu anomaly in waters is Eu rich minerals in host rocks of the geothermal areas. The less distinct Ce anomaly in geothermal systems indicates the reducing conditions. According to the calculations of the transport modes, the REEs are transported in the form of $LnSO_4^+$, $LnHCO_3^{2-}$, $LnCO_3^+$ and Ln^{3+} in the AGF and $LnCO_3^+$ and Ln^{3+} complexes in the SGF and IGF. On the other hand, the contents of REE in waters depend on their individual properties, such as the atomic numbers, the temperature and pH of the fluid.

References

Akkuş, İ., Akıllı, H., Ceyhan, S., Dilemre, A., Tekin, Z. 2005. Türkiye Jeotermal Kaynakları Envanteri, Maden Teknik Arama Genel Müdürlüğü Envanter Serisi-201, Ankara.

Arslan, M., Aslan, Z. 2006. Mineralogy, Petrography and Whole-Rock Geochemistry of the Tertiary Granitic Intrusions in the Eastern Pontides, Turkey, Journal of Asian Earth Sciences, 27, pp.177-193.

Arslan, M., Temizel, İ., Abdioğlu, E., Kolaylı, H., Yücel, C., Boztuğ, D., Şen, C. 2013. "40Ar-39Ar dating, whole-rock and Sr-Nd-Pb isotope geochemistry of post-collisional Eocene volcanic rocks in the southern part of the Eastern Pontides (NE Turkey): Implications for magma evolution in extension-induced origin", Contribution to Mineralogy and Petrology, 166, pp.113-142.

Bau, M., Dulski, P. 1999. Comparing yttrium and rare earths in hydrothermal fluids from the Mid-Atlantic Ridge: implications for Y and REE behaviour during near-vent mixing and for the Y/Ho ratio of proterozoic seawater. Chem Geol 155(1-2): pp.77-90.

Bragin I.V., Kharitonova N.A., Chelnokov, G.A., Aseeva, A.V., Chudaev, O.V. 2018. REY geochemistry in groundwater from Paratunka geothermal area (Kamchatka peninsula, Far East of Russia), Environmental Earth Sciences, 77, 376p.

Büyük, M. 1978. Fatsa (Sarmaşık) Kaplıcası Hidrojeoloji Etüdü, Maden Tetkikve Arama Genel Müdürlüğü Rapor No: 6082, Ankara (unpublished).

Craddock, P.R, Bach, W. 2010. Insights to magmatic-hydrothermal processes in the Manus back-arc basin as recorded by anhydrite. Geochim Cosmochim Acta 74(19): pp.5514–5536.

De Carlo, E.H., Wen, X.Y., Irving, M.1998. The influence of redox reactions on the uptake of dissolved Ce by suspended Fe and Mn oxide particles. Aquat. Geochem. 3, pp.357–389.

Embley, R.W., Baker, E.T., Butterfield, D.A., Chadwick, W.W., Lupton, J,E., Resing, J.A., de Ronde, C.E.J., Nakamura, K.I., Tunnicliffe, V., Dower, J.F., Merle, S.G. 2007. Exploring the submarine ring of fire: Mariana Arc—Western Pacific. Oceanography 20(4): pp.68–79

Erzenoğlu, Z., Tangaç, Ö.F. 1986. Ordu- Fatsa (Sarmaşık) Kaplıcası Ilıca-1 Sıcak Su Sondajı Kuyu Bitirme Raporu: Maden Tetkik ve Arama Genel Müdürlüğü Rapor No: 7890, 11p. Ankara (unpublished).

Evcimen, Ö., Karslı, O. 2012. İkizdere Plütonu'nun (KD Türkiye) U-Pb Jeokronolojisi, Petrolojisi ve Jeodinamik Önemi, 65.Türkiye Jeoloji Kurultayı 2-6 Nisan/April, 366p.

Fırat Ersoy, A. 2001. Ilıcaköy (İkizdere-Rize) Sıcak Su Kaynaklarının Hidrojeolojisi, (MSc Thesis), Karadeniz Teknik Üniversitesi Fen Bilimleri Enstitüsü.

Gammons C.H., Wood, S.A., Pedrozo, F., Varekamp, J.C., Nelson, B.J., Shope, C.L., Baffico, G. 2005. Hydrochemistry and rare earth element behavior in a volcanically acidified watershed in Patagonia, Argentina. Chem Geol 222: pp.249-267

Gedik, A., Ercan, T., Korkmaz, S., Karataş, S. 1992. Rize- Fındıklı- Çamlıhemşin Arasında (Doğu Karadeniz) Yer Alan Magmatik Kayaçların Petrolojisi ve Doğu Pontidlerdeki Bölgesel Yayılımları, Türkiye Jeoloji Bülteni, C. 35, pp.15-38, Ankara.

Göb, S., Loges, A., Nolde, N., Bau, M., Jacob, D.E., Markl, G. 2013. Major and trace element compositions (including REE) of mineral, thermal, mine and surface waters in SW Germany and implications for water– rock interaction. Appl Geochem 33: pp.127-152.

Göksu, E. 1996. 1/500.000 ölçekli Türkiye Jeoloji Haritası Samsun Paftası açıklaması, Maden Tetkik ve Arama Genel Müdürlüğü yayını, Ankara.

Gustafsson, J.P. 2012. Visual MINTEQ ver. 3.0. Dept of Land and Water Resources Engineering, Stochholm, Sweden (E-mail: gustafjp@kth.se).

Güven, İ. H. 1993. "Doğu Pontidler'in 1/250.000 Ölçekli Kompilasyonu", Maden Tetkik ve Arama Genel Müdürlüğü, Ankara.

Gürsel, F. 1991. Ayder (Çamlıhemşin-Rize) ve Çevresinin Jeotermal Enerji Yönünden İncelenmesi, (MSc Thesis), Karadeniz Teknik Üniversitesi Fen Bilimleri Enstitüsü.

Gündüz, M. 1999. Rize-İkizdere-Ilıcaköy Sıcaksu Sahası Hidrojeoloji İncelemesi, (MSc Thesis) Hacettepe Üniversitesi, Fen Bilimleri Enstitüsü.

Haas, J.R., Shock, E.L., Sassani, D.S.1995. Rare earth elements in hydrothermal systems: estimates of standard partial molar thermodynamic properties of aqueous complexes of the rare earth elements at high pressures and temperatures. Geochim Cosmochim Acta 59: pp.4329–4350.

Kara, İ. 1997. Türkiye Termal Ve Mineralli Sular Envanteri (Artvin) Maden Tetkik ve Arama Genel Müdürlüğü Rapor No: 10261, 19p. Ankara (unpublished).

Kartal, T. 1972. Rize-Ayder Kaplıcası Hidrojeoloji Raporu: Maden Tetkik ve Arama Genel Müdürlüğü Rapor No: 5689, 20p. Ankara (unpublished).

Karslı, O., Aydın, F., Sadıklar, M.B. 2004. The Morphology and Chemistry of K-Feldspar Megacrysts from Ikizdere Pluton: Evidence for Acid and Basic Magma Interactions in Granitoid Rocks, NE-Turkey: Chemie der Erde-Geochemistry 64, pp.155-170.

Ketin, İ. 1966. Anadolu'nun tektonik birlikleri. Maden Tetkik ve Arama Dergisi no. 66, pp.20-34, Ankara.

Klinkhammer, G., German, C.R., Elderfield, H., Greaves, M.J., Mitra, A. 1994. Rare earth elements in hydrothermal fluids and plume particulates by inductively coupled plasma mass spectrometry. Mar Chem 45 (3): pp.179–186

Moller, P. 2001. The behavior of REE and Y in water-rock interactions. Water-Rock Interaction. In: Proceedings of the 10th International Symposium. Rotterdam: Balkema, Netherlands, vol 2, pp.989-992.

Okay, A. İ., Tüysüz, O. 1999. "Tethyan sutures of northern Turkey", In: Durand, B., Jolivet, L., Hovarth, F., Séranne, M. (eds), The Mediterranean Basins: Tertiary Extension within the Alpine Orogen Tethyan Sutures of Northern Turkey. Geological Society, London, Special Publications, 156, pp.475-515.

Özbeşikçi, A., Kırcı, M., Uysal, M. 1981. Ordu–Giresun–Gümüşhane-Samsun Yörelerindeki Manganez Zuhurlarına Ait Prospeksiyon Rapor no: 7162, Maden Tetkik ve Arama Genel Müdürlüğü. Ankara (unpublished).

Özsayar, T., Pelin, S., Gedikoğlu, A. 1981. Doğu Pontidlerde Kretase, KTÜ., Yerbilimleri Dergisi, 2, pp.65-114.

Shakeri, A., Ghoreyshinia, S., Mehrabi, B., Delavari, M. 2015. Rare earth elements geochemistry in springs from Taftan geothermal area SE Iran. J Volcanol Geotherm Res 304: pp.49-61.

Sun, S.S., McDonough, W.F. 1989. Chemical and isotopic systematics of oceanic basalts; implications for mantle composition and processes. In: Magmatism in the ocean basins. Saunders, A.D. and Norry, M.J. (Editors), Geological Society of London, London. 42: pp.313-345.

Terlemez, İ., Yılmaz, A. 1980. Ünye-Ordu-Koyulhisar-Reşadiye Arasında Kalan Yörenin Stratigrafisi, TJK Bülteni, 23/2, pp.179-192, Ankara.

Temizel, İ., 2002. İkizce (Ünye-Ordu) Yöresi Volkanik Kayaçlarının Petrografik, Jeokimyasal ve Petrolojik İncelenmesi, (MSc Thesis), Karadeniz Teknik Üniversitesi Fen Bilimleri Enstitüsü, Trabzon.

Temizel, İ., Arslan, M., Ruffet, G. Peucat, J.J. 2012. Petrochemistry, Geochronology and Sr–Nd İsotopic Systematics Of The Tertiary Collisional And Post-Collisional Volcanic Rocks From The Ulubey (Ordu) Area, Eastern Pontide, Ne Turkey: Implications For Extension-Related Origin And Mantle Source Characteristics, Lithos, 128, pp.126-147.

Temizel, İ., Arslan, M., Yücel, C., Abdioğlu, E., Ruffet, G. 2016. "Geochronology and geochemistry of Eocene-aged volcanic rocks around the Bafra (Samsun, N Turkey) area: Constraints for the interaction of lithospheric mantle and crustal melts", Lithos, 258-259, pp.92-114.

Uzel, Ö. F., Gündüz, M. 1998. Yıldız, S., Rize- İkizdere Kaplıcası sıcak su sondajı Ilıcaköy-1 ve Ilıcaköy-2 kuyu bitirme raporu: Maden Tetkik ve Arama Genel Müdürlüğü Rapor No: 10213, 11p. Ankara (unpublished).

Wood, S, A. 1990. The aqueous geochemistry of the rare-earth elements and yttrium. 1. Review of available low-temperature data for inorganic complexes and the inorganic REE speciation of natural waters. Chem Geol 82(C): pp.159-186.

Yücel, C. 2013. "Trabzon-Giresun arasındaki Tersiyer volkanitlerinin petrografisi, 40Ar-39Ar jeokronolojisi, petrokimyası, Sr-Nd-Pb izotop jeokimyası ve petrolojisi", Karadeniz Teknik Üniversitesi, Fen Bilimleri Enstitüsü, PhD Thesis, 406p.

Zhang, Y., Tan, H., Zhang, W., Wei, H., Dong, T. 2016 Geochemical constraint on origin and evolution of solutes in geothermal springs in western Yunnan, China. Chemie der Erde, 76, pp.63-75.

Bulletin of the Mineral Research and Exploration

http://bulletin.mta.gov.tr

Appearance features of clayey mixtures having fly ashes

Fatma DAĞCI[a] , Nazlı İpek KUL GÜL[a] and Niyazi Uğur KOCKAL[a*]

[a]Department of Civil Engineering, Akdeniz University, 07058, Antalya, Turkey.

Research Article

ABSTRACT

The use of wastes has become very significant and widespread in terms of sustainable production of clayey mixtures, since the wastes provide many advantages. In this study, the effects of two different types of fly ash, which were wastes of Seyitomer and Cayirhan thermal power plants, on the color change of brick samples with various amount of fly ash ranging between 0 to 60% at different sintering temperatures were investigated. As a result, traditional red colored bricks could be produced with fly ash without using a separate raw material to meet the color requirements. It was found that desired colors for special architectural applications could also be achieved by using fly ash.

1. Introduction

Clay minerals are found in different forms in nature, they are divided into various classes according to their mineralogical properties, crystal structures, chemical contents, areas of use and physical properties.

The most known products of ceramics, one of the main uses of clays, are bricks, pottery, tiles and porcelain (Semiz, 2017). Ceramic products firstly emerged in Anatolia 8000 years ago. These products that became a part of human life at a certain stage of civilization are used in many areas such as architectural elements, decoration material and kitchen ware. Ceramic products can be considered as almost entirely domestic goods, so it is important to create added value in Turkey. Turkey is the sixth producer of ceramic tiles in the World and the third producer of ceramic tiles in Europe as a producer of ceramic tiles (TCF, 2018).

Color plays an active role in defining the properties and visual characteristics of materials (Ware, 2013). Therefore, the color difference is a physical quality parameter that is used in many fields from health sector to the food sector, from food to material science. This parameter can be measured by simple devices or even with visual inspection. Colorimeters have two chromatic coordinates that are red-green and yellow-blue and lightness channels. These devices also include glass filters derived from the characteristics of a standard human observer (Ware, 2013).

Fly ash and bottom ash are the primary products of coal burning process called as Coal Combustion Products (CCPs) and have been used as raw materials in various applications for about 80 years (Heidrich et al., 2013). Firing coal at thermal power plants' furnace over 1000 ° C results in the formation of fly ash by electrostatic filters or mechanical precipitation of the particles formed from the flue gases (ECOBA, 2010).

Studies for reuse of fly ash to produce materials such as bricks, ceramics, cement, concrete, glass, lightweight aggregates are still in progress all around the world (Eliche-Quesada et al., 2017). Karaman et al. (2006) were found that there was a negative relationship between the compressive strength and color measurement parameters of bricks (lightness

and chromaticity coordinates). The relationship between the compressive strength and lightness, chromaticity coordinate of yellow-blue could be defined as linear regression equations. On the other hand, the relationship between the compressive strength and chromaticity coordinate of red-green was weak. Eliche-Quesada et al. (2017) found out that the mechanical properties of conventional clay bricks and bricks contained 20% of fly ash which were sintered at 1000°C were quite similar. According to Kockal (2012*a, b*), it was found that the shrinkage, water absorption and strength properties of commercial ceramic tiles were close to those obtained with fly ash substitution in the ceramic mixture. Kockal (2015) determined that at sintering temperature of 1130°C, the addition of fly ash to ceramic tiles resulted in reduced water absorption and increased shrinkage and strength. At 1210°C, compressive strength and shrinkage decreased and water absorption increased.

According to Turkish Statistical Institute (TUIK)'s data in 2016, total of 19.5 million tonnes of waste was generated in thermal power plants, of which 87.8% were ash and slag waste. While 83.3% of the total waste was disposed, only a small amount such as 16.7% was sent to waste recovery plants and mines (TUIK, 2018). For this reason, the aim of this study is to investigate the color changes of the clayey mixtures substituted by fly ash to be used to produce ceramic materials. In the study, two different fly ashes of Cayirhan and Seyitomer thermal power plants were used at different ratios and the mixtures were exposed to sintering at different temperatures. The color changes of these mixtures were measured by chroma meter and lightness factor and chromaticity coordinates of the samples were obtained and color differences were calculated. As well as, the experimental results were compared and discussed.

2. Materials and Methods

2.1. Materials

Chemical compositions of all raw materials are given in table 1. The clay was obtained from the Elmalı region of Antalya, Turkey. Fly ashes were obtained from Seyitömer (SFA) and Çayırhan (CFA) thermal power plants respectively located in Kütahya and Ankara, Turkey. Clay was replaced with both of the fly ashes at different percentages by weight. Moreover, tap water was used as a constituent of brick samples to give suitable shape to the samples.

2.2. Preparation of Brick Samples

In the study to obtain brick samples, six different mixtures (clay + fly ash) were prepared, in the amount of fly ash ranging between 0 and 60% by weight in 10% intervals. These mixtures were prepared identically for both types of the fly ashes (CFA and SFA). Homogenous mixtures were obtained by mixing with the addition of nearly 0.5 gram of water for each mixture.

In order to carry out the experiments, samples were produced in the shape of a cylinder. Samples with a diameter of 20 mm and a height of between 20 to 27 mm were prepared in order to obtain aspect ratio (d/h) of nearly 1. The total amounts of the mixtures were set at the optimum amounts to keep the height of these samples between the specified values. The mass values of the mixtures was determined separately for each percentage of fly ash through trial and error; the mass of samples containing 0% fly ash was 18 grams (water + clay) and 60% fly ash (water + clay + fly ash) was 14 grams. Cylinder samples were molded with a hydraulic press of 15 tonnes under 110 bar pressure and 10 seconds of time for each percentage of fly ash.

After pressing, the fresh samples were dried at 80°C to obtain constant mass for about 2 h. Then, the oven dried fresh samples were sintered at three different temperatures that were 850,950 and 1050°C in a muffle furnace. The sintered samples are coded as shown in table 2. Loss on ignition values of all sintered samples are given in figure 1, 2. In this table and figures "S" represents SFA and "C" represents CFA.

Table 1- Chemical compositions of raw materials.

Raw Materials	Na_2O	MgO	Al_2O_3	SiO_2	P_2O_5	SO_3	K_2O	CaO	TiO_2	Cr_2O_3	MnO	Fe_2O_3
SFA	0.66	3.65	24.89	51.04	0.08	0.32	2.31	3.12	0.90	0.10	0.12	11.79
CFA	9.18	8.29	13.11	34.90	0.72	2.81	2.68	21.93	0.51	<0.0007	0.08	5.43
Clay	0.57	8.12	15.04	34.13	0.35	0.08	2.13	27.95	0.70	0.11	0.13	10.11

Table 2- Codes of brick samples.

Sintering Temperature (°C)	Fly Ash Content of Brick Samples (%)						
	0	**10**	**20**	**30**	**40**	**50**	**60**
850	K-850	10 S-850/ 10 C-850	20 S-850/ 20 C-850	30 S-850/ 30 C-850	40 S-850/ 40 C-850	50 S-850/ 50 C-850	60 S-850/ 60 C-850
950	K-950	10 S-950/ 10 C-950	20 S-950/ 20 C-950	30 S-950/ 30 C-950	40 S-950/ 40 C-950	50 S-950/ 50 C-950	60 S-950/ 60 C-950
1050	K-1050	10 S-1050/ 10 C-1050	20 S-1050/ 20 C-1050	30 S-1050/ 30 C-1050	40 S-1050/ 40 C-1050	50 S-1050/ 50 C-1050	60 S-1050/ 60 C-1050
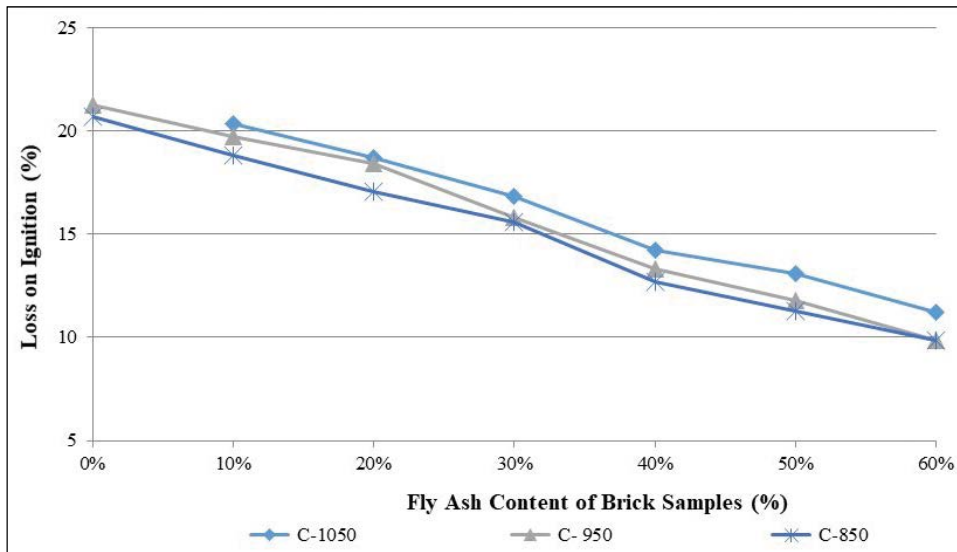
Figure 1- Loss on Ignition versus Fly Ash Content of Brick Samples containing CFA.
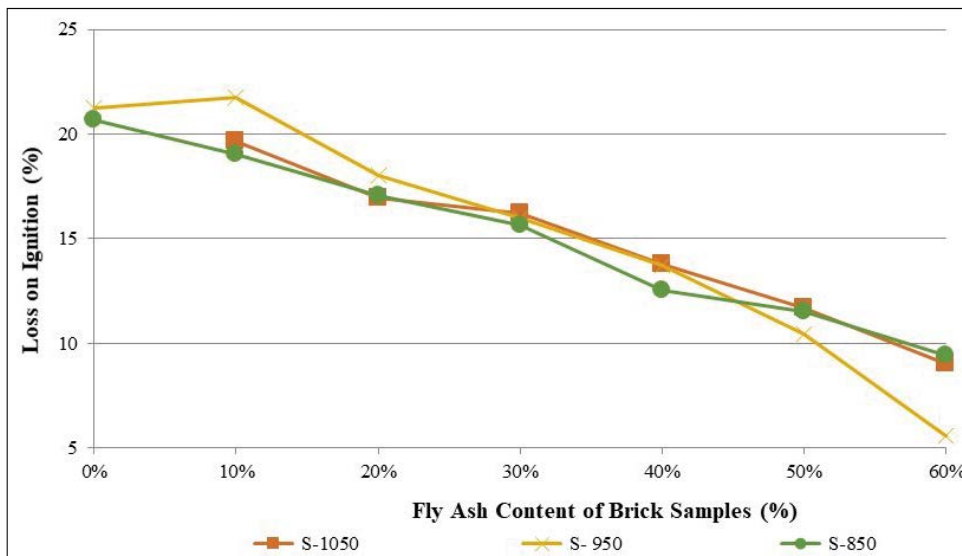
Figure 2- Loss on Ignition versus Fly Ash Content of Brick Samples containing SFA.

2.3. Experimental Methods

The chemical analyses of the raw materials were carried out by X-Ray Fluorescence (XRF). Loss on ignition values of all sintered samples were calculated by the equation below:

$$LOI = \frac{w_f - w_s}{w_f} \times 100 \tag{1}$$

where W_f is the weight of oven-dried fresh samples and W_s is the weight of sintered samples.

The sintered samples were measured with the FRU Chroma Meter colorimetrically. The color difference (E) was calculated by the following equation with the sample's lightness factor (L) and chromaticity in other words chromaticity coordinates a (red) and b (yellow):

$$\Delta E = \sqrt{\Delta L^2 + \Delta a^2 + \Delta b^2} \qquad (2)$$

3. Results and Discussion

In terms of the production of sustainable ceramic products, the wastes such as fly ash could be used to replace flux agents. These agents are generally alkaline and alkali oxides (K_2O, Na_2O, MgO, CaO) of the raw material that allow proper sintering at low temperatures. In addition, these wastes control the plasticity and shrinkage of the ceramics and so enable us to save raw materials and energy (Sultana et al., 2015; Kockal, 2012b).

Actually because of this, the color variations of the clay mixtures with substitution of different types of fly ashes were examined. Furthermore, the effects of sintering temperature, fly ash content and type on color change and lightness factors were investigated.

The results obtained from the measurements of chroma meter on the sintered samples were as indicated in table 3. The results given are the average of the measurements. During the sintering process at 1050°C, control samples lost their structural integrity. Therefore, the pronounced samples were not measured.

Table 3- Color measurement results of the brick samples.

	K-1050	10 S-1050	20 S-1050	30 S-1050	40 S-1050	50 S-1050	60 S-1050
L	--	64.23	62.09	57.58	54.79	52.84	51.09
a	--	9.77	10.34	11.61	12.24	12.98	13.67
b	--	22.90	21.76	20.65	19.45	18.70	18.49
E	--	68.88	66.60	62.26	59.42	57.53	56.02
	K-1050	10 C-1050	20 C-1050	30 C-1050	40 C-1050	50 C-1050	60 C-1050
L	--	67.62	69.36	69.67	69.91	69.95	69.27
a	--	8.17	6.12	5.47	4.97	4.61	4.64
b	--	22.81	22.20	21.48	20.88	20.21	19.19
E	--	71.82	73.08	73.11	73.13	72.95	72.02
	K-950	10 S-950	20 S-950	30 S-950	40 S-950	50 S-950	60 S-950
L	66.12	65.07	62.97	62.16	59.96	59.29	57.69
a	9.65	10.14	10.92	11.56	12.79	13.90	13.91
b	23.54	22.84	22.32	22.09	22.89	24.43	23.21
E	70.85	69.70	67.69	66.97	65.45	65.62	63.72
	K-950	10 C-950	20 C-950	30 C-950	40 C-950	50 C-950	60 C-950
L	66.12	65.97	65.57	65.72	65.32	64.48	64.88
a	9.65	8.65	8.35	7.85	7.62	7.35	7.06
b	23.54	21.79	20.68	19.18	18.19	17.22	16.17
E	70.85	70.01	69.26	68.90	68.23	67.14	67.23
	K-850	10 S-850	20 S-850	30 S-850	40 S-850	50 S-850	60 S-850
L	63.60	62.67	62.14	62.05	62.12	61.73	61.33
a	10.13	10.01	10.37	10.58	10.76	10.74	10.98
b	22.20	21.48	22.04	21.91	22.02	21.35	21.49
E	68.12	67.00	66.74	66.65	66.77	66.19	65.91
	K-850	10 C-850	20 C-850	30 C-850	40 C-850	50 C-850	60 C-850
L	63.60	63.65	63.72	63.38	62.51	62.57	62.15
a	10.13	9.36	8.64	8.22	7.69	7.56	7.15
b	22.20	20.93	19.77	18.60	17.17	16.70	15.30
E	68.12	67.65	67.27	66.56	65.28	65.20	64.40

For SFA-containing brick samples, there was an inverse relationship between the fly ash content and lightness factor (L) at all sintering temperatures.

Considering the lightness factor in CFA-containing brick samples, it was observed that there was a slight fluctuation differently from the samples with SFA. The rise in the lightness factor of brick samples is due to the decline in the amount of Fe_2O_3 and organic materials (Kockal, 2012*a*). Thus, the increment in the lightness factor of SFA-containing brick samples was based on extreme Fe_2O_3 content even higher than the clay as seen in table 1. Besides, almost constant L values of CFA-containing brick samples could be attributed to the balancing effect of low Fe_2O_3 content and loss on ignition values. Chromaticity coordinates (a and b), which were another criteria of color change, gave dissimilar results for SFA and CFA containing samples. Foremost, it was seen that red color (a) increased and yellow color (b) decreased in brick samples containing SFA at 1050°C. In fact, this situation could be visible in figure 3a. Furthermore, there was reduction between 10C-1050 to 60C-1050 for both of red and yellow colors by 43% and 16% respectively, as could be noticed roughly in figure 3b.

The color of ceramic products can vary from light red to dark brown depending on rise of the amount of Fe_2O_3. In order to obtain glazed or unglazed white ceramic products, the amount of Fe_2O_3 should be in the range of 1-2% (Dondi et al., 2014). Because the Fe_2O_3 content of the SFA was as high as about 12%, the red color became darker for 60S-1050. On the other hand, since the content of Fe_2O_3 of CFA was lower than clay and the content of CaO (which has white color) was quite higher than SFA and nearly the same with clay, CFA-contained samples' color experienced lightening at large ratios.

Taking the results of 950°C into consideration, it was recognized that the brick samples containing SFA and K-950 showed stagnate trend for the chromaticity coordinates of yellow (Figure 4a) but the red color trend nearly was the same as it was at 1050°C. In addition to this, CFA-containing brick samples displayed decrement on the chromaticity coordinates of red and yellow (Figure 4b). It was identified that the color changes due to the amount of fly ash demonstrated nearly stable state for both types of fly ash at the sintering temperature of 950 °C. At the sintering temperature of 850°C, the deviation of the chromaticity coordinates of red between K-850 and 60S-850 was only 8%. The chromaticity coordinates of yellow of K-850 and 60S-850 changed slightly with a value of 3% reduction (Figure 5a).

These results suggest that there was almost no change in the colors of brick samples with the
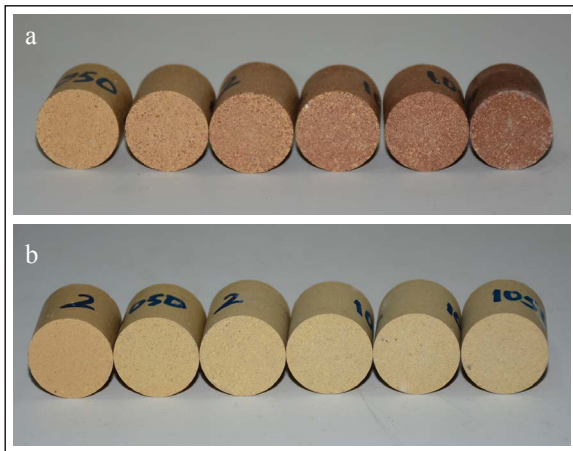
Figure 3- a*) SFA-containing brick samples sintered at 1050°C
*The figure shows the brick samples containing 10% fly ash on the left hand and 60% fly ash on the right hand, so the fly ash content increases from left to the right.
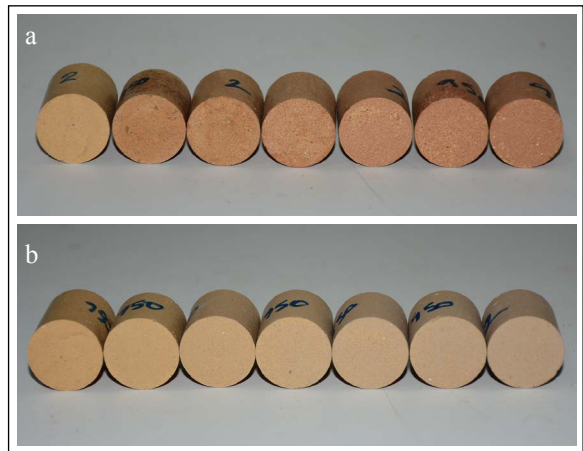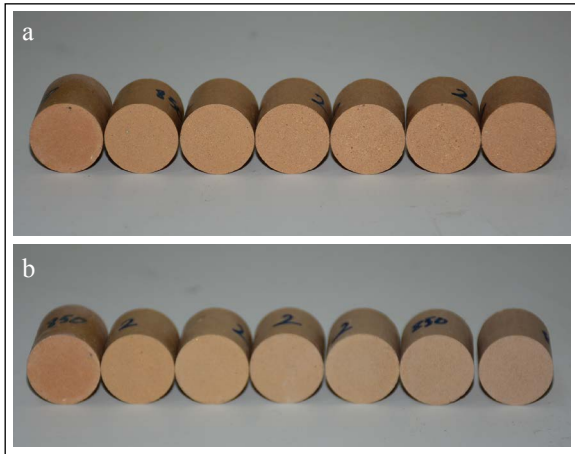b*) CFA-containing brick samples sintered at 1050 °C
*The figure shows the brick samples containing 10% fly ash on the left hand and 60% fly ash on the right hand, so the fly ash content increases from left to the right.

Figure 4- a*) SFA-containing brick samples sintered at 950°C *The figure shows the brick samples containing 0% fly ash on theleft hand and 60% fly ash on the right hand, so the fly ash content increases from left to the right.
b*) CFA-containing brick samples sintered at 950°C *The figure shows the brick samples containing 0% fly ash on the left hand and 60% fly ash on the right hand, so the fly ash content increases from left to the right.

Figure 5- a*) SFA-containing brick samples sintered at 850°C*The figure shows the brick samples containing 0% fly ash on the left hand and 60% fly ash on the right hand, so the fly ash content increases from left to the right.
b*) SFA-containing brick samples sintered at 850°C*The figure shows the brick samples containing 0% fly ash on the left hand and 60% fly ash on the right hand, so the fly ash content increases from left to the right.

variation of fly ash content at the sintering temperature of 850°C. The chromaticity coordinates of red and yellow lessened at a nearly close rate of 30%, as K-850 compared with 60C-850 (Figure 5b).

It was seen that the general tendency was in the direction of cutting down the color difference with the rise of the fly ash ratio for all brick samples. It was noted that lightness (L) and color difference fell off with a rise of the sintering temperature 850 to 1050 for the samples coded as 40 S, 50 S and 60 S at the constant fly ash content. The amount of this decrement was found to be at most for 60 S-coded samples. 60 S-950 reduced in lightness by 5.9% and color difference by 3.3%; 60 S-1050 declined in lightness by 16.7% and color difference by 15% compared to 60 S-850 (Figure 6).
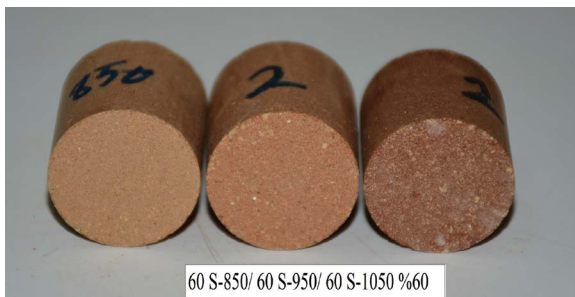
Figure 6- Brick samples containing 60% SFA (constant ratio) sintered at different temperatures.

As well as, for all brick samples containing SFA, the chromaticity coordinate of red was directly related to the content of fly ash and the sintering temperature, but yellow color was inversely proportioned.

It was stated that the liquid phase formed by increasing the sintering temperature decreased the porosity. As a result of this, the crack formation was minimized and mechanical behaviours such as bending strength developed (Celik, 2010).

It was observed that SFA containing samples with a constant content of fly ash, despite including the same amount of Fe_2O_3, the red color increased and the lightness decreased thanks to the liquid phase formation at high sintering temperature. Lastly, the evaluation was performed for CFA-containing brick samples with respect to sintering temperatures. It was detected that the chromaticity coordinates of red had decrement and reversely, yellow color had increment (Figure 7).
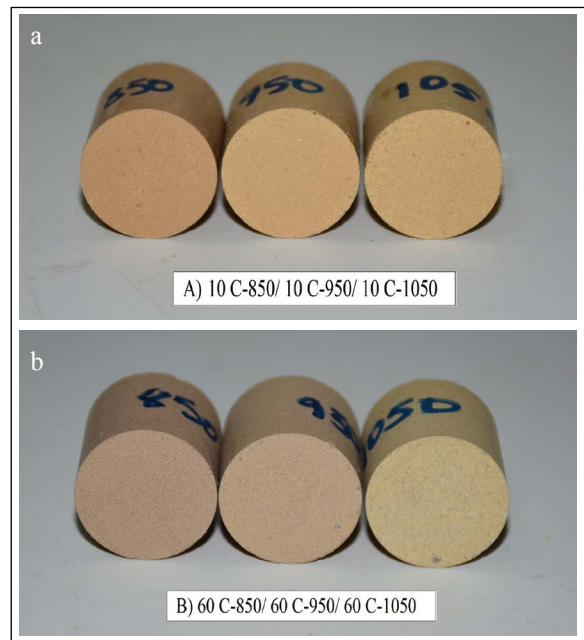
Figure 7- a) Brick samples containing 10% CFA (constant ratio) sintered at different temperatures. b) Brick samples containing 60% CFA (constant ratio) sintered at different temperatures.

4. Conclusions

Some reasonable conclusions were obtained according to experimental studies.

➢ As the fly ash ratio and the sintering temperature increased the red color coordinate decreased for CFA-containing samples and increased for the SFA-containing samples. In other words, both of two fly ash types led to different colors for the brick samples.

➢ The clay used in the experiment is also the raw material of the brick producers and another clay type is practically used to provide the red color in the industry to meet ordinary request of the consumers. Thus, this study resulted in the use of fly ash, a waste, instead of the secondary raw material. Nevertheless, by consumption of fly ash, saving the secondary raw material and energy will be achieved.

➢ Especially SFA, which caused significant increase in red color, promises hope for conventional brick production.

➢ Moreover, in some architectural applications, different colors are desired. It was inferred that different types and contents of fly ash could be used to meet this requirement in the brick production. This situation will ensure that there is no need for additional glazing and painting operations for these specific applications.

References

Celik, H. 2010. Technological characterization and industrial application of two Turkish clays for the ceramic industry. Applied Clay Science, 50(2), 245-254.

Dondi, M., Raimondo, M., Zanelli, C. 2014. Clays and Bodies For Ceramic Tiles: Reappraisal and Technological Classification. Applied Clay Science, 96, 91-109.

Eliche-Quesada, D., Sandalio-Pérez, J. A., Martínez-Martínez, S., Pérez-Villarejo, L., Sánchez-Soto, P. J. 2017. Investigation of use of coal fly ash in eco-friendly construction materials: fired clay bricks and silica-calcareous non fired bricks. Ceramics International, 44(4), 4400-4412.

ECOBA (European Coal Combustion Products Association) 2010 Statistics. http://www.ecoba.com/ecobaccpprod.html. April 25, 2018.

Heidrich, C., Feuerborn, H. J., Weir, A. 2013. Coal combustion products: a global perspective. World of Coal Ash Conference 22-25 April 2013, Kentucky, 22-25.

Karaman, S., Gunal, H., Ersahin, S. 2006. Assesment of clay bricks compressive strength using quantitative values of colour components. Construction and Building Materials, 20(5), 348-354.

Kockal, N. U. 2012a. Properties and microstructure of porous ceramic bodies containing fly ash. Journal of building physics, 35(4), 338-352.

Kockal, N. U. 2012b. Utilisation of different types of coal fly ash in the production of ceramic tiles. Boletín de la Sociedad Española de Cerámica y Vidrio, 51(5), 297-304.

Kockal, N. U. 2015. Optimizing Production Parameters of Ceramic Tiles Incorporating Fly Ash Using Response Surface Methodology. Ceramics International, 41(10), 14529-14536.

Semiz, B. 2017. Characteristics of clay-rich raw materials for ceramic applications in Denizli region (Western Anatolia). Applied Clay Science, 137, 83-93.

Sultana, M. S., Ahmed, A. N., Zaman, M. N., Rahman, M. A., Biswas, P. K., Nandy, P. K. 2015. Utilization of hard rock dust with red clay to produce roof tiles. Journal of Asian Ceramic Societies, 3(1), 22-26.

TCF (Turkish Ceramic Federation). 2018. http://www. serfed. com/tr/content.php?content_id=125. April 25.

TUIK (Turkish Statistical Institute). 2018. Thermal Power Plant Water, Wastewater and Waste Statistics. http://tuik.gov.tr/PreHaberBultenleri.do?id=24873. April 23.

Ware, C. 2013. Information Visualization: Perception for Design, Elsevier, 513 p.

Bulletin of the Mineral Research and Exploration

http://bulletin.mta.gov.tr

Statistical approach by factor and cluster analysis on origin of elements from the Hamit Plutonic (Turkey) rock samples

Fusun YALCIN[a*] , Daniel G. NYAMSARI[b] , Nurdane ILBEYLI[b]   and Rifat BATTALOĞLU[c]

[a]Akdeniz University, Department of Mathematics, 07058, Antalya, Turkey.
[b]Akdeniz University, Department of Geological Engineering, 07058, Antalya, Turkey.
[c]Niğde Ömer Halisdemir University, Department of Chemistry, 51200, Niğde, Turkey.

ABSTRACT

The Hamit pluton forms part of the Central Anatolian Crystalline Complex. It is located N-NE of Kaman (Kirsehir). It covers an area of about 120 km². The geochemical contents of 63 rock samples collected from this pluton were analyzed for their origin, homogeneity and relationship with crustal rocks. Their element contents were determined by using X-Ray Fluorescence spectroscopy. The samples were divided into 2 major groups based on their similarities: Group 1 contained 63.5% of the samples and indicated they were formed from melts whose contents might have evolved greatly due to crustal assimilation; while the 36.5% of samples belonged to Group 2, and show minimal evolution of the melt. According to the variation in K/Rb ratio versus SiO_2 and the Rb/Zr versus SiO_2 the initial melt had experience great evolution due to crustal assimilation. The initial melt is considered to have contained "most" of SiO_2, TiO_2, Fe_2O_3, MnO, MgO, CaO, P_2O_5, Sr, Zn, Cu, Ni, Co, Cr, Ba, Nd, Sc and V that formed the pluton, while "majority" of the Al_2O_3, Nb, Zr, U, Th, Pb, Ga, Rb, Ce and La are considered to have been derived from crustal contamination, and "almost all" of Na_2O, K_2O and Y are considered to have originated from crustal assimilation.

1. Introduction

Practically, the term "alkaline" is used to encompass a wide range of igneous rocks, all of which do not conform to this rigid definition. Carbonatites, for example, are certainly silica-deficient but are rarely alkali-rich (Fitton and Upton, 1987). Alkaline plutonic rocks are large scale intrusive igneous rocks containing an excess of alkali oxides (Na_2O + K_2O) over silica and/or alumina with respect to alkali. The excess alkali in these rocks cannot be accommodated in feldspar alone and so they appear in feldspathoids, sodic pyroxenes, sodic amphiboles and other alkali-rich phases (Fitton and Upton, 1987).

Alkaline rocks are usually important for their geochemical contents as they can host or be associated with most of the world's resources of niobium (Nb), tantalum (Ta), rare earth elements (REE) (Fitton and Upton, 1987) and mostly associated with economic deposits of apatite (Verplanck et al., 2014) and with diamonds (Mitchell, 1991).

The Central Anatolian Crystalline Complex is made up of metamorphic rocks overthrust by ophiolitic units and intruded by a number of calc-alkaline to alkaline plutons (Göncüoğlu et al., 1991) as shown in figure 1. One of the alkaline pluton in the complex is the Hamit pluton, which is surrounded by the Paleozoic Kaman metamorphics, the Mesozoic Karakaya ultramafics and the Cenozoic cover units. The Hamit pluton is
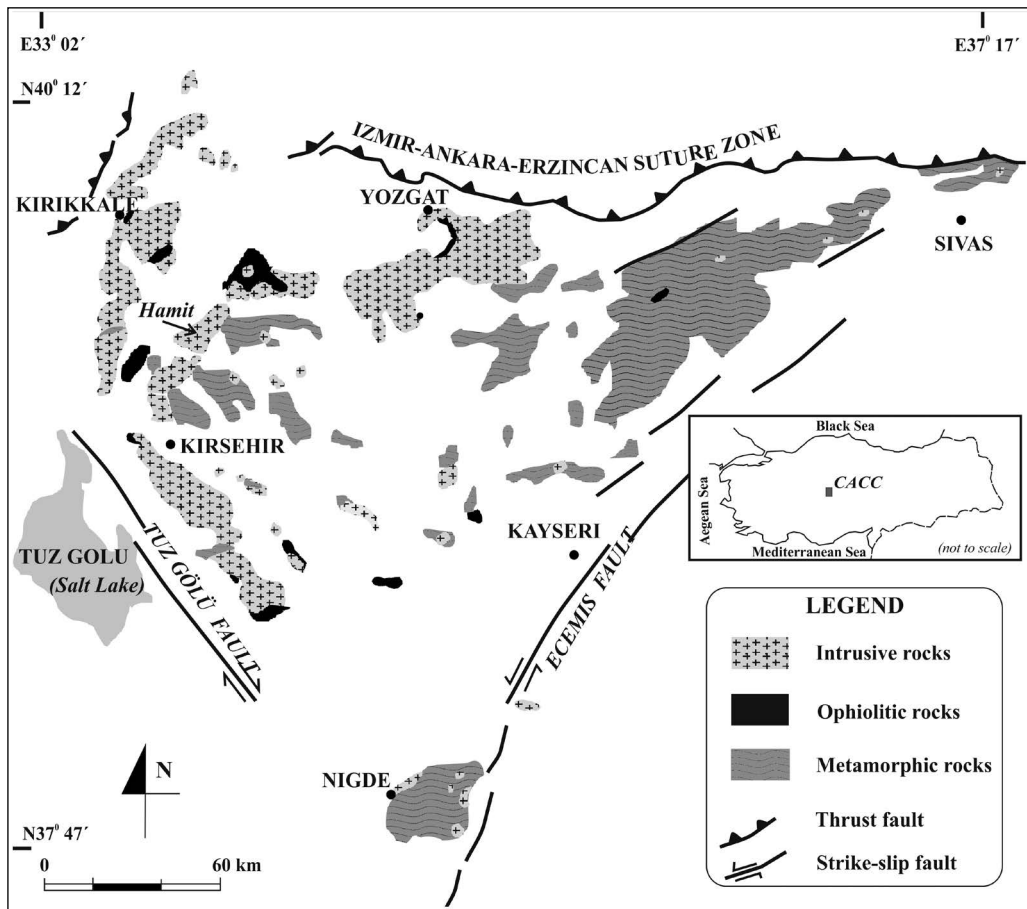
Figure 1- Geological setting of the Central Anatolian Crystalline Complex (after Bingöl, 1989).

situated in N-NE of Kaman and covers an area of about 120 km² containing nepheline syenite, pseudoleucite syenite, alkali feldspar syenite and quartz syenite. The alkaline-peralkaline Hamit intrusive rocks show comparable field to the petrographic and geochemical characteristics with A-type granites (Ilbeyli, 2004). The aim of this study is to use factor and cluster analysis to: examine the homogeneity of the samples' contents and study the origin and relationship of the elements in the parental magma that eventually lead to the formation of these plutonic rocks.

The use of factor analysis is this study is tied to the fact that it could show not only chemical changes during alteration but also chemical variation in the rocks (Gill, 1972). Meanwhile according to Yalcin et al. (2013) cluster analysis can be used to identify similarly or homogeneously combining samples. These methods have also been used in interpreting geochemical data by several different authors in their publications (Child, 1970; Lawley and Maxwell, 1971; Jöreskog et al., 1976; Facchinelli et al., 2001;

Kumru and Bakac, 2003; Boruvka et al., 2005; Yalcin and İlhan, 2008; Akbarpour et al., 2013; Yalcin et al., 2013; Yalcin and Ilbeyli, 2014, 2015; Ilbeyli and Yalcin, 2015).

2. Materials and Method

Sixty-three (63) representative rock samples (Ilbeyli, 1999) were collected from along the Hamit pluton and store in plastic bags with the use of a hammer and a sledgehammer. The location of every sample was noted with the use of a GPS and transported to the University of Durham, United Kingdom where they were prepared for X-Ray Fluorescence to determine their element contents. In the laboratory, the samples were prepared one by one. Their sizes were first reduced with the use of a hammer and a jaw crusher, after which they were reduced to a homogenized powder form using an agate ball mill and then pressed into pellets. Before the preparation of each sample, the apparatus was washed

with water and purified with washed with 10% HNO$_3$ acid to prevent contamination from other samples, and then dried with compressed air. The major and trace elements were then determined using pressed powder pellets by X-ray fluorescence spectrometry (XRF) at the University of Durham, United Kingdom using an automated Philips PW 1400 spectrometer with a Rh anode tube.

Major Elements: From the 63 samples analyzed, the main analytes for alkaline rocks are composed of averages as follows: SiO$_2$ (60.02%), Al$_2$O$_3$ (19.45%), CaO (2.87%), Na$_2$O (4.51%), K$_2$O (8.10%). SiO$_2$ and K$_2$O both have an approximately right symmetric distribution (skewness ranging between 0 and 0.5) implying most of their values are close to and lower than the mean value. CaO has a moderately skewed distribution with its skewness in the range of 0.5 and 1, while Al$_2$O$_3$ and Na$_2$O are highly and right skewed (skewness > 1). This indicates most of their values were lower than the mean value with extreme values higher than the mean value, as confirmed by the median values 18.98 (Al$_2$O$_3$) and 4.30 (Na$_2$O), which are lower than their respective mean values; as shown on table 1 below.

Trace Elements: 15 trace elements were analyzed. The averages of six of the significant trace element analytes are: Ba (599.37 ppm), Sr (550.74 ppm), Zr (351.92 ppm), Rb (303.15 ppm), Th (79.63 ppm) and Nb (39.97 ppm). Ba and Sr (with Skewness of 0.73 and 0.59 respectively) have a moderately right skewed distribution while Zr, Rb and Nb (with skewness 1.25, 1.16 and 1.52 respectively) show a highly right skewed distribution and Th shows an approximately symmetrical distribution. Out of the other nine trace elements, 7 of them (Pb, V, Ga, U, Cu, Ni, and Cr) show highly right skewed distribution while Zn shows approximately symmetric distribution and Co shows a moderately skewed distribution; as shown on table 1 below.

Rare Earth Elements – REE: 5 REE where analyzed. They have averages in ppm as follows Ce (171.56), La (105), Nd (51.49), Y (34.59) and Sc (3.64). According to their distribution patterns, La (-0.24) and Nd (-0.35) both have an approximately symmetric distribution, while Ce (-0.99), Y (0.87) and Sc (0.96) show moderately skewed distribution; as shown on table 1 below.

The box plot, figure 2, shows the anomalous concentration of an elements' distribution within

Table 1- Summary of statistical description of the various elements in the samples analyzed.

	SiO$_2$	TiO$_2$	Al$_2$O$_3$	Fe$_2$O$_3$	MnO	MgO	CaO	Na$_2$O	K$_2$O	P$_2$O$_5$	Ba	Sr	Zr	Rb	Th
N	63.00	63.00	63.00	63.00	63.00	63.00	63.00	63.00	63.00	63.00	63.00	63.00	63.00	63.00	63.00
Minimum	52.52	0.04	14.50	0.42	0.00	0.02	0.15	1.78	5.86	0.00	22.30	57.70	20.20	173.80	2.30
Maximum	72.24	0.74	25.86	6.49	0.15	3.02	7.15	8.32	11.30	0.44	2082.10	1452.50	996.70	559.30	160.20
Mean	60.02	0.38	19.45	3.10	0.09	0.76	2.87	4.51	8.10	0.13	599.37	550.74	351.92	303.15	79.63
Median	60.96	0.31	18.98	2.21	0.11	0.31	1.93	4.30	8.01	0.04	168.80	198.60	332.10	283.80	67.00
Skewness	0.10	0.32	1.40	0.60	-0.35	1.47	0.79	1.18	0.35	0.93	0.73	0.59	1.25	1.16	0.36
Kurtosis	-1.32	-0.91	2.50	-0.96	-1.34	0.97	-0.86	3.06	-0.08	-0.74	-1.21	-1.56	1.37	1.87	-0.63
Std. Deviation	5.17	0.20	2.15	1.83	0.05	0.94	2.38	1.18	1.18	0.15	660.59	524.05	232.20	79.70	35.75
	Zn	Pb	V	Nb	Ga	U	Cu	Ni	Cr	Co	Ce	La	Nd	Y	Sc
N	63.00	63.00	63.00	63.00	63.00	63.00	63.00	63.00	63.00	63.00	63.00	63.00	63.00	63.00	63.00
Minimum	8.40	40.80	0.60	8.20	12.20	0.00	0.00	0.00	0.00	0.00	6.30	14.60	3.60	2.00	0.00
Maximum	156.50	146.30	125.50	101.00	41.00	44.70	36.80	31.80	52.80	16.90	290.30	182.60	103.80	104.30	11.50
Mean	65.27	62.54	46.44	39.97	20.23	10.73	10.52	8.78	8.76	4.79	171.56	105.38	51.49	34.59	3.64
Median	59.50	59.20	32.80	37.20	19.60	9.10	5.00	6.40	3.40	3.00	178.40	103.10	53.50	36.80	2.70
Skewness	0.38	2.35	1.03	1.52	1.75	1.53	1.04	1.26	1.74	0.98	-0.99	-0.24	-0.35	0.87	0.96
Kurtosis	-0.51	6.17	-0.10	2.80	4.98	2.82	-0.41	1.41	3.39	-0.19	1.70	0.64	-0.02	2.87	0.22
Std. Deviation	34.34	19.57	34.96	19.33	5.20	9.77	11.19	7.10	11.12	4.86	58.78	37.97	21.96	18.09	2.97

the samples. In all the samples, SiO_2, TiO_2, Fe_2O_3, MnO, CaO, K_2O, P_2O_5, Sr, Th, Zn, Cu, Co, Ba, Nd and Sc, show no anomalous concentration and most of them also display an approximately symmetric to moderately skewed distribution. Al_2O_3 shows high anomaly concentrations in 3 samples (S15, S28 and S31) and low anomaly in 1 sample (S56); MgO shows high anomalies in 4 samples (S5, S6, S9 and S13); Na_2O shows high anomalous concentrations in 5 samples (S15, S16, S17, S20, and S41) and low anomalies in 2 samples (S29 and S30); Nb has high anomaly concentrations in 4 samples (S28, S29, S30 and S31) and low in 4 samples (S33, S35, S40 and S56); Zr shows very high anomalies in 8 of the samples (S15, S16, S17, S20, S28, S29, S30 and S31). Rb shows high anomalies in 2 samples (S29 and S30); Y shows high anomalies in 2 samples (S44 and S46); Ce shows high anomalies in 2 samples (S30 and S36) and low anomalies in 4 samples (S33, S34, S40 and S56); and La has high anomalies in 2 samples (S30 and S31) and low anomalies in 4 samples (S33, S39, S40 and S56).

Correlation: Considering the major determinant element of an alkaline rock (SiO_2, Al_2O_3, Na_2O and K_2O), the coefficient correlation matrix presented on table 2 reveals that SiO_2 shows no significant positive relationship with any of the elements; rather they show very strong negative/weak relationship (where $r < -0.7$) with TiO_2, Fe_2O_3, MnO, MgO, CaO, P_2O_5, Sr, Zn, Co, Ba, Nd, Sc and V. Meanwhile there exist "strong" positive relationship ($r > 0.7$) between Al_2O_3 and Nb and Zr; and between CaO and MnO, Sr, Cu, Ni, Ba, Nd and Sc. A moderately strong positive relationship (where $r > 0.5$) exists between Al_2O_3 and U, Ga, Zn, Ce and La; between CaO and Zn and Y; between Na_2O and Pb; between K_2O and Rb. Whereas there exists moderately negative (moderately weak) relationship (where $-0.7 < r < -0.5$) between SiO_2 and Cu, Ni and Ce; and between MgO and K_2O; and weak negative relationship (where $-0.5 < r < 0$) between CaO and Na_2O, K_2O, Th and Rb; between Na_2O and Fe_2O_3, MgO, P_2O_5, Cu, Co, Sc and V; between K_2O and P_2O_5, Sr, Cu, Ni, Co, Ba, Sc and V.

On the other hand, considering the rest of the elements constituted in the rock samples, we notice that a "very strong" positive correlational relationship ($r > 0.9$) is demonstrated among the following elements: between TiO_2 and Fe_2O_3, CaO, P_2O_5, Co and V; between Fe_2O_3 and MgO, CaO, P_2O_5, Co and V; between MgO and CaO, P_2O_5, Co; between CaO and
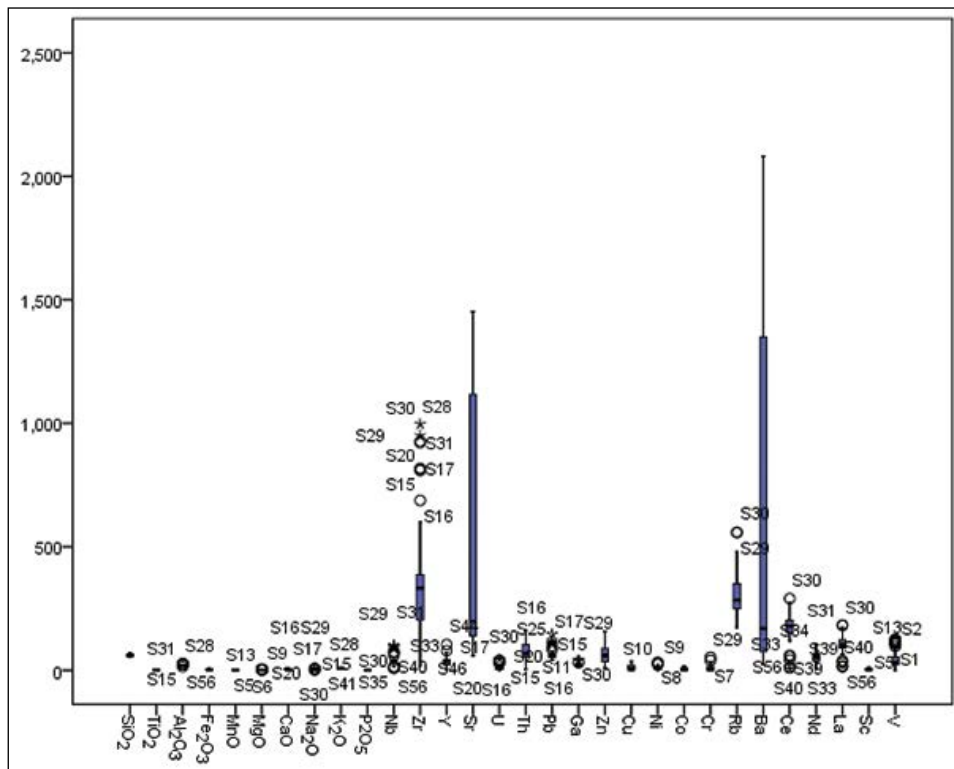
Figure 2- Distribution of the elements' concentration within the various samples of the Hamit Pluton.

Table 2- Coefficient correlation between the elements in samples analyzed from of the Hamit Pluton.

	SiO₂	TiO₂	Al₂O₃	Fe₂O₃	MnO	MgO	CaO	Na₂O	K₂O	P₂O₅	Nb	Zr	Y	Sr	U	Th	Pb	Ga	Zn	Cu	Ni	Co	Cr	Rb	Ba	Ce	Nd	La	Sc	V
SiO₂	1																													
TiO₂	-.772**	1																												
Al₂O₃	-.380**	-.199	1																											
Fe₂O₃	-.858**	.969**	-.083	1																										
MnO	-.789**	.799**	-.055	.814**	1																									
MgO	-.728**	.886**	-.178	.928**	.650**	1																								
CaO	-.807**	.929**	-.193	.962**	.812**	.903**	1																							
Na₂O	.076	-.427**	.271*	-.361**	-.010	-.422**	-.301*	1																						
K₂O	.149	-.353**	.300*	-.404**	-.219	-.506**	-.451**	-.130	1																					
P₂O₅	-.782**	.933**	-.159	.965**	.700**	.962**	.940**	-.384**	-.465**	1																				
Nb	-.335*	-.068	.819**	-.023	.053	-.148	-.119	.070	.293*	-.159	1																			
Zr	-.480**	.031	.772**	.160	.186	.075	.102	.117	.024	.052	.865**	1																		
Y	-.342*	.495**	-.147	.413**	.645**	.244	.421**	-.212	.088	.282*	.105	.060	1																	
Sr	-.785**	.853**	-.044	.892**	.711**	.771**	.863**	-.231	-.362**	.884**	-.131	.082	.191	1																
U	-.297	-.122	.578**	-.016	.204	-.056	-.040	.384**	.084	-.087	.598**	.674**	.015	-.096	1															
Th	.227	-.348*	.304*	-.387**	-.209	-.441**	-.441**	.160	.270*	-.474**	.589**	.456**	.063	-.490**	.405**	1														
Pb	-.309*	-.034	.464**	.033	.310*	-.095	.055	.541**	-.113	-.077	.510**	.590**	.101	.068	.531**	.312*	1													
Ga	-.380*	.027	.653**	.149	.032	.154	.039	-.078	.081	.099	.660**	.768**	-.137	.067	.572**	.352**	.350**	1												
Zn	-.846**	.521**	.569**	.621**	.586**	.491**	.540**	-.063	.009	.509**	.609**	.738**	.191	.553**	.563**	.114	.439**	.692**	1											
Cu	-.692**	.833**	-.119	.853**	.649**	.861**	.804**	-.345**	-.373**	.885**	-.143	.016	.302*	.754**	.102	-.441**	-.119	.106	.465**	1										
Ni	-.629**	.693**	.003	.725**	.540**	.801**	.711**	-.244	-.455**	.742**	.098	.260*	.281*	.529**	.076	-.199	.238	.242	.410**	.643**	1									
Co	-.743**	.905**	-.182	.941**	.685**	.953**	.915**	-.407**	-.477**	.959**	-.141	.070	.300*	.829**	-.062	-.434**	-.079	.115	.495**	.853**	.737**	1								
Cr	-.419**	.358**	.198	.410**	.227	.470**	.304*	-.223	-.106	.412**	.182	.311*	.107	.272*	.176	.070	-.008	.456**	.450**	.441**	.443**	.371**	1							
Rb	.237	-.425**	.362**	-.444**	-.367**	-.469**	-.478**	-.069	.564**	-.498**	.579**	.452**	-.026	-.476**	.283*	.712**	.163	.465**	.145	-.459**	-.271*	-.472**	.104	1						
Ba	-.738**	.819**	-.023	.858**	.642**	.779**	.813**	-.272*	-.374**	.875**	-.140	.074	.200	.960**	-.042	-.485**	.033	.117	(	.797**	.579**	.818**	.288*	-.468**	1					
Ce	-.643**	.413**	.533**	.421**	.515**	.227	.320*	-.017	.154	.260*	.760**	.695**	.397**	.293*	.453**	.526**	.504**	.530**	.784**	.224	.327*	.257	.332**	.360**	.244	1				
Nd	-.803**	.768**	.153	.753**	.776**	.547**	.702**	-.197	.021	.612**	.337*	.338**	.532**	.638**	.098	.030	.221	.208	.732**	.508**	.409**	.591**	.297	-.058	.520**	.775**	1			
La	-.472**	.235	.517**	.243	.358*	.072	.182	.097	.087	.089	.783**	.730**	.339**	.114	.423**	.649**	.542**	.506**	.653**	.004	.246	.091	.230	.438**	.054	.929**	.660**	1		
Sc	-.703**	.767**	-.095	.814**	.610**	.753**	.828**	-.314*	-.367**	.778**	-.043	.147	.170	.750**	-.126	-.365**	-.004	.094	.541**	.574**	.495**	.779**	.204	-.407**	.659**	.307*	.674**	.195	1	
V	-.799**	.934**	-.147	.955**	.758**	.932**	.945**	-.378**	-.416**	.930**	-.040	.127	.442**	.781**	-.111	-.363**	.002	.096	.530**	.773**	.773**	.926**	.393**	-.434**	.727**	.379**	.732**	.251*	.824**	1

**. Correlation is significant at the 0.01 level (2-tailed).   *. Correlation is significant at the 0.05 level (2-tailed).

P_2O_5, Co and V; between P_2O_5 and Co and V; between Sr and Ba; between Co and V; and between Ce and La.

In addition, there exist "strong" positive relationships (r > 0.7) between TiO_2 and MnO, MgO, Sr, Cu, Ba, Nd and Sc; between Fe_2O_3 and MnO, Sr, Cu, Ni, Ba, Nd, La and Sc; between MnO and P_2O_5, Sr, Nd and V; between MgO and Sr, Cu, Ni, Ba, Sc and V; between P_2O_5 and Sr, Cu, Ni, Ba and Sc; between Nb and Zr, Ce and La; between Zr and Ga, Zn and La; between Sr and Cu, Co, Sc and V; between Th and Rb; between Zn and Ce and Nd; between Cu and Co, Ba and V; between Ni and Co and V; between Co and Ba and Sc; between Ba and V; between Ce and Nd; between Nd and V; and between Sc and V.

There exist weak relationships between Fe_2O_3 and Th and Rb; between MnO and Rb; between MgO and Th and Rb; between P_2O_5 and Th and Rb; between Sr and Th and Rb; between Th and Cu, Co, Ba, Sc and V; between Cu and Rb; and between Co and Rb.

Regression: Regression analysis has been done to determine the relationship of SiO_2 with other elements (Table 3). According to the adjusted R^2 value, 99.7% of the total variability in SiO_2 is explained by the all the other elements, while the ANOVA (variant analysis) indicates model has a significant explanatory power. This therefore implies the Model SUMMARY has a very strong; explanatory power on SiO_2 and that the numbers of samples used in this analysis were sufficient.

Cluster Analysis: Hierarchical clustering analysis was done to group the samples according to their similarity or homogeneity. The most similarly or homogeneously combining samples are 17 and 20 followed by: 43-51, 19-21, 22-24, 5-10, 9-13, 3-5, 57-60, 43-53 and 46-47. The most dissimilar samples are 1 and 15, followed by: 1-12, 15-32, 1-3, 15-16, 3-4, 32-57, 3-6, 3-18, 27-30, 32-33 and 4-11. Samples 1, 2,

3 and 15 show the highest number of most dissimilar combination with other samples, occurring 4 times among the 15 highly most dissimilar combining cluster samples; followed by 32 (3 times), 4 (3 times) and 33 (2 times).

According to the dendrogram, the most similar combined samples are divided into 7 clusters. They include Cluster 1 (samples 17, 20, 15, 28, 31, 29, 30), which closely linked to Cluster 2 (only sample 16); Cluster 3 (samples 59, 61, 57, 60, 62, 63, 58, 34, 35, 50, 43, 51, 53, 37, 49, 54, 41, 42, 36, 46, 47, 44, 45, 32, 38, 48, 52, 55, 40, 56, 33 and 39); Cluster 4 (samples 1 and 2); Cluster 5 (samples 4, 14, 7 and 11); Cluster 6 (samples 6, 23, 22, 24, 25, 9, 13, 5, 10, 3, 8, 19, 21, 26, 27 and 18); and Cluster 7 (only sample 12); as shown on figure 3a below.

It can be observed from the dendrogram that the elements are divided in 4 different cluster groups, each of which contains elements showing relatively close correlational relationship. They include Cluster 1 (MnO, P_2O_5, TiO_2, MgO, Fe_2O_3, CaO, Sc, Na_2O, Co, K_2O, Cu, Ni, Cr, Al_2O_3, Ga, U, SiO_2, Pb, Nd, V, Nb, Y, Zn, Th and La), Cluster 2 (Rb and Ce), Cluster 3 (Zr), Cluster 4 (Sr and Ba). Cluster 1 and more closely related directly. This grouping shows some similarity among the elements, as shown on figure 3b.

Factor Analysis: Table 4 (a, b and c), shows the results of the Principal Component Analysis (PCA) of the elements. In the retained 3 components, all the elements are well represented with at least 63.3% of the elements having a proportion > 0.7, of their variance explained by the retention factor and 93.3% of the elements have proportion of their variances > 50% (> 0.5) explained by the retention factor; whereas just 6.7% (2/30) of the elements (Y and Cr) have > 0.5 of their variance that is not explained by the retention factor table 4a.

Table 3- Data Regression of samples content of the Hamit Pluton using Model SUMMARY (a) and ANOVA (b).

Model SUMMARY[a]		R	R Square	Adjusted (Adj.) R Square	Std. Error of the Estimate	
1		.999[b]	.999	.997		.26691
ANOVA[a]		Sum of Squares	df	Mean Square	F	Sig.
1	Regression	1654.239	29	57.043	800.697	.000[b]
	Residual	2.351	33	.071		
	Total	1656.590	62			
a. Dependent Variable: SiO_2 ; b. Predictors: (Constant), V, Pb, Ga, K_2O, Th, Cr, Y, U, Al_2O_3, Ba, Na_2O, Ni, Rb, Sc, Cu, Nd, Zr, MnO, Co, Nb, La, Zn, CaO, Ce, Sr, P_2O_5, TiO_2, MgO, Fe_2O_3						
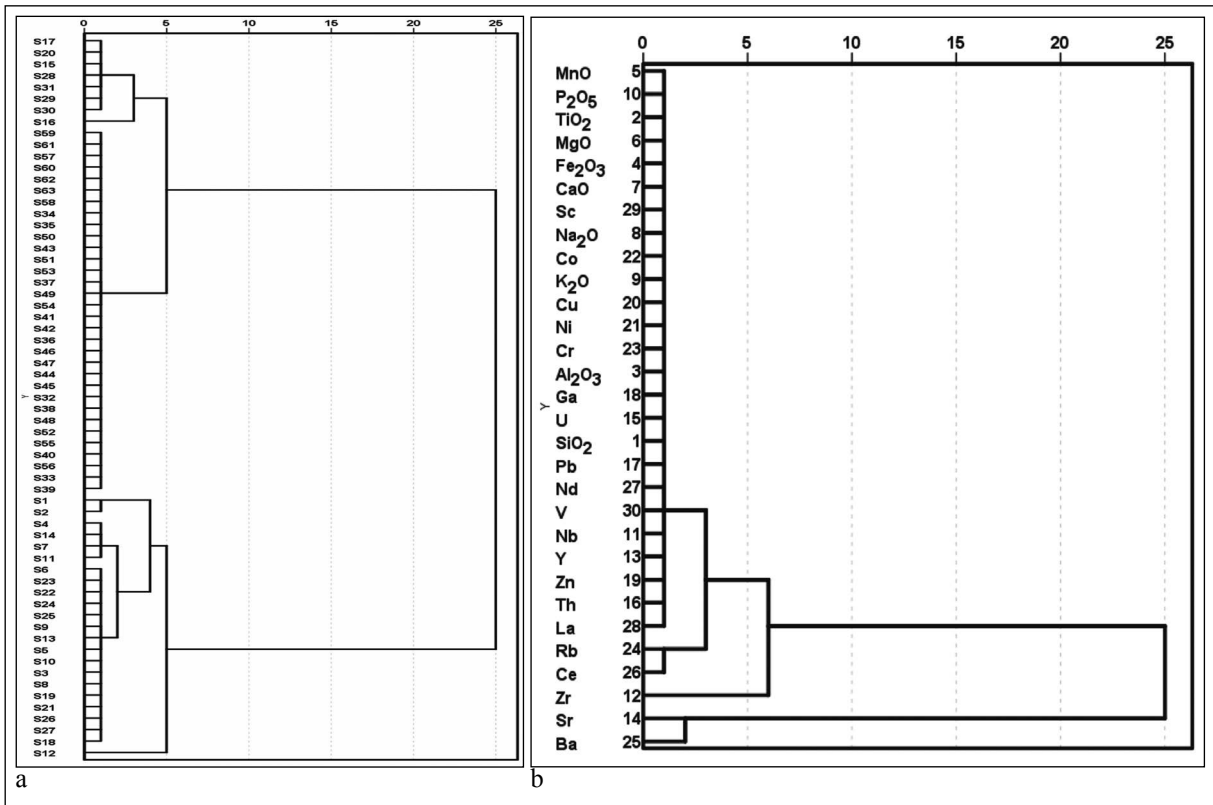
Figure 3- a) Dendrogram of Hierarchical Cluster analysis of samples of the Hamit Pluton. b) Elements dendrogram of the Hamit Pluton samples.

Table 4a- Proportion of elements' variance explained in the Hamit Pluton samples.

	Communalities			Communalities	
	Initial	Extraction		Initial	Extraction
SiO_2	1.000	.907	Zr	1.000	.861
TiO_2	1.000	.967	Nd	1.000	.823
Al_2O_3	1.000	.721	La	1.000	.821
Fe_2O_3	1.000	.993	Sr	1.000	.818
MnO	1.000	.688	Ba	1.000	.783
MgO	1.000	.899	Cu	1.000	.763
CaO	1.000	.942	Rb	1.000	.744
Na_2O	1.000	.538	Th	1.000	.690
K_2O	1.000	.538	Sc	1.000	.675
P_2O_5	1.000	.962	U	1.000	.643
V	1.000	.931	Ga	1.000	.595
Co	1.000	.915	Ni	1.000	.587
Ce	1.000	.911	Pb	1.000	.573
Zn	1.000	.885	Y	1.000	.474
Nb	1.000	.873	Cr	1.000	.249

Extraction Method: Principal Component Analysis.

The 3 components retained contribute for 75.903% of the total variable's variance with the least total Eigenvalues > 2.0 (Table 4b). The Factor 1 with initial Eigenvalue 13.684, explains 45.613% of the total variable variance constituting the largest number of the strongest correlational relationships with 56.7%

of the elements as presented on table 4c (TiO_2, Fe_2O_3, MgO, CaO, P_2O_5, Co, V – all with r > 0.9 –; MnO, Sr, Zn, Cu Ni, Ba, Nd, Sc – all with r > 0.7 –; Cr – with r < 0.5 –; and SiO_2 with r < -0.89); Factor 2 with Eigenvalue 7.077, explains 23.592% of the total variable's variance and constitutes the strongest

Table 4b- Proportion of elements' variance explained in the Hamit Pluton samples.

Total Variance Explained						
Component	Initial Eigenvalues			Extraction Sums of Squared Loadings		
	Total	% of Variance	Cumulative %	Total	% of Variance	Cumulative %
1	13.684	45.613	45.613	13.684	45.613	45.613
2	7.077	23.592	69.204	7.077	23.592	69.204
3	2.010	6.699	75.903	2.010	6.699	75.903
Extraction Method: Principal Component Analysis.						

Table 4c- Component matrix of elements in the Hamit Pluton samples.

Component Matrixᵃ				Component Matrixᵃ			
	Component				Component		
	1	2	3		1	2	3
SiO_2	-.893	-.312	.107	Th	-.344	.700	.287
TiO_2	.953	-.149	.191	Pb	.111	.625	-.412
Al_2O_3	-.007	.802	-.278	Ga	.211	.723	-.170
Fe_2O_3	.992	-.083	.036	Zn	.679	.646	-.086
MnO	.823	.085	.054	Cu	.849	-.194	-.064
MgO	.923	-.213	-.054	Ni	.754	.030	-.131
CaO	.957	-.164	.000	Co	.933	-.211	-.021
Na_2O	-.318	.239	-.616	Cr	.438	.236	.035
K_2O	-.392	.325	.528	Rb	-.402	.656	.390
P_2O_5	.955	-.222	-.041	Ba	.853	-.171	-.161
Nb	.049	.931	.059	Ce	.478	.787	.250
Zr	.239	.877	-.187	Nd	.773	.327	.345
Y	.411	.089	.545	La	.308	.823	.221
Sr	.884	-.157	-.108	Sc	.814	-.108	.007
U	.058	.707	-.373	V	.952	-.118	.102

Extraction Method: Principal Component Analysis.
a. 3 components extracted.

correlational relationships with 33.3% of the elements (Nb with r > 0.9, Al_2O_3, Zr, U, Th, Pb, Ga, Rb, Ce and La – all with r > 0.7); and Factor 3 constituting strongest correlational relationship of 10% of the elements (Na_2O < -0.5, K_2O and Y – all with r > 0.5), has initial Eigenvalue 2.010 explaining 6.699% of the total variable variance. In summary, 56.7% of all the elements show their strongest positive relation in component 1, while 33.3% of them show their strongest positive relationship in component 2 and 10% in component 3. Scree plot diagram (Figure 4) also shows that there are three components for these elements.

3. Discussion

The boxplot, figure 2, actually reveals particular samples with elements that could possibly have affected the fairly normal distribution of the elements with the Hamit Pluton. 88.24% (15/17) of the elements (SiO_2, TiO_2, Fe_2O_3, MnO, CaO, K_2O, P_2O_5, Sr, Th, Zn,

Cu, Co, Ba, Nd and Sc; with the exception of LREEs La and Ce) have skewness ranging from approximately symmetrical to moderately skew.

Comparing figure 2 and figure 3a, Cluster 1 contain samples with most of the anomalous concentration of elements – only in some or all of these samples that high anomalous concentration of Al_2O_3, Nb, Zr, Rb are observed. La and Na_2O show both high and low anomaly, except in S41; Cluster 3 contains majority of the samples, that is 50.8% (32/63); and in contrast to Cluster 1, some of its samples instead show low anomalous concentration of Al_2O_3, Nb, Ce and La, with exceptions of high anomalous concentrations of Na_2O (S41), Y (S44 - S46) and Ce (S36). Cluster 6 is the second largest cluster with 25.4% (16/63) of the samples. Here only few samples S5, S6, S9 and S13 do have anomalous concentrations (MgO, one of the abundant oxides in the earth crust). In Clusters 4, 5 and 7 no sample was identified with an anomalous concentration of any elements.
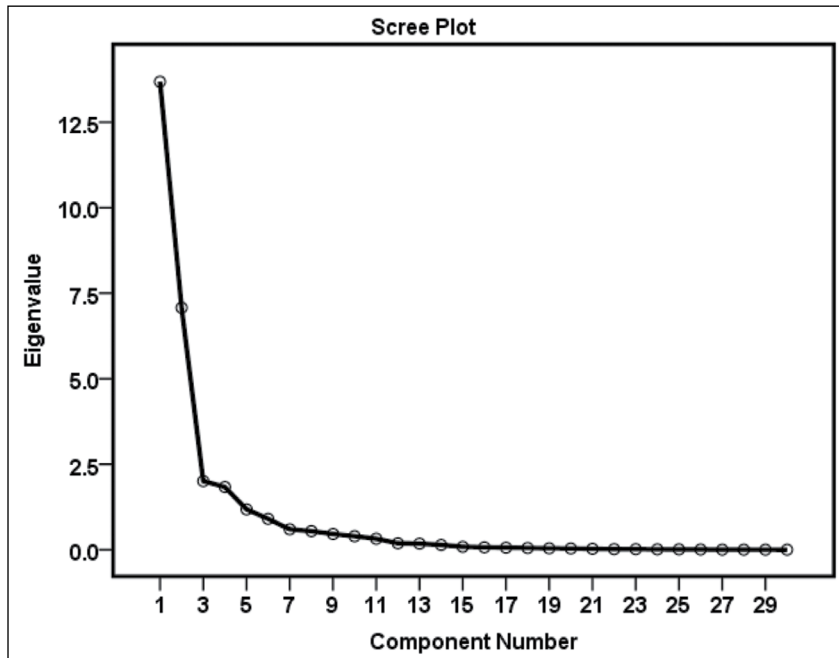
Figure 4- Scree plot showing a visual presentation of factor analysis.

It can be observed from the dendrogram (Figure 3a) that the 7 clusters can be grouped into two, with each group containing clusters with samples that show close correlation with each other. That is Group 1 (clusters 1, 2 and 3) and Group 2 (clusters 4, 5, 6 and 7). It is clear that the 2 groups of clusters of the samples show a great disparity in their similarity of element content. Group 1 contains all the samples showing most of the anomalous concentrations of major, trace and REEs (but for 4 samples in Group 2 indicating anomalous concentrations only in MgO). It is also observed that all the elements indicating anomalous concentration in Group 1 are well-loaded in the second component of the Principal Component Analysis (PCA) as shown on table 5, a probable indication that samples of Group 1 may have probably being originated from a different source and most likely crustal contamination.

According to correlation analysis of the samples, the fact that the samples show possibility in homogenous combination of elements, it means their elements could possibly be from the same source or origin. In addition, elements with the "very strong" and "strong" correlational relationships are also considered to be from the same "initial" source (Yalcin et al., 2015).

Majority of the elements demonstrating a "very strong" correlational relationship ($r > 0.8$) according to Pearson correlation coefficient are best-loaded on component 1 (Table 4c) are mostly heavy and/or high temperature elements and mostly mantle abundant elements.

Comparing the trace element averages (Figure 5) of the Hamit pluton to those of the mantle and earth crust, concentrations of Zr, Sr, Rb, Ba and Ce are distinctly higher than those of the earth crust, which in turn are also much higher than those of the mantle, whereas average values for Ni and Cr in the Hamit pluton is far much lower than those of the mantle and almost similar to those of the earth crust. It could generally be observed that the averages of trace element values of the Hamit pluton are much similar to those of the earth crust than to those of the mantle.

The pattern of the 3 component matrix extraction and Pearson coefficient correlation matrix do indicate some similarities. All the elements signifying strong to moderately positive correlation with Al_2O_3 are all located within the component 2, where the highest proportion of their variances are explained; all those indicating a strong negative correlational relationship with SiO_2 are loaded on the first component where a greater proportion of their variances are also explained.

Pearson coefficient correlation of variables explain majority of the elements with their strongest
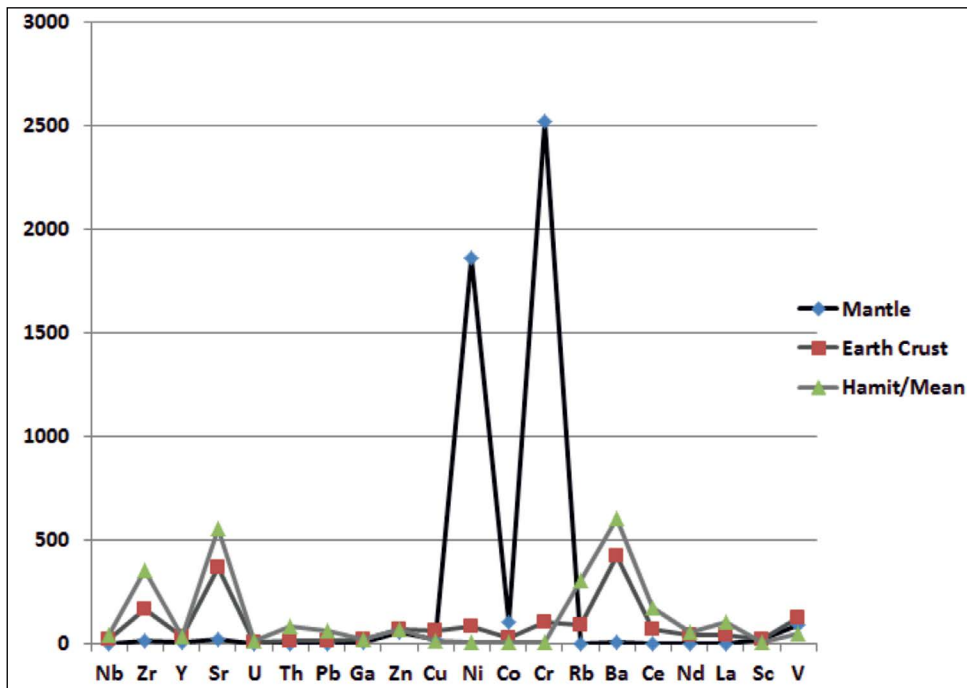
Figure 5- Comparing trace element averages in the Hamit Pluton to those of the mantle (Palme and O'Neill, 2005) and earth crust (Greenwood and Earnshaw, 1997; Lide, 2008).

correlation coefficient located in component 2, with the exception of Rb, Ce and Zr, are grouped alongside the elements of component 1, with the exception of Sr and Ba.

Ba and Sr are not being grouped with the other elements of component 1 by the Pearson variable correlation, rather grouped together separately. They are thought to have being of same source with the initial magma, which was probably and relatively very rich in Ba and Sr. The high concentration of Zr is thought to have resulted from a crustal contamination relatively rich in Zr.

Considering that most of the well-loaded elements in component 1 are mostly related to partial melting from the mantle, it was labeled to be the initial melt content of the plutonic rocks; component 2 as elements with much contribution from the crustal interaction; and component 3 as mostly crustal contamination; considering the abundance of Na_2O, K_2O and Y in the earth crust.

There was insignificant crustal contamination of MgO, Ni and Cr in some samples that might have resulted to their skewed distribution. La and Ce though are respectively left approximately symmetric to moderately skewed distribution; they are well-loaded on the second component with elements showing right skewed distribution. This could imply a significant and insignificant quantity of these elements might have come from a source different from the initial melt.

Crustal Contamination Test: LILE (e.g. Rb and K) and Zr are incompatible with respect to the major crystallizing mineral assemblage (plagioclase, augite, magnetite, and hornblende) and ratios like K/Rb and Rb/Zr do not significantly change by fractional crystallization of this assemblage (Davidson et al., 1987). Implying that variations in these ratios are preferably related to crustal contamination by assimilation and fractional crystallization processes (Davidson et al., 1987). The examination of the samples (Figure 6) illustrates wider range variance of K/Rb and Rb/Zr ratios with respect to SiO_2; indicating significant crustal assimilation is involved during the evolution of the entire plutonic suite.

4. Conclusion

The initial magma that resulted to the formation of the Hamit plutonic rock suite experienced some degree of evolution due to crustal assimilation.
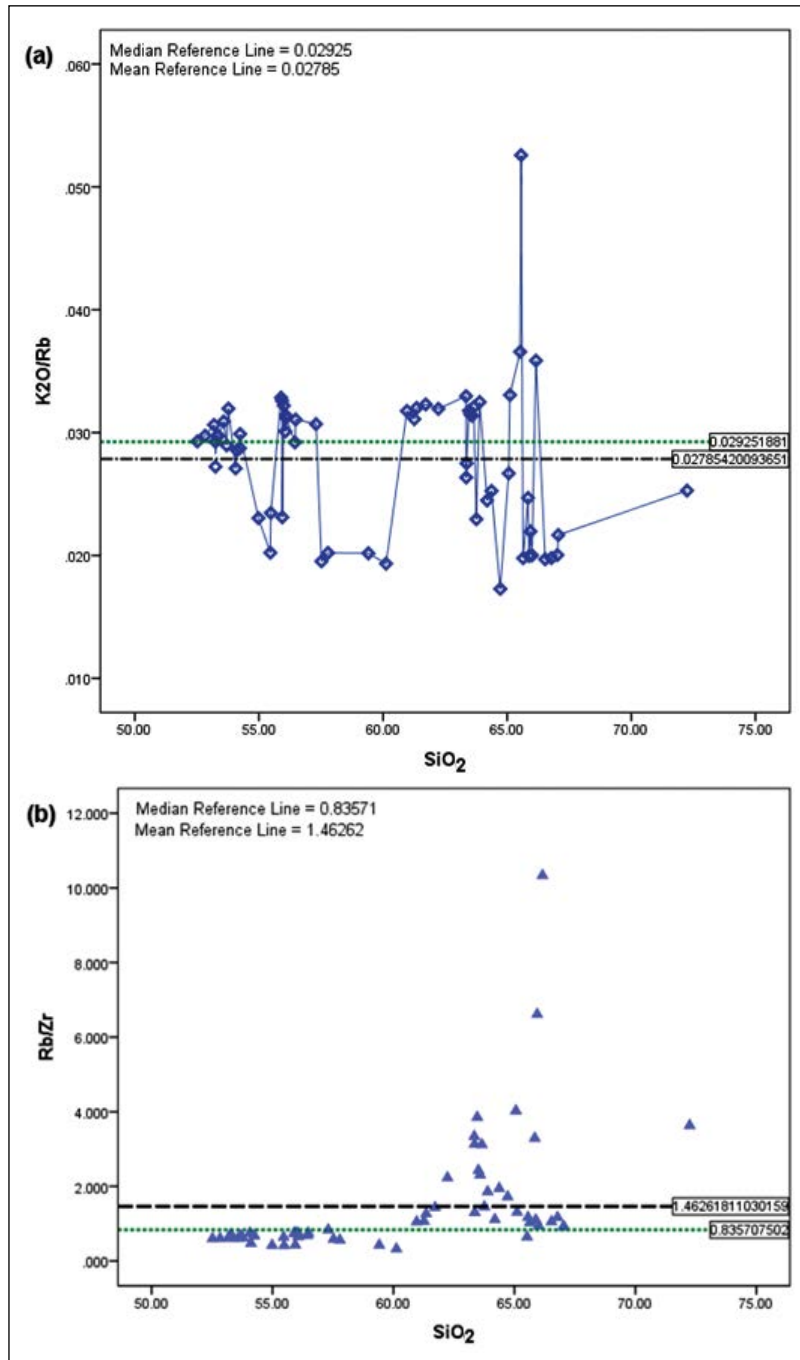
Figure 6- Variations of (a) K$_2$O/Rb vs. SiO$_2$ and (b) Rb/Zr vs. SiO$_2$.

The 63 samples studied could be divided into major 2 groups: 63.5% in Group 1 (samples 15, 16, 17, 20, 28, 29, 30, 31, 32, 33, 34, 35, 36, 37, 38, 39, 40, 41, 42, 43, 44, 45, 46, 47, 48, 49, 50, 51, 52, 53, 54, 55, 56, 57, 58, 59, 60, 61, 62 and 63) and 36.5% in Group 2 (samples 1, 2, 3, 4, 5, 6, 7, 8, 9, 10, 11, 12, 13, 14, 18, 19, 21, 22, 23, 24, 25, 26 and 27); with Group 1 containing mostly samples formed from melts whose

contents might have evolved greatly due to crustal assimilation.

The initial melt is thought to have contained "most" of the SiO$_2$, TiO$_2$, Fe$_2$O$_3$, MnO, MgO, CaO, P$_2$O$_5$, Sr, Zn, Cu, Ni, Co, Cr, Ba, Nd, Sc and V that formed the pluton, while "majority" of the Al$_2$O$_3$, Nb, Zr, U, Th, Pb, Ga, Rb, Ce and La are thought to

have been derived from the crustal contamination, and "almost all" of the Na$_2$O, K$_2$O and Y are thought to have originated from crustal assimilation

Generally, trace element values of the Hamit pluton are much similar to those of the crust than to those of the mantle, discrediting thoughts that the mantle could be a likely source for the magma. The initial magma is thought to have been very rich in Sr and Ba before subsequent contamination by the crust.

Acknowledgement

References

Akbarpour, A., Gholami, N., Azizi, H., Torab, F.M. 2013. Cluster and R-mode factor analyses on soil geochemical data of Masjed-Daghi exploration area, northwestern Iran. Arabian Journal of Geosciences 6: 3397-3408.

Bingöl, E. 1989. Geological map of Turkey, 1:2 000 000. Mineral Research and Exploration Institute, Ankara.

Boruvka, L., Vacek, O., Jehlicka J. 2005. Principal component analysis as a tool to indicate the origin of potentially toxic elements in soils. Geoderma 128: 289-300.

Child, D. 1970. The essential of factor analysis. Hold Rinehart and Winston Ltd, London, 107 pp.

Davidson, J.P., Ferguson, K.M., Colucci, M.T., Dungan, M.A. 1987. The origin of magmas from the San Pedro-Pellado Volcanic Dokhan Volcanics complex, S. Chile: multicomponent sources and open system evolution. Contributions to Mineralogy and Petrology 100: 429-445.

Facchinelli, A., Sacchi, E., Mallen, L. 2001. Multivariate statistical and GIS-based approach to identify heavy metal sources in soils. Environmental Pollution 114: 313-324.

Fitton, J.G., Upton, B.G.J. 1987. Alkaline Igneous Rocks. Geological Society Special Publication No. 30, pp. ix-xiv.

Gill, R.C.O. 1972. The geochemistry of the Grønnedal-Ika alkaline complex, South Greenland. PhD Thesis, University of Durham, UK (unpublished).

Göncüoğlu, M. C., Toprak, V., Kuşcu, İ., Erler, A., Olgun, E., 1991. Orta Anadolu Masifinin Batı Bölümünün Jeolojisi, Bölüm 1-Güney Kesim: TPAO Rapor No. 2909, Ankara (unpublished).

Greenwood, N.N., Earnshaw, A. 1997. Chemistry of the Elements 2nd edition. Oxford: Butterworth-Heinemann.

Ilbeyli, N. 1999. Petrogenesis of Collision-related Plutonic Rocks, Central Anatolia (Turkey). PhD Thesis, University of Durham, Durham, UK (unpublished).

Ilbeyli, N. 2004. Field, Petrographic and Geochemical Characteristics of the Hamit Alkaline Intrusion in the Central Anatolian Crystalline Complex, Turkey. Turkish Journal of Earth Sciences 13: 269-286.

Ilbeyli, N., Yalcin, F. 2015. Application of Factor Analysis Method to the Alkaline Geochemical Data from Central Anatolia (Turkey). Goldschmidt 2015 Abstracts, 3314.

Jöreskog, K.G., Klovan, J.E., Reyment, R.A. 1976. Geological Factor analysis. Elsevier, Amsterdam, 178 pp.

Kumru, M.N., Bakac, M. 2003. R-mode Factor Analysis Applied to the Distribution of Elements in Soils from the Aydın Basin, Turkey. Journal of Geochemical Exploration 77: 81-91.

Lawley, D.N., Maxwell, A.E. 1971. Factor analysis as a statistical method. 2nd edition Butterworth and Co., Ltd., London, 153 pp.

Lide, D.R. 2008. CRC Handbook of Chemistry and Physics, 88th edition. Boca Raton, Florida: Taylor, Francis Group.

Mitchell, R.H. 1991. Kimberlites and Lamproites: Primary Sources of Diamond. Geoscience Canada, Volume 18, Number 1, pp. 1-16.

Palme, H., O'Neill, H.St.C. 2005. Cosmochemical Estimates of Mantle Composition. pp. 1-38 in the Mantle and Core. Edited by Richard W. Carlson. Oxford: Elsevier Ltd.

Verplanck, P.L., Van Gosen, B.S., Seal, R.R., McCafferty, A.E. 2014. A deposit model for carbonatite and peralkaline intrusion-related rare earth element deposits. U.S. Geological Survey Scientific Investigations Report 2010-5070-J, 72 pp.

Yalcin, F., Ilbeyli, N. 2014. Multivariation Statistics Determination of the Hamit Alkaline Plutonic Rocks (Kirsehir-Turkey). 30th International Conference on Alkaline, Kimberlite and Carbonatite Magmatism Abstracts, 228.

Yalcin, F., Ilbeyli, N. 2015. Cluster Analysis Applied to Alkaline Geochemical Data (Hamit, Turkey). ICJMS'2015 - The 28th International Conference of the Jangjeon Mathematical Society, Antalya, Turkey, 128.

Yalcin, M.G., Ilhan, S. 2008. Major and Trace Element Geochemistry of Terra Rossa Soil in the Kucukkoras Region, Karaman, Turkey. Geochemistry International (Geokhimia) 46: 1038-1054.

Yalcin, M.G., Simsek, G., Ocak, S.B., Yalcin, F., Kalayci, Y., Karaman, M.E. 2013. Multivariate Statistics and Heavy Metals Contamination in Beach Sediments from the Sakarya Canyon, Turkey. Asian Journal of Chemistry 25: 2059-2066.

Bulletin of the Mineral Research and Exploration

http://bulletin.mta.gov.tr

Mineral resource estimation using a combination of drilling and IP-Rs data using statistical and cokriging methods

Kamran MOSTAFAEI[a*]   and Hamidreza RAMAZI[a]

[a]Faculty of Mining and Metallurgical Engineering, Amirkabir University of Technology (Tehran Polytechnic), Iran.

Research Article

ABSTRACT

The aim of this research is the mineral resource estimation using a combination of drilling and IP-Rs data. Therefore the approach of this paper is to study the correlation of induced polarization (IP) and Electrical resistivity (Rs) data with drilling data in order to grade estimation and mineral resource estimation. Reducing the boreholes number and optimization of the boreholes location is another aim of this research. The Abassabad copper mine located in Miami-Sabzevar mineralization belt northeast Iran was chosen as a case study. Within the borehole locations, geophysical profiles were designed and surveyed. After IP-Rs data inversion, 2D sections were prepared. The 3D block models of IP-Rs were constructed by geostatistical methods. The correlation between IP-Rs and drilling data were examined by statistical and geostatistical methods using regression, multivariate regression analysis, and cokriging. Based on the mentioned methods copper grade was estimated and the 3D block models of Cu grade were constructed. Obtained models were checked and compared with real Cu model compiled according to drilling data which was done after geophysical measurements. Results showed that the regression between IP data and Cu grade was more appropriate with least error. Rs data are not suitable for Cu estimation, due to changing intervals which led to increasing estimation error. Based on the suggestions of this paper, we could reduce the number of boreholes to 30% of the initial number and optimize the boreholes locations.

1. Introduction

Ore reserve modelling and estimation play crucial part in mineral exploration and exploration planning and require an extensive database that make it a costly and time-consuming process. Mineral exploration is a complex process which is carried out through integration of different methods. Building a 3D model of a deposit is the main goal of mineral exploration. The main issue is to acquire more information in less time and by lower costs. Grade estimation is the most important phase which can have a major effect on mining feasibility and its future management (Tahmasebi and Hezarkhani, 2012). Ore modeling and reserve estimation was done according to exploration studies results, such as boreholes and exploratory drifts, which are located in a grid. (Wang Q. et al., 2011).

There are numerous researches regarding ore modeling and grade estimation including ore reserve estimation by fuzzy modeling based on the spatial variability (Tutmez et al., 2007); ore reserve estimation using fractal methods in China (Wang Q. et al., 2010) using Wavelet Neural Network (WNN) and Artificial Neural Network (ANN) methods for mineral deposit evaluation (Li et al., 2010); grade estimation and reserve evaluation for Iron ore deposit in Iran (Shademan et al., 2013); grade estimation and modeling using support vector machine methods (Li

et al., 2013), combination of geostatistical and fractal methods in order to assessment of mineral resource in the Tongshan porphyry copper deposit (Wang G. et al., 2013) and management of resources and reserve in Brazil (Seccatore et al., 2014). It is noted that grade estimation and ore reserve estimation of these studies were based on drilling results.

Geophysical methods especially IP-Rs methods are widely used in earth sciences including mineral exploration, engineering geology, environmental studies and etc. We can be mentioned some case as follow; Gold-silver deposit exploration by IP in Russia (Gurin et al., 2015), Uranium mineralization detection in India (Biswas and Sharma, 2016), Bitumen exploration in Iran using IP-Rs (Mashhadi et al., 2017), detection deeply buried cave in Spain using combination of IP-Rs and gravity (Martinez-Moreno et al., 2013), sinkhole investigation in urban area using ERT and GPR (Sevil et al., 2017), investigation of coal washing waste pile in Iran by geoelectrical methods (Jodeiri et al., 2014) , investigation of landfill leaching plume using 2D and 3D ERT (Maurya et al., 2017).

In mineral exploration, geophysical surveys are predominantly carried out for anomaly separation and delineation of geological structures. However, there are some studies about grade and reserve estimation by geophysical methods including copper grade estimation in blast holes using prompt gamma neutron activation analysis (PGNAA) in Chuquicamata copper mine in Chile (Charbucinski et al., 2003), investigation of organic pollutions effect on IP-Rs measurements in laboratory based on its results detection of pollution zone in Aveiro, Portugal (Martinho and Almeida, 2006), ore reserve estimation by VES and chemical analyses (Ehinola et al., 2009), correlation between geoelectrical data and aquifer parameters in evaluation of ground water potential (Batte et al., 2010), estimation of Ni grade using crosshole seismic velocity tomography in Canada (Perozzi et al., 2012), coal quality estimation using borehole geophysical data (Webber et al., 2013), reserve estimation of limestone and sand using geoelectrical data (Ushie et al., 2014) and predicting the pyrite oxidation and transport process in coal waste pile using resistivity methods in Iran (Jodeiri et al., 2016), At large, these studies include three subjects: I) estimation of hydraulic parameters of aquifer and hydrogeological

parameters by geoelectrical data; II) estimation of grade and chemical parameters using well logging geophysical data and III) evaluation of lithology and dynamic parameters using geophysical methods that used in geotechnical investigations.

The attempt of this research was to combine geophysical induced polarization (IP) and resistivity (Rs) and drilling data to enhance copper ore modeling and grade estimation. In contrast of drilling, IP-Rs surveying is fast, continuous and cheap so it can cover more areas. Therefore combination of IP-Rs and drilling, can save time and cost in exploration. Therefore, in the first stage of this study, IP-Rs surveys were carried out in the available borehole locations and then inversion and modeling of IP-Rs data was conducted. After that the relationship between grade and IP-Rs has been checked and established in the borehole locations using statistical methods including regression and multivariate regression analyses (MRV) and cokriging. Finally, the 3D block model of the deposit was constructed that used for grade prediction and ore reserve calculation in the all of the study area. Studying the spatial relationships of IP and Cu on one hand and applying the spatial regression to predicting the Cu grade based on the other regionalized variable is a new method which has been assessed in one case study.

2. Methods

2.1. Induced Polarization and Resistivity (IP-Rs)

In mineral exploration, geophysical methods are used for measurement of physical features of bodies or rocks, also especially, for identification of differences between studied targets. Geophysical exploration can be used to detection the mineralization properties by measuring physical properties directly (Gadallah and Fisher, 2009). Recently, application of geophysical exploration is increasing due to optimization in cost and time (Mostafaie and Ramazi, 2015). The base of geophysical methods is the identifying the contrasts of physical properties in materials. (Telford et al., 1990). Geophysical method(s) selection for a mineral deposit exploration depended on physical properties of mineral target and its accompanied rocks geological setting, and also its topography. Integrated geophysical methods are commonly used in mineral exploration to obtain qualified results and more

certain results (Mandal et al., 2013; Biswas et al., 2014; Mandal et al., 2015). Electrical resistivity (Rs) and induced polarization (IP) are the most commonly used and the oldest subset of geophysical exploration (White et al., 2003; Dahlin and Loke, 2015). The measured parameter in geoelectrical surveys is apparent resistivity that shows by Rs (Loke and Dahlin, 2002). The base of IP method is the study of secondary electric fields that generated in ground by electric currents. IP observation are performed in time or frequency domains. In the time domain, the decay voltage is measured as a function of time while in the frequency domain, apparent resistivity p, is measured at two or more frequencies, generally below 10 Hz. The measured parameter in IP survey is apparent chargeability (Dahlin et al., 2002).

There are many arrays in IP-Rs surveying, but dipole - dipole, pole - dipole, Wenner and Schlumberger arrays are the most commonly used. Dipole - dipole array that is more conventional in profiling is sensitive to horizontal resistivity variations but very low sensitivity to vertical variations. It also has low depth of investigation compared to other conventional arrays like Wenner and Schlumberger. The other disadvantage of dipole - dipole array is that its pseudo-sections could be very different from the real geological structures (Loke, 2015).Wenner and Schlumberger arrays cannot be used for profiling. Although the conventional arrays (e.g. Dipole-Dipole, pole- Dipole, Wenner, and Schlumberger) have been used in many mineral exploration studies successfully, in some topographical and geological conditions especially in thin and high dip-angle mineralized vines, these arrays may not lead to satisfying results (Mostafaie and Ramazi , 2015).

Regarding the mentioned factors and problems, Ramazi and Mostafaei (2013) tried to design a new array, which lacks some of the mentioned problems, provides a good image of the subsurface, and can be used practically in the field, especially for one channel measurement systems. The designed array is named CRSP that is the abbreviation of (Combined Resistivity Sounding and Profiling). CRSP is a combination of sounding and profiling which can lead to good results in mentioned geological conditions (Ramazi and Mostafaie, 2013). This array (CRSP array) has successfully been applied in many exploration and/or site investigation projects using

IP-Rs studies. For more information on CRSP array please refer to Ramazi and Mostafaie, 2013; Ramazi and Jalali, 2014; Mostafaie and Ramazi, 2015; Amini and Ramazi, 2016*a, b*.

2.2. Regression

Regression is a subset of statistical methods that used to estimate the relationship between variables. Regression has several techniques for modeling and analyzing variables that focus on identifying the relationship between a dependent variable and one or more independent variables (Howarth, 2001). Regression techniques are widely used for prediction, and also used to understand which among the independent variables are related to the dependent variable, and to explore the forms of these relationships (Armstrong, 2012).

According to data and research goal, there are several types of regression such as linear, logistic, polynomial, ridge and etc., (Faul et al., 2009). Linear regression is the simplest type of the regressions where there are two correlated random variables; X and Y. The outcomes generate a cloud of data in the plane X-Y and we want to determine the best affine function Y=aX+b that fits the observations (Howarth, 2001). In most cases, including this study, linear regression dose not satisfactory results so we should use the nonlinear regression that include several methods. The polynomial models can be used in those situations where the relationship between variables is curvilinear. Sometimes a nonlinear relationship in a small range of explanatory variable can also be modeled by polynomials (Helsel and Hirsch, 2002). This model depends on the number of variables. For one variable the polynomial model is given by eq.1.

$$Y = B_0 + B_1 x_1 + B_2 x^2 + ... + B_n x^n \qquad (eq.1)$$

Where

Y; dependent variable*, x;* independent variable, B_0 to B_n*;* constant number

2.3. Multivariate Regression Analyses (MRA)

Functions obtained from regression analyses are usually used to describe the relationship between response and predictor variables (Chiou et al., 2016). Multivariate regression analysis is a method with one

dependent and many independent variables (Braglia et al., 2012; Zhang and Goh, 2016). In this method, it is assumed that a dependent variable (Y) is expressed as the function of independent variable (Xi):

Y=f (Xi)

The regression type depends on the type of obtained function so that if the function was linear the regression is called linear and if the function was non-linear the regression is called non- linear (Granian et al., 2015).

The general form of the model is as follows:

$$y = \alpha_0 + \alpha_1 x_1 + \alpha_2 x_2 + ... + \alpha_n x_n + \varepsilon \qquad \text{(eq.2)}$$

That in this function y is dependent variable, x_1 to x_n are independent variables and a_0 to a_n are regression coefficient. In linear regression analysis, the regression coefficients are calculated by least square method. In linear regression analysis, correlation coefficient (R^2) can be obtained from the following equation:

$$R^2 = \frac{\sum_{i=1}^{n}(\hat{Y}_i - \overline{Y})^2}{\sum_{i=1}^{n}(Y_i - \overline{Y})^2} = 1 - \frac{\sum_{i=1}^{n}(Y_i - \hat{Y}_i)^2}{\sum_{i=1}^{n}(Y_i - \overline{Y})^2}$$

In this equation $\hat{Y}i$ is calculated value of ith sample of dependent variable, $\overline{Y}$ is mean of the variable and Y_i is the value of ith sample of the dependent variable (Braglia et al., 2012). If R^2 is close to 1, it means the result is desirable if R^2 is closed to zero this means that dependent and independent variables have not correlation (Mogaji, 2016).

Multivariate regression has been shown to suitable model for various earth sciences studies. Over the past few years, multivariate regression analysis was used widely in different earth sciences for predicting various objectives (e.g., Noori et al., 2010 ; Khanlari et al, 2012; Mokhtari, 2014; Habibi et al., 2014; Granian et al., 2015). Therefore, multivariate linear regression has been used to obtain the relationship between IP, Rs and copper grade in the Abassabad copper mine.

2.4. Cokriging

Geostatistics aims at providing quantitative descriptions of natural variables distribute in space or in time and space (Chiles and Delfiner, 2012). Geostatistics is the application of statistical estimation

techniques considering the spatial correlation between data. Spatial correlation data, including distance and direction, can be expressed in mathematical form, considering the spatial structure. Spatial structure is studied by means of a variogram in geostatistics (Mostafaie et al., 2014). Geostatistical methods was developed for estimation of the regionalized variables such as grade in ore body at a known location. Regionalized variables are variables of a phenomenon defined in space (and/or time) that possesses a certain structure (Kumar et al., 2007). Kriging is an optimal interpolation based on regression against observed z values of surrounding data points, weighted according to spatial covariance values. Cokriging is kriging using information from one or more correlated secondary variables, or multivariate kriging in general (Bohling, 2005). The cokriging procedure is a natural extension of kriging when a multivariate variogram or covariance model and multivariate data are available (Wackernagel, 2003). Cokriging and kriging are subset of the geostatistical methods used for estimation and interpolation. These methods are generalized form of univariate and multivariate linear regression for estimation at a point, an area or within a volume. Cokriging methods are used to take advantage of the covariance between two or more regionalized variables that are related, and are appropriate when the main attribute of interest is sparse, but related secondary information is abundant (Deutsch and Journel, 1998).

The information available on a natural phenomenon is rarely limited to the values assumed by a single variable over set of sample points. In the most real studies (especially earth science) involve more than on variable, so we have to use the multivariate generalization of kriging which is named cokriging (Chiles and Delfiner, 2012). Using auxiliary variables we can improve the precision of a main variable. auxiliary variables usually are cheap in measuring so we can reduce the number of observations for the main variable that it is expensive and needed for optimizing the interpolations (Knotters, et al., 1995). A variable of interest is cokriged at a specific location from data about itself and about auxiliary variable in the neighborhood. The data set may not cover all data variables at all sample locations. Ordinary cokriging requires at least on data value about the variable of interest, while simple cokriging, relying on its knowledge of the mean, can be performed with data solely about the auxiliary variables (Wackernagal,

2003). As mentioned before, cokriging method consisted of one primary and one secondary variable. Moreover, spatial structure should be studied in any geostatistical method. So in the cokriging analyses, the cross semi-variogram (or cross-variogram) should be determined in prior (Hooshmand, et al., 2011). There are some method for coregionalization model investigation such as: linear model of coregionalization (LMC); Markov-type model; intrinsic linear model (Madani and Emery, 2018). The linear model of coregionalization (LMC) is the one of the approach to simultaneously model direct and cross variogram in a multivariate setting. An LMC is suitable in cokriging and cosimulation (Leuangthong et al., 2008, Goulard and Voltz, 1992).

The measurements available for different variables in given domain may be located either at the same sample points or at different points for each variables. Complete heterotopy: the variables have been measured on different sets of sample points and have no sample locations in common. Partial heterotopy: some variables share some sample locations. Isotopy: data is available at all sampling points (Wackernagal, 2003). The sampling is partially heterotopic in this study. By considering the data located in a neighborhood of the target location and data distribution situation, the search strategies to select neighboring data will be selected. There are some search strategies including: collected neighborhood,

multi-collected neighborhood, full neighborhood (Chiles and Delfiner, 2012, Madani and Emery, 2018). In collected cokriging only retained secondary data are the ones available at the target location (Madani and Emery, 2018). The collected cokriging and full cokriging have been used in this study.

For more information about Cokriging in ore modeling and grade estimation refer to Knotters et al., 1995; Boezio et al., 2011 and Xu et al., 2015.

3. Case Study-Abassabad Copper Mine

The Abassabad cooper mine is an active mine that is located 120 km East of Shahrud, Semnan Province, Northeastern Iran. This mine is located 10 km north of Abassabad village, named Abassabad copper mine. The location map are presented in figure 1.

From the geological point of view, Abassabad is a part of a wide mineralization belt named Miami-Sabzevar copper belt. There are many lithology units in all of the Miami-Sabzevar copper belt including 2 major geological units: igneous rocks (porphyritic andesite and tracchyandesite) and sedimentary rocks (limestone with marl). Mineralization has occurred in the contact of andesite and limestone. The geology map of Abassabad was presented in figure 2. Based on the geology map there are some lithology units include porphyritic tracchyandesite, conglomerate,
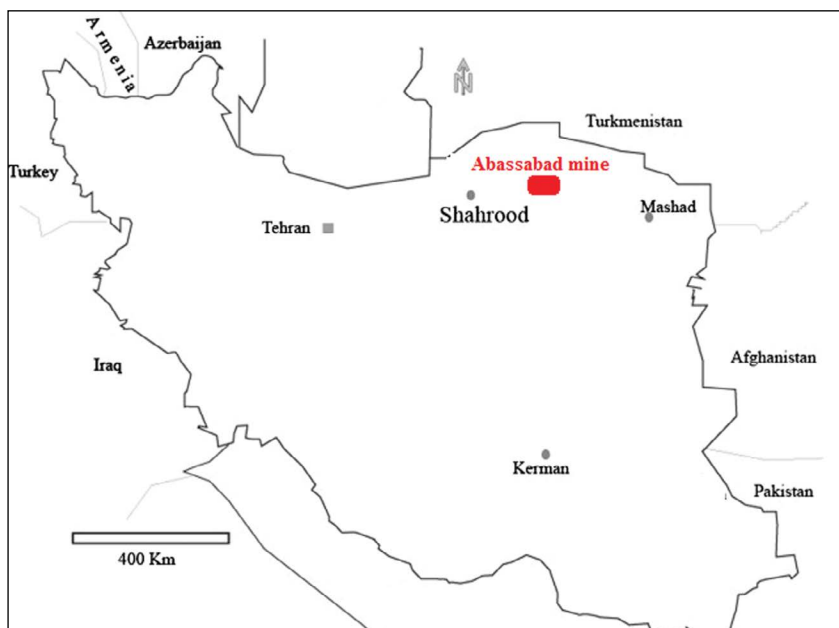
Figure 1- Location of Abassabad copper mine (case study) in Iran.
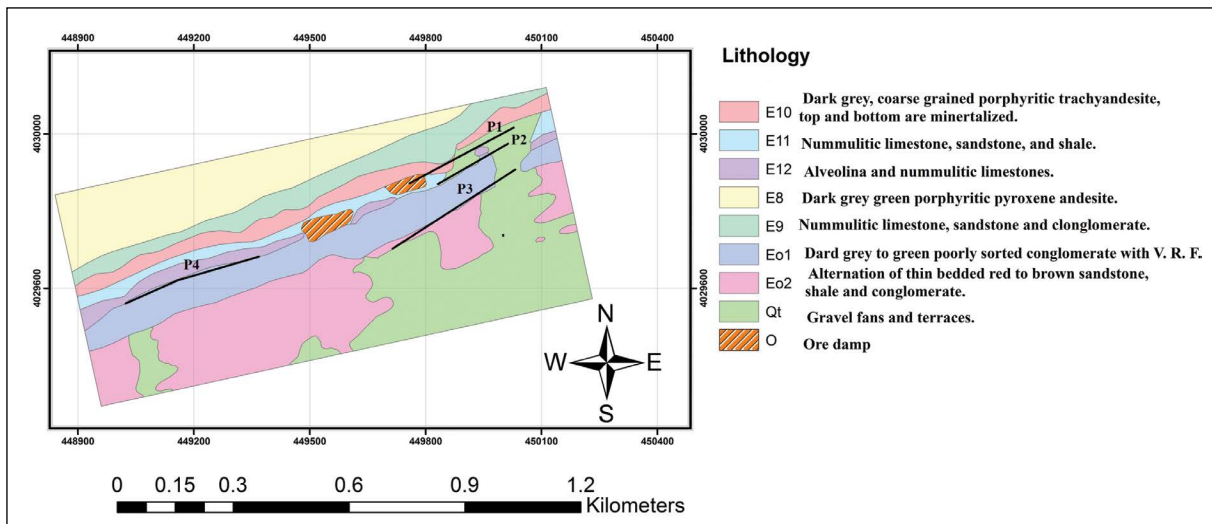
Figure 2- Geological map of Abbasabad copper mine (study area) and IP-Rs profiles location.

limestone, sandstone and shale. Quaternary alluvium occur in some locations. Sedimentary rocks consist of limestone, and in some parts clay minerals were converted to marl. Mineralogy studies shows that limestone is a geochemical barrier to settle the copper content. Limestone caused deposition of copper minerals so mineralization has occurred in the contact of andesite and limestone. According various studies such as; to mineralogy, petrology, alteration and economic geology, this deposit is Manto-type copper deposit (Salehi et al., 2016).

4. Results

In this research, the integration of IP-Rs data and grade data for construction of 3D block model and resource estimation was investigated. For this purpose, the Abassabad copper mine was selected which is an active copper mine in the Semnan Province, Northeastern Iran. In the first step, geophysical surveying was performed in the exploratory boreholes. Then, inversion of obtained data carried out using Res2Dinv software package and 2D sections were prepared. Based on the geostatistical methods, 3D block model of IP-Rs were prepared in the study area. In the second step, the relationship of IP-Rs data and the copper grade was checked out. Based on correlation between IP and Cu grade obtained by regression, Cu grade was estimated in all of the study area and the 3D model of Cu grade was prepared. Then the relationship of IP-Rs data and Cu grade were calculated by multivariate regression analyses (MRA).

Based on the MRA results, Cu grade was estimated and the 3D model of Cu grade was obtained. Based on the obtained model, 7 boreholes were proposed. The accuracy of grade estimation and prepared models was checked out by new exploratory boreholes. Then prepared models -using regression and MRA methods- were reviewed and remodeled by adding new drilling data. For more accuracy and comparison, cokriging was used. Relationship of IP values and Cu grade was examined and Cu grade was estimated and then, 3D model of Cu was prepared using cokriging. Finally estimated Cu grade and obtained Cu models were compared. Prepared models based on the IP-Rs data and Cu grade were compared with real block model of Cu grade.

4.1. Geophysical Results

In the first stage, location of profiles were detected then data surveying was done. Data inversion was done by Res2Dinv and the 2D imaging of profiles is prepared. The 3D model of data was prepared based on geostatistical methods. Also for the determination of the IP-Rs data thresholds, statistical methods and fractal methods were used. The result of 3D modeling was checked out by geostatistical methods and drilling results.

4.1.1. Designing and Surveying Data

Based on the exploratory borehole plan, the IP-Rs profiles were designed. Geophysical profile position was chosen in a way that it covers most of exploration boreholes (Figure 3). According to the mineralization
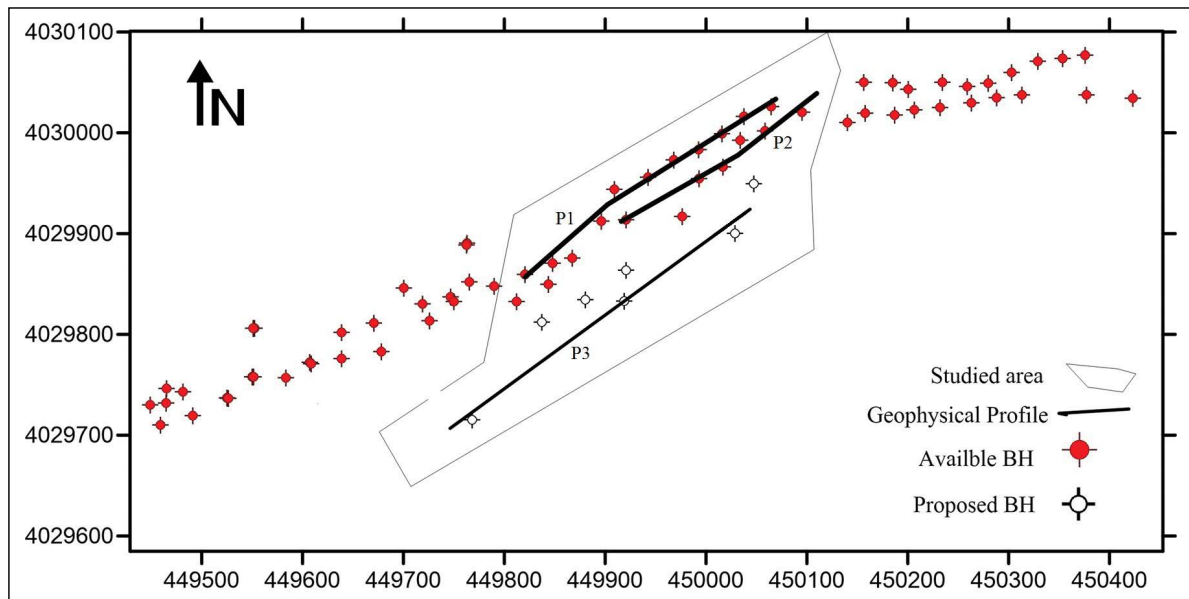
Figure 3- Map of study area in Abbasabad mine and the location of available BH and geophysical profiles also proposed BH after geophysical modeling.

type, mine situation and surveying conditions, CRSP (combined resistivity sounding and profiling) array was selected for this investigation. CRSP array is a combined array which can lead to useful results in the various topographical and geological conditions (Ramazi and Mostafaie, 2013). Therefore, IP-Rs data have been surveyed by using CRSP array. Generally, 4 profiles were designed and surveyed. Three profiles P1, P2 and P3 are parallel. P1 and P2 were surveyed along borehole profiles with 10 meters electrode spacing. P3 and P4 were surveyed for the evaluation of IP-Rs results, therefore along these profiles there are no exploration boreholes. P3 was located 50 meters south of P1 and P2, and is also parallel to them. The electrode spacing of P3 is 20 meters. P4 is located 500 meters from the western part of the others by 10 m electrode spacing. Finally, 2000 points were read in the length of all profiles. In each point, resistivity and induced polarization in time domain have been recorded. Also the drilling data of 20 boreholes was available.

Data acquisition has been carried out according to designed plan field in 09/01/2017 to 09/22/2017. In order to check the data quality, several measurements were randomly repeated in the field. The surveyed data was revised, the data accuracy was checked out, and then data processing was done.

4.1.2. Inversion Results

As mentioned earlier in this paper, IP-Rs data inversion was done in the first stage resulted in 2D IP-Rs imaging. The resistivity and IP data sets were inverted using the RES2DINV software. To prepare IP-Rs sections, the resistivity and IP data sets were inversed by the Newton and Gauss–Newton methods, from the RES2DINV software package (Loke and Dahlin, 2002). In the inversion process number of iterations were 5. The best iteration was selected based on the RMS error and geological situations. The RMS error level is between 3.2% to 5.5% for IP data, and RMS error is between 8% to 12.5% for resistivity data. The inversion results determined as IP and resistivity sections shown by the surfer software. Inversion results and compiled sections are presented in figure 4 for profiles 1 to 4. Anomaly values were defined based on the fractal methods. Due to the data, the "concentration–area" method (Ferdows and Ramazi, 2015) has been used in this research for separation of the anomalous value from the background. The obtained threshold correlated with drilling results and the obtained threshold was modified. The threshold of the inversed IP data is equal to 25 mV/V and the threshold of inversed Rs data is 250 Ωm. According to the obtained results of the geophysical study and those correlated with the drilling data, it may be say that resistivity and IP
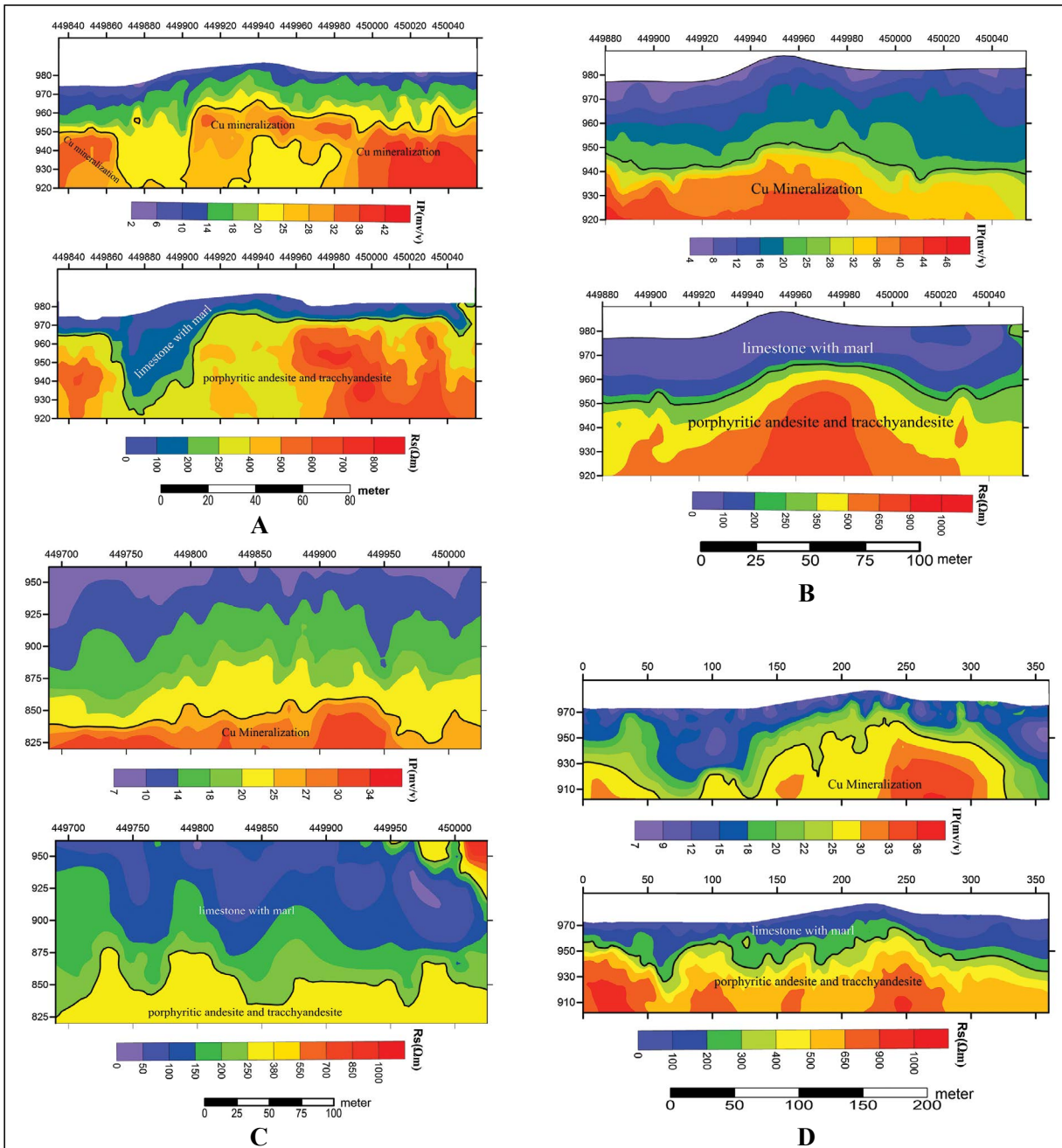
Figure 4- Inverted resistivity (Rs) and induced polarization (IP) sections with topography; A) Profile1, B) Profile2, C)Profile3, D) Profile4.

section could detect mineralization zones so well. In the profile locations, the mineralization was traced with acceptable accuracy by a high value of resistivity and IP. The efficiency of IP-Rs in the Abassabad copper mine is high and this investigation reduced and optimized the drilling operation efficiently. For further investigation and optimization of the exploration boreholes, we need a 3D model of the study area. By

a 3D model, we can investigate the area between the profiles and also all of the study area.

4.1.3. 3D Modeling

After inversion and preparation of 2D sections presented in figure 4, the 3D models of IP-Rs data were obtained based on the geostatistical methods. In this study, data of P1, P2 and P3 were used for modeling,

because these profiles were parallel and the distance between them was less. As mentioned, P4 is located 500 meters from the western part of the other profiles, so we cannot use it in modelling. In geostatistics, the variables with spatial structure are investigated. In the other word, spatial structure is essential for using geostatistical methods. The variogram is a fundamental tool in geostatistics for investigating spatial structure because it provides critical parameters for various Kriging estimators. Accuracy of the proposed parameters from the variogram are of crucial importance and can have significant positive or negative influence on the estimated blocks (Mostafaie et al., 2014). In order to study the spatial structure, the data were reviewed and variography was carried out. According to the above factors and applying the

related software such as (SGeMS) (Bohling, 2007) experimental variogram for data were calculated and presented scientifically. Variogram for various parameters such as different azimuth and dip were calculated. The appropriate theoretical models based on the least square differences were fitted to the variogram (Figures 5 to7).

Variogram models and parameters for maximum range; median range and minimum range that are perpendicular each other and essential for modeling are presented in table 1 briefly. The angels of anisotropy were obtained for X, Y and Z respectively, -30, 0 and 120.

In the next step, 3D modeling was done based on the obtained parameters of the variography. Datamine
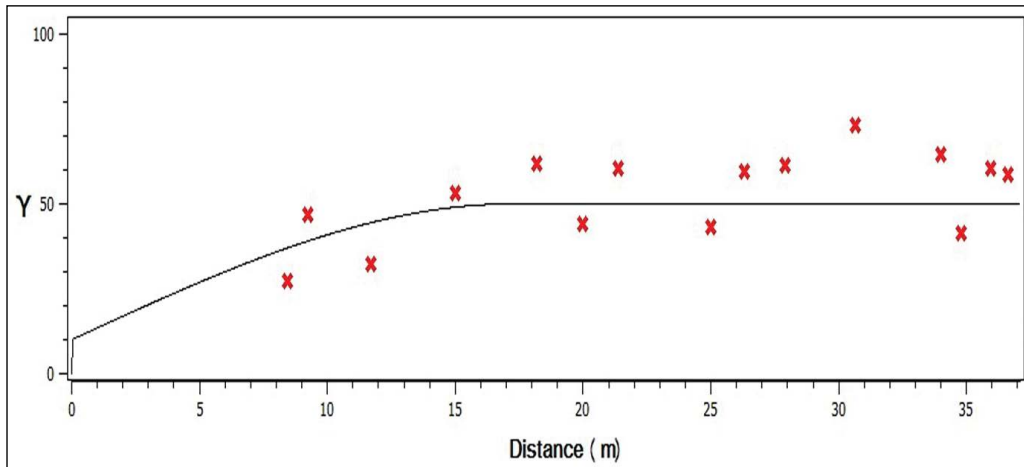
Figure 5- Variogram model for minimum range of data (azth: 330, dip: 30).
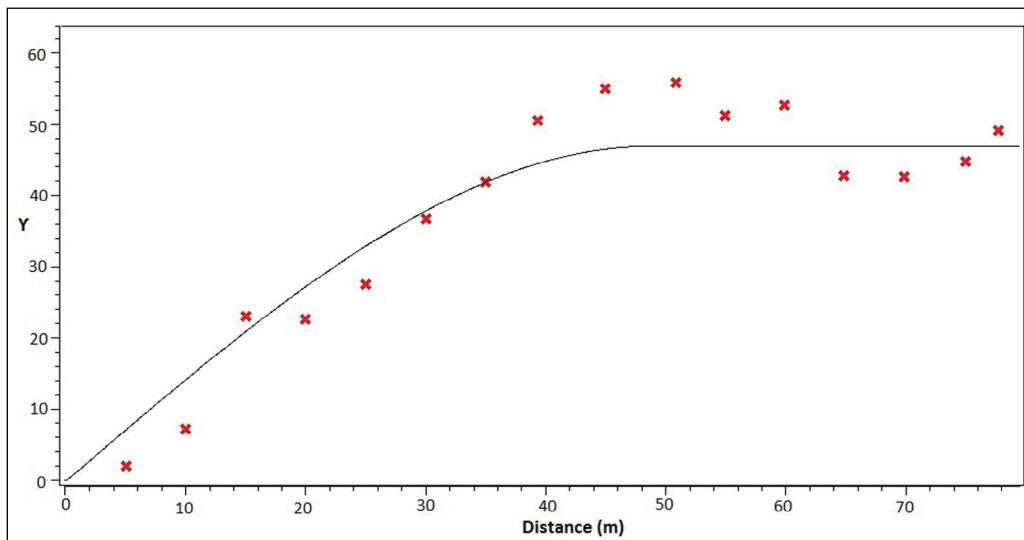
Figure 6- Variogram model for median range of data (azth: 150, dip: 60).
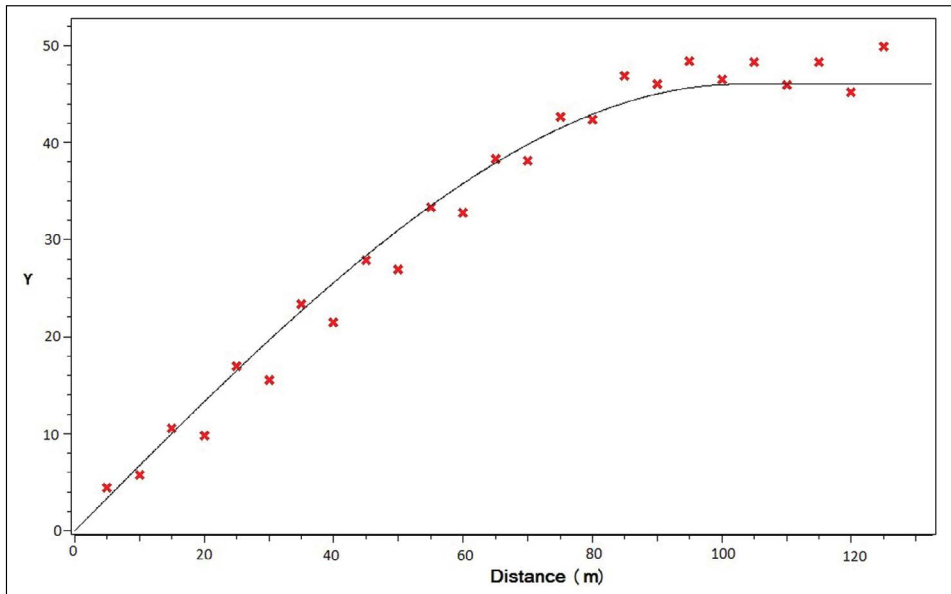
Figure 7- Variogram model for maximum range of data (azth: 60, dip: 0).

Table 1- Obtained parameters of presented variogram.

Azimuth	Dip	Model	Range(m)	Sill(mv/v)²	Nugget effect(mv/v)²
330	30	Spherical	18	50	10
150	60	Spherical	50	50	0
60	0	Spherical	102	50	0

Studio3 software package was used to prepare 3D models. The input data of Datamine Studio3 software were two-dimensional modeling results obtained from inversion. As we know the output of inversion including X, Y, Z, IP-Rs for each point that were prepared to input dataset as continuous data according to the setting of Datamine database. The input data were composited and the composite length was selected 5 meters. Then, the 3D block models of IP-Rs were prepared by Datamine Studio software. The two models include induced polarization (IP) and Resistivity (Rs) are presented as a 3D block model in figures 8 and 9, respectively. It should be noted that the block size were identical and equal to 5 meters in the whole of the model. In these models, IP-Rs parameter distribution has been shown with high accuracy and the mineralization zone is marked in different directions. Maximum value of the IP is 45 mv/v and the maximum value of resistivity is 850 Ωm. The threshold of IP is 25 mv/v and the Rs threshold is 250 Ωm. IP-Rs models show that high values of IP-Rs are the anomalous values. In the other word, anomaly value is the location with high value of the IP-Rs. Based on the 2D section and the 3D model of geophysical results, 7 boreholes were proposed

and drilled (Figure 3). Drilling data confirmed the geophysical results. In the drilling planning of this mine, boreholes were drilled at a distance of 30 meters. By geophysical modelling the mineralization zone and it's characterizes including; depth, thickness, continuity were determined. Geophysical modelling showed that mineralization zone has an acceptable continuity. So the boreholes are not needed at a distance of 30 meters, and using the boreholes at intervals more than 60 meters we can obtained required data to mineralization identify. Therefore using geophysical results we were able to reduce the borehole number significantly

According to drilling results, the database includes boreholes and geophysical models was constructed. In order to better correlation the drilling and IP-Rs data combined and composited. After data composite, dataset was selected to correlation studying (Table 2).

4.2. Regression Results

As mentioned before, one of the main goal of this research is to estimate Cu grade based on the IP-Rs data in order to use regression method. Firstly,

186
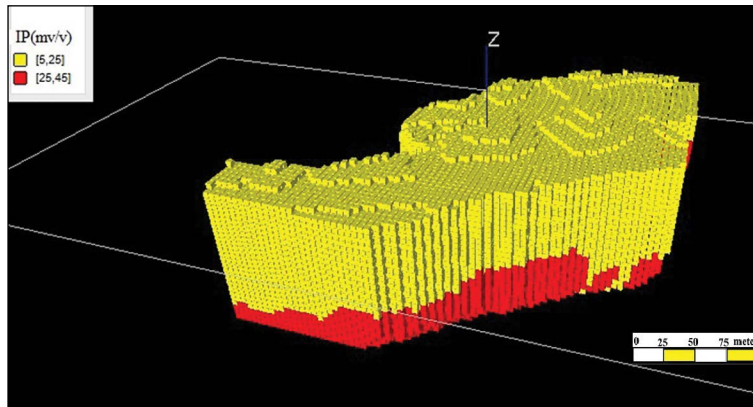
Figure 8- The results of modeling as a 3D block model for IP data in study area.
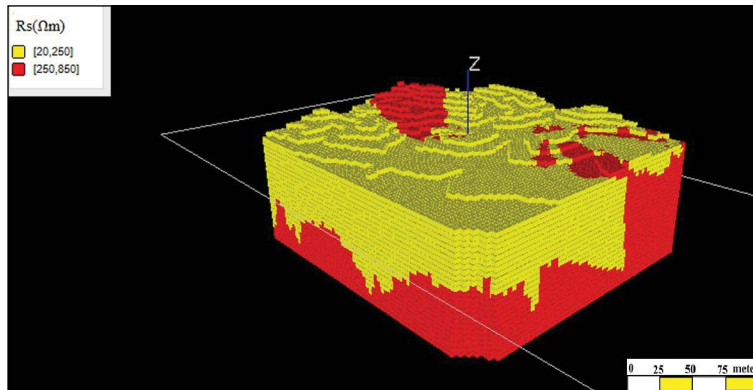
Figure 9- The results of modeling as a 3D block model for Rs data in study area.

Table 2- The statistical description of used data in this study.

Parameter	Symbol	No. of samples	Max.	Ave.	Min.	Std. dev.
Induce polarization	IP	106	46.45	25.75	11.370521	7.91
Resistivity	Rs	106	735.1	362.7	81.585678	179.5
Cu grade	Cu	106	5.4	0.74	0.002	1.08

primary statistical analysis of data was performed. In regression analysis, the relationship among variables is examined. For this purpose, correlation between IP and Cu grade were checked out. So, IP was assumed as an independent variable and Cu assumed as dependent. Therefore there is a function; Y=f(X) that X= IP and Y= Cu.

After checking the correlation between IP and Cu, the best equation was selected and the obtained result is presented in figure 10. As mentioned previously, there are several type of regression. So the polynomial regression type is selected as the best type of regression and the obtained equation (eq.3) is as fallow;

$Y= 0.0043x^2 \; 0.13x \mid 1.002$

where; X=IP, Y=Cu eq.3

The R-sq of equational.1 is about 75%, and the S is about 4.9% in this analyze that it is acceptable. It is notable that S is the standard deviation of the distance between the data values and fitted values.

Based on the IP, copper reserve was estimated in all of the study area according to equation1 and the 3D model of estimated copper was constructed (Figure 11). In this copper mine, Cut of grade was considered as 0.1%, so the model consists of two group: values less than 0.1% and values more than 0.1% in the presented models. The dimensions of the block model are selected 5*5*5 meters. Based on the block model, estimated Cu reserve is about 2.11 million ton (Table 3).

The correlation between Rs and Cu grade was checked out. The correlation coefficient between Rs

187
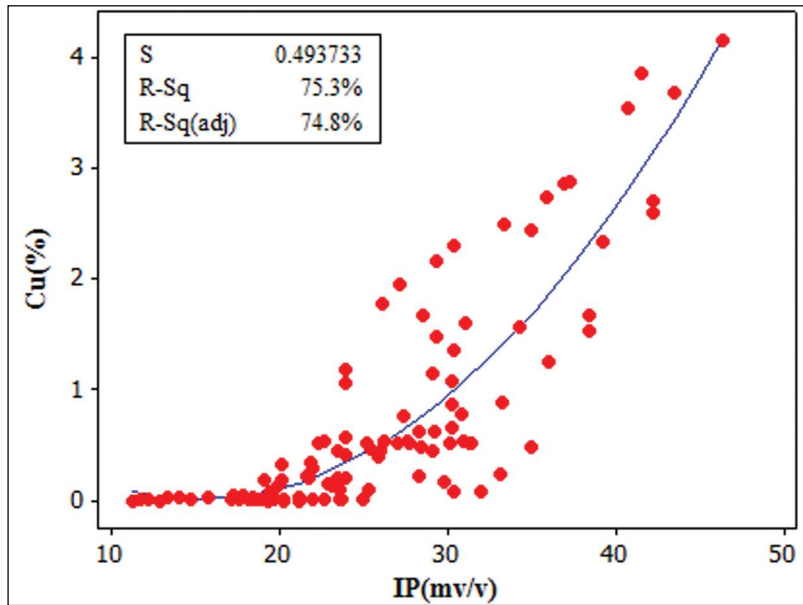
Figure 10- Diagram of Cu grade versus IP.
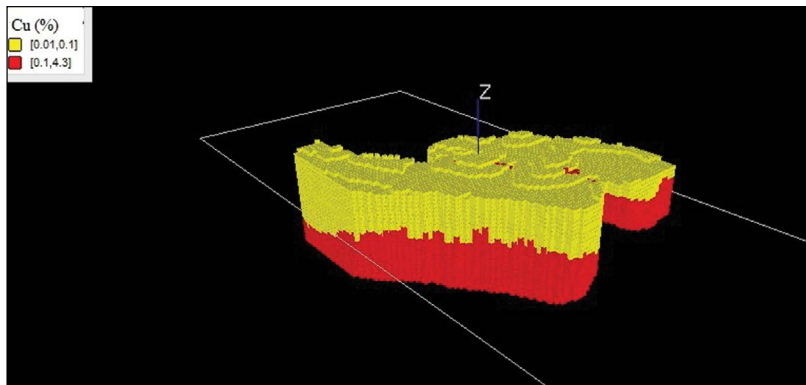
Figure 11- 3D model of the estimated Cu based on the regression results.

Table 3- Result summaries of estimated Cu using regression.

Min (%)	Max (%)	Cutoff grade (%)	Mean (%)	Block size(m)	Estimated ore(million ton)
0.05	4.2	0.1	0.78	5x5x5	2.11

and Cu grade is less than 50% that is not a satisfactory value. Therefor its results were not used in copper estimation.

4.3. Multivariate Regression Analyses (MRA) Result

In the previous part, we checked out the correlation between IP and Cu grade, and now we want to investigate the correlation between IP-Rs and Cu grade simultaneously. In the other word, we want to check the IP-Rs influence on Cu estimation together. So we used the Multivariate Regression Analyses (MRA), because as mentioned, MRA was used for

examination of one dependent and more independent variables relation. In this paper, IP-Rs values were considered as independent variables and Cu grade were considered as dependent variable in order to predict the Cu grade by IP-Rs parameters using Minitab software. As mentioned in the previous parts-2.2 regression- there are several type of regression, also in the multivariate regression analyses, there are several type of regression. After the studying these types polynomial type is selected. Then the best equation with high R-Sq. was selected based on trial and error method. The obtained equation is presented as eq.4.

Cu (%) = 5587 + 6.80 IP - 0.120 Rs - 6002 (Rs)$^{0.1}$ - 0.143 (IP)^2 - 51.0 Ln (IP) + 620 Ln (Rs) + 0.00130 (IP)^3 + 288 (Rs)$^{0.3}$ (eq.4)

Correlation Coefficient = 67.3%

Based on the eq.2 the Cu grade in the study area was estimated and the Cu 3D block model was prepared (Figure 12). The Cu reserve was estimated about 2.46 million ton (Table 4).

We mentioned cokriging method as consisted of one primary and one secondary variable. The primary statistical analyses shoed that correlation between IP and Cu is more than correlation between Rs and Cu, also the Rs data variation range is more than IP which causes an increase in estimation error level. Therefore Rs data were not used in cokriging estimation. In this paper, primary variable was Cu grade and secondary variable was IP data. Due to abundance of IP data, we attempted to estimate Cu grade using IP data. As mentioned in cokriging cross-variogram is necessary, so variography was done based on the linear model of coregionalization (LMC). At first, variography of IP and Cu grade was performed. Subsequently, cross-variogram of IP and Cu grade was calculated and required parameters were obtained (Figures 13 to 15).
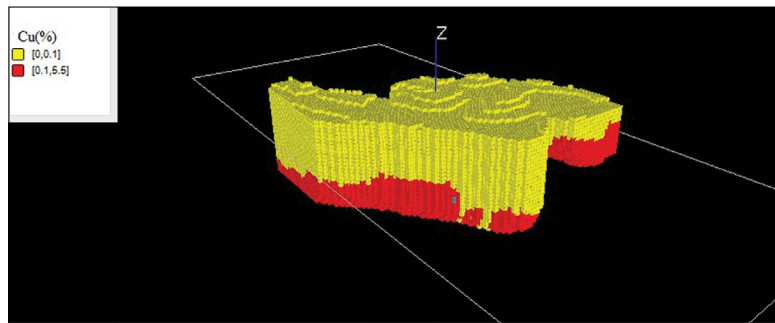
Figure 12- 3D model of estimated Cu based on the MRA results.

Table 4- Results summaries of estimated Cu using MLR.

Min (%)	Max (%)	Cutoff grade (%)	Mean (%)	Block size(m)	Estimated ore(million ton)
0	8	0.1	1.43	5x5x5	2.46
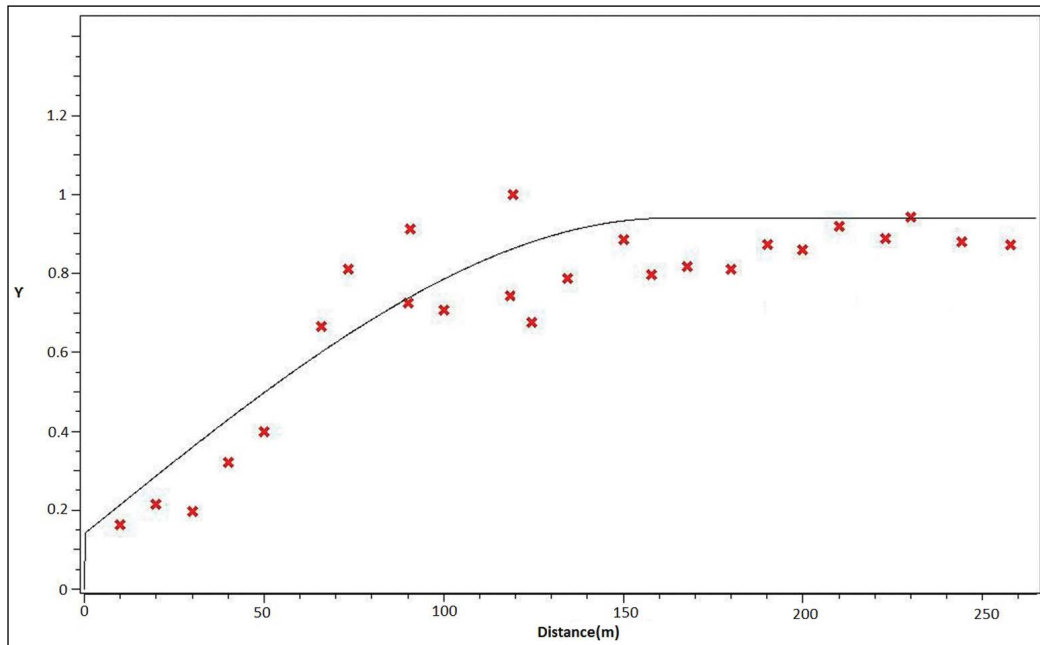
Figure 13- Variogram model for IP data.
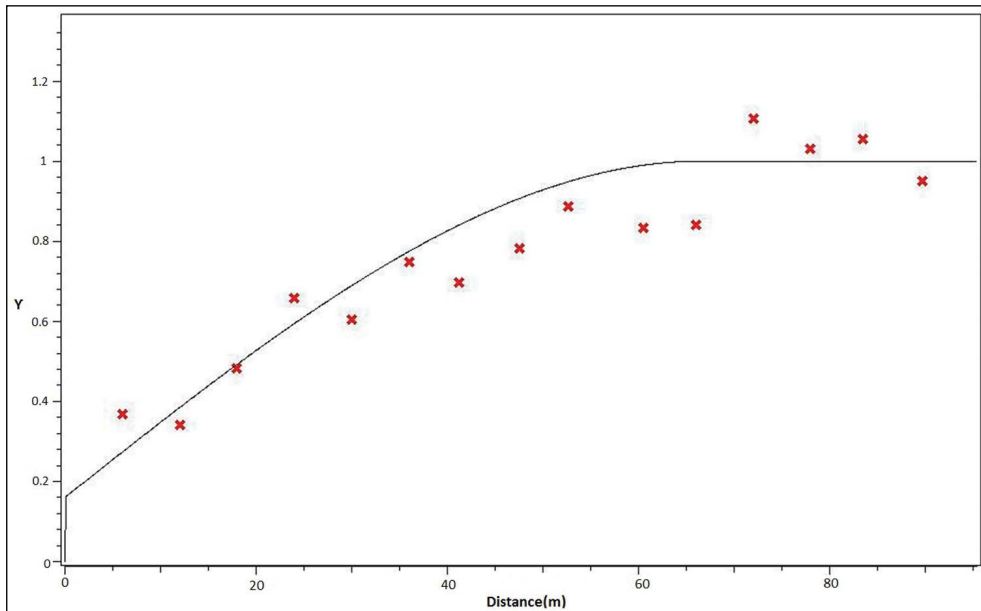
Figure 14- Variogram model for Cu data.
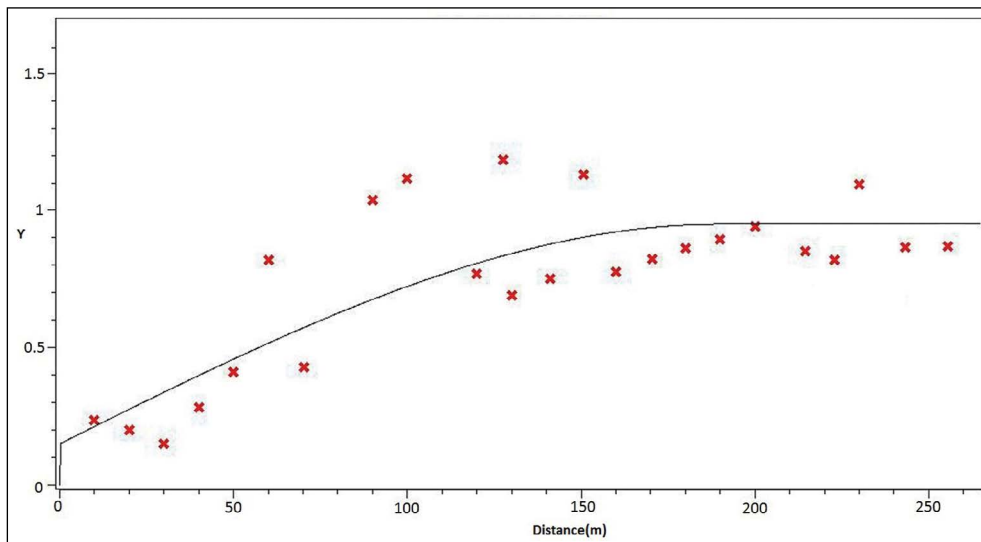
Figure 15- Cross-variogram model for IP and Cu.

The standardized variograms and their parameters presented in (Table 5).

Then according to the variogram parameters, Cu grade was estimated and the 3D block model of Cu grade was constructed by SGeMS software (Figure 16) and the results presented in table 6. In the estimation maximum and minimum of data equal to 3 and 15 respectively and also the search radius considered 60 meters in the cokriging estimation process. Ordinary type of cokriging (OK) was used for estimation. The secondary data (IP data) covers

Table 5- The summaries of used parameters in cokriging based on the standardized variograms.

Experimental semivariogram	Fitted model	sill	Range(m)	Nugget effect
IP	Spherical	1	150	0.18
Cu	Spherical	1	65	0.35
Cross	Spherical	1	185	2.6
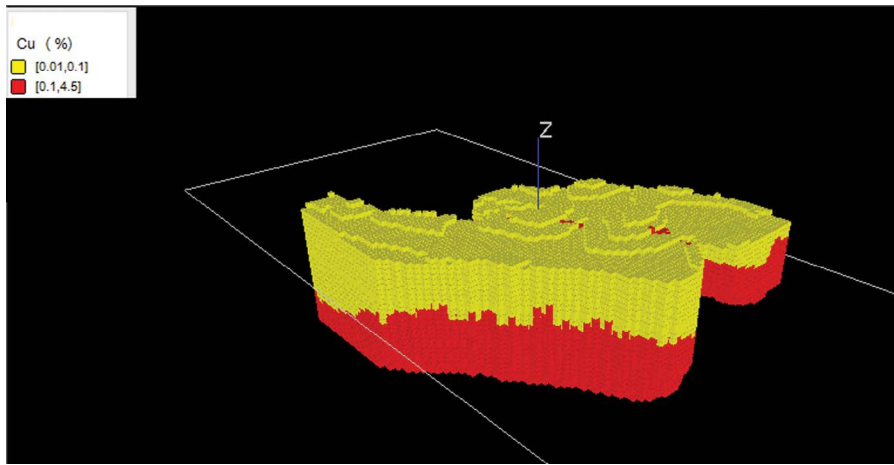
Figure 16- The 3D block model of Cu estimation using cokriging.

Table 6- Results summaries of estimated Cu using cokriging.

Min (%)	Max (%)	Cutoff grade (%)	Mean (%)	Block size (m)	Estimated ore (million ton)
0	4.44	0.1	0.92	5*5*5	1.85

the whole domain because we want to estimate the Cu grade based on the 3D block model of IP data (Figure 8 in 4.1.3). Given that the secondary data is more than primary data, so we used the full cokriging and also collected cokriging with Markov Model 2 (MM2). The results of full cokriging that it was used all data are better and acceptable, so we presented the full cokriging results in this paper. For more details see in section 4.2. Cokriging and presented explanations in (Wackernagal, 2003; Chiles and Delfiner, 2012; Madani and Emery, 2018).

5. Discussion

The Miami-Sabzevar copper belt is a wide mineralization zone that it is currently under reconnaissance and exploration. This vast areas of this belt entails high cost and time-consuming exploration activity. Thus the main goal of this research was to devise an exploration plan to overcome this hurdle. Geophysical methods are among the cheapest and fastest so we decided to use geophysical methods combined with drilling results in ore modeling. For this purpose, the active mine of Madan Bozorg in the Miami-Sabzevar belt was selected as a case study.

At first, the application of the IP-Rs methods was investigated through devising survey profiles. In the borehole locations 2 profiles were designed and surveyed. In this location, there were 20 boreholes. Obtained data was inverted and 2D sections of IP-

Rs were prepared. IP-Rs results were compared with drilling results. Then in the locations that there is no boreholes, 2 profiles were designed and surveyed. Also these data were inverted and sections were prepared (see 4.1.2). In the next stage, 3D models of IP-Rs data were prepared by geostatistical methods and the correlation between Cu grade and IP-Rs was examined. To checking obtained results, 7 exploratory boreholes were proposed, and drilled. Drilling results showed that the geophysical method could detect anomalous region for Cu mineralization, significantly. Moreover, the correlation between Cu grade and IP-Rs is appropriate and applicable (see 4.1.2).

Based on the drilling, the database includes 20 boreholes (available boreholes and drilled boreholes after geophysical modeling) was constructed. The correlation between Cu grade and IP-Rs were revised and investigated. For this purpose regression, MRA and cokriging were used and according to the obtained correlation, Cu grade was estimated in the study area. The 3D block model of the estimated Cu grade was constructed (see; 4.2, 4.3, 4.4).

As mentioned before the case study is an active copper mine, so the extraction block model based on the measured copper grade is available. The mineral reserve estimation results according to the measured copper grade presented briefly (Table.7). The obtained results showed that the estimated copper is about 1.95 million ton with 0.71% mean.

Table 7- Results summaries of estimated Cu based on the measured copper grade in Abbasabad copper mine.

Min (%)	Max (%)	Cutoff grade (%)	Mean (%)	Block size (m)	Estimated ore (million ton)
0.006	6.8	0.1	0.71	5*5*5	1.95

The obtained models based on the combination of IP-Rs and drilling data were compared were compared with actual Cu models, according to this we can say the obtained results are acceptable.to better comparison, we calculated the estimation error of obtained models over the actual model (Table 8).

Table 8- The error level of estimation methods over actual model.

No.	Method	Estimation error
1	Regression	8.2%
2	MLA	26.1%
3	Cokriging	5.1%

Results showed that the model constructed by the cokriging method is close to reality with minimum error. Beside cokriging method, the results of the regression method (correlation between IP and Cu) is better. Due to the smoothing effect of the cokriging, the estimated copper is less than the actual result. The results of MRA methods are of most error due to consideration of the simultaneous effect of IP-Rs values. The Rs data variation range is more than of IP data, so estimation of Cu grade entails more error rather than regression and cokriging methods.

Conclusion

IP-Rs methods have been used successfully in the copper detection in the Abassabad copper mine with highest efficiency. Through geostatistical methods, we were able to construct 3D models for IP-Rs data that surveyed in 2D which were confirmed by drilling results.

The number of boreholes could be decreased from 20 to 7 in two places with acceptable results by geophysical modeling that led to significant cost saving.

Correlation between Cu grade and IP-Rs were examined and calculated using regression, MRA and cokriging methods and based on them, Cu grade was estimated and the 3D block model of Cu was constructed.

Results proved that Cu estimation using IP data is of better quality than Rs data, because of high variation

of Rs data that increases error rate. However, Rs data can be used for geological prediction.

Results of this paper shows that the location and number of additional boreholes can be optimized by the combination of geophysical data and drilling results. We could reduce the number of boreholes and the cost of the exploration operation significantly. Based on these results, we devised exploration plan for the other areas of the Miami-Sabzevar mineralization belt.

References

Amini, A., Ramazi, H. 2016a. Anomaly enhancement in 2D electrical resistivity imaging method using a residual resistivity technique, the journal of the Southern African Institute of Mining and Metallurgy, vol. 116, 1–8. http://dx.doi.org/10.17159/2411-9717/2016/v116n2a7

Amini, A., Ramazi, H. 2016b. Application of Electrical Resistivity Imaging for Engineering Site Investigation, A Case Study on Prospective Hospital Site,Varamin, Iran, Acta Geophysica, 64(4), 2200–2213. http://doi.org/10.1515/acgeo-2016-0100

Armstrong, J. S. 2012. Illusions in regression analysis International Journal of Forecasting, 28, 689–694

Batte, A. G., Barifaijo. E., Kiberu. J. M., Kawule, W., Muwanga, A., Owor, M., Kisekulo, J. 2010. Correlation of geoelectric data with aquifer parameters to delineate the groundwater potential of hard rock terrain in central Uganda. Pure and Applied Geophysics, 167(12), 1549–1559. http://doi.org/10.1007/s00024-010-0109-x

Biswas, A., Sharma, S. P. 2016. Integrated geophysical studies to elicit the structure associated with Uranium mineralization around South Purulia Shear Zone, India: A Review. Ore Geology Reviews, 72, 1307-1326.

Biswas, A., Mandal, A., Sharma, S. P., Mohanty, W. K. 2014. Delineation of subsurface structure using self-potential, gravity and resistivity surveys from South Purulia Shear Zone, India: Implication to uranium mineralization. Interpretation, 2(2), T103-T110.

Boezio, M. N. M., Costa, J. F. C. L., Koppe, J. C. 2011. Ordinary Cokriging of Additive Log-Ratios for Estimating Grades in Iron Ore Deposits, Proceedings of the 4th International Workshopon Compositional Data Analysis 1–10.

Bohling, G. 2005. KRIGING, C&PE 940, 1–20. ttp://people.ku.edu/~gbohling/cpe940.

Bohling, G. 2007. S-GeMS Tutorial Notes in Hydrogeophysics: Theory, Methods, and Modeling, Boise State University, Boise, Idaho, 1–26.

Braglia, M., Carmignani, G., Frosolini, M., Zammori, F. 2012. Data classification and MTBF prediction with a multivariate analysis approach. Reliability Engineering and System Safety, 97(1), 27–35. http://doi.org/10.1016/j.ress.2011.09.010

Charbucinski, J., Malos, J., Rojc, A., Smith, C. 2003. Prompt gamma neutron activation analysis method and instrumentation for copper grade estimation in large diameter blast holes. Applied Radiation and Isotopes, 59, 197–203. http://doi.org/10.1016/S0969-8043(03)00163-5

Chiles, J.P., Delfiner, P. 2012 Geostatistics: modeling Spatial Uncertainty, Hoboken, N.J., Wiley.

Chiou, J., Yang, Y., Chen, Y. 2016. Multivariate functional linear regression and prediction. Journal of Multivariate Analysis, 146, 301–312. http://doi.org/10.1016/j.jmva.2015.10.003

Dahlin, T., Loke, M. H. 2015. Negative apparent chargeability in time-domain induced polarisation data. Journal of Applied Geophysics, 123, 322–332. http://doi.org/10.1016/j.jappgeo.2015.08.012.

Dahlin, T., Leroux, V., Nissen, J. 2002. Measuring techniques in induced polarisation imaging. Journal of Applied Geophysics, 50(3), 279–298. http://doi.org/10.1016/S0926-9851(02)00148-9.

Deutsch, C.V., Journel, A.G. 1998. GSLIB: Geostatistical Software Library and User's Guide, second edition. Oxford, UK: Oxford University Press.

Ehinola, O. A., Oladunjoye, M. A., Gbadamosi, T. O. 2009. Chemical composition, geophysical mapping and reserve estimation of clay deposit from parts of Southwestern Nigeria, Journal of Geology and Mining Research, 1(3), 57–66.

Faul, F., Erdfelder, E., Buchner, A., Lang, A. G. 2009. Statistical power analyses using G*Power 3.1: Tests for correlation and regression analyses. Behavior Research Methods, 41 (4), 1149–1160. http://doi.org/10.3758/BRM.41.4.1149.

Ferdows, M. S., Ramazi, H. 2015. Application of the fractal method to determine the membership

function parameter for geoelectrical data (case study : Hamyj copper deposit , Iran). Journal of Geophysics and Engineering, 12. 909–921.

Gadallah, M. R., Fisher, R. 2009. Exploration geophysics. Berlin. Springer. http://doi.org/10.1007/978-3-540-85160-8

Goulard, M., Voltz, M. 1992 Linear Coregionalization Model: Tools for Estimation and Choice of Cross-Variogram Matrix, Mathmatical Geology, 24(3),269-286.

Granian, H., Hassan, S., Asadi, H. H., John, E., Carranza, M. 2015. Multivariate regression analysis of lithogeochemical data to model subsurface mineralization: a case study from the Sari Gunay epithermal gold deposit, NW Iran. Journal of Geochemical Exploration, 148, 249–258. http://doi.org/10.1016/j.gexplo.2014.10.009

Gurin, G., Tarasov, A., Ilyin, Y., Titov, K. 2015. Application of the Debye decomposition approach to analysis of induced-polarization profiling data (Julietta gold-silver deposit, Magadan Region) Russian Geology and Geophysics 56, 1757–1771. http://doi.org/10.1016/j.rgg.2015.11.008

Habibi, M. J., Mokhtari, A. R., Baghbanan, A., Namdari, S. 2014. Journal of Petroleum Science and Engineering Prediction of permeability in dual fracture media by multivariate regression analysis. Journal of Petroleum Science and Engineering, 120, 194–201. http://doi.org/10.1016/j.petrol.2014.06.016

Helsel, B. D. R., Hirsch, R. M. 2002. Hydrologic Analysis and Interpretation; Chapter A3 Statistical Methods in Water Resources. Techniques of Water-Resources Investigations of the United States Geological Survey.

Hooshmand, A., Delghandi, M., Izadi, A., Aali, K. A. 2011. Application of kriging and cokriging in spatial estimation of groundwater quality parameters, African Journal of Agricultural Research, 6(14), 3402–3408.

Howarth, R. J. 2001. A History of Regression and Related Model-Fitting in the Earth Sciences (1636? -2000), Natural Resources Research 10(4),241-286.

Jodeiri, B., Ramazi, H., Faramarz, S., Ardejani, D., Moradzadeh, A. 2014. Integrated Time-Lapse Geoelectrical–Geochemical Investigation at a Reactive Coal Washing Waste Pile in Northeastern Iran, NE Iran, Mine Water and the Environment, 33: 256-265.

Jodeiri, B., Faramarz, S., Ardejani, D., Ramazi, H., Moradzadeh, A. 2016. Predicting pyrite oxidation

and multi-component reactive transport processes from an abandoned coal waste pile by comparing 2D numerical modeling and 3D geoelectrical inversion, International Journal of Coal Geology, 164: 13-24

Khanlari, G. R., Heidari, M., Momeni, A. A., Abdilor, Y. 2012. Prediction of shear strength parameters of soils using arti fi cial neural networks and multivariate regression methods. Engineering Geology, 131–132, 11–18. http://doi.org/10.1016/j.enggeo.2011.12.006

Knotters, M., Brus, D. J., Voshaar, J. H. O. 1995. A comparison of kriging , co-kriging and kriging combined with regression for spatial interpolation of horizon depth with censored observations, Geoderma, 67, 227–246.

Kumar, D., Ahmed, S., Krishnamurthy, N. S., Dewandel, B. 2007. Reducing ambiguities in vertical electrical sounding interpretations: A geostatistical application, Journal of Applied Geophysics, 62(1), 16–32. http://doi.org/10.1016/j.jappgeo.2006.07.001

Leuangthong, O., Daniel Khan, K., Deutsch, C.V. 2008. Solved problem in geostatisitcs, Chapter 9: Multiple Variable.

Li, X., Xie, Y., Guo, Q., Li, L. 2010. Adaptive ore grade estimation method for the mineral deposit evaluation. Mathematical and Computer Modelling, 52(11–12), 1947–1956. http://doi.org/10.1016/j.mcm.2010.04.018.

Li, X., Li, L., Zhang, B., Guo, Q. 2013. Neurocomputing Hybrid self-adaptive learning based particle swarm optimization and support vector regression model for grade estimation. Neurocomputing, 118, 179–190. http://doi.org/10.1016/j.neucom.2013.03.002.

Loke, M.H., 2015, Tutorial: 2-D and 3-D electrical imaging surveys: (Revision date: 17th October 2015), (www.geotomosoft.com)

Loke, M. H., Dahlin, T. 2002. A comparison of the Gauss − Newton and quasi-Newton methods in resistivity imaging inversion, Journal of Applied Geophysics, 49, 149–162.

Madani, N., Emery, X. 2018. A comparison of search strategies to design the cokriging neighborhood for predicting coregionalizaed variables, Stochastic Environmental Research and Risk Assessment, https://doi.org/10.1007/s00477-018-1578-1

Mandal, A., Biswas, A., Mittal, S., Mohanty, W. K., Sharma, S. P. Sengupta, D., Sen, J., Bhatt, A. K. 2013. Geophysical anomalies associated with uranium mineralization from Beldih mine, South Purulia Shear Zone, India. Journal Geological Society of India, 82(6), 601-606.

Mandal, A., Mohanty, W.K., Sharma S.P., Biswas, A., Sen, J., Bhatt, A. K. 2015. Geophysical signatures of uranium mineralization and its subsurface validation at Beldih, Purulia District, West Bengal, India: a case study.Geophysical Prospecting, 63(2), 713-726. https://doi.org/10.1111/1365-2478.12205.

Martinho, E., Almeida, F. 2006. 3D behaviour of contamination in landfill sites using 2D resistivity/IP imaging: Case studies in Portugal. Environmental Geology, 49(7), 1071–1078. http://doi.org/10.1007/s00254-005-0151-7

Martínez-Moreno, F.J., Pedrera, A., Ruano, P., Galindo-Zaldívar, J., Martos-Rosillo, S., González-Castillo, L., Sánchez-Úbeda, J.P., Marín-Lechado, C. 2013. Combined microgravity, electrical resistivity tomography and induced polarization to detect deeply buried caves: Algaidilla cave (Southern Spain). Engineering Geology, 162, 67-78, doi: 10.1016/j.enggeo.2013.05.008.

Mashhadi, S.R., Mostafaei, K., Ramazi, H. 2017. Improving bitumen detection in resistivity surveys by using induced polarisation data, Exploration Geophysics. https://doi.org/10.1071/EG17032.

Mogaji, K. A. 2016. Geoelectrical parameter-based multivariate regression borehole yield model for predicting aquifer yield in managing groundwater resource sustainability. Integrative Medicine Research, 10(4), 584–600. http://doi.org/10.1016/j.jtusci.2015.12.006

Mokhtari, A. R. 2014. Hydrothermal alteration mapping through multivariate logistic regression analysis of lithogeochemical data. Journal of Geochemical Exploration, 145, 207–212. http://doi.org/10.1016/j.gexplo.2014.06.008

Mostafaie, K., Ramazi, H. 2015. Application of electrical resistivity method in sodium sulfate deposits exploration, case study: Garmab, Iran. Journal of Biodiversity and Environmental Sciences, 6(2), 2220–6663. Retrieved from http://www.innspub.net

Mostafaie, K., Ramazi, H. R., Jalai, M. 2014. Application of Integrated Geophysical and Geostatistical Methods in Amiriyeh Site Classification. Geodynamics Research International Bulletin (GRIB), (2) 2,1-15.

Maurya, P.K., Ronde, V.K., Fiandaca, G., Balbarini, N., Auken, E., Bjerg, L.P., Christiansen, A.V. 2017 Detailed landfill leachate plume mapping using 2D and 3D electrical resistivity tomography- with

correlation to ionic strength measured in screens. Journal of Applied Geophysica, 138:1-8.

Noori, R., Khakpour, A., Omidvar, B., Farokhnia, A. 2010. Expert Systems with Applications Comparison of ANN and principal component analysis-multivariate linear regression models for predicting the river flow based on developed discrepancy ratio statistic. Expert Systems With Applications, 37(8), 5856–5862. http://doi.org/10.1016/j.eswa.2010.02.020

Perozzi, L., Gloaguen, E., Rondenay, S., McDowell, G. 2012. Using stochastic crosshole seismic velocity tomography and Bayesian simulation to estimate Ni grades: Case study from Voisey's Bay, Canada. Journal of Applied Geophysics, 78, 85–93. http://doi.org/10.1016/j.jappgeo.2011.06.036

Ramazi, H., Mostafaie, K. 2013. Application of integrated geoelectrical methods in Marand (Iran) manganese deposit exploration. Arabian Journal of Geosciences, 6(8), 2961–2970. http://doi.org/10.1007/s12517-012-0537-2

Ramazi, H., Jalali, M. 2014. Contribution of geophysical inversion theory and geostatistical simulation to determine geoelectrical anomalies. Stud. Geophys. Geod. 59: 97–112.

Salehi, L., Rasa, I., Alirezaei, S., Kazemi Mehrnia, A. 2016. The Madan Bozorg, volcanic-hosted copper deposit, East Shahroud; an example of Manto type copper deposits in Iran, Journal of Geoscience, 25(98): 93-104.

Seccatore, J., Marin, T., Tomi, G. De, Veiga, M. 2014. A practical approach for the management of resources and reserves in Small-Scale Mining. Journal of Cleaner Production, 84, 803–808. http://doi.org/10.1016/j.jclepro.2013.09.031

Sevil, J., Gutierrez, F., Zarroca, M., Desira, G., Carbonela, D., Guerrero, J., Linares, R., Roque, C., Fabregat, I. 2017. Sinkhole investigation in an urban area by trenching in combination with GPR, ERT and high-precision leveling. Manteled evaporate karst of Zaragoza city, NE Spain. Engineering Geology 213: 9-20

Shademan, Kh M., Madani,H., Hassani, H., Moarefvand, P. 2013. Determining the Best Search Neighbourhood in Reserve Estimation , using Geostatistical Method: A Case Study Anomaly No 12A Iron Deposit in Central Iran, Journal Geological Society of India , 81(12), 581–585.

Tahmasebi, P., Hezarkhani, A. 2012. A hybrid neural networks-fuzzy logic-genetic algorithm for grade estimation. Computers and Geosciences, 42, 18–27. http://doi.org/10.1016/j.cageo.2012.02.004

Telford, W. M., Geldart, L. P., Sheriff, R. E. 1990. Applied Geophysics. Cambridge University Press, Cambridge. http://doi.org/10.1180/minmag.1982.046.341.32

Tütmez, B., Tercan, A. E., Kaymak, U. 2007. Fuzzy Modeling for Reserve Estimation Based on Spatial Variability. Mathematical Geology, 39(1),87-111. http://doi.org/10.1007/s11004-006-9066-4

Ushie, F., Harry, T., Affiah, U. 2014. Reserve Estimation from Geoelectrical Sounding of the Ewekoro Limestone at Papalanto , Ogun State , Nigeria , Journal of Energy Technologies and Policy 4(5), 28–33.

Wackernagal, H. 2003. Mutivariate Geostatistics; an introduction with applications, Springer sciences.

Wang, G., Pang, Z., Boisvert, J. B., Hao, Y., Cao, Y., Qu, J. 2013. Quantitative assessment of mineral resources by combining geostatistics and fractal methods in the Tongshan porphyry Cu deposit (China). Journal of Geochemical Exploration, 134, 85–98. http://doi.org/10.1016/j.gexplo.2013.08.004

Wang, Q., Deng, J., Liu, H., Yang, L., Wan, L., Zhang, R. 2010. Fractal models for ore reserve estimation. Ore Geology Reviews, 37(1), 2–14. http://doi.org/10.1016/j.oregeorev.2009.11.002

Wang, Q., Deng, J., Liu, H., Wang, Y., Sun, X., Wan, L. 2011. Fractal models for estimating local reserves with different mineralization qualities and spatial variations. Journal of Geochemical Exploration, 108(3), 196–208. http://doi.org/10.1016/j.gexplo.2011.02.008

Webber, T., Costa, J. F. C. L., Salvadoretti, P. 2013. Using borehole geophysical data as soft information in indicator kriging for coal quality estimation. International Journal of Coal Geology, 112, 67–75. http://doi.org/10.1016/j.coal.2012.11.005

White, R. M. S., Collins, S., Loke, M. H. 2003. Resistivity and IP arrays, optimised for data collection and inversion. Exploration Geophysics, 34(4), 229. http://doi.org/10.1071/EG03229

Xu, H., Sun, J., Russell, B., Innanen, K. 2015. Porosity prediction using cokriging with multiple secondary datasets, CREWES Research Report, 27, 1–13.

Zhang, W., Goh, A. T. C. 2016. Geoscience Frontiers Multivariate adaptive regression splines and neural network models for prediction of pile drivability. Geoscience Frontiers, 7(1), 45–52. http://doi.org/10.1016/j.gsf.2014.10.003.

Bulletin of the Mineral Research and Exploration

http://bulletin.mta.gov.tr

Landslide susceptibility mapping using information value and frequency ratio for the Arzew sector (North-Western of Algeria)

Roukh ZINE EL ABIDINE[a*]   and Nadji ABDELMANSOUR[a]

[a]*Laboratory of Geo resources, Environments and Natural Risks, Oran 2 Mohamed Benahmed University, Faculty of Earth Science and the universe, B.P1 1524 El-M'Naouar. Oran31000. Algeria.*

ABSTRACT

Geological hazards present one of the most important constraints for the development of the Arzew sector (Oran province), North Western of Algeria. Landslides are considered us one of the most common phenomena in the study area and especially in the hilly area. For minimizing and reducing the consequences of this problem, it is necessary to carry out preliminary studies on the cartography of the different zones exposed to the slope instability phenomena. The main objective of this study is to perform the landslide susceptibility mapping by statistical models and GIS techniques for the Arzew area. To achieve this goal, an analytical approach was carried out. Firstly, a landslide inventory map was prepared using previous inventory maps, satellite images, aerial photos and field surveys. Secondly seven conditioning factors such as slope degree, aspect, lithology, land use, distance to the streams, distance to the road and altitude were exploited to assess landslide susceptibility. Thirdly, the weight value for each class of the conditioning factors was determined using Frequency Ratio (FR) and Information Value (IV) models based in GIS functionalities. Consequently, Landslide Susceptibility Maps (LSMs) were produced by the classification process of the global Landslide Susceptibility Indexes (LSIs) into five classes. Finally, for experiment verification, the LSMs obtained with the FR and IV models were confirmed comparing LSMs with landslide inventory map using both the Receiver Operating Characteristics (ROC) and the Seed Cell Area Index (SCAI) models. The area under curve (AUC) results, demonstrate that the IV method more performance (89.03%) for LSM than FR method (85.57%). Furthermore, the validation results using SCAI also confirmed that the IV model was more accurate than FR model. The models employed in this study are capable to resolve the issue of the landslide susceptibility of the study area. The produced susceptibility maps can be used for future land use planning and can be considered as a powerful tool to resolve the spatial distribution of the risk associated to landslides.

1. Introduction

Landslides was considered one of the most frequent and damaging natural hazards threatening the human lives, economic, big projects and properties in northern part of Algeria (Benaissa et al., 1989; Guemache et al., 2011; Hadji et al., 2017; Djerbal et al., 2017). Oran region, located in north western of Algeria, known for its complex geology (recent tectonic and seismic activity), is particularly exposed to the landslide hazard. To minimize landslides consequences, it requires a rational land use in the spatial planning. As a solution, landslide susceptibility maps were considered the principal tool for predicting risk.

The susceptibility to landslides is the probability of spatial occurrence of the landslide for several factors

of environmental predisposition (slope, aspect, land use, lithology, etc) for a given area (Thiery, 2007; Guzzetti et al., 2005). The GIS techniques are the most important tools enable quickly generate this type of thematic maps.

The landslide susceptibility mapping can be estimated by the use of several methods based on GIS techniques. Many studies have used frequency ratio for assessing landslide susceptibility such as (Akgün et al., 2008; Yalçın et al., 2011; Youssef et al., 2015). Other studies have used Logistic regression model to evaluate landslide susceptibility (Gorsevski et al., 2006*b*; Yılmaz, 2010; Bai et al., 2011; Pourghasemi et al., 2013; Raja et al., 2017). The statistical index model (information value) is also used to resolve the thematic of landslide susceptibility (Bui et al., 2011; Cui et al., 2016; Aghdam et al., 2016). The weight of evidence model has also used by many researches (Regmi et al., 2010; Özdemir and Altural, 2013). The analytical hierarchy process (AHP) (Gorsevski et al., 2006*c*; Ercanoglu et al., 2008; Intarawichian and Dasananda, 2010; Chen et al., 2016; Ghosh et al., 2017), fuzzy set (Pradhan, 2011; Sezer et al., 2011), the Support Vector Machine (SVM) method (Ballabio and Sterlacchini, 2012; Peng et al., 2014; Pradhan et al., 2017) and artificial neural network (Yılmaz, 2009; Conforti et al., 2014; Chen et al., 2017) were applied to the landslide hazard zoning.

In Algeria, landslide susceptibility mapping presents a novel approach for prevention of the risks linked to the landslides. So far, few attempt at landslide susceptibility were applied in Algeria (Hadji et al., 2013; Djerbal and Melbouci, 2013; Hadji et al., 2014; Bourenane et al., 2015; Achour et al., 2017; Hadji et al., 2017; Dahoua et al., 2017; Mahdadi et al., 2018).

Landslide susceptibility zonation is indispensable for land-use management and should become an official document for various future projects (Gorsevski et al., 2006a; Corominas et al., 2014). The geographical position of the study area has the particularity of being an economic and tourism ultimate center, requires preliminary studies in the planning and risks management. To define landslide prone area, the present research destined to mapping landslide susceptibility for the Arzew sector (Northwestern of Algeria).

In this study, simple method was used to landslide susceptibility mapping, by following three essential steps: The first one consist to collect the data input, the second one, calculated the landslide susceptibility index using two models based on GIS. Step three, establishment and validation of the output data.

2. General Characteristics of the Study Area

The study area is part of the Oran coastal, northwest of Algeria, located between the UTM coordinates WGS84 zone 30 (3976894.08 m, 3954859.17 m) latitude and (715833.47 m, 747107.72 m) longitude (Figure 1), were the area of this region is 308.06 km².

The geomorphological unities of the study area is characterized by the presence of plains, mountains and plateaus, the altitude range between (0 and 625) meters on the reliefs (Figure 1). Arzew climate is part of the semi-arid Mediterranean bioclimatic stage, of which highly developed hydrographic network which has a flow conforming to the topography of the region. Towards the north, the hydrography has a flow directed towards the sea, while towards the south the superficial flow feeds several endoergic structures, represented by several lakes and sebkha (Figure 2).

The study area is part of the alpine belt, containing Paleozoic, Mesozoic, highly tectonized, largely metamorphosed units (Ciszak, 1993). According to the geological maps (Gourinard, 1952*a,b*) four units in the study area are made up of three apparent and distinct geological entities (Figure 3). They are distributed from east to west respectively; Kristel Mountain, Borosse and Orousse Mountains, the fourth entity presented by Djebel Essebouaa. Djebel Borosse and more complex than Djebel Orousse, both are constituted by relatively thick carbonate and calcaro-schistose formations. Milled limestones truncated by dominant erosion surfaces. Their impressive abrupt cliffs are formed by schist characterized by a overlapping structure of Neogene to Plio-Quaternary age (Perrodon, 1957; Fenet, 1975; Thomas, 1985). The Miocene subdivided into two sedimentary cycles. The first post-nappe cycle presented by green marls located between the southern flank of Djebel Essebouaa and the plateau of Boufatis for the second cycle is preceded by an active erosion phase accompanied by an accumulation of continental series to the East of Oran. Marlins and cineretic formations rely on deposits of Canastel's first post-nappe cycle (Oran cliffs - Canastel).
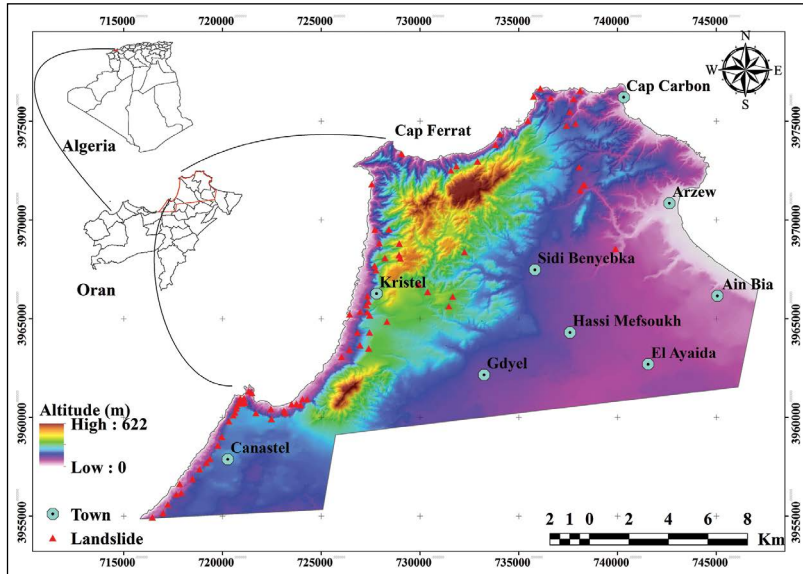
Figure 1- Location of study area.
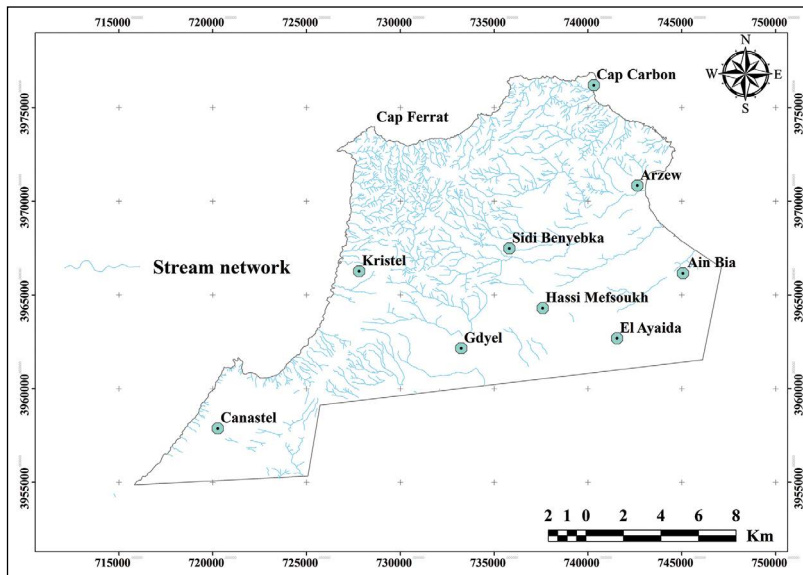
Figure 2- Streams network map of the study area.

The South and East of the Arzew massif, marked by marly outcrops and gypsum, the upper Miocene is covered by the Pliocene. The latter is often confused with the quaternary lands. The term Plio-Quaternary, which is vague and imprecise, gives rise to various confusions. In this context, we agree with Thomas 1985 nomenclature for Pliocene and Quaternary terrains: PI: represented by sandy conglomerates, marls and marine sands laterally at the foot of the schistose massifs, to continental conglomeratic deposits. These deposits are of Tabianian age. The PII cycle: it is represented by the formation of the Golf of Arzew. These lumacheles pass laterally (in some places) to sandy dunes, or marls and sands in the center of the basin (Telamine lake and Arzew salt). The Pleistocene is often formed by rube silt and gray silt with Lateral equivalents represented either by shell sands, dunes or even fluvio-lacustrine clays. A calcareous crust (pink to reddish-brown slab) develops on various facies in relation to the shaping of the ablation surfaces correlative to the deposits of type playa.
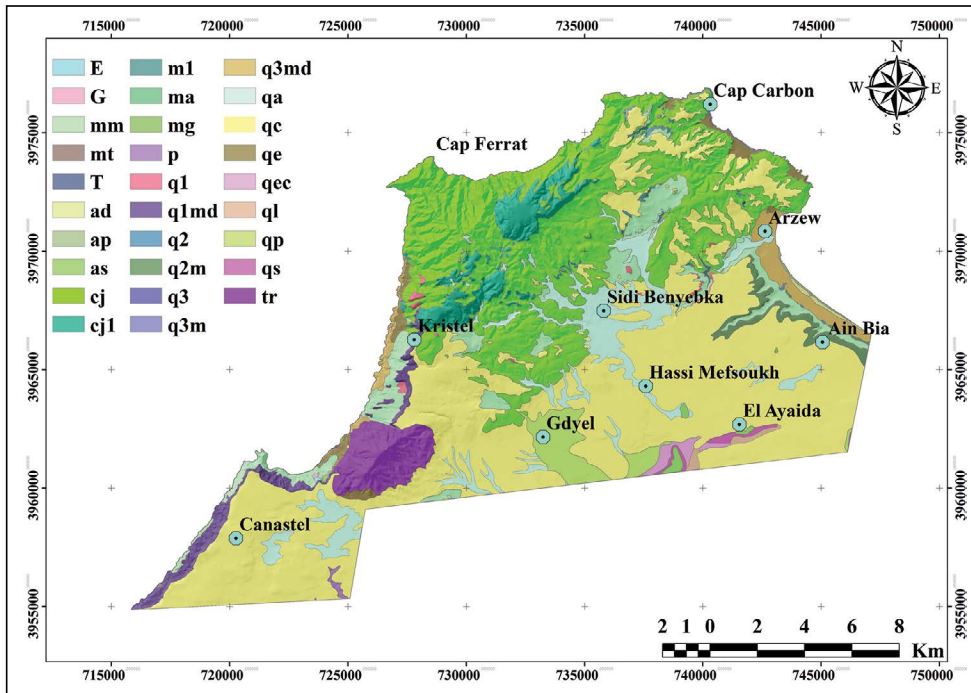
Figure 3- Lithological map of the study area, ad: dune vives, as: low salted bottoms vegetation; Ap: beach, p: marly more or less sandy; Q1: marine Pleistocene (Calabrian); Q1m: lumachelle; Q1md: dune marine; Q2: intermediate marine Pleistocene; Q2m: marine lumachelle, Q3: recent marine Pleistocene; Q3m: scallop lumachelle; Q3md: marine dune; Qa: continental quaternary associated with alluvium; Qc: carapace and topsoil more or less encrusted; Qe: eboule; Qec: carapace and topsoil more or less encrusted and collapsed; Q1: Pleistocene marine ancient level; Qp: continental quaternary (clay lake); Qs base salted bottom with vegetation; M1: algae limestone; Mm: gray marl; Mg: fine sand with yellow marl; Mt: white marl-limestone; Cj1: limestone marmorised sometimes dolomitized; Cj: schist; Tr: permo-triace (purplish schist); E: eruptive (green rocks); G: diapirism (gypsum); T source deposit (Gourinard 1952 *a,b*).

3. Landslide Inventory

Landslide inventory mapping is one of the key process of landslide susceptibility modeling (Fell et al., 2008; Corominas et al., 2014). Satellites images, aerial photos, GPS, reviews, articles, internal reports and fields' survey provide important tools to establish landslide inventory map. This map contains a landslide position that arises in the past. In this study, the landslide positions were identified using existence data base, satellite images, aerial photos, Google Earth, and field surveys. Eventually, data base contains more than 80 polygons. Figure 4 illustrate the spatial distribution of landslide location in the Arzew sector, Algeria. In this study we used landslides classification developed by Cruden and Varnes 1996. Landslides are grouped into three types: rotational, translational and compound slide. Figure 5 illustrates some example of landslide affected the study area.

4. Conditioning Factors

Generally, mass movement result from the combination of triggers and aggravating factors, particularly the lithological, structural and geotechnical characteristics, slope angle, groundwater, surface water and seismic… etc. Their distribution over time is irregular and their frequency is conditioned by extreme natural events.

The conditioning-factors used in this research are slope angle, slope exposure, lithology, land use, altitude, distance to the streams and distance to the road. They are generated by different sources (Table 1). However, the topographic attributes such as slope angle, slope exposure and altitude were derived from Digital Elevation Model (DEM). The DEM was established accordingly by digitization and interpolation of the topography map curves extracted from a 1:25000 scale topographical maps
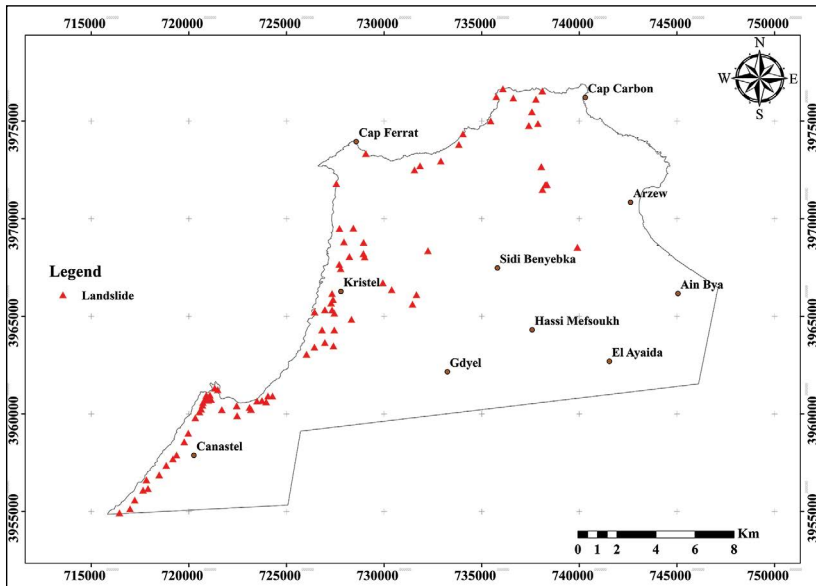
Figure 4- Landslide spatial distribution map.
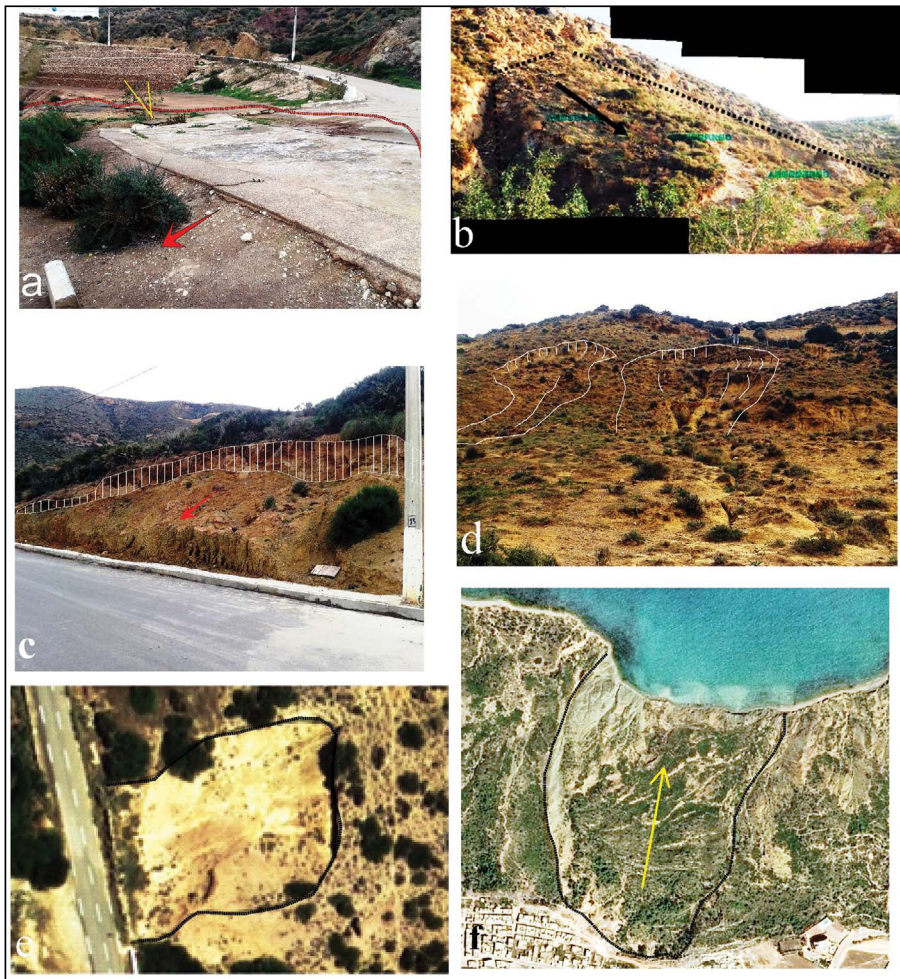
Figure 5- Example of different type of landslides mapped in the study area a) translational slide, b) rotational slide (Benabdellah, 2010), c) rotational slide, d) compound slide, e) rotational slide (aerial photography); f) translational slide (satellite image SPOT 6).

Table 1- Information source for the various parameters used in the landslides susceptibility mapping .

Setting	Maps	Sources of informations
Landslide inventory	Landslide inventory map	Satellite images (SPOT6), Google Earth, aerial photography, field surveys and bibliographic data.
Topography	DEM	Creation of DEM by digitization and interpolation the contours lines extracted from 1/25000 scale topographical maps.
Morphometric	Slope map Slope Exposure map Altitude map	Derived from DEM
Geological	Lithological map	Digitization lithological formations from 1/50000 scale geological maps
Hydrology	Distance to the streams map	Digitization the stream network from the 1/25000 scale topographic maps.
Land use	Land use map Distance to the road map	Land use map (BNEDER 2011), satellite image, field surveys.

(Figure 1), the lithology was extracted from a 1:50000 scale geological maps and furthermore the both land use map and distance to the road map are extracted from a 1:25000 scale land use map of Oran elaborated by National office of studies for rural development (Beneder, 2011), field survey and satellite images.

4.1. Slope Angle

Slope degrees allowed to increases acculturation of the slope movement, that's why this parameter presented one of the aggravating landslide factors. using DEM and GIS functions, slope degree were classified into 5 classes: 0-10°, 10-20°, 20-30°, 30-50° and >50° (Figure 6).

4.2. Slope Exposure (Aspect)

Aspect considered as the exposition of slope, it is measured clockwise in degree from 0 to 360 °, the values that are less than 1 represents flat area. Aspect also presents an essential conditioning factor in landslide susceptibility process. Figure 7 illustrates the aspect map of the Arzew sector with nine classes.

4.3. Lithology

Lithology considered the most important conditioning factor because each lithological unit has landslide susceptibility level (Yeşilnacar and Topal, 2005). In the current study, lithological map was prepared by digitization of a 1:50000 scale geological maps. Based on geotechnical and geomorphological
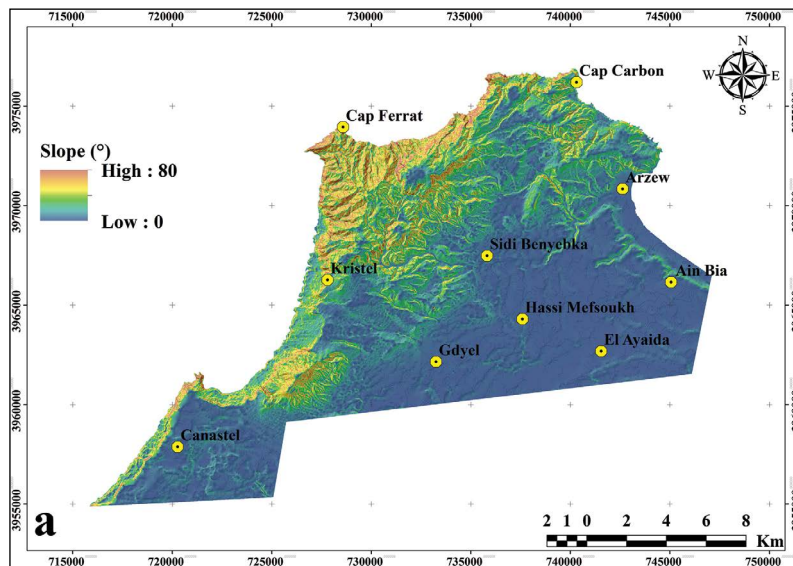
Figure 6- Slope map of the study area.
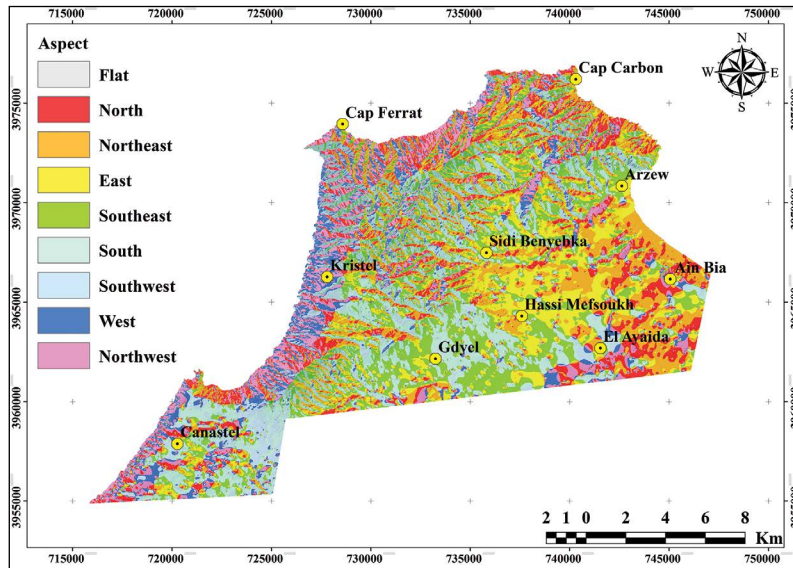
Figure 7- Aspect map of the study area.

characteristics, they were classified into four classes using ArcGIS software (Table 2).

4.4. Distance to the Streams

Generally, landslides developed near streams where flow velocity is sufficiently to erode the lower part of talus. For this distance to the streams were integrated in landslide susceptibility estimation, using Euclidean distance function in ArcGIS, streams buffer zone were established and classified in six classes (0-100, 100-200, 200-300, 300-400, 400 -500, > 500).

4.5. Land Use

Barren and little vegetative land makes talus more prone to erosion and sliding (Gomes et al. 2005), so land use considered an important parameters included in this study. Land use map of Arzew sector produced by digitization of 1/25000 scale land use map of the

Oran (Figure 8), it is reclassified into four classes (Table 2).

4.6. Distance to the Road

During the road construction, the anthropogenic actions influencing landslide, and that is through by destroy vegetation, application of external loads (Bourenane et al., 2015). Accordingly, the distance to the road considered an important parameter in this study. In current study, distance to the road divided into 5 zones using an interval of 150m: (0-150, 150-300, 300-450, 450-600, >600).

4.7. Altitude

Slope movement intensity increases with altitude increasing, in this research, DEM were used to perform altitude map based on Reclassify function in Arc GIS. From 0 to 622, altitude classified into 6

Table 2- Classification of lithology and land us.

Lithology	Class1	Q3, Ad, Qs, Ql, Qa, Qc, Ap, As, P, Q2, Qec, T, Qp, Qs.
	Class2	Tr, Cj1, Cj.
	Class3	Q2m, Mg, Q3m, Q3md, Ml.
	Class4	Ma, Mt, Qe, Q1md, Mm, E, G.
Land use	Class1	Forest, Fruit crops, Olive growing, Water body.
	Class2	Maquis wooded, maquis.
	Class3	Wine-growing, Mixed cropping, Vegetable growing, big culture, urban.
	Class4	Mines, Bare soil.
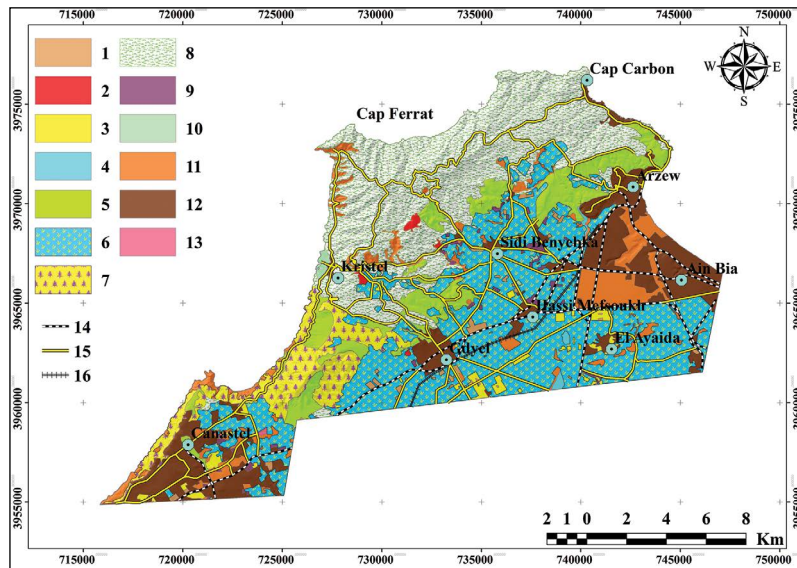
Figure 8- Land use map of study area. 1 fruit crops, 2 mines, 3 vegetable growing, 4 water body, 5 forests, 6 big culture, 7 maquis wooded, 8 maquis, 9 olive growing, 10 mixed cropping, 11 bare land, 12 urban, 13 wine-growing, 14 major road, 15 secondary road, 16 rail road.

classes: 0-100, 100-200, 200-300,300-400, 400-500 and >500 (Figure 9).

5. Landslide Susceptibility Mapping

In this paper, statistical index method and frequency ratio were applied to mapping landslide susceptibility. Weight of each causative factors class was defined by the combination of each parameter and landslide inventory map. By combination following decision rules (addition, division, multiplication …etc), weight of each conditioning factors class was defined. Finally, classification of landslide susceptibility index using natural break (jenks) and validation of landslide susceptibility maps comparing LSMs and inventory map. Figure 10 illustrates the flowchart of methodology used in this research.

5.1. Frequency Ratio Method

The fundamental concept of this method is to calculate the ratio between the density of phenomena
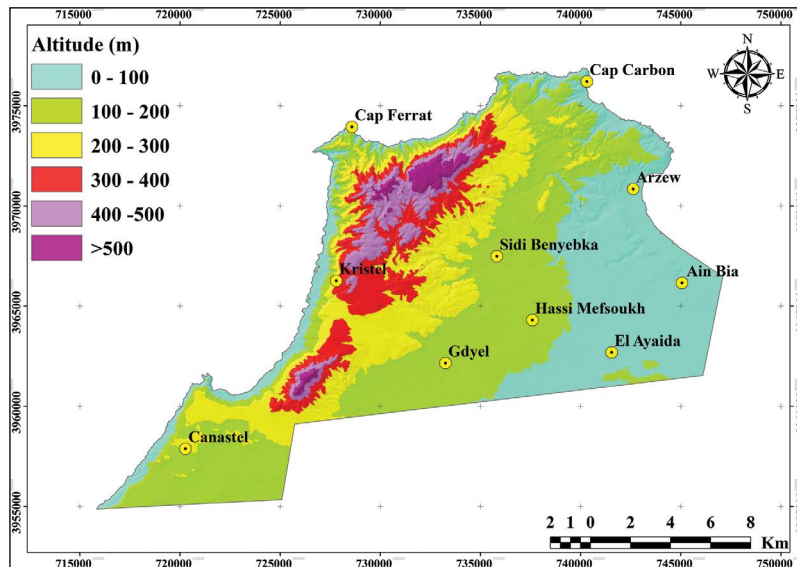
Figure 9- Altitudes map of study area.
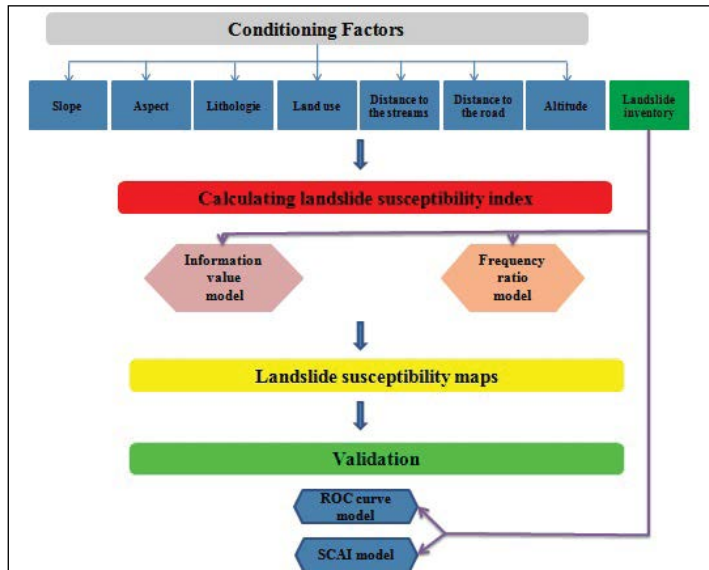
Figure 10- Methodology flowchart for the process work.

in a given class and the density of the same class. (Lee and Talib, 2005).LSI expressed using following Equation: (Equation 1)

$$LSI \quad Fr1 + Fr2 + Fr3 + ... + Frn \quad (1)$$

In the statistical analysis between landslide occurrence ratio and ratio of each class in conditioning factor, the average value of Fr is equal to 1. If the value is >1, indicate maximal correlation and a value lower than 1 present minimal correlation. Table 3 shows the results of this application.

As a result, for the slope degree, FR increased with increasing of the slope degree, the class (>50) has maximum value (3.995), while the class (0 − 10) has the minimum value (0.338). Aspect analyses show that the maximum FR value (3.454) is for Northwest, followed by West (2.573), North (2.025) and Flat (1.915), indicating the maximal probability of landslide occurrence. Frequency results of lithology parameter indicate that the gray marl, white marl-limestone, gypsum and dune marine with maximum FR value (10.397) are most prone to landslide. The FR values greater than 1 are distributed at the distance closer to the streams (0-100) and (100-200) indicating a high probability of landslide occurrence. For the proximity to the road give respectively, value 1.125, 1.507 and 1.710 for the distance (300 - 450), (450-600) and > 600. Correlation between land use and landslide indicate that the landslide commonly occurred in

barren area (4.086) and maquis area (1.759). The combination between altitude and landslide inventory, showed that landslides mostly appeared from 0 to 100m.

Using equation 1, LSI values range from 1.15 to 27.13. Using reclassify function, the LSI map was reclassified into five classes: very low (39.07%), low (31.46%), moderate (19.80%), high (4.72%) and very high (4.93%) (Figure 11a-c).

5.2. Information Value Method

The statistical method used in this study is proposed by Yin and Yan, 1988 and modified by van Westen, 1993, is based on the comparison between the spatial distribution of phenomena and their various factors. First, the method is based on a statistical analysis using Equation (2)

$$W(i) = \frac{Npix(Si)/Npix(Ni)}{\sum Npix(si)/\sum Npix(Ni)} \quad (2)$$

W (i) is the weight of each class (for example the weight of class 10 ° of the slope), Npix (Si) is the number of slip pixels in classes i, Npix (Ni) is the number of pixels in class i. the dominator is the ratio between number of pixels all landslide and total pixels in the study area. In a second step, the probability of occurrence of landslides in each class is determined by Equation (3):

Table 3- Spatial relationship between each factor contributing to a landslide and the landslide using the FR and information value models.

Parametre	Classes	% of total area (a)	% of landslide area (b)	Frequency Ratio (b/a)	Information value (Wi)
Slope (°)	0-10	69.477	23.526	0.338	-1.102
	10-20	14.877	36.920	2.481	0.889
	20-30	09.710	23.138	2.382	0.848
	30-50	05.813	15.929	2.739	0.988
	>50	00.211	00.485	3.995	1.365
Aspect	Flat	00.042	0.0811	1.915	0.613
	North	11.744	23.792	2.025	0.669
	Northeast	14.347	10.149	0.705	-0.385
	East	15.546	02.908	0.187	-0.713
	Southwest	18.028	02.696	0.149	-1.937
	South	15.056	02.015	0.133	-2.047
	Southwest	08.081	05.734	0.709	-0.380
	West	07.409	19.066	2.573	0.908
	Northwest	09.712	33.554	3.454	1.202
Lithology	Class 1	55.022	03.612	0.065	-2.727
	Class 2	32.656	04.205	0.128	-2.053
	Class 3	03.462	00.075	0.021	-3.833
	Class 4	08.858	92.210	10.397	2.337
Distance to the stream	0-100	41.838	48.409	1.157	0.174
	100-200	22.937	26.137	1.139	0.159
	200-300	11.845	11.370	0.959	-0.012
	300-400	07.346	05.855	0.797	-0.198
	400-500	05.402	03.201	0.592	-0.494
	500-600	04.565	02.989	0.654	-0.394
	600-700	03.865	01.379	0.356	-2.414
	>700	02.198	00.656	0.298	-2.592
Land use	class1	10.469	07.164	0.684	-0.396
	class2	32.693	57.516	1.759	0.457
	class3	49.122	03.791	0.077	-1.119
	class4	07.714	31.527	4.086	1.390
Distance to the road	0-150	28.604	08.318	0.290	-1.251
	150-300	21.739	17.740	0.816	-0.219
	300-450	15.284	17.796	1.125	0.101
	450-600	10.137	15.283	1.507	0.394
	> 600	24.233	41.460	1.710	0.226
Altitude	0-100	28.062	66.072	2.354	0.843
	100-200	39.549	25.429	0.642	-0.454
	200-300	18.001	05.789	0.321	-1.147
	300-400	08.671	02.709	0.312	-1.176
	400-500	04.125	0000	000	000
	> 500	01.590	0000	000	000

$$Pr(i) = \ln \frac{Npix(Si)/Npix(Ni)}{\sum Npix(si)/\sum Npix(Ni)} \qquad (3)$$

Finally, the landslides susceptibility index (LSI) of the terrain is determined by the sum of all factors (Equation 4) after the integration of the probability of occurrence of slips in each class.

$$LSI = \sum_{i=1}^{n} \ln \frac{Npix(Si)/Npix(Ni)}{\sum Npix(si)/\sum Npix(Ni)} \qquad (4)$$

The combinations of the thematic maps with landslide inventory map in ArcGIS allow calculating the number of pixels of the landslide in each class. The information value method allowed us to calculate the weight of each class (Table 3). Positive and negative results of LSI mean that the highest values indicate a great possibility of sliding. The final calculated LSI values of the study area range from -11.98 to 7.53. The LSI map was classified into five classes using natural breaks (jenks) method (very low 19.12%, low 33.3%,
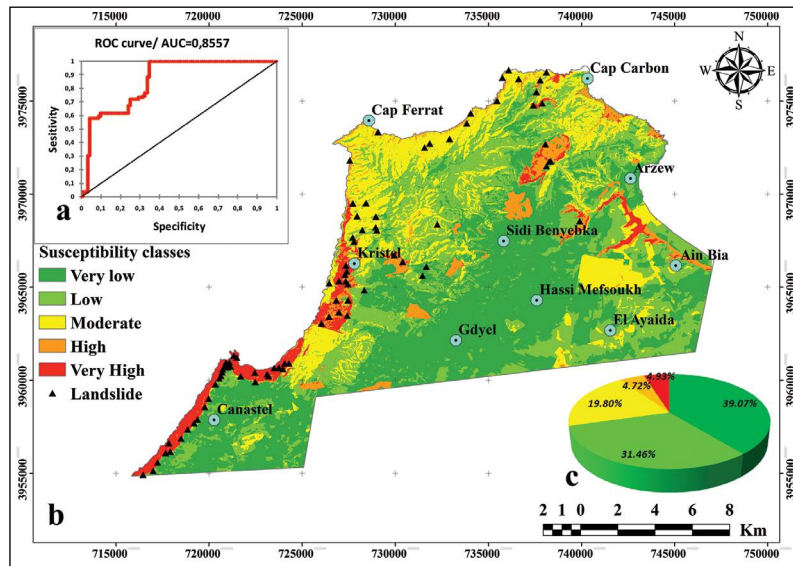
Figure 11- a) ROC curve of the LSM provide by frequency model, b) Landslide susceptibility map produced using frequency model, c) distribution pie-chart of the landslide susceptibility classes.

moderate 24.46%, high 18.34% and very high 4.75%) (Figure 12b, c).

5.3. Validation

For validation process, two statistical methods were used to evaluate the performance of the LSMs obtained. Both of ROC curve and SCAI methods are based on the combination of the landslide susceptibility and landslide inventory map. ROC curve have comparing 30% of landslides with the two LSMs. The AUC value was 85.57% for FR model (Figure 10a), and 89.03 for IV model (Figure 11a). Comparing the obtained results of Area under curve for the two models indicate that the use of the IV for landslide susceptibility zoning provide more accurate prediction in comparing the FR model .
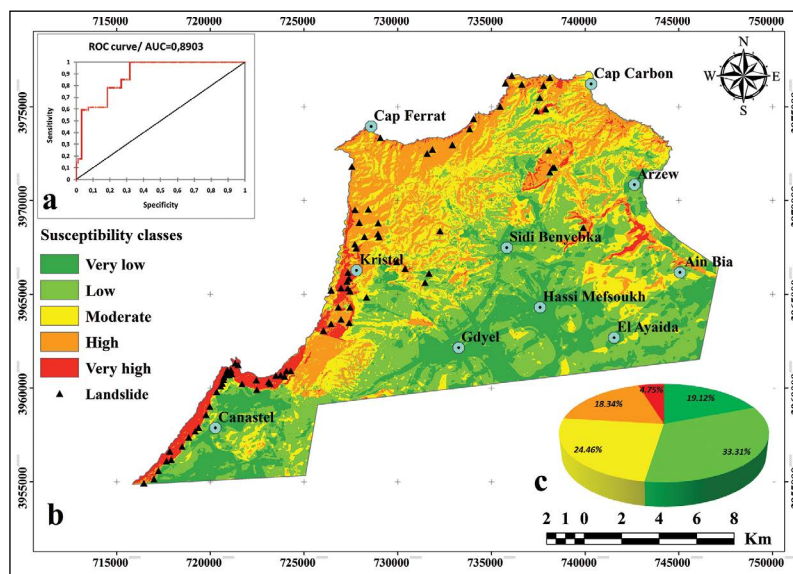
Figure 12- a) ROC curve of the LSM provide by bivariate statistical model, b) Landslide susceptibility map produced using information value model, c) Distribution pie-chart of the landslide susceptibility classes.

Oriented solution based about the SCAI method was proposed to compare the results of two methods according to the LSM. The SCAI method was cited by Süzen and Doyuran, 2004 as validation tool of landslide susceptibility map. In order to evaluate SCAI, we use the following Equation:

$$SCAI = \frac{SAP}{LP} \qquad (5)$$

Were, SAP are the percentages of susceptibility area and LP is the percentage of landslide.

According to the table 4, very high and high classes have contained the minimum SCAI, for the low and very low classes contain maximal SCAI value. The obtained results of the SCAI method, confirmed that the IV method more performance than FR method .

Table 4- The densities of landslide occurrence among the landslide susceptibility classes for the two models.

Model	FR			IV		
Susceptibility classes	Area (%)	Seed (%)	SCAI	Area (%)	Seed (%)	SCAI
Very low	39,07	2,01	19,44	19.12	0.27	70.81
Low	31,46	2,5	12,58	33.31	2.08	16.01
Moderate	19,8	3,33	5,95	24.46	4.80	5.09
High	4,72	5,7	0,83	18.34	10.68	1.71
Very high	4,93	86,44	0,06	4.75	82.15	0.05

6. Conclusion

Geological risk, related to landslide presented a strong danger for the socio-economic of regions located in North part of Algeria; however, the investigations about the landslide problem in Algeria which have already been published are rare and scattered. In recent literature a few attempt at landslide were applied in the North eastern of Algeria. The present study confirmed that the North western of Algeria was also suffered from slope movement problem. The selected region was lacked a precondition studies, maps and documents to define landslide prone area and mitigate landslide consequences.

In this article, two landslide susceptibility maps of the Arzew sector North western of Algeria were established. The FR and VI methods were used to define relationship between landslides spatial distribution and the predisposing factors.

The AUC results using ROC curve indicate that the use of information value model (89.03%) for established LSM provide more accurate prediction in comparing with frequency ratio (85.57%).

In other hand, the results of Seed Cell Area Index (SCAI) model, also confirmed that the landslide susceptibility map elaborate by the information value method is more accurate than the other model used in this work.

Mapping field susceptible of the landslides for the Arzew area can be evaluated by the use of other models and it can be developed by the combination of many others data.

The proposed models experimented can be considered as a powerful tool for decision makers to the revision of the PDAU (master plan of planning and development), furthermore, this document may serve local communities and planners in choosing suitable locations for future projects and take preventive measures about landslide prone area (high and very high landslide susceptibility classes).

References

Achour, Y., Boumezbeur, A., Hadji, R., Chouabbi, A., Cavaleiro, V., Bendaoud, E. A. 2017. Landslide susceptibility mapping using analytic hierarchy process and information value methods along a highway road section in Constantine, Algeria. Arabian Journal of Geosciences 10:194.

Aghdam, I., N., Varzandeh, M.H.M., Pradhan, B. 2016. Landslide susceptibility mapping using an ensemble statistical index (Wi) and adaptive neuro-fuzzy inference system (ANFIS) model at Alborz Mountains (Iran). Environmental Earth Sciences 75:553.

Akgün, A., Dağ, S., Bulut, F. 2008. Landslide susceptibility mapping for a landslide-prone area (Findikli, NE of Turkey) by likelihood-frequency ratio and weighted linear combination models. Environmental Geology 54:1127-1143.

Bai, S., Lü, G., Wang, J., Zhou, P., Ding, L. 2011 GIS-based rare events logistic regression for landslide-susceptibility mapping of Lianyungang, China. Environmental Earth Sciences 62:139-149.

Ballabio, C., Sterlacchini, S. 2012. Support vector machines for landslide susceptibility mapping: the Staffora River Basin case study, Italy. Mathematical geosciences 44:47-70

Benabdellah, M. 2010. Mis en évidence des phénomènes contrôlant le littoral oranais (de la Calère a la pointe de Canastel) : étape fondamentale pour une cartographie des risques géologiques. Mémoire de magister, Université d'Oran, 258p.

Benaissa, A., Cordary, D., Gioraud, A. 1989. Les mouvements de terrain dans la zone urbaine de Constantine (Algérie). Bulletin of the International Association of Engineering Geology-Bulletin de l'Association Internationale de Géologie de l'Ingénieur 40:85-90

Beneder. 2011. Carte d'occupation du sol wilaya d'Oran notice explicative. Bureau national d'études pour le développement rural, Rapport inédite, 13p.

Bourenane, H., Bouhadad, Y., Guettouche, MS., Braham, M. 2015. GIS-based landslide susceptibility zonation using bivariate statistical and expert approaches in the city of Constantine (Northeast Algeria). Bulletin of Engineering Geology and the Environment 74:337-355.

Bui, D.T., Lofman, O., Revhaug, I., Dick, O. 2011. Landslide susceptibility analysis in the Hoa Binh province of Vietnam using statistical index and logistic regression. Natural Hazards 59:1413.

Chen, W., Li, W., Chai, H., Hou, E., Li, X., Ding, X. 2016. GIS-based landslide susceptibility mapping using analytical hierarchy process (AHP) and certainty factor (CF) models for the Baozhong region of Baoji City, China. Environmental Earth Sciences 75:63.

Chen, W., Pourghasemi, H. R., Zhao, Z. 2017. A GIS-based comparative study of Dempster-Shafer, logistic regression and artificial neural network models for landslide susceptibility mapping. Geocarto International 32:367-385.

Ciszak, R. 1993. Evolution géodynamique de la chaîne tellienne en Oranie (Algérie occidentale) pendant le Paléozoïque et le Mésozoïque vol 20. Laboratoire de géologie sédimentaire et paléontologie, Thèse de doctorat, Université Paul Sabatier, 513p.

Conforti, M., Pascale, S., Robustelli, G., Sdao, F. 2014. Evaluation of prediction capability of the artificial neural networks for mapping landslide susceptibility in the Turbolo River catchment (northern Calabria, Italy). Catena 113:236-250.

Corominas, J., Van Westen, C., Frattini, P., Cascini, L., Malet, J. P., Fotopoulou, S., Catani, F., Van DenEeckhaut, M., Mavrouli, O., Agliardi, F., Pitilakis, K., Winter, M.G., Pastor, M., Ferlisi, S., Tofani, V., Herva´s, J., Smith, J.T., 2014. Recommendations for the quantitative analysis of landslide risk. Bulletin of Engineering Geology and the Environment 73, 209–263.

Cruden, D.M, Varnes, D.J. 1996. Landslide Types and Processes, Special Report, Transportation Research Board, National Academy of Sciences, 247: 36-75.

Cui, K., Lu, D., Li, W. 2016. Comparison of landslide susceptibility mapping based on statistical index, certainty factors, weights of evidence and evidential belief function models. Geocarto International:1-21.

Dahoua, L., Yakovitch, S., Hadji, R. 2017.GIS-based technic for roadside-slope stability assessment: an bivariate approach for A1 East-West highway, North Algeria. Mining Science 24.

Djerbal, L., Khoudi, I., Alimrina, N., Melbouci, B., Bahar, R. 2017 Assessment and mapping of earthquake-induced landslides in Tigzirt City, Algeria. Natural Hazards:1-21.

Djerbal, L., Melbouci, B. 2013. Contribution to the mapping of the landslide of Aïn El Hammam (Algeria). In: Advanced Materials Research,. Trans Tech Publ, pp 332-336.

Ercanoğlu, M., Kasmer, O., Temiz, N. 2008. Adaptation and comparison of expert opinion to analytical

hierarchy process for landslide susceptibility mapping. Bulletin of Engineering Geology and the Environment 67:565-578.

Fell, R., Corominas, J., Bonnard, C., Cascini, L., Leroi, E., Savage, WZ. 2008 .Guidelines for landslide susceptibility, hazard and risk zoning for land use planning. Engineering Geology 102:85-98.

Fenet, B. 1975. Recherches sur l'alpinisation de la bordure septentrionale du Bouclier africain à partir de l'étude d'un élément de l'orogène nord-maghrébin : les monts du Djebel Tessala et les massifs du littoral oranais, Thèse de doctorat, Université de Nice, 310p.

Ghosh, K., Bandyopadhyay, S., De, S.K. 2017. A Comparative Evaluation of Weight-Rating and Analytical Hierarchical (AHP) for Landslide Susceptibility Mapping in Dhalai District, Tripura. In: Environment and Earth Observation. Springer, pp 175-193.

Gomes, A., Gaspar, J., Goulart, C., Queiroz, G. 2005. Evaluation of landslide susceptibility of Sete Cidades Volcano (S. Miguel Island, Azores). Natural Hazards and Earth System Science 5:251-257.

Gorsevski, P.V., Gessler, P.E., Boll, J., Elliot, W.J., Foltz, R.B. 2006*a*. Spatially and temporally distributed modeling of landslide susceptibility. Geomorphology 80:178-198.

Gorsevski, P.V., Gessler, P.E., Foltz, R.B., Elliot, W.J. 2006*b*. Spatial prediction of landslide hazard using logistic regression and ROC analysis. Transactions in GIS 10:395-415.

Gorsevski, P.V., Jankowski, P., Gessler, P.E. 2006*c*. An heuristic approach for mapping landslide hazard by integrating fuzzy logic with analytic hierarchy process. Control and Cybernetics 35:121-146.

Gourinard, Y. 1952*a*. Carte géologique détaillée de l'Algérie. Feuille Arzew (127) 2ème idition, Serv. Carte Géol. Alger, Algérie.

Gourinard, Y. 1952*b*. Carte géologique détaillée de l'Algérie. Feuille Oran (159) 2ème idition, Serv. Carte Géol, Alger, Algérie.

Guemache, M.A., Chatelain, J.L., Machane, D., Benahmed, S., Djadia, L. 2011. Failure of landslide stabilization measures: the Sidi Rached viaduct case (Constantine, Algeria). Journal of African Earth Sciences 59:349-358.

Guzzetti, F., Reichenbach, P., Cardinali, M., Galli, M., Ardizzone, F. 2005. Landslide hazard assessment in the Staffora basin, northern Italian Apennines. Geomorphology 72:272-299.

Hadji, R., Boumazbeur, A., Limani, Y., Baghem, M., el Madjid Chouabi, A., Demdoum, A. 2013. Geologic, topographic and climatic controls in landslide hazard assessment using GIS modeling: a case study of Souk Ahras region, NE Algeria. Quaternary International 302:224-237.

Hadji, R., Limani, Y., Demdoum, A. 2014. Using multivariate approach and GIS applications to predict slope instability hazard case study of Machrouha municipality, NE Algeria. In: Information and Communication Technologies for Disaster Management (ICT-DM), 1st International Conference on, 2014. IEEE, pp 1-10.

Hadji, R., Rais, K., Gadri, L., Chouabi, A., Hamed, Y. 2017. Slope failure characteristics and slope movement susceptibility assessment using GIS in a medium scale: a case study from Ouled Driss and Machroha municipalities, Northeast Algeria. Arabian Journal for Science and Engineering 42:281-300.

Intarawichian, N., Dasananda, S. 2010. Analytical Hierarchy Process For Landslide Susceptibility Mapping In Lower Mae Chaem Watershed, Northern Thailand. Suranaree Journal of Science & Technology 17.

Lee, S., Talib, J.A. 2005. Probabilistic landslide susceptibility and factor effect analysis Environmental geology 47:982-990

Mahdadi, F., Boumezbeur, A., Hadji, R., Kanungo, D.P., Zahri, F. 2018. GIS-based landslide susceptibility assessment using statistical models: a case study from Souk Ahras province, NE Algeria. Arabian Journal of Geosciences 11:476

Özdemir, A., Altural, T. 2013. A comparative study of frequency ratio, weights of evidence and logistic regression methods for landslide susceptibility mapping: Sultan Mountains, SW Turkey. Journal of Asian Earth Sciences 64:180-197.

Peng, L., Niu, R., Huang, B., Wu, X., Zhao, Y., Ye, R. 2014. Landslide susceptibility mapping based on rough set theory and support vector machines: A case of the Three Gorges area, China. Geomorphology 204:287-301.

Perrodon, A. 1957. Etude géologique des bassins néogènes sublittoraux de l'Algérie occidentale. Thèse de doctorat, Université d'Oran, 301p.

Pourghasemi, H., Moradi, H., Aghda, S.F. 2013. Landslide susceptibility mapping by binary logistic regression, analytical hierarchy process, and statistical index models and assessment of their performances. Natural Hazards 69:749-779.

Pradhan, B. 2011. Manifestation of an advanced fuzzy logic model coupled with Geo-information techniques

to landslide susceptibility mapping and their comparison with logistic regression modeling. Environmental and Ecological Statistics 18:471-493.

Pradhan, B., Jebur, M.N., Abdullahi, S. 2017. Spatial Prediction of Landslides Along Jalan Kota in Bandar Seri Begawan (Brunei) Using Airborne LiDAR Data and Support Vector Machine. Laser Scanning Applications in Landslide Assessment. Springer, pp 167-178.

Raja, NB., Çiçek, I., Türkoğlu, N., Aydın, O., Kawasaki, A. 2017. Landslide susceptibility mapping of the Sera River Basin using logistic regression model. Natural Hazards 85:1323-1346.

Regmi, N.R., Giardino, J.R., Vitek, J.D. 2010. Modeling susceptibility to landslides using the weight of evidence approach: Western Colorado, USA. Geomorphology 115:172-187.

Sezer, E.A., Pradhan, B., Gökçeoğlu, C. 2011. Manifestation of an adaptive neuro-fuzzy model on landslide susceptibility mapping: Klang valley. Malaysia Expert Systems with Applications 38:8208-8219.

Süzen, M., Doyuran, V. 2004. A comparison of the GIS based landslide susceptibility assessment methods: multivariate versus bivariate. Environmental geology 45:665-679.

Thiery, Y. 2007. Susceptibilité du Bassin de Barcelonnette (Alpes du Sud, France) aux'mouvements de versant': cartographie morphodynamique, analyse spatiale et modélisation probabiliste. Thèse de doctorat, Université de Caen, 445p.

Thomas, G. 1985. Géodynamique d'un bassin intramontagneux Le bassin du Bas Chélif occidental (Algérie) durant le Mio-Plio-Quaternaire. Thèse de doctorat, Université de Pau, 594p.

Van Westen, C. J. 1993. Application of geographic information systems to landslide hazard zonation. ITC Publication, Vol.15. International Institute for Aerospace Survey and Earth Sciences, Enschede 245pp.

Yalçın, A., Reis, S., Aydınoğlu, A., Yomralıoğlu, T. 2011. A GIS-based comparative study of frequency ratio, analytical hierarchy process, bivariate statistics and logistics regression methods for landslide susceptibility mapping in Trabzon, NE Turkey. Catena 85:274-287.

Yeşilnacar, E., Topal, T. 2005. Landslide susceptibility mapping: a comparison of logistic regression and neural networks methods in a medium scale study, Hendek region (Turkey). Engineering Geology 79:251-266.

Yılmaz, I. 2009. A case study from Koyulhisar (Sivas-Turkey) for landslide susceptibility mapping by artificial neural networks Bulletin of Engineering Geology and the Environment 68:297-306.

Yılmaz, I. 2010. Comparison of landslide susceptibility mapping methodologies for Koyulhisar, Turkey: conditional probability, logistic regression, artificial neural networks, and support vector machine. Environmental Earth Sciences 61:821-836.

Yin, K., Yan, T. 1988. Statistical prediction model for slope instability of metamorphosed rocks. In: Proceedings of the 5th International Symposium on Landslides. sl]:[sn], pp 1269-1272.

Youssef, A.M., Al-Kathery, M., Pradhan, B. 2015. Landslide susceptibility mapping at Al-Hasher area, Jizan (Saudi Arabia) using GIS-based frequency ratio and index of entropy models. Geosciences Journal 19:113-134.

Bulletin of the Mineral Research and Exploration

**BULLETIN OF THE
MINERAL RESEARCH AND EXPLORATION**

CONTENTS

Geological structures mapping using aeromagnetic prospecting and remote sensing data in the karstic massif of Beni Mellal Atlas, Morocco

Ikram BOUTIRAME[a*] , Ahmed BOUKDIR[aID], Ahmed AKHSSAS[bID] and Ahmed MANAR[cID]

[a]*Sultan Moulay Slimane University, Faculty of Sciences and Technics, Department of Geology, Post box 523, Beni Mellal/Morocco.*
[b]*Mohamed 5 University, Mohammadia School of Engineers, Laboratory of Applied Geophysics, Geotechnics, Engineering Geology and Environment, Post box765, Agdal, Rabat/Morocco.*
[c]*Ministry of Energy, Mines and sustainable development, Postbox 6208, Agdal, Rabat/Morocco.*

Research Article

ABSTRACT

The current study exposes the results of aeromagnetic data interpretation and a combined analysis of 1-A sentinel radar image that cover the study area of Beni Mellal Atlas in order to describe the structural geometry and to understand its tectonic evolution.The map of the reduced to pole of residual magnetic field highlights various magnetic anomalies with high amplitudes that correspond to Jurassic-Cretaceous basaltic formations outcropping synclinal basins of Beni Mellal Atlas. The interpretation of magnetic data using tilt derivative (TDR), horizontal gradient technique coupled to upward continuation and Euler Deconvolution allows us to distinguish the fractures network that is affecting the study area. In order to complete this analysis, the Sentinel-A radar image is processed and filtered using SNAP ESA Sentinel-1 toolbox software to extract lineaments. The final structural map reveals four faults groups oriented respectively NE-SW, ENE-WSW to E-W, N-S and NW-SE Their depths estimated by the application of Euler deconvolution exceed 1500 m.Thoses faults have played a major role in structural evolution of Beni Mellal Atlas.

1. Introduction

The detection of geological lineaments such as faults, fractures, lithological contacts...etc., is a crucial step for the success of hydrogeological and mining research studies. These linear structures may contain mineralization or constitute potential pathways for groundwater flow, particularly in the karstic area (Khamis et al., 2014; Dauteuil et al., 2016). The karstic massif of Beni Mellal, which is the object of this study, is a bordering mountain range where the rise of the carbonate rocks overlooks Tadla plain from 2400 m (Benzaquen, 1963; Rolley, 1973; Monbaron, 1982). The Beni Mellal Atlas –Tadla plain junction zone, known as the Beni Mellal Dir, is a highly undulating zone with steep-slope valleys (Benzaquen,

1963) and is characterized by a dense vegetation cover that hides the geological formations and obstructs the discrimination of fracture network. It is therefore necessary to use indirect methods such as remote sensing and geophysical prospecting to overcome these difficulties.

Remote sensing is widely used in geological and structural mapping (Srivastava and Bhattacharya, 2006; Alonso-Contes, 2011; Adiri et al., 2017). The use of this technique becomes more effective when combined with complementary data such as geophysical. In fact, remote sensing can extract multitude of data about the structure and composition of the Earth's surface using satellite image acquisition and interpretation processes. The radar images provide

the information on the subsoil roughness and texture and highlight the relief of the structural discontinuities. Thus, they have a strong potential for the geological studies and in particular structural evaluations owing to their independence to environmental conditions (e.g. climatic conditions, density of vegetation cover, rugged topography ...).

Numerous studies have been carried out using radar remote sensing tools in structural mapping (Mansour and Ait Brahim, 2005; Corgne et al., 2010). In Morocco, Adiri et al. (2017) have made a comparison between remote sensing data multi-sources (optical and radar remote sensing) for automatic lineaments extraction in the region of Sidi Flah-Bouskour inlier, Anti-Atlas Morocco. Because of its high sensitivity to geomorphology, the Sentinel-1 radar sensor gives better results than optical sensors. In reality, each geological formation is characterized by a particular radar texture that corresponds to a defined magnetic, gravimetric or electrical anomaly. The synergy of geophysical data and radar images makes it possible to gather precise geological informations to determine the fractures network (Ranganai et al., 2008; Megwara et al., 2014; Ejep et al., 2017; Boutirame et al., 2018).

The aim of this study is the lineament mapping in the Beni Mellal Atlas based on the combination of airborne magnetic data and Sentinel-1 image interpretation. The fractures deduced from this study checked against field measurements and observations to characterize its spatial distribution in the study area on the one hand, and to be able to understand its structural and geological origin on the other hand.

1.1. Description of Study Area

1.1.1. General Context

The Beni Mellal Atlas, the subject of this study, corresponds to the north occidental edge of the central High Atlas (Rolley, 1973). It is located in the south of Tadla plain, outskirts of the junction between High and Middle Atlas. Its highest point is R'Nim mountain that reaches 2411m above sea level (Figure 1a and b). A decrease in altitude is observed from south to north, it moves up from 1000 m (El Ksiba) on the edge of the Atlas to less than 500 m in Tadla plain. The karstic massif of Beni Mellal Atlas is formed; essentially; by fractured carbonate deposits of Lower and Middle Jurassic, constituting the main outcrops of the mountainous area that overhangs Beni Moussa
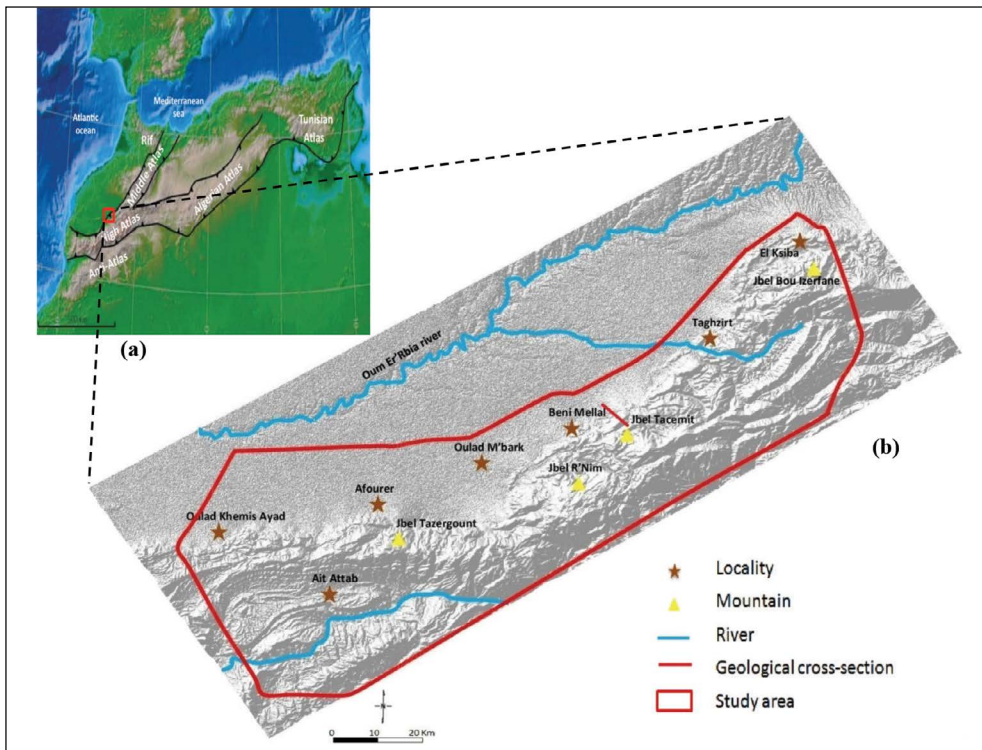
Figure 1- a) Map of North Africa showing the location of the study area on digital topography; b) Shaded relief of Sentinel-1A image showing the study area limits.

plain. Thoses formations carried in altitudes, present typical karst forms such as dolines, avens, caves and sinkholes (Bouchaou, 1988).

1.1.2. Geological Setting

The Beni Mellal Atlas is an open and flattened anticline that abruptly dominates Beni Moussa plain through a fault system, the most important one is the North Atlasic Fault (Tadla overlap). It is the key area of Central High Atlas (Guezal et al., 2013), its geological history is therefore linked to this intracontinental chain (Michard,1976; Mattauer et al., 1977; Ziegler et al., 1995), whose various structural elements are a result of geodynamic evolution that began with distal tectonics at the end of Paleozoic and during Mesozoic by the opening of Tethys sea (Du Dresnay, 1972; Laville and Harmand, 1982; Beauchamp,1988 and Piqué et al., 1998). Its northern border is characterized by a succession of overlapping structural units that rest on the Liassic and Tertiary

thrusts of Dir (Figure 2c). The Mesozoic formations consist of massive carbonates of Lower and Middle Jurassic, detrital Bathonian-Early Cretaceous deposits ("red-layer" formations), and Cretaceous carbonates and terrigenous deposits (Figure 2a).

The Mesozoic serie rests on a Paleozoic basement deformed during the Hercynian orogeny (Hoepffner et al., 2006). It begins with Triassic rocks formed of red clays with basaltic intercalations. The Lower and Middle Lias consist of bedded limestones and dolomites surmounted by chocolate marls of Toarcian-Aalenian age. The Upper Jurassic and Lower Cretaceous are characterized by red detrital deposits knows in the literature as «red beds» (Souhel, 1996; Haddoumi, 1988). This "red beds" formation is composed of three lithostratigraphical units forming large basins (Jenny et al., 1981). We distinguish from bottom to top: Guettioua formation, Iouaridene formation and detrital doposits of Jbel Sidal formation (Charrière et al., 2005; Haddoumi et al., 2010). This
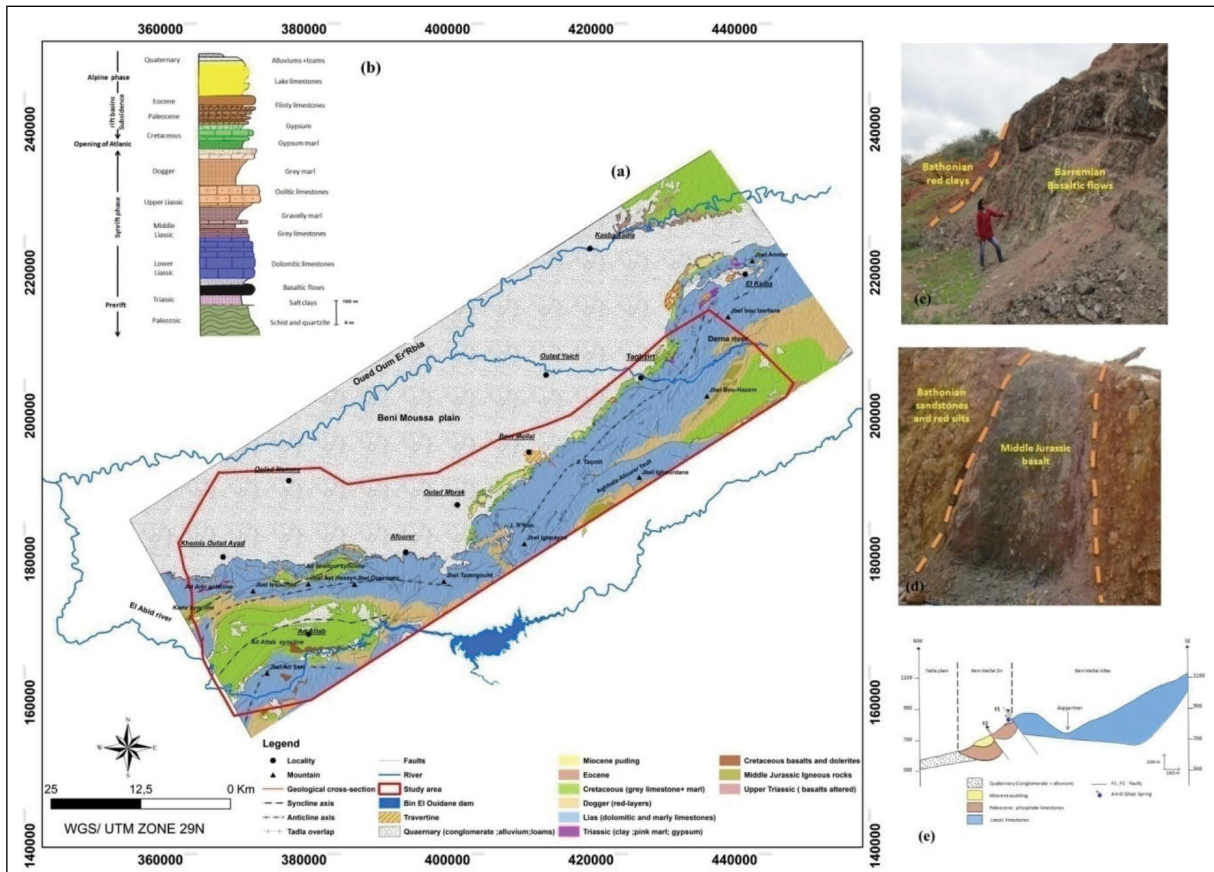
Figure 2- a) Geological map of the study area (Benzaquen, 1963; Monbaron, 1985 and Verset, 1985), b) Litho-stratigraphic log of Beni Mellal Atlas, c) Pictures showing basaltic flows in Beni Mellal Atlas, d) NW-SE geological cross-section showing the different units of the study area: Tadla plain, piemont and mountainous zone of Beni Mellal Atlas.

important detrital deposit has been accompanied by Juarrasic-Cretaceous magmatic occurrences. The latter, outcrop in the synclinal basins of Beni Mella (Guezal et al., 2013) represented as two successive horizons interbedded in the sandstone-detrital series of "red beds" (Jenny et al., 1981; Haddoumi, 1988; Souhel, 1996) (Figure 2b):

- Basaltic horizon B1: outcrops on the northern flank of Ait Attab syncline. This basaltic complex consists of volcanoclastic deposits placed in the upper part of Guettioua formation (Michard et al., 2011);

- Basaltic horizon B2: is associated with the base of Jbel Sidal formation and thicker compared to the previous one, this second episode is effected during the Barremian with the form of three massive flows separated by red clays (Bardon et al., 1978; Souhel, 1996).

The Tertiary serie is presented by phosphated limestones and Maestrichtian-Paleocene marls. The Mesozoic and Tertiary cover is unconformably capped by Mio-Pliocene lake limestones and Quaternary alluviums (Jabour and Nakayama, 1988; Beauchamp, 1988).The mainly carbonate marine sedimentation during the lower and middle Lias and the detrital deposits during the lower Bathonian-Cretaceous (Souhel, 1987; Haddoumi, 1988) were controlled by a tectonics extension oriented NW-SE. Indeed, during the lower and middle Lias two major faults were active: the Beni Ayat border fault and the Ait Seri fault which delimits in the north the Ait Seri block (Figure 3) where a reef-facies carbonate platform is deposited. The Toarcian's marly deposits obscure the Ait Seri fault, and at the same time the tectonic activity is transferred to another fault called Karia fault that appears between the Karia and Ait Imelloul blocks. The distensive synsedimentary tectonics continues with the appearance of "Issoumer fault" bordering and tipping the Ait Attab block to the west (Figure 3).

2. Data and Method

2.1. Aeromagnetic Data Processing

The airborne magnetic data, which is used in this study, was obtained from the Ministry of Mines and Energy of Rabat in form of two residual magnetic field maps with a scale of 1: 100,000 (Beni Mellal
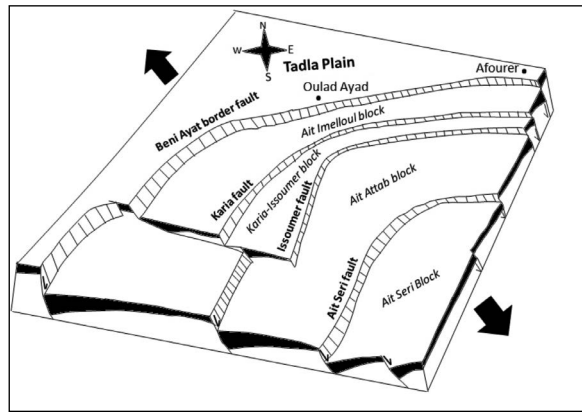
Figure 3- Schematic model showing the paleogeography of Ait Attab region during Jurassic.

and Afourer sheets). These data result from an aeromagnetic study carried out in the Central High Atlas by the African Geophysical Company in 1970. The data was acquired by a magnetic equipment type C.S.F Caesium Steamer on board a plane type 680 FL. At a barometric altitude of 2600 m, the aeromagnetic survey carried out consisted of flight lines oriented NW-SE and spaced 3.5 to 4 km apart, and transverse lines oriented NE-SW with 10 to 15 km spacing. The two residual magnetic field maps were scanned and digitized using ArcGIS software, then processed by applying several mathematical filters and transformation operators using Geosoft Oasis Montaj software (version 8.3) namely the horizontal gradient, Tilt-Derivative and Euler Deconvolution.The application of these filters has allowed the elaboration of several maps, which we refer to in the review and structural interpretation of the magnetic results.

2.1.1. Residual Magnetic Field and Reduction to the Pole (RTP)

The residual magnetic field map (Figure 4) highlights the existence of magnetic maxima and minima showing important variation of the magnetization in the subsoil with magnetic field values oscillating between 960 and 1064 nT. In order to better visualize these magnetic anomalies and to facilitate the analysis and the structural interpretation of results, the residual aeromagnetic field has been reduced to pole (RTP). This reduction makes it possible to eliminate the anomalies distortion caused by inclination of the earth's magnetic field (El Gout et al., 2009) by transforming the magnetic anomaly as if it were located at the north magnetic pole and to
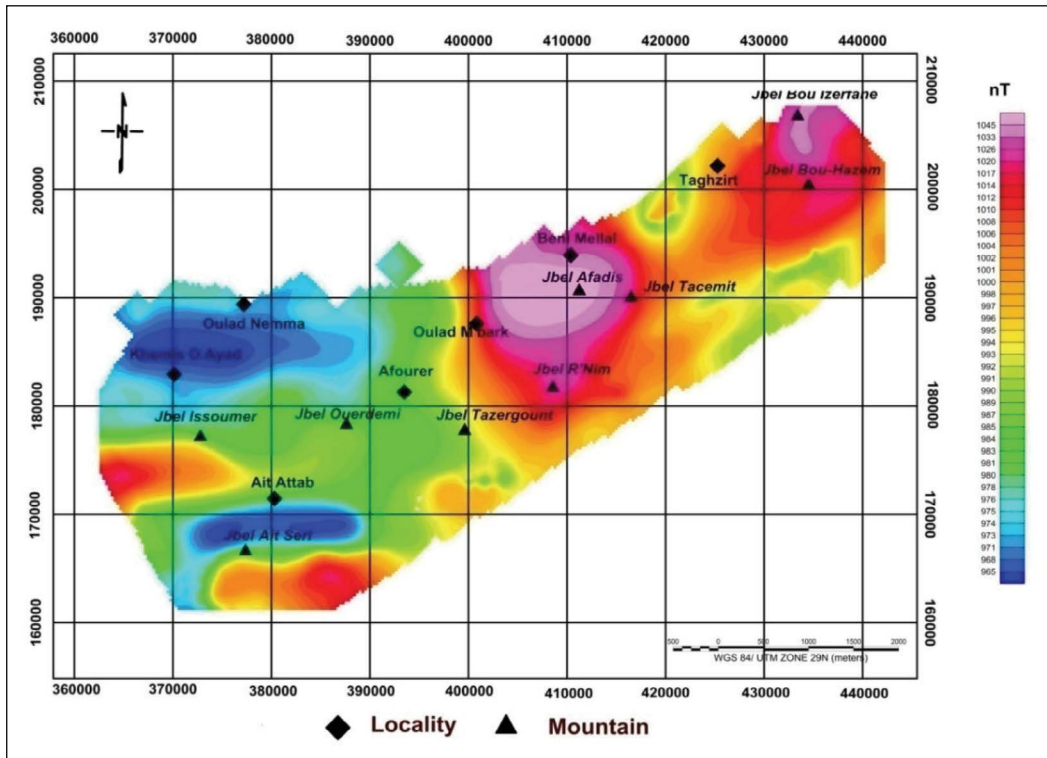
Figure 4- Residual magnetic field of the study area.

replace back anomalies on the apex of the sources that create them, provided that the magnetization is not remanent (Debeglia, 2005).

The analysis of (Figure 5) the reduced to the pole residual magnetic map reveals the existence of several magnetic anomalies of different shapes and amplitudes. It shows high magnetic responses in the center, South-West and the north-east extremity of the study area (P1, P2, P3, P4, P5, and P6), while the low magnetic anomalies (N1 and N2) in blue and green colors are observed in the western and eastern parts of Beni Mellal Atlas.

2.1.2. Tilt Angle Transformation "Tilt-Derivative" (TDR)

In order to obtain as much information as possible from initial aeromagnetic data, we applied the Derivative Tilt Operator (TDR) (or Tilt angle) using the following geomagnetic field elements: inclination I = 45°14' north and declination D = 7°12' west, corresponding to aeromagnetic survey that dates from October 1975. The usefulness of this transformation operator lies in the fact that it enhances all the magnetic anomalies either with small or large amplitudes (Miller

and Singh, 1994; Salem et al., 2008). It calculates the arctangent of the ratio of vertical derivative to total horizontal derivative of the magnetic field T (Salem et al., 2008). The equation of this transformation is as follows:

$$\Theta = \tan^{-1} \left[\frac{\frac{\delta T}{\delta Z}}{\sqrt{\left(\frac{\delta T}{\delta x}\right) + \left(\frac{\delta T}{\delta y}\right)}} \right] \qquad (1)$$

The map of the reduced residual magnetic field transformed by the method of "Tilt Derivative" (Figure 6) facilitates the structural interpretation of magnetic data and makes it possible to locate the linear structures such as the faults (Amar et al.,2012 and Amar, 2013). Indeed, the zero contours lines of TDR filter (θ = 0) mark the abrupt change between two different magnetic sources which consequently correspond to the contact between these sources.

2.1.3. Boundary Analysis Method: Horizontal Gradient

With the objective of better exploit this magnetic data and to highlighting the different structural axis that defines the deep structure of the study area,
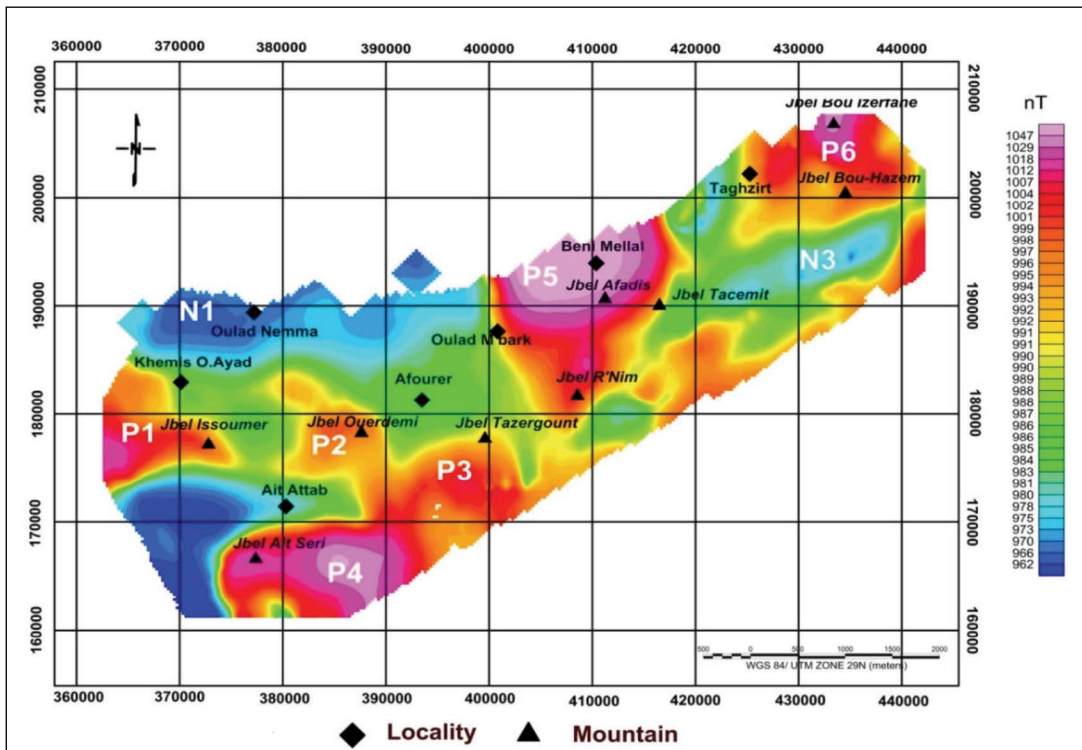
Figure 5- Reduced to pole of residual magnetic field map.
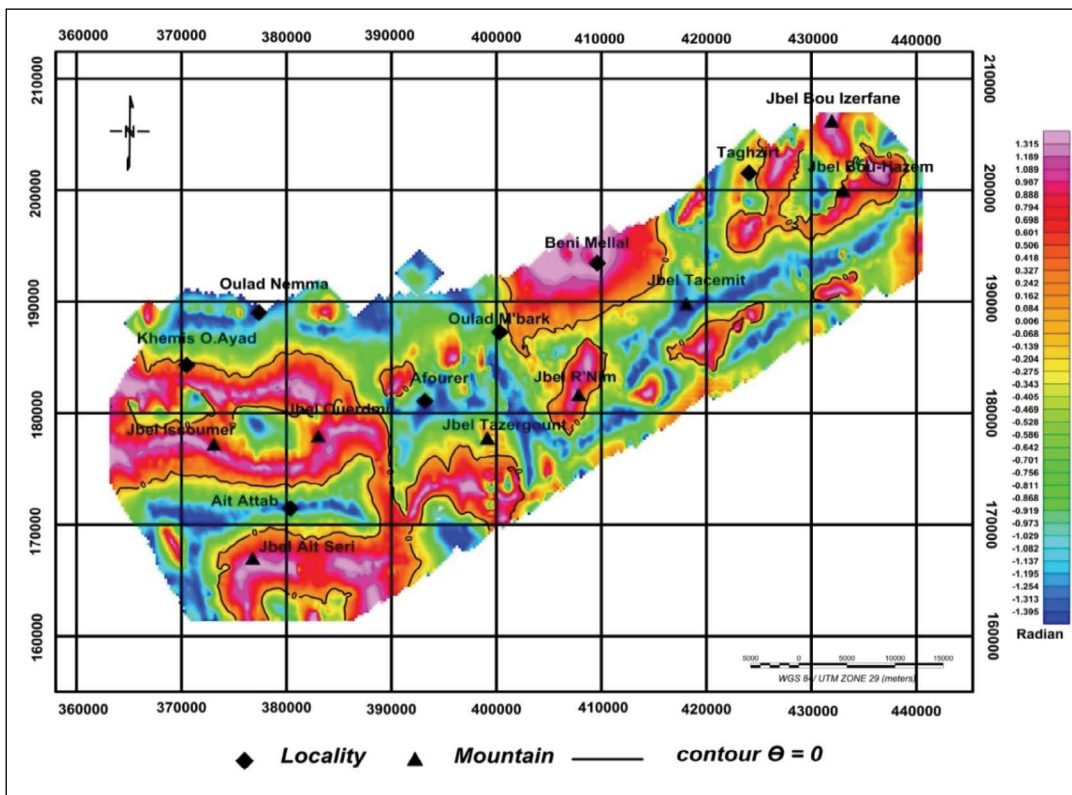
Figure 6- Tilt-Derivative magnetic map.

we have applied a multi-scale analysis method of magnetic contacts, based on, the joint use of horizontal gradient and the upward continuation techniques. This method, used by several authors (Everaerts and Mansy, 2001; Abderbi and Khattach, 2011), allows on one hand to locate the zones with rapid variation of the magnetic field caused by the lithological change or the presence of geological discontinuities (fractures, faults…), and determine the dip direction of thoses geological structures on the other hand. Indeed, the magnetic anomalies correspond to inflection points which transform after the horizontal gradient calculation into local maxima. These maxima are located above the geological contacts that present magnetic susceptibility contrasts (Van Senden et al., 1990). In order to determine the dip direction of thoses structures, a series of upward continuation has been carried out at different altitudes. For each level the horizontal gradient of the residual magnetic field is calculated and its local maxima are determined. If the structures are vertical, the maxima obtained at each altitude are superimposed. However, their migration with the upwards continuation indicates the dip direction (Figure 7).

2.1.4. Euler Deconvolution

The Euler Deconvolution method was used to estimate the location of anomalous sources on the horizontal plane and their depths (Thompson, 1982; Reid et al., 1990; Moreau et al., 1996). This technique is based on the resolution of the Euler homogeneity equation (1) using the structural index N (Reid et al., 1990) which measures the rate of potential field changes. This index varies as a function of the geometry of the detected source (Oruç and Selim, 2011).

$$(x-x0) \left(\frac{dM}{dx}\right) + (y-y0) \left(\frac{dM}{dy}\right) + (z-z0) \left(\frac{dM}{dz}\right) = N*(B-M) \quad (1)$$

Where (x0, y0, z0) are the coordinates of the magnetic source, M represents the total field measured at (x,y,z), B is the regional value of the total field and N indicates the structural index.

In the current study, we applied the Euler Deconvolution method to the residual magnetic field reduced to pole using a structural index equal to zero (N = 0) with a window size of 10*10 and a maximum
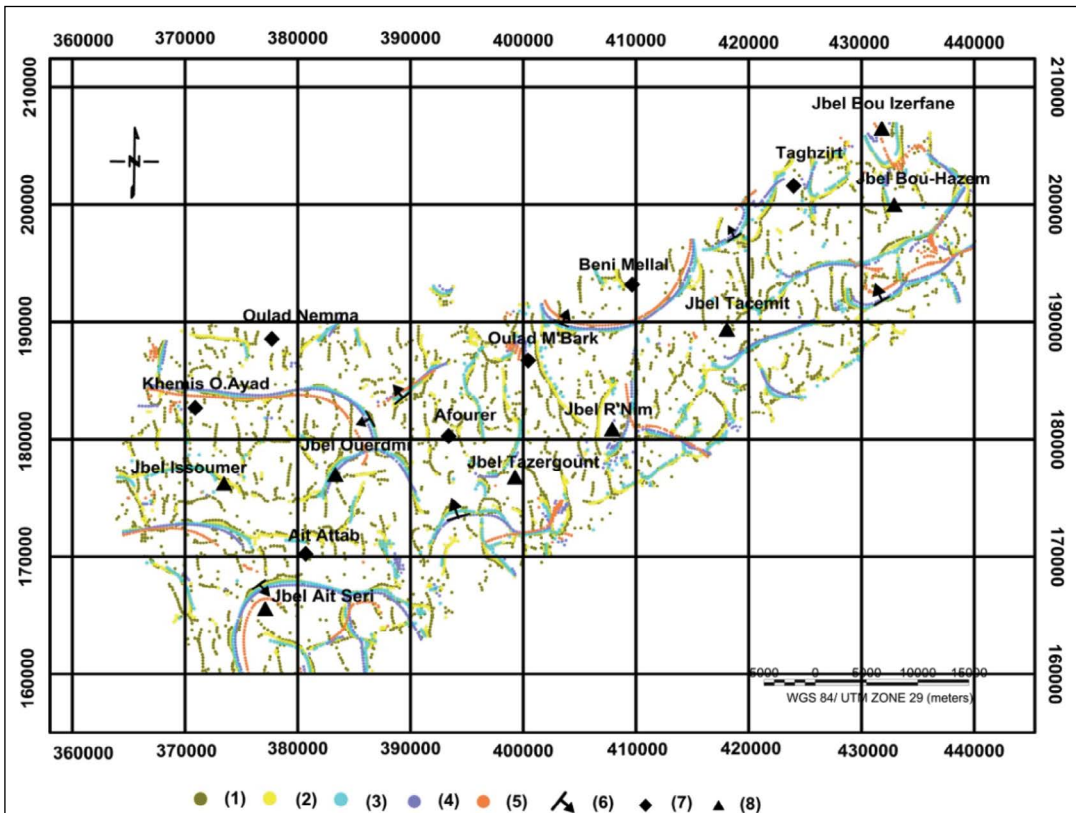
Figure 7- Superposition of the horizontal gradient maxima and its upward continuations at different altitudes: 1) 0 m; 2) 500 m; 3) 1 km; 4) 2 km; 5) 4 km. 6) dipping direction; 7) locality; 8) mountain.

relative error of 15%. A digital Elevation Model was used to remove the Euler solutions whose elevation is higher than the altitude ground.

2.2. Remote Sensing Data Processing

To achieve our objective, a Sentinel-1A radar image is used in this study. This image was acquired on 2 April 2017 in C-band ($\lambda = 5.66$ cm) (Table 1). It was processed and analyzed by a free and open source software "SNAP ESA Sentinel-1 toolbox S1TBX". It is available on the official website of European Space Agency ESA.

Table 1- Sentinel-1A image characteristics.

Radar image	Sentinel-1A data
Acquisition time	02 April 2017
Acquisition orbit	Descending
Polarization	C-band (5.4GHz)
Polarization	VV-VH
Data product	Level-1 GRD

The raw radar image has undergone preliminary processing that consists of radiometric, atmospheric and geometric correction to mitigate the atmospheric effects and topographic disturbances affecting the recorded information quality (Corgne et al., 2010). Thereafter, a "refined Lee" filter has been applied to the radar image to eliminate the flicker effect (speckle reduction) (Lee et al., 1999). For improving the lineaments perception; spatial filters were applied to the pre-treated radar image as per the four main directions N-S; NE-SW; NW-SE and E-W (Figure 8).

The interpretation and extraction of lineaments was done visually (manual extraction). Indeed, Hobbs, 1912 described the lineaments as any significant line that reveals the hidden architecture of the subsoil and having a well-defined structural signification. In our study, the lineaments location is mainly identified by their effect on the landscape (Lachaine, 1999), a change in texture or geometric shape or else by the hydrographic network disturbance. To avoid taking into consideration all linear structures with anthropogenic origin (crest line, road, paths, electrical power lines,, cultivated areas, etc.), the processed radar image has been superimposed with the topographic and land cover maps of the study area to eliminate them during the lineaments extraction. The figure 9 shows the visual interpretation results of Sentinel-1 image.

The analysis of this map shows a difference in the lineament distribution in the study area. Indeed, the
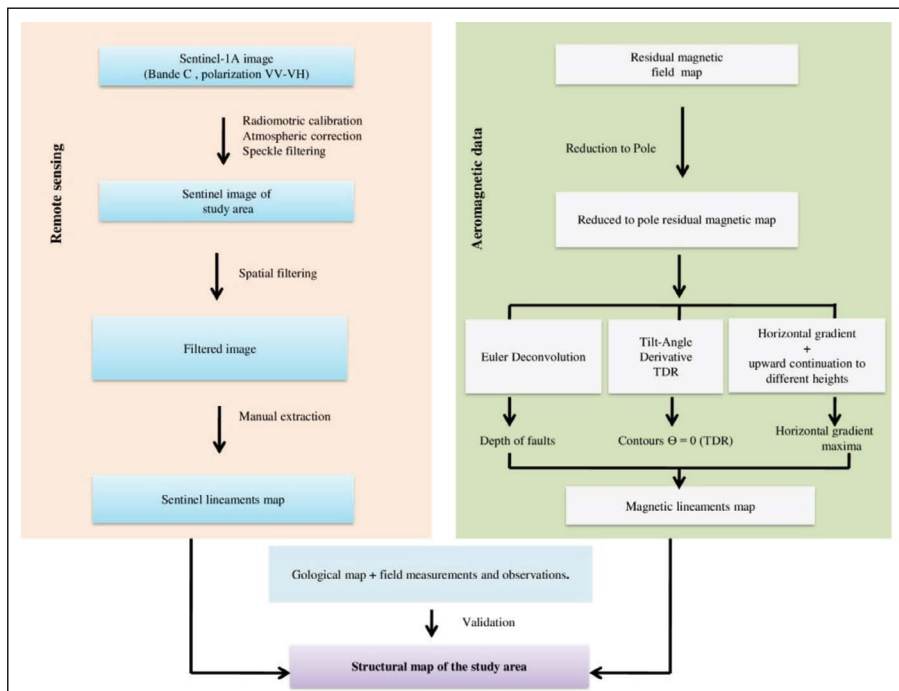
Figure 8- Flowchart of adopted methodology for lineament mapping.
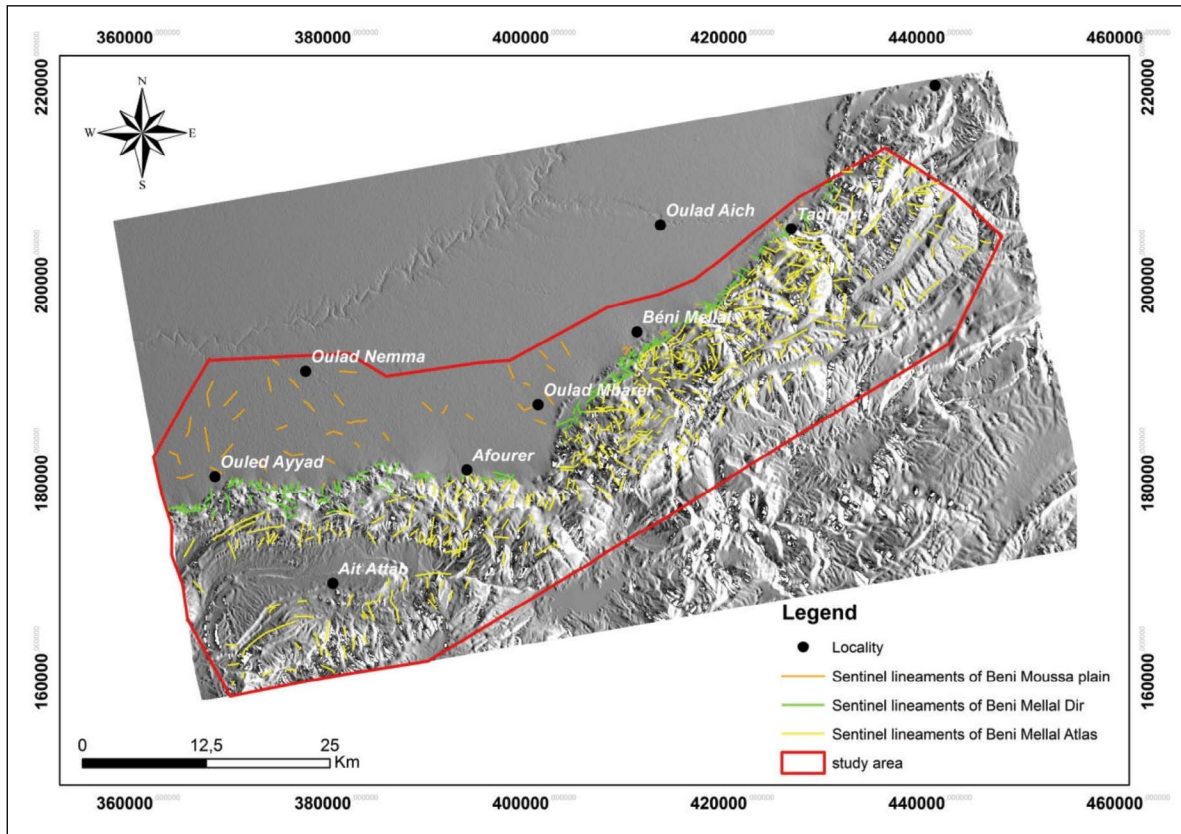
Figure 9- Extracted lineaments from processing Sentinel-1 image (Boutirame et al., 2018).

fracture density becomes more important when we go from the Beni Moussa plain towards the mountainous area of Beni Mellal Atlas. This latter presents a high lineament density with a predominance of NE-SW to ENE-WSW trending.This is related to the dolomitic and limestone nature of the Jurassic formations that occupy the totality of Beni Mellal Atlas. While the Beni Mousa plain shows a low fracture density due to of the presence of quaternary deposits which mask the deep faults affecting the Cenozoic cover of this plain. In the piedmont of Beni Mellal, the junction zone between Beni Mellal Atlas and the Beni Moussa plain, the main directional peaks that predominate this transition zone are oriented E-W and ENE-WSW, they are inherited from Late Variscan period (Du Dresney,1975; Mattauer et al., 1977).

3. Results and Discussion

The map of the reduced residual magnetic field to the pole (Figure 5) made it possible to distinguish several high and weak amplitudes anomalies,

characterized by an intensity values pair (high values in red to pinkish and weak values in blue). The observed magnetic signatures generally show a NE-SW to ENE-WSW and E-W trend in its orientation. To determine the geological sources of these magnetic anomalies, the geological map was superimposed with the magnetic data reduced to pole. In the western part of the study area, four geomorphological and structural zones have been identified; thoses zones correspond to two depressions and two high regions separated by major structural accidents (Figure 10). We distinguish from north to south: Beni Moussa plain (N1), the border zone of Afourer Atlas (P1, P2 and P3), Ait Attab syncline zone (N2) and the Ait Rhouja-Ait Seri zone (P4). The positive anomaly P1 reflects the magnetic signature of Ait Arki anticline occupied by the Triassic gypsum and basaltic formations.These formations have revealed at a depth of 1490 m in the KMS1 oil drilling, carried out near the Khemis Oulad Ayad locality (B.R.P.M., 1971).

The areas with high anomalies (P2, P3 and P4) are attributed to basaltic flows intercalated between
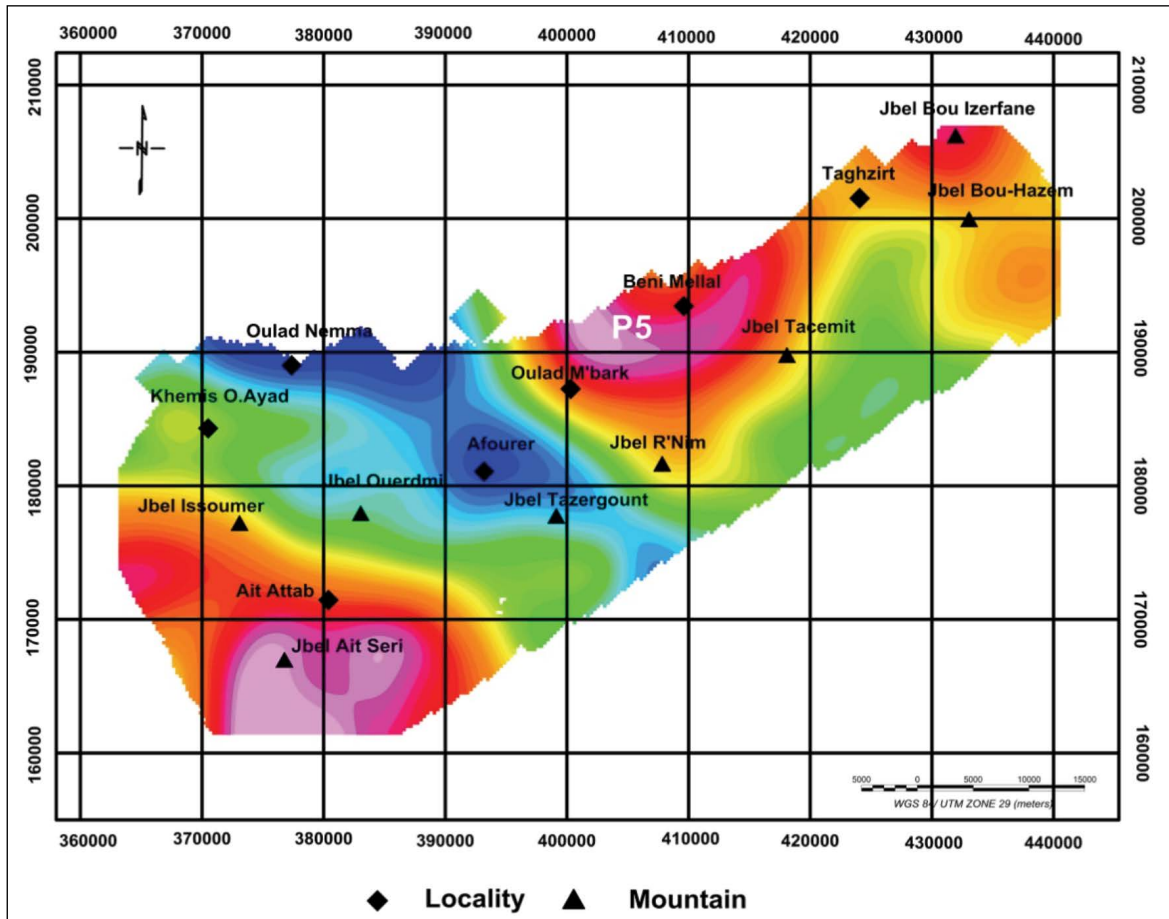
Figure 10- Upward continuation map for 4 km generated from RTP of residual magnetic field.

the mid-Jurassic "red beds" (Souhel 1996; Michard et al., 2011). These basaltic flows result from two middle Jurassic and early Cretaceous magmatic events (Monbaron 1981; Jenny et al., 1981) (Figure 5), that confirms to us these high magnetic anomalies are generated by these magnetic formations. In the eastern part of the study area, the geological outcrops are mainly presented by Liassic carbonates. The magnetic anomaly P5 does not seem to have a corresponding surface expression, thereby suggesting that its source is deeply buried. Indeed, this anomaly, whose the center is located in the west of Beni Mellal, persists to a continuation of 4 km, witnessing its deep origin (Figure 11).

The second anomaly P6, located at the western extremity of the study area appears to be correlated with the presence of Middle Jurassic magmatic intrusions in Taghzirt region and upper Triassic argillites in some locations (Rolley 1978; Haddoummi et al., 2010). The negative magnetic

anomalies N1, N2 and N3 correspond respectively, to the Quaternary cover of the Tadla plain, the Ait Attab syncline whose heart is occupied by the Cretaceous carbonate and terrigenous formations; finally; to the Liassic slab of the Atlas Afourer that overcomes the Beni Moussa plain. These formations are characterized by a weak magnetic susceptibility responsible for the low signature compared to previous ones.

The TDR map (Figure 6) has made it possible to identify the magnetic anomalies already detected by the reduced residual magnetic field map. The zero contour lines (inclination angle θ =0) corresponds to geological contacts such as faults, fracture zones or lithological boundaries (Salem et al., 2008). Indeed, the projection of the Tilt derivative map on the geological map of the study area reveals the existence of a fault systems mainly oriented in ENE-WSW, E-W, N-S and NW-SE. Thoses directions characterize the Atlasic Chain evolution during Mesozoic and Cenozoic periods (Choubert and Faure-Muret, 1960-
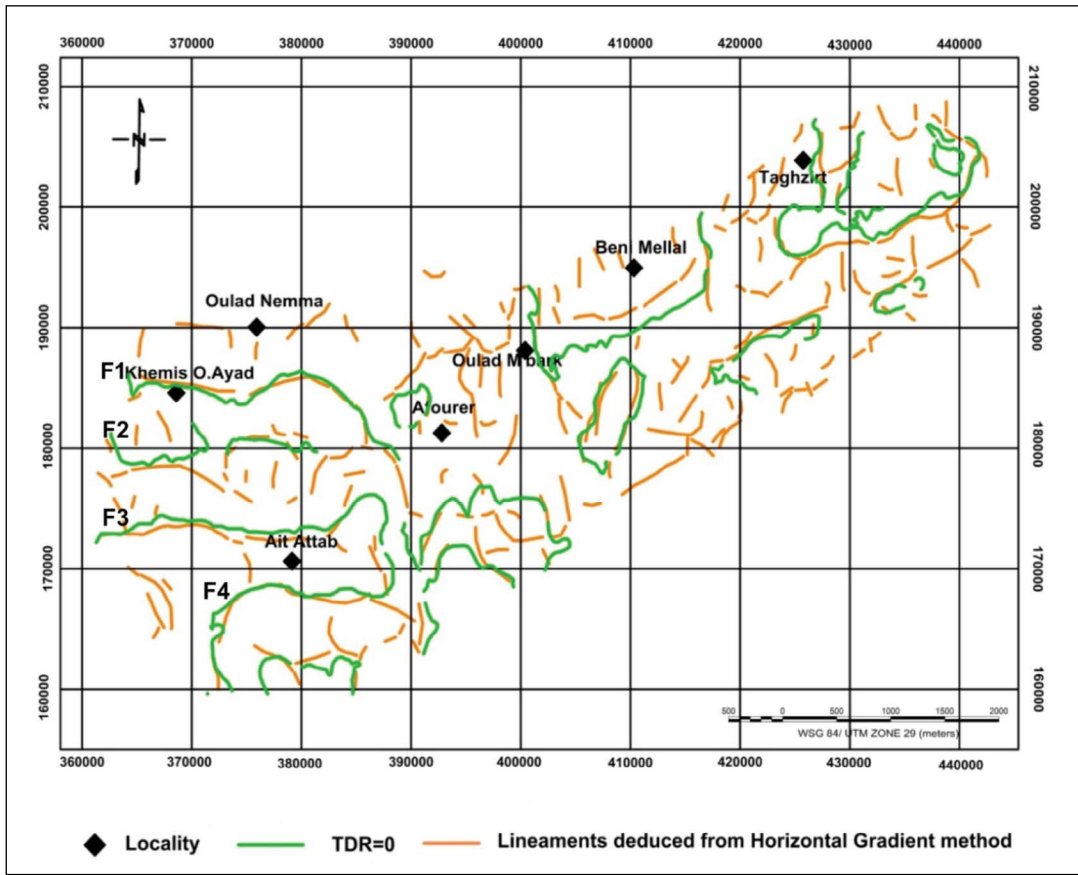
Figure 11- Magnetic lineaments map.

1962; Sadki, 1992; Zouine, 1993). We distinguish several major structures (Figure 11):

- Fault F1, named Beni Ayat border fault or the northern Atlasic fault, is an overlapping fault which constitute an abnormal contact with the deformed Mesozoic deposits of the Atlasic Chain (Afourer Atlas) on the cenozoic tabular layers of Tadla plain (Benzaquen, 1963, Du Dreseney, 1975; Mattauer et al., 1977) (Figure 3). Previous geological and structural studies (Rolley, 1973; Monbaron, 1982) have already revealed this fault. Its path draws a morphostructural and discontinuous line oriented E-W and hidden in some places by the Quaternary cover of Tadla plain. In Afourer Atlas, this fault is marked by argillites and altered basalts as outcrops of the upper Triassic (Ensslin, 1992);

- Fault F2 is called "Karia fault", is delimited in the north by the Ait Imelloul block and in the south by that of Karia-Issoumer. This fault breaks the Karia syncline, which is reduced first to a pinch of Dogger

and upper Liassic before reappearing beyond this fault in the form of a depressed zone incorporated in the Middle Liassic, which obviously, towards the east becomes the Ait Imelloul syncline (Figure 3);

- Fault F3 is known in the literature by the Issoumer border fault (Du Dresnay, 1975; Souhel; Canerot, 1989). This is a major accident falls within a synsedimentary extensional tectonic context which has controlled marine sedimentation during the Dogger and detrital deposition during the Bathonian (Souhel, 1996; Ibouh et al., 2000). This fault is responsible for the Ait Attab block tipping towards the West (Choubert, Faure-Muret, 1960-1962=; Jenney, 1984) (Figure 3). It was previously revealed by the seismic profile KT6 which extends from the Tadla plain in the North-West to the southern flank of the Ait Attab syncline in the South-East (Jabour and Nakayama, 1988; Hafid, 2006);
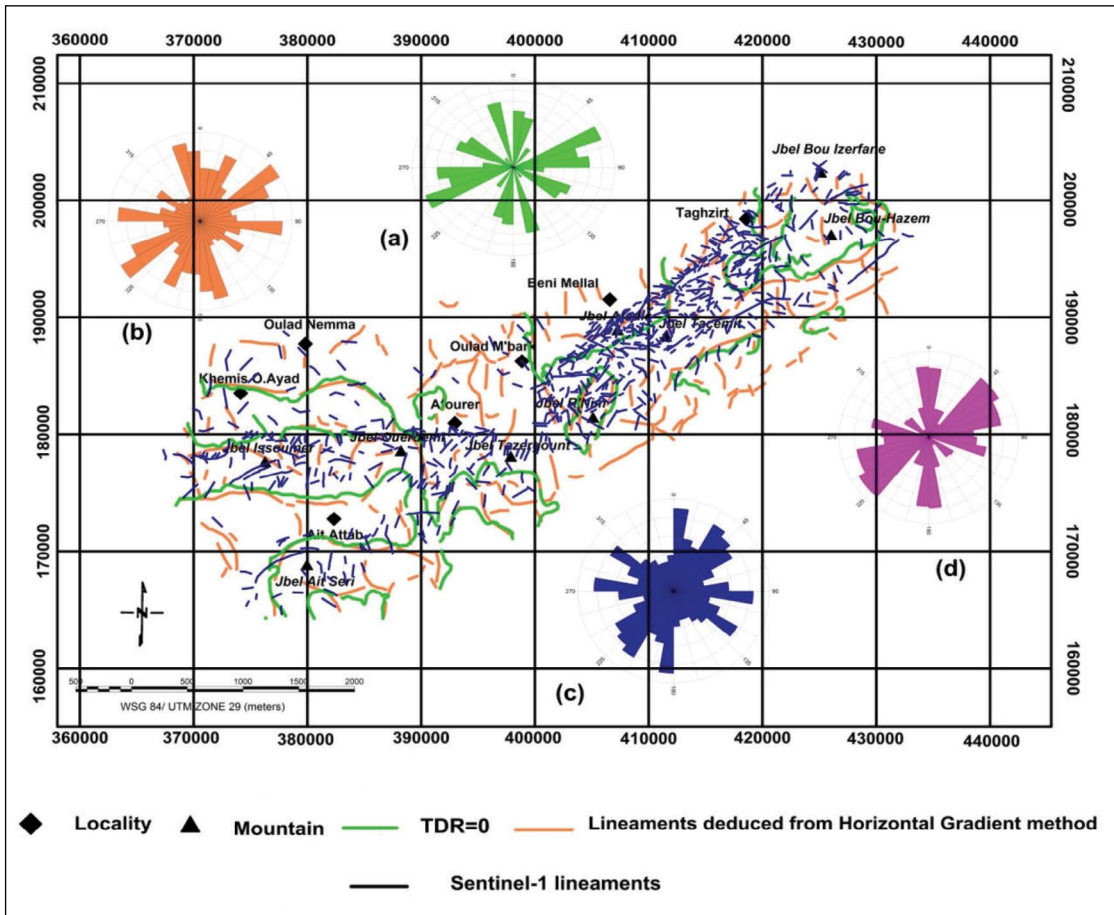
Figure 12- Fractures network map of the study area and rose diagram of highlighted directions obtained from: a) - TDR transformation; b) - Gradient horizontal method; c) – Sentinel-1 image; d) - field measurements.

- Fault F4 "Ait Seri Border Fault": This reverse fault overlaps the lower and middle Liassic carbonate formations towards the north-west with the infra-Aptian red sandstones. Activated during lower and middle Liassic (Du Dresnay, 1972), this fault delimits the Ait Seri block (Figure 3) on which a reef-facies carbonate platform is deposited (Rolley, 1978).

In addition to major structures enhanced by the Tilt-angle transformation, several annex faults of these structures affect the study (Figure 11). The location of the local maxima from the horizontal gradient at various altitudes using reduced to pole aeromagnetic data facilitates the magnetic anomalies interpretation. Indeed, the horizontal gradient achieves local maxima over or near contacts separating two rock units with different magnetism (Fred et al., 2017). The alignment of these magnetic peaks reflects the geological discontinuities that can be interpreted in terms of faults or fractures.

The result obtained by the application of the horizontal gradient technique coupled to the upward continuation shows that the study area is controlled by four major families fractures trending NE-SW to ENE-WSW (N40-70°), E-W (N90-100°), N-S (N170-180°) and NW-SE (N130°) (Figure 12). These directions are associated with syn-sedimentary faults inherited from Pan-African and Hercynian Orogeny (Du Dresnay, 1975; Michard, 1976; Mattauer et al., 1977; Chorowicz et al., 1982; Piqué et al., 1998, 2007). In fact, during the upper Triassic-lower Cretaceous, these faults have controlled the opening and the subsidence of Atlasic basins in the form of rift basins by blocks tipping towards the north-west (Chorowicz et al., 1982; Chafiki, 1994 and Ensslin, 1992). The faults oriented N-S, have also been highlighted by horizontal gradient method, they are related to a submeridian compression phase relative to Alpine orogeny (upper Eocene-Quaternary) (Matteur et al., 1977; Monbaron, 1982; Morel et al., 2000). On

the other hand, the family of faults oriented NW-SE (N120-130°), are dimly represented in the study area. They are associated with transverse faulting showing a strike-slip character (Fadile, 1987; Chafiki, 1994; Souhel and Canerot, 1989). During middle Jurassic (Bajocian-Bathonian), these faults have reactivated to normal faults delineating the semi-grabens of high atlasic basin under the influence of an intense compression of WNW-ESE direction. The numerical processing of Sentinel 1-A image has provided similar results to thoses obtained from the airborne magnetic data analysis (Figure 12). The rose diagram reveals lineaments oriented N-S (N10 ° and N170-180 °); E-W (N90-100 °). NE-SW (N30-70°) and NW-SE (N120-130°) (Figure 12).

The Euler solutions obtained go hand in hand with the structure of lineaments deduced from the application of the horizontal gradient and TDR transformation (Figure 13). The depths obtained are between 0 and more than 1500 m. The lineaments retraced by the Euler solutions are oriented mainly ENE-WSW to E-W and NW-SE.

The E-W trending lineaments display a depth exeeds 1500 m, which testify their deep origin. Thoses latter affect the anticlinal structures of Beni Mellal Atlas. During the Triassic-Jurassic period, the Ait Attab sector was submitted to an NW-SE extension by playing the faults oriented ENE-WSW to E-W to strike-slip faults. In the Afourer Atlas of Afourer, the Ait Attab syncline is bordered by two major faults: the Isoummer fault (F3) in the North-West and the Ait Seri fault (F4) in the South-East. Thoses two faults correspond to potential detachment levels of the Meso-Cenozoic cover. In fact, it is a "thin skin" cover characterized by a cover detachment at the base of the Triassico-Jurassic series and bordered by two ramp anticlines of "fault-bend fold" type (Issoumer and Ait Seri anticlines).The south-eastern flank of the Ait Attab syncline thrusts the Ait Seri anticline; with a liassic heart; through a back-thrust that probably
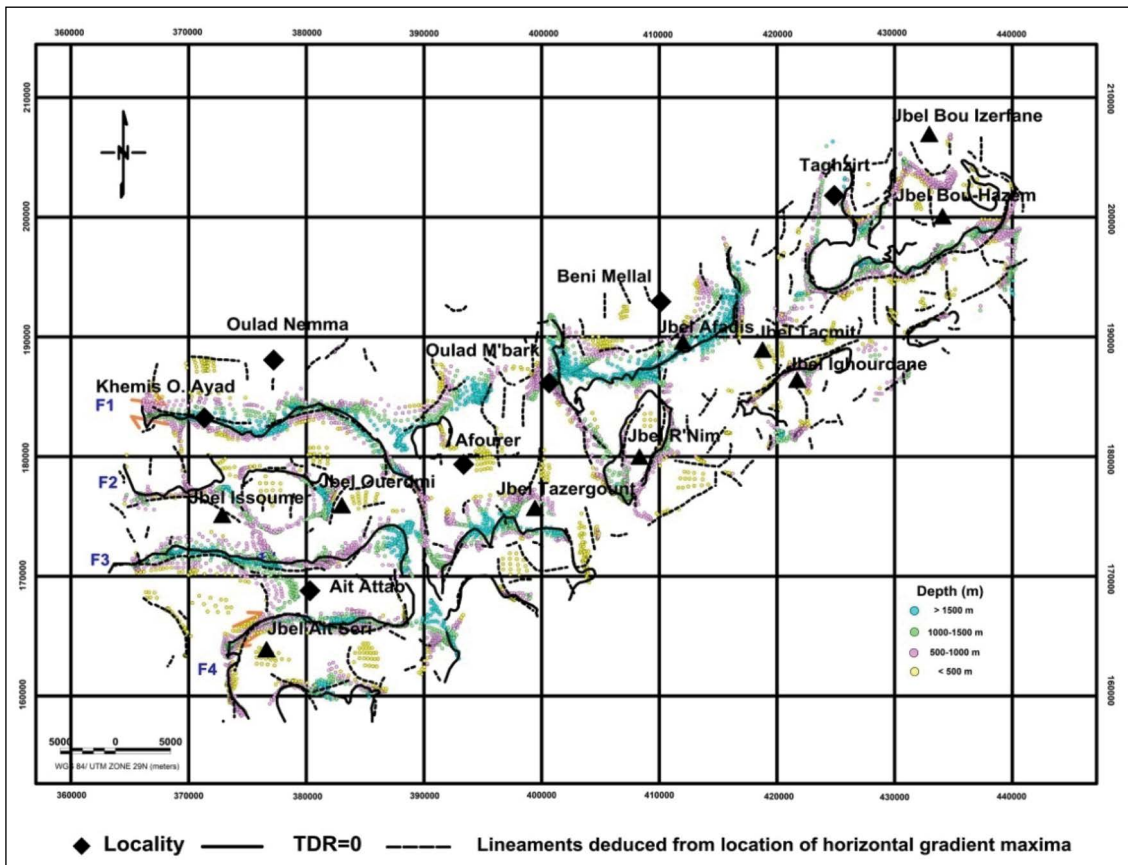
Figure 13- Superposition of Euler solutions and magnetic lineaments deduced from application of horiozontal gradient and TDR transformation.

allows to compensate the blockage of overlap movement responsible for the advance of the detached sedimentary cover towards downstream (Beni Moussa plain). This overlap movement begins on the ramp detachment of the Ait Seri fault F4, after its blocking against the Cenozoic formations of Tadla plain, the faulting play was transferred in-depth on the ramp of Issoumer fault F3.

The magnetic lineaments obtained by the structural interpretation of aeromagnetic data are correlated with the lineaments extracted from the Sentinel 1-A radar image. The directional families of fractures measured in the field are mainly trending N10°, N40-75° and N170-180°. These directions merge with the karstic cavities developed on the lower Jurassic limestone of Beni Mellal Atlas (Bienfait, 1978). The fracture set trending N40-70° is related to hercynian deformation which shows a brittle tectonic materialized by the replay of the major faults NE-SW.

4. Conclusion

The current study relies on the fusion of aeromagnetic data as well as the radar remote sensing. It aims to define the directions of the main structural elements in Beni Mellal Atlas and to understand their tectonic origin. In fact, the map of the reduced to pole of residual magnetic field has allowed highlighting many magnetic anomalies of varying shapes, amplitudes and depths. From a geological view, the most important anomalies are matched with the presence of basaltic flows that resulted from two magmatic events during Bathonian and Lower Cretaceous. The use of tilt angle derivative (TDR), the horizontal gradient technique combined with the upward continuation (until 4 km) and the euler deconvoluion method has allowed highlighting magnetic alignments that correspond to faults. The most important ones are extended along the main structural accidents which are already recognized by classical geological studies (Monbaron, 1981; Rolley, 1973; Fadile, 1987). In fact, the TDR map made it possible to determine the major structural accidents that across Beni Mellal Atlas (the border Atlasic fault, Issoumer fault, Ait Seri fault) and contribute to its subdivision into collapsed blocks. The NE-SW to ENE-WSW, E-W and N-S directions dominate magnetic faults trends that fit into the same directional families obtained from sentinel image processing. The

major lineaments with the N40-70° direction represent normal synsedimentary faults, they are crosscut by the N-S (N170-180°) trending faults that are related to tectonic submeridian alpine compression (Matteur et al., 1977; Monbaron, 1981).Thoses faults influenced the thickness variation of the sedimentary cover, which reflects a collapse movement of the basement relating to a synsedimentary distensive tectonics active since the Triassic to the lower Cretaceous.

The Euler solutions confirm and redraw, in general, the lineaments obtained by the magnetic data and Sentinel-1image interpretation. The estimated depths vary between 0 m and more than 1500 m. The E-W trending lineaments diplay a depth exeeds 1500 m, which testify their deep origin. They affect the basics deposits of the Triassic layers and the Liassic carbonates, thus reflecting that the study area has undergone a thin-skinned deformation. Indeed, this paleo-stress field played a primodial role in the structuring of the Beni Mellal Atlas including Afourer Atlas whose presence of a major faults system allowed to divide the sector into collapsed blocks and tipped to the north-west. Below the Issoumer and Ait Seri faults, detachment ramps located at the base of the Lias and inside the Triassic serie are the cause of the Meso-Cenozoic cover detechment that comes to thrust towards the N-W the atlasic border zone and the Cretaceous and Tertiary deposits of Tadla Plain. Thoses structural results present a useful informations to guide hydrogeological prospecting campaigns in Beni Mellal Atlas.

References

Abderbi, J., Khattach, D. 2012. Apport des données aéromagnétiques et gravimétriques à l'étude de la structure géologique des Hauts Plateaux méridionaux, Maroc.Journal of Hydrocarbons Mines and Environmental Research. 2(2), 111-118. Amar, M. 2013.

Adiri, Z., El Harti, A., Jellouli, A., Lhissou, R., Maacha, L., Azmi, M., Zouhair, M., Bachaoui, E.M. 2017. Comparison of Landsat-8, ASTER and Sentinel

1 satellite Remote Sensing data in Automatic Lineaments Extraction: a case study of Sidi Flah-Bouskour inlier, Moroccan Anti Atlas, Advances in Space Research, 60, 2355-2367.

Alonso-Contes, C. A. 2011. Lineament mapping for groundwater exploration using remotely sensed imagery in a karst terrain : Rio Tanama and Rio de Arecibo basins in the northern karst of Puerto Rico. Master's Thesis, Michigan Technological University, 70p.

Amar, M. 2013. Apport de l'analyse structurale et de la géophysique à la reconnaissance du système aquifere du Haut Atlas oriental, Maroc. Thèse doctorat, Université Moulay Ismail Meknès.

Amar, M., Manar, A., Boualoul, M. 2012. Apport de la cartogrpahie aéromagnétique à l'édentification structurale du systéme aquifere des sources de l'Oasis de Figuig (Maroc). Bulletin de l'Institut Scientifique,Rabat,section Sciences de la Terre,2012,34,29-40.

B.R.P.M., 1971. Historique du sondage pétrolier de Khemis Oulad Ayad N°3000/36 (KMS1). Permis de Béni Moussa

Bardon, C., Bossert, A., Hamzeh, R., Westphal, M. 1978. Paléomagnétisme des formations paléo-volcaniques du Crétacé inférieur dans l'Atlas de Béni-Mellal (Maroc). Notes Service et mémoire Géologique Maroc, 39(272), 7-26.

Beauchamp, J. 1988. Triassic sedimentation and rifting in the High Atlas (Morocco), in Triassic-Jurassic Rifting: Continental Breakup and the Origin of the Atlantic Ocean and Passive Margins, W. Mainspeizer, Elsevier Sci., New York,447 – 497.

Benzaquen, M. 1963.Bordure septentrionale de l'Atlas de Béni Mellal. Contribution à l'étude géologique de la région d'El Ksiba. Notes et Mém. Serv. Géol. Maroc 22(170), 20-45.

Bienfait, P. 1978. Note relative aux cavités dans la région de Béni Mellal (Maroc). Direction de la région Hydraulique de Béni Mellal (D.R.H), 27p.

Bouchaou, L. 1988. Hydrogéologie du bassin des sources karstiques du complexe calcaire haut atlasien du Dir de Béni Mellal (Maroc). Thèse Doctorat 3ème cycle. Univ. Franche Comté, 182p, Besançon.

Boutirame, I., Boukdir, A., Akhsass, A., Boutirame, F., Manar. A., Aghzzaf, B. 2018. Contribution of gravity data and Sentinel-1 image for structural mapping. Case of Beni Mellal and Beni Moussa plain (Morocco).E3S Web Conferences, 37, 05002.

Chafiki, D. 1994. Dynamique sédimentaire à l'articulation plate-forme - bassin : exemple du Lias de la région de Béni- Mellal (Haut-Atlas central, Maroc). Thèse 3ème cycle, Université Cadi Ayyad, 185 p, Marrakech.

Charrière, A., Haddoumi, H., Mojon, P.O. 2005. Découverte du Jurassique supérieur et d'un niveau marin du Barrémien dans les « Couches rouges » continentales du Haut Atlas central marocain : implications paléogéographiques et structurales. Comptes rendus Palevol, 4, 385–394.

Chorowicz, J., Alem, M., Bahmad, A., Chariai, H., EL Kochri, A., Medina, F., Tamain, G. 1982. Les anticlinaux éjectifs du Haut Atlas : résultat de tectoniques atlasiques superposées. C. R. Acad. Sci. Paris, 294, 271-274.

Choubert, G., Faure Muret, A. 1960-1962. Evolution paléogéographique et structurale des domaines méditerranéens et alpins d'Europe « Tome 1 ». Evolution du domaine atlasique marocain depuis les temps paléozoïques. Mém. hors série, Soc. Géol. France, 1, 447-527.

Corgne, S., Magagi, R., Yergeau, M., Sylla, D. 2010. An integrated approach to hydro-geological lineament mapping of a semi-arid region of West Africa using Radarsat-1 and GIS. Remote Sensing of Environment ,114, 1863–1875.

Dauteuil, O., Moreau, F., Qarqori, K. 2016. Structural pattern of the Saïss basin and Tabular Middle Atlas in northern Morocco: hydrological implications. J Afr Earth Sci, 119, 150–159.

Debeglia, N. 2005. Estimation de la direction d'aimantation pour une réduction au pôle optimale du champ magnétique. BRGM/RP-54059-FR, 34 p.

Du Dresnay, R. 1972. Les phénomènes de bordure des constructions carbonatées du Lias moyen du Haut Atlas central (Maroc). C.R. Acad. Des Sc. Paris, 275, 341-344, 535-537.

Du Dresnay, R.1975. Influence de l'héritage structural tardi-hercynien et de la tectonique contemporaine sur la sédimentation jurassique, dans le sillon marin du Haut- Atlas, Maroc. 9ème Congrès international de Sédimentologie, Nice, 103-108.

Ejep, J.S., Olasehinde,P., Appollonia, A., Okunlola, I. 2017. Investigation of Hydrogeological Structures of Paiko Region, North-Central Nigeria Using Integrated Geophysical and Remote Sensing Techniques. Geosciences, 7, 122-140.

El Gout, R., Khattach, D., Houari, M. R. 2009. Etude gravimétrique du flanc nord des Béni Snassen (Maroc nord oriental): implications structurales et hydrogéologique.. Bull. Ins Sci., Rabat, section Sciences de la Terre, 31, 61-75.

Ensslin, R. 1992. Cretaceous synsedimentary tectonics in the Atlas system of Central Morocco, Geol. Rundsch., 81, 91-104.

Everaerts, M., Mansy, J.L. 2001. Le filtrage des anomalies gravimétriques, une clé pour la compréhension des structures tectoniques du Boulonnais et de l'Artois (France), Bulletin de la Société Géologique de France 172, 3, 267–274.

Fadile, A., 1987.Structure et évolution alpine du haut Atlas central sur la transversale Aghbala-Imilchil (Maroc). Thèse de 3ème cycle Univ. Paul Sabatter, 300p, Toulouse (no published).

Fred, Y., Pérez, C., López-Loera, H., Fregoso-Becerra, E., Yutsis, V., Martínez-Ruíz,V.J., Dávila-Harris, P. 2017. Caracterización de lineamientos estructurales y sus implicaciones hidrogeológicas en la cuenca de Villa Hidalgo (San Luis Potosí) integrando métodos geofísicos potenciales. Boletín de la Sociedad Geológica Mexicana, 69 (3), 555 – 576.

Guezal, J., El Baghdadi, M., Barakat, A. 2013. Les Basaltes de l'Atlas de Béni-Mellal (Haut Atlas Central, Maroc) : un Volcanisme Transitionnel Intraplaque Associé aux Stades de L'évolution Géodynamique du Domaine Atlasique. Anuár do Anuário do Instituto de Geociências, 36 (2), 70-85.

Haddoumi, H. 1988. Les Couches rouges (Bathonien à Barrémien) du synclinal des Aït Attab (Haut Atlas central, Maroc) ; étude sédimentologique et stratigraphique. Thèse de 3éme cycle, Université de Nancy I, 133 p.

Haddoumi, H., Charrière, A., Mojon, P.O. 2010. Stratigraphie et sédimentologie des « Couches rouges » continentales du Jurassique-Crétacé du Haut Atlas central (Maroc) : implications paléogéographiques et géodynamiques. Comptes rendus Geobios, 43, 431-451.

Hafid, M. 2006. Styles structuraux du Haut Atlas de Cap Tafelney et de la partie septentrionale du Haut Atlas occidental: tectonique salifère et relation entre l'Atlas et l'Atlantique. Notes et Mém. Serv. géol. Maroc, 465, 172p.

Hoepffner, C., Houari, M.R., Bouabdelli, M., 2006. Tectonics of the North African Variscides (Morocco,Western Algeria), an outline, in Frizon de Lamotte D., Saddiqi O., Michard A. (Eds.), Recent Developments on the Maghreb Geodynamics. C. R. Geosci. 338, 25-40.

Hobbs, W.H. 1912. Earth features and their meaning: an introduction to geology for the student and the general reader. Macmillan, New-York, 506 p.

Ibouh, H., Chafiki, D., Bouabdelli, M., Souhel, A., El Bchari, F., Elhariri, KH., Canerot, J. 2000. Rôle de la tectonique distensive du Toarcien inférieur dans l'évolution de la chaîne haut-atlasique centrale du Maroc. Strata,1, 10, 103-105.

Jabour, H., Nakayama, K. 1988. Basin modeling of Tadla basin, Morocco, for hydrocarbon potential, AAPG bull., 72, 1059-1073.

Jenny, J., Le Marrec A., Monbaron, M. 1981. Les Couches rouges du Jurassique moyen du Haut Atlas central (Maroc) : corrélations lithostratigraphiques, éléments de datations et cadre tectono-sédimentaire. Bull. Soc. Géol. France, 23, 6, 627–639.

Khamis, M., Basheer, A., Rabeh, T., Khalil, A., Essam Eldin. A. A., Sato, M. 2014. Geophysical assessment of the hydraulic property of the fracture systems around Lake Nasser-Egypt: in sight of polarimetric borehole radar. NRIAG Journal of Astronomy and Geophysics, 3, 7-17.

Lachaine, G. 1999. Structures géologiques et linéaments, Beauce (Québec). Mémoire de maitrise, Département de géographie et de télédétection, Université de Sherbrooke, 83 pp.

Laville, E., Harmand, C. 1982. Évolution magmatique et tectonique du bassin intracontinental mésozoïque du Haut Atlas (Maroc) : un modèle de mise en place synsédimentaire de massifs "anorogéniques" liés à des décrochements, Bull. Soc. géol. Fr., XXIV, 2, 213–227.

Lee, J. S., Grunes, M. R., et de Grandi, G., 1999. Polarimetric SAR speckle filtering and its implication for classification. IEEE Transactions on Geoscience and Remote Sensing, 37, 2363–2373.

Mansour, M., Ait Brahim, L. 2005.Apport de la Télédétection radar et du MNT à l'analyse de la fracturation et la dynamique des versants dans la Région de Babtaza, Rif, Maroc. Télédétection, 5, 95-103.

Mattauer, M., Tapponier, P., Proust, F. 1977. Sur les mécanismes de formation des chaines intracontinentales. L'exemple des chaines atlasiques du Maroc. Bull. Soc. Géol. France, 19, 521-526.

Michard, A. 1976. Elément de géologie marocaine. Éditions du service géologique du Maroc, Note et Mém, 252.

Michard, A., Saddiqi, O., Chalouan A., Rjimati, E., Mouttaqi, A. 2011. In Nouveaux Guides géologiques et miniers du Maroc / New Geological and Mining Guidebooks of Morocco. Notes et Mémoires du Service géologique du Maroc, 556-564.

Miller, H.G., Singh, V. 1994. Potential field tilt – a new concept for location of potential field sources; J. Appl. Geophys. 32, 213–217.

Monbaron, M. 1981. Sédimentation, tectonique synsédimentaire et magmatisme basique l'évolution paléogéographique et structurale de l'Atlas de Béni Mellal (Maroc) au cours du Temps Mésozoïque, ses incidences sur la tectonique atlasique. Ecologea Géol. Helv, 74(3), 625-638.

Monbaron, M. 1982. Précisions sur la chronologie de la tectogénèse atlasique. C.R. Acad. Sc. Paris : t. 294, 2, 883-885.

Monbaron, M. 1985.Carte géologique du Maroc au 1/100 000ème, feuille Béni Mellal. Notes et Mém. Serv. Géol. Maroc, no: 341.

Moreau, F., Gibert, D. et Saracco, G. 1996. Filtering non-stationary geophysical data with orthogonal wavelets, Geophysical Research Letter, 23, 407-410.

Morel, J.L., Zouine, E.M., Andrieux, J., Faure-Muret, A. 2000. Déformations néogènes et quaternaires de la bordure nord haut-atlasique (Maroc) : rôle du socle et conséquences structurales. Journal of African Earth Sciences, 30, 119-131.

Oruc, B., Selim H. 2011 Interpretation of magnetic data in the Sinop area of Mid Black Sea, Turkey, using tilt derivative, Euler deconvolution, and discrete wavelet transform; J. Appl. Geophys. 74 194–204.

Piqué, A., Aït Brahim, L., Aït Ouali, R., Amrhar, M., Charroud, M., Gourmelen, C., Laville, E., Rekhiss, F., Tricart, P. 1998. Évolution structurale des domaines atlasiques du Maghreb au Méso-Cénozoïque ; le rôle des structures héritées dans la déformation du domaine atlasique de l'Afrique du Nord. Bull. Soc. géol. France 169, 6, 797–810.

Piqué, A., Soulaimani, A., Hoepffner, C., Bouabdelli, M., Laville, E., Amrhar, M., Chalouan, A. 2007. Géologie du Maroc. Editions GEODE, Marrakech.

Ranganai, R.T., Ebinger, C.J. 2008. Aeromagnetic and Landsat TM Structural Interpretation for identifying regional groundwater exploration targets, south-central Zimbabwe Craton. J. Appl. Geophys., 65, 73–83.

Reid, A. B., Allsop, J.M., Granser, H., Millet, A. J., Somerton, I.W. 1990, Magnetic interpretation in three dimensions using Euler deconvolution: Geophysics, 55, 80–91.

Rolley, J.P. 1973. Etude géologique de l'Atlas d'Afourer - Haut-Atlas central - Maroc. Stratigraphie. Thèse Doctorat 3ème cycle, Univ. de Grenoble, 100 p, Grenoble.

Rolley, J.P. 1978. Carte géologique du Maroc au 1/100.000: feuille d'Afourer. Notice explicative. Notes et Mémoires du Service Géologique du Maroc, 247, 247 bis: 1-103.

Sadki, D. 1992. Le Haut Atlas central (Maroc) – stratigraphie et paléontologie du Lias supérieur et du Dogger inférieur : dynamique du bassin et des peuplements. Thèse Doct. d'Etat; Univ. Cadi Ayyad, Marrakech, 331 p.

Salem, A., Williams, S., Fairhead, J.D., Smith, R., Ravat, D.J. 2008. Interpretation of magnetic data using tilt-angle derivatives; Geophysics, 73, L1–L10.

Souhel, A. 1996. Le Mésozoïque dans le Haut Atlas de Béni-Mellal (Maroc). Stratigraphie, sédimentologie et évolution géodynamique. Mémoire de Thèse d'État, Université Caddi Ayad, 235 p, Marrakech.

Souhel, A., Canerot, J. 1989. Polarités sédimentaires téthysienne puis atlantique : l'exemple des couches rouges jurassico-crétacées du Haut-Atlas central (Maroc). Sci. Géol., Mém., 84, 39-46.

Srivastava, P.K., Bhattacharya, A.K. 2006. Groundwater assessment through an integrated approach using remote sensing, GIS and resistivity techniques: A case study from a hard rock terrain. Int. J. Rem. Sens., 27, 4599–4620.

Thompson, D.T., 1982. EULDPH: A new technique for making depth estimates from magnetic data: Geophysics, 47(1), 31–37.

Van Senden, D.C., Portielje, R., Borer,A. 1990. Vertical exchange due to horizontal density gradients in lakes; the case of Lake Lucerne. Aquatic Science, 52p.

Verset, Y. 1985.Carte géologique du Maroc au 1/100 000ème, feuille Kasba Tadla. Notes et Mém. Serv. Géol . Maroc, n°340.

Ziegler, P., Cloetingh, S., Wees, J. 1995. Dynamics of intraplate compressional deformation: The Alpine foreland and other examples, Tectonophysics, 252, 7 – 60.

Zouine, El. 1993. Géodynamique récente du Haut Atlas. Evolution de sa bordure septentrionale et du Moyen Atlas sud-occidental au cours du Cénozoïque. Doct. Etat, Es-Sc. Nat. Univ. Mohamed 5 Fac. Sciences, 330 p, Rabat (unpublished).

Bulletin of the Mineral Research and Exploration

http://bulletin.mta.gov.tr

Simulation of a salt dome using 2D linear and nonlinear inverse modeling of residual gravity field data

Soheyl POURREZA[a]   and Farnush HAJIZADEH[a*]

[a]Faculty of Mining Engineering,Urmia University, Urmia, Iran.

Research Article

ABSTRACT

In gravity field inversion we usually dealing with underdetermined problems and for obtaining realistic solutions can introduce a depth-weighting function to the inversion algorithm. We employ a linear inversion method for determining the underground density distribution of the gravity causative mass. The validation and accuracy of method is tested on two synthetic gravity anomaly from different models, while the data are noise- free and corrupted with noise. In this paper, We also invert the 2D gravity anomaly produced by a salt dome from the northwest of Iran. The salt domes in the region under investigation are a rich source of Potash. The inverted structure demonstrate on average a depth to top and bottom of 27 m and 65 m, respectively. For comparison, we also have simulated the salt dome using the nonlinear inverse modeling. The results are mostly similar.

1. Introduction

Gravity investigation has been used widely over the years for inverse modeling of various buried geological structures and deposit mass, especially in mineral reconnaissance projects (Mandal et al., 2013; Biswas et al., 2014*a, b*; Mandal et al., 2015; Biswas and Sharma, 2016). The nonuniqueness in the linear inverse problem of gravity, i.e., the existence of a large variety of distribution of undersurface density models that generate a similar gravity effect on measurement plane, hesitate the reliability of solution (Skeels, 1947; Parker, 1973; Biswas, 2015; 2016; Singh and Biswas, 2016; Biswas et al., 2017). In order to obtain the correct unique solution and minimizing the ambiguities, various researchers have been proposed different algorithms to increase the amount of extracted information from inversion for simulating the geometry of a density distribution due to a distinct gravity anomaly, as the proposed model be geologically realistic (Srivastava et al., 2007; Ganguli and Dimri, 2013; Biswas, 2015; Ganguli et al., 2015; Singh and Biswas, 2016; Biswas et al., 2017).

Tsuboi (1983) introduce a simple but effective approach based on equivalent stratum technique to estimate 3D topography of a density interface. Oldenburg (1974) proved that the Parker's expression could be applied in order to specify the geometry of the density distribution from the residual gravity anomaly. The geological maps and petrophysical data from rock samples were used to to approximate the model parameters to realistic values (Farquharson et al., 2008; Williams, 2008; Heincke et al., 2010; Lelièvre et al., 2012; Tschirhart et al., 2013; 2017). Kamm et al. (2015) used the petrophysical information for joint inversion of magnetic and gravity. Moreover, there are uniform and permanent models in the inversion of gravity and magnetic fields and their derivatives (Biswas, 2018; Lalongo et al., 2014).

Using a joint inversion of multiple data sets can also diminish the nonuniqueness of the inverse problem, examples of joint inversion of gravity and magnetic data are given by, e.g., Zeyen and Pous (1993), Gallardo and Meju (2003), and Pilkington (2006) using deterministic inversion techniques

and by Bosch and McGaughey (2001) and Bosch et al. (2006) using stochastic methods. Shamsipour et al. (2010, 2011, 2012) proposed the cokriging as a geostatistical method and conditional simulation for the discrete 3-D inversion of magnetic and gravity data respectively, including geological restrictions.

One way to eliminate this ambiguity is to put a appropriate geometry shape to the anomalous mass with a known density followed by inversion of gravity anomalies (Chakravarthi and Sundararajan, 2004). Although customary geometry models may not be geologically realistic, they are usually being sufficient to analyze causative mass of many isolated gravity anomalies (Abdelrahman and El-Araby, 1993). The interpretation of such an anomaly aims essentially to compute the parameters such as depth, shape, and radius of the gravity anomaly causative body such as geological structures , mineral mass and artificial underground structures (Singh and Biswas, 2016; Biswas, 2015). Thus, in this case deal with the nonlinear inverse modeling.

Several graphical and numerical methods have been developed for analyzing residual gravity anomalies caused by simple bodies, such as Saxov and Nygaard (1953) and Bowin et al. (1986). The methods include, for example, Fourier transform (Odegard and Berg, 1965; Sharma and Geldart,1968); Mellin transform (Mohan et al., 1986); Walsh transforms techniques (Shaw and Agarwal, 1990); ratio techniques (Hammer, 1977; Abdelrahman et al., 1989); least-squares minimization approaches (Gupta, 1983; Lines and Treitel, 1984; Abdelrahman, 1990; Abdelrahman et al., 1991), different neural networks (Salem et al., 2001; Osman et al., 2006; 2007; Al-garni, 2013; Eshaghzadeh and kalantari, 2015; Eshaghzadeh and Hajian, 2018); very fast simulated annealing (Biswas et al., 2017; Biswas, 2015; 2016) Particle swarm optimization (Singh and Biswas, 2016); effective quantitative interpretations using the least-squares method (Gupta, 1983) based on the analytical expression of simple moving average residual gravity anomalies are yet to be developed. Abdelrahman and El-Araby (1993) introduced an interpretive technique based on fitting simple models convolved with the same moving average filter as applied to the measured gravity. A simple approach introduced by Essa (2007) is applied to determine the shape factor and depth of simple features from residual gravity anomalies along the profile. Another automatic method, e.g. the least-squares method, was offered by Asfahani and Tlas (2008), by which the depth and amplitude coefficient can be specified.

In this study, we employ the linear inverse modeling technique using depth weighting parameter as resolution enhancer and one-norm (also known as the L1 norm or mean norm) as stopping criteria in inversion algorithms for a real gravity data due to a salt dome in the north of the Zanjan province, Iran. The salt domes situated in the north of the Zanjan province and the south of the East Azerbaijan province are volumetrically small and near the surface. These salt domes are the rich resources of the Potash.

2. Computing the Kernel Matrix

For inverting the gravity data and calculating a 2D density distribution corresponding to the gravity anomaly, it is necessary that the gravity response due to the ground of the sub-surface as has been divided to several prisms be computed at the surface. For a 2-D model, as shown in figure 1, the gravity response of all the rectangular prisms at the observation point i, is given by:

$$g_i = \sum_{j=1}^{M} P_{ij} d_j, \quad i = 1, ..., N \qquad \text{(equation 1)}$$

where M and N denote the number of blocks and the number of observations, respectively, d_j is the density of the jth block and P_{ij} is matrix of geometric element or kernel matrix which presenting the influence of the jth block on the ith gravity value. In order to calculate the kernel matrix P_{ij}, the gravity response of the 2D prism using equation developed by Last and Kubik (1983) is estimated, as:

$$p_{ij} = 2G \left[\begin{array}{l} (x_i - x_j + \frac{d}{2}) \log(\frac{r_2 r_3}{r_1 r_4}) + d \log(\frac{r_4}{r_3}) - \\ (z_j + \frac{h}{2})(\theta_4 - \theta_2) + (z_j - \frac{h}{2})(\theta_3 - \theta_1) \end{array} \right], \qquad \text{(equation 2)}$$

where;

$$r_1^2 = (z_j - \frac{h}{2})^2 + (x_i - x_j + \frac{d}{2})^2,$$

$$r_2^2 = (z_j + \frac{h}{2})^2 + (x_i - x_j + \frac{d}{2})^2,$$

$$r_3^2 = (z_j - \frac{h}{2})^2 + (x_i - x_j - \frac{d}{2})^2,$$

$$r_4^2 = (z_j + \frac{h}{2})^2 + (x_i - x_j - \frac{d}{2})^2,$$

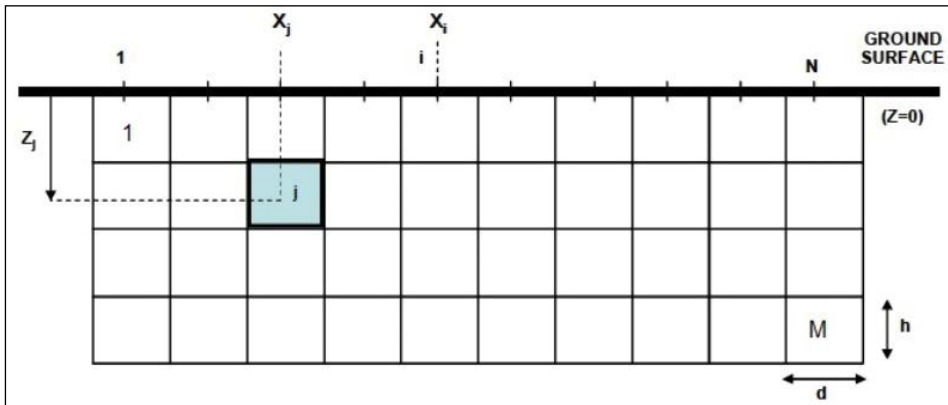Figure 1- A simple 2D model of the inversion domain as has been divided to several blocks with a dimension of i×j.

and

$$\theta_1 = \tan^{-1}(x_i - x_j + \frac{d}{2})/(z_j - \frac{h}{2}),$$

$$\theta_2 = \tan^{-1}(x_i - x_j + \frac{d}{2})/(z_j + \frac{h}{2}),$$

$$\theta_3 = \tan^{-1}(x_i - x_j - \frac{d}{2})/(z_j - \frac{h}{2}),$$

$$\theta_4 = \tan^{-1}(x_i - x_j - \frac{d}{2})/(z_j - \frac{h}{2}),$$

Here G is the gravitational constant, d and h are the width and height of the each block.

3. Inversion Method

In most of the inverse modeling cases, we deal with the underdetermined problems, i.e. the number of unknowns is much greater than the number of observed data. For a general underdetermined system of linear equations, i.e. $d=Pf$ where d is the column vector of the observed gravity field data, f is the column vector of the unknown, i.e. density, and P is the kernel rectangular matrix, the minimum norm solution is defined as the model that fits the data exactly which is given by (Menke, 1984):

$$f = P^T (PP^T)^{-1} d,$$ (equation 3)

The super script T denotes the matrix transposition. This expression usually leads to an unrealistic density distribution. We can solve the inversion problem using the weighted–damped least-squares method, as (Last and Kubik, 1983):

$$f = W_f^{-1} P^T (P W_f^{-1} P^T + W_n^{-1})^{-1} d,$$ (equation 4)

If assumed that there are M prisms of unknown density (number of model parameters) and N observed gravity data (Figure 1), therefore, f is a $M×1$ vector of the unknown density and d is a $N×1$ vector of the observed gravity data. The density weighting matrix (W_f), noise-weighting matrix (W_n) and kernel matrix (P) have also the dimensions $M×M$, $N×N$ and $N×M$, respectively. The density weighting matrix is given by (Last and Kubik, 1983):

$$\left[W_f^{(k-1)} \right]_{ii}^{-1} = \left[f_i^{(k-1)} \right]^2 + \varepsilon,$$ (equation 5)

where k is the iteration and constants ε is the perturbation number as should be chosen as small as possible without causing numerical inconstancy, generally is assumed about 10^{-10} to 10^{-13}. The noise-weighting matrix is defined at each iteration as:

$$W_n^{-1} = l_0^2 diag \left(P w_f^{-1} P^T \right),$$ (equation 6)

As the l_0 is a priori estimated noise/signal ratio. The weighting functions are specifically designed to minimize the area of the model, that is, to maximize its compactness. After computing the density amount of each block in each iteration, the gravity effect of the blocks whose estimated values are greater than the initial defined amount, must be eliminated. The formulation is (Last and Kubik, 1983):

$$g_i^k = g_i - b \sum_j P_{ij} H \left[f_j^{(k-1)} / b \right], \quad i = 1,...,N,$$ (equation 7)

where b is being the target density and H denotes the Heaviside step function, as here, whose value is zero for smaller or equal values to one and one for values larger than one,

$$H[n] = \begin{cases} 0, & n \leq 1 \\ 1, & n > 1 \end{cases} \qquad \text{(equation 8)}$$

It is worth mentioning, the Heaviside step function is used to eliminate the gravity effect of the blocks whose the estimated density are greater than the target density from the gravity data. When the density value of the specific block gets bigger than a interface density (b), the algorithm establishes the density of the block equal to b and automatically separates the block in the next iterative during inversion process. This is achieved by subtracting its gravity effect from the total gravity anomaly and assigning it a very large weight, thus the equation 7, estimate a reduced gravity data vector in each step (Last and Kubik, 1983).

The method consists of an iterative procedure in which the weighting matrices alter at each iteration until an acceptable convergence of the solution is obtained and eventually a compact final model is generated (Last and Kubik, 1983). In inverting gravity data due to a causative mass, the evaluated density distribution related to buried structure tend to concentrate near the surface. For nullifying the natural decay of the kernels and maximizing the depth resolution, a depth weighting function is inset in the problem. Li and Oldenburg (1998) offered to employ a depth weighting function such as:

$$w_z = \frac{1}{(z + z_o)^z}; \qquad \text{(equation 9)}$$

where z is the depth of the layers and z_0 depends on the cell size of the model and the observation height of the gravity data.

In this paper, we employ the one-norm ($L1$ norm) as a criterion for stopping the iteration process in inversion algorithms. The $L1$ norm has the form:

$$L1 \ norm : \ \|e\|_1 = \left[\sum_k |e_k| \right], \qquad \text{(equation 10)}$$

Where the e is the difference between the observed gravity data and inverted gravity data due to the evaluated model from the density distribution at each iteration. As soon as the $L1$ norm achieve the lowest amount which usually coincides with minimum area of the density distribution, the iteration is terminated. We can summarize the inversion process as the following algorithm,

Input: d, P, ε, l_0

Output: f

for i=1:k do

Calculate: W_f, W_n

Compute: $f, L1$

If $L1_{(i-1)} < L1_i$

Break

end

Apply: *Heaviside function*

Compute: d

end

4. Synthetic Models

The proficiency and validity of the compact inversion method is illustrated with two set of synthetic gravity data. We assign the ε and l_0 as 10^{-10} and 0.1 respectively, for inverting the theoretical gravity data. Figure 2(a) shows the gravity response to the assumed model in figure 2(b) where the subsurface ground has been partitioned into 15×10 prisms as the dimension of each prism is 10 m × 5 m. As is shown in figure 2b, the 2D model include 12 prisms whose the density contrast is -1000 kg/m³. The inverted gravity corresponding to the resulted causative body from inverting the observed gravity (Figure 2c), is displayed in figure 2(a). This inverted model that is exactly similar of the original causative body, achieved at 8th iteration, where the L1 norm as the stopping criterion attain the smallest amount. The L1 norm, reduces intensely from its initial value of 0.71 mGal at the first iteration to 0.031 mGal at the end of the 5th iteration and then gradually reaches zero (very close to zero) mGal at the 8th iteration (Figure 6a).

Figure 3(a) shows the computed gravity for the assumed model in figure 3(b) where the subsurface inversion domain has been divided into 25×10 blocks of dimension 4 m × 5 m. Therefore, the whole domain is 100 m × 50 m and the total number of blocks is M=250. considering figure 3b can see that the 2D model include 18 prisms whose the density contrast is -1000 kg/m³. In recent theoretical model, the inversion domain has been composed of the smaller blocks than the first model. figures 4 (a), 4(b) and 4(c) represent the inferred density distribution from the inversion
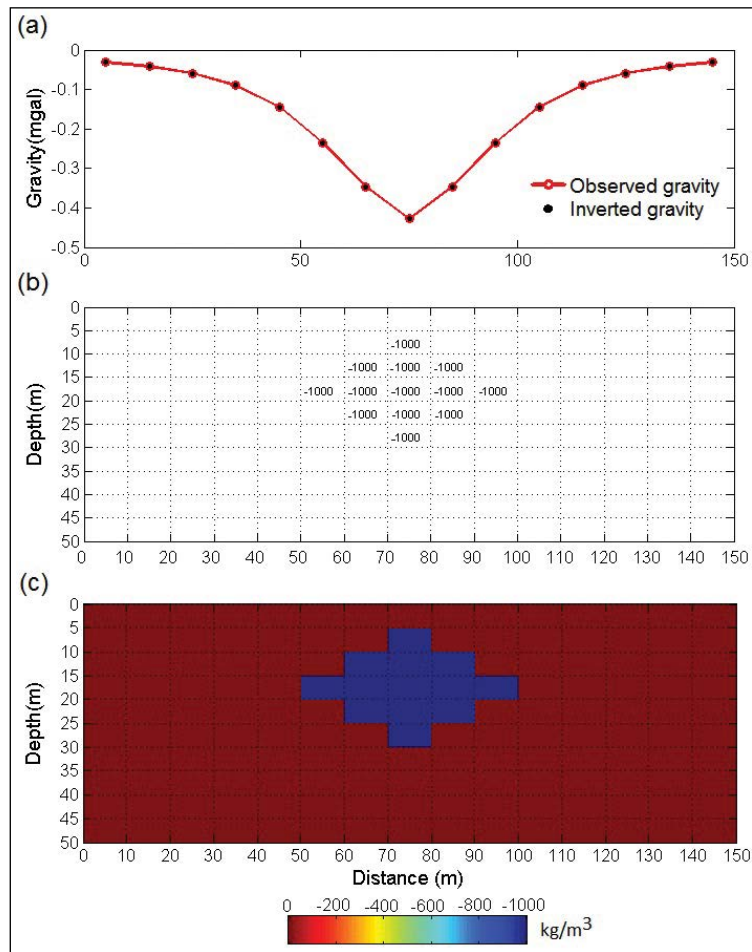
Figure 2- a) Observed and inverted gravity due to b) assumed model and c) inverted model, respectively.

the observed gravity after 3rd, 5th and 7th iterations, respectively. At 7th iteration, L1 norm amount is minimum one. Figure 6(b) exhibit the variations the L1 norm values versus the iteration during inversion for the observed gravity in figure 3(a). With attention to figures 4 can clearly find during inversion process the number of the blocks which are masked with high density decrease. The 3rd iteration produced a spread-out density distribution, but at the 5th iteration the compactness has been increased, as at the 7th iteration the minimum area of the blocks with maximum density, regardless to the sign of density, has been yielded. The inverted gravity due to the resulted model in figure 4(c) is shown in figure 3(a).

The efficiency of the inversion approach in the presence of error is tested after adding 10% random noise to the gravity data in figure 3(a). The noise corrupted synthetic gravity data has been brought in figure 5(a). Figures 5 (b), 5(c) and 5(d) demonstrate

the configuration of density distribution between prisms resulted from the inversion the observed gravity data corrupted with noise at 5th, 7th and 9th iterations, respectively. With the iterations proceeding, the area of the interpreted structure is diminishes as at the 7th iteration a fairly compact model is inferred. By the 9th iteration the procedure give a almost converged results to the desired initial model. The L1 norm value decreases gradually from its initial value of 0.727 mGal at the first iteration to 0.078 mGal at the 9th iteration (Figure 6c), where L1 norm amount is minimum. Therefore, the figure 5(d) shows the most similar shape to the assumed causative body by inversion the gravity data corrupted with random noise. The inverted gravity data due to interpreted model in figure 5(d) has been shown in figure 5(a).

We also studied the stability of the inversion technique for the observed gravity data with a higher level of noise, as it corrupted with 15% random noise
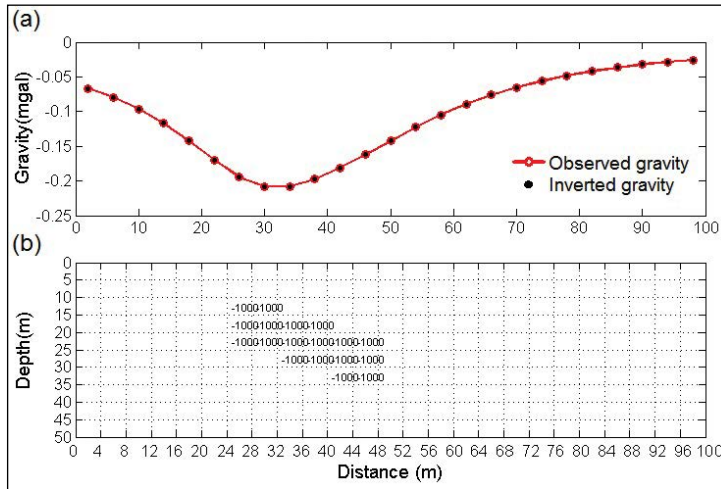
Figure 3- a) observed and inverted gravity b) assumed model
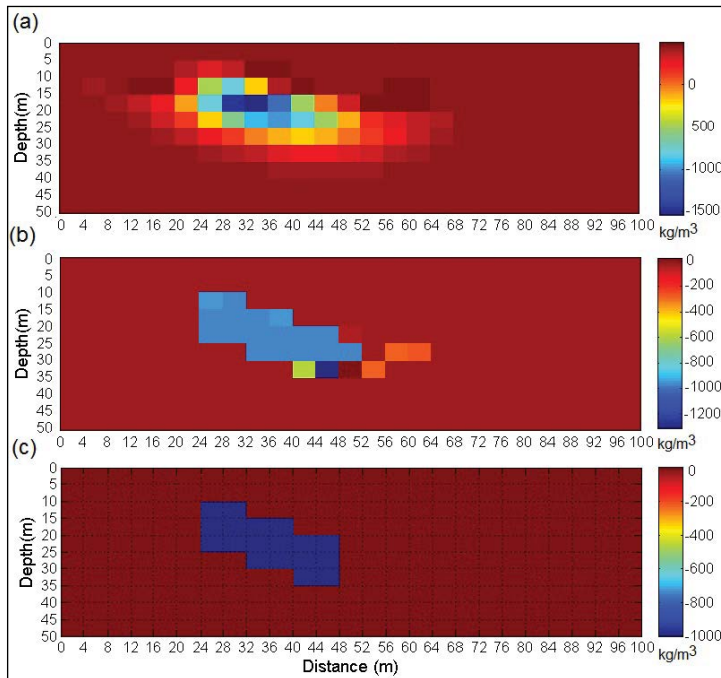
Figure 4- Inverted models at a) 3rd, b) 5th and c) 7th iterations, respectively

(Figure 7a). The interpreted density distribution is shown in figure 7(b) as the buried structure has been specified by the black line. The algorithm stopped at 14th iteration, where the L1 norm became 1.32 mGal. Considering the inferred results prove the validity of the inverse modeling method.

The analysis of the synthetic models, with and without random noise, eventuate the satisfactory results which confirm the performance and stability of the inversion method.

5. Field Example

The region under study is situated in the north of the Zanjan province, the northwest of Iran. Miocene stage in this area are characterized by rapid subsidence, deposition, and facies changes in both marine and continental sedimentary basins as Miocene units in the study region include sequences of Marl, Salt and Chalk. Figure 8 show the geological map of the region under investigation. The gravity measurement region is approximately even morphologically. The height
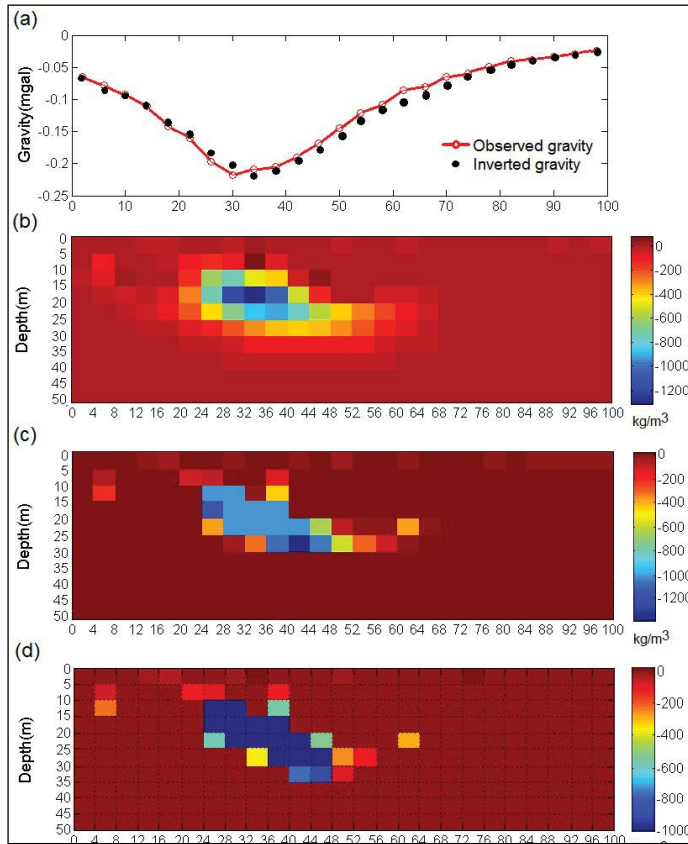
Figure 5- a) Observed gravity due to model in figure 3(b) as corrupted with 10% noise and inverted gravity b) inverted model at 5th iteration, c) inverted model at 7th iteration and d) inverted model at 9th iteration
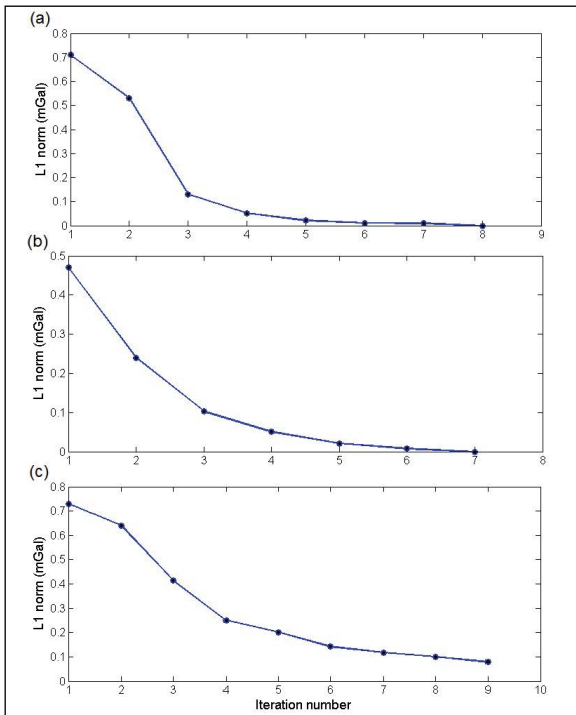
Figure 6- Variations L1 norm values versus iteration number for analyzing a) the observed gravity data in figure 2(a), b) the observed gravity data in figure 3(a), c) the noisy observed gravity data in figure 4(a)

variations the region under evaluation is illustrated in figure 9.

The salt domes in this area are the result of the upward movement of the Neogene evaporative materials as their connection with the mother salt layer have been interrupted (Figure 10). The depth of these salt domes is shallow and their volume is low. These salt dome have mostly high percentage of Potash.

The main salt dome in the region under consideration is Aji-chay salt dome. An area that the gravity studies has been performed, with a white rectangular on figure 8 has been determined. Figure 11 show the computed Bouguer gravity anomaly after making the necessary corrections. The Bouguer gravity anomaly map demonstrate a dominant regional gravity field which increase from south to north. After removing a trend (degree 2) from the Bouguer anomaly, the residual (local) gravity anomalies which
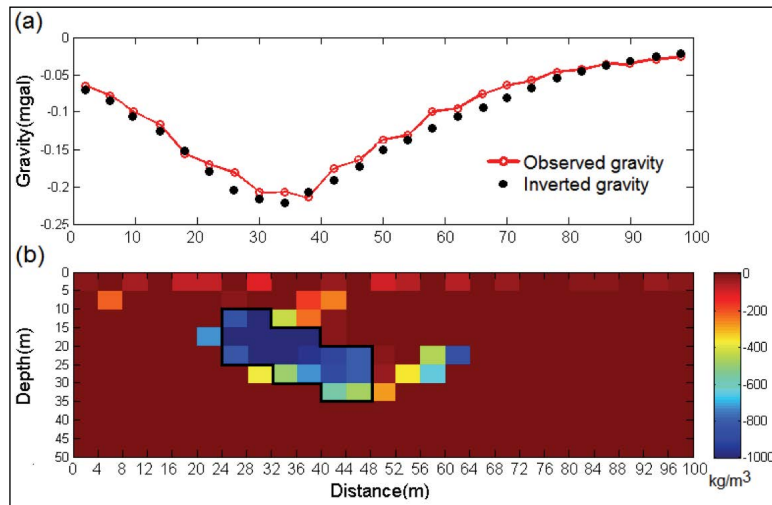
Figure 7- a) Observed gravity due to model in figure 3(b) as corrupted with 15% noise and inverted gravity due to b) inverted model. the initial assumed model outlined with black line.
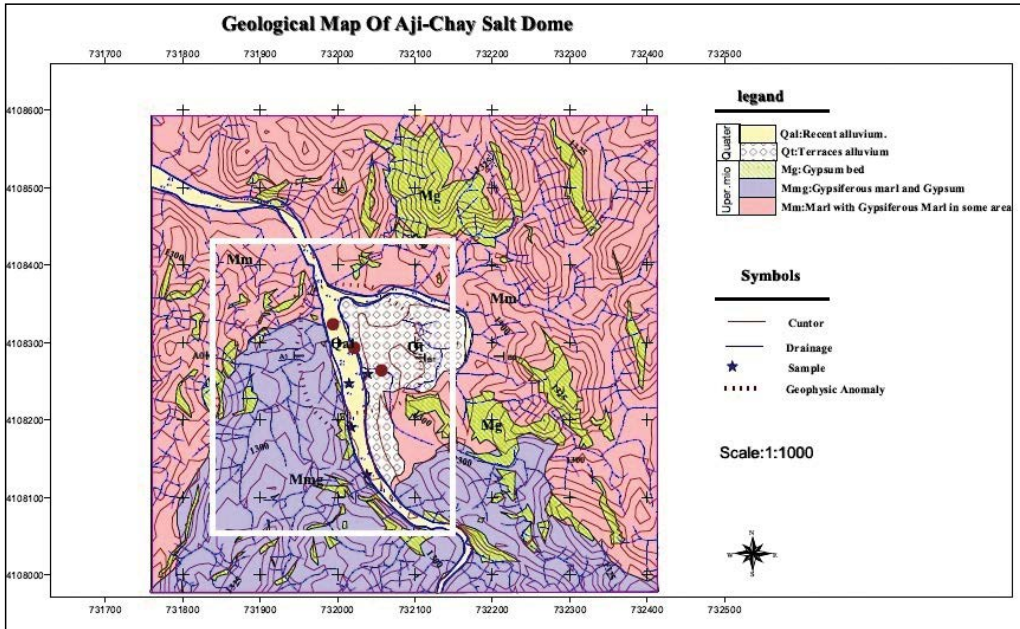
Figure 8- The geological map of area under investigation.

are our desire, are appeared (Figure 12). Because of the less density of the salt dome than around domain, it is recognizable on the residual gravity anomalies map with negative anomaly.

From negative anomaly due to the salt dome was sampled at 17 points with about 11.3 m interval along profile *AB*. Profile *AB* in anomaly is specified in E-W direction, which is shown in figure 12.

The variation of the gravity field along profile AB is shown in figure 13 (a). For inverting the observed gravity, we divided the inversion domain into 33×21 blocks of dimension 5.8 m in the x direction and 5 m in the y direction. Therefore, the whole domain is 192 m × 105 m, i.e. 20160 m². The ε and initial l_0 values were specified as 10^{-12} and near to zero respectively. We have also considered the average density of the salt dome about 2200 kg/m³. Considering the geological formation, sediments and layer material
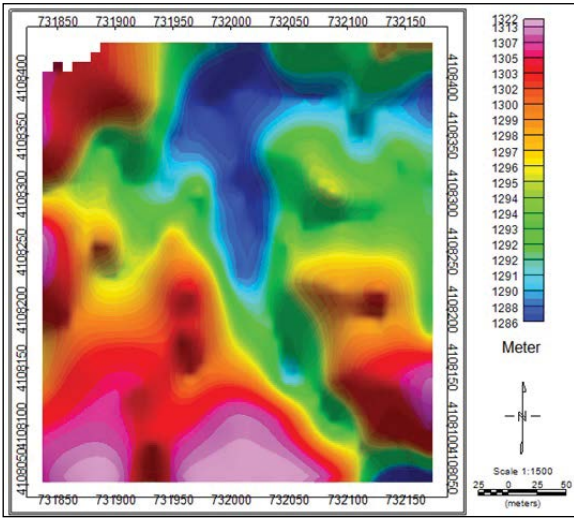
Figure 9- The topography map of the region under gravity survey.
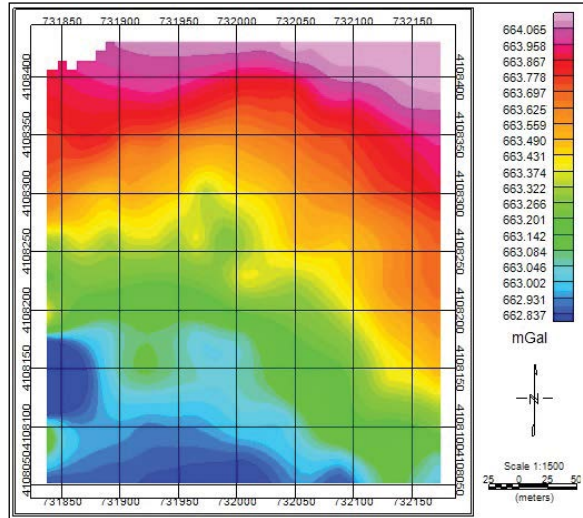
Figure 11- The Bouguer gravity anomaly map of the area under evaluation.
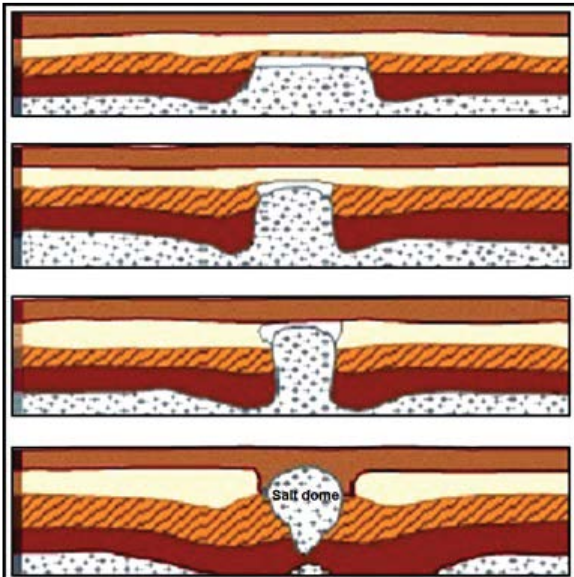
Figure 10- The process of salt dome formation in the region of the northwest of Iran.
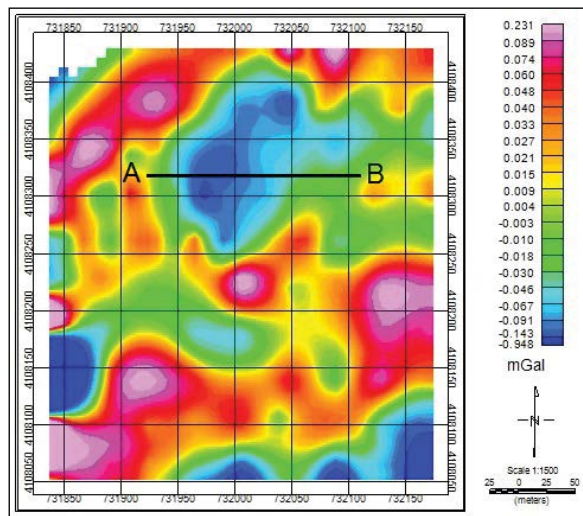
Figure 12- The residual gravity anomalies map of the area under evaluation. The position of the profile AB over the negative gravity anomaly due to the salt dome has been specified.

of the area under investigation, the average density of subsurface domain is given as 2500 kg/m³. Then, the density contrast was taken to be -300 kg/m³. Figure 13 (b) display the distribution of the inverted density after 18 iterations. The estimated L1 norm for each iteration is shown in figure 14. The L1 norm lessen from the its initial value of 1.576 mGal at the first iteration to 0.162 mGal at the 18th iteration

The inverted gravity produced by the determined densities for juxtaposed prisms is shown in figure 13 (a). The density distribution demonstrate the

geometry of the salt dome whose main concentration is at a depth of 42 m and a horizontal distance of 60 m from the profile AB origin, where the density contrast is about -300 kg/m³. By getting away from the center of salt dome in all directions, because of admixing the salt with sediment and alluvial material the density contrast amount diminish. The simulated salt dome show a elongation in the diffusion of the density towards east (right). If we consider the density contrast of -200 kg/m³ as the salt dome limited area, therefore it have a depth to top of about 27 m and a depth to bottom of about 65 m.

For comparison, we have used from ModelVision software in order to nonlinear inverse modeling of the measured gravity data due to the salt dome. The gravity sampling was accomplish at 33 points with 10 m interval along the profile A′B′ which depicted on the gravity anomaly of the salt dome, as is shown in figure 15(a). The variation of the gravity field along profile A′B′ is shown in the upper part of figure 15(b) (black line). We have considered a spherical initial model situated on the profile A′B′ whose the location of horizontal and vertical cross-section (violet circle) has been presented in figure 15(a) and the down part of the figure 15(b), respectively. The blue line in the upper part of figure 15(b) indicate the gravity anomaly caused by the assumed model.

The software tries to minimize the error between the observed gravity and inverted gravity (the upper part of figure 16 b) by changing the model parameters,

i.e. the depth to top and bottom and radiuses in three directions. The horizontal and vertical cross-section of the final model are displayed through figure 16(a) and the down part of the figure 16(b). The estimated upper and lower surfaces depth of inferred model are about 25 m and 73 m, respectively and the maximum horizontal extension is about 70 m.

6. Conclusions

In this paper, a compact inversion method based on introduced approach by Last and Kubik (1983) is employed. For increasing the depth resolution and eluding the tendency of placement the structure too close to the surface is used a depth weighting function in the inversion algorithm. The convergence and consistency of the proposed method was evaluated with two synthetic gravity data, with and without random noise, due to two theoretical models. The L1
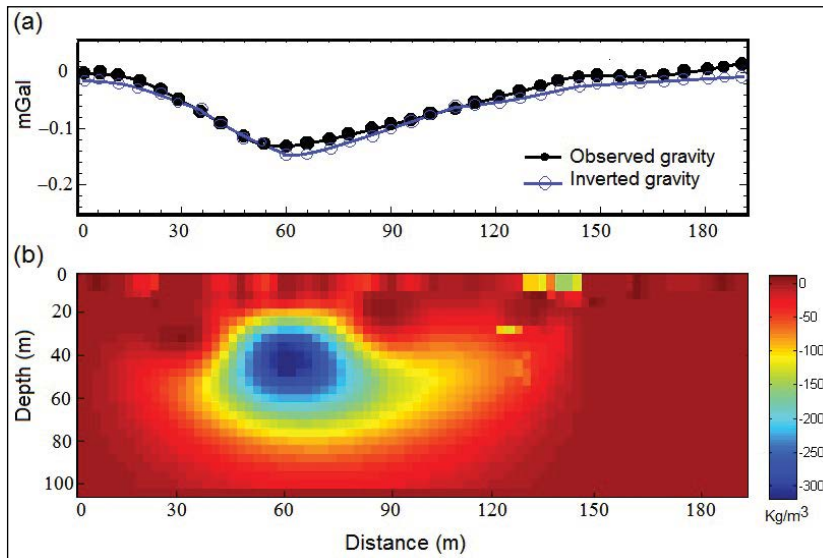
Figure 13- a) Observer gravity along profile AB and inverted gravity due to b) inverted structure.
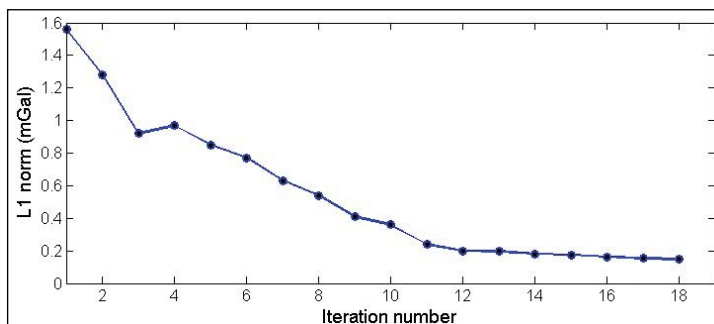
Figure 14- Variations L1 norm values versus iteration number during inversion of the real gravity data.

norm was considered as the stopping criterion of the iteration. The inverted density from interpretation the synthetic data are completely similar to the assumed models. We have inverted a real 2D gravity data set due to a salt dome using the linear inversion method. Usually for low N/S values a satisfying convergence of the solution is obtained. For real gravity data, we have considered a near to zero value for l_o until the noise was interpreted geologically, in other words, noise-weighting matrix be determined based on the estimated density in the each iteration.

The inverted density has been distributed smoothly overall the inversion domain where the centralization of the high density contrast (about -300 kg/m³)

indicate the core of salt dome. The modeled domain shows that with increasing distance from the core of salt dome, the density contrast dwindle, therefore the interface between salt deposit and surroundings is not a sharp and distinct border.

We also analyzed the real gravity data using the ModelVision software. The inferred structure from nonlinear inversion, i.e. ModelVision software, show good conformity with inverted structure from linear inversion, i.e. proposed method. With respect to the results can infer that the described inversion technique is a powerful and practicable instrument for interpreting the gravity field.
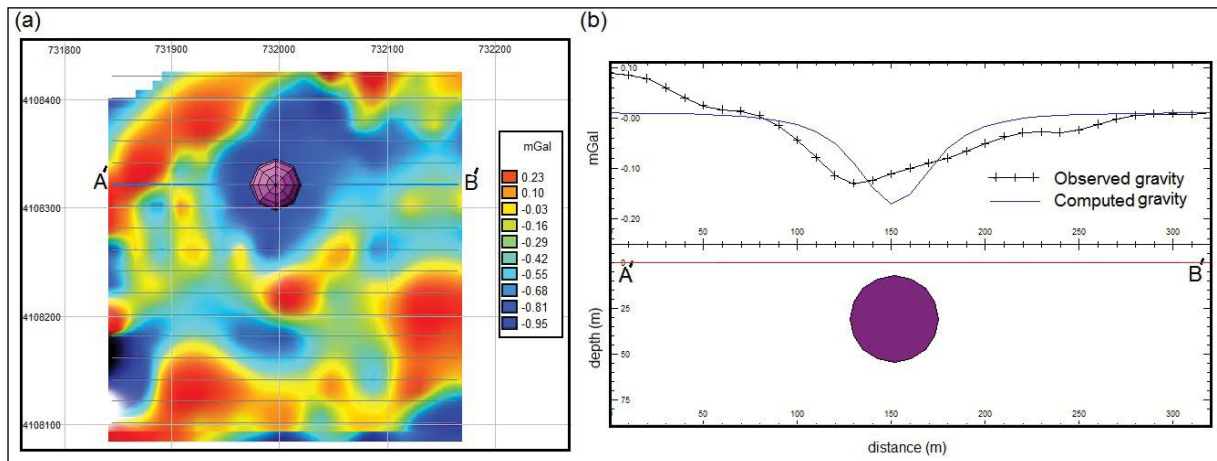
Figure 15- a) The horizontal cross-section of the initial model situated on the gravity anomaly of the salt dome where the profile A′B′ go across. b) gravity field changes through the profile A′B′ (black line) and calculated gravity (blue line) due to the initial model as the vertical cross-section of it has been displayed.
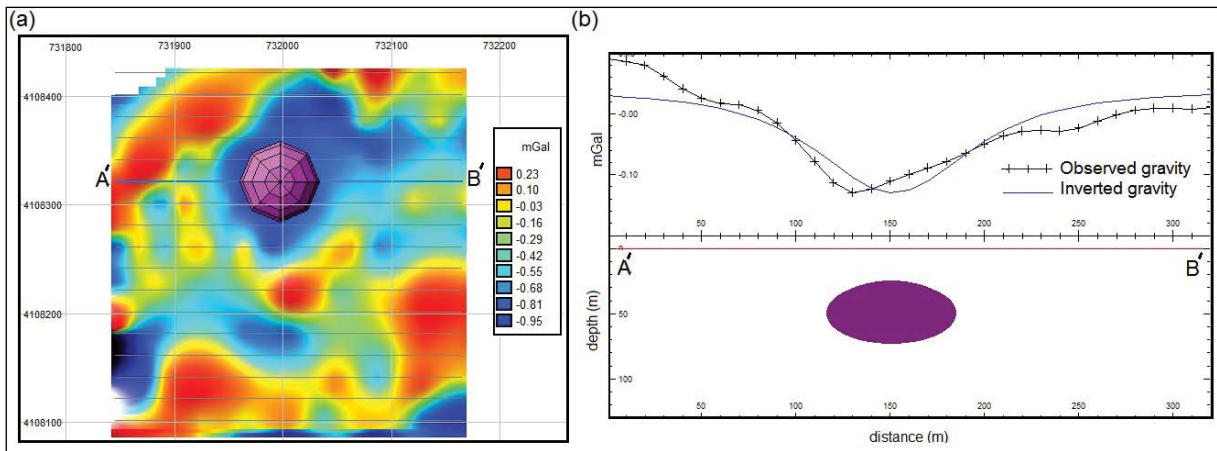
Figure 16- a) Horizontal cross- section of the final inferred model using the nonlinear inversion of gravity data of the profile A′B′. b) The inverted gravity produced by the resulted structure (blue line). The vertical cross-section of the final inversion model has been shown in the down part of the Figure 15(b).

References

Abdelrahman, E.M. 1990. Discussion on "A least-squares approach to depth determination from gravity data" by O. P. Gupta. Geophysics, 55, 376-378.

Abdelrahman, E.M., El-Araby, T.M. 1993. A least-squares minimization approach to depth determination from moving average residual gravity anomalies. Geophysics, 58,1779–1784.

Abdelrahman, E.M., El-Araby, H.M. 1993. Shape and depth solutions from gravity using correlation factors between successive least-squares residuals. Geophysics, 59, 1785–1791.

Abdelrahman, E.M., Bayoumi, A.I., Abdelhady, Y.E., Gobashy, M.M., El-Araby, H.M. 1989. Gravity interpretation using correlation factors between successive least-squares residual anomalies. Geophysics, 54, 1614-1621.

Abdelrahman, E.M., Bayoumi, A.I., El-Araby, H.M. 1991. A least-squares minimization approach to invert gravity data. Geophysics, 56, 115-l 18.

Al-Garni, M.A. 2013. Inversion of residual gravity anomalies using neural network. Arab J Geosci, 6,1509–1516.

Asfahani, J., Tlas, M. 2008. An automatic method of direct interpretation of residual gravity anomaly profiles due to spheres and cylinders. Pure and Applied Geophysics, 165/5, 981–994.

Biswas, A. 2015. Interpretation of residual gravity anomaly caused by a simple shaped body using very fast simulated annealing global optimization. Geoscience Frontiers, 6/6, 875–893.

Biswas, A. 2016. Interpretation of gravity and magnetic anomaly over thin sheet-type structure using very fast simulated annealing global optimization technique. Modeling Earth Systems and Environment, 2/1, 30.

Biswas, A. 2018. Inversion of source parameters from magnetic anomalies for mineral /ore deposits exploration using global optimization technique and analysis of uncertainty. Natural Resources Research, 27/1, 778–107.

Biswas, A., Sharma, S. P. 2016. Integrated geophysical studies to elicit the structure associated with Uranium mineralization around South Purulia Shear Zone, India: A Review. Ore Geology Reviews, 72, 1307–1326.

Biswas, A., Mandal, A., Sharma, S. P., Mohanty, W. K. 2014a. Delineation of subsurface structure using self-potential, gravity and resistivity surveys from South Purulia Shear Zone, India: Implication to uranium mineralization. Interpretation, 2/2, T103–T110.

Biswas, A., Mandal, A., Sharma, S. P., Mohanty, W. K. 2014b. Integrating apparent conductance in resistivity sounding to constrain 2D Gravity modeling for subsurface structure associated with uranium mineralization across South Purulia Shear Zone. International Journal of Geophysics, Article ID 691521, 1–8.

Biswas, A., Parija, M. P., Kumar, S. 2017. Global nonlinear optimization for the interpretation of source parameters from total gradient of gravity and magnetic anomalies caused by thin dyke. Annals of Geophysics, 60/2, G0218, 1–17.

Bosch, M., McGaughey, J. 2001. Joint inversion of gravity and magnetic data under lithological constraints. The Leading Edge, 20, 877–881.

Bosch, M., Meza, R., Jiménez, R., Hönig, A. 2006. Joint gravity and magnetic inversion in 3D using Monte Carlo methods: Geophysics, 71/4, G153–G156.

Bowin, C., Scheer, E., Smith, W. 1986. Depth estimates from ratios of gravity, geoid, and gravity gradient anomalies. Geophysics, 51, 123-136.

Chakravarthi, V., Sundararajan, N. 2004. Ridge regression algorithm for gravity inversion of fault structures with variable density. Geophysics, 69, 1394–1404.

Eshaghzadeh, A., Kalantary, R.A. 2015. Anticlinal Structure Modeling with Feed Forward Neural Networks for Residual Gravity Anomaly Profile, 8th congress of the Balkan Geophysical Society, DOI: 10.3997/2214-4609.201414210.

Eshaghzadeh, A., Hajian, A. 2018. 2-D inverse modeling of residual gravity anomalies from Simple geometric shapes using Modular Feed-forward Neural Network, Annals of Geophysics. 61,1, SE115.

Essa, K.S. 2007. A simple formula for shape and depth determination from residual gravity anomalies. Acta Geophysica, 55/2, 182–190.

Farquharson, C. G., Ash, M. R., Miller, H. G. 2008. Geologically constrained gravity inversion for the Voisey's Bay ovoid deposit. The Leading Edge, 27, 64–69.

Gallardo, L. A., Meju, M. 2003. Characterization of heterogeneous near-surface materials by joint 2D inversion of DC and seismic data: Geophysical Research Letters, 30, L1658.

Ganguli, S.S., Dimri, V. P. 2013. Interpretation of gravity data using eigen image with Indian case study: A SVD approach. Journal of Applied Geophysics, 95, 23-35.

Ganguli, S.S., Lashin, A.A., Al Arifi, N.S., Dimri, V. P. 2015. Design of Gravity energy filter to enhance signal-to-noise ratio of gravity measurements. Jour. of Ind. Geophy. Union, 19/3, 333-338.

Gupta, O.P. 1983. A least-squares approach to depth determination from gravity data. Geophysics, 48, 357-360.

Hammer, S. 1977. Graticule spacing versus depth discrimination in gravity interpretation. Geophysics, 42, 60-65.

Heincke, B., Jegen, M., Moorkamp, M., Chen, J., Hobbs, R.W. 2010. Adaptive coupling strategy for simultaneous joint inversions that use petrophysical information as constraints: 80th Annual International Meeting, SEG, Expanded Abstracts, 29, 2805–2809.

Ialongo, S., Fedi, M., Florio, G. 2014. Invariant models in the inversion of gravity and magnetic fields and their derivatives. Journal of Applied Geophysics, 110, 51-62.

Kamm, J., Lundin, I.A., Bastani, M., Sadeghi, M., Pedersen, L.B. 2015. Joint inversion of gravity, magnetic, and petrophysical data — A case study from a gabbro intrusion in Boden, Sweden. Geophysics, 80/5, B131–B152.

Last, B. J., Kubik, K. 1983. Compact gravity inversion, Geophysics,48, 713-721.

Lelièvre, P.G., Farquharson, C.G., Hurich, C.A. 2012. Joint inversion of seismic traveltimes and gravity data on unstructured grids with application to mineral exploration. Geophysics, 77, K1–K15.

Li, Y., Oldenburg, D. W. 1998. 3-D inversion of gravity data. Geophysics, 63, 109-119.

Lines, L.R., Treitel, S. 1984. A review of least-squares inversion and its application to geophysical problems. Geophys. Prosp, 32, 159-186.

Mandal, A., Biswas, A., Mittal, S., Mohanty, W. K., Sharma, S. P. Sengupta, D., Sen, J., Bhatt, A. K. 2013. Geophysical anomalies associated with uranium mineralization from Beldih mine, South Purulia Shear Zone, India. Journal Geological Society of India, 82/6, 601–606.

Mandal, A., Mohanty, W. K., Sharma, S. P., Biswas, A., Sen, J., Bhatt, A. K. 2015. Geophysical signatures of uranium mineralization and its subsurface validation at Beldih, Purulia District, West Bengal, India: A case study. Geophysical Prospecting, 63, 713–726.

Menke, W. 2012. Geophysical Data Analysis: Discrete inverse theory (MATLAB Edition), Elsevier Inc., New York, 293 s.

Mohan, N.L., Anandababu, L., Rao, S. 1986. Gravity interpretation using the Melin transform, Geophysics. 51, 114-122.

Odegard, M.E., Berg, J.W. 1965. Gravity interpretation using the Fourier integral. Geophysics, 30, 424-438.

Oldenburg, D. W. 1974. The inversion and interpretation of gravity anomalies. Geophysics, 39/4, 526-536.

Osman, O., Muhittin, A.A., Uçan, O.N. 2006. A new approach for residual gravity anomaly profile interpretations: Forced Neural Network (FNN). Ann. Geofis, 49, 6.

Osman, O., Muhittin, A.A., Uçan, O.N. 2007. Forward modeling with Forced Neural Networks for gravity anomaly profile. Math. Geol, 39, 593-605.

Parker, R. L. 1973. The Rapid Calculation of Potential Anomalies. Geophysical Journal of the Royal Astronomical Society, 31, 447-455.

Pilkington, M. 2006. Joint inversion of gravity and magnetic data for twolayer models. Geophysics, 71/3, L35–L42.

Salem, A., Ravat, D., Johnson, R., Ushijima, K. 2001. Detection of buried steel drums from magnetic anomaly data using a supervised neural network. J. Environ. Eng. Geophys, 6,115-122.

Saxov, S., Nygaard, K.1953. Residual anomalies and depth estimation. Geophysics, 18, 913-928.

Shamsipour, P., Marcotte, D., Chouteau, M., Keating, P. 2010. 3D stochastic inversion of gravity data using cokriging and cosimulation. Geophysics 75, I1–I10.

Shamsipour, P., Chouteau, M., Marcotte, D. 2011. 3D stochastic inversion of magnetic data. Journal of Applied Geophysics 73, 336–347.

Shamsipour, P., Marcotte, D., Chouteau, M. 2012. 3D stochastic joint inversion of gravity and magnetic data. Journal of Applied Geophysics 79, 27–37.

Sharma, B., Geldart, L.P. 1968. Analysis of gravity anomalies of two-dimensional faults using Fourier transforms. Geophys. Prosp, 77-93.

Shaw, R. K., Agarwal, N.P. 1990. The application of Walsh transforms to interpret gravity anomalies due to some simple geometrically shaped causative sources: A feasibility study. Geophysics, 55, 843-850.

Singh, A., Biswas, A. 2016. Application of global particle swarm optimization for inversion of residual gravity anomalies over geological bodies with idealized geometries. Natural Resources Research, 25/3, 297–314.

243

Skeels, D. C. 1947. Ambiguity in gravity interpretation, Geophysics, 12, 43-56.

Srivastava, R.P., Vedanti, N., Dimri, V.P. 2007. Optimal Design of a Gravity Survey Network and its Application to Delineate the Jabera-Damoh Structure in the Vindhyan Basin, Central India. Pure & App. Geophy, 164/10, 2009-2022.

Tschirhart, V., Morris, W. A., Jefferson, C.W., Keating, P., White, J. C., Calhoun, L. 2013. 3D geophysical inversions of the north-east Amer Belt and their relationship to the geologic structure. Geophysical Prospecting, 61, 547–560.

Tschirhart, V., Jefferson, C.W., Morris, W.A. 2017. Basement geology beneath the northeast Thelon Basin, Nunavut: insights from integrating new gravity, magnetic and geological data. Geophysical Prospecting, 65, 617-636.

Tsuboi, C. 1983. Gravity, 1st edn. George Allen ve Unwin Ltd, London, 254 pp.

Williams, N. C. 2008. Geologically-constrained UBC-GIF gravity and magnetic inversions with examples from the Agnew-Wiluna Greenstone Belt, Western Australia: Ph.D. thesis, University of British Colombia.

Zeyen, H., Pous, H. 1993. 3-D joint inversion of magnetic and gravimetric data with a priori information. Geophysical Journal International, 112, 244–256.

Bulletin of the Mineral Research and Exploration

Nummulites sireli Deveciler (junior homonym of *N. sireli* Alan) renamed as *Nummulites ercumenti* nom. nov.

Ali DEVECİLER[a*]

[a]Department of Geological Engineering, Ankara University, 06830, Ankara, Turkey.

Discussion

ABSTRACT

A new published species under the scope of this journal (*Nummulites sireli* Deveciler) was renamed as *Nummulites ercumenti* nom.nov for being a junior homonym of an another *Nummulites* species.

1. Introduction

A homonym is described as an identical taxon name which belongs to a different taxon. According to the ICZN (International Code of Zoological Nomenclature), the first published name is accepted as the senior homonym and is to be used as a valid name. The rest become junior homonyms that should be replaced with appropriate new names.

This discussion introduces the replacement of *Nummulites sireli* Deveciler with *Nummulites ercumenti* as nomen novum for being the junior homonym of *Nummulites sireli* Alan.

2. Systematic Paleontology

Nummulites ercumenti nom. nov.

2019 *Nummulites sireli,* Deveciler (junior homonym of *Nummulites sireli* Alan 2010; p. 99-102, pl. 9, figs. 1-9, unpublished), p. 124-125, pl. 1, figs. 1-12.

Derivation of name: After Dr. Ercüment Sirel, for his valuable contributions on the systematics of larger benthic foraminifera paleontology.

Remark: Deveciler (2019) described and figured *Nummulites sireli* as a new species in the Lutetian limestones of Çayraz section (Haymana-Ankara). However it was revealed that the same name has been previously given to a different Bartonian nummulitid in Akçadağ-Malatya region by Alan (2010) within the scope of her unpublished PhD Thesis. Therefore *Nummulites sireli* Deveciler, 2019 was accepted as the junior homonym of *Nummulties sireli* Alan, 2010 and the new species in Deveciler (2019) has been renamed as *Nummulites ercumenti* nom. nov.

3. Conclusions

Giving the same name to different taxons is a very common issue in various palaeontological studies,. In this study to avoid from the future taxonomic confusions, *Nummulites sireli* Deveciler, 2019 was renamed as *Nummulites ercumenti* nom. nov. because of being the junior homonym of *Nummulites sireli* Alan, 2010.

References

Alan, B. 2010. Malatya havzasındaki sığ denizel sedimanların Eosen (Orta-Geç Eosen) bentik foraminifer tanımlaması ve biyostratigrafisi. PhD thesis, Ankara Üniversitesi Fenbilimleri Enstitüsü, 249 p. Ankara (unpublished).

Deveciler, A. 2019. A new species of *Nummulites* Lamarck (Nummulitidae, Foraminiferida) from central Turkey. Bulletin of the Mineral Research and Exploration 158, 121-139.

ACKNOWLEDGEMENT

Bulletin of the Mineral Research and Exploration Notes to the Authors

1. Aims of Publication

- To announce and share researches in all fields of geoscientific studies in Turkey with geoscientists worldwide.

- To announce scientific researches and practices on geoscientific surveys carried out by the General Directorate of Mineral Research and Exploration (MTA) to the public.

- To use the journal as an effective media for international publication exchange by keeping the journal in high quality, scope and format.

- To contribute to the development of Turkish language as a scientific language.

2. Scope

At least one of the following qualifications is required for publishing the papers in the Bulletin of Mineral Research and Exploration.

2.1. Research Articles

2.1.1. Original Scientific Researches

- These articles cover and contribute to the main subjects of the earth sciences, the original scientific researches and its results related to all aspects of disciplines in geoscience like exploration and evaluation of the underground sources and environmental problems, and

- The studies, which apply new aspects and methods for the solution of problems about the earth sciences and researches, which apply new aspects and methods for the solution of the problems, in the engineering sciences carried out in MTA.

2.1.2. Review Articles

These papers include comphrehensive scholarly review articles that summarize and critically assess previous geoscientific researches with a new perspective and reveal a new approach.

2.2. Discussion/Reply

- This type of article is intended for the discussion of papers that have already been published in the latest issue of the Bulletin. The discussion/reply type articles, which criticize all or a part of a recently published article, are published in the following

first issue if it is submitted within six months after the publication of the Bulletin.

- The discussions are sent to the corresponding author of the original paper to get their reply before publication. The discussions abut the paper with two or more authors are sent only to the corresponding author.

- If the review article is not published within the prescribed preiod then it is published alone. Later sent replies are not published. Re-criticising of the replies is not allowed.

- The authors should obey the rules of scientific ethics and discussions in their discussion/reply papers. The papers in this category should not exceed four printed pages of the journal including figures and tables etc. The format of the papers should be compatible with the "Spelling Rules" of the Bulletin.

2.3. Short Notes

- The short notes part of the Bulletin covers short, brief and concisely written research reports for papers including the data obtained from ongoing and/or completed scientific researches and practices related to geoscience and new and/or preliminary factual findings from Turkey and worldwide.

- The short notes will follow a streamlined schedule and will normally be published in the following first or second issue shortly after submission of the paper to the Bulletin.

- This type of articles should not exceed four printed pages of the journal including figures, tables and an abstract.

3. Submission and Reviewing of Manuscripts

- Manuscript to be submitted for publishing in the Journal must be written clearly and concisely in Turkish and/or English and prepared in the Bulletin of Mineral Research and Exploration style guidelines. All submissions should be made online at the http://.dergi.mta.gov.tr website.

- The manuscript submitted for reviews must not have been published partially or completely previously in another journal.

- The rejected manuscripts are not returned back to

author(s) whereas a letter of statement indicating the reason of rejection is sent to the corresponding author.

- Submitted manuscripts must follow the Bulletin style and format guidelines. Otherwise, the manuscript which does not follow the journals' style and format guidelines, is given back to corresponding author without any reviewing.

- Every manuscript which passes initial Editorial treatise is reviewed by at least two independent reviewers selected by the Editors. Reviewers' reports are carefully considered by the Editors and associated editors.

- The manuscript that need to be corrected with the advices of reviewer(s) is sent back to corresponding author(s) to assess and make the required corrections suggested by reviewer(s) and editors. The authors should prepare a letter of well-reasoned statement explaining which corrections are considered or not.

- If there are any suggestions given by editors and referees that are not accepted and corrected by the author, then it should be sent to the Editor's Office with corrected copies of the report explaining the reason for not accepting these suggestions and corrections.

- Figures and tabless should be 1/3 of the main text.

- To be published in the Bulletin of Mineral Research and Exploration, the printed lenght of the manuscript should not exceed 30 printed pages of the journal including an abstract, figures and tables. The publication of longer manuscripts will be evaluated by Editorial Board if it can be published or not.

- The authors must do the reviewer's corrections and proposals in 60 days and must upload to the system.

- At the printing stage after the last control, the first print of the manuscript are sent to the author/authors in pdf version and asked from the author/authors to make the press control.

4. Publication Language and Periods

- The Bulletin of Mineral Research and Exploration is published at least twice a year and each issue is published both in Turkish and English. Thus, the manuscripts are accepted in Turkish or English. The spelling and punctuation guidelines of Turkish Language Institution are preferred for the Turkish issue. However, the technical terms related to geology are used in accordance with the decision of the Editorial Board.

5. Spelling Draft

Manuscripts should be written in word format in A4 (29.7 x 21 cm) size and double-spaced with font size Times New Roman 10-point, margins of 25 mm at the sides, top and bottom of each page.

The formulas requiring the use of special characters and symbols must be submitted by the symbols part of the Microsoft Office Word Program on computer.

Initial letters of the words in sub-titles must be capital. The first degree titles in the manuscript must be numbered and left-aligned, 10 point bold Times New Roman must be used. The second degree titles must be numbered and left-aligned, they must be written with 10 point normal Times New Roman. The third degree titles must be numbered and left-aligned, they must be written with 10 point italic Times New Roman. The fourth degree titles must be left-aligned without having any number; 10 point italic Times New Roman must be used. The text must continue placing a colon after the title without paragraph returns (See: Sample article: http://bulletin.mta.gov.tr).

One line spacing must be left after paragraphs within text.

Paragraphs must begin with 0.5 mm indent.

The manuscript must include the below sections respectively;

o Title Page

o The Name and Surname of the author and * sign (Adress, e-mail adres must be given at the bottom of the page)

o Abstract

o Key Words

o Introduction

o Body

o Discussion

o Conclusion

o Acknowledgements

o References

5.1. Title Page

The title must be short, specific and informative and written with small letters font size Times New Roman 10-point bold. The title mustn't contain the subjects insufficiently processed in the article.

5.2. Author(S)'S Name, Addresses and Email Address

- The name and surname of the author/authors must be written without affiliations. Name must be written in small letters, the surname must be written in capital letters.

- At the affiliation (work adres) written after the name and the surname of the author/authors only the name of the company must be written, the author's job mustn't be written.

- Information about the adresses must be given at the next line as 10-point and italic.

- ORCID number should be taken from www.orcid. org and placed below the address.

- At the articles with two or more than two authors, the numbers must be written above the surnames of the authors, the informations about their adresses must be given at the next line by leaving one space line. Also, at this part the corresponding author must be indicated by the (*) symbol and the telephone, FAX and e-mail address of the corresponding author must be given.

- Abbreviations must not be made while writing the name of the uthor and the affiliation adres. Adresses must be given in Turkish in the Turkish version, in English in the English version.

- At the end of the article the name of the corresponding author and contact informations must be added.

5.3. Abstract

- The abstract must be understandable before having a look at the text.

- The abstract should state briefly the overall purpose of the research, the aim of the article, its contributions to the known theories, new data, principle results and major conclusions.

- Tha abstract must contain short and brief sentences.

- Addressing other sections and illustrations of the text or other writings must be avoided.

- The information, which have not been mentioned in the text, must not be in the abstract.

- The article must be written as one paragraph, preferably. Please provide an abstract which doesn't exceed 200 words.

- The abstract must be written with 10-point, normal Times New Roman in single-spaced lines.

- "Abstract" must not be given for the writings that will be located in "Short Notes" section.

- The English abstract must be under the title of "Abstract".

5.4. Key Words

Immediately after the abstract, please provide up to 5 key words and with each words seperated by comma. These key words will be used for indexing purposes.

5.5. Introduction

- The introduction section should state the objectives of the work, research methods, location of the study area and provide an adequate and brief background by avoiding a detailed literature survey.

- Non-standard or uncommon classifications or abbreviations should be avoided. But if essential, then they must be defined at their first mention and used consistently thereafter. Seperate paragraphs could be organized for each of the subjects at the introduction part. If it is necessary, the subtitle can be given for each of them (for example method, material, terminology etc.).

- When pre-information is needed for facilitating the understanding of the text, this section can also be used (for example, statistical data, bringing out the formulas, experiment or application methods, and others).

5.6. Body

- In this chapter, there must be data, findings and opinions that are intended to convey to the reader about the subject. The body section forms the main part of the article.

- The data used in other sections such as "Abstract", "Discussions", and "Results" are caused by this section.

- While processing the subject, the care must be taken not to go beyond the objective highlighted in the "Introduction" section. The knowledge, which

do not contribute to the realization of the purpose of the article or are useless for conclusion, must not be included.

- All data used and the opinions put forward in this section must prove the findings obtained from the studies or they must be based on a reference by citation.

- The guidance and methods to be followed in processing subjects vary according to the characteristics of the subjects mentioned. Various topic titles can be used in this section as many as necessary.

5.7. Discussions

- Discussion of the data and findings that are objectively transferred in the Main Text section of the article should be done in this section. This must be written as a seperate section from the results section.

5.8. Conclusions

- The main conclusion of the study provided by data and findings of the research should be stated concisely and concretely in this section.

- The subjects that are not mentioned sufficiently and/or unprocessed in the body section must not be included in this section.

- The conclusions can be given in the form of substances in order to emphasize the results of the research and to make the expression understandable.

5.9. Acknowledgements

- In this section, the significant contributions made in the realization of investigation that form the topic of the paper is specified. While specifying contributions, the attitude diverted the original purpose of this section away is not recommended. Acknowledgements must be made according to the following examples.

- This study was carried out within scope of ....project.

- I/we would like to thank to ……… for contributing to the development of this article with his/her critiques.

- Academic and/or authoritorial affiliations are written for the contributions made because of requirement of ordinary task.

- For example:

- "Prof. Dr. İ. Enver Altınlı has led the studies".

- "The opinions and warnings of Dr. Tandoğan Engin are considered in determining the chemistry of chrome minerals."

- The contributions made out of the requirement of ordinary task:

- For example:

- "I would like to thank to Professor Dr. Melih Tokay who gives the opportunity to benefit from unpublished field notes"; "I would like to thank to the preliminary-Plan Chief Engineer Ethem Göğer, State Hydraulic Work, 5th Zone". Academic and / or task-occupational titles are indicated for such contributions.

- The contributions, which are made because of requirement of ordinary task but do not necessitate responsibility of the contributor mustn't be specified.

- For example:

- Sentences such as "I would like to thank to our General Manager, Head of Department or Mr. / Mrs. President ……………who has provided me the opportunity to research" must not be used.

5.10. References

- All references cited in the text are to be present in the reference list.

- The authors must be sure about the accuracy of the references. Publication names must be written in full.

- Reference list must be written in Times New Roman, 9-point type face.

- The reference list must be alphabetized by the last names of the first author of each work.

- If an author's more than one work is mentioned, ranking must be made with respect to publication year from old to new.

- In the case that an author's more than one work in the same year is cited, lower-case alphabet letters must be used right after publication year (for example; Saklar, 2011*a, b*).

- If the same author has a publication with more than one co-author, firstly the ones having single author

are ranked in chronological order, then the ones having multiple authors are ranked in chronological order.

- In the following examples, the information related to works cited is regulated in accordance with different document/work types, considering punctuation marks as well.

- If the document (periodic) is located in a periodical publication (if an article), the information about the document must be given in the following order: surnames of the author/authors, initial letters of author's/ authors' first names. Year of publication. Name of the document. Name of the publication where the document is published, volume and/ or the issue number, numbers of the first and last pages of the document.

For example:

Pamir, H.N. 1953. Türkiye'de kurulacak bir hidrojeoloji enstitüsü hakkında rapor. Türkiye Jeoloji Bülteni 4, 1, 63-68.

Barnes, F., Kaya, O. 1963. İstanbul bölgesinde bulunan Karbonifer'in genel stratigrafisi. Maden Tetkik ve Arama Dergisi 61,1-9.

Robertson, A.H.F. 2002. Overview of the genesis and emplacement of Mesozoic ophiolites in the Eastern Mediterranean Tethyan region. Lithos 65, 1-67.

- If more than one document by the same authors is cited, firstly the ones having single name must be placed in chronological order, then the ones having two names must be listed in accordance with chronological order and second author's surname, finally the ones having multiple names must be listed in accordance with chronological order and third author's surname.

- If the document is a book, these are specified respectively: surnames of the author/authors, initial letters of author's/authors' first names. Year of publication. Name of the book (initial letters are capital). Name of the organization which has published the book, name of the publication wherethe document is published, volume and/ or the issue number, total pages of the book.

For example

Meriç, E. 1983. Foraminiferler. Maden Tetkik ve Arama Genel Müdürlüğü Eğitim Serisi 23, 280p.

Einsele, G. 1992. Sedimentary Basins. Springer-Verlag, p 628.

- If the document is published in a book containing the writings of various authors, the usual sequence is followed for the documents in a periodic publication. Then the editor's surname andinitial letters of their name /names are written. "Ed." which is an abbreviation of the editor word is written in parentheses. Name of the book containing the document (initial letters are capital). Name of the organization which has published the book. Place of publication, volume number (issue number, if any) of the publication where the document is published, numbers of the first and last page of the document.

For example:

Göncüoğlu, M.C., Turhan, N., Şentürk, K., Özcan, A., Uysal, Ş., Yalınız, K. 2000. A geotraverse across northwestern Turkey. Bozkurt, E., Winchester, J.A., Piper, J.D.A. (Ed.). Tectonics and Magmatism in Turkey and the Surrounding Area. Geological Society of London Special Publication 173, 139-162.

Anderson, L. 1967. Latest information from seismic observations. Gaskell, T.F. (Ed.). The Earth's Mantle. Academic Press. London, 335-420.

- If name of a book where various authors' writings have been collected is specified, those must be indicated respectively: book'seditor/editors' surname/surnames, and initial letters of their name/names. "Ed." which is an abbreviation of the editor word must be written in parentheses. Year of Publication. Name of the book (initial letters are capital). Name of the organization which has published the book, total pages of the book.

For example:

Gaskel, T.F.(Ed.)1967. The Earth's Mantle. Academic Press, 520p.

- If the document is an abstract published in a Proceedings Book of a scientific activity such as conference/symposium/workshop …etc. , information about the document must be given in the following order: surnames of the author/authors, initial letters of author's/authors' first names. Year of publication. Title of the abstract. Name, date and place of the meeting where the Proceedings Book is published, numbers of the first and last pages of the abstract in the Proceedings Book.

For example:

Yılmaz, Y. 2001. Some striking features of the Anatolian geology. 4. International Turkish Geology Symposiums 24-28 September 2001, London, 13-14.

Öztunalı, Ö., Yeniyol, M. 1980. Yunak (Konya) yöresi kayaçlarının petrojenezi. Türkiye Jeoloji Kurumu 34. Bilim Teknik Kurultayı, 1980, Ankara, 36

- If the document is one of the unpublished documents as report, lecture notes, and so on., information about the document must be given by writing the word "unpublished" in parentheses to the end of information about the document after it is specifiedin accordance with usual order which is implemented for a document included in a periodic publication.

For example:

Özdemir, C. Biçen, C. 1971. Erzincan ili, İliç ilçesi ve civarı demir etütleri raporu. General Directorate of Mineral Research and Exploration Report No: *4461*, 21 p. Ankara (unpublished).

Akyol, E. 1978. Palinoloji ders notları. EÜ Fen Fakültesi Yerbilimleri Bölümü, 45 p., İzmir (unpublished).

- The followings must be specified for the notes of unpublished courses, seminars, and so on: name of the document and course organizer. Place of the meeting. Name of the book, corresponding page numbers.

For example:

Walker, G. R. Mutti, E. 1973.Turbidite facies and facies associations. Pacific Section Society for Sedimentary Geology Short Course. Annaheim. Turbitides and Deep Water Sedimantation, 119-157.

- If the document is a thesis, the following are written: surname of the author, initial letter of the author's first name. Year of Publication. Name of the thesis. Thesis type, the university where it is given, the total number of pages, the city and "unpublished" word in parentheses.

For example:

Seymen, İ. 1982. Kaman dolayında Kırşehir Masifi'nin jeolojisi. Doçentlik Tezi, İTÜ Maden Fakültesi, 145 s.İstanbul (unpublished).

- Anonymous works must be regulated according to publishing organization.

For example:

MTA. 1964. 1/500.000 ölçekli Türkiye Jeoloji Haritası, İstanbul Paftası. Maden Tetkik ve Arama Genel Müdürlüğü, Ankara.

- The date, after the name of the author, is not given for on-printing documents; "in press" and / or "on review" words in parenthesis must be written. The name of the article and the source of publication must be specified, volume and page number must not be given.

For example:

o Ishihara, S. The granitoid and mineralization. Economic Geology 75th Anniversary (in press).

- Organization name, web address, date of access on web address must be indicated for the information downloaded from the Internet. Turkish sources must be given directly in Turkish and they must be written with Turkish characters.

For example:

o ERD (Earthquake Research Department of Turkey). **http://www.afad.gov.tr**. March 3, 2013.

- While specifying work cited, the original language must be used; translation of the title of the article must not be done.

6. Illustrations

- All drawings, photographs, plates and tables of the article are called "illustration".

- Illustrations must be used when using of them is inevitable or they facilitate the understanding of the subject.

- While selecting and arranging the illustrations' form and dimensions, page size and layout of the *Bulletin* must be considered, unnecessary loss of space must be prevented as much as possible.

- The pictures must have high quality, high resolution suitable for printing.

- The number of illustrations must be proportional to the size of the text.

- All illustrations must be sent as separate files independent from the text.

- While describing illustrations in the text, abbreviations must be avoided and descriptions must be numbered in the order they are mentioned in the text.

- Photographs and plates must be given as computer files containing EPS, TIFF, or JPEG files in 600 dpi and higher resolutions (1200 dpi is preferred) so that all details can be seen in the stage of examination of writing.

6.1. Figures

- Drawings and photos (except for the plates in the text) will be evaluated together as "Figure" and they must be numbered in the order they are mentioned in the text.

- The figures published in the Bulletin of Mineral Research and Exploration must be prepared in computer considering the dimensions of single-column width 7.4 m or double-column width 15.8 cm. Figure area together with the writing at the bottom should not exceed 15.8x21in maximum.

- Unnecessasry details must not be given in figures or care must be taken not to use much space for information transfer.

- Figures must be arranged in such a way to be printed in black/white or colored.

- The figure explanations being justified in two margins must be as follows:

Figure 1- Sandıklı İlçesinin (Afyon); a) güneybatısının jeolojik haritası, b) İnceleme alanının genel dikme kesiti (Seymen 1981), c) Türkiye'nin önemli neotektonik yapıları (Koçyiğit 1994'den değiştirilerek).

Figure 1- a) Sandıklı ilçesinin güneybatısının jeolojik haritası, b) İnceleme alanının genel dikme kesiti (Seymen, 1981), c) Türkiye'nin önemli neotektonik yapıları (Koçyiğit 1994'den değiştirilerek).

- Drawings must be made by well-known computer programs painstakingly, neatly and cleanly.

- Using fine lines, which can disappear when figures shrinks, must be avoided. Symbols or letters used in all drawings must be in Times New Roman and not less than 2 mm in size when shrink.

- All standardized icons used in the drawings must be explained preferably in the drawing or with figure caption if they are too long.

- Linear scale must be used for all drawings. Author's name, figure description, figure number must not be included into the drawing.

- Photos must be in quality and quantity that will reflect the objectives of the subject.

6.2. Plates

- Plates must be used when needed a combination of more than one photo and the publication on a special quality paper.

- Plate sizes must be equal to the size of available magazine pagespace.

- Figure numbers and linear scale must be written under each of the shapes located on the Plate.

- The original plates must be added to the final copy which will be submitted if the article is accepted.

- Figures and plates must be independently numbered. Figures must be numbered with Latin numerals and plates with Roman numerals (e.g., Figure1, Plate I).

- There must be no description text on Figures.

6.3. Tables

- All tables must be prepared preferably in word format in Times New Roman fonts.

- Tables together with table top writing must not exceed 15x8 cm in size.

- The table explanations being justified in two margins must be as follows:

Table 1- Hydrogeochemical analysis results of geothermal waters in the study area.

7. Nomenclature and Abbreviations

- Non-standard and uncommon nomenclature abbreviations should be avoided in the text. But if essential, they must be described as below: In cases where unusual nomenclatures and unstandardized abbreviations are considered to be compulsory, the followed way and method must be described.

- Full stop must not be placed between the initials of words for standardized abbreviations (MER, SHW, etc.).

- Geographical directions must be abbreviated in English language as follows: N, S, E, W, NE …etc.

- The first time used abbreviations in the text are presented in parenthesis, the parenthesis is not used for subsequent uses.

- The metric system must be used as units of measurement.
- Figure, plate, and table names in the article must not be abbreviated. For example, "as shown in generalized stratigraphic cross-section of the region (Figure 1…………..."

7.1. Stratigraphic Terminology

Stratigraphic classifications and nomenclatures must be appropriate with the rules of International Commision on Stratigraphy and/or Turkey Stratigraphy Committee. The formation names which have been accepted by International Commision on Stratigraphy and/or Turkey Stratigraphy Committee should be used in the manuscript.

7.2. Paleontologic Terminology

Fossil names in phrases must be stated according to the following examples:

o For the use of authentic fossil names;

e.g. Limestone with *Nummulites*

o When the authentic fossil name is not used;

o e.g. nummulitic Limestone

o Other examples of use;

e.g. The type and species of *Alveolina / Alveolina* type and species

- Taxonomic ranks must be made according to the following examples:
- The names of the fossils should be stated according to the rules given below:

o For the first use of the fossil names, the type, spieces and the author names must be fully indicated;

Alveolina aragonensis Hottinger, 1960, not reference

Alveolina cf. *aragonensis* Hottinger, 1960, not reference

Alveolina aff. *aragonensis* Hottinger, 1960, not reference

o When a species is mentioned for the second time in the text;

A.aragonensis

*A.*cf.*aragonensis*

*A.*aff. *aragonensis*

It is accepted as citation if stated as *Alveolina aragonensis* Hottinger (1960). Cited Hottinger (1960), stated in the Reference section.

- The statement of plates and figures (especially for the articles of paleontology):

a for the statement of species mentioned in the body text; **Borelis vonderschmitti** (Schweighauser, 1951)

(Plate, Figure, Figure in the body text).

b. When cited for other articles;

1951 *Neoalveolina vonderschmitti* Schweighauser, page 468, figure 1-4, figure in body text.

1974 *Borelis vonderschmitti* (Schweighauser), Hottinger, page 67, plate 98, figure 1-7.

c. For the citation in the text

(Schweighauser, 1951, page, plate, figure, figure in the body text)

(Hottinger, 1974, page, plate 97, figure 67, plate 98, figure 1-7, figure in the body text).

Ordo: Foraminiferida Eichwald, 1830 Super family: Alveolinacea Ehrenberg, 1939 Family: Borelidae Schmarda, 1871 Type genus: *Borelis* de Montfort, 1808 Type species: *Borelis melenoides* de Montfort, 1808; *Nautilus melo* Fitchel and Moll, 1789	Not reference, Not stated in the Reference section
Borelis vonderschmitti (Schweighauser, 1951) (Plate, Figure, Figure in Body Text)	Schweighauser, 1951 not reference
1951 *Neoalveolina vonderschmitti* Schweighauser, page 468, figure 1-4	Cited Scweighauser (1951), stated in the Reference section.
1974 *Borelis vonderschmitti* (Schweighauser), Hottinger, page, 67, plate 98, figure 1.7	Cited Hottinger (1974), stated in the Reference section.

8. Citations

All the citiations in the body text must be indicated by the last name of the author(s) and the year of publication, respectively. The citations in the text must be given in following formats.

- For publications written by single author:

- It is known that fold axial plain of Devonian and Carboniferious aged units around Istanbul is NS oriented (Ketin, 1953, 1956; Altınlı, 1999).

- Altınlı (1972, 1976) defined the general characteristics of Bilecik sandstone

- For publications written by two authors:

- The upper parts of the unit contain Ilerdian fossils (Sirel and Gündüz, 1976; Keskin and Turhan, 1987, 1989).

- For publications written by three or more authors:

According to Caner et al. (1975) Alıcı formation reflects the fluvial conditions.

The unit disappears wedging out in the East direction (Tokay et al., 1984).

- If reference is not directly obtained but can be found in another reference, cross-reference should be given as follows:

- It is known that Lebling has mentioned the existence of Lias around Çakraz (Lebling, 1932: from Charles, 1933).

9. Reprints

The author(s) will receive 2 two hard copies of the related issues.

10. Copyright and Conditions of Publication

- It is a condition of publication that work submitted for publication must be original, previously unpublished in whole or in part.

- It is a condition of publication that the authors who send their publications to the Bulletin of Mineral Research and Exploration hereby accept the conditions of publication of the Bulletin in advance.

- All copyright of the accepted manuscripts belong to MTA. The author or corresponding author on behalf of all authors (for papers with multiple authors) must sign and give the agreement under the terms indicated by the Regulations of Executive Publication Committee. Upon acceptance of an article, MTA can pay royalty to the authors upon their request according to the terms under the "Regulations of Executive Publication Committe" and the "Regulations of Royalty Payment of Public Office and Institutions"

All the information and forms about the Bulletin of Mineral Research and Explorations can be obtained from http://bulletin.mta.gov.tr